

# Measurement and Modeling of Detonation-Driven Shock Tube Flows

Thesis by  
Donner Thomas Schoeffler

In Partial Fulfillment of the Requirements for the  
Degree of  
Doctor of Philosophy



CALIFORNIA INSTITUTE OF TECHNOLOGY  
Pasadena, California

2025  
Defended March 31, 2025

© 2025

Donner Thomas Schoeffler  
ORCID: 0000-0002-1932-5986

All rights reserved except where otherwise noted



## ACKNOWLEDGMENTS

I have had the privilege to be Professor Joe Shepherd's student for five years, in which time I have grown enormously from his mentorship and teaching in the laboratory, at the blackboard, and in our many weekly meetings. I am deeply grateful for his unfaltering patience, support, and friendship, which have made this a singular experience in my life.

I have been fortunate to share my time in the Explosion Dynamics Lab with Branson Davis, Conor Martin, Charline Fouchier, Ken Matsuoka, and Yunliang Qi. I have greatly enjoyed working with everyone and learning from their many interesting projects. I would also like to acknowledge all of the former EDL members, from whose past work and retired experiments I learned a great deal, especially during my early years in the lab. I am very grateful for our closeness and camaraderie with the Caltech Hypersonics Group, and I would especially like to thank Professors Hans Hornung and Joanna Austin, both of whom also supported and encouraged this work. My thanks goes to Liza Bradulina for her essential assistance over the years and to Noel Esparza-Duran for his engineering support and friendship. This work was possible because of the sponsorship by the Office of Naval Research, under grant number N00014-22-1-2141 with Dr. Eric Marineau.

More than anyone, my wife, Sara, has supported me through this work, and I will always be most dearly grateful.

## ABSTRACT

The detonation driver is a device for generating the strong shock waves used in high-enthalpy hypersonic flow research facilities. The dynamic production of high-pressure and high-temperature driver gas has several advantages for shock-tube performance, however the unsteady gas dynamics of detonation waves also introduces several challenges. These are investigated here analytically and experimentally.

For forward-mode operation, where the detonation propagates into the shock-tube diaphragm, the detonation Taylor wave attenuates the driven shock, and a model is needed to predict the resulting shock dynamics. This is accomplished by first analyzing the problem of plane shock decay generally. A new approximate solution is formulated for the classic piston start-stop problem and shown to be a significant advancement over predecessors. This result is applied to the shock decay from a detonation driver, and a two-parameter model is fit to simulation data, yielding a method for predicting shock trajectories from shock-tube initial conditions.

A small-scale shock tube is designed and constructed using a detonation driver that is operable in both the forward and reverse mode. A transparent driven section is used with large field-of-view shadowgraphy to perform novel time-resolved shock speed measurements. These are used to calibrate the decay model for a forward-mode driver and enable unique observations of shock-speed oscillations, resulting from diaphragm rupture and detonation initiation processes. Results are also obtained for shock tube operation with a conventional high-pressure helium driver.

The gradients and fluctuations in post-shock flows are characterized using a heterodyne focused laser interferometer, a new instrument with advanced capabilities for measuring large phase changes with high resolution. As a development upon the FLDI, spatial filtering characteristics are preserved, and both differential and absolute phase data are acquired simultaneously, enabling a new technique for measurement of gas densities. The instrument is developed, experimentally validated, and then used to probe detonation-driven shock tube flows, achieving phase measurements of over 100 radians with milliradian resolution in a 10 MHz bandwidth. Results from forward-mode operation find that a hydrogen-oxygen driver produces remarkably disturbance-free flows. For reverse-mode operation, the amplitude of flow oscillations is found to be positively correlated with the contact-surface sound-speed ratio, and frequencies are consistent with first-order lateral acoustic waves.

## PUBLISHED CONTENT AND CONTRIBUTIONS

Schoeffler, D. T. and Shepherd, J. E. (2023). Decay of shock waves in detonation-driven shock tubes. In *34th International Symposium on Shock Waves, Volume 2: Applications 1*. Springer Singapore.

Schoeffler, D. T. and Shepherd, J. E. (2024). Decay of plane shock waves in equilibrium flows. *Under consideration for J. Fluid Mech.*

# TABLE OF CONTENTS

Acknowledgments . . . . .	iii
Abstract . . . . .	iv
Published Content and Contributions . . . . .	v
Table of Contents . . . . .	vi
List of Illustrations . . . . .	viii
List of Tables . . . . .	xvii
Chapter I: Introduction . . . . .	1
1.1 Motivation . . . . .	1
1.2 The Detonation-Driven Shock Tube . . . . .	4
1.3 Review of Prior Work on Detonation Drivers . . . . .	7
1.4 Areas for Further Research . . . . .	11
1.5 Outline . . . . .	14
Chapter II: Decay of Plane Shock Waves in Equilibrium Flows . . . . .	16
2.1 Formulation . . . . .	20
2.2 Shock-Change Equations . . . . .	23
2.3 Shock Decay Model . . . . .	30
2.4 Initial Shock Decay Rate . . . . .	33
2.5 Numerical Simulations . . . . .	35
2.6 Summary . . . . .	49
Chapter III: Modeling Forward-Mode Detonation-Driven Shock Decay . . . . .	52
3.1 Problem Formulation . . . . .	52
3.2 Simulation Methods . . . . .	57
3.3 Results: Shock Decay . . . . .	59
3.4 Results: Post-Shock Flow . . . . .	65
3.5 Implications of Shock Decay Model . . . . .	66
3.6 Summary & Conclusions . . . . .	71
Chapter IV: Time-Resolved Shock Speed Measurements: Methods . . . . .	72
4.1 GALCIT Unsteady Shock Tube (GUST) . . . . .	72
4.2 Detonation Speed Measurement . . . . .	75
4.3 Shadowgraphy Methods . . . . .	77
4.4 Verification . . . . .	82
4.5 Summary . . . . .	88
Chapter V: Time-Resolved Shock Speed Measurements: Results & Analysis . . . . .	90
5.1 Results: Forward-Mode Detonation Driver . . . . .	90
5.2 Results: Reverse-Mode Detonation Driver . . . . .	101
5.3 Results: Helium Driver . . . . .	106
5.4 Discussion . . . . .	107
5.5 Conclusions . . . . .	110

Chapter VI: Heterodyne Focused Laser Interferometer: Theory, Methods, and Validation . . . . .	111
6.1 Theory . . . . .	115
6.2 Methods . . . . .	133
6.3 Validation . . . . .	140
6.4 Conclusions . . . . .	147
Chapter VII: Heterodyne Focused Laser Interferometer: Results . . . . .	150
7.1 Additional Methods . . . . .	150
7.2 Results: Forward-Mode Detonation Driver . . . . .	157
7.3 Results: Reverse-Mode Detonation Driver . . . . .	164
7.4 Results: Helium Driver . . . . .	170
7.5 Frequency Analysis . . . . .	171
7.6 Discussion . . . . .	179
7.7 Summary & Conclusions . . . . .	181
Chapter VIII: Conclusions & Future Work . . . . .	183
8.1 Conclusions . . . . .	183
8.2 Future Work . . . . .	185
Bibliography . . . . .	188
Bibliography . . . . .	188
Appendix A: Additional Material on Plane Shock Decay . . . . .	201
A.1 Irreversible Chemical Reaction . . . . .	201
A.2 Implementation of Prior Theories . . . . .	202
Appendix B: Additional Methods & Data: Shock Speed Measurements . . . . .	207
B.1 Detonation Spectrum . . . . .	207
B.2 Calibration Methods . . . . .	207
B.3 Post-Processing Algorithm . . . . .	209
B.4 Shot Conditions . . . . .	214
B.5 Shock Speed Data . . . . .	217
B.6 All Calibration Factors . . . . .	221
Appendix C: Ultra-Sensitive FLDI Using Balanced Detection . . . . .	222
Appendix D: Additional HFLI Methods . . . . .	227
D.1 Optical Construction . . . . .	227
D.2 Beam Profiling . . . . .	228
D.3 Spherical Aberration . . . . .	230
D.4 IQ Demodulation . . . . .	232
D.5 Noise and Drift . . . . .	234
Appendix E: Additional HFLI Data . . . . .	237
E.1 Shot Conditions . . . . .	237
E.2 Additional Data: Absolute Phase . . . . .	242
E.3 Additional Data: Differential Phase . . . . .	255
E.4 Additional Data: Amplitude . . . . .	256
Appendix F: Additional Data: Pressure Measurements . . . . .	269
F.1 Vibration Isolation . . . . .	269
F.2 Shot Data . . . . .	270
Appendix G: Engineering Drawings . . . . .	282

## LIST OF ILLUSTRATIONS

<i>Number</i>	<i>Page</i>
1.1 Ideal one-dimensional structure of a plane detonation wave propagating in a closed tube. . . . .	5
1.2 Space-time diagrams of detonation-driven shock tube operation . . .	6
1.3 Pressure-velocity diagram for initial wave interactions in a detonation-driven shock tube. . . . .	8
2.1 Space-time diagram of shock decayed by a centered expansion wave .	19
2.2 Shock-change coefficients in a perfect gas for a range of $M$ and $\gamma$ . . .	30
2.3 $K^{-1}$ for a range of $M$ and $\gamma$ . . . . .	30
2.4 Shock decay model and its power-law approximate solution for a perfect gas . . . . .	32
2.5 Variation in $\alpha$ with $M$ and $\gamma$ . . . . .	32
2.6 $B^{-1}$ for a range of $M$ and $\gamma$ . . . . .	35
2.7 Variation in $\beta$ with $M$ and $\gamma$ , where $\beta$ is given by (2.68). . . . .	36
2.8 Example of shock displacement calculation using cross correlation of pressure gradients. . . . .	37
2.9 Early evolution of velocity, pressure, and their gradients for $M_0 = 7$ and $\gamma = 1.4$ . . . . .	39
2.10 Estimates of $\dot{M}_0$ using shock-change equations with unperturbed gradients in incident simple wave. . . . .	40
2.11 Comparison of various theories for the decay of a $M_0 = 3$ and $\gamma = 1.4$ shock with simulation results and our model. . . . .	41
2.12 Comparison for the decay of a $M_0 = 7$ and $\gamma = 1.4$ shock. . . . .	41
2.13 Time-evolution of (a) $M$ from numerical simulations and model predictions and (b) model error. . . . .	42
2.14 Relative error in model prediction for $M$ at end of simulated time . .	42
2.15 Terms from second-order shock-change equation (2.54) evaluated from simulation data for $M_0 = 7$ $\gamma = 1.4$ . . . . .	43
2.16 Maximum value of $\epsilon$ , which quantifies the perturbation by the reflected wave. . . . .	43

2.17	Shock-change coefficients $K^{-1}$ and $B^{-1}$ for shock Mach numbers up to 20 in a $\gamma = 1.4$ gas and in equilibrium air initially at 50 kPa, 300 K air (21% $O_2$ and 79% $N_2$ ). . . . .	44
2.18	Thermodynamics for simulations of shocks in equilibrium air . . . .	45
2.19	Comparison between numerical simulations and model predictions for strong shocks in equilibrium air initially at 50 kPa and 300 K. . .	46
2.20	Parameters for power-law approximation of decay model for equilibrium air at 50 kPa and 300 K. . . . .	46
2.21	Variation of (a) $\Gamma$ and (b) $a_1 \partial_a \Gamma$ along $M_0 = 15$ post-shock isentrope, where $v_2$ is the post-shock specific volume. . . . .	47
2.22	Initial (a) particle velocity and (b) pressure for simulations of shock decay by the simple wave from a constant-deceleration piston for $M_0 = 7$ and $\gamma = 1.4$ . . . . .	50
2.23	Time evolution of (a,b,c) shock speed and (d,e,f) model error for $M_0 = 7$ and $\gamma = 1.4$ shocks decayed by the simple wave from a constant-deceleration piston for three values of the scale parameter, $\sigma$ . . . . .	50
3.1	Initial conditions for the simplified model problem . . . . .	53
3.2	(a) rarefaction wave curves and (b) isentropes for detonation products from stoichiometric mixtures of ethylene-oxygen . . . . .	54
3.3	Map of variables for simulation cases examining the combined effects of pressure and sound speed ratios . . . . .	56
3.4	Time evolution of driven shock Mach number for simulation of base case. . . . .	60
3.5	Space-time diagram generated from integration along characteristics of simulation data for the base parameter set. . . . .	60
3.6	Comparison of the mean shock Mach number in the plateau region from numerical simulations with the result from the model . . . . .	61
3.7	Shock decay parameter fit to propagation law for all simulation cases . . . . .	62
3.8	Shock decay properties plotted against multivariate correlations with pressure and sound speed ratios . . . . .	63
3.9	Decay properties from sensitivity study of secondary independent variables, where each quantity was varied individually about the base case. . . . .	64
3.10	Comparison of distance along driven section when shock reaches plateau period calculated using model formulae and from simulations. . . . .	64

3.11	Comparison of shock decay model with numerical simulations including finite-rate dissociation in the air test gas. The decay model assumes chemically frozen flow. . . . .	65
3.12	Space-time diagram with color corresponding with $\log(\rho/\rho_1)$ . . . .	66
3.13	Pressure and density profiles at various axial positions . . . . .	67
3.14	Calculations of ZND induction zone length and CJ sound speed for $C_2H_4 + 3O_2$ with various diluents . . . . .	69
3.15	Calculations of forward-mode detonation-driven shock decay for four driver mixtures . . . . .	70
4.1	Diagram of detonation-driven shock tube with transparent polycarbonate driven section. . . . .	73
4.2	Diagram of detonation driver. Detonation is initiated and shaped in channels of inner sleeve, which is shown unwrapped in (c). . . . .	74
4.3	Diagram of optical ports for measuring detonation time-of-arrival . .	75
4.4	Example of signals used to measure detonation speed . . . . .	76
4.5	Detonation speed measurements for three driver mixtures. . . . .	76
4.6	Diagram of large field-of-view shadowgraphy setup. . . . .	77
4.7	Example full field-of-view shadowgraph, showing width of polycarbonate tube and narrow measurement FOV. . . . .	78
4.8	Post-processing steps to obtain frame-to-frame shock displacement .	80
4.9	Example of raw and low-pass filtered shock speed signal obtained from post-processing algorithm . . . . .	80
4.10	eCDFs for errors from simulated shadowgraphy measurements of shock speed . . . . .	82
4.11	Shock speed measurements from six shots at the same condition. . . .	83
4.12	Shock shadowgraph signals from wide and narrow fields of view. . .	83
4.13	Shadowgraph frames are plotted as space-time diagrams with corresponding speed measurements . . . . .	85
4.14	Comparison of shock-speed measurement using two post-processing algorithms. . . . .	86
4.15	Large FOV frames showing curved shock. . . . .	86
4.16	Simulated shadowgraphs of flat and curved shocks . . . . .	87
4.17	Effect of sinusoidal variation in shock-curvature on simulated shock-speed measurements. . . . .	88
5.1	Pressure measurements showing detonation striking diaphragm . . .	91



5.2	Forward-mode detonation-driven shock speed measurements for various pressure ratios. . . . .	92
5.3	Mean ratio of shock speed measurement to ideal model, $c$ . . . . .	93
5.4	Forward-mode detonation-driven shock speed measurements compared with calibrated model. . . . .	94
5.5	Effect of diaphragm thickness on (a) shock speed and (b) space-time diagram. All conditions use $P_{41} = 50$ kPa $C_2H_4 + 3O_2$ driver gas and $P_1 = 6.5$ kPa air driven-section gas. . . . .	94
5.6	Effect of diaphragm thickness on $c$ for three pressure ratios. . . . .	95
5.7	Effect of absolute pressure with scaled diaphragm thickness. . . . .	95
5.8	Effect of driver gas mixture on forward-mode detonation-driven (a) shock speeds and (b) space-time diagrams. . . . .	96
5.9	Comparison of experiment and model for hydrogen-oxygen driver, where $P_{41} = 87$ kPa, $P_1 = 32.12$ kPa, and diaphragm thickness is $25.4 \mu m$ . . . . .	97
5.10	Time-frequency analysis of data from Figure 5.2(d). . . . .	98
5.11	Peak frequencies from periodograms computed for entire shock speed records. . . . .	99
5.12	Photograph of rigid cross of thin flat plates used to mechanically support plastic diaphragms to prevent bulging. . . . .	100
5.13	Effect of mechanically supporting diaphragm on (a) high-pass filtered shock speed signals and (b) power spectra computed from first third of signals in (a). . . . .	100
5.14	Deflection of Mylar diaphragms with varied thicknesses from driver pressurization. . . . .	101
5.15	Reverse-mode detonation-driven shock speed measurements for various pressure ratios. Driver gas is $C_2H_4 + 3O_2$ and diaphragm thickness is $25.4 \mu m$ for all cases. . . . .	102
5.16	Shock speed fractional attenuation per unit meter calculated from slope of measurement fits. . . . .	103
5.17	Peak frequencies obtained from power spectra of pressure-ratio data. . . . .	103
5.18	Diaphragm effects on shock speed for constant pressure ratio. All cases use a $C_2H_4 + 3O_2$ driver mixture. . . . .	104
5.19	Effect of driver mixture on driven shock speed, where each case uses 100 kPa driver gas and 10 kPa air driven-section gas. . . . .	105
5.20	Periodograms from driver-mixture data in Figure 5.19. . . . .	105

5.21	Ratio of peak frequencies from shock speed power spectra with characteristic transverse frequency, $a_2/d$ . . . . .	106
5.22	Shock speed measurements and power spectral densities for various test gases . . . . .	107
5.23	Measurements of shock speed using unheated high-pressure helium driver for two pressure ratios . . . . .	108
6.1	Block diagram of frequency down converter. . . . .	122
6.2	Block diagram of IQ demodulator. . . . .	124
6.3	Illustration of phase unwrapping using IQ data. . . . .	125
6.4	Power spectral density of synthetic signal with band-limited Gaussian noise and 80 dB SNR. . . . .	128
6.5	Histograms of IQ data calculated from simulated signals with four different SNRs. . . . .	128
6.6	Phase noise from IQ data with band-limited additive Gaussian noise. . . . .	129
6.7	Comparison of absolute and differential focused laser interferometer transfer functions . . . . .	131
6.8	Diagram of heterodyne focused laser interferometer. . . . .	133
6.9	Power spectra compare heterodyne signal from detector D1 with background signals in (a) and the local oscillator (LO) in (b). . . . .	139
6.10	RMS phase noise measurements in 10 kHz to 10 MHz band for various sampling rates . . . . .	140
6.11	Typical phase signals for resting interferometer. . . . .	141
6.12	Comparison of measurements of 100 kHz ultrasonic waves using a conventional FLDI, the differential HFLI, and absolute HFLI. . . . .	142
6.13	Ratio of differential to absolute phase signals comparing measurements with analytical result (6.55). . . . .	142
6.14	Diagram of open-ended shock-tube experimental setup for validating HFLI dynamic response. . . . .	143
6.15	Comparison between differential phase measurements from a conventional and heterodyne FLDI . . . . .	144
6.16	Unwrapped phase signals from four shots at 54-psi condition . . . . .	145
6.17	Signal amplitudes from IQ data for four shots at 54-psi condition and $d = 2.5$ mm. . . . .	146
6.18	Representative time steps of density profiles from numerical simulations of open-ended shock-tube validation experiment. . . . .	147

6.19	Comparison between experimental measurements of absolute phase change using heterodyne interferometer and phase signals modeled from numerical simulations for four cases . . . . .	148
7.1	Diagram of GUST with stainless-steel driven section ports for optical access and pressure transducers. . . . .	150
7.2	Comparison of isentropes from pressure and density measurements with thermodynamic calculations. Density is obtained from interferometer. . . . .	152
7.3	(a) pressure and (b) absolute phase data from 25 kPa $C_2H_4 + 3O_2$ detonation. . . . .	153
7.4	Comparison of measured and calculated CJ isentrope for a 25 kPa $C_2H_4 + 3O_2$ detonation. . . . .	154
7.5	Comparison shock-speed measurements using shadowgraphy and pressure sensor time of arrival . . . . .	155
7.6	Examples of post-shock phase value identified for representative shot conditions. . . . .	155
7.7	(a) Vibrational relaxation times for $O_2$ in air. (b) comparison of post-shock densities for vibrationally frozen and equilibrium gases . .	157
7.8	Forward-mode comparison between results from experiments and numerical simulations . . . . .	158
7.9	Detailed view of post-shock data from Figure 7.8, plotted in density units. . . . .	160
7.10	Forward-mode post-shock density data for supported and unsupported diaphragms . . . . .	161
7.11	P7 pressure data for shots with a supported and unsupported diaphragm	162
7.12	Forward-mode post-shock density data for different diaphragm thicknesses in (a) and materials in (b) . . . . .	162
7.13	Forward-mode post-shock density data for three driver mixtures and two pressure conditions . . . . .	164
7.14	Reverse-mode post-shock density measurements for four $P_1$ pressures	165
7.15	Reverse-mode post-shock density measurements for four $P_1$ pressures	166
7.16	Reverse-mode post-shock density measurements for two diaphragm thicknesses . . . . .	166
7.17	Reverse-mode post-shock density measurements for three driver mixtures and two pressure conditions . . . . .	167

7.18	Reverse-mode post-shock density measurements for three test gases and two pressure conditions . . . . .	168
7.19	Additional reverse-mode data at more pressure conditions where argon is the test gas. . . . .	169
7.20	Measurements of root-mean-square post-shock density fluctuations using a reverse-mode driver . . . . .	170
7.21	Post-shock density data for six pressure conditions using a cold high-pressure helium driver. . . . .	172
7.22	Background subtracted data for forward-mode detonation-driven shocks with a 50 kPa $C_2H_4 + 3O_2$ driver and air test gas. . . . .	173
7.23	Power spectra of data with (colored) and without (black) background-subtraction. . . . .	173
7.24	Peak frequencies from power spectra of density data for (a) forward-mode and (b) reverse-mode detonation drivers. . . . .	174
7.25	Space-time diagrams illustrating four possible modes for a plane disturbance to propagate between the observation plane and the shock wave. . . . .	175
7.26	Comparison between experimentally measured frequency ratio and calculated Doppler shifts for a plane wave disturbance and reverse-mode data. . . . .	176
7.27	Comparison between experimentally measured frequency ratio and calculated Doppler shifts for a plane wave disturbance and forward-mode data. . . . .	179
7.28	Comparison between post-shock density data for the three driver types where shock Mach numbers are all similar. . . . .	180
7.29	A second comparison between post-shock density data for the three driver types where shock Mach numbers are all similar, where the forward-mode driver uses hydrogen. . . . .	180
A.1	Effect of $Q$ on $K^{-1}$ for $\gamma = 1.2$ . . . . .	202
A.2	Solutions of shock decay model for nonzero $Q$ . . . . .	203
B.1	Spectra of luminous detonation products and flash lamp . . . . .	207
B.2	Photograph of alignment tool positioned on polycarbonate tube. . . . .	208
B.3	Calibration image used to obtain pixel size, FOV position, and verify unity magnification. . . . .	209
B.4	(a) linear array of shadows from the alignment tool. In (b), the image is vertically averaged and inverted. Peaks are identified. . . . .	210

B.5	Measured rib positions from alignment tool are compared with their known true positions. . . . .	210
B.6	Spatial variation of magnification from differentiating measured rib positions. . . . .	211
B.7	Shock speed measurements for forward-mode shot condition numbers 1 to 10. Solid line is measurement, dashed line is model. Driver length is 438.6 mm. . . . .	217
B.8	Shock speed measurements for forward-mode shot condition numbers 11 to 22. Solid line is measurement, dashed line is model. Driver length is 438.6 mm. . . . .	218
B.9	Shock speed measurements for reverse-mode shot condition numbers 23 to 31. Solid line is measurement, dashed line is model. . . . .	219
B.10	Shock speed measurements for reverse-mode shot condition numbers 32 to 37. Solid line is measurement, dashed line is model. . . . .	220
B.11	Shock speed measurements for shot condition numbers 38 and 39 using high-pressure helium driver. Solid line is measurement, dashed line is model. . . . .	220
B.12	Calibration factors for all tested shot conditions. . . . .	221
C.1	Schematic for FLDI modified to implement balanced detection. . . . .	223
C.2	Comparison of signals obtained using FLDI with balanced detection and differential amplification . . . . .	224
C.3	Comparison of power-spectra of signals obtained using FLDI with balanced detection and differential amplification . . . . .	224
C.4	Comparison of power-spectral densities from balanced FLDI with white-noise sources . . . . .	226
D.1	Diagram of heterodyne focused laser interferometer. . . . .	227
D.2	Diagram of optical table constructed from 0.75-in plywood and steel channels. All free-space optics are rail-mounted. . . . .	229
D.3	Foci pair using Thorlabs BP209-VIS in “slit” mode. . . . .	230
D.4	Focused beam diameter measurements using Thorlabs BP209-VIS in “knife-edge” mode. . . . .	230
D.5	Beam $M^2$ measurement. . . . .	231
D.6	Fringe patterns obtained from homodyne interferometer setup. . . . .	231
D.7	Schematic of analog IQ demodulation system. . . . .	233
D.8	Comparison of phase measurement using analog and digital IQ demodulation. . . . .	234

D.9	Laser noise measurements. . . . .	235
D.10	Comparison between phase signals measured using a reference beam that was fiber-coupled versus in free-space. . . . .	236
E.13	Differential phase measurement from shot 405. . . . .	255
E.14	Power spectral densities for differential and absolute phase measure- ments from shot 405. . . . .	256
E.15	Amplitude modulation from heterodyne signal obtained for shot 400.	257
E.16	Amplitude modulation compared with background reference signal and estimates of their power spectral densities. . . . .	258
E.25	Shock $\Delta t$ estimate using cross-correlation of amplitude signals. . . .	267
E.26	Comparison between shock speed measurement techniques for two shot conditions. . . . .	268
F.1	Comparison between pressure measurements using a PCB mounted in an aluminum and in a plastic plug. . . . .	269
F.2	Post-shock pressure signal spectrum for PCB mounted in an alu- minum and in a plastic plug. . . . .	270

## LIST OF TABLES

<i>Number</i>	<i>Page</i>
3.1	Examples of perfect gas parameters for equilibrium detonation products 56
3.2	Values of $P_{41}$ corresponding with calculations in Figure 3.15 . . . . . 71
5.1	Comparison of RMS shock speed oscillation amplitudes between driver techniques . . . . . 110
7.1	GUST pressure transducer positions . . . . . 151
7.2	Diaphragm material properties . . . . . 163
7.3	Experimental frequency ratio, $f_l/f_s$ , and predicted Doppler shift of first-order lateral waves, $b_L$ . . . . . 178
B.1	Shot conditions and model parameters for forward-mode driver ex- periments . . . . . 215
B.2	Shot conditions and model parameters for reverse-mode driver ex- periments . . . . . 216
B.3	Shot conditions for high-pressure helium driver . . . . . 216
D.1	Optical components of interferometer . . . . . 228
D.2	Electrical components of interferometer . . . . . 228
E.1	Shot conditions for HFLI measurements. . . . . 237

*Chapter 1***INTRODUCTION****1.1 Motivation**

The shock tube is a laboratory apparatus used to generate plane shock waves in gases. Its basic construction and operation are simple: two coaxial pipes are separated by a diaphragm, where one is filled with a desired test gas, and the other is pressurized until the diaphragm ruptures. The high-pressure gas rapidly expands into the other pipe section, compressing the test gas through a shock wave that is driven down the length of the tube. The shock wave impulsively heats, compresses, and accelerates the test gas, and this ability to rapidly do work gives the shock tube its unique utility.

Shock tubes find widespread application in fluid dynamics and chemical physics research, and, in particular, shock-tube-based facilities are some of the only laboratory methods capable of reproducing at scale the high flow velocities seen in hypersonic flight. Relevant flows are characterized not only by high Mach numbers but also by high total enthalpies, which produce a complex coupling between the flow and molecular processes like chemical dissociation and vibrational relaxation. Ground testing capabilities are essential for investigating these physics, and the impulsive operation of a shock tube is leveraged in order to attain the enormous powers needed to generate these flows. Advancing shock-tube technology for these applications is therefore a major and continuing area for research.

**1.1.1 Hypervelocity Flow Research Facilities**

Hypervelocity flow research facilities build upon the basic shock tube with primarily two designs (Hornung, 2010). In reflected shock tunnels, the primary shock wave is reflected at the shock-tube end, generating a high-pressure high-temperature stagnant gas volume that is subsequently accelerated in a steady expansion through a nozzle to high velocities. The very high temperatures in the stagnated gas volume lead to oxygen dissociation and the formation of nitric oxide. Subsequent expansion through the nozzle causes the gas thermodynamic state to “freeze” at some composition distinct from air. This is a facility-specific effect and can be significant (Olivier, 2016), illustrating the importance of experimental research in different types of facilities.



These issues are substantially mitigated in an expansion tube because the shocked test gas is never stagnated prior to reaching the test section. In an expansion tube, the shock tube is connected to a third coaxial pipe section at an even lower pressure, so that acceleration to hypervelocity is instead achieved through an unsteady expansion.

After its first development (Trimpi, 1962), widespread use of expansion tubes was hampered by observations of noisy, unusable free-stream test flows (Norfleet et al., 1966). Paull and Stalker (1992) analyzed the transmission and propagation of acoustic perturbations in these flows and identified the importance of the primary contact-surface sound-speed ratio, which gives guidance on how to tune facility operating conditions. Conclusions from this work have been employed to successfully operate several expansion tubes (Dufrene et al., 2007, Dufrene, 2013).

Paull and Stalker considered the acoustic wave perturbations to originate from the driver, arguing that observations of structured test flow perturbations with dominant frequencies are the result of frequency focusing from a possibly broadband noise source. Other than originating from the driver, Paull and Stalker do not identify the generating mechanism of acoustic waves, however this is essential in order to develop engineering strategies for mitigating them.

Diaphragm techniques are an example of another important engineering trade when designing and operating expansion tubes. Large diameter facilities require thick metal diaphragms to withstand initial pressures. Rupture is violent and produces a significant portion of the audible noise during facility operation, as discussed by Erdos and Bakos (1994). Additionally, diaphragms are prone to shed particulate into the flow during rupture. The particulate is accelerated to high velocities and can be exceedingly damaging, leading to off-axis operation in some of the largest facilities (Dufrene, 2013), which reduces the advantages of having a large area core flow.

Free-stream noise and diaphragm considerations are tied to the shock-tube driver technology employed. Different techniques exist to obtain the high performances required for these research facilities.

### **1.1.2 Driver Technologies**

Generation of strong shocks at relevant pressures requires a high-performance driver. Shock-tube performance is almost entirely driven by the ratio of driver and test gas sound speeds. Since the test gas is fixed by application, driver technologies endeavor to maximize driver gas sound speeds. At any temperature, the gas with the highest

sound speed is hydrogen. However, high-pressure hydrogen poses serious hazards since it is highly flammable in air. Consequently, the vast majority of shock-tube research employs helium.

The main strategy for increasing driver gas sound speeds is to heat the gas to raise its temperature. Some facilities use helium or hydrogen and statically heat it (MacLean et al., 2010). In free-piston-driven facilities, a piston is used to adiabatically compress the driver gas to high pressure and temperature (Stalker, 1967). A third technique is to heat the gas via combustion.

To obtain the highest sound speeds, combustion-heated drivers employ hydrogen-oxygen driver mixtures, however these are sensitive and prone to transition to detonation. In early work on combustion drivers, Hertzberg and Smith (1954) observed that when diaphragms were weak resulting shock waves were anomalously strong, likely a consequence of incipient detonation. Nagamatsu and Martin (1959) highly diluted their hydrogen-oxygen mixture with helium to suppress transition to detonation. However, instead of suppressing it, a detonation wave can intentionally be initiated, and the very large pressures and temperatures generated can be taken advantage of to drive strong shocks. This is the detonation driver.

Detonation drivers are attractive as a method for mitigating some of the negative diaphragm effects discussed above. Detonations are fast (2-3 km/s), and so high pressures and temperatures are generated dynamically. Consequently, in the detonation-driven facility, the shock-tube diaphragm only has to withstand the pressure difference prior to initiation, approximately 3-5% of the detonation pressure. This enables the use of thinner diaphragms.

Since the detonation driver only requires fuel and oxygen, dependence on helium is eliminated. This is a major advantage since helium is a scarce resource with growing demand and rising price (Kramer, 2023). Shock tube facilities typically do not employ any methods for helium recapture, and so experiments using large quantities can be prohibitively expensive.

Detonation driver gas is very hot (4000-5000 K), and only cools modestly through the shock-tube isentropic expansion (2000 K). Consequently, sound-speed ratios across detonation-driven shock tube contact surfaces are large (Lawson and Austin, 2018), and so the theory by Paull and Stalker (1992) indicates the possibility for free-stream noise issues in expansion tube applications. Operation of a large-scale detonation-driven expansion tube has indeed shown significant test-flow unsteadiness (Jiang

et al., 2015).

The motivation for this work is to investigate the detonation driver as a method for generation of strong shocks in an expansion tube research facility. Expansion tube technology is important for the research of hypervelocity flows, complementing capabilities provided by other facilities to access different flow conditions but also to cross-validate results and eliminate doubts from facility-specific effects. Use of the detonation driver for an expansion tube is attractive for its high-performance capabilities and possible elimination of some diaphragm concerns. However, the quality of flows generated needs to be investigated given known challenges of expansion tubes.

## 1.2 The Detonation-Driven Shock Tube

The phenomenology of gaseous detonation waves will be briefly presented first before returning to their application in shock-tube drivers. In a detonation driver, the detonation wave is used as a tool to do work. Consequently, the following presentation will be cursory. Key references to the historical development of detonation theory are given by Fickett and Davis (1979) and Lee (2008).

A detonation wave is a coupled shock and combustion wave that can propagate through a premixed volume of fuel and oxidizer. Energy release from exothermic reactions in the shock-heated medium supplies the work required to push the shock forward. The Chapman-Jouguet (CJ) condition states that the detonation wave will propagate at the speed which drives the post-shock flow sonic in the shock-fixed frame. From this condition and the medium's energy release, a detonation wave speed can be calculated that accurately models the behavior of real detonations.

Chemical reactions require a finite time to progress, and these establish the intrinsic length scales of a detonation wave. For a steady theoretically one-dimensional structure, the reaction zone formed behind a shock is described by the ZND model, after Zel'dovich, von Neumann, and Döring. For a detonation propagating at the CJ speed, the ZND structure terminates at the CJ state.

It was discovered experimentally that detonation waves in gases do not propagate as predicted by one-dimensional theory, exhibiting a rich variety of different behaviors. Chemical reaction rates are highly sensitive to post-shock temperatures, and this coupling between reaction rates and detonation shock speed provides a mechanism for instability. The effect of the unstable detonation structure is to give it a length scale distinct from but correlated with predictions by one-dimensional theory.

Detonation length scales become important when they are comparable to those of geometric confinement, namely tube diameters. These length scales are often quantified by a detonation cell size. This metric is imprecise, given the highly variable detonation structure depending upon gas chemistry, thermodynamics, and geometric confinement. However, for cell sizes much less than tube diameters, a spanwise average of the detonation wave can be modeled again as approximately one-dimensional.

The gas processed by a detonation wave exits the reaction zone with a high velocity. In a closed tube, the end caps do not allow any gas flow and so establish zero-velocity boundary conditions. In order to match this boundary condition, high velocity detonation products must be brought to a halt. This is accomplished by an unsteady expansion, known as the Taylor-Zel'dovich (TZ) wave, which is approximately self-similar.

From the above elements, an ideal one-dimensional model can be formed for the detonation wave propagating in tubes. Figure 1.1 illustrates this structure. The wave propagating at the CJ speed is followed by a very small reaction zone that terminates at the CJ state. The TZ wave expands detonation products and extends over roughly half of the distance the wave has propagated.

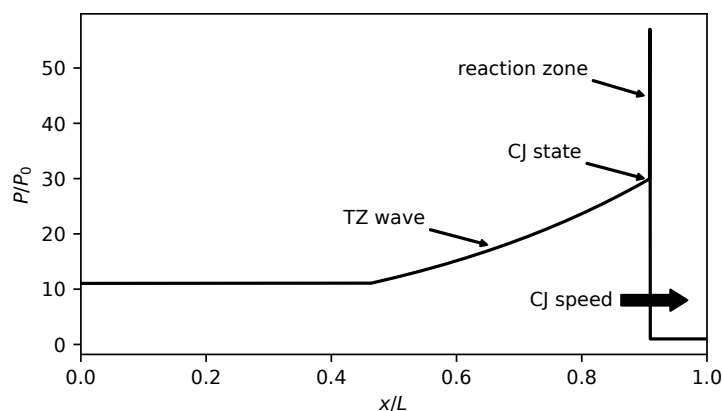


Figure 1.1: Ideal one-dimensional structure of a plane detonation wave propagating in a closed tube.

In a detonation driver, the detonation wave can be initiated to propagate either forward into the shock-tube diaphragm, or in the reverse direction away from the diaphragm. These distinguish the two operation modes, and space-time diagrams for each illustrate the wave dynamics in Figure 1.2.

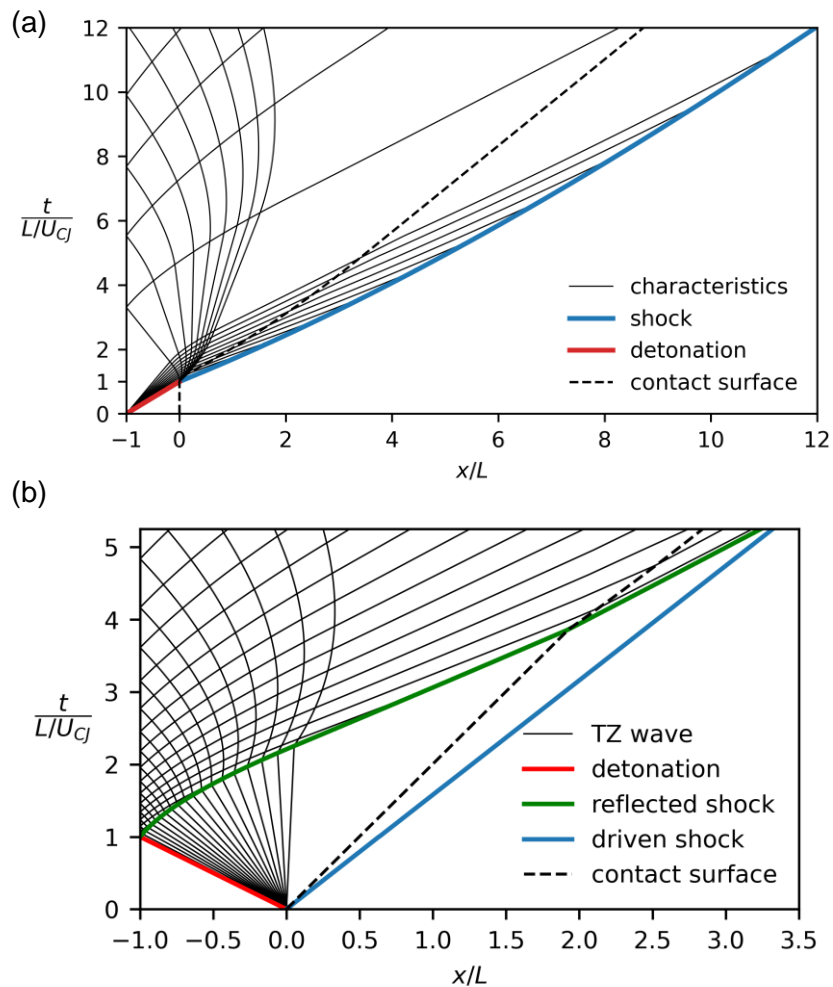


Figure 1.2: Space-time diagrams of shock tube operation with an (a) forward-mode and (b) reverse-mode detonation driver. Coordinates are nondimensionalized using the driver length,  $L$ , and CJ speed,  $U_{CJ}$ .

In the forward mode, detonation reaction zone length scales are small, and so transients from the finite reaction zone structure are confined to early time, which is also substantially influenced by diaphragm rupture effects. Neglecting these early-time effects, the shock-tube can be modeled as if it is driven by the CJ state. However, the CJ state is the head of the TZ wave, which immediately transmits through the contact surface and interacts with the driven shock, causing its strength to decay from the beginning of its formation.

In the reverse-mode, the detonation is initiated at the diaphragm and propagates upstream. The backwards propagating detonation drives the shock-tube by isentropically expanding the CJ state through an extended TZ wave to a positive velocity.

Upon impact with the driver end wall, the detonation and TZ wave reflect a shock that accelerates through the TZ wave and overtakes the primary shock at later time. In this configuration, the driven shock is theoretically steady but of weaker strength relative to the initial speed attained with the forward mode.

As with conventional shock-tube techniques, the initial shock speed can be obtained from a pressure-velocity diagram. Figure 1.3 shows that the only difference between the forward and reverse mode is the sign of the CJ gas velocity, i.e., it is positive for a forward-mode driver and negative for a reverse-mode driver. For perfect gases, this is shown by the detonation-driven shock tube equation,

$$\frac{P_{42}}{P_1} = \frac{1 + \frac{2\gamma_1}{\gamma_1 + 1}(M_s^2 - 1)}{\left(1 - \frac{\gamma_{42} - 1}{\gamma_1 + 1} \frac{a_1}{a_{42}} \frac{M_s^2 - 1}{M_s} \pm \frac{\gamma_{42} - 1}{2} M_{42}\right)^{2\gamma_{42}/(\gamma_{42}-1)}}, \quad (1.1)$$

+ forward, - reverse ,

where  $\gamma$  is the ratio of specific heat capacities,  $a$  is the sound speed, and  $M_s$  is the driven shock Mach number. Subscript 1 denotes the driven gas, and subscript 42 denotes the CJ state, which is distinguished from the unburnt driver gas, denoted in this work by subscript 41. Equation (1.1) is the same as for a typical shock tube with the addition of the  $M_{42}$  term in the denominator, which is the local Mach number of the flow,  $u_{42}/a_{42}$ , where  $u$  is the lab-frame gas velocity. Initial shock speeds obtained from a detonation driver can be calculated for perfect gases from (1.1) and for real gases from numerical calculation of the pressure-velocity diagram.

The detonation driver is not a new technique and has seen relatively recent widespread adoption in several large-scale hypersonic flow research facilities. Next, the prior work on detonation drivers will be reviewed.

### 1.3 Review of Prior Work on Detonation Drivers

The earliest work on the use of detonation waves in a shock-tube driver was by Bird (1957). Bird identified each operation mode and highlighted some of the challenges posed by the unsteady wave interactions.

Following Bird, there were a few experimental studies of detonation drivers. Waldron (1958) spark ignited hydrogen-oxygen mixtures at the diaphragm and reported measurements of large shock attenuation, despite using a form of reverse-mode operation. Coates and Gaydon (1965) investigated a method for mitigating shock

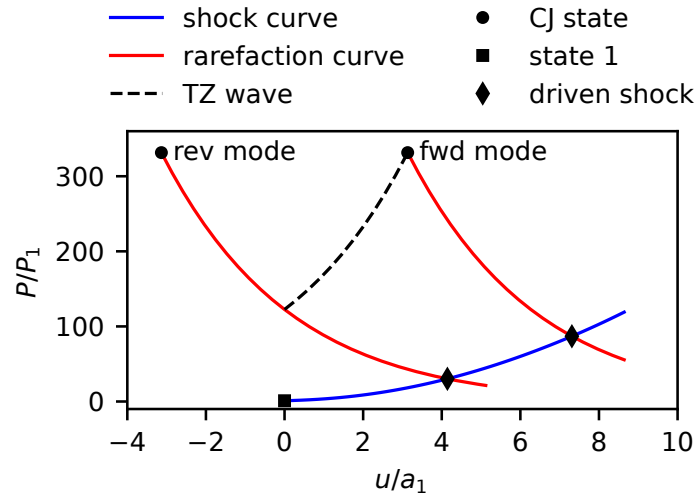


Figure 1.3: Pressure-velocity diagram for initial wave interactions in a detonation-driven shock tube.

attenuation using an auxiliary light-gas driver to shock initiate detonation in forward-mode operation. The contact surface from this auxiliary driver provides a means of supporting the detonation and thereby shortening or eliminating the TZ wave. Additionally, if the shock wave was sufficiently weak that the reactants did not ignite, then upon impact with the secondary diaphragm a detonation was promptly initiated and propagated upstream. This is a novel form of reverse-mode operation. Lee (1967) also performed experiments with a reverse-mode detonation driver, instead initiating the detonation using an exploding bridge wire at the diaphragm.

Attenuation by the TZ wave was a known problem for forward-mode operation, however Balcerzak and Johnson (1966) recognized that the driver could be made sufficiently long to reduce the significance of shock attenuation. They used the method of characteristics to analyze forward-mode detonation-driven expansion tube operation and concluded that the magnitude of unsteadiness during a facility's test flow could be made negligible.

Following this early work, there was little development on detonation drivers until Yu et al. (1992) presented the first use of a detonation-driven reflected-shock tunnel, TH2 at RWTH Aachen University. The facility employs a reverse-mode detonation driver, where detonation is initiated in a separate tube that launches the wave transversely into the diaphragm. They presented results for hydrogen-oxygen mixtures at 1 MPa, and discuss operation at higher pressure. Such significant detonation pres-

tures posed serious structural concerns, and so a low-pressure damping section was added to the upstream end of the driver. This damping section is now a common feature on other reverse-mode-driven facilities. Additional work on detonation-driven TH2 is described by Grönig et al. (1998) and Olivier (2016).

After Bakos and Erdos (1995) investigated methods for improving the performance of the 6-in diameter expansion tube HYPULSE at GASL,<sup>1</sup> the facility was upgraded for operation with a forward-mode detonation driver using shock-initiation of hydrogen-oxygen-helium mixtures. Bakos et al. (1996) presented an experimental and computational study of detonation-driven HYPULSE in expansion tube mode. Instead of totally eliminating the TZ wave, they noted that it could be used to compensate for the viscous pressure rise resulting from shock-tube boundary layers. This study demonstrated the performance gain by transitioning from a traditional light-gas driver to a detonation driver, enabling operation with higher test gas pressures, greatly increasing the total pressures achievable in test flows. The facility was later operated also as a detonation-driven reflected shock tunnel (Erdos et al., 1997). Driver-gas contamination is important for reflected-shock tunnels, and detonation driver considerations were studied by Chue et al. (2003).

Stuessy et al. (1998) presented a 6-in diameter detonation-driven reflected-shock tunnel at the University of Texas at Arlington. After exploring spark initiation, they modified the facility to use shock initiation, also identifying the potential gain by eliminating the TZ wave. They used hydrogen-oxygen with pressures up to 8 atm. These results are combined with those from GASL by Lu et al. (2000) and further expanded upon by Lu and Wilson (2003). Later, Peace and Lu (2018a) explored the initial shock speed transmitted by a forward-mode detonation, and Jayamani and Lu (2022) investigated attenuation by viscous effects and heat transfer in a small-diameter (19 mm) shock tube. A variant on the shock-initiated detonation driver is to use an auxiliary reverse-mode detonation driver. This was studied by Chen et al. (2004).

Significant work on detonation drivers has been performed at the Chinese Academy of Sciences (CAS), culminating in the construction of several large-scale research facilities, all employing detonation driver techniques. Beginning with early work at CAS, Hongru (1999) reviewed detonation driver techniques, and identified that forward-mode decay could be reduced by increasing the driver length. Experiments were presented for a driver-driven length ratio of 0.8 with an additional area con-

---

<sup>1</sup>The facility is now at Purdue University.



traction at the diaphragm, and it was concluded that shock attenuation could be sufficiently reduced for useful application of forward-mode operation. Jiang et al. (2002) further investigated area-change geometries to mitigate TZ wave decay both computationally and experimentally. They determined the optimal geometry to be a cavity ring: a large divergence upstream of the diaphragm where the detonation expands and reflects in upon itself, leading to a transient rise in pressure that reduces the mean gradients behind the detonation. These results were discussed further by Jiang et al. (2007) and Jiang et al. (2011) for application in the JF-10 reflected-shock tunnel. The JF-10 driver implements the cavity ring with three sections of varied diameter and length. The main driver is 150 mm in diameter, opens up to 300 mm in the cavity ring, and then reduces to 100 mm prior to the primary diaphragm (Jiang and Yu, 2016). The driver is over 6-m long and operated with 3 MPa pressures.

Jiang et al. (2015) applied the cavity ring concept to the expansion tube JF-16 using hydrogen-oxygen mixtures up to 1.5 MPa. They found significant test flow noise and attributed it to the contact-surface sound-speed ratio, referencing the theory by Paull and Stalker (1992). JF-16 uses a large area ratio, reducing from 150-mm in the driver to 68-mm in the driven section.

Jiang and Yu (2016) reviewed detonation driven facilities at the Chinese Academy of Sciences including the huge JF-12 reflected-shock tunnel. JF-12 uses a 99-m long reverse-mode detonation driver with a 400-mm inner diameter. They describe operation using 3.0 MPa of acetylene-oxygen or 3.5 MPa of hydrogen-oxygen for different shot conditions. A new facility, JF-22, with similar size and methods to JF-12 has been built to access conditions at higher Mach numbers and flight altitudes (Hu et al., 2025).

With large initial driver pressures, metal diaphragms are still required, and Zhao et al. (2005) found forward-mode operation often led to diaphragm fragmentation. This was controlled using a clever technique of initiating the detonation at the diaphragm to open it just prior to arrival of the forward-running detonation, mitigating diaphragm fragmentation from detonation impact. Yamanaka et al. (2002) used lower driver pressures and investigated different diaphragm materials including scored copper. Mylar was found to perform the best, followed by deeply-scored copper.

The detonation driver has now been in regular use for the operation of hypersonic research facilities for over 30 years. Both the forward-mode and reverse-mode driver are used, where shock attenuation from forward-mode operation has been

mitigated with three strategies: large driver-to-driven section length ratios to stretch the TZ wave, shock-initiation of the detonation with an auxiliary driver to shorten the TZ wave, and a cavity-ring geometry upstream of the diaphragm to raise TZ wave pressures from shock reflection. The majority of these facilities have been reflected-shock tunnels, except for HYPULSE and JF-16, and in almost all cases hydrogen is the driver fuel of choice due to its high sound speed. There are several areas for further research to advance detonation driver technology particularly with applications toward expansion tube facilities.

## **1.4 Areas for Further Research**

### **1.4.1 Detonation-Driven Shock Decay**

As is now well-established, the forward-mode detonation driver generates a decaying shock wave. Prior work has focused on engineering strategies for reducing this attenuation with an auxiliary driver or area-change geometry. Shock-initiation reintroduces many of the undesirable traits of light-gas drivers, like thick diaphragms with particulate ejection. Performance of the facility is then limited to the performance of the light-gas driver instead of the detonation driver. The area-change geometries investigated by Jiang et al. (2002) pose a different challenge. The shock reflection process produces significant strong transverse shocks in the driver gas. Although Jiang et al. (2002) report that their reflected-shock tunnel flows were stable and free from oscillations, their simulations do clearly show the strong perturbations expected from intuition. These are a major concern for application to expansion tubes.

Although there are engineering solutions and substantial facility calibrations, the elementary gas dynamics of plane shock decay from these drivers has not been modeled. Plane shock decay is a historic problem in gas dynamics and can be reduced to the classic piston start-stop problem, where a piston impulsively drives a shock, and then impulsively stops generating a centered expansion wave. These waves interact, and the plane shock decays. This is a challenging analytical problem for strong shocks because the flow is non-homentropic and non-self-similar. A solution to this problem provides direct insight to the motion of plane shocks in a detonation-driven facility. Although this is of interest purely as a novel problem in fluid dynamics, an efficient analytical model has basic utility in the design and operation of these facilities, e.g., in the consideration of alternative driver gas mixtures. Developing these models is one objective of this thesis.

### 1.4.2 Shock Speed Measurement

Models for shock motion need to be compared against experimental measurements. Measurements of shock speed are a cornerstone of shock-tube techniques, since shock speed is the critical quantity that characterizes a shock-tube's performance. All quantities that describe the post-shock flow can be calculated from knowledge of the shock speed. Accurate measurement of shock speeds is therefore essential to their use in shock tubes.

Ideal shock-tube theory predicts that shock waves are exactly steady, and so theoretically only two measurements of the shock's time-of-arrival at two known positions are required to determine the shock speed. This has translated into the actual practice of using a small number of time-of-arrival gauges to discretely sample shock position and estimate shock speed. A time-of-arrival gauge is anything with a fast response to the shock arrival. Pressure transducers, ion gauges, and thin-film gauges are common examples. From shock arrival times, a mean shock speed can be measured for the position halfway between the gauges. This measurement can be accurate even for a decaying shock wave, however measurement resolution is coarse. Increased measurement resolution is important when considering a decaying shock wave, since now the acceleration must be captured.

Over the history of shock-tube research, many sources of shock unsteadiness have been identified, such as from shock-tube boundary layers (Mirels, 1957) and finite diaphragm opening times (White, 1958). Consequently, it is common practice to use a linear array of time-of-arrival gauges, from which the rate of shock attenuation can be estimated. This has proven important for the calibration of many shock-tube facilities (Petersen and Hanson, 2001). However, the decaying shock from a detonation-driver is expected to exhibit stronger and time-varying attenuation, slowing by 50% within a few driver lengths. To obtain accurate measurements of these trajectories, improved resolution is required.

The only method known to the author for high-resolution shock-speed measurements along the length of a shock tube is a microwave velocimeter. The technique requires shocks of sufficient strength to ionize the gas. This produces a surface that microwaves coupled into the shock tube can reflect from. Blum and Dunn (1966) present an early example measuring the Doppler shift of reflected waves and give references to earlier work. The technique has found recent use by Dufrene (2013) and Straede et al. (2024) for measurements in expansion tubes. Haloua et al. (2000) used the technique to observe galloping detonations, another reflective surface. For

shock waves in inert gases with modest strengths, gases are not ionized and this technique cannot be used. Indeed, an important virtue of the expansion tube is the ability to preserve the gas composition, motivating use of reduced shock speeds.

High-resolution detonation speed measurements are made using streak cameras, where a one-dimensional image is streaked across a photosensitive medium at high speed. This is possible because detonation fronts are highly luminous, so streak images show this emission on effectively a space-time diagram. In another technique, Crane et al. (2022) were able to finely sample detonation position using an array of fiber-coupled photodetectors mounted to a transparent detonation tube. Inert shocks do not radiate strongly and so do not have this advantage.

Visualization techniques, like schlieren or shadowgraphy, can be employed to image shock motion. High-resolution measurements of shock speed enabled Damazo and Shepherd (2017) to make unique observations of unexpectedly high-speed shocks from normal detonation reflection. Typical implementations of these techniques are in facility test sections, which allow for optical transmission, and so some adaptation is required to use visualization methods along the length of a shock tube.

With an application toward capturing the dynamics of detonation-driven shock waves, another major objective for this thesis is to develop a technique to perform high-resolution shock speed measurements.

### **1.4.3 Advanced Interferometric Techniques**

Shock speeds only give information on the immediate post-shock flow. The gradients and fluctuations in the flow following the shock are what is actually important regarding a facility's test flow, particularly with respect to the expansion tube. Measurement of these quantities requires different techniques.

There are many different diagnostics used to characterize shock tube flows. Wall-mounted pressure transducers are ubiquitous but often give low-fidelity results due to facility vibrations. Pitot probes are essential to characterizing free-stream flows, and there have been recent advances with static pressure probes (Yu et al., 2024). Laser absorption spectroscopy techniques are uniquely capable of measuring gas compositions, temperatures, pressures, and even velocities (Hanson et al., 2016). However, interferometric techniques are uniquely sensitive to the acoustic perturbations of interest in expansion tubes and in this work.

The Focused Laser Differential Interferometer (FLDI) is a laser diagnostic currently in widespread use. First developed by Smeets and George (1973), it was popularized

by Parziale et al. (2012), who used it to measure free-stream noise and boundary layer disturbances in the T5 free-piston reflected-shock tunnel. The instrument is easy to align and vibration insensitive, immediately setting it apart from many other interferometric techniques. The focused beams provide a low-pass filtering effect enabling improved sensitivity at the focus with some resistance to boundary layer flows along test section walls. However, signal-to-noise ratios are limited by free-stream densities, which can be low in expansion tubes. In these applications, Lawson (2021) identified laser noise to be a major obstacle for improved measurements.

A powerful optical technique is to use heterodyne interferometry. Interference between two beams with different frequencies produces a signal at the beat frequency, the difference between the two optical frequencies. Detection of this heterodyne signal can be performed in frequency bands free from laser noise, totally eliminating this as an issue. Additionally, new signal processing methods are possible, enabling direct phase measurement. This gives the potential for *absolute* phase measurements instead of *differential* measurements. Advancing interferometric techniques by employing heterodyne detection and applying the instrument for measurements of detonation-driven shock tube flows is another major objective for this work.

## 1.5 Outline

In this chapter, the motivation, background, and objectives for this thesis were detailed.

In Chapter 2, the problem of plane shock decay is analyzed generally. A new model is formulated for this classic problem, validated against numerical simulations, and shown to predict shock motion with accuracy much improved upon prior work. These results are used in Chapter 3 to model the shock decay from forward-mode detonation drivers. The decay model is formulated from perfect-gas simulations but is shown to remain accurate for more general thermodynamics of real gases.

Chapter 4 presents the experimental facility and methods used to make time-resolved shock-speed measurements. Chapter 5 presents measurements of shock speed from forward-mode, reverse-mode, and helium-driven operation. Novel results include the ability to perform frequency analysis of shock speeds and unique observations of shock speed oscillations.

In Chapter 6, the theory and methods used to construct a heterodyne focused laser interferometer are discussed, and the instrument's response is validated against a set of experiments. The heterodyne technique enables new high-resolution mea-

surements of density perturbations, and results from interrogating detonation-driven post-shock flows are presented in Chapter 7.

Finally, conclusions and areas for future work are given in Chapter 8.

## *Chapter 2*

### DECAY OF PLANE SHOCK WAVES IN EQUILIBRIUM FLOWS

Schoeffler, D. T. and Shepherd, J. E. (2024). Decay of plane shock waves in equilibrium flows. *Under consideration for J. Fluid Mech.*

Shock decay is fundamental to numerous problems in fluid mechanics, resulting from either the geometric or unsteady expansion of the post-shock flow. Geometric effects have been famously modeled by Whitham's geometric shock dynamics (Whitham, 1999, Chapter 8). However, predicting shock decay from the interaction with an unsteady wave in a general medium remains a challenging problem to describe analytically because a shock's motion is coupled with the post-shock flow. Predictive models for this wave interaction are important because it is fundamental to many problems in shock wave physics. In detonation physics, it is essential to the unsteady shock front of gaseous detonations (Jackson and Short, 2013), to critical phenomena like minimum ignition energy (Eckett et al., 2000), and to the operation of detonation-driven shock tubes (Jiang et al., 2002). The interaction causes the shock attenuation in experiments using flyer plates (Fowles, 1960) and laser-driven shocks (Cottet and Romain, 1982). Application of geometric methods to problems like spherical blast wave propagation is substantially complicated by the unsteady wave interaction (Best, 1991). The interaction of an unsteady expansion with a shock is isolated for plane shock waves in equilibrium flows, and so this problem is the focus of this chapter. With modern computational methods it is straightforward to directly simulate these one-dimensional shock dynamics, however, analytical methods remain essential for physical insight, time-efficient solutions, and analysis of experimental and computational data.

Many shock propagation theories have been developed over nearly a hundred years of research. A common analytical approach is to specify the conservation equations to the shock discontinuity and combine them with the Rankine-Hugoniot equations. A single equation can be derived, and early formulations by Cassen and Stanton (1948) and Chen and Gurtin (1971) showed how shock acceleration is determined by the balance of the post-shock pressure gradient with geometric divergence or chemical reaction, respectively. The resulting equation is often unnamed but sometimes referred to as the shock-change equation (Fickett and Davis, 1979) or as

singular surface theory (Wright, 1976). A family of shock-change equations can be derived that relate shock acceleration to a derivative of any post-shock flow variable (Radulescu, 2020).

For one-dimensional equilibrium flows, predicting a shock's motion from these equations requires an additional condition on the post-shock flow, and this condition is typically what distinguishes different shock propagation theories and determines their accuracy for a given problem. Taylor (1939) developed a first theory by approximating the post-shock pressure gradient as constant. Chandrasekhar (1943) obtained a solution for weak shock pulses by assuming the velocity and sound speed to be spatially linear. Friedrichs (1948) first solved the problem of a weak plane shock decayed by a centered expansion in a perfect gas. This specific problem has seen significant attention since it is the simplest formulation for a shock decayed by an unsteady wave. Burnside and Mackie (1965) specifically analyzed the initial decay rate of the shock. Ardavan-Rhad (1970) and Sharma et al. (1987) developed models also assuming linearity of the post-shock velocity distribution. Fowles (1960) derives a similar theory to Friedrichs using a Murnaghan equation of state. For general one-dimensional shocks (planar, cylindrical, and spherical), Brinkley and Kirkwood (1947) derived a second-order shock propagation equation using a condition on the similarity of shock energy over time. Many other theories have come from efforts to model the non-self-similar motion of blast waves when the shock strength is finite and the upstream pressure is nonzero. These theories are not reviewed here but are described in monographs by Korobeinikov (1991), Sachdev (2004), and Lee (2016), which also discuss some of the other theories above.

The shock-change equation formalism was also used by Chester (1954), Chisnell (1957), and Whitham (1958) to model the effect of a nonuniform upstream medium on a shock's motion, particularly due to quasi-one-dimensional area changes. They neglected the coupling between the shock's motion and the post-shock flow, which is equivalent to assuming that all incoming  $C^+$  characteristics originate from a region of uniform flow. Whitham developed the theory into his shock dynamics (Whitham, 1999, Chapter 8) and identified that the method's fundamental assumption is

$$\partial_t P + \rho a \partial_t u = 0 \quad (2.1)$$

at the shock front, where  $P$  is the pressure,  $\rho$  is the density,  $a$  is the sound speed, and  $u$  is the particle velocity. The approximation has enabled expedient and reasonably accurate estimation of shock motion for a wide range of problems. However,



for problems with rapid geometric expansion, such as in blast waves and shock diffraction (Skews, 1967), coupling with the post-shock flow cannot be ignored and so the accuracy of (2.1) is worse. The effect of incoming disturbances on Chester-Chisnell-Whitham (CCW) theory was studied by Rośaciszewski (1960), Oshima et al. (1965), and Yousaf (1974, 1982), and *ad hoc* methods (Ridoux et al., 2019) have been developed to remedy this issue for numerical implementations of geometric shock dynamics (Henshaw et al., 1986). Best (1991) sought to include the effect of incoming disturbances by extending the approximation (2.1) to higher orders.

Shock propagation theories are not limited to approximations on first-order post-shock derivatives but can be formulated for any higher-order derivative. If a shock-change equation is derived for each term in the series expansion of a dependent variable, then an infinite hierarchy of equations can be obtained, and truncation of the series expansion provides a sufficient condition to solve all lower-order equations. Friedlander (1958) presents this theory in detail for sound pulses, where higher-order equations provide corrections to geometric acoustics. Similarly, since geometric shock dynamics is obtained from (2.1), Best (1991) derived higher-order corrections using a series expansion in terms of

$$\partial_t^{n-1}(\partial_t P + \rho a \partial_t u) = 0. \quad (2.2)$$

An alternative approach is given by Sharma and Radha (1994), who use a series expansion in space of the post-shock pressure, so that truncation at order  $n$  is given by

$$\partial_x^n P = 0. \quad (2.3)$$

Although arbitrarily higher-order shock propagation equations can be derived, enabling in principle arbitrarily accurate solutions, the utility of these methods is limited because higher-order equations become exceedingly cumbersome to derive and the accuracy achievable at any given order is not clear. Additionally, higher-order equations require initial conditions at every lower order. These initial conditions cannot be arbitrary, since they must be compatible with a series expansion of a solution to the governing equations. Obtaining these initial conditions is itself a difficult problem.

The difficulty of these higher-order theories is highlighted for the problem of plane shock decay. Plane shock waves in a uniform medium can only decay from the interaction with a simple wave, which entirely determines the resulting shock motion.

In the simplest case, the wave is self-similar and centered, and a space-time diagram for the interaction with a shock is shown in Figure 2.1. The shock interaction generates a wave propagating along  $C^-$  characteristics, which perturbs the post-shock flow from purely the incident simple wave. For an arbitrary flow variable,  $q$ , the perturbed quantity in the post-shock flow can be written simply as

$$q = q^{(0)} + q^{(1)}, \quad (2.4)$$

where  $q^{(0)}$  is given by the unperturbed incident simple wave and  $q^{(1)}$  is the perturbation. An infinite hierarchy of shock-change equations can be obtained by a series expansion of  $q$  at the shock front. The series expansion can be truncated to solve the system of equations, however this introduces truncation error not only from the perturbation, but also the incident wave. Instead, if only the series expansion for the perturbation is truncated,

$$\partial_x^n q^{(1)} = 0, \quad (2.5)$$

then the system of equations can be solved including the effect of the unperturbed simple wave at all orders. The problem is then reduced to identifying the appropriate variable to use for  $q$  and obtaining initial conditions for the perturbed wave. The subject of this chapter is the development, implementation, and validation of this theory for the decay of plane shocks.

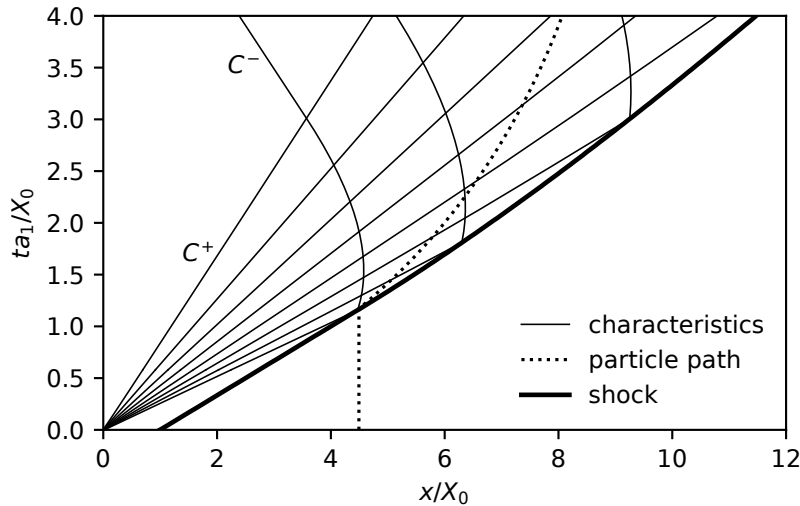


Figure 2.1: Space-time diagram of a shock decayed by a centered expansion wave. This diagram was generated from numerical simulation results presented later in this work for a Mach 3 shock and isentropic exponent  $\gamma = 1.4$ .  $X_0$  is the shock's initial distance from the origin, and  $a_1$  is the upstream sound speed.

Since shock wave phenomena are important in many diverse media, an important point is that theories using the shock-change equation formalism can be derived for a general equation of state. This has been used before by some authors. Brinkley and Kirkwood (1947) derive their theory for a general equation of state, Best (1991) implements a Tait equation of state, and Singh and Arora (2021) applied Sharma & Radha's theory to a van der Waals gas. However, most prior work only considers a perfect gas model. The theory presented in this chapter is derived for a general equation of state.

The structure of this chapter is as follows. In Section 2.1, the problem of a shock decayed by an arbitrary simple wave is formulated. From analysis of the simple wave motion, it will be shown that an optimal truncation term is the second gradient of velocity,  $u_{xx}$ , which is identically zero throughout a centered expansion in a perfect gas. The shock-change equation for  $u_{xx}$  is derived in Section 2.2. The derivation is developed by defining coefficients for each first-order shock-change equation, which enables a compact presentation of the second-order results. The second-order ordinary differential equation and strong and weak shock solutions are discussed in Section 2.3. In order to implement the shock decay model for any given simple wave interaction, the initial shock decay rate is required. A solution for the perturbed initial condition is given in Section 2.4. Finally, Section 2.5 presents the major results of this chapter, where the present model is compared with numerical simulations and several prior theories.

## 2.1 Formulation

An initially steady plane shock wave decays when overtaken by a simple expansion wave. The properties of the expansion wave determine the rate of decay of the shock over time. Any simple wave can be modeled as having originated from the motion of some piston. If a piston impulsively accelerates to speed  $u_2$  and impulsively stops after time  $\tau_p$ , then a shock with speed  $U_0$  is driven ahead of a centered expansion wave that overtakes the shock at later time. Figure 2.1 depicts the resulting space-time diagram for a Mach 3 shock, where the time when the piston stops is  $t = 0$ . Coordinates are scaled by the shock position when the piston stops, which is given by

$$X_0 = (U_0 - u_2)\tau_p. \quad (2.6)$$

The space-time diagram shows the  $C^-$  characteristics of the reflected wave. The particle path drawn intersects the point at which the shock begins decaying and

so bounds the region of nonuniform entropy behind the shock. The nonuniform entropy and reflected wave perturb the incident simple wave.

The theory of simple waves is discussed in many books, e.g., Thompson (1972) and Landau and Lifshitz (1987). The equations describing any simple wave for a general equation of state are

$$x = (u + a(u))t + f(u), \quad (2.7)$$

$$du - \frac{da}{\Gamma - 1} = 0 \quad \text{on } C^- \text{ characteristics}, \quad (2.8)$$

where  $f(u)$  is some function that satisfies the boundary conditions given by the piston motion and  $\Gamma$  is the fundamental derivative of gas dynamics (Thompson, 1971).

If the piston is impulsively stopped, then all characteristics are centered at the stopping point and (2.7) becomes

$$x = (u + a(u))t. \quad (2.9)$$

Equation (2.9) is also obtained asymptotically from (2.7) as  $t \rightarrow \infty$ , because on a given  $C^+$  characteristic  $f(u)$  is constant and so becomes much smaller than  $(u + a(u))t$ . Using (2.8), the velocity gradient in the centered wave is given by

$$u_x = \frac{1}{\Gamma t}, \quad (2.10)$$

which shows that  $u_x$  is spatially uniform, except for any variation in  $\Gamma$ . If the medium is a perfect gas, then  $\Gamma = (\gamma + 1)/2$  is constant, where  $\gamma$  is the ratio of specific heat capacities, and the first and second velocity gradients are

$$u_x = \frac{2}{(\gamma + 1)t} \quad (2.11)$$

$$u_{xx} = 0. \quad (2.12)$$

The second gradient,  $u_{xx}$ , is exactly zero everywhere throughout the wave. From (2.8), it is straightforward to show that the second gradient of sound speed,  $a_{xx}$ , is also zero everywhere. Second order derivatives of all other dependent variables are nonzero. The temperature, pressure, and density throughout the wave are given by

$$\begin{aligned} T &= T_0 \left( \frac{a}{a_0} \right)^2, \\ P &= P_0 \left( \frac{a}{a_0} \right)^{\frac{2\gamma}{\gamma-1}}, \\ \rho &= \rho_0 \left( \frac{a}{a_0} \right)^{\frac{2}{\gamma-1}}, \end{aligned} \quad (2.13)$$

where the subscript 0 denotes a reference state in the isentropic flow. For values of  $\gamma$  where  $n = 2\gamma/(\gamma - 1)$  is an integer, then the lowest-order gradients of  $T$ ,  $P$ , and  $\rho$  to vanish are

$$\partial_x^3 T = 0, \quad (2.14)$$

$$\partial_x^{n+1} P = 0, \quad (2.15)$$

$$\partial_x^{n-1} \rho = 0. \quad (2.16)$$

For  $\gamma = 5/3$ ,  $n = 5$ , and for  $\gamma = 7/5$ ,  $n = 7$ . In Best's truncation term (2.2), partial derivatives with respect to time are used. For all second order derivatives, including mixed partials, only  $u_{xx}$  and  $a_{xx}$  are zero. This can be seen by suitably differentiating (2.9) and (2.13).

For a centered expansion in a perfect gas,  $u_{xx}$  and  $a_{xx}$  can only be nonzero behind a decaying shock due to the perturbation by reflected waves. The proposed model is to neglect this perturbation and apply  $u_{xx} = 0$  at the shock, which is a sufficient condition to obtain a second-order shock propagation equation. The term  $u_{xx}$  is chosen over  $a_{xx}$  due to the simpler derivation and because it is continuous through jumps in the entropy gradient, such as across the particle path in figure 1.2. Note that this model is only applied in the limit approaching the shock position from behind, and so it is independent of discontinuities in  $u_{xx}$ , e.g., at the head of the reflected wave.

For an arbitrary simple wave in a general medium,  $u_{xx} \neq 0$ , and so this variation must be accounted for. If  $\Gamma$  is not constant, then

$$\frac{u_{xx}}{u_x^2} = -\frac{\Gamma - 1}{\Gamma} \partial_a \Gamma, \quad (2.17)$$

where  $\partial_a \Gamma$  is the variation of  $\Gamma$  with the equilibrium sound speed at constant entropy. For many cases, (2.17) may be sufficiently small that it can be neglected, for example, this will be shown for equilibrium air. In cases where this approximation cannot be made, then the  $u_{xx}$  in the unperturbed incident wave must be evaluated for each characteristic.

If the piston slows to a halt monotonically but its motion is otherwise general, then  $u_x$  and  $u_{xx}$  are given by

$$u_x = \frac{1}{\Gamma t + f'(u)}, \quad (2.18)$$

$$u_{xx} = -\left(\frac{\partial \Gamma}{\partial a}\right)_s (\Gamma - 1)t + f''(u) u_x^3, \quad (2.19)$$

and, for a perfect gas,

$$\frac{u_{xx}}{u_x^2} = -\frac{f''(u)}{(\gamma + 1)t/2 + f'(u)}. \quad (2.20)$$

By neglecting only the perturbation to  $u_{xx}$  by reflected waves, the unperturbed value given by (2.20) can still be used to evaluate  $u_{xx}$  at the shock. However, as discussed previously, the simple wave from a general piston deceleration rapidly approaches the self-similar centered expansion as time advances. So, an additional approximation is to still apply  $u_{xx} = 0$  at the shock and use (2.20) to estimate the additional induced error. This is equivalent to approximating the incident simple wave as a centered expansion with an equivalent initial velocity gradient  $u_x$ , which determines the initial shock decay rate.

The tendency toward a self-similar solution is a feature of many fluid mechanics problems, including shock propagation. Strong decaying shocks over sufficiently large time approach a self-similar limit described by Zel'dovich and Raizer (1967). In this limit,  $u_{xx}$  again equals zero, including behind the decaying shock, even if  $u_{xx} \neq 0$  initially from a general piston motion and the reflected perturbation. Uniformity of the velocity gradient in self-similar flows is a property discussed by Pert (1980) and motivated the work by Sharma et al. (1987). Indeed, Chandrasekhar (1943) and Ardavan-Rhad (1970) both also use similar models. The difference here is that  $u_{xx}$  is assumed to be zero only at the shock front, and no assumptions are made about the flow further behind the shock.

This shock decay model will be compared with numerical simulations to test the three factors that cause  $u_{xx}$  to deviate from zero. First, simulations of shocks decayed by a centered expansion in a perfect gas will evaluate the magnitude of the perturbation by the shock interaction, since  $u_{xx}^{(0)} = 0$  exactly. Second, simulations of shocks decayed by a centered expansion in equilibrium air will provide one example of a general equation of state that significantly departs from a perfect gas. Third, simulations of shocks decayed by the simple wave generated from the constant deceleration of the piston will examine the departure from  $u_{xx}^{(0)} = 0$ .

## 2.2 Shock-Change Equations

The aim of the following derivation is to obtain the shock-change equation that relates plane shock motion with post-shock values of  $u_{xx}$ . Aspects of the derivation appear in many previous articles, including recent work (Radulescu, 2020). However, other than the main results, a useful feature of the present derivation is the formulation of coefficients for each shock-change equation. These coefficients can be evaluated

independent of any problem and provide a substantially more compact approach for deriving higher-order shock-change equations for a general equation of state. In this work, equilibrium flow is specified throughout because nonequilibrium phenomena, such as vibrational relaxation or exothermic chemical reaction, are also coupled with the shock motion. These effects are included in many shock-change equation derivations (Fickett and Davis, 1979, Sharma and Radha, 1994), however they are beyond the scope of the present work. Equilibrium flow assumes that the time scale of these phenomena is either much greater or smaller than characteristic flow time scales. Vincenti and Kruger (1965) describe equilibrium flows in detail.

The equations of motion for equilibrium flow in one dimension, neglecting diffusion of mass, momentum, and energy, are

$$\frac{D\rho}{Dt} + \rho \frac{\partial u}{\partial x} = 0, \quad (2.21)$$

$$\frac{Du}{Dt} + \frac{1}{\rho} \frac{\partial P}{\partial x} = 0, \quad (2.22)$$

$$\frac{DP}{Dt} - a^2 \frac{D\rho}{Dt} = 0, \quad (2.23)$$

where  $a$  is the equilibrium sound speed. An equation of state closes the system and can be specified generally, for example, as  $a = a(P, \rho)$ . It is useful as a first step to combine the continuity and energy equation, which gives

$$\frac{DP}{Dt} + \rho a^2 \frac{\partial u}{\partial x} = 0. \quad (2.24)$$

Consider a shock propagating with speed  $U(t)$  and position  $X(t)$  into an otherwise uniform flow with conditions given by  $u_1$ ,  $P_1$ , and  $\rho_1$ , where subscript 1 denotes the upstream state. The derivation in the case of a nonuniform upstream flow is given by Schoeffler and Shepherd (2023). Although the shock is unsteady, the discontinuous jump in flow variables can still be found by control volume analysis and is given instantaneously at all time by the Rankine-Hugoniot equations,

$$\rho_2 w_2 = \rho_1 w_1, \quad (2.25)$$

$$P_2 + \rho_2 w_2^2 = P_1 + \rho_1 w_1^2, \quad (2.26)$$

$$h_2 + w_2^2/2 = h_1 + w_1^2/2, \quad (2.27)$$

where subscript 2 denotes the post-shock state,  $h$  is the enthalpy, and  $w$  is the flow velocity in the shock-fixed frame, i.e.,  $w = U - u$ . With an equation of state, the

Rankine-Hugoniot equations can be solved for the post-shock state, where each quantity can be written generally as

$$\begin{aligned}
 w_2 &= w_2(w_1, P_1, \rho_1), \\
 P_2 &= P_2(w_1, P_1, \rho_1), \\
 \rho_2 &= \rho_2(w_1, P_1, \rho_1), \\
 a_2 &= a_2(P_2, \rho_2), \\
 &= a_2(w_1, P_1, \rho_1).
 \end{aligned} \tag{2.28}$$

Assuming  $u_1 = 0$ , then  $w_1 = U(t)$ . Since  $w_1 = U(t)$  is not constant, the post-shock quantities are varying with time, and so the flow is nonuniform. The resulting gradients behind the shock are described by the conservation equations, (2.22) and (2.24), evaluated at the shock discontinuity, i.e.,

$$\begin{aligned}
 \left. \frac{Du}{Dt} \right|_2 + \frac{1}{\rho_2} \left. \frac{\partial P}{\partial x} \right|_2 &= 0, \\
 \left. \frac{DP}{Dt} \right|_2 + \rho_2 a_2^2 \left. \frac{\partial u}{\partial x} \right|_2 &= 0.
 \end{aligned} \tag{2.29}$$

The time-variation of any post-shock variable can be obtained by differentiating (2.28), e.g., for the post-shock pressure,

$$\frac{dP_2}{dt} = \frac{\partial P_2}{\partial w_1} \dot{U}(t), \tag{2.30}$$

where  $\dot{U}(t)$  is the shock acceleration. The partial derivative coefficient is only a function of the shock Hugoniot and instantaneous shock speed. The time derivative of the post-shock quantity  $P_2$  is equivalent to a total derivative of the field variable evaluated at the shock's position,  $P(X(t), t)$ , i.e.,

$$\frac{dP_2}{dt} = \left. \frac{\partial P}{\partial t} \right|_2 + U(t) \left. \frac{\partial P}{\partial x} \right|_2. \tag{2.31}$$

This derivative is analogous to the material derivative in the conservation equations and so is referred to here as a shock derivative. Material derivatives can be expressed in terms of shock derivatives by

$$\left. \frac{D}{Dt} \right|_2 = \frac{d}{dt} + (u_2 - U) \left. \frac{\partial}{\partial x} \right|_2. \tag{2.32}$$

Applying (2.32) to the (2.29) gives

$$\begin{aligned}
 \frac{du_2}{dt} + (u_2 - U)u_{x,2} + \frac{P_{x,2}}{\rho_2} &= 0, \\
 \frac{dP_2}{dt} + (u_2 - U)P_{x,2} + \rho_2 a_2^2 u_{x,2} &= 0,
 \end{aligned} \tag{2.33}$$



where subscript notation has been adopted for partial differentiation. The equations can now be combined to eliminate either the pressure or velocity gradient. Eliminating the pressure gradient and simplifying gives

$$\frac{dP_2}{dt} + \rho_2 w_2 \frac{du_2}{dt} + \rho_2 a_2^2 \eta u_{x,2} = 0, \quad (2.34)$$

where

$$\eta = 1 - \frac{w_2^2}{a_2^2}. \quad (2.35)$$

The shock derivatives can be expanded in terms of the shock acceleration by differentiating (2.28) as shown in (2.30). Equation (2.34) becomes

$$u_{x,2} = -\frac{1}{\rho_2 a_2^2 \eta} \left[ \frac{\partial P_2}{\partial w_1} + \rho_2 w_2 \frac{\partial u_2}{\partial w_1} \right] \dot{U}. \quad (2.36)$$

This result can be expressed compactly as

$$u_{x,2} = F \dot{M}, \quad (2.37)$$

where  $\dot{M} = \dot{U}/a_1$  and

$$F = -\frac{a_1}{\rho_2 a_2^2 \eta} \left[ \frac{\partial P_2}{\partial w_1} + \rho_2 w_2 \frac{\partial u_2}{\partial w_1} \right]. \quad (2.38)$$

The coefficient  $F$  is dimensionless and only a function of the shock Hugoniot. Equation (2.37) represents one of a family of shock-change equations that relate first-order derivatives of post-shock flow variables with the shock acceleration. All first-order shock-change equations can be expressed similarly in terms of a coefficient multiplying the shock acceleration to give any post-shock flow derivative.

Shock-change equations for all other post-shock flow derivatives can be derived using (2.37). The equation for the pressure gradient can be derived from the momentum equation (2.22),

$$\begin{aligned} \frac{1}{\rho_1 a_1} \frac{\partial P}{\partial x} \Big|_2 &= -\frac{\rho_2}{\rho_1 a_1} \frac{Du}{Dt} \Big|_2, \\ &= -\frac{\rho_2}{\rho_1 a_1} \left[ \frac{du_2}{dt} - w_2 \frac{\partial u}{\partial x} \Big|_2 \right], \\ &= -\frac{\rho_2}{\rho_1} \left[ \frac{\partial u_2}{\partial w_1} - \frac{w_2}{a_1} F \right] \dot{M}, \\ &= G \dot{M}, \end{aligned} \quad (2.39)$$

where  $G$  is the corresponding coefficient for the pressure gradient. The shock-change equation for the density gradient can be obtained from (2.21) and is

$$\left. \frac{a_1}{\rho_1} \frac{\partial \rho}{\partial x} \right|_2 = H \dot{M}, \quad (2.40)$$

$$H = \frac{a_1}{\rho_1 w_2} \left( a_1 \frac{\partial \rho_2}{\partial w_1} + \rho_2 F \right). \quad (2.41)$$

With  $G$  and  $H$ , coefficients for any other thermodynamic quantities can be derived using the equation of state. For example, the sound speed gradient is given by

$$\left. \frac{\partial a}{\partial x} \right|_2 = E \dot{M}, \quad (2.42)$$

$$E = \rho_1 a_1 \left. \frac{\partial a}{\partial P} \right|_2 G + \frac{\rho_1}{a_1} \left. \frac{\partial a}{\partial \rho} \right|_2 H, \quad (2.43)$$

where the partial derivative coefficients are thermodynamic functions.

All of the above are first-order shock-change equations. By differentiating the conservation equations, a similar procedure of substitution can be used to obtain higher-order shock-change equations. The gradients of (2.22) and (2.24) are

$$\frac{\partial}{\partial x} \left( \frac{Du}{Dt} + \frac{1}{\rho} \frac{\partial P}{\partial x} \right) = 0, \quad (2.44)$$

$$\frac{\partial}{\partial x} \left( \frac{DP}{Dt} + \rho a^2 \frac{\partial u}{\partial x} \right) = 0. \quad (2.45)$$

Expanding the derivatives gives

$$u_{tx} + u_x^2 + uu_{xx} - \frac{1}{\rho^2} \rho_x P_x + \frac{1}{\rho} P_{xx} = 0, \quad (2.46)$$

$$P_{tx} + u_x P_x + u P_{xx} + \rho_x a^2 u_x + 2\rho a a_x u_x + \rho a^2 u_{xx} = 0, \quad (2.47)$$

and by re-expressing time derivatives as shock derivatives we have

$$\frac{du_x}{dt} - w u_{xx} + u_x^2 - \frac{1}{\rho^2} \rho_x P_x + \frac{1}{\rho} P_{xx} = 0, \quad (2.48)$$

$$\frac{dP_x}{dt} - w P_{xx} + u_x P_x + \rho_x a^2 u_x + 2\rho a a_x u_x + \rho a^2 u_{xx} = 0. \quad (2.49)$$

Eliminating  $P_{xx}$  gives a single equation,

$$\begin{aligned} \frac{dP_x}{dt} + \rho w \frac{du_x}{dt} + \rho w u_x^2 - \frac{w}{\rho} \rho_x P_x + u_x P_x \\ + \rho_x a^2 u_x + 2\rho a a_x u_x + (\rho a^2 - \rho w^2) u_{xx} = 0. \end{aligned} \quad (2.50)$$

The shock derivatives of post-shock gradients can be found from differentiating the first-order shock-change equations, i.e.,

$$\frac{1}{\rho_1 a_1} \frac{dP_{x,2}}{dt} = G' \dot{M}^2 + G \ddot{M}, \quad (2.51)$$

$$\frac{du_{x,2}}{dt} = F' \dot{M}^2 + F \ddot{M}, \quad (2.52)$$

where  $\ddot{M}$  is the second time derivative of the shock Mach number, and  $F'$  and  $G'$  are

$$F' = \frac{dF}{dM}, \quad G' = \frac{dG}{dM}. \quad (2.53)$$

Therefore, by replacing all post-shock gradients with their corresponding shock-change equation and grouping terms, equation (2.50) can be simply expressed as

$$\ddot{M} + K \dot{M}^2 + L a_1 u_{xx,2} = 0, \quad (2.54)$$

where  $K$  and  $L$  are second-order shock-change coefficients given by

$$K = \left[ G' + MF' + MF^2 - \frac{\rho_1^2}{\rho_2^2} MGH + FG + \frac{a_2^2}{a_1^2} HF + 2 \frac{\rho_2 a_2}{\rho_1 a_1} EF \right] (G + MF)^{-1}, \quad (2.55)$$

$$L = \frac{\rho_2 a_2^2}{\rho_1 a_1^2} \eta (G + MF)^{-1}. \quad (2.56)$$

Similar to the first-order results,  $K$  and  $L$  are dimensionless and valid for an arbitrary equation of state, where the only assumption has been that the flow is in thermodynamic equilibrium. Equation (2.54) is the desired second-order shock-change equation for  $u_{xx}$ .

Sharma and Radha (1994) instead formulate a second-order shock-change equation in terms of  $P_{xx}$ , and Best (1991) uses  $\partial_t(P_t + \rho a u_t)$ . These equations can be derived using (2.54). To obtain the equation for  $P_{xx,2}$ , (2.54) is substituted into (2.48), which gives upon simplification

$$\ddot{M} + J \dot{M}^2 + N \frac{P_{xx,2}}{\rho_1} = 0, \quad (2.57)$$

where the coefficients are

$$J = \frac{F' + M \frac{\rho_1 K}{\rho_2 L} + F^2 - \frac{\rho_1^2}{\rho_2^2} GH}{F + \frac{\rho_1 M}{\rho_2 L}}, \quad (2.58)$$

$$N = \frac{\rho_1}{\rho_2} \left( F + \frac{\rho_1 M}{\rho_2 L} \right)^{-1}. \quad (2.59)$$

The coefficients for Best's formulation are more complex and therefore derived separately in Appendix A.2.5.

For a perfect gas, the equation of state is given by the ideal gas law, and the heat capacities are constant. All of the shock-change coefficients can be re-expressed as functions of only  $M$  and  $\gamma$ . Some of the coefficients are given here explicitly,

$$F = -\frac{2}{\gamma + 1} \frac{3M^2 + 1}{M(M^2 - 1)}, \quad (2.60)$$

$$G = -\frac{2(M^2 + 1)}{(\gamma - 1)M^2 + 2} - \frac{2(3M^2 + 1)}{(\gamma + 1)(M^2 - 1)}, \quad (2.61)$$

$$H = -\frac{2(\gamma + 1)M^2(3(\gamma - 1)M^4 - (\gamma - 3)M^2 + 2(\gamma + 2))}{(M^2 - 1)((\gamma - 1)M^2 + 2)^3}, \quad (2.62)$$

$$K = \frac{-3M((9\gamma - 7)M^4 + 10(\gamma + 1)M^2 - 3\gamma + 13)}{(M^2 - 1)((7\gamma - 5)M^4 + 2(\gamma + 5)M^2 - \gamma + 3)}, \quad (2.63)$$

$$L = -\frac{(\gamma + 1)(M^2 - 1)^2((\gamma - 1)M^2 + 2)}{2(7\gamma - 5)M^4 + 4(\gamma + 5)M^2 - 2\gamma + 6}. \quad (2.64)$$

The coefficient for the sound speed gradient,  $E$ , can be obtained from (2.43) using the perfect gas equation of state,

$$a = \sqrt{\gamma P / \rho}. \quad (2.65)$$

Using the above formulae, Figure 2.2 plots the coefficients for varying  $M$  and  $\gamma$ . Except for  $E$ , all of the coefficients are uniformly negative.  $E$  crosses zero for some value of  $M$  and  $\gamma$ , which means that when a shock decays through this Mach number, the sound speed gradient changes sign from negative to positive. Except for  $L$ , all of the coefficients exhibit an inverse dependence on  $M$ , tending toward negative infinity as  $M \rightarrow 1$ . This is, of course, partially a consequence of how we have chosen to define the coefficients. They could have instead been defined so that their product with the a flow gradient gives the shock acceleration. In Figure 2.2(e), the inverse dependence of  $K$  on  $M$  is particularly striking, with curves for different  $\gamma$  nearly indistinguishable. To see this better,  $K^{-1}$  is plotted in Figure 2.3, illustrating that it is nearly linear in its dependence on  $M$  with slopes converging as  $M \rightarrow 1$ .

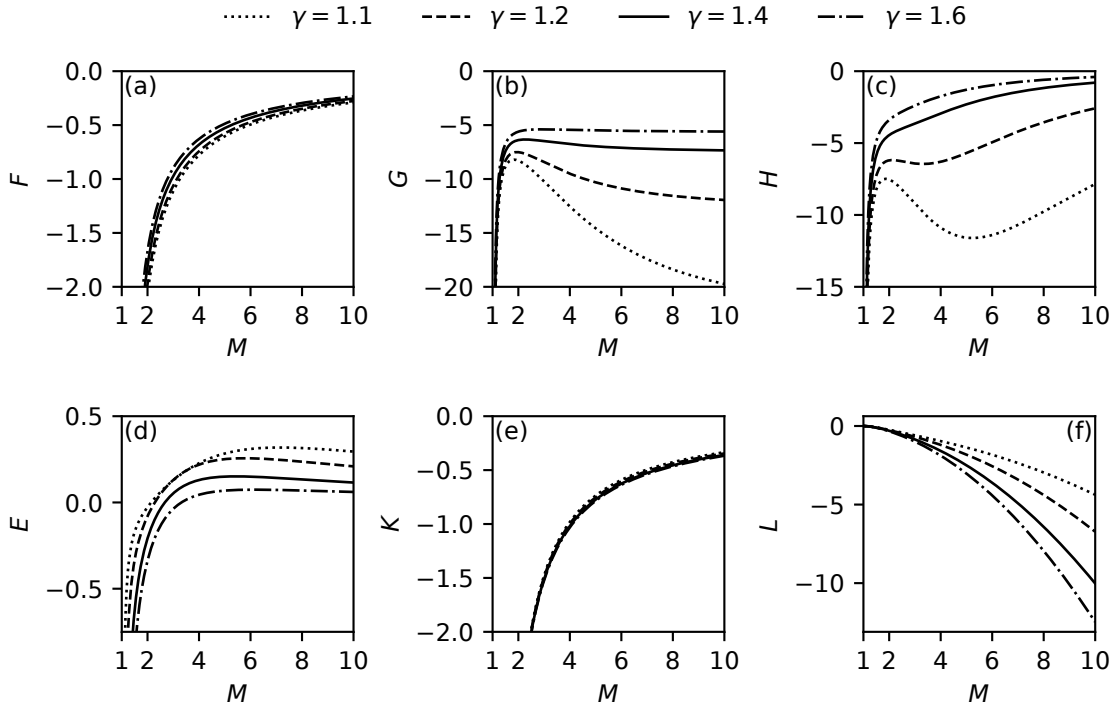


Figure 2.2: Shock-change coefficients in a perfect gas for a range of  $M$  and  $\gamma$ .

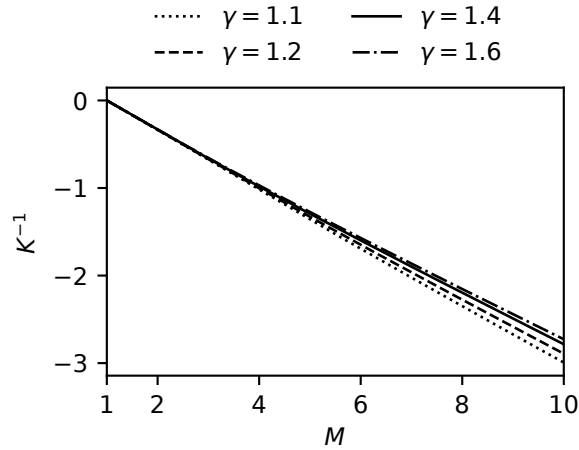


Figure 2.3:  $K^{-1}$  for a range of  $M$  and  $\gamma$ .

### 2.3 Shock Decay Model

For a known incident simple wave, the unperturbed second velocity gradient  $u_{xx,2}^{(0)}$  can be used to close the shock-change equation (2.54) and solve for the shock Mach number time evolution. As discussed in Section 2.1,  $u_{xx,2}^{(0)} = 0$  exactly for centered expansion waves in a perfect gas and can be applied as a model for arbitrary simple waves with a general equation of state. By applying this to (2.54), then the following

shock propagation equation is obtained

$$\begin{aligned}\ddot{M} + K\dot{M}^2 &= 0, \\ M(0) &= M_0, \\ \dot{M}(0) &= \dot{M}_0,\end{aligned}\tag{2.66}$$

where  $K = K(M)$  is given by (2.55) for a general equation of state and (2.63) for a perfect gas. The system of equations (2.66) describes an initial value problem, which can be numerically integrated for known initial conditions and equation of state to obtain the solution  $M(t)$ .

For a perfect gas, the near linear behavior of  $K^{-1}$  in Figure 2.3 suggests approximating it as

$$K \approx K(M_0) \frac{M_0 - 1}{M - 1},\tag{2.67}$$

where  $K(M_0)$  is the value of  $K$  at the initial condition. With this approximation, (2.66) can be integrated analytically, and the solution is

$$\begin{aligned}\delta(t) &= \frac{1}{(1 + \beta t/\alpha)^\alpha}, \\ \delta(t) &= \frac{M(t) - 1}{M_0 - 1}, \quad \beta = \frac{-\dot{M}_0}{M_0 - 1}, \quad \alpha = -\frac{1}{K(M_0)(M_0 - 1) + 1}.\end{aligned}\tag{2.68}$$

The solution has the functional form of a power law, where the exponent  $\alpha$  is determined by the function  $K$ .  $\beta$  is the initial shock decay rate and provides the time scale for the shock's evolution.

The shock decay model (2.66) was integrated for a range of initial shock Mach numbers and  $\gamma$  using a fourth order Runge-Kutta scheme. The results are shown in Figure 2.4 with the power-law approximation (2.68), where the time coordinate is scaled by the initial shock acceleration. Compared with numerically integrating (2.66), the approximate solution (2.68) is reasonably accurate with errors larger for increasing  $\gamma$  and  $M_0$ . For  $M_0 = 10$  and  $1 \leq \gamma \leq 5/3$ , the error given by the approximate solution when  $\delta = 0.4$  is less than 1.4%, and when  $\delta = 0.2$  it is less than 4.7%. Values for the power law exponent,  $\alpha$ , are plotted in Figure 2.5.

The shock acceleration can be obtained by differentiating (2.68) and is

$$\frac{\dot{M}}{M_0 - 1} = \frac{-\beta}{(1 + \beta t/\alpha)^{\alpha+1}}\tag{2.69}$$

$$\tau_d = \left( \frac{-\dot{M}}{M - 1} \right)^{-1} = \frac{1}{\beta} + \frac{t}{\alpha}.\tag{2.70}$$

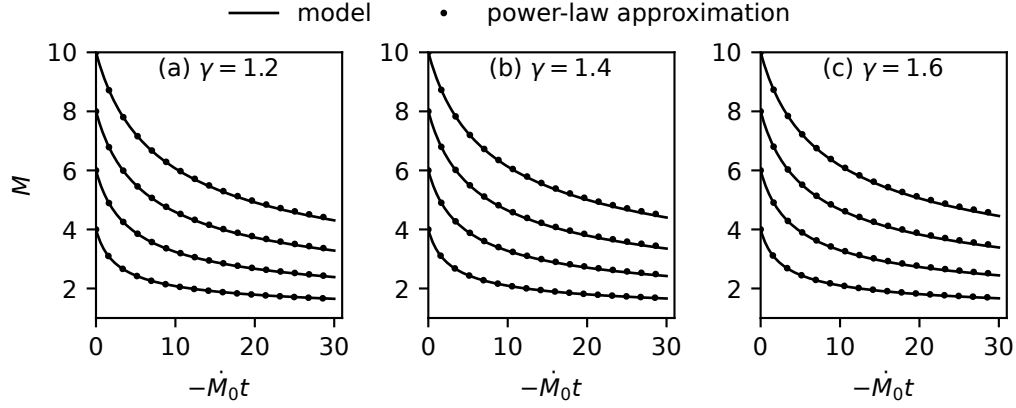


Figure 2.4: Shock decay model and its power-law approximate solution for a perfect gas with (a)  $\gamma = 1.2$ , (b)  $\gamma = 1.4$ , and (c)  $\gamma = 1.6$ .

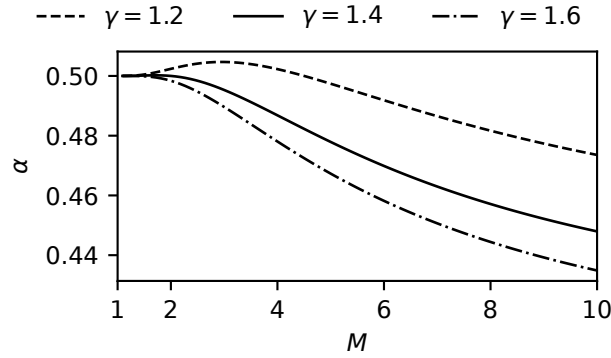


Figure 2.5: Variation in  $\alpha$  with  $M$  and  $\gamma$ .

The time scale of local unsteadiness for a particle processed by the decaying shock is given by  $\tau_d$ . Equation (2.70) shows that  $\tau_d$  increases linearly with time as the shock decays.

The weak shock limit for  $\alpha$  is obtained from a series expansion about  $M_0 = 1$  and is

$$\alpha = \frac{1}{2} + O((M_0 - 1)^4). \quad (2.71)$$

The leading-order term is the  $1/2$  power that is well known to be the solution for weak shock decay from Friedrichs (1948). Notably, this approximation is good to four orders in  $(M_0 - 1)$  and independent of  $\gamma$ .

The strong shock limit,  $1/M_0 \rightarrow 0$ , gives

$$\alpha = \frac{7\gamma - 5}{4(5\gamma - 4)} + O(M_0^{-2}), \quad (2.72)$$

where in this case  $\delta = M/M_0$  and  $\beta = -\dot{M}_0/M_0$ .

The power-law approximation has important correspondence with self-similar theories. Self-similar solutions typically apply in some asymptotic limit for a given problem (Barenblatt and Zel'dovich, 1972). For strong shocks, in the limit of large time, when  $\beta t/\alpha \gg 1$ , the typical formulation of self-similar shock propagation is obtained,

$$M \sim At^{-\alpha}, \quad (2.73)$$

where  $A = M_0(\beta/\alpha)^{-\alpha}$  and  $\alpha$  is interpreted as the similarity exponent. In our model,  $\alpha$  for strong shocks is given by (2.72), which provides a good approximation for the similarity exponents reported by Zel'dovich and Raizer (1967) for the problem of an impulsive load (note that the exponent is defined differently here). The agreement is not surprising since the self-similar solution results in  $u_{xx} = 0$ , so the assumptions of the present model will yield exact results for such cases. This suggests that the general formulation for  $K$  could be used to obtain similarity exponents for other equations of state by examining the limit of  $M \rightarrow \infty$ .

## 2.4 Initial Shock Decay Rate

When a simple wave first overtakes an initially steady shock, then the initial shock acceleration,  $\dot{M}_0$ , is required to implement the shock decay model (2.66). This quantity is not generally known and must be estimated. Rough estimates can be obtained by using a first-order shock-change equation with a gradient in the incident simple wave, however the first-order gradient is instantaneously perturbed by the interaction. A clear illustration of this is to compare the velocity and pressure gradients for a given shock acceleration, which cannot simultaneously match the gradients in the simple wave. The ratio of the pressure gradient to the velocity gradient in the incident simple wave is

$$\frac{1}{\rho_1 a_1} \frac{P_x}{u_x} = \frac{\rho_2 a_2}{\rho_1 a_1}, \quad (2.74)$$

and the ratio behind a shock is

$$\frac{1}{\rho_1 a_1} \frac{P_x}{u_x} = \frac{G}{F}. \quad (2.75)$$

These two quantities are generally not equal. For moderate strength shocks in gases with  $1 \leq \gamma \leq 5/3$ , then

$$\frac{G}{F} \frac{\rho_1 a_1}{\rho_2 a_2} > 1, \quad (2.76)$$



which increases for greater  $M$  and smaller  $\gamma$ . Clearly, both the pressure and velocity gradients behind a decaying shock wave cannot be simultaneously matched to the incident gradients of a simple wave. The wave reflected by the interaction is necessary to match flow gradients with the values given by shock-change equations. The initial gradients are perturbations of the incident values.

The perturbed post-shock state can be modeled as

$$\begin{aligned} u &= u^{(0)} + u^{(1)}, \\ P &= P^{(0)} + P^{(1)}, \end{aligned} \quad (2.77)$$

where superscript (0) terms describe the incident simple wave, and superscript (1) terms describe the perturbation by the reflected wave.  $u$  and  $P$  are the flow variables in the general region behind the shock. The approximation is that  $u^{(0)} \gg u^{(1)}$  and  $P^{(0)} \gg P^{(1)}$ . Then, to leading order, the  $C^+$  characteristic equation is (Landau and Lifshitz, 1987, §104)

$$\left[ \frac{\partial}{\partial t} + (u^{(0)} + a^{(0)}) \frac{\partial}{\partial x} \right] \left( u^{(1)} + \frac{P^{(1)}}{\rho^{(0)} a^{(0)}} \right) = 0, \quad (2.78)$$

and so gradients along  $C^+$  characteristics are given by

$$u_x^{(1)} + \frac{P_x^{(1)}}{\rho^{(0)} a^{(0)}} - \frac{P^{(1)}}{(\rho^{(0)} a^{(0)})^2} \frac{\partial \rho^{(0)} a^{(0)}}{\partial x} = 0. \quad (2.79)$$

When the simple wave initially overtakes the shock, the reflected wave only perturbs the derivatives of post-shock flow variables, so that at the shock

$$\begin{aligned} u_2^{(1)} &= 0, \\ P_2^{(1)} &= 0, \end{aligned} \quad (2.80)$$

and (2.79) becomes

$$u_{x,2}^{(1)} + \frac{P_{x,2}^{(1)}}{\rho_2 a_2} = 0. \quad (2.81)$$

The perturbation (2.77) can be applied to the shock-change equations, giving

$$F \dot{M} = u_{x,2}^{(0)} + u_{x,2}^{(1)}, \quad (2.82)$$

$$\rho_1 a_1 G \dot{M} = P_{x,2}^{(0)} + P_{x,2}^{(1)}. \quad (2.83)$$

From a  $C^-$  characteristic through the simple wave, the unperturbed gradients are related by

$$u_{x,2}^{(0)} - \frac{P_{x,2}^{(0)}}{\rho_2 a_2} = 0. \quad (2.84)$$

Equations (2.81) and (2.84) can be used to eliminate the pressure gradient terms from (2.83), which gives

$$\rho_1 a_1 G \dot{M} = \rho_2 a_2 (u_{x,2}^{(0)} - u_{x,2}^{(1)}), \quad (2.85)$$

and (2.85) can be combined with (2.82) to eliminate the perturbation term,  $u_{x,2}^{(1)}$ . The result is

$$\frac{1}{2} \left( F + \frac{\rho_1 a_1}{\rho_2 a_2} G \right) \dot{M} = u_{x,2}^{(0)}. \quad (2.86)$$

For a given simple wave incident upon a shock with initial velocity gradient  $u_{x,2}^{(0)}$ , the shock-change equation (2.86) can be used to compute the initial shock acceleration, where the resulting velocity and pressure gradients are consistent with an acoustic perturbation to the incident simple wave. It is convenient to express (2.86) with a new coefficient,

$$B = \frac{1}{2} \left( F + \frac{\rho_1 a_1}{\rho_2 a_2} G \right), \quad (2.87)$$

the inverse of which is plotted in figure 2.6 for a perfect gas with various  $\gamma$ .

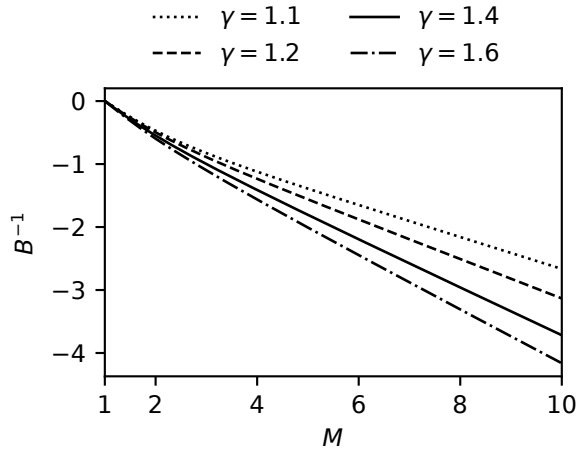


Figure 2.6:  $B^{-1}$  for a range of  $M$  and  $\gamma$ .

Equation (2.86) can be used to calculate the initial shock decay rate,  $\beta$ , defined by (2.68). For a centered wave in a perfect gas,  $u_{x,2}^{(0)}$  is given by (2.11), where  $t$  is the time when the wave first intersects the shock. Figure 2.7 plots  $\beta$  for various  $\gamma$ .

## 2.5 Numerical Simulations

### 2.5.1 Methods

Numerical simulations were performed using the open-source finite-volume CFD toolbox OpenFOAM-9 (Greenshields, 2021) and the solvers implemented in the

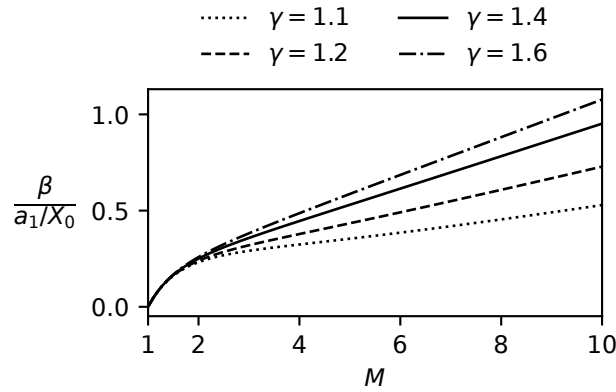


Figure 2.7: Variation in  $\beta$  with  $M$  and  $\gamma$ , where  $\beta$  is given by (2.68).

library blastFoam-5 (Heylman et al., 2021). The equations of motion are solved in conservative form, so that the tracked variables are  $\{\rho, u, e\}$ . Fluxes are interpolated using the scheme by Kurganov et al. (2001) and limited using the functions by van Albada et al. (1997) and van Leer (1974). Second-order Runge-Kutta time integration was used. Various validation cases are included in the blastFoam library, including the relevant test problem of interacting blast waves from Woodward and Colella (1984).

For simulations of centered expansion waves, the initial condition corresponds with the time when the piston impulsively stops,  $t = 0$ , as described in section 2.1. At this time, post-shock conditions for  $P$ ,  $T$ , and  $u$  are uniform from the left domain boundary,  $x = 0$ , up to the shock position at  $x = 1$ . A zero velocity boundary condition at  $x = 0$  causes a centered expansion to form as time advances.

For all simulations, the grid resolution was  $2.5 \cdot 10^3$  cells per unit length, i.e., the initial distance of the shock from the left boundary. Time steps were adjusted to preserve a maximum Courant number of 0.25. Time steps were written to file at a rate adjusted based on the expected initial shock acceleration. The criterion chosen was  $\beta \Delta t = 0.001$ , where  $\Delta t$  is the sampling interval. Simulations were run until shocks had decayed to approximately  $\delta = 0.4$ . The domain lengths were adjusted accordingly. Typical simulation domains were  $5 \cdot 10^4$  cells with  $3 \cdot 10^3$  time steps written to file. A grid-resolution study including post-processing methods was performed for  $M = 10$  and  $\gamma = 1.4$  for resolutions up to  $10^4$  per unit length and confirmed grid independence of the results.

Shock speeds were measured from simulation results using a cross-correlation al-

gorithm. For every pair of sampled time steps, the cross-correlation of the pressure gradient was computed, and the resulting correlation peak provides an estimate for the shock displacement. Because the numerical shock profile approximates an error function, pressure gradients and their cross correlation are accurately modeled by a Gaussian. Hence, the computed cross-correlations were fit to a Gaussian of the form

$$f(x) = ae^{b(x-x_0)^2}, \quad (2.88)$$

where  $a$ ,  $b$ , and  $x_0$  are fit parameters.  $x_0$  provides a sub-grid-resolution estimate for the shock displacement. This algorithm was chosen for giving much less noisy data than, for example, computing the shock speed from the post-shock pressure or directly differentiating shock position data. Figure 2.8 illustrates the algorithm. In (a), two pressure gradients are shown, and their cross-correlation is fit to a Gaussian in (b).

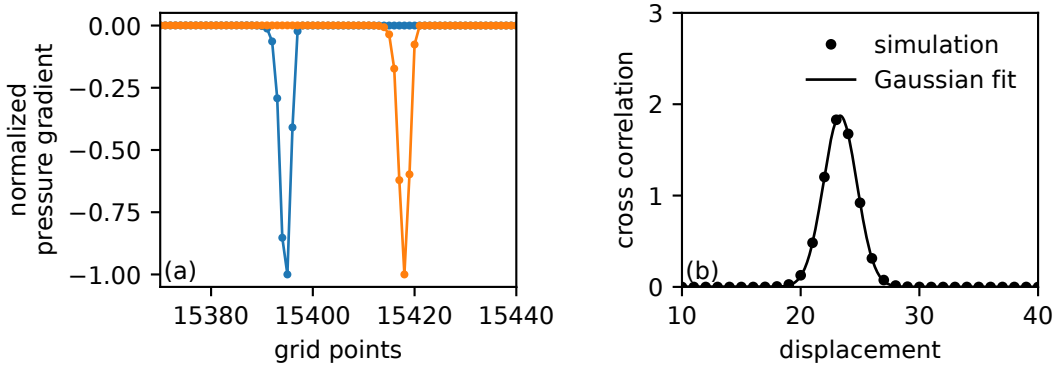


Figure 2.8: Example of shock displacement calculation using cross correlation of pressure gradients.

In order to quantify residual terms in the second-order shock-change equation (2.54), it was necessary to compute  $\ddot{M}$ , which requires numerically differentiating  $M$  twice. This is prone to significant noise, so a smoothing algorithm was employed. Data for  $M$  were smoothed using the Whitaker smoother as described by Eilers (2003). This algorithm was chosen because it does not require interpolation at domain boundaries and so distortion is reduced when compared to other common smoothers. Distortion is nonetheless nonzero, so for estimation of the initial shock acceleration,  $\dot{M}_0$ , a cubic polynomial was fit to the first 100 points of  $M$ , and its derivative was evaluated at the time when the shock begins decaying.

The decay model (2.66) was solved numerically using a fourth-order Runge-Kutta integrator, where  $\dot{M}_0$  was computed using (2.86). For perfect gas calculations,  $K$  is given by (2.63). For calculations of strong shock waves in equilibrium air,  $K$  is given by (2.55), and all shock-change coefficients were computed using Cantera (Goodwin et al., 2021) and the Shock and Detonation Toolbox (Kao et al., 2020). This was done by computing the equilibrium post-shock state for a range of shock speeds, and numerically differentiating the resulting data.

Thermodynamics for equilibrium air composed of 21%  $O_2$  and 79%  $N_2$  were computed with Cantera using the ninth-order polynomials given by McBride et al. (2002) including ionic species. For implementation of equilibrium air in OpenFOAM, the equation of state was specified using tabular look-up methods available in blastFoam, where  $P$  and  $T$  are given in terms of tabular data of  $\rho$  and  $e$ . The data tables were generated using Cantera.

### 2.5.2 Centered Expansion in a Perfect Gas

The time evolution of velocity, pressure, and their gradients is shown in figure 2.9 for a representative case with  $M_0 = 7$  and  $\gamma = 1.4$ . Artifacts in the gradients at the shock front were eliminated by downsampling the data by a factor of five before computing the gradient. The leftmost contour corresponds to a time just before the expansion wave is incident upon the shock, and subsequent contours are after the shock has begun decaying. The interaction reflects a left-propagating wave along  $C^-$  characteristics, which introduces kinks in the velocity and pressure profiles. Although not obvious from (a) and (c), they are apparent in the velocity and pressure gradients in (b) and (d) as step discontinuities. This discontinuity propagates along the leading characteristic of the reflected wave and in (b) is not to be mistaken for a small numerical artifact that is apparent in early profiles. The pressure gradient in (d) shows a kink between the step discontinuity and the shock front, which corresponds to the particle path that bounds the region of nonuniform entropy. These features in both the velocity and pressure profiles are clearly weak compared with the gradients introduced by the incident centered wave, which is consistent with the claim made in section 2.4 that they can be modeled as perturbations.

The initial shock acceleration,  $\dot{M}_0$ , was measured from simulation results and compared with the value predicted using three estimates. The relative error of these three estimates is shown in figure 2.10 for three values of  $\gamma$  and  $M_0$  ranging from 1.5 to 10, where the relative error is given by  $\dot{M}_{0,\text{est}}/\dot{M}_{0,\text{sim}} - 1$ . As discussed in

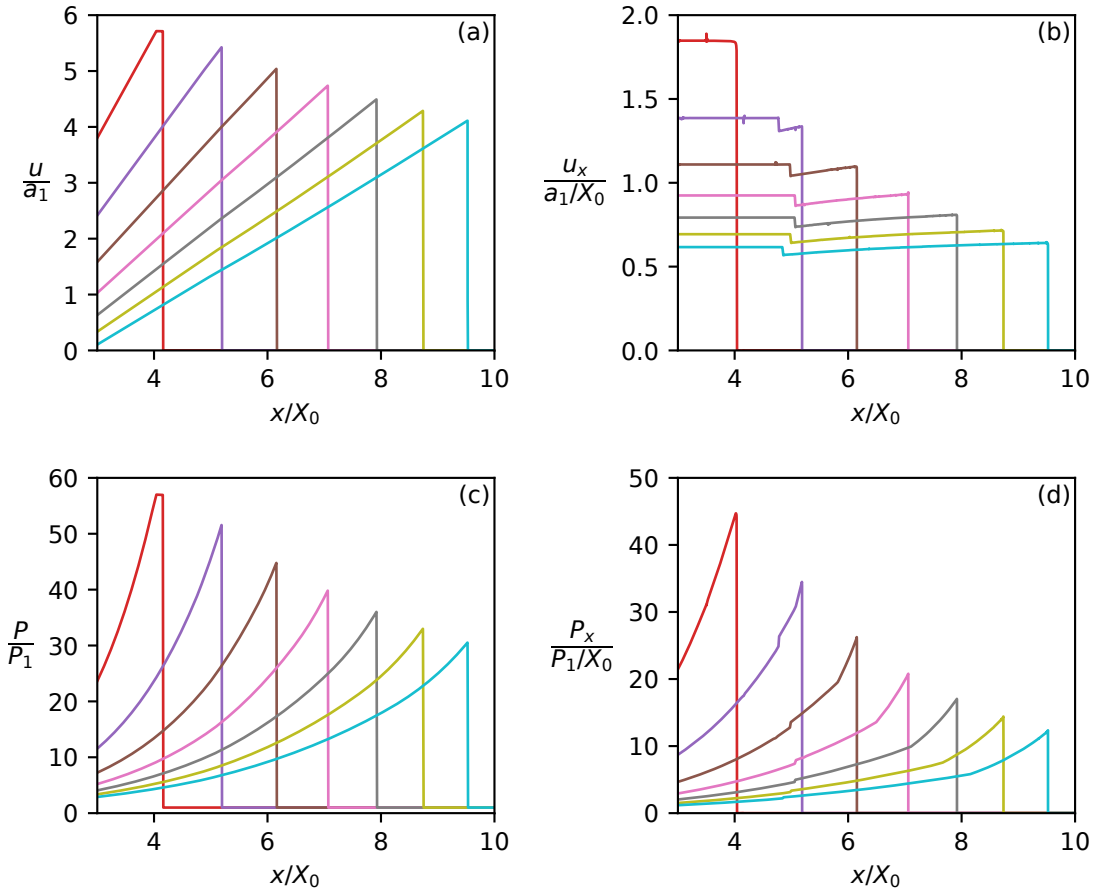


Figure 2.9: Early evolution of velocity, pressure, and their gradients for  $M_0 = 7$  and  $\gamma = 1.4$ . The leftmost profile corresponds to  $t = 0.381\sqrt{\gamma}$ , just prior to wave incidence, and  $\Delta t = 0.127\sqrt{\gamma}$  between each subsequent profile.

section 2.4,  $u_{x,2}^{(0)}$  and  $P_{x,2}^{(0)}$  are the velocity and pressure gradients in the incident centered expansion, unperturbed by the reflected wave from the interaction with the shock. Using these quantities and their shock-change equations directly introduces significant error for small  $\gamma$  and large  $M_0$ . The method described in section 2.4 uses the shock-change coefficient,  $B$ , that takes into account the effect of a weak acoustic perturbation and is effectively an average of the two other methods. The result is that  $u_{x,2}^{(0)}/B$  is a consistently more accurate prediction of  $\dot{M}_0$ . The average error is uniformly 0.5%, and this is attributed in part to the numerical methods.

In Figure 2.11 results from a simulation for  $M_0 = 3$  and  $\gamma = 1.4$  are used to evaluate the accuracy of various theories from prior work including the new model given by (2.66). Solutions by Chandrasekhar (1943), Brinkley and Kirkwood (1947), Friedrichs (1948), Sharma et al. (1987), Best (1991), and Sharma and Radha (1994)

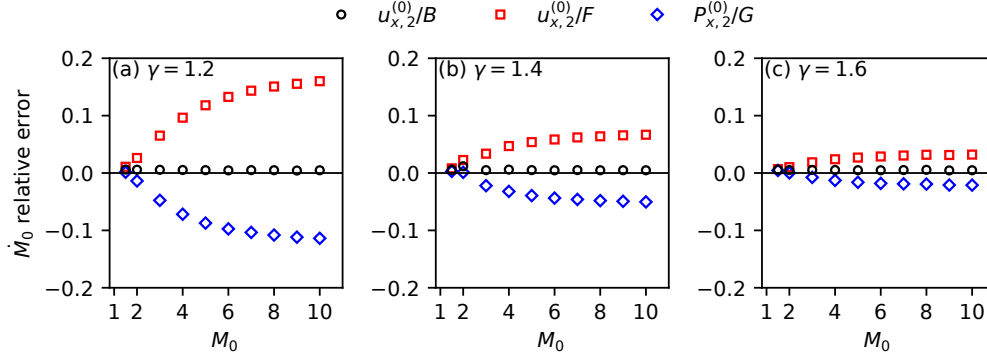


Figure 2.10: Estimates of  $\dot{M}_0$  using shock-change equations with unperturbed gradients in incident simple wave compared with values measured from numerical simulations.

are plotted. Details on implementation of these theories are described in Appendix A.2. It is important to note that, except for Friedrichs (1948) and Sharma et al. (1987), all theories require the initial shock acceleration to be known, so the solution (2.86) was used for this. Clearly, the present model is most accurate, nearly indistinguishable from the simulation results. Theories by Chandrasekhar (1943) and Brinkley and Kirkwood (1947) are both also quite accurate, and so they are compared with the present model and simulation results for a stronger shock,  $M_0 = 7$ , in Figure 2.12. In this case, the other models begin to diverge from the simulation results, but the present model still closely agrees.

The present model is compared to three simulation cases in Figure 2.13 with  $M_0 = 3$ ,  $M_0 = 6$ , and  $M_0 = 9$  for  $\gamma = 1.4$ . The time-evolution of the relative error between the model and simulation, given by  $M_{\text{model}}/M_{\text{sim}} - 1$ , is shown in (b). Shock decay is slightly faster for the model, such that errors are uniformly negative. For  $M_0 = 3$ , it appears that the error approaches a constant value, but for  $M_0 = 6$  and  $M_0 = 9$  it is still increasing in magnitude. Although the duration in time of each simulation is not the same, they capture the same amount of shock decay,  $\delta = 0.4$ .

Since errors are largest at final simulation time, they are plotted in Figure 2.14 for all simulated cases. The dependence on  $\gamma$  is shown with additional data for  $M_0 = 7$  in (b). Error is larger for smaller  $\gamma$  and increasing  $M_0$ . For shock decay up to  $\delta = 0.4$ , error for  $\gamma = 1.2$  is less than 3%, error for  $\gamma = 1.4$  is less than 2%, and error for  $\gamma = 1.6$  is less than 1%. For  $M_0 = 7$ , error is nearly 7% for  $\gamma = 1.01$ .

Other than the estimate for  $\dot{M}_0$ , the only assumption in the model is that  $u_{xx,2} = 0$ , and so the nonzero errors in Figure 2.14 illustrate that this is not exactly true. Although

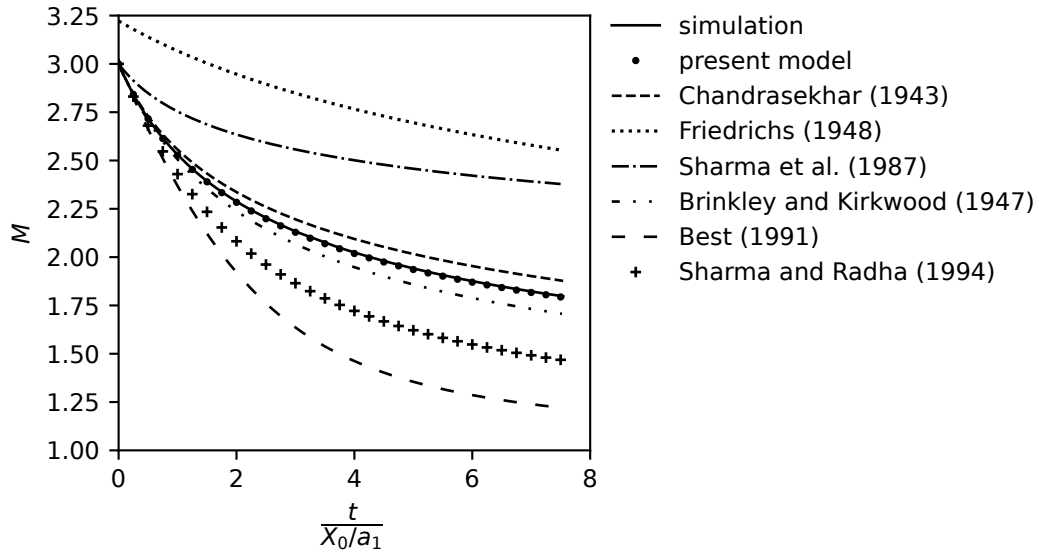


Figure 2.11: Comparison of various theories for the decay of a  $M_0 = 3$  and  $\gamma = 1.4$  shock with simulation results and our model.

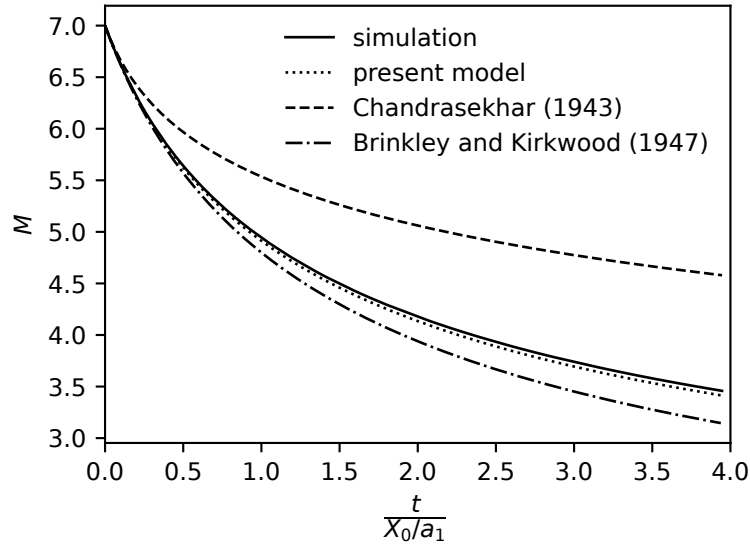


Figure 2.12: Comparison for the decay of a  $M_0 = 7$  and  $\gamma = 1.4$  shock.

$u_{xx,2} = 0$  in the initial centered expansion, the interaction with the shock generates a perturbation to the flow resulting in a nonzero value for  $u_{xx,2}$ . The shock-change equation for  $u_{xx,2}$  (2.54) is analytically exact, and so can be used to compute the magnitude of the perturbation from simulation data. In Figure 2.15, the terms of (2.54) are plotted for the simulation case  $M_0 = 7$  and  $\gamma = 1.4$ , where  $K$  is computed



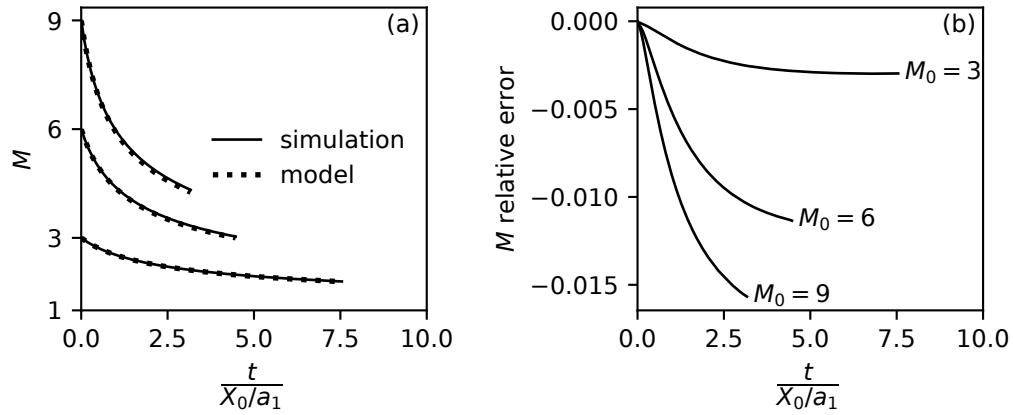


Figure 2.13: Time-evolution of (a)  $M$  from numerical simulations and model predictions and (b) model error. All cases are for  $\gamma = 1.4$ .

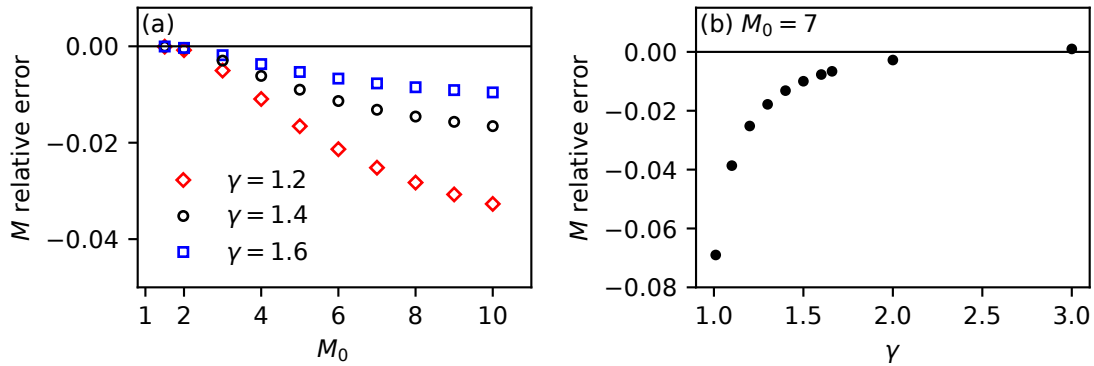


Figure 2.14: Relative error in model prediction for  $M$  at end of simulated time, corresponding to  $\delta = 0.4$ . Dependence on  $\gamma$  is shown with more data in (b) for  $M_0 = 7$ .

using the simulated  $M$ . In (a),  $\ddot{M}$  and  $-K\dot{M}^2$  are nearly indistinguishable. From (2.54), their difference is the residual term  $a_1 Lu_{xx,2}$ , which is plotted in (b) and shows a small nonzero value initially, before rapidly decreasing to near zero. The initial magnitude of the terms in (a) is roughly twenty times greater than the initial value in (b), which shows that the perturbation is small compared to the terms in (a) and illustrates why the approximation  $u_{xx,2} = 0$  produces such accurate predictions of the shock propagation.

The exact shock-change equation (2.54) can be reformulated to obtain a small

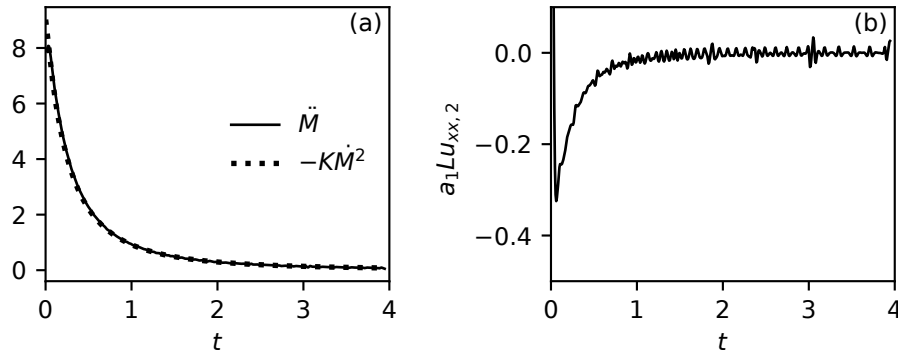


Figure 2.15: Terms from second-order shock-change equation (2.54) evaluated from simulation data for  $M_0 = 7$   $\gamma = 1.4$ , where quantities are nondimensionalized using time scale  $X_0/a_1$ .

parameter in terms of  $u_{xx,2}$ ,

$$\ddot{M} + K\dot{M}^2 (1 + \epsilon) = 0, \quad (2.89)$$

$$\epsilon = a_1 \frac{L u_{xx,2}}{K \dot{M}^2}. \quad (2.90)$$

Now, the model  $u_{xx,2} = 0$  can be considered the limit of  $\epsilon \ll 1$ . The maximum value for  $\epsilon$  is at time  $t = 0$  when the perturbation is strongest. This is estimated from simulation data and plotted in Figure 2.16, which shows that  $\epsilon$  is largest for decreasing  $\gamma$  and increasing  $M_0$ , consistent with the errors in Figure 2.14.

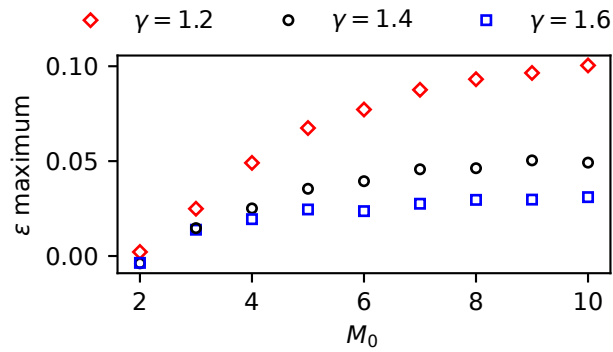


Figure 2.16: Maximum value of  $\epsilon$ , which quantifies the perturbation by the reflected wave.

In contrast, for the analogous formulations used by Best (1991) and Sharma and Radha (1994), where the equivalent residual term is defined by  $\partial_t(P_t + \rho a u_t)$  and

$P_{xx}$ , respectively, the residual term is never small because the gradients are never small in the incident simple wave, regardless of the reflected perturbation. For example, the equation for  $P_{xx,2}$  is

$$\ddot{M} + J\dot{M}^2 (1 + \hat{\epsilon}) = 0 \quad (2.91)$$

$$\hat{\epsilon} = \frac{NF^2}{J} \frac{P_{xx,2}}{\rho_1 u_{x,2}^2}. \quad (2.92)$$

In a centered expansion in a perfect gas,  $P_{xx,2}$  at the head of the wave is given by

$$\frac{P_{xx,2}}{\rho_1} = \frac{\gamma + 1}{2} \frac{\rho_2}{\rho_1} u_{x,2}^2. \quad (2.93)$$

Neglecting the perturbation by the reflected wave, then for  $\gamma = 7/5$  and  $M = 5$ ,  $\hat{\epsilon} = 5.37$ , whereas for the  $u_{xx,2}$  formulation  $\epsilon = 0$ , exactly.

### 2.5.3 Centered Expansion in Equilibrium Air

Figure 2.17 shows calculations of the shock-change coefficients relevant to the decay model,  $K$  and  $B$ , for  $M$  up to 20. In (a)  $K^{-1}$  remains roughly linear. In (b),  $B^{-1}$  diverges significantly from  $\gamma = 1.4$ , indicating that for a given  $u_x^{(0)}$ , the initial shock decay rate is greater in equilibrium air.

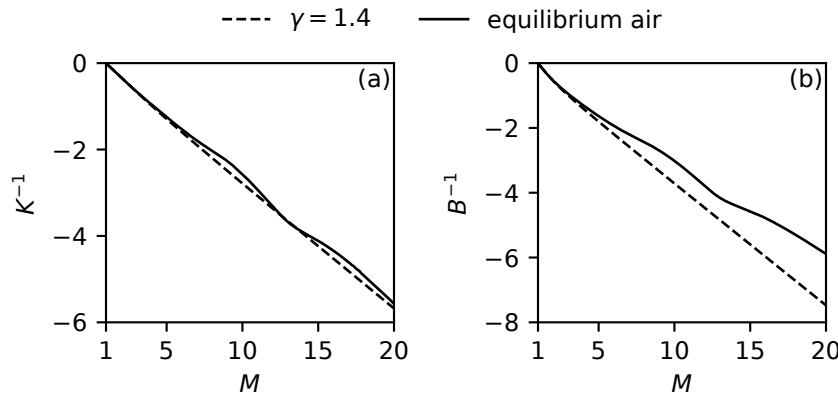


Figure 2.17: Shock-change coefficients  $K^{-1}$  and  $B^{-1}$  for shock Mach numbers up to 20 in a  $\gamma = 1.4$  gas and in equilibrium air initially at 50 kPa, 300 K air (21%  $O_2$  and 79%  $N_2$ ).

Simulations were performed for three shock Mach numbers (5, 10, and 15) in air initially at 50 kPa and 300 K. In Figure 2.18(a), the shock Hugoniot and isentrope are plotted. Also shown is the chemically frozen Hugoniot. Figure 2.18(b) shows the tabular data for  $P(\rho, e)$ , where  $P$  is normalized by the chemically frozen pressure,  $P_{fr}$ , at the same  $\rho$  and  $e$ . The shock Hugoniot and isentropes are also plotted in

Figure 2.18(b), where the area bounded by the curves contains all thermodynamic states accessed by the simulated flow.

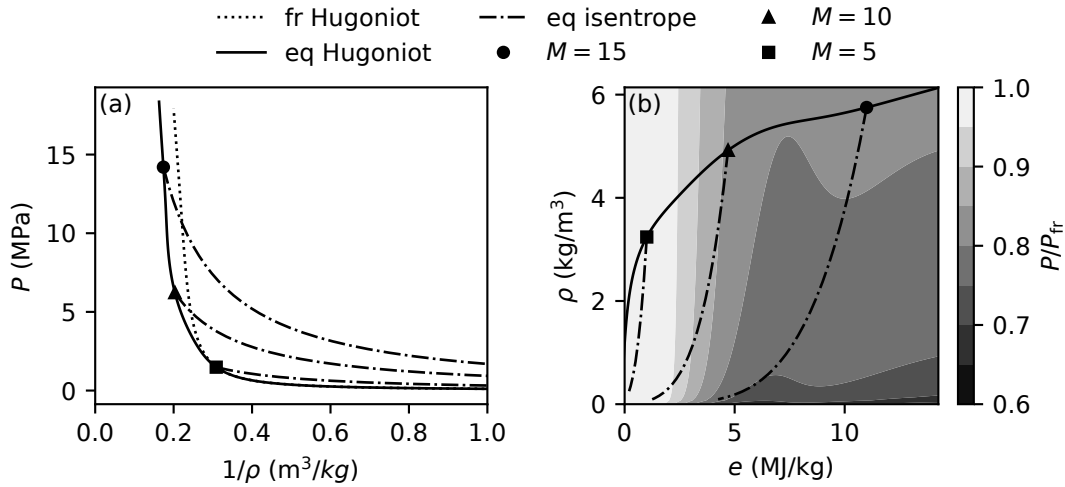


Figure 2.18: Thermodynamics for simulations of shocks in equilibrium air. (a) shock Hugoniot and isentropes, (b) contours of tabular data for  $P = P(\rho, e)$ . Abbreviations “fr” and “eq” denote chemically frozen and equilibrium, respectively.

Results from numerical simulations are compared with model predictions in Figure 2.19. The time-evolution of the shock Mach number is shown in (a), (b), and (c), and the relative error is shown in (d). The model accuracy is excellent with error less than 1% for both  $M_0 = 5$  and  $M_0 = 10$  cases and less than 2% for  $M_0 = 15$ . This clearly shows that the model is effective even for equations of state very different from a perfect gas. Results for  $\gamma = 1.4$  are also shown for comparison. The large error can be attributed to the discrepancy in  $B^{-1}$  shown in 2.17(b).

The power-law approximation can also be applied for problems with general equations of state, where  $K(M_0)$  is computed accordingly. Figure 2.20 shows  $\alpha$  and  $\beta$  for  $M$  up to 20. The non-monotonic behavior of  $\alpha$  as  $M_0$  increases is due to the sequential effects of vibrational excitation, chemical dissociation, and ionization in equilibrium air. Similar behavior can be observed from plots of  $\gamma$  (Henderson and Menart, 2008).

The interaction with the centered wave for equilibrium air did not introduce a larger perturbation to the incoming simple wave than for a perfect gas. As discussed in 2.1, the other source for nonzero  $u_{xx,2}$  is in variation of  $\Gamma$  on  $C^+$  characteristics in the simple wave.  $\Gamma$  and  $a_1 \partial_a \Gamma$  are plotted in figure 2.21 along the post-shock isentrope of the  $M_0 = 15$  case. These values can be used with (2.54) to estimate the maximum

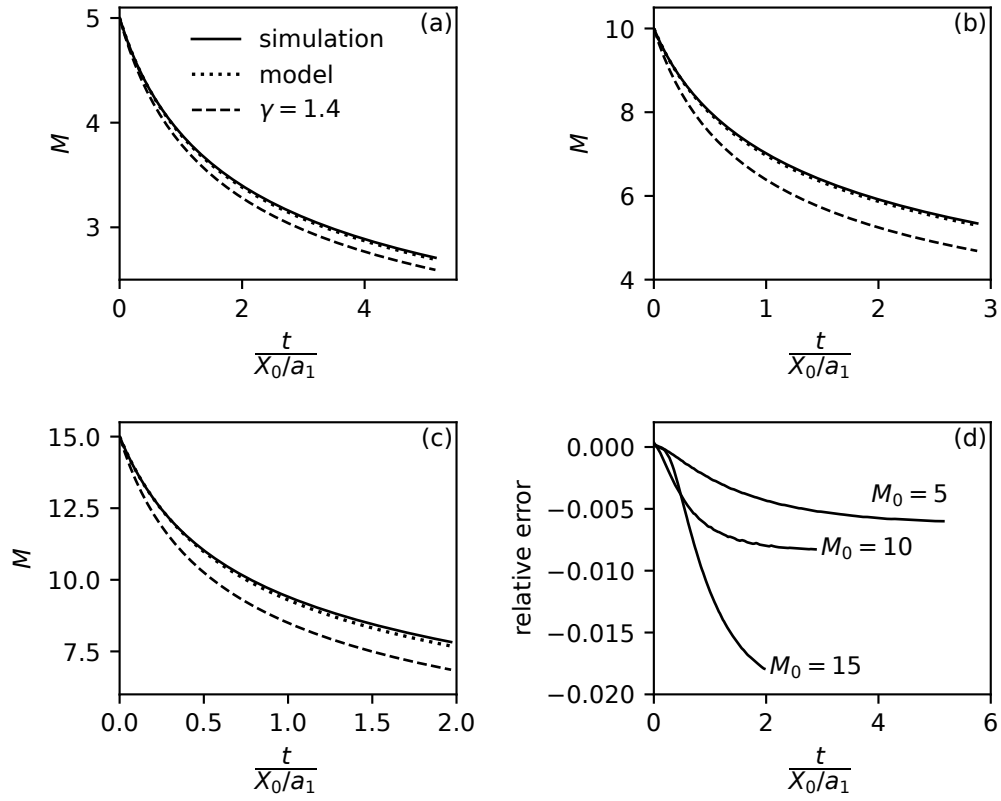


Figure 2.19: Comparison between numerical simulations and model predictions for strong shocks in equilibrium air initially at 50 kPa and 300 K.

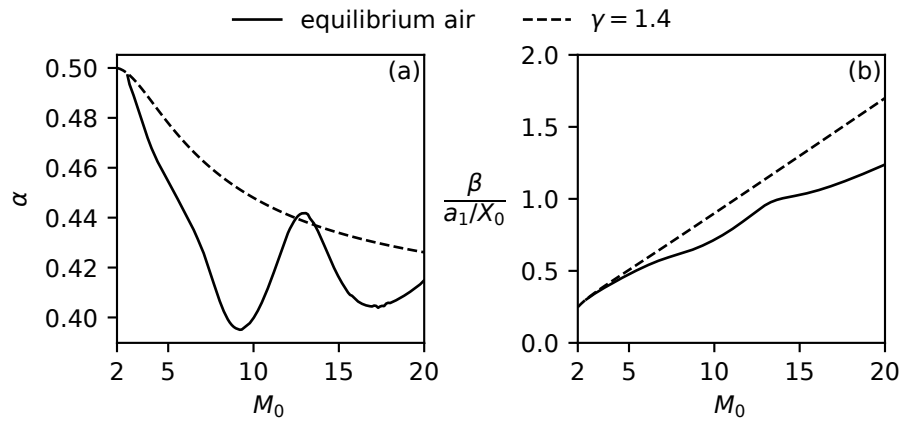


Figure 2.20: Parameters for power-law approximation of decay model for equilibrium air at 50 kPa and 300 K.

$\epsilon$ , where  $\epsilon$  is given by

$$\begin{aligned}\epsilon &= a_1 \frac{Lu_{xx,2}}{K\dot{M}^2}, \\ &= -a_1 \frac{LF^2}{K} \frac{\Gamma - 1}{\Gamma} \partial_a \Gamma.\end{aligned}\tag{2.94}$$

For  $M_0 = 15$ ,  $LF^2/K = 2.16$ . Then, using the maximum values shown in figure 2.21 for  $\Gamma$  and  $a_1 \partial_a \Gamma$  gives  $\epsilon \leq .014$ . So, for equilibrium air at these conditions, the effect of nonconstant  $\Gamma$  is negligible, and the model assumption that  $u_{xx,2} \approx 0$  holds.

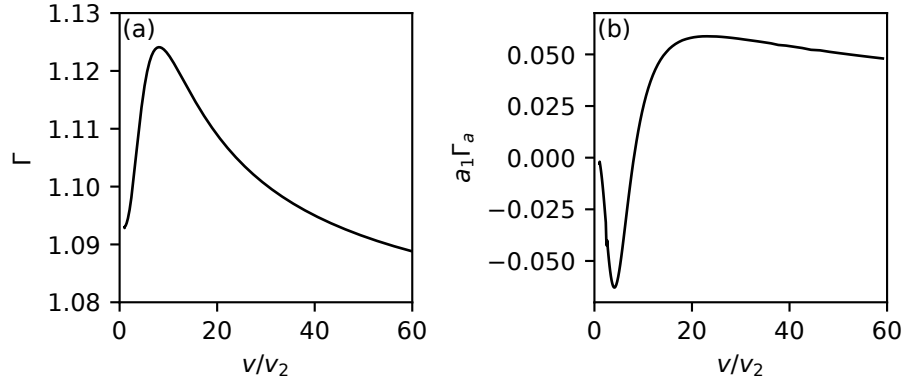


Figure 2.21: Variation of (a)  $\Gamma$  and (b)  $a_1 \partial_a \Gamma$  along  $M_0 = 15$  post-shock isentrope, where  $v_2$  is the post-shock specific volume.

### 2.5.4 Simple Wave from the Constant Deceleration of a Piston in a Perfect Gas

If the piston does not impulsively stop, but instead slows at a gradual rate, then a non-self-similar simple wave is generated. If the piston slows with a constant acceleration to a halt, then the piston velocity,  $v$ , and position,  $X_p$ , over time are given by the piecewise expressions

$$v = \begin{cases} u_2(1 - t/\tau_s) & 0 \leq t \leq \tau_s \\ 0 & t \geq \tau_s \end{cases}, \quad X_p = \begin{cases} u_2 t \left(1 - \frac{t}{2\tau_s}\right) & 0 \leq t \leq \tau_s \\ \frac{u_2 \tau_s}{2} & t \geq \tau_s \end{cases}, \quad (2.95)$$

where  $\tau_s$  is the time when the piston is fully stopped. The solution for the simple wave is given by (2.7), where  $f(u)$  is obtained from the piston path. The procedure is demonstrated for an exponential piston by Zel'dovich and Raizer (1967), however in that case the result is implicit. For a constant-deceleration piston, all quantities can be found explicitly throughout the wave. At the piston face,  $u = v$  and so

$$f(v) = X(t(v)) - (v + a(v))t(v), \quad (2.96)$$

where time is expressed in terms of the piston speed, i.e.,  $t = \tau_s(1 - v/u_2)$ . For a perfect gas, the sound speed is given by

$$a(u) = \frac{\gamma - 1}{2}(u - u_2) + a_2, \quad (2.97)$$

and so (2.96) can be simplified to obtain the general expression for  $f(u)$  in the simple wave,

$$f(u) = \frac{u_2 \tau_s}{2} \left( 1 - \left( \frac{u}{u_2} \right)^2 \right) - \left[ \frac{\gamma + 1}{2} u - \frac{\gamma - 1}{2} u_2 + a_2 \right] \left( 1 - \frac{u}{u_2} \right) \tau_s. \quad (2.98)$$

With  $f(u)$ ,  $u(x, t)$  throughout the simple wave can be obtained from (2.7),

$$\begin{aligned} \frac{u}{u_2} = & 1 - \frac{a_2}{\gamma u_2} - \frac{\gamma + 1}{2\gamma} \frac{t}{\tau_s} \\ & + \frac{1}{\gamma} \sqrt{\left( \frac{\gamma + 1}{2} \frac{t}{\tau_s} \right)^2 + 2\gamma \left( \frac{x}{u_2 \tau_s} - \frac{t}{\tau_s} \right) - (\gamma - 1) \frac{a_2}{u_2} \frac{t}{\tau_s} + \left( \frac{a_2}{u_2} \right)^2}. \end{aligned} \quad (2.99)$$

The sound speed can be obtained from (2.97), and other quantities follow from isentropic relations.

The velocity gradients,  $u_x$  and  $u_{xx}$ , are found by differentiating (2.99). The result for  $u_{xx}$  can be simply expressed as

$$u_2 u_{xx} = -\gamma \tau_s u_x^3, \quad (2.100)$$

which is valid throughout the wave.

With the additional time scale,  $\tau_s$ , a single additional dimensionless variable distinguishes resulting shock motions given by  $\sigma = \tau_s/\tau_p$ , where  $\tau_p$  is the duration of the constant velocity phase of the piston motion. For  $\sigma \rightarrow 0$ , a centered expansion wave is obtained. For  $\sigma \rightarrow \infty$ , there is no initial steady phase of the piston motion, and the shock is formed decaying at the piston face. In this limit, the maximum value for  $u_{xx}$  at the shock is at  $t = 0$  and given by

$$\frac{a_1 u_{xx,2}}{u_{x,2}^2} = -\gamma \frac{a_1}{a_2}, \quad (2.101)$$

which can be used to estimate  $\epsilon$  from the exact shock-change equation and is equal to

$$\epsilon = -\gamma \frac{LF^2}{K} \frac{a_1}{a_2}. \quad (2.102)$$

For  $M_0 = 7$  and  $\gamma = 1.4$ ,  $\epsilon = -0.61$ , which is clearly not small and shows that the general piston motion introduces a significant deviation from the  $u_{xx,2} = 0$  model.

For decreasing  $\sigma$ , there is more time for the simple wave to approach the linear-velocity profile of a centered expansion, and so the  $u_{xx,2} = 0$  model accuracy is expected to increase. For larger  $\sigma$ , where  $u_{xx,2}$  is non-negligible, we can still use

the value in the unperturbed wave and neglect the disturbance by reflected waves. In this case, (2.100) is used in the shock-change equation (2.54). Instead of directly computing the velocity gradient, it is estimated using its shock-change equation and the value for the shock acceleration.  $u_{xx,2}$  is then approximated by

$$u_{xx,2} = -\gamma\tau_s(F\dot{M})^3/u_2, \quad (2.103)$$

which enables (2.54) to be solved as a second-order initial value problem. The initial shock acceleration is still given by (2.86), where the velocity gradient at the head of the unperturbed wave is

$$u_{x,2}^{(0)} = \left[ \frac{\gamma+1}{2}t_0 + \frac{a_2}{u_2}\tau_s \right]^{-1}. \quad (2.104)$$

In order to numerically simulate the shock decay by these simple waves, three cases for a shock with  $M_0 = 7$  and  $\gamma = 1.4$  were considered with values of  $\sigma = 0.25$ ,  $\sigma = 0.5$ , and  $\sigma = 1.0$ . The simulation was initialized using data computed from the above formulae. For all cases, the initial condition was chosen for a time before the wave is incident upon the shock. The initial conditions are shown in figure 2.22. For  $\sigma = 0.5$  and  $\sigma = 0.25$ , the piston velocity is not zero at the beginning of the simulation. For these cases, the left boundary condition is set to the constant piston velocity at the beginning of the simulation, so that the piston is no longer slowing. Characteristics from the wall do not reach the shock within simulation time.

Results from numerical simulations are plotted with the model prediction in figure 2.23. Subplots (a), (b), and (c) show that, as expected, as  $\sigma$  increases the agreement with the  $u_{xx,2} = 0$  model decreases. Accordingly, subplots (d), (e), and (f) show that the error increases. Also plotted in figure 2.23 are the model results from using the unperturbed value of  $u_{xx,2}$  in the incident simple wave, which was approximated using (2.103). This achieves less than 2% error for all cases, which is similar to the error in section 2.5.2 for  $M_0 = 7$  and  $\gamma = 1.4$ . These results show that even for non-self-similar simple waves, the shock-propagation model obtained by neglecting only perturbations to the incident second velocity gradient remains accurate.

## 2.6 Summary

A model for the decay of plane shock waves in equilibrium flows with an arbitrary equation of state was formulated using a shock-change equation for the second velocity gradient behind the shock,  $u_{xx}$ . In contrast to prior work, instead of neglecting all higher-order gradients, only the perturbation to those gradients by



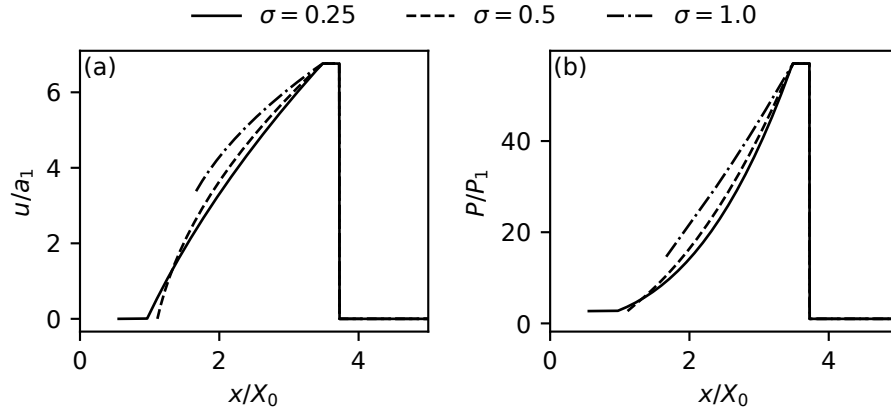


Figure 2.22: Initial (a) particle velocity and (b) pressure for simulations of shock decay by the simple wave from a constant-deceleration piston for  $M_0 = 7$  and  $\gamma = 1.4$ .

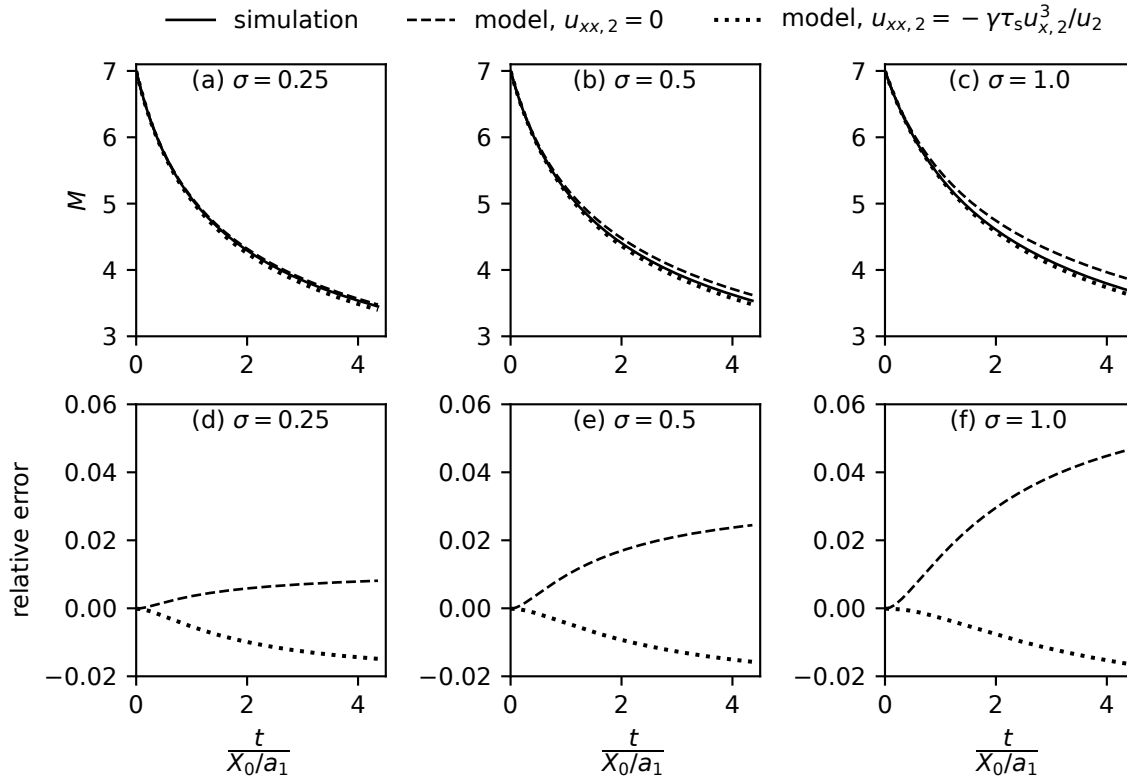


Figure 2.23: Time evolution of (a,b,c) shock speed and (d,e,f) model error for  $M_0 = 7$  and  $\gamma = 1.4$  shocks decayed by the simple wave from a constant-deceleration piston for three values of the scale parameter,  $\sigma$ .

the shock interaction is neglected. For centered expansion waves in a perfect gas,  $u_{xx} = 0$  exactly throughout the wave, and therefore also behind a decaying shock

if the perturbation is neglected. Comparison with numerical simulations showed that these perturbations are indeed sufficiently small to obtain accurate solutions for the shock trajectory. For a general equation of state,  $u_{xx} \neq 0$  in the incident simple wave due to variation in the fundamental derivative of gas dynamics,  $\Gamma$ . For a centered wave in equilibrium air, it was shown that this variation is small, and  $u_{xx} = 0$  remains an accurate model even for a Mach 15 shock. For an arbitrary simple wave,  $u_{xx} \neq 0$  and must be accounted for. This can still be accomplished by neglecting the perturbation from the shock interaction, which was shown to be effective for the simple wave generated by the constant deceleration of a piston in a perfect gas. Since simple waves converge to a self-similar solution, then in some cases  $u_{xx} = 0$  can still be used for arbitrary simple waves and remains a good initial estimate.

The value of the analytical results obtained in this chapter is in their generality and simple formulation. The model can be readily implemented through numerical solution of a simple ordinary differential equation (2.66), where  $K$  is given for an arbitrary equation of state in (2.55) and for a perfect gas in (2.63). The initial shock acceleration can be computed from (2.86), where  $u_x^{(0)}$  is the velocity gradient in the incident simple wave, which is given by (2.10). A useful result from this analysis is an approximate power-law formulation, which remains accurate even for cases with strong shocks in equilibrium air. Although not detailed in this article, the model can be used for shocks in media with irreversible endothermic or exothermic reactions, such as overdriven detonation waves. An example of this is described in Appendix A.

## *Chapter 3*

### MODELING FORWARD-MODE DETONATION-DRIVEN SHOCK DECAY

Schoeffler, D. T. and Shepherd, J. E. (2023). Decay of shock waves in detonation-driven shock tubes. In *34th International Symposium on Shock Waves, Volume 2: Applications 1*. Springer Singapore.

An essential characteristic of forward-mode detonation drivers is that the nonuniform driver gas causes the driven shock wave to decay from the beginning of its formation. Prediction of shock decay is important not only to properly choose the shock's strength for processing the test gas, but also because the decaying shock introduces unsteadiness in the post-shock flow, which can pose serious limitations for facilities where the test gas is meant to simulate some steady, hypervelocity flow. Nonetheless, unsteady shock waves may be used if the time scale of their unsteadiness is sufficiently large compared to a facility's test time. This is determined in practice by experimentally characterizing a given facility or by numerical simulation. Expedient methods for estimating performance are important, and so a model is needed to predict detonation-driven shock decay.

In Chapter 2 it was shown that the motion of plane shock waves acted upon by simple waves can be accurately approximated by a power law. In this chapter, this result will be applied to the problem of shock decay from a forward-mode detonation driver. A model problem will be formulated, and numerically simulated for a range of independent variables. The problem is first simulated assuming both driver and test gases are perfect, i.e., with constant heat capacities. This will be shown to be accurate for modeling detonation products, however the approximation is not so good for shocks in air. These inaccuracies will be addressed using simulations with thermally equilibrated air including a finite-rate reaction model.

#### **3.1 Problem Formulation**

The intrinsically multidimensional cellular detonation structure can be modeled as a one-dimensional reaction zone in a spanwise mean, terminating in the equilibrium Chapman-Jouguet (CJ) state. Behind the CJ state is an unsteady expansion wave, known as the Taylor-Zel'dovich (TZ) wave when self-similar. Two length scales are

present in this formulation of the one-dimensional detonation wave: the reaction zone width and the detonation propagation distance, i.e., the driver length. The reaction zone width scales with some characteristic detonation cell size, which is typically small compared to the driver length for all pressures and mixtures of interest here. So, the reaction zone may be neglected from analysis, and the CJ-TZ detonation structure remains. Additionally, wall effects like viscous attenuation and heat transfer are neglected, which is appropriate for sufficiently small driver length-to-diameter ratios (Radulescu and Hanson, 2005).

The initial condition for the detonation-driven shock tube, as modeled here, is when the CJ state is incident with the contact surface separating shock tube sections, as shown in Figure 3.1. The typical enumeration of shock tube gas states is used here with a modification to also describe relevant states in the detonation driver, which are the initial, unreacted gas state 41, the CJ state 42, and the TZ wave plateau state 43. These subscripts are used throughout, particularly for the CJ state. The strategy taken in this work is to numerically simulate the evolution of this initial condition.

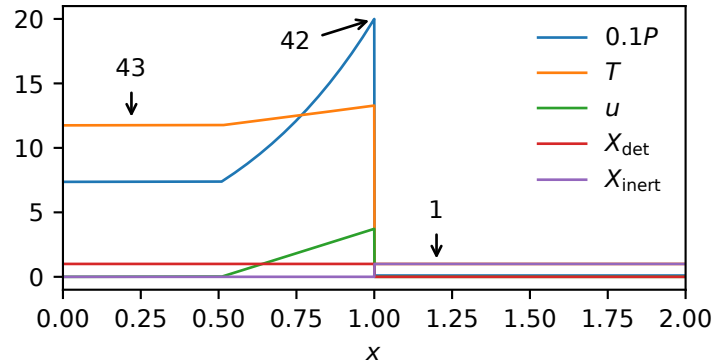


Figure 3.1: Initial conditions for the simplified model in terms of pressure, temperature, velocity, and mole fractions for detonation driver gas,  $X_{\text{det}}$ , and inert shock tube gas,  $X_{\text{inert}}$ , where enumeration 42 and 43 identifies the CJ and TZ-plateau states, respectively.

The problem will first be modeled assuming the detonation products and inert driven-section test gas to be perfect gases. The temperatures are so high in fuel-oxygen detonation products that chemical reactions remain much faster than fluid mechanic length scales, such that flows can be accurately modeled as in chemical equilibrium (Cooper, 2004). The specific heat capacity ratio for the detonation products can therefore be defined using the equilibrium conditions of the CJ state

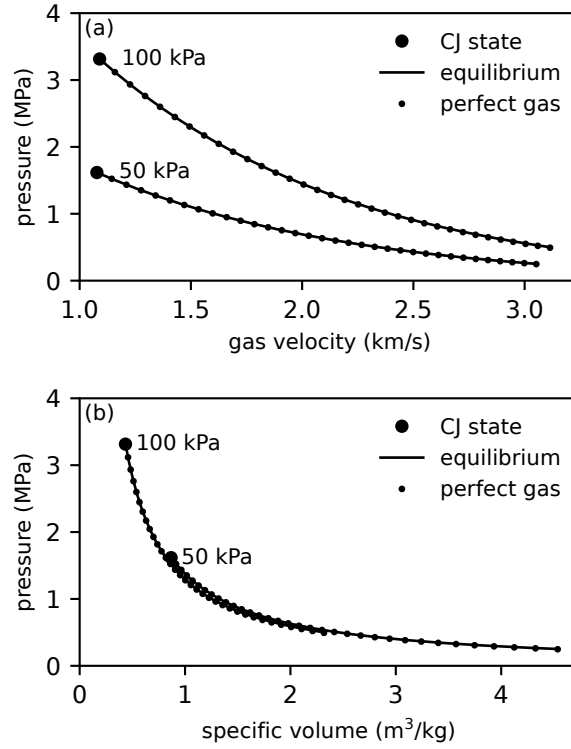


Figure 3.2: (a) rarefaction wave curves and (b) isentropes for detonation products from stoichiometric mixtures of ethylene-oxygen initially at 300 K and two initial pressures of 50 and 100 kPa.

and is calculated here by

$$\gamma_{42} = \rho_{42} a_{42}^2 / P_{42} , \quad (3.1)$$

where  $a_{42}$  is the equilibrium sound speed. A single value for  $\gamma_{42}$  remains accurate throughout subsequent isentropic expansion of the CJ state. Rarefaction wave curves and isentropes are plotted in Figure 3.2 for equilibrium and perfect gas calculations and show that (3.1) is accurate. All calculations are performed using the Shock and Detonation Toolbox (Kao et al., 2020). Note that the mean molecular weight of the gas changes as equilibrium is maintained through the expansion. Consequently, temperatures calculated using the perfect-gas model are incorrect. However, since density and pressure are accurately modeled on the isentrope and chemical equilibrium is assumed, the fluid dynamics are unaffected.

Strong shocks in air and other non-monatomic gases produce significant relaxation of internal energy modes and possibly dissociation, and so the perfect-gas model is not generally reliable. Nonetheless, the perfect-gas model is simple, facilitates analysis

with a reduced number of independent variables, and provides essential insight into the gas dynamics. Results from perfect-gas simulations will be analyzed first, then evaluated against those with non-constant heat capacities and a finite-rate reaction model.

The simplified model problem has six independent, dimensionless variables describing all conditions. They are

$$\frac{P_{42}}{P_1}, \quad \frac{a_{42}}{a_1}, \quad M_{42}, \quad \gamma_{42}, \quad \gamma_1, \quad \frac{W_{42}}{W_1}, \quad (3.2)$$

which are, respectively, the pressure ratio, the sound speed ratio, the local CJ Mach number in the lab-frame, the CJ gas specific heat ratio, the driven gas specific heat ratio, and the ratio of molecular weights. The only additional variable not present in typical shock tube analysis is  $M_{42} = u_{42}/a_{42}$ , which quantifies the driver gas velocity in the lab-frame. The molecular weight ratio is only included as it is necessary to compute the temperature, which is unimportant for the present problem. Because of the self-similar TZ wave, all length scales can be normalized by the driver length. The nonuniformity from the TZ wave is a result of the boundary conditions and does not require any additional variables to describe.

All quantities in (3.2) were independently investigated here. A base parameter set is used throughout the study to vary parameters about. Quantities for the base case are

$$\begin{aligned} \frac{P_{42}}{P_1} = 200, \quad \frac{a_{42}}{a_1} = 3.7, \quad M_{42} = 0.85, \\ \gamma_{42} = 1.14, \quad \gamma_1 = 1.4, \quad \frac{W_{42}}{W_1} = 0.79, \end{aligned} \quad (3.3)$$

which were chosen to be values typical for stoichiometric ethylene-oxygen at standard temperature and pressure and air driven gas, although they are typical for other mixtures as well. The initial condition given by the base case is shown in Figure 3.1. The primary variables considered for shock tube operation were the pressure ratio and sound speed ratio. Quantities  $M_{42}$  and  $\gamma_{42}$  are only determined by the detonation gas mixture, and typical values for many mixtures are  $M_{42} \in [0.8, 0.85]$  and  $\gamma_{42} \in [1.1, 1.2]$ . To illustrate this, Table 3.1 lists values for  $M_{42}$  and  $\gamma_{42}$  calculated for various mixtures. The only parameter for the inert shock tube gas is  $\gamma_1$ .

Although the evolution of the initial condition is numerically simulated, the initial speed of the driven shock can be directly computed using a pressure-velocity diagram. Because of the nonzero gas velocity, either a rarefaction or shock may be reflected from the contact surface interaction, determined by the position of the CJ

Table 3.1: Examples of perfect gas parameters for equilibrium detonation products

mixture	$M_{42}$	$\gamma_{42}$
$\text{C}_2\text{H}_4 + 3\text{O}_2$	0.85	1.14
$\text{C}_2\text{H}_4 + 3\text{O}_2 + 4\text{Ar}$	0.83	1.16
$2\text{H}_2 + \text{O}_2$	0.84	1.13
$4\text{H}_2 + \text{O}_2$	0.82	1.15

state relative to the shock curve. The boundary dividing these wave reflections is defined by when  $P_{42} = P_2$  and  $u_{42} = u_2$ . For the present independent variables, this occurs when the following is satisfied

$$M_{42} \frac{a_{42}}{a_1} = \frac{1}{\gamma_1} \frac{P_{42}/P_1 - 1}{\sqrt{\frac{\gamma_1 + 1}{2\gamma_1} (P_{42}/P_1 - 1) + 1}} . \quad (3.4)$$

All simulation cases were chosen to be on the side of the boundary where an expansion is reflected. Cases used to examine the effect of only pressure and sound speed ratios are plotted with the wave-reflection boundary in Figure 3.3. The initial shock Mach number,  $M_0$ , is given by the detonation-driven shock-tube equation (1.1).

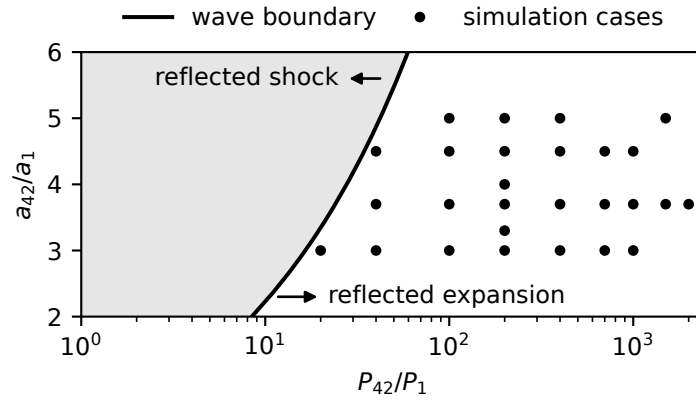


Figure 3.3: Map of variables for simulation cases examining the combined effects of pressure and sound speed ratios. All are located to the right of the boundary defining reflection of expansion or shock waves at the diaphragm for  $M_{42} = 0.85$ ,  $\gamma_{42} = 1.14$ , and  $\gamma_1 = 1.4$ .

In order to characterize the decaying shock wave, the power law formulation derived in Chapter 2 for the strong shock limit is used. Therefore, the decay parameter,  $\delta$ , is defined by the time-varying shock Mach number,  $M(t)$ , normalized by its initial

speed,  $M_0$ , i.e.,

$$\delta = \frac{M(t)}{M_0} . \quad (3.5)$$

The weak shock formulation is more accurate for some conditions, however subsequent model formulae are more complicated.

The shock propagation law is

$$\delta = \frac{1}{(1 + \beta t/\alpha)^\alpha} , \quad (3.6)$$

where  $\beta$  is the positive initial decay rate,  $\beta = -\dot{\delta}_0$ , and normalizes the time variable. The exponent,  $\alpha$ , characterizes the shape of the trajectory. Larger values of  $\alpha$  correspond with faster decay for a given value of  $\beta$ . Both parameters determine the rate of shock decay and hence the magnitude of unsteadiness generated in the post-shock flow.

In Chapter 2, the power law (3.6) was derived for the strong shock limit of (2.66), where  $\beta$  was defined by the incident simple wave and  $\alpha$  was defined only by the shock Mach number. This model arose from neglecting perturbations to the second velocity gradient,  $u_{xx,2}$ , which is zero for centered waves. When considering non-self-similar waves,  $u_{xx,2} \neq 0$ , and so the decay model was modified to incorporate this nonzero term. The simple wave that decays the forward-mode detonation-driven shock is not centered due to the interaction with the left-propagating wave generated at the diaphragm. The shock is decayed immediately upon formation, and so there is no time for the transmitted simple wave to propagate and approach self-similarity again. Therefore, analytical treatment of this problem requires incorporating the effect of  $u_{xx,2} \neq 0$ . The strategy taken in this work is to instead use (3.6) to fit simulation data.

## 3.2 Simulation Methods

Evolution of the detonation-driven shock tube initial condition was directly simulated using the same methods as those described in Chapter 2 with minor differences. Perfect gas simulations used OpenFOAM-7 and blastFoam-4, whereas reactive calculations used OpenFOAM-9 and blastFoam-5.

### 3.2.1 Perfect Gas

Simulations were performed using variables normalized by the inert shock tube gas initial state, i.e.,

$$P = \frac{\tilde{P}}{\tilde{P}_1}, \quad T = \frac{\tilde{T}}{\tilde{T}_1}, \quad u = \frac{\tilde{u}}{\tilde{u}_{\text{ref}}}, \quad W = \frac{\tilde{W}}{\tilde{W}_1}, \quad t = \frac{\tilde{t}\tilde{u}_{\text{ref}}}{\tilde{L}}, \quad x = \frac{\tilde{x}}{\tilde{L}}, \quad (3.7)$$



where  $\tilde{u}_{\text{ref}} = \sqrt{\tilde{R}\tilde{T}_1/W_1}$ ,  $\tilde{R}$  is the universal gas constant,  $\tilde{L}$  is the driver length, and the tilde identifies dimensional quantities. Simulation results are reported below using the same normalizations except for the reference velocity, where the sound speed,  $a_1$ , is used instead. The sound speed and  $\tilde{u}_{\text{ref}}$  are related by  $\tilde{a}_1/\tilde{u}_{\text{ref}} = \sqrt{\gamma_1}$ , hence simulation time is reported with a square-root  $\gamma_1$  factor.

For a given set of shock tube variables, the initial condition was computed separately, discretely sampled, and mapped onto a uniform simulation grid, from which the simulation was initiated. All simulation cases were run until the major features of the shock evolution were developed, typically  $t_{\text{sim}} \geq 3.0\sqrt{\gamma_1}$ . Time steps were sampled every  $\Delta t = 0.001\sqrt{\gamma_1}$ .

The driven shock Mach number was computed in post-processing at each sampled time step using the post-shock pressure and the perfect gas shock jump equation. Numerically differentiating discrete simulation data is prone to introducing large errors and then necessitates substantial use of smoothing algorithms. For perfect-gas calculations, the post-shock pressure was used to calculate the shock Mach number, a repeatable technique that minimizes use of smoothing methods and reduces the error introduced into computed quantities. The time evolution of the shock velocity exhibits several kinks, which were identified using the large spikes in the second derivative of shock velocity after smoothing the data with a Savitzky-Golay filter. No smoothing is otherwise applied to the shock Mach number results presented below.

Numerical simulations and post-processing algorithms were both verified for grid independence using the base case with grid resolutions of  $1 \cdot 10^3$ ,  $2 \cdot 10^3$ , and  $4 \cdot 10^3$  cells per driver length. All simulations presented here used  $2 \cdot 10^3$  cells per driver length, and the shock tube length was varied depending on the case so that all shocks reached similar points in their evolution. Total cell count for each case ranged from  $4 \cdot 10^4$  to  $8 \cdot 10^4$ .

Results from thirty six simulations are described below, which examined the influence of all independent variables. Primary focus was on the effect of pressure and sound speed ratios, and the twenty seven pertaining simulation variables are shown in Figure 3.3. Sensitivity of the base case to other variables was examined with cases where  $\gamma_{42} \in \{1.1, 1.14, 1.2\}$ ,  $M_{42} \in \{0.8, 0.825, 0.85\}$ , and  $\gamma_1 \in \{1.2, 1.3, 1.4, 1.5, 1.66\}$ .

### 3.2.2 Reacting Gas

As shown above in Section 3.1, the perfect-gas model remains accurate for fuel-oxygen detonation products. Simulations are therefore simplified by only considering real gas effects in the shocked driven section test gas.

Chemical reaction introduces additional length scales, and so results are not as readily nondimensionalized. For these problems, a driver length of 0.5 m is used, which is similar to the driver length used in experiments discussed later in this work. The perfect-gas study is general, while reacting gas calculations are performed to check model accuracy for conditions relevant to later experiments. As such, typical driver conditions are calculated for 50 or 100 kPa of stoichiometric ethylene-oxygen.

In this work, shocks up to roughly  $M_s = 8$  are considered, where dissociation time scales become small relative to those of a typical shock tube. The initial detonation-driven shock speed can still be calculated for equilibrium flows by solving for the pressure and velocity equilibrium condition numerically using, e.g., the Shock and Detonation Toolbox. This is sufficient to calculate the initial shock speed for forward-mode operation.

To prepare initial conditions, all thermodynamic and shock wave calculations are performed using Cantera (Goodwin et al., 2021) and the Shock and Detonation Toolbox (Kao et al., 2020). Both Cantera calculations and OpenFOAM simulations use the NASA-7 polynomial data (McBride et al., 1993). For shocks in air (21% O<sub>2</sub>, 79% N<sub>2</sub>), finite-rate kinetics tabulated by Johnston and Brandis (2014) are used.

Using NASA-7 polynomials to compute heat capacities assumes the gas to be in vibrational equilibrium. No calculations were performed that modeled finite-rate relaxation of these modes.

## 3.3 Results: Shock Decay

### 3.3.1 Perfect Gas

The time evolution of the driven shock Mach number for the base set of independent variables (3.3) is shown in Figure 3.4. The Mach number continuously decays from the initial speed to an apparently quasi-steady plateau period, after which the shock continues to decay further. These three periods of the shock Mach number evolution were obtained in all simulations.

A space-time diagram of the base simulation case was computed by directly integrating along the characteristics. The result is shown in Figure 3.5, where the

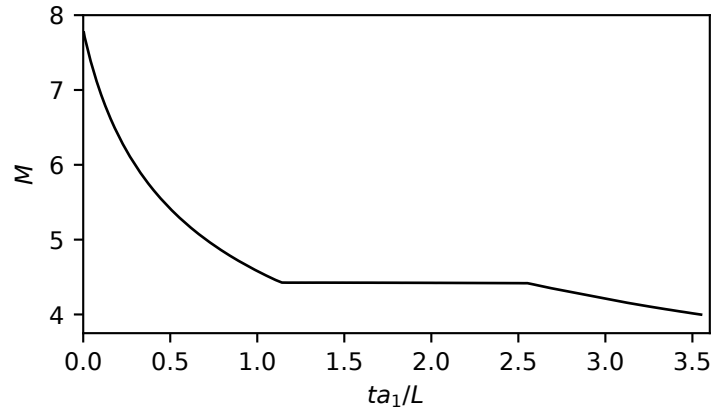


Figure 3.4: Time evolution of driven shock Mach number for simulation of base case.

reflection of characteristics at the end wall and shock front are tracked. Characteristic reflections at the contact surface are important but not included here. The space-time diagram illustrates the origin of the three regions of the shock Mach number evolution shown in Figure 3.4. The shock initially decays from attenuation by the transmitted TZ wave. However, since the TZ wave is finite, once the final characteristic intersects the shock, a region of approximately steady propagation is reached. After sufficient time, the centered expansion wave from the initial contact surface interaction reflects from the driver end wall and catches up with the shock wave, which causes it to decay further.

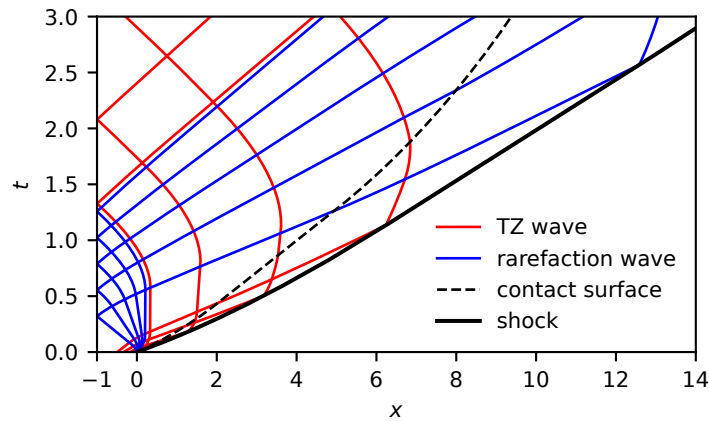


Figure 3.5: Space-time diagram generated from integration along characteristics of simulation data for the base parameter set.

The shock Mach number is only approximately steady during the plateau period

between the first and second phases of decay. The variation that does occur is substantially smaller than the variation during periods of shock decay, such that the plateau period is comparably steady. Unsteadiness in this period results from wave interaction with the contact surface. The shock Mach number in this period can be accurately approximated using the detonation-driven shock tube equation for the *reverse-mode* driver. This is because the plateau propagation period is driven by the TZ wave plateau state. Isentropic expansion of the TZ-wave gas is just a continuation of the isentropic expansion from the CJ state. This is only an approximate solution for the forward-mode plateau state because derivation of requires that the post-shock state is homentropic, which is not true due to the prior wave decay. The  $C^+$  characteristic drawn from the contact surface to the plateau-state shock does not have a constant Riemann invariant. Pressure and velocity are also not necessarily uniform in this region due to the compression wave reflected by a decaying shock. These effects are nonetheless weak, and Figure 3.6 shows that the approximation provides an accurate prediction for the mean shock Mach number in this region for all simulation cases.

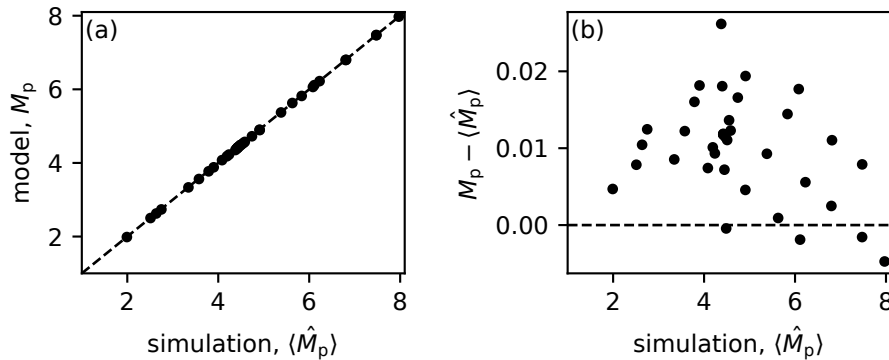


Figure 3.6: (a) Comparison of the mean shock Mach number in the plateau region from numerical simulations,  $\langle \hat{M}_p \rangle$ , with the result from the model,  $M_p$ , given by (1.1) for the reverse-mode driver. Residuals are shown in (b).

Even for moderate pressure ratios, the quasi-steady plateau period is only reached after the shock has traveled several driver lengths. Reverse-mode detonation drivers utilize this condition by initiating the detonation at the diaphragm and reducing the effective TZ wave or driver length. It is unrealistic to access this plateau period in forward-mode operation without using shock initiation to shorten the TZ wave (Bakos et al., 1996). Therefore, in order to otherwise use the forward-mode driver, the driven shock wave during its initial period of decay must be exploited, which

requires a characterization of its decay properties.

The shock decay parameter (3.5) in the first period of shock decay was fit to the propagation law (3.6) for all simulation cases, and both the fit and its residuals are shown in Figure 3.7. The root-mean-square error between data and fit across all simulations is  $7 \cdot 10^{-4}$ , proving the propagation law to describe the shock decay exceptionally well. The conclusions from this are several-fold. Foremost, the decaying shock propagates according to a power law in time as formulated by (3.6) to within some negligible error. There are only two properties of this propagation: the power-law exponent,  $\alpha$ , and the time scale or initial decay rate,  $\beta$ . The fitting of simulation data to (3.6) therefore provides measurements of these quantities,  $\alpha$  and  $\beta$ , which may be used to examine effects of independent variables on the resulting shock decay.

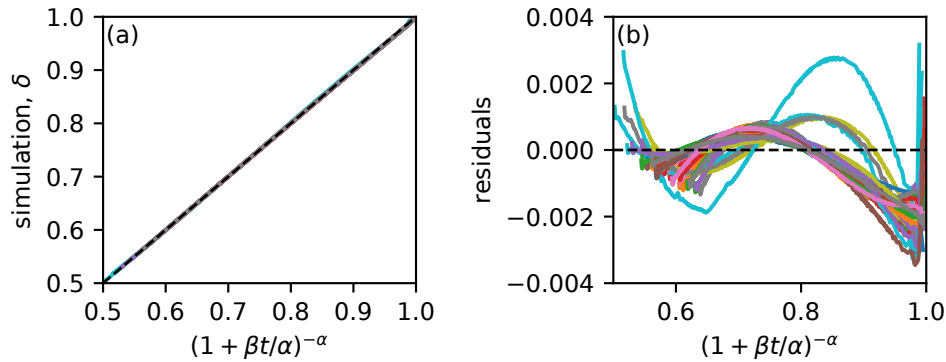


Figure 3.7: (a) The shock decay parameter (3.5) for all simulation cases is plotted against a fit to the propagation law (3.6) with corresponding residuals plotted in (b), where residuals are  $\delta - (1 + \beta t / \alpha)^{-\alpha}$ .

The shock decay properties,  $\alpha$  and  $\beta$ , for simulations where the pressure and sound speed ratios were varied together are plotted against multivariate correlations in Figure 3.8. The fits are

$$\beta = 0.814 \left( \frac{P_{42}}{P_1} \right)^{-0.337} \left( \frac{a_{42}}{a_1} \right)^{1.75} \quad (3.8)$$

$$\alpha = \left( \frac{\log(P_{42}/P_1) - 15.2}{42.16} \right)^2 \log(P_{42}/P_1) + \frac{a_{42}/a_1 - 2.15}{63.17}, \quad (3.9)$$

The power-law exponent,  $\alpha$ , could be separated into a linear combination of independent functions of the pressure and sound speed ratios. Dependence on the sound speed ratio could be linearly fit, but a more complicated dependence on the

pressure ratio required a cubic fit to the logarithm. Although cumbersome and not theoretically motivated, the functional form was chosen because it effectively fits the data. The pressure ratio dependence exhibits a maximum at  $P_{42}/P_1 \approx 160$ . Increasing the pressure ratio further decreases  $\alpha$ . Decreasing the sound speed ratio decreases  $\alpha$ .

The correlation for  $\beta$  in Figure 3.8(b) shows that the initial decay rate increases strongly with increasing the sound speed ratio and decreases with increasing the pressure ratio. This is important for facility operation. In order to reduce unsteadiness in the test gas it is desired to reduce the decay rate of the shock wave. This can be done by increasing the pressure ratio and decreasing the sound speed ratio, which has the double effect of reducing the exponent,  $\alpha$ , and decreasing the initial decay rate,  $\beta$ . Dependence of  $\beta$  on the sound speed ratio is particularly strong, nearly quadratic. For example, a reduction of sound speed ratio from 3.7 to 3 reduces the initial decay rate by 30%. Since the shock Mach number is directly proportional to both the pressure and sound speed ratios, the ratios can be varied to preserve the same shock Mach number while decreasing the shock unsteadiness.

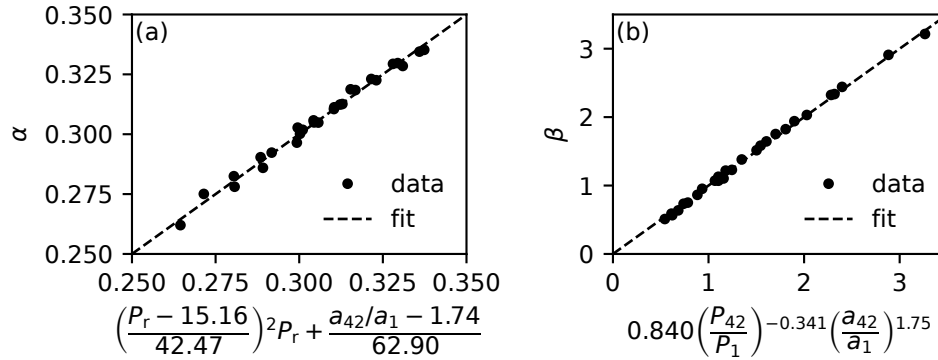


Figure 3.8: Shock decay properties plotted against multivariate correlations with pressure and sound speed ratios, where  $P_r = \log(P_{42}/P_1)$ .

The other three independent variables of interest are  $\gamma_1$ ,  $\gamma_{42}$ , and  $M_{42}$ . Figure 3.9 plots  $\alpha$  and  $\beta$  for simulation cases where the base case is perturbed about these three variables independently. For all, the variation in both  $\alpha$  and  $\beta$  is small, less than 3% for the variable ranges tested, which confirms that the effects of pressure and sound speed ratios are primary. A single simulation case with unity molecular weight ratio was performed to confirm its irrelevance to the present problem. Results were identical to the base case, except in the temperature variable, as expected.

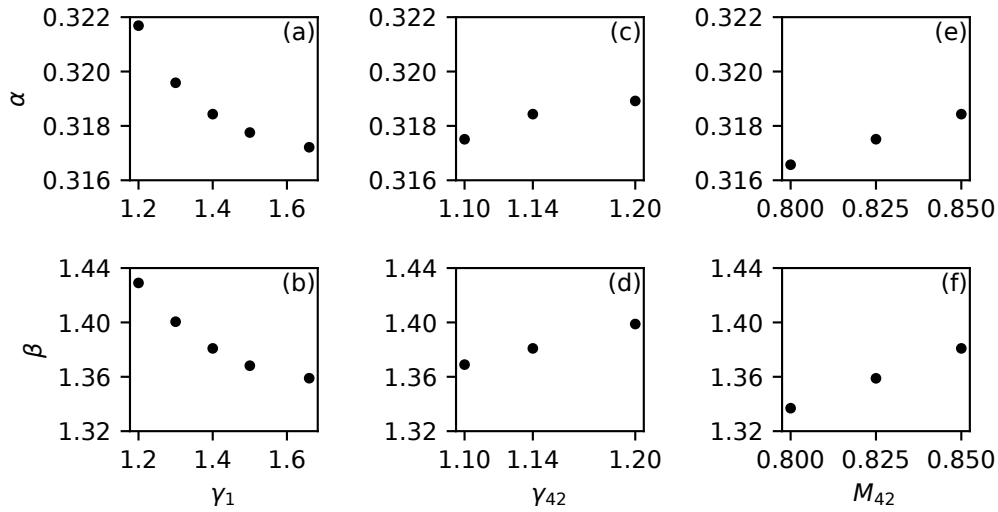


Figure 3.9: Decay properties from sensitivity study of secondary independent variables, where each quantity was varied individually about the base case.

Since the shock speed in the plateau period can be predicted using (1.1), then the decay model can be used to estimate the time or position when the decaying shock reaches the plateau period. A comparison between results using model formulae and simulations is shown in Figure 3.10, illustrating that for the majority of cases the model is accurate. Note that distance is normalized by the driver length.

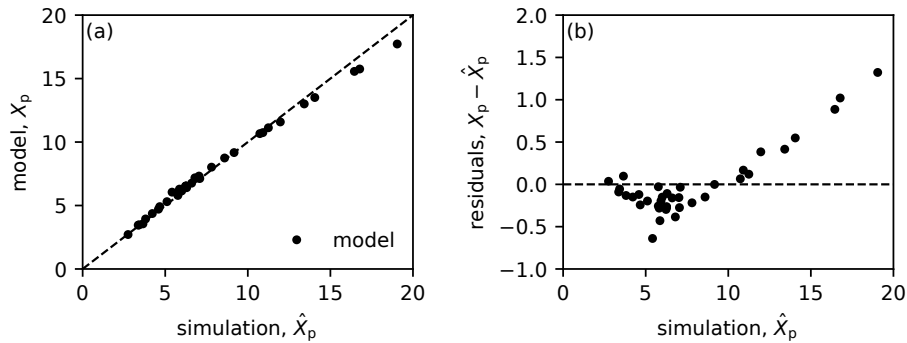


Figure 3.10: Comparison of distance along driven section when shock reaches plateau period calculated using model formulae and from simulations.

### 3.3.2 Reacting Gas

The decay model above can now be compared against calculations for air with a non-constant heat capacity and finite-rate reactions. Results from simulations are shown in Figure 3.11 for four shot conditions, where the air pressure is varied

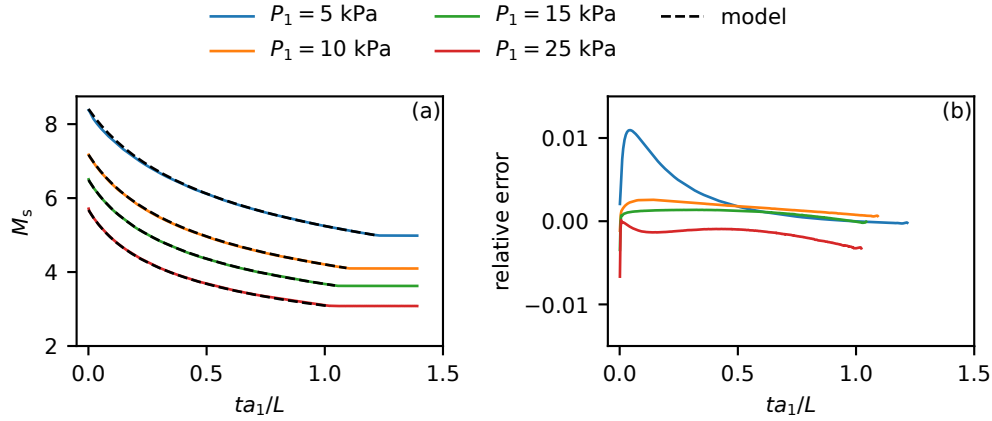


Figure 3.11: Comparison of shock decay model with numerical simulations including finite-rate dissociation in the air test gas. The decay model assumes chemically frozen flow.

and  $P_{41} = 50$  kPa for all cases. Also shown in Figure 3.11 are predictions from the shock decay model described above, where the initial shock speed is computed using the chemically-frozen shock Hugoniot (vibrational equilibrium), and the decay parameters  $\beta$  and  $\alpha$  are evaluated using the perfect-gas correlations (3.9). Relative model errors, given by  $M_{s,model}/M_{s,sim} - 1$ , are shown in (b).

These results show that the decay model remains accurate, even for shocks in real gases for the conditions examined here. The chemically-frozen initial shock speed and Hugoniot were chosen because they were more accurate than if chemical-equilibrium was assumed. Consequently, the chemically-frozen Hugoniot is used for all shock decay calculations below. For stronger shocks, dissociation effects likely become more significant and may need to be incorporated.

### 3.4 Results: Post-Shock Flow

The bulk of this work has so far focused exclusively on the shock propagation itself. However, the flow behind the shock is what is of interest for all shock-tube applications. An important consequence of using a decaying shock is that the post-shock flow has nonuniform temperature and density even in the plateau period. To show these effects, results from a single simulation are considered here for  $P_{41} = 50$  kPa ethylene-oxygen and  $P_1 = 5$  kPa air. Based on above results, these calculations were performed assuming air to be chemically frozen (vibrationally equilibrated).

Figure 3.12 shows a space-time diagram with color map corresponding to  $\log(\rho/\rho_1)$ . The shock is easily identifiable as the crisp diagonal boundary. The contact surface is



visible following the shock as a negative jump in density. Four red lines are plotted, which correspond to the axial position where pressure and density are plotted in Figure 3.13(a) and (b), respectively.

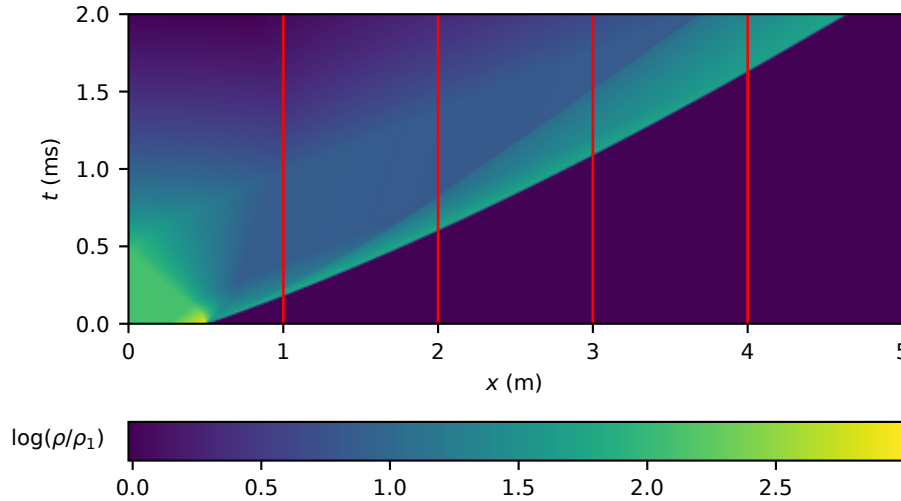


Figure 3.12: Space-time diagram with color corresponding with  $\log(\rho/\rho_1)$  for simulation with  $P_{41} = 50$  kPa ethylene-oxygen,  $P_1 = 5$  kPa air.

Pressure and density profiles show the post-shock flow as the shock decays toward the plateau period. The plateau is evident from the pressure data as a region of constant pressure that is overtaking the shock. The contact surface lies within this plateau period. As shown in (b), shocked air in this plateau period does not have uniform density, because each particle path was processed by a shock with different strength. The kink in the  $x = 3.0$  profile shows the boundary defined by the last TZ wave characteristic. These results are relevant to designs using shock-initiated detonation, which attempt to shorten or eliminate the TZ wave. If there is any shock decay, then there will be a region of nonuniform entropy, regardless of whether the shock subsequently reaches a period of steady propagation.

### 3.5 Implications of Shock Decay Model

From comparison with simulation results, the shock decay model, in particular the power-law formulation, has been shown to be highly useful for predicting the time evolution of shock speed. There are several implications from these results that will be discussed below.

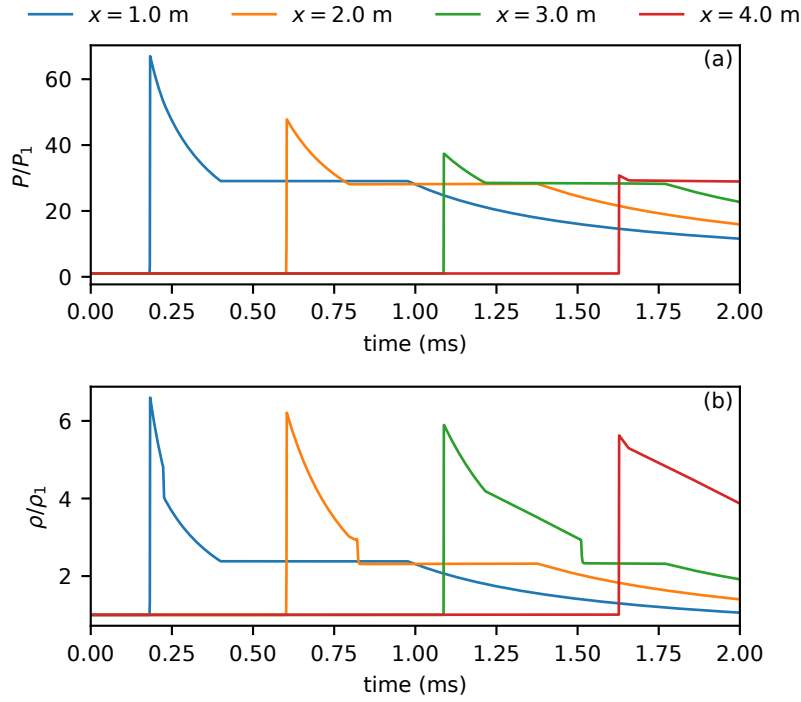


Figure 3.13: Pressure and density profiles at various axial positions for simulation with  $P_{41} = 50$  kPa ethylene-oxygen,  $P_1 = 5$  kPa air.

### 3.5.1 Shock Decay Formulae

At this point, it is useful to present some formulae that result from the shock decay model. The shock acceleration is given by

$$\begin{aligned} \frac{\dot{M}}{M_0} &= \frac{-\beta}{(1 + \beta t/\alpha)^{\alpha+1}} = \frac{-\beta\delta}{1 + \beta t/\alpha}, \\ \frac{\dot{M}}{M} &= \frac{-\beta}{1 + \beta t/\alpha} = -\beta\delta^{1/\alpha}, \end{aligned} \quad (3.10)$$

which gives the interesting result that the time scale defined by the local decay rate,  $\tau_d = (-\dot{M}/M)^{-1}$ , increases with time as

$$\tau_d = \frac{1}{\beta} + \frac{t}{\alpha}. \quad (3.11)$$

Many shock-change coefficients vary linearly with  $M$  for strong shocks, hence (3.11) indicates that the corresponding gradients are decreasing like  $\sim t^{-1}$ . Equation (3.11) provides the time scale for the post-shock unsteadiness when the shock has processed the relevant region of the test gas.

The model relates shock speed with time, but it can be integrated to be reformulated in terms of shock position,  $X$ ,

$$\delta = \left( 1 + \frac{1 - \alpha}{\alpha} \frac{\beta}{M_0} X \right)^{-\alpha/(1-\alpha)}, \quad (3.12)$$

which shows that the spatial decay rate is scaled by  $M_0$ .

Shock tubes are calibrated based on the shock wave that ultimately processes the test gas. In expansion tubes and shock tunnels, this is only a small volume of gas at the end of the shock tube. Hence, it is useful to consider the shock properties at this position. For a shock-tube with length  $L_s$  and driver length  $L_d$ , the shock wave at the output of the shock tube is described by

$$M = M_0 \left( 1 + \frac{1 - \alpha}{\alpha} \frac{\beta}{M_0} \frac{L_s}{L_d} \right)^{-\alpha/(1-\alpha)}. \quad (3.13)$$

Equation (3.13) can be used to calculate  $\dot{M}$  from (3.10).

### 3.5.2 Reducing the Decay Rate

Shock unsteadiness is directly proportional to  $\beta$ . The time scale of the initial decay rate scales with the driver length. So, the simplest strategy for reducing shock decay is to use a driver as long as possible.

As mentioned above, another method for reducing  $\beta$  is to reduce  $a_{42}/a_1$ . Since the test gas is fixed, this requires reducing the CJ state sound speed. This can be accomplished in practice by diluting the driver mixture with a heavy gas. However, the detonation reaction zone is highly sensitive to post-shock temperatures, and dilution with a gas that has even a modest heat capacity can significantly impact detonation stability. Lower detonation temperatures lead to increased reaction zone lengths and larger detonation cells. Hence, significant dilution with, e.g.,  $N_2$  or  $CO_2$  could render the mixture undetonable. Noble gases can be used to dilute driver mixtures since they are monatomic and so have minimal heat capacity. Contenders are argon, krypton, and xenon.

Figure 3.14 shows calculations for ethylene-oxygen detonations with various amounts of these diluents. As expected,  $CO_2$  and  $N_2$  cause a rapid increase in induction-zone length, whereas it is only modestly affected by noble gas dilution. Krypton and xenon are by far the most effective at reducing sound speeds. Unfortunately, these gases are quite rare and expensive. This leaves only argon as a viable diluent. 50% argon dilution of ethylene-oxygen results in a modest 15% reduction of the CJ sound speed. If krypton could be used, then 50% dilution would result in a 34% reduction.

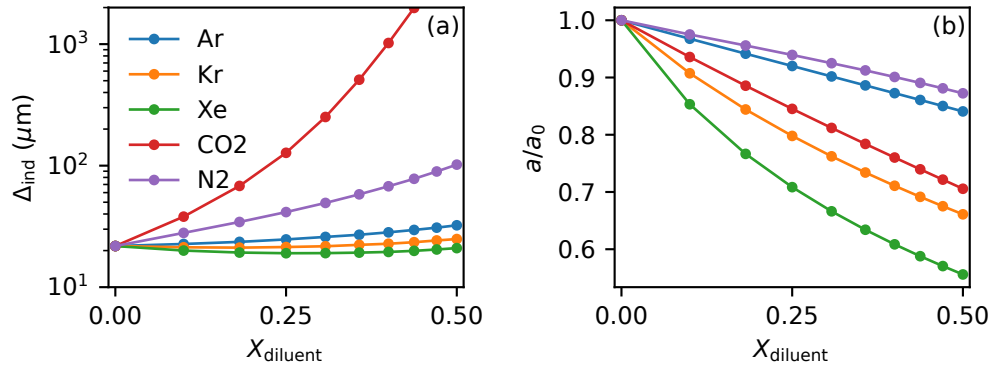


Figure 3.14: Calculations of ZND induction zone length and CJ sound speed for 1 bar of  $\text{C}_2\text{H}_4 + 3\text{O}_2$  with various diluents. Sound speed data in (b) are normalized by the undiluted CJ value,  $a_0$ .

### 3.5.3 Driver Mixture Effects

The performance of different driver mixtures can be investigated using the decay model. Prior work has largely focused only on the initial condition. This is inaccurate because it does not capture the rate at which a given shock will decay. These calculations were performed for four mixtures:  $\text{C}_2\text{H}_4 + 3\text{O}_2$ ,  $2\text{H}_2 + \text{O}_2$ ,  $\text{C}_2\text{H}_4 + 3\text{O}_2 + 4\text{Ar}$ , and  $\text{C}_2\text{H}_4 + 3\text{O}_2 + 4\text{Kr}$ . Pressures were varied to examine several effects. Results from these calculations are shown in Figure 3.15, where trajectories are calculated up to the predicted plateau-state shock speed and are plotted against the spatial coordinate. Note that the normalization by  $L_d$  is included explicitly in the axis label for clarity, but this is no different from the dimensionless  $X$  variable used above. All cases use a constant  $P_1$  pressure of 10 kPa air. The  $P_{41}$  pressure is adjusted for each set of calculations. These pressures are listed in Table 3.2.

In (a), initial driver pressures are constant and equal to 100 kPa. Undiluted ethylene-oxygen produces the strongest shock. Dilution reduces the CJ sound speed and pressure and therefore shocks are initially weaker. The shock for the hydrogen case decays rapidly, crossing trajectories for both diluted ethylene cases.  $P_{41}$  pressures are important to consider as they determine the diaphragms required to stand off initial pressure differences. Thinner diaphragms are possible for ethylene mixtures over hydrogen mixtures, because initial pressures are lower.

In (b), initial driver pressures are adjusted so that the CJ pressure,  $P_{42}$ , is the same for each mixture, approximately 3.31 MPa. This is most relevant to considering a given facility's peak operating pressure, since structural loading is determined by

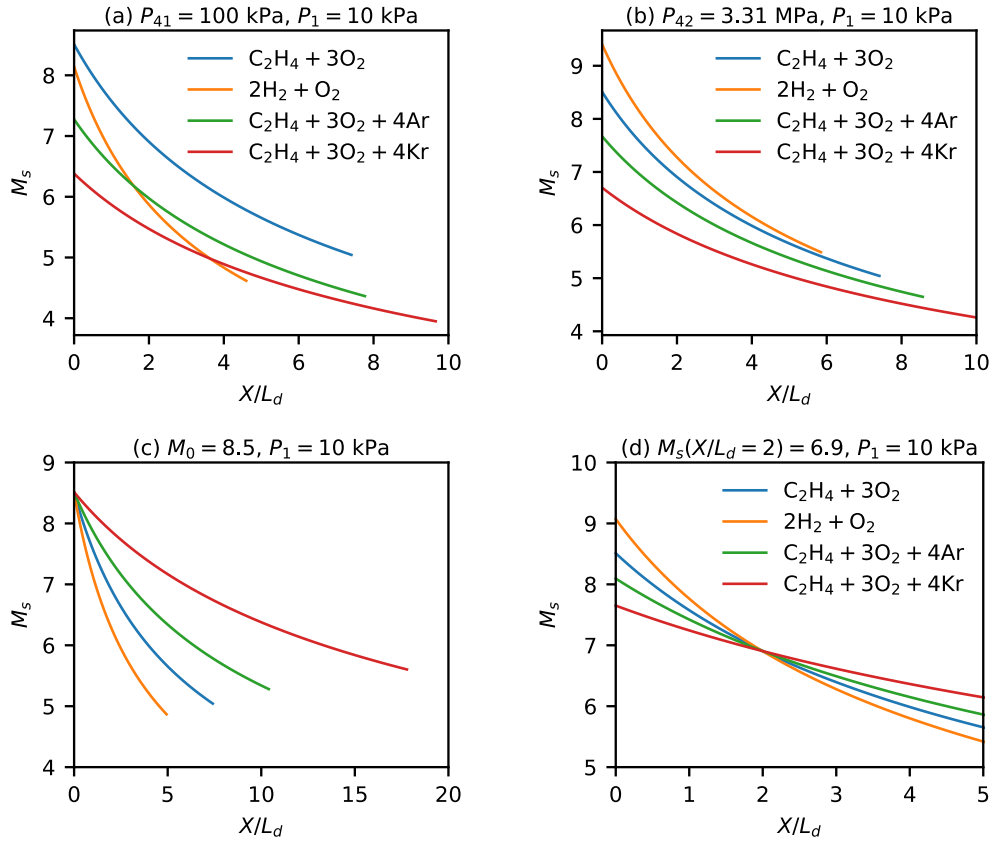


Figure 3.15: Calculations of forward-mode detonation-driven shock decay for four driver mixtures. Each subplot shows calculations for different  $P_{41}$  pressures.

the CJ pressure and not initial pressures. With its greater sound speed, the hydrogen mixtures drives a notably stronger shock, but it decays toward the undiluted ethylene trajectory.

In (c), driver pressures are adjusted so that the initial shock Mach number,  $M_0$ , is the same for each. This was approximately  $M_0 = 8.5$ . This comparison shows clearly the effects of different values for  $\beta$ . The hydrogen case decays more rapidly than the diluted-ethylene cases. What is also striking about these calculations is the enormous increase in gas required to compensate for dilution. From Table 3.2, the argon-diluted pressure must be more than doubled to obtain the same initial shock speed. However, this is compensated for by the reduced decay.

In (d), driver pressures are adjusted so that the decayed shock Mach number at a position  $X/L_d = 2$  is the same for each case. This is meant to model a shock tube with a driven-to-driver length ratio of 2. Hence, these calculations are the ones most

relevant to real shock-tube operation.

Table 3.2: Values of  $P_{41}$  corresponding with calculations in Figure 3.15

mixture	(a) $P_{41}$ (kPa)	(b) $P_{41}$ (kPa)	(c) $P_{41}$ (kPa)	(d) $P_{41}$ (kPa)
$\text{C}_2\text{H}_4 + 3\text{O}_2$	100	100	100	100
$2\text{H}_2 + \text{O}_2$	100	174	118	151
$\text{C}_2\text{H}_4 + 3\text{O}_2 + 4\text{Ar}$	100	126	205	162
$\text{C}_2\text{H}_4 + 3\text{O}_2 + 4\text{Kr}$	100	126	445	247

### 3.6 Summary & Conclusions

In this chapter, the strong-shock power law formulation derived previously was applied to empirically fit perfect-gas numerical simulation data. Exceptional agreement was found for all conditions simulated. Multivariate correlations were used to relate the propagation law fit parameters to key independent variables, namely the pressure and sound speed ratios. This model was shown to remain accurate for simulations including air with a non-constant heat capacity and finite-rate reactions.

The decay model was used to investigate various driver mixtures. Hydrogen mixtures with their elevated sound speed produce the highest initial performance for a forward-mode detonation driver. However, the subsequent shock decay must be taken into account, since the high sound speed results in more rapid decay.

Driver dilution with a heavy gas was considered to reduce sound speeds and thereby reduce expected decay rates. Argon is the only realistic contender, unless krypton or xenon can be obtained affordably. Calculations show that heavy gas dilution does reduce decay rates, however, at the cost of requiring increased  $P_{41}$  pressures.

An important consideration is to minimize the initial pressure difference across the diaphragm. For lower pressures, thinner diaphragms can be used, and this could possibly be advantageous. In these cases, hydrocarbon mixtures are preferred over hydrogen, as was demonstrated here with ethylene. Minimally, this shows the utility of using driver gases other than hydrogen, which has been the focus of prior work almost exclusively. For laboratory experiments, it is convenient to use lower  $P_{41}$  pressures because of typical instrumentation ranges and safety. Consequently, the majority of experiments in this work used ethylene as the driver fuel.

## *Chapter 4*

### TIME-RESOLVED SHOCK SPEED MEASUREMENTS: METHODS

A small-scale shock tube was constructed to experimentally characterize the shock waves generated by a detonation driver in both forward-mode and reverse-mode operation. The shock tube was constructed to also enable operation with a conventional high-pressure helium driver for comparison with the detonation driver. This chapter presents the facility and the methods used to perform time-resolved shock speed measurements. These new techniques were employed so that the shock acceleration behavior could be confidently compared with shock decay modeling. Additionally, the method is able to resolve frequency behavior in the shock motion, providing new insight into these dynamics in shock tubes. Results from this study are presented in the next chapter.

#### **4.1 GALCIT Unsteady Shock Tube (GUST)**

The shock tube constructed for the present experiments is diagrammed in Figure 4.1. The shock tube has a continuous 76.2-mm inner diameter with a driver length of 438.6 mm and driven-section length just over 2 m. The driven section uses a transparent off-the-shelf polycarbonate tube with a 6.35-mm wall thickness and 0.76-mm internal diameter tolerance. The extruded plastic surface was sufficiently smooth to directly seal against with O-rings. The detonation driver and diaphragm closure were rigidly mounted to an I-beam, so that detonation thrust forces were not transmitted to the polycarbonate tube.

Figure 4.1 shows the position of two pressure transducers on either side of the diaphragm. These sensors (PCB piezotronics 113B26) were digitized at 14 bit and 2.5 MS/s (NI PXI-6133). The driver-side transducer was used for timing and to characterize the incident detonation wave.

The driver initiates detonation in the main tube by implosion of an annular wave formed in outer channels. This detonation imploder was built and extensively characterized in several previous studies (Grunthaner et al., 2001, Jackson, 2005, Jackson and Shepherd, 2007). Diagrammed in Figure 4.2, the driver is composed of concentric aluminum tubes with channels milled on the outer surface of the

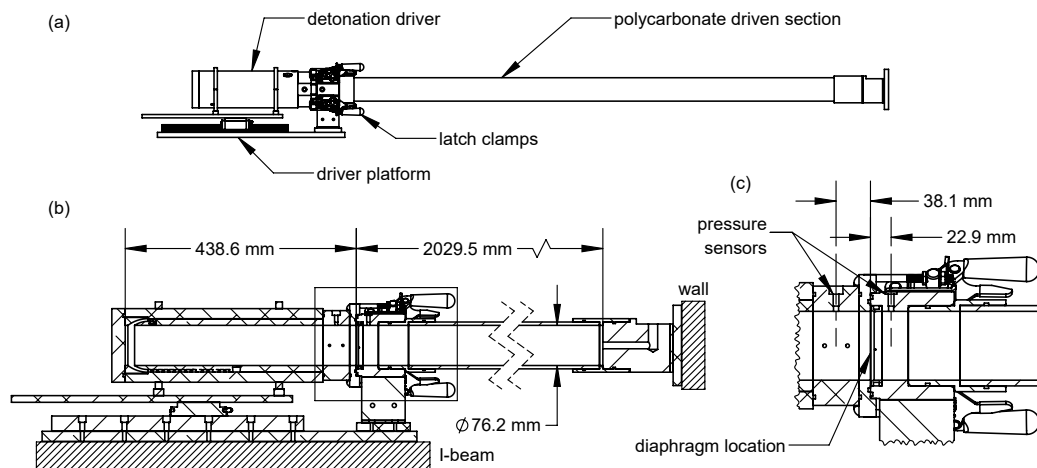


Figure 4.1: Diagram of detonation-driven shock tube with transparent polycarbonate driven section.

inner tube. The detonable mixture is ignited in the outer channels where obstacles facilitate transition to detonation, and the channels uniformly spread the wave into an annular detonation. Figure 4.2(c) shows the inner sleeve unwrapped. At one end, the detonation exits the outer channels and is redirected into the inner core where the detonation implodes, transitions to a plane wave, and propagates down the length of the driver. The driver could be flipped so that the detonation imploded either at the upstream end wall or at the shock tube diaphragm, enabling either forward or reverse-mode operation.

After evacuating to less than 100 mTorr, the driver mixture was prepared using the method of partial pressures and mixed with a recirculating pump for 2 minutes. Three driver mixtures were used in the present work: stoichiometric ethylene-oxygen, hydrogen-oxygen, and ethylene-oxygen diluted with 50% argon. High-purity synthetic air (20.91%  $O_2$ ) was used as the driven section test gas for the majority of shots. For other test gases, an additional recirculating pump was used to mix the driven section for 2 minutes.

Static fill pressures were measured using transducers with 0.5% reading accuracy and nominal variation typically within 10 Pa of the set point. Temperatures in the driver and driven section were recorded using K-type thermocouples. Driver temperature typically rose a few degrees over the course of several shots, so that the mean temperature was 23.5°C with standard deviation 0.7°C. Driven-section temperatures were typically 22.5°C.



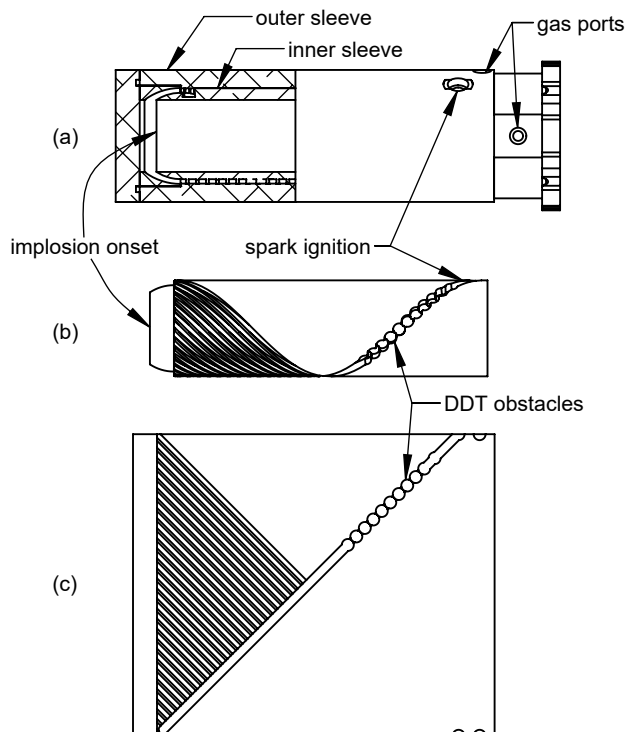


Figure 4.2: Diagram of detonation driver. Detonation is initiated and shaped in channels of inner sleeve, which is shown unwrapped in (c).

Mylar diaphragms were used for all detonation driver experiments. Three diaphragm thicknesses were used: 12.7, 25.4, and 50.8  $\mu\text{m}$ . The driver was also operated as a high-pressure helium driver, where it was pressurized with helium until diaphragm rupture. 1100-O aluminum was used for these diaphragms with 0.15-mm and 0.30-mm thicknesses. Diaphragms were not scored and a knife-blade cutter was not used, however good shot-to-shot repeatability was still obtained. A Heise 300 psig dial gauge was used to measure driver pressure for these experiments.

Over the course of the several hundred shots performed in GUST, a regular observation has been the significance of damage from Mylar diaphragm particulate. Although diaphragms were thin, significant particulate is generated by diaphragm rupture, and particulate is accelerated to high velocities. The stainless-steel plug at the shock-tube end is significantly pitted from impact of this particulate.

In Appendix G, all engineering drawings for this facility and other components are included. A schematic of the facility's gas supply system is also included.

## 4.2 Detonation Speed Measurement

The detonation driver design included a component to make detonation speed measurements. A pair of fiber-coupled optical ports, spaced by 25.4 mm, viewed the inside diameter through 1-mm diameter apertures. Fibers routed detonation luminosity to a pair of photodetectors, the signals from which were used to estimate detonation time-of-flight. Figure 4.3 illustrates the setup.

The 1-mm apertures were made from center drilling set screws that could be advanced flush with the tube inside diameter. It was found that covering the aperture with Kapton tape was sufficient to prevent the detonation from propagating through the 1-mm hole. This was important for obtaining crisp signals. Usually, the tape had to be replaced every few shots especially for higher pressure conditions. Multimode fibers with a 1-mm core (Thorlabs M35L01) were used to improve transmission to the two amplified photodetectors (Thorlabs PDA100A).

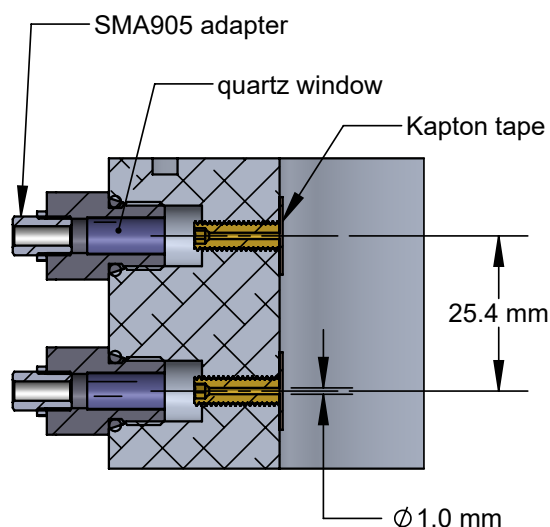


Figure 4.3: Diagram of closely-spaced fiber-coupled optical ports for measuring detonation time-of-arrival.

Photodetector signals were passed through an analog 20 kHz 8<sup>th</sup>-order Bessel high-pass filter (Krohn-Hite 3384) to effectively differentiate the signal, giving sharper pulses. The pulses were then digitized (LeCroy 44Xs-A). Detonation time-of-arrival was identified from 50% of the pulse rise time. Figure 4.4 shows an example of these signals. The ringing after the pulse is from the filter's step response as well as fluctuations in luminosity.

Figure 4.5 shows examples of detonation speed measurements for the driver mixtures considered. Detonations were typically observed to propagate within 2% of the CJ

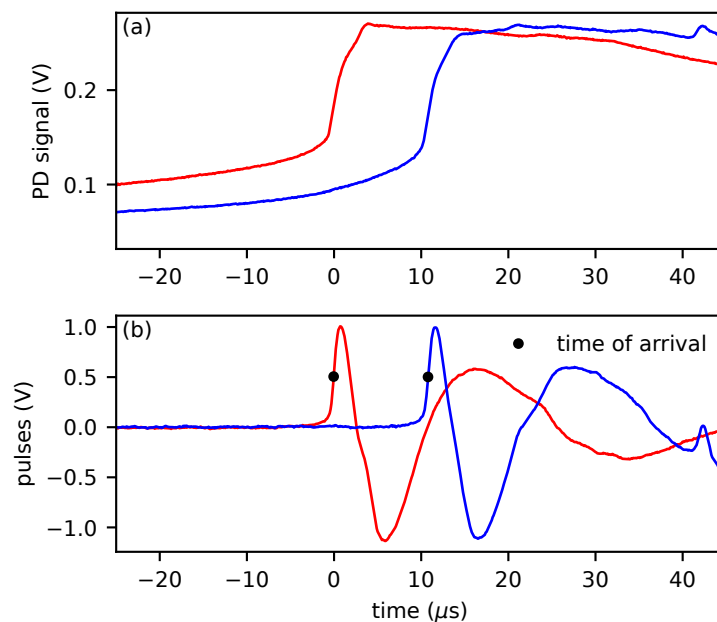


Figure 4.4: Example of photodetector (PD) signals in (a) and filtered signal pulses in (b) used to measure detonation speed.

speed. There is greater scatter for hydrogen data. This is partly suspected to be from the greater CJ speed (2.8 km/s for hydrogen-oxygen vs 2.3 km/s for ethylene-oxygen). Shots where a larger deviation from CJ speed was observed were repeated. In all experiments performed in GUST, no sensitivity to variations in detonation speed was observed. These measurements nonetheless provided a useful verification of detonation driver operation.

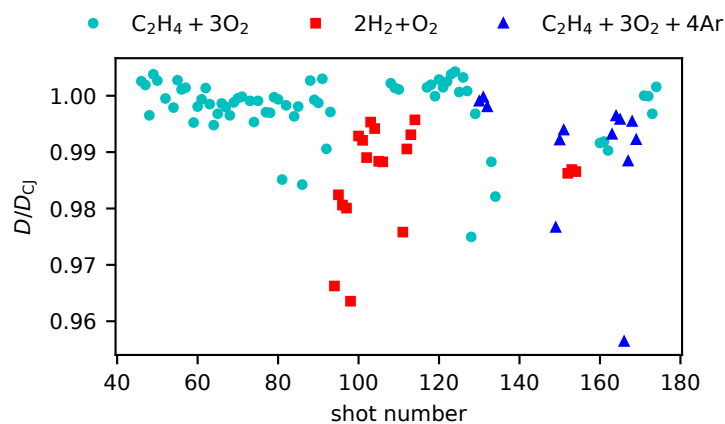


Figure 4.5: Detonation speed measurements for three driver mixtures.

### 4.3 Shadowgraphy Methods

#### 4.3.1 Optical Setup

Shock propagation along the tube was recorded using high-speed shadowgraphy with a field-of-view (FOV) just over 500-mm wide. Shadowgraphy was chosen for its high sensitivity to shock waves and its modest requirements for optical quality, which was important for visualization through the polycarbonate tube. The setup, diagrammed in Figure 4.6, was built on rails so that it could be translated along the tube length.

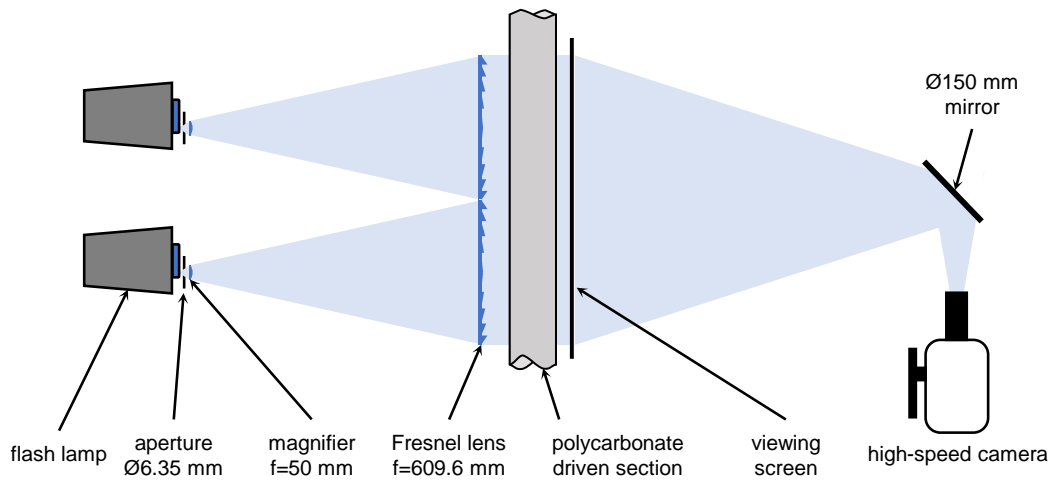


Figure 4.6: Diagram of large field-of-view shadowgraphy setup.

The light sources used were a pair of flash lamps (Elinchrom D-Lite 4) which generated approximately 1 ms of broadband white light in a 400 J flash. Only a small section of the ring-shaped flash tube was used by positioning a 6.35-mm diameter aperture directly in front of a portion of the tube. Light from the rest of the flash tube was obstructed from entering the system.

Each flash lamp was collimated by a 279.4-mm square Fresnel lens with 609.6-mm focal lengths (Edmund Optics 32-691). Just after the 6.35-mm aperture, a 50-mm focal length lens was used to increase the system's numerical aperture and increase throughput. Collimated light was transmitted through the polycarbonate tube and was incident on a viewing screen located less than 15 mm from the tube. The viewing screen was a 220-grit sandblasted acrylic panel.

The viewing screen was recorded by a high-speed camera (Phantom v2512) using an 85-mm Nikon lens. The camera was configured to use a 1280×16 pixel FOV along the tube centerline with a 830 kfps framing rate and a 265 ns exposure. Figure 4.7 shows a large FOV image of the polycarbonate tube and a 450-mm scale, used

for spatial calibration. The narrow FOV used for high-speed imaging along the tube centerline is highlighted. The dark vertical band down the middle is due to non-focusing margins of the Fresnel lenses. More details regarding the calibration of this optical setup are described in Appendix B.

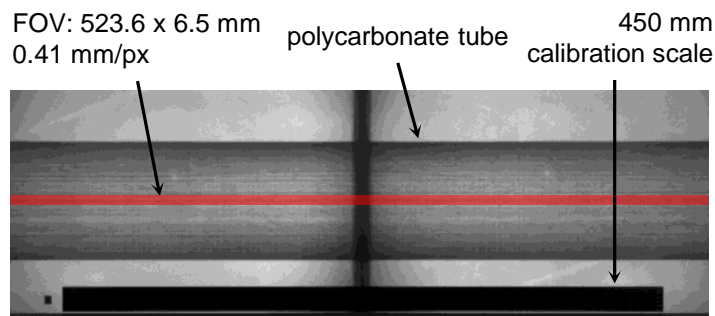


Figure 4.7: Example full field-of-view shadowgraph, showing width of polycarbonate tube and narrow measurement FOV.

Optical throughput was found to be important for competing with the luminosity of detonation products, which otherwise worsened shadowgraph contrast. Filtering this emission was not an option because the spectrum emitted by luminous detonation products and diaphragm material substantially overlapped with the flash lamp spectrum. Spectra were acquired for both the flash lamps and detonation products using an Ocean Optics FX spectrometer and are given in Appendix B.

Some issues were encountered with electrical pickup from the high-frequency circuit used to ionize and flash the flash tube. This issue was eliminated by using G-10 optical posts for the aperture and 50-mm lens.

Geometric distortion is a known challenge of quantitative shadowgraphy (Settles, 2001). The construction implemented here minimizes distortion by locating the viewing screen directly adjacent to the tube. Due to the finite source size and collimation by Fresnel lenses, which exhibit strong chromatic aberration, the depth of field is small with resolution decreasing from 2.0 lp/mm on the near side of the tube to 0.9 lp/mm on the far side of the tube, relative to the screen. This was measured with a USAF 1951 target without the polycarbonate tube in place. With the polycarbonate tube, resolution is decreased further to 0.5 lp/mm and varies along the tube length and degree of degradation. The polycarbonate tube required replacement roughly every 100 shots due to optical degradation. Mylar diaphragm debris would either scratch or stick to the inner surface, and the high temperatures from shock reflection blackened the end of the tube over time.

### 4.3.2 Post-Processing Algorithm

The shadowgraphy videos were post-processed to obtain measurements of shock position and speed. Each frame was background subtracted and vertically averaged. The signals were then filtered in space and time to eliminate signal from detonation-product luminosity and diaphragm fragments. Inter-frame displacements of the shock shadow signal were measured using the peak from signal cross-correlation. Sub-pixel correlation peaks were estimated using the three-point-Gaussian fit, commonly used in digital particle-image velocimetry (Willert and Gharib, 1991). The above post-processing steps are illustrated in Figure 4.8 and the code used to implement this algorithm is reproduced in Appendix B.

The resulting displacements for each frame pair give the shock speed over time in units of pixels per frame. These were transformed to laboratory coordinates using a spatial calibration of the viewing screen and the camera framing rate. After the algorithm was applied, data were resampled to a uniform grid. The signals showed significant high-frequency noise, and so time-series data are Savitzky-Golay filtered with fourth-order polynomials and 25 points per window, effectively a 55 kHz low-pass filter (Schafer, 2011). Figure 4.9 shows an example of raw and filtered signals obtained from one shot using the above post-processing algorithm. Uncertainty bounds are also shown which are described in the next section.

### 4.3.3 Uncertainty Analysis

Shock speed measurement uncertainty comes from two sources: geometric accuracy of shadowgraphs and the post-processing algorithm.

Shock shadowgraphs are assumed to be one-to-one between their position on the viewing screen and the shock's actual position in the shock tube. Geometric accuracy is limited by the optical components, including distortion by the polycarbonate tube, and their alignment. A calibration plate with 37 1.27-mm wide vertical grid lines, spaced 6.35-mm apart, was placed in the narrow measurement FOV, and the position of grid line shadows was compared with the true geometric positions on the plate. This was used to align the optical setup so that the average magnification was unity, however there was some variation across each lens with a maximum deviation of roughly 1%. This also includes uncertainty in the screen's spatial calibration.

Processing shock shadowgraph movies into speed measurements introduces error from the signal-to-noise ratio, the finite resolution, and variability in the signal shape. This was estimated by simulating the signal processing algorithm.

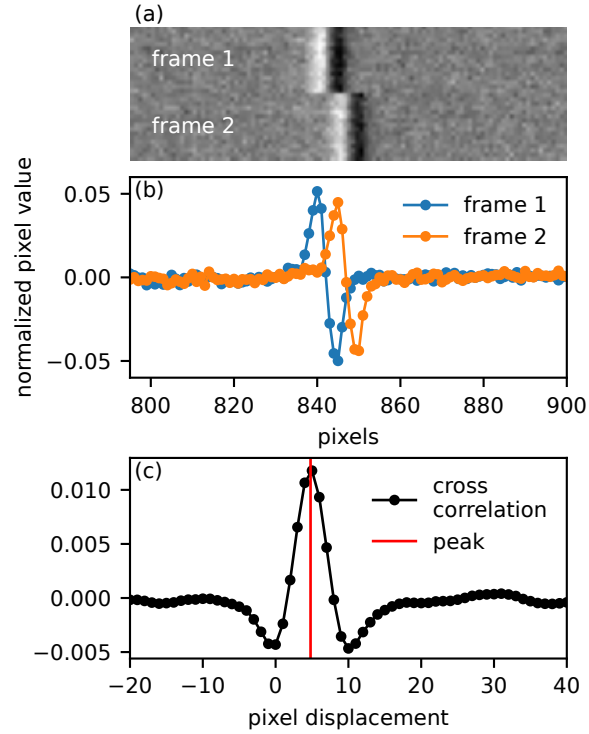


Figure 4.8: Post-processing steps to obtain frame-to-frame shock displacement. (a) shows exemplary pair of shock shadowgraph frames. (b) shows the signals from vertically averaging and filtering the frames. (c) shows the signals' cross-correlation and sub-pixel peak estimate.

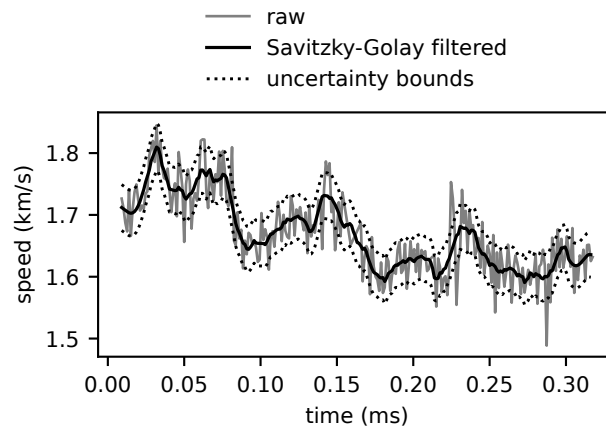


Figure 4.9: Example of raw and low-pass filtered shock speed signal obtained from post-processing algorithm. Uncertainty bounds are also shown.

A simulated shock is assumed to propagate through the shadowgraph field of view at a constant speed  $U_s$ . The shock shadowgraph image was modeled as the first

derivative of a Gaussian,

$$G(x, s, x_0) = -A \frac{(x - x_0)}{s} \exp \left( -\frac{(x - x_0)^2 + s^2}{2s^2} \right), \quad (4.1)$$

normalized so that  $G(x_0 + s, s, x_0) = -A$ , where  $A$  is the amplitude and  $s$  determines the signal width. The function  $G$  is evaluated on a 1280 pixel grid. As the shock travels through the tube with speed  $U_s$ , the position of the shadowgraph translates as  $x_0 = U_s t$ . The parameter  $s$  determines the width of the signal, where the average from experimental data was 2.4 pixels, ranging from 1.2 to 3.6. Measurement signals were normalized by the bit depth and background subtracted, resulting in signal amplitudes ranging from 0.02 to 0.08.<sup>1</sup> Noise in each pixel was experimentally measured and is modeled as additive white Gaussian noise with a variance of 0.0015.

The post-processing algorithm was simulated for a range of constant shock speeds, where variation in the signal amplitude and width was modeled by sampling from a uniform distribution for each simulated frame. The initial sub-pixel position of the shock was also varied for each iteration. For each speed,  $5 \cdot 10^4$  iterations were performed. Resulting histograms of algorithm error were not normally distributed, so empirical cumulative distribution functions (eCDFs) were generated for each shock speed, and a 95% algorithm uncertainty bound was chosen. Figure 4.10 shows example eCDFs in (a) and values of the uncertainty bound for each simulated shock speed in (b), ranging from 0.5 km/s to 3 km/s. There is variability, so the algorithm uncertainty is bounded at 20 m/s for all shock speeds.

The combination of the above sources of uncertainty gives the following expression for error in reported shock speed measurements

$$\epsilon = 0.01U_s + 20 \text{ m/s}, \quad (4.2)$$

where deviations from the true shock speeds in 95% of measurements are expected to lie within this bound. Other sources of uncertainty like variation in detonation speed are negligible in comparison and so are neglected.

Measurement error in facility pressures and temperatures also contributes uncertainty to predictions using the ideal one-dimensional model described above. Due to generally small variation in the model exponent,  $\alpha$ , only error in  $M_{s,0}$  and  $\beta$  was considered. The net effect on these quantities was calculated to be less than 0.5% for the conditions tested here.

---

<sup>1</sup>This shows the shock shadowgraph contrasts achieved with this technique.



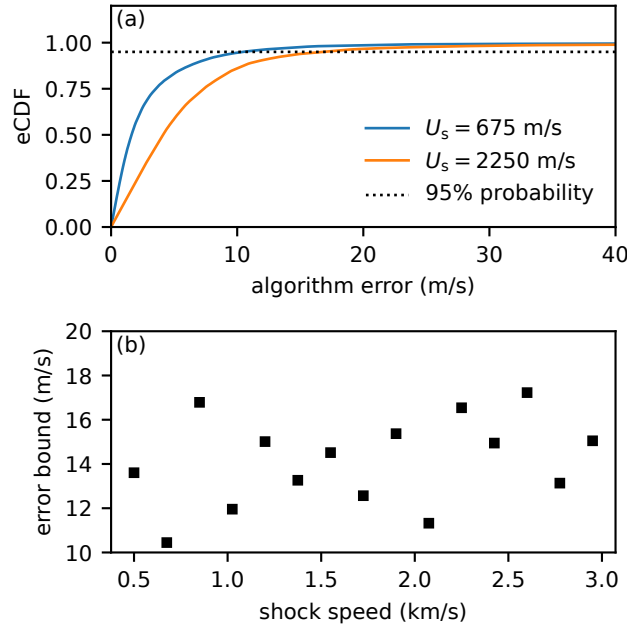


Figure 4.10: (a) eCDFs for two shock speeds. (b) 95% algorithm error bound from eCDFs.

## 4.4 Verification

### 4.4.1 Repeatability

In order to investigate many shot conditions, results from only one experiment for a given condition and tube axial position are used. This was found to be acceptable because of good shot-to-shot repeatability. From a set of six shots at the same condition and axial position, a standard deviation of 10 m/s was obtained. This includes the algorithm error described above. Since  $2\sigma$  is within the algorithm bound, shot-to-shot variation is within known uncertainty. Repeatability was regularly verified for other shot conditions during the progression of experiments.

### 4.4.2 Increased Spatial Resolution

The nominal shadowgraphy configuration used a wide FOV with 0.41 mm/px resolution. The example shadowgraphs in Figure 4.8 show that the shock is imaged on only a small number of pixels. To verify the shock structure was being sufficiently resolved, data were acquired for a narrow FOV configuration with 0.15 mm/px resolution. Figure 4.12 shows a comparison between shadowgraph signals obtained using the nominal wide FOV and a narrow FOV. The lower spatial resolution result from the wide FOV is shown to be sufficient at resolving the signals.

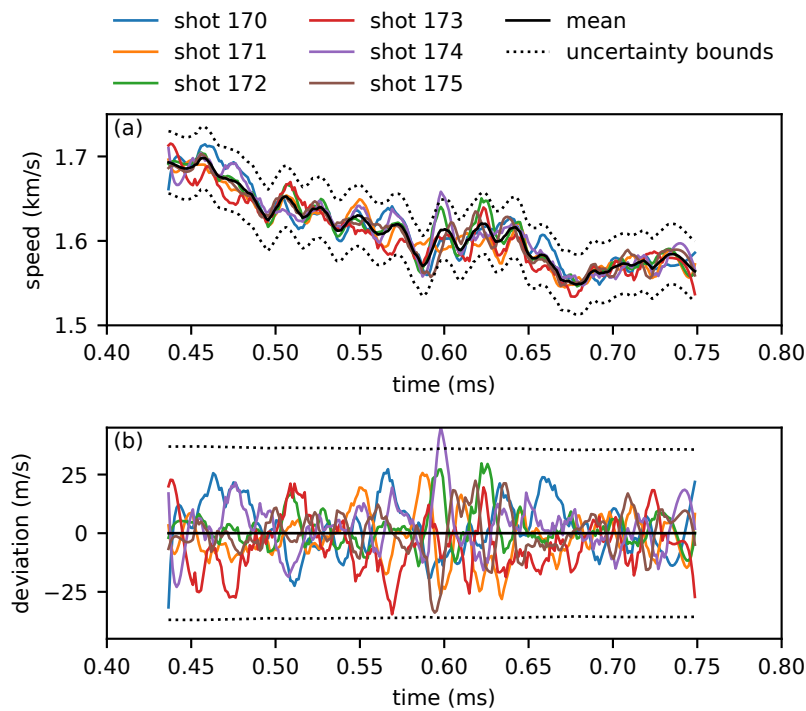


Figure 4.11: Shock speed measurements from six shots at the same condition.

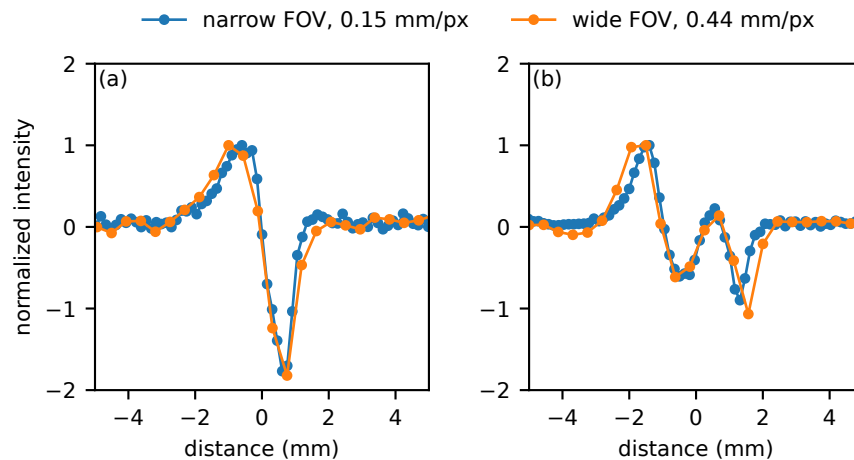


Figure 4.12: Shock shadowgraph signals from wide and narrow fields of view.

#### 4.4.3 Shock Shape & Motion

The measurement examples above show fluctuating shadowgraph signals and shock speeds, which were features of all experimental data. Shadowgraph signals regularly bifurcated, showing two dark or bright bands, instead of the typical Gaussian-derivative shape associated with shock shadowgraphs. The cross-correlation algorithm accurately measures displacement of a static signal, but it must be considered

how these signal shape fluctuations affect shock speed measurements. This will be addressed in this section.

Figure 1.2 shows these signal fluctuations in detail from one shot. (a) and (c) are constructed as space-time diagrams with signals incremented vertically with time. Data in (c) follow directly after data in (a). The unfiltered shock speed measurements using the cross-correlation algorithm for the selection of frames in (a) and (c) are shown in (b) and (d), respectively, as the black line on top of shock speed from the entire record in red. The shadowgraph signals in (a) initially show two positive peaks, where one peak propagates to the right through the signal. By the last frame in (a), the typical Gaussian-derivative shape is attained again, which persists until roughly  $94 \mu\text{s}$  in (c). Over this time period, the shock speed measurement shows a phase of acceleration and deceleration superimposed on the background shock decay.

The shock-speed oscillations are not merely a consequence of using the cross-correlation algorithm on a varying signal. Figure 4.14 shows a comparison with shock speed measured by tracking the signal minimum. The signal minimum, or the darkest position of the shadow, can be used to identify a single position for the shock. The peak-tracking method gives a noisier measurement, however both algorithms capture the same oscillatory behavior with a period of roughly  $75 \mu\text{s}$ .

The fine motion in the shock shadow signals is believed to be from fluctuations in the shock shape. Figure 4.16 shows large FOV shadowgraphs that captured the full tube diameter. The shadowgraphs are background subtracted and have their contrast stretched (the saturation is from the luminous detonation products). The shock shadow is curved, most clearly seen in (b), and this curvature varies with time.

A curved shock can produce the shadowgraph signal fluctuations observed above. Shadowgraphy is sensitive to the second derivative of changes in the medium's refractive index  $n$ , and the resulting change in optical intensity  $I$  can be approximated as (Merzkirch, 1987)

$$\frac{\Delta I}{I} \propto \int \left( \frac{\partial^2}{\partial x^2} + \frac{\partial^2}{\partial y^2} \right) (\log n) dz, \quad (4.3)$$

where  $x$  and  $y$  define the plane normal to the ray path, which propagates along the  $z$ -axis for small deflections. Since  $n \propto \rho$ , the shadowgraph obtained from a density field can be simulated by taking the second derivative normal to the optical axis and then integrating along the optical axis. This was done for some simple shock shapes

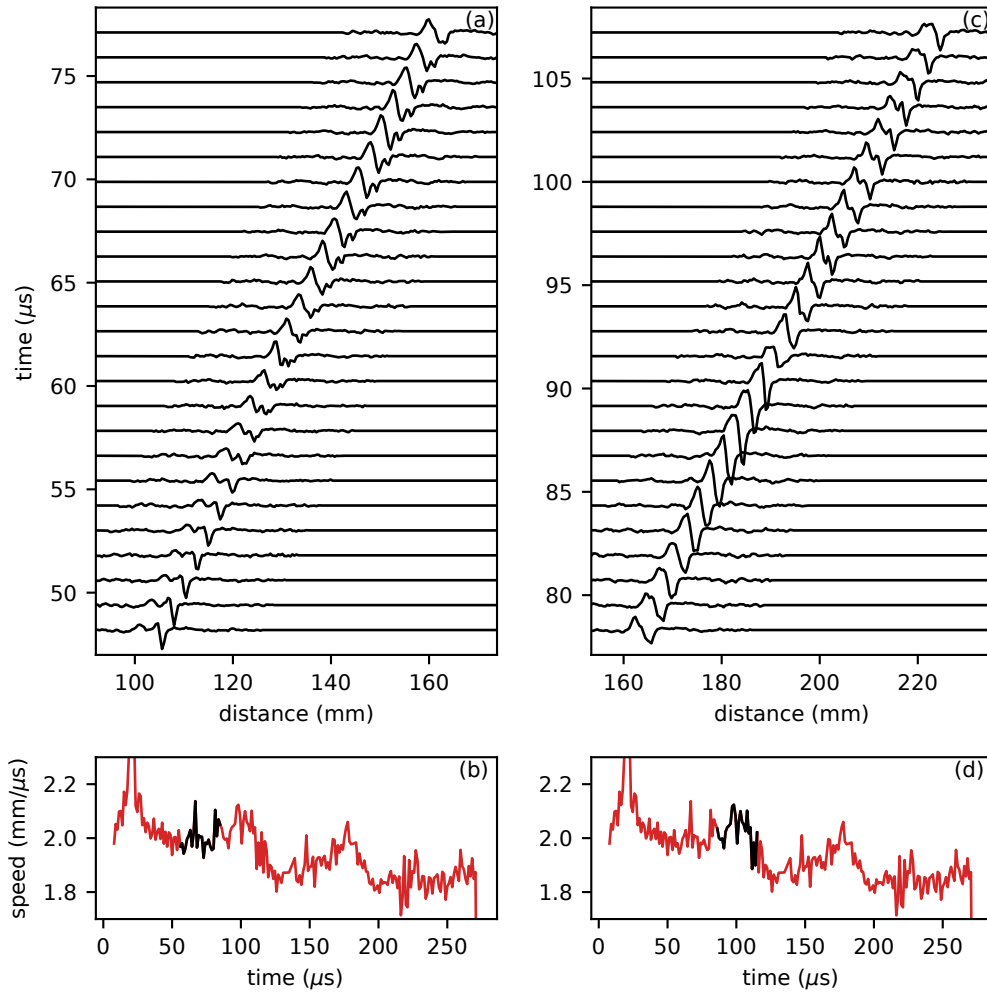


Figure 4.13: Shadowgraph frames are plotted as space-time diagrams in (a) and (c) with speed measurements from corresponding frames in (b) and (d), respectively. Shock speed from the entire record is plotted in red and from the frame selection in black.

shown in Figure 4.16. The domain of high density  $\rho$  is defined using a constant radius of curvature, and, in order to give the shock a finite thickness, the density fields were passed through a Gaussian filter. The shadowgraphs obtained from these density fields are shown in (d-f). The expected Gaussian derivative appears in (d), however the signal is distorted in (e) and (f) from the shock curvature. The convex shock in (c) is most similar to the shock's appearance in Figure 4.15. As the shock curvature deviates from zero, the shock shadow signal therefore appears to split and recombine. Whether the two peaks are positive or negative also indicates if the shock is concave (negative) or convex (positive).

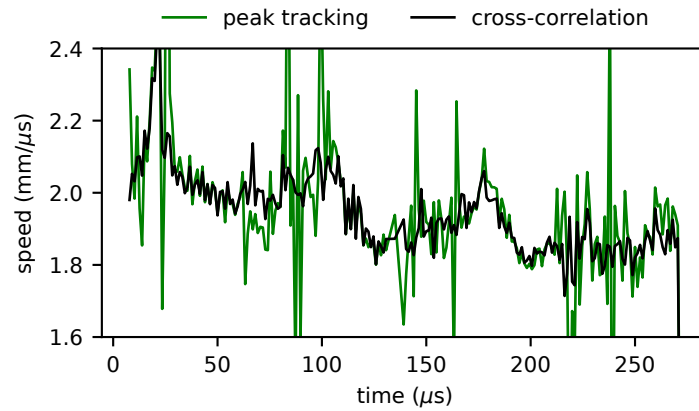


Figure 4.14: Comparison of shock-speed measurement using two post-processing algorithms.

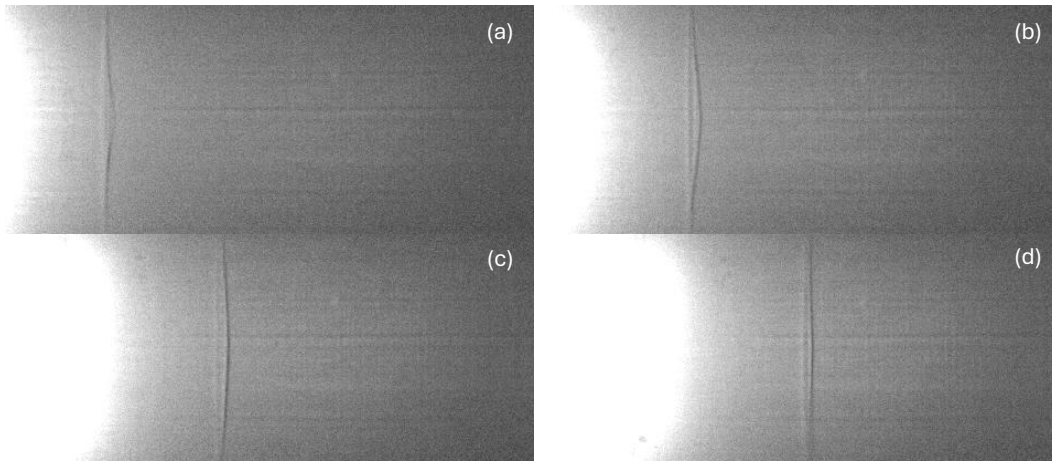


Figure 4.15: Large FOV frames showing curved shock.

It is believed that the shadow signal fluctuations are a consequence of these variations in shock shape, and the fluctuations introduce some structure to the shock speed measurements using the cross-correlation algorithm. To assess the impact on measurements, the cross-correlation algorithm was applied to simulated shadowgraph signals from a shock with constant mean speed and oscillatory curvature. Figure 4.17(a) compares a simulated and experimental shadowgraph signal for a time with peak shock curvature, illustrating that the simulation provides a reasonable model for the observed shadowgraph signals. The curvature was simulated to oscillate sinusoidally with a period of  $75 \mu\text{s}$ , similar to what is shown in Figure 4.13, and the simulated signal was propagated with a constant speed of  $2 \text{ km/s}$ . Figure 4.17(b) shows the resulting simulated shock speed measurement plotted with the speed of

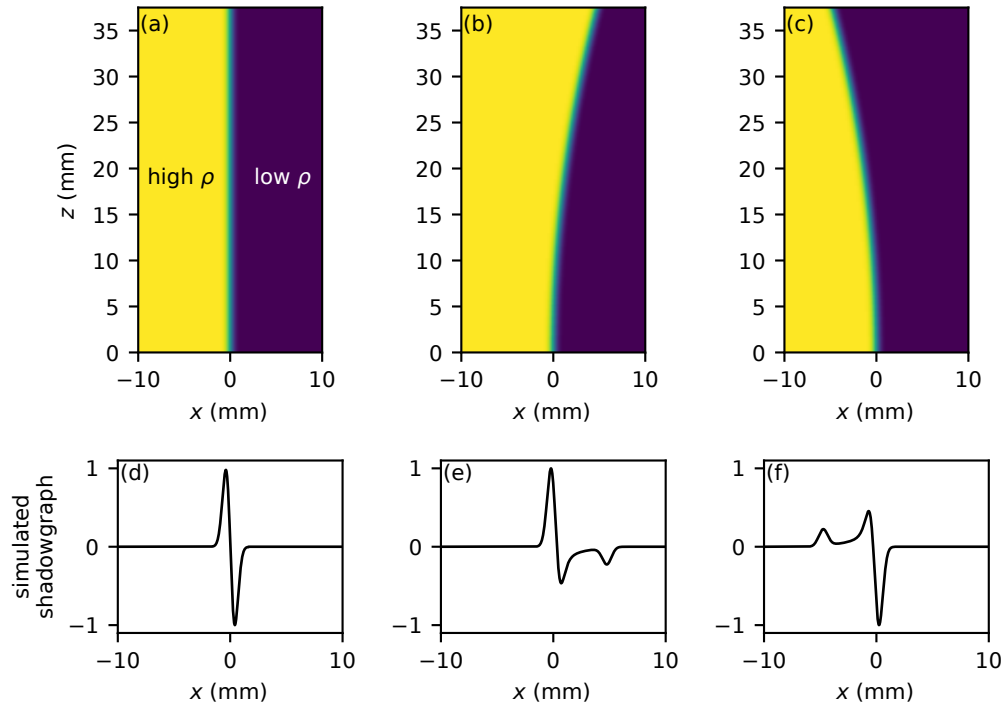


Figure 4.16: Simulated shadowgraphs of flat and curved shocks. Density color map in (a-c) with corresponding shadowgraphs in (d-f).

the curved shock's apex. Clearly, the sinusoidal variation in shock curvature, and therefore oscillations in the shadowgraph signal, introduces a perturbation to the measured shock speed. The perturbation is in-phase with the curvature oscillation, however it is not sinusoidal and does not show the same amplitude as the apex speed. This illustrates that frequency analysis of shock speed measurements gives useful insight into the shock dynamics, however care must be taken in interpreting the amplitude of these oscillations.

These simulations show the limitations of identifying a single shock speed for the dynamics of real shocks in a shock tube. A single shock speed only completely defines the dynamics for a shock with constant curvature. Real shocks, however, may exhibit more complicated dynamics with surfaces that change shape over time, and so a single shock speed is an incomplete description. The present experimental methods are capable of capturing the temporal variation of shock speeds, enabling new insight into these dynamics.

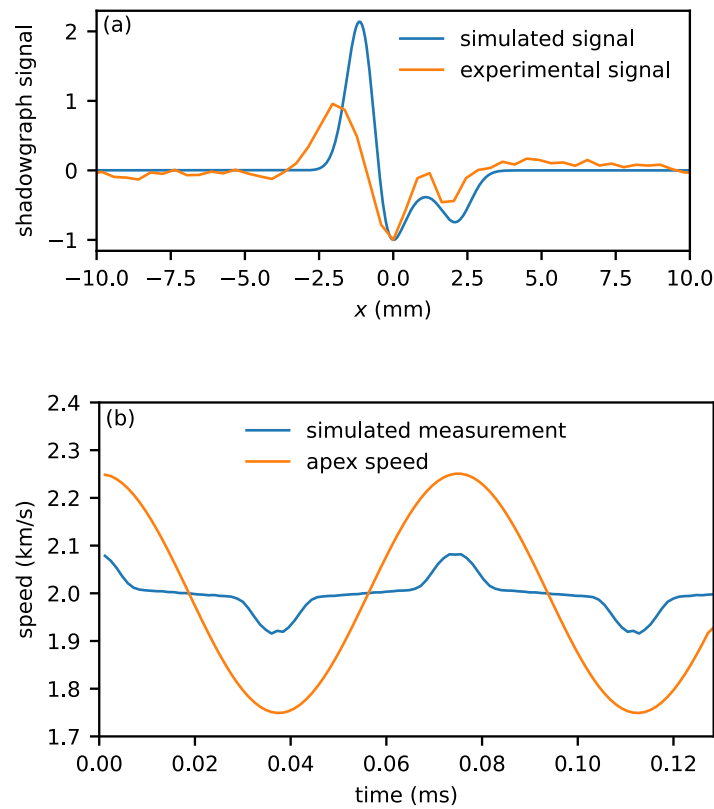


Figure 4.17: (a) Comparison between simulated and experimental shadowgraph signals. (b) Shock-speed measurement using cross-correlation algorithm for simulated shadowgraph signals with sinusoidal variation in shock curvature.

#### 4.5 Summary

In order to make high-resolution shock speed measurements, a shadowgraphy technique was devised for shock visualization through the transparent driven section of a shock-tube. The facility, GUST, and the technique were presented in this chapter, and shock-speed measurement accuracy was quantified. Some representative data were used to verify methods. In particular, measurements for a single shot condition were shown to be highly repeatable. Wide FOV shadowgraph signals were compared with those with increased spatial resolution, illustrating that the imaging resolution used is sufficient. Finally, perturbations to the shadowgraph signal were shown to be consistent with a time-varying shock curvature, and simulated signals were used to show that these signal perturbations introduce corresponding perturbations to shock-speed measurements. These results illustrate the challenge of identifying a single shock speed for the dynamics of a shock with time-varying curvature, however the present techniques may still be used to make measurements

of the periodicity of these shock oscillations.

In the next chapter, results from applying this technique toward the measurement of detonation-driven shock waves will be presented.



## *Chapter 5*

### TIME-RESOLVED SHOCK SPEED MEASUREMENTS: RESULTS & ANALYSIS

In this chapter, time-resolved shock speed measurements using the shadowgraphy technique described in Chapter 4 are presented. Shot conditions used for these experiments are tabulated in Appendix B. Experiments were performed using a forward-mode detonation driver, reverse-mode detonation driver, and a high-pressure helium driver. Results are from a total of 132 individual experiments, comprising 39 distinct shot conditions. Pressures, diaphragm thicknesses, and driver mixtures were varied. Three mixtures were used for the detonation driver corresponding to a nominal mixture ( $\text{C}_2\text{H}_4+3\text{O}_2$ ), a high-sound-speed mixture ( $2\text{H}_2+\text{O}_2$ ), and a low-sound-speed mixture ( $\text{C}_2\text{H}_4+3\text{O}_2+4\text{Ar}$ ).

Experimental results are compared throughout this chapter with model predictions. For forward-mode results, calculations use the decay model presented in Chapter 3. For reverse-mode and helium-driven conditions, only the initial shock Mach number is calculated. For all of these, the test gas is assumed chemically frozen. Model parameters are given with tabulated shot conditions in Appendix B.

#### **5.1 Results: Forward-Mode Detonation Driver**

##### **5.1.1 Diaphragm Rupture**

In the forward-mode driver, the detonation propagates downstream and strikes the shock tube diaphragm, which ruptures and leads to shock formation. The resulting unsteady shock motion is established by the initial condition of the detonation at the diaphragm. This condition is important to examine, so pressure measurements from the transducer directly upstream of the diaphragm in the driver are first briefly presented.

The pressure measurements are shown in Figure 5.1 for three diaphragm thicknesses and compared with the TZ wave at the transducer position, which is annotated in Figure 4.1. The first jump in pressure is from the incident detonation, followed by decay from the TZ wave, and then there is a second jump in pressure. This second jump is consistent with a shock reflected from the diaphragm when the detonation makes impact. The density of the solid material is greater than the CJ state by two

to three orders of magnitude, so that a shock is always reflected.

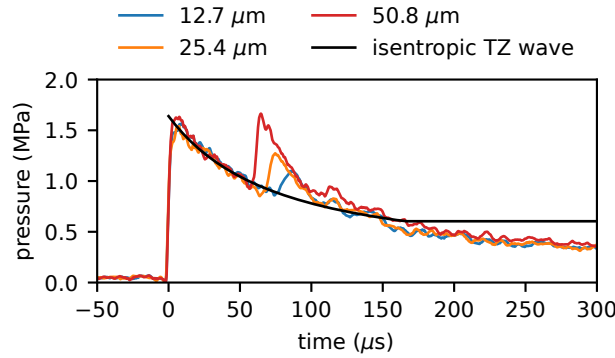


Figure 5.1: Pressure measurements showing detonation striking diaphragm. Transducer is 38.1-mm upstream of the diaphragm. Conditions are 50 kPa of  $\text{C}_2\text{H}_4 + 3\text{O}_2$ .

The high pressures from the shocked detonation products cause diaphragm fragmentation, and the forces accelerate the diaphragm downstream. Thinner diaphragms are lighter and accelerate faster, resulting in a more rapid expansion of the driver gas and so a faster attenuation of the reflected shock. Therefore, for thinner diaphragms, the reflected shock is observed later in time at a weaker magnitude, as shown in Figure 5.1. Additionally, pressure data are clearly consistent with the TZ wave prior to arrival of the reflected shock, which indicates that over this time scale boundary layer effects are negligible. This is important because it means that the isentropic detonation profile can be used to compute shock-tube initial conditions, neglecting diaphragm effects.

### 5.1.2 Pressure Ratio

Shock-tube performance is typically tuned by adjusting the pressure ratio. For the forward-mode detonation driver, both the initial shock speed and decay rate are affected. Shock speed measurements for six pressure ratios are shown in Figure 5.2, increasing from (a) to (f), where the driver pressure was a constant 50 kPa for all cases and the driven section pressure was varied. Also plotted are predictions from the decay model. As expected, significant shock decay is observed in all cases. Generally good agreement with the model is obtained for lower pressure ratios, however agreement worsens as the pressure ratio increases.

The mean ratio of shock speed measurements with model calculations, given by

$$c = \left\langle \frac{U_{s,\text{exp}}}{U_{s,\text{model}}} \right\rangle, \quad (5.1)$$

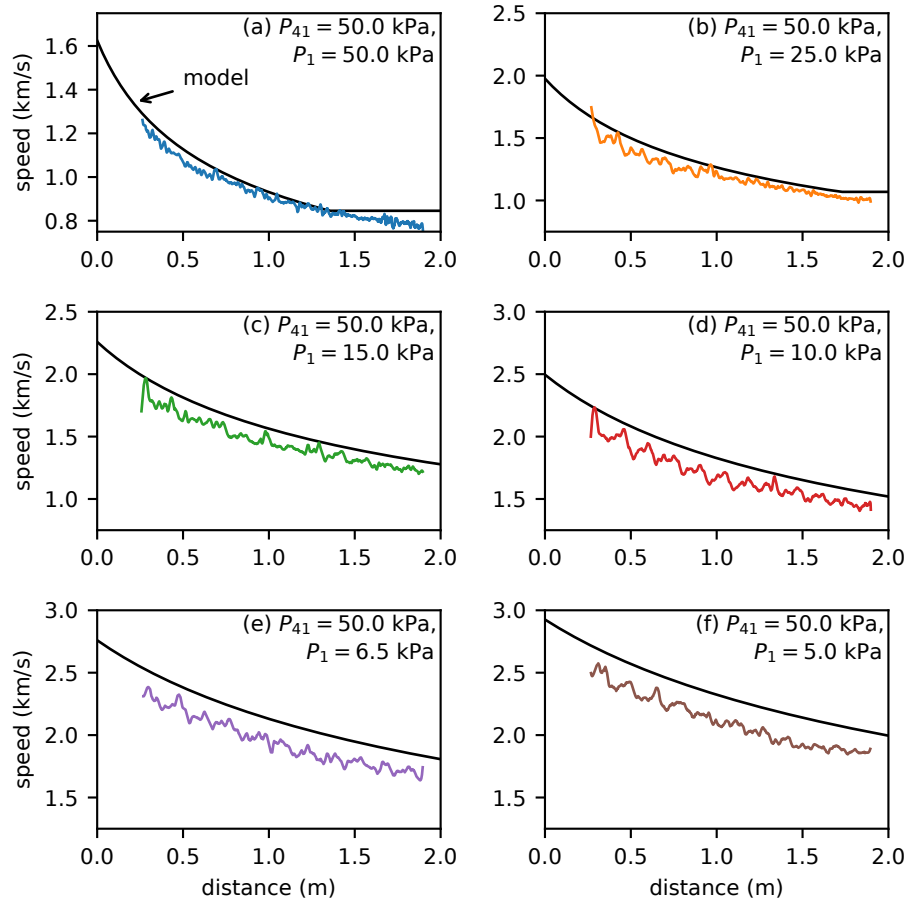


Figure 5.2: Forward-mode detonation-driven shock speed measurements for various pressure ratios, where unburnt driver pressure is  $P_{41} = 50$  kPa for all cases and driven section pressure,  $P_1$ , is varied. All cases use a  $\text{C}_2\text{H}_4 + 3\text{O}_2$  driver mixture and  $12.7 \mu\text{m}$  Mylar diaphragm. The ideal shock decay model is shown by the black line in each subplot.

quantifies deviations from the ideal theory. This is calculated only for data in the initial decay period, i.e., with velocities above the predicted steady shock speed in the plateau period. Note that (5.1) is calculated using the time-series data, since this is more consistent with the decay model. Values for  $c$  for each pressure ratio above are plotted in Figure 5.3, where uncertainty in both measurements and model are combined. Clearly, the deviation from the ideal model cannot be accounted for by measurement uncertainty. The fit shown is

$$c \approx 0.059 \left( \frac{P_{41}}{P_1} \right)^{-1} + 0.927. \quad (5.2)$$

Although mean error in the model is not negligible, it predicts the shock decay rate

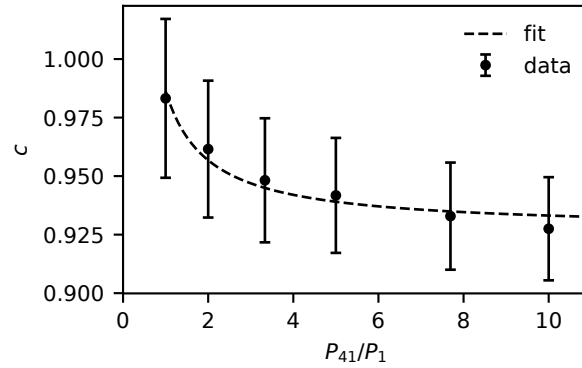


Figure 5.3: Mean ratio of shock speed measurement to ideal model,  $c$ , for each pressure ratio in Figure 5.2.

reasonably well, so  $c$  can be used as a correction to the shock decay model,

$$U_{s,\text{exp}} \approx \frac{cU_{s,0}}{\left(1 + \frac{\beta}{\alpha} \frac{a_1 t}{L_d}\right)^\alpha}, \quad (5.3)$$

$$U_{s,\text{exp}} \approx \frac{cU_{s,0}}{\left(1 + \frac{1-\alpha}{\alpha} \frac{\beta}{cU_{s,0}} \frac{a_1 X}{L_d}\right)^{\alpha/(1-\alpha)}}, \quad (5.4)$$

where (5.4) is the decay model in spatial coordinates from (3.12). Figure 5.4 shows the experimental data replotted with the calibrated model using (5.4).

### 5.1.3 Diaphragm Effects

Figure 5.5 shows the effect of Mylar diaphragm thickness on shock speed measurements in (a) and on the space-time diagram in (b). As the diaphragm thickness increases, the measured shock speeds are uniformly reduced, deviating further from the ideal model. The space-time diagram shows that the increased diaphragm thickness results in a delay in shock arrival time, indicating that the thicker diaphragms increase the shock formation time.

Similar results were obtained for two other pressure ratios, and the ratio  $c$  for these conditions is shown in Figure 5.6. As the diaphragm thickness increases,  $c$  deviates further from unity for all three pressure ratios. Data for each pressure ratio are fit to lines and extrapolated to zero diaphragm thickness. The nonzero intercepts indicate that there is potentially an additional effect responsible for the model discrepancy. The intercepts are not much greater than the values for  $12.7 \mu\text{m}$

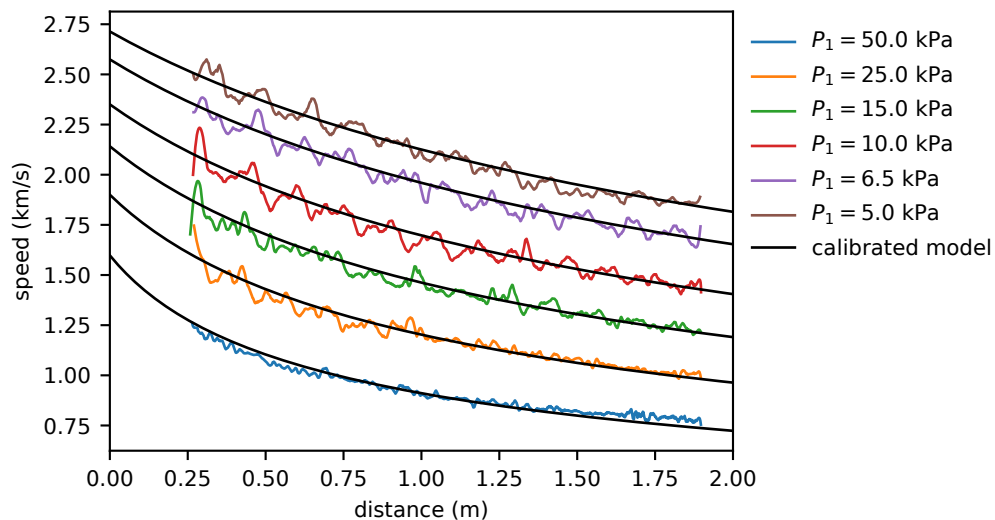


Figure 5.4: Forward-mode detonation-driven shock speed measurements compared with calibrated model.

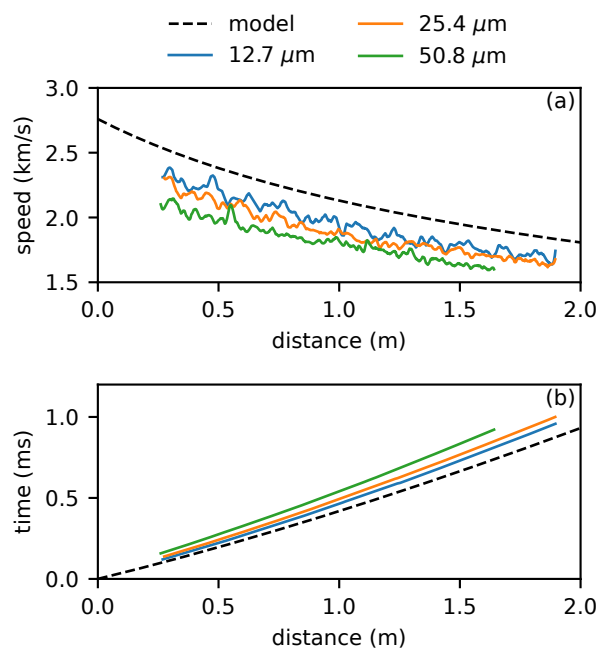


Figure 5.5: Effect of diaphragm thickness on (a) shock speed and (b) space-time diagram. All conditions use  $P_{41} = 50$  kPa  $C_2H_4 + 3O_2$  driver gas and  $P_1 = 6.5$  kPa air driven-section gas.

diaphragms, suggesting that insignificant improvement is obtained from using even thinner diaphragms.

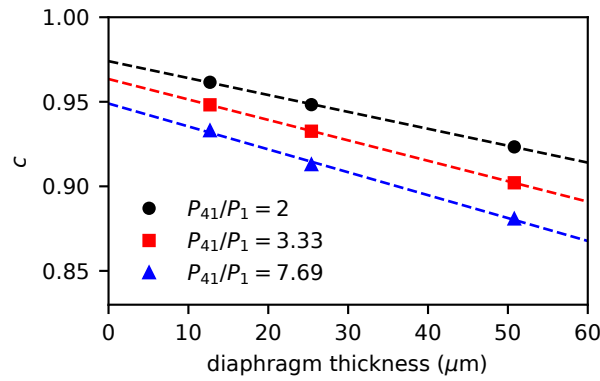


Figure 5.6: Effect of diaphragm thickness on  $c$  for three pressure ratios. Dashed curves are linear fits.

Non-ideal diaphragm effects are due to its shape, mass, and strength. Diaphragm opening times are typically related to its mass. Figure 5.7 shows shock speed measurements for six shot conditions, where three pressure ratios are tested at higher absolute pressures. The diaphragm thickness is also scaled, so that the expected force per diaphragm mass is constant. The results for each pressure ratio are on top of each other, indicating that for conditions with matched diaphragm dynamics the model discrepancy is the same.

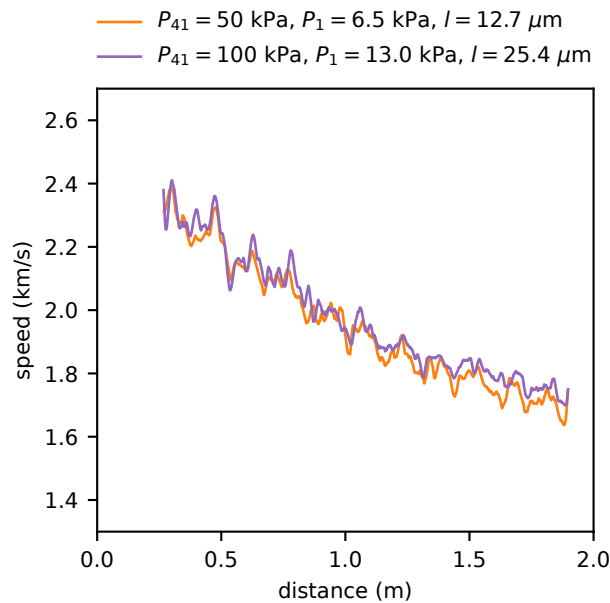


Figure 5.7: Effect of absolute pressure with scaled diaphragm thickness.

### 5.1.4 Driver Mixture

Figure 5.8 compares shock speed measurements in (a) and space-time diagrams in (b) for three driver mixtures, where the driver pressure and shock tube pressure ratios were chosen to produce the same CJ pressure and initial shock Mach number, and hence similar diaphragm dynamics. Since the initial shock speed should be similar, the subsequent shock motion shows the effect of the driver gas sound speed. The hydrogen-oxygen mixture has a high sound speed and so a larger initial decay rate,  $\beta$ , resulting in more rapid decay overall. In contrast, the argon-diluted mixture has a lower sound speed and so lower overall shock decay. These observations are consistent with model predictions.

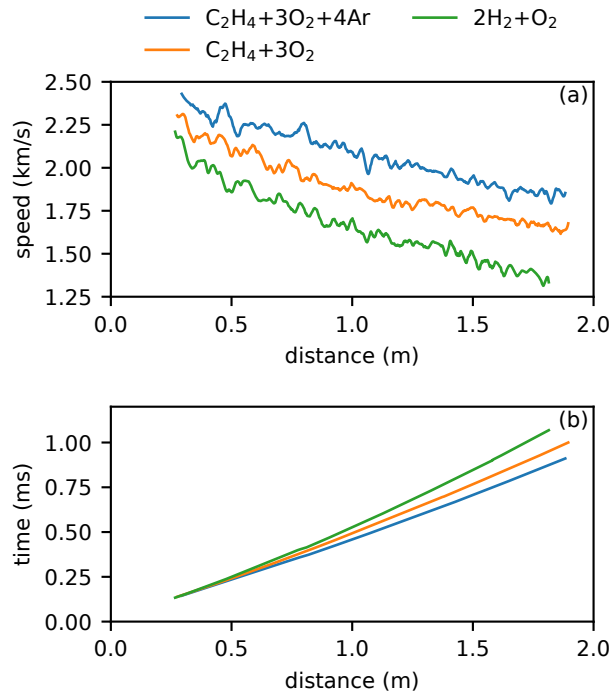


Figure 5.8: Effect of driver gas mixture on forward-mode detonation-driven (a) shock speeds and (b) space-time diagrams. Conditions are chosen so that ideal initial shock speed and CJ pressure are the same for the three cases. Conditions are numbers 13, 19, and 22 from Table B.1.

Because of the faster shock decay generated by the hydrogen-oxygen mixture, the ideal model predicts that the shock should reach the steady speed phase much earlier in the measurement region. This is shown in Figure 5.9. The experimental shock decay follows the model decay until the model reaches the steady shock speed, where the experiment shows that the shock continues decaying well below the steady shock

speed. The steady shock speed in this region is determined by the TZ wave plateau state, which is not influenced by diaphragm effects. Shock decay below this speed indicates other effects, namely wall heat transfer and viscous attenuation.

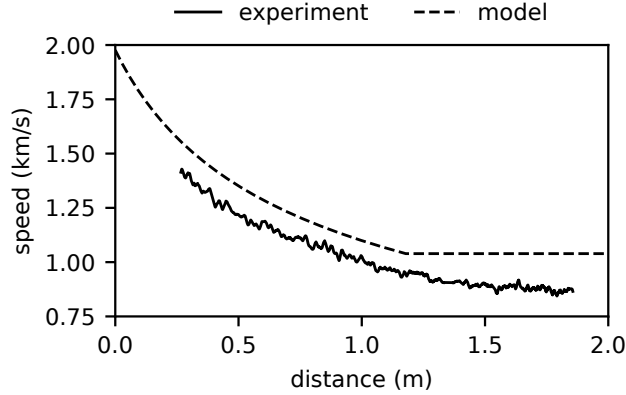


Figure 5.9: Comparison of experiment and model for hydrogen-oxygen driver, where  $P_{41} = 87$  kPa,  $P_1 = 32.12$  kPa, and diaphragm thickness is  $25.4 \mu\text{m}$ .

### 5.1.5 Time-Frequency Analysis

The time-resolved shock speed measurements in this work enable observations of higher-frequency shock motion. In many of the above plots there is clearly an oscillatory component to the shock speed, particularly for the higher pressure ratios in Figure 5.2.

To analyze these frequencies, the shock speed measurements are high-pass filtered (HPF) using a Savitzky-Golay filter with a 4 kHz cut-off (4th order polynomials with a window of 325 samples). High frequencies were passed by subtracting the Savitzky-Golay filtered signal from the unfiltered signal. This is not necessary for spectral analysis, but useful for visualizing the time-series oscillations.

Signals exhibit time-varying frequencies and amplitudes, so a coarse time-frequency analysis is implemented. For the condition in Figure 5.2(d), the signal record is segmented into thirds, and a periodogram is computed for each third using a Hann window. Periodograms are estimates of the power spectrum (Oppenheim and Schaffer, 2010), and here they are computed using SciPy (Virtanen et al., 2020). Record lengths are too short to afford any useful averaging.

The segmented signal and corresponding estimates of power spectral density (PSD) are plotted in Figure 5.10(a) and (b), respectively. There is a prominent peak



frequency that decreases with time, which is plotted in (c). The discrete Fourier transform (DFT) resolution is used for the peak frequency error bounds. Also plotted in (c) is the characteristic frequency of an acoustic plane wave propagating along the tube diameter in the post-shock flow. This frequency is  $a_2/d$ , where  $a_2$  is the post-shock sound speed and  $d$  is the tube diameter. Figure 5.10(c) shows that the measured frequencies are consistently higher than this acoustic frequency.

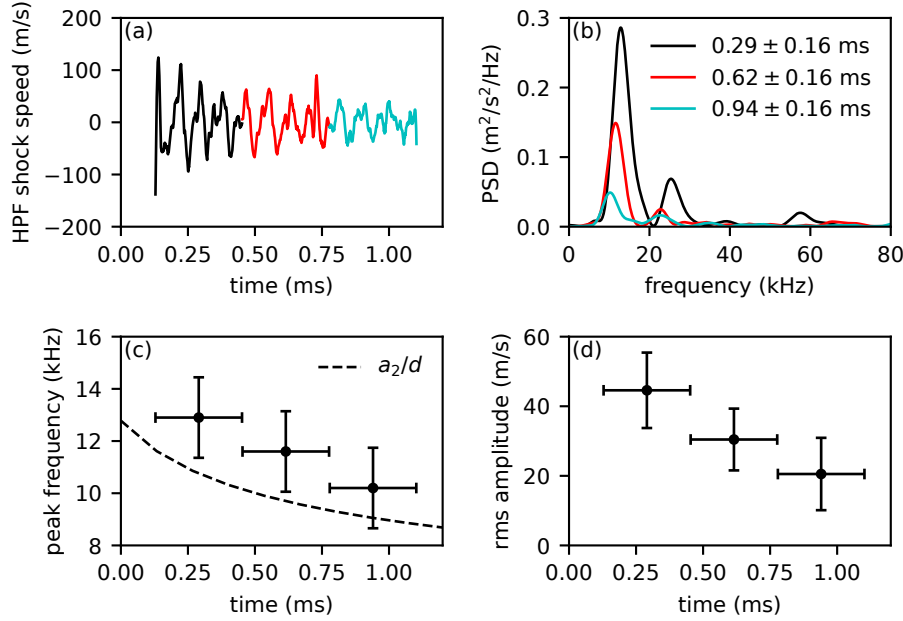


Figure 5.10: Time-frequency analysis of data from Figure 5.2(d). (a) shows high-pass filtered signal, segmented into thirds. (b) shows periodograms of these segments using a Hann window. (c) shows PSD peak frequency over time, and (d) shows signal amplitude in 50 kHz bandwidth over time.

The signal amplitude is evaluated by integrating Figure 5.10(b) up to 50 kHz. Signal above 50 kHz was averaged to obtain a noise spectral density. This calculation is performed on the signal without the low-pass filtering used for plots of time variation. The root-mean square (RMS) signal amplitudes are plotted over time in Figure 5.10(d). The signal in (a) is not sinusoidal and more closely resembles a sawtooth waveform, for which the peak amplitude is related to the RMS value by a factor of  $\sqrt{3}$ . Applying this factor to (d) gives peak shock oscillation amplitudes of nearly 100 m/s, as observed in (a).

If the periodogram is calculated instead for the entire record, then the peak frequency obtained is an average of those in (c). This is useful for comparing oscillation frequencies between shot conditions. Figure 5.11 shows these peak frequencies for

the different pressure ratio conditions. Periodograms for these conditions are given in Appendix B. The peak frequency clearly increases as the pressure ratio increases, and the trend follows that of the reference frequencies given by  $a_2/d$ , illustrating the dependence on post-shock sound speed.

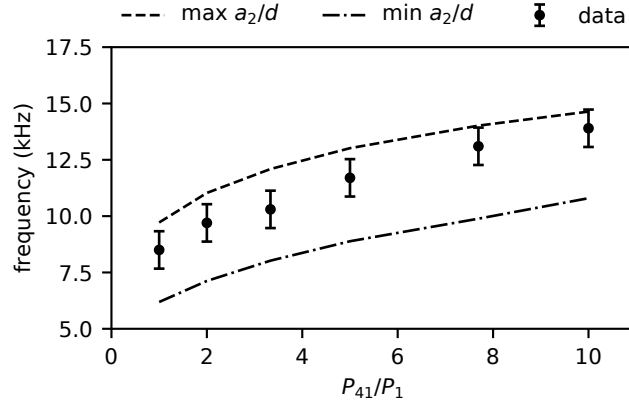


Figure 5.11: Peak frequencies from periodograms computed for entire shock speed records.

### 5.1.6 Diaphragm Bulge

A principal source for the shock speed oscillations in the above results was identified to be the bulging of plastic diaphragms. This was first identified by observing that oscillation amplitude is reduced by using thicker diaphragms for the same shot condition. However, if the thicker diaphragm was statically pre-loaded to a much higher initial pressure difference and therefore plastically stretched, then the initial diaphragm bulge was increased and higher oscillations in the shock speed were observed again.

A straight-forward remedy for this issue is to mechanically support the diaphragm with a rigid cross of thin flat plates. A photograph of this is shown in Figure 5.12, where the plates are 1.27-mm thick stainless steel. Unlike diaphragm cutters, these plates must be sufficiently blunt to not prematurely tear the diaphragm.

The effect of mechanically supporting the diaphragm is shown in Figure 5.13. The spectra in (b) are computed only for the first third of each record. The RMS signal amplitude in the first third of the record is  $53.3 \pm 13.1$  m/s and  $22.5 \pm 14.0$  m/s for the unsupported and supported diaphragms respectively. Clearly, mechanically supporting the diaphragm substantially reduces the large amplitude oscillations in shock speed. An additional advantage of supporting the diaphragm is that it reduces

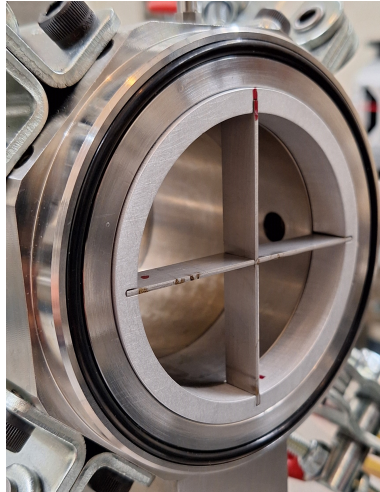


Figure 5.12: Photograph of rigid cross of thin flat plates used to mechanically support plastic diaphragms to prevent bulging.

the initial static diaphragm loading and hence enables even thinner diaphragms to be used.

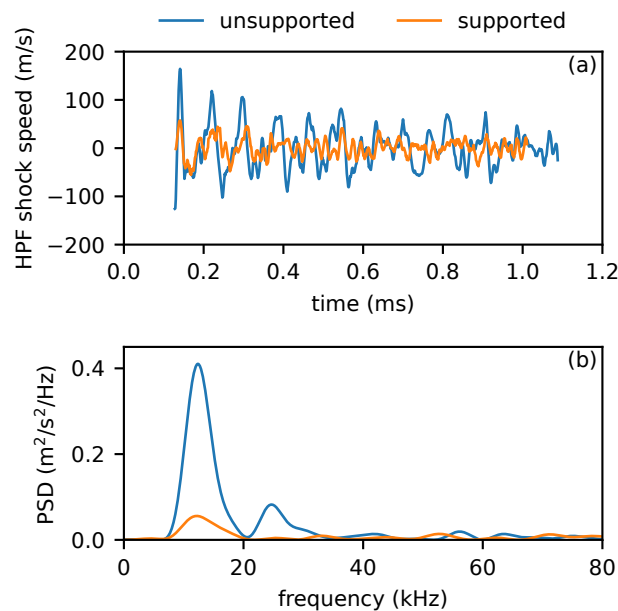


Figure 5.13: Effect of mechanically supporting diaphragm on (a) high-pass filtered shock speed signals and (b) power spectra computed from first third of signals in (a).

Diaphragms were found to bulge quite substantially. This was measured by removing the driven section and pressurizing the driver with a diaphragm in place. The diaphragm deflection was measured with a laser tape measure, and the results are

shown in Figure 5.14. For most typical shock-tube conditions, the diaphragm is bulging 10-15 mm, roughly 30% of the tube radius.

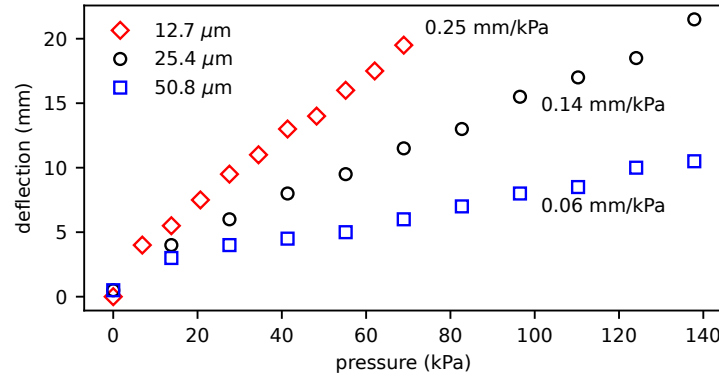


Figure 5.14: Deflection of Mylar diaphragms with varied thicknesses from driver pressurization.

## 5.2 Results: Reverse-Mode Detonation Driver

In the reverse-mode driver, the detonation is initiated at the diaphragm and propagates upstream, driving an ideally steady shock in the test gas. In this work, the detonation is initiated at the diaphragm by imploding an annular detonation formed in channels external to the main tube inner diameter.

### 5.2.1 Pressure Ratio

Results for six pressure ratios are shown in Figure 5.15, where the driver pressure is constant and the driven-section pressure is varied. As expected, the shocks are approximately steady, exhibiting substantially less decay than from the forward-mode driver. A new feature of these measurements seen in (a) through (d) is a jump in shock speed resulting from the arrival of the shock reflected by the detonation when it impacts the upstream driver end wall. The TZ wave also reflects and attenuates the reflected shock. So after being overtaken by the reflected shock, the primary shock is also decaying.

For lower pressure ratios in Figure 5.15(a) and (b), agreement with predictions given by ideal theory is excellent. As the pressure ratio increases, the shocks are observed to be slower than as predicted and there is nonzero shock attenuation. The effective shock attenuation is calculated by fitting the data with a line that intersects the ideal value at the diaphragm position. The slope of this line is normalized by the calculated shock speed and plotted in Figure 5.16. Attenuation per meter shows

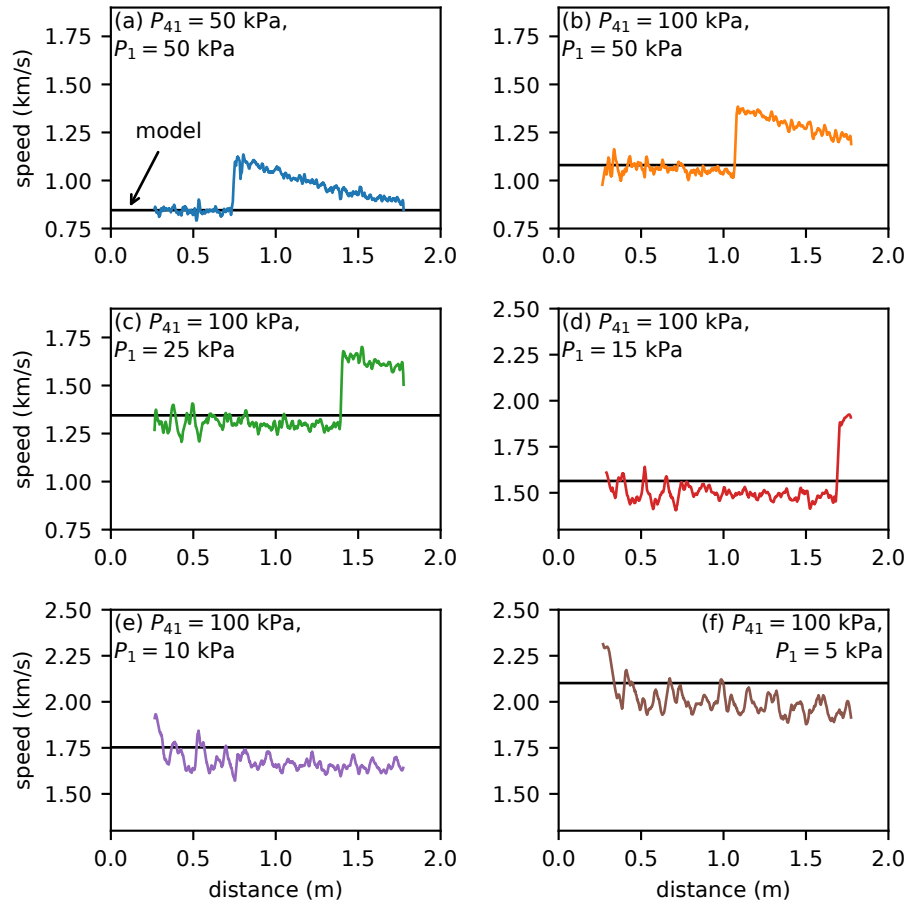


Figure 5.15: Reverse-mode detonation-driven shock speed measurements for various pressure ratios. Driver gas is  $\text{C}_2\text{H}_4 + 3\text{O}_2$  and diaphragm thickness is  $25.4 \mu\text{m}$  for all cases.

an inverse dependence with pressure ratio, increasing rapidly for lower values and slower for larger values, approaching nearly 5% per meter. This attenuation likely illustrates wall boundary layer effects.

Similar to results from the forward-mode driver, significant oscillation is observed in shock speed measurements, particularly for higher pressure ratios. By inspection, oscillation amplitudes are larger at early time, but analysis shows that peak frequencies are constant throughout the measurement record. The dominant frequency is therefore estimated using periodograms with a Hann window of the entire record length prior to reflected shock arrival. The dominant frequency from Figure 5.15(b) through (f) is plotted in Figure 5.17. The characteristic transverse acoustic frequency,  $a_2/d$ , is also plotted. The observed frequencies are uniformly much higher than  $a_2/d$  with a ratio varying from 1.2 to 1.4.

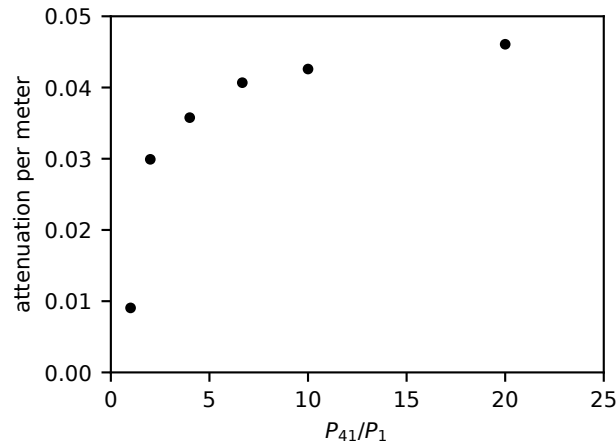


Figure 5.16: Shock speed fractional attenuation per unit meter calculated from slope of measurement fits.

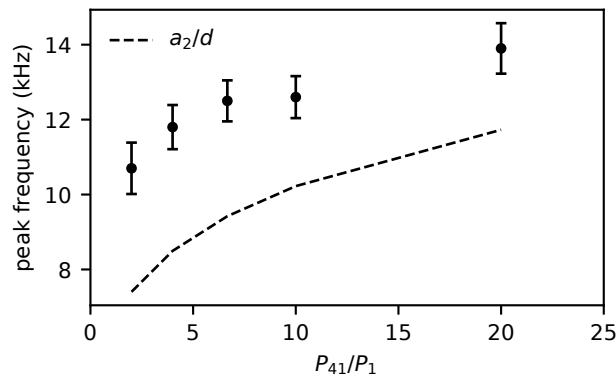


Figure 5.17: Peak frequencies obtained from power spectra of pressure-ratio data.

### 5.2.2 Diaphragm Effects

Diaphragm effects are shown in Figure 5.18, where the nominal pressure ratio is constant but the diaphragm-inertia conditions are varied. Although the frequency content appears qualitatively different, the overall shock speed and attenuation per meter is approximately the same for the four conditions. In (d), the diaphragm is mechanically supported as described for the forward-mode driver. Interestingly, the oscillatory component appears to be improved by this, indicating that for the reverse-mode the shock oscillations are not originating from the diaphragm bulge.

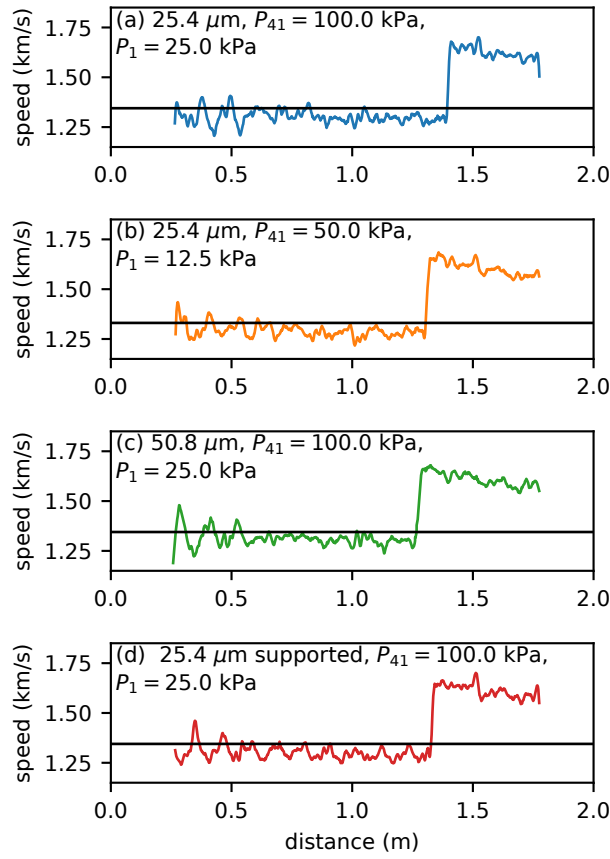


Figure 5.18: Diaphragm effects on shock speed for constant pressure ratio. All cases use a  $\text{C}_2\text{H}_4 + 3\text{O}_2$  driver mixture.

### 5.2.3 Driver Mixture

Driver mixture effects are shown in Figure 5.19 for one pressure ratio. The reflected shock is seen to arrive earlier for the hydrogen-oxygen mixture and later for the argon-diluted mixture, as expected from the different detonation speeds and driver gas sound speeds. For the hydrogen-oxygen case, the shock appears to be slower than expected from ideal theory with more rapid attenuation.

Periodograms for the three cases are shown in Figure 5.20 with  $a_2/d$  plotted as a vertical line. The variation in  $a_2/d$  between the three cases is small enough to lie within the thickness of the single plotted line. The spectra show that as the driver gas sound speed increases, the oscillation frequency increases, departing further from  $a_2/d$ . The ratio of the dominant frequency with  $a_2/d$  is plotted in Figure 5.21 against the sound speed ratio  $a_{42}/a_1$  for two pressure ratios, illustrating the frequency-dependence on driver gas sound speed.

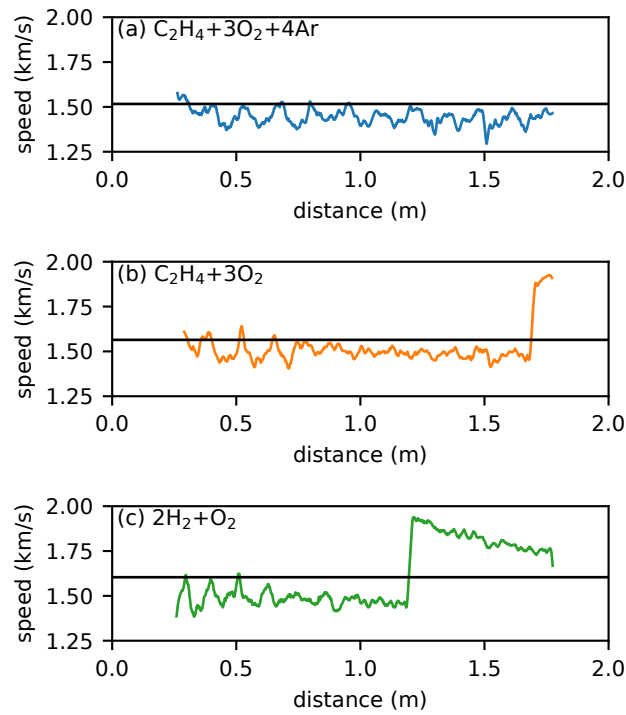


Figure 5.19: Effect of driver mixture on driven shock speed, where each case uses 100 kPa driver gas and 10 kPa air driven-section gas.

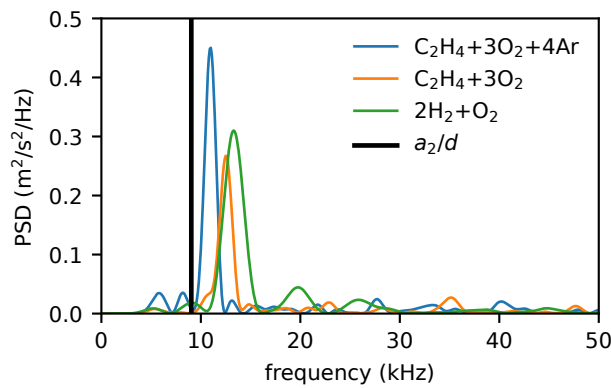


Figure 5.20: Periodograms from driver-mixture data in Figure 5.19.

Since shock speed oscillation frequency is increased for greater driver gas sound speeds, but otherwise not affected by diaphragm conditions, the oscillations in reverse-mode shocks are suspected to originate from the detonation initiation process. Jackson (2005) showed that very high peak pressures are obtained from detonation implosion. Some component of the reflected shocks inevitably transmit into the driven gas. The dependence on driver gas sound speed indicates either that



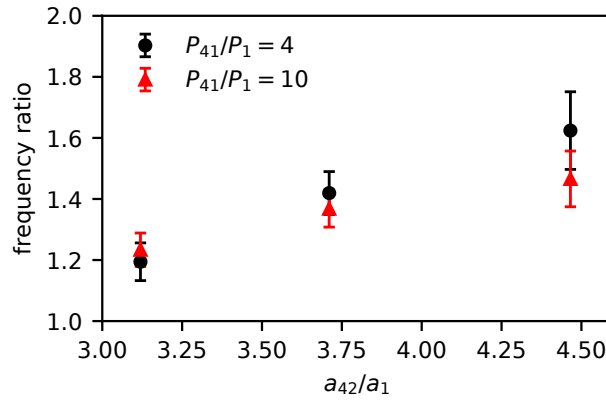


Figure 5.21: Ratio of peak frequencies from shock speed power spectra with characteristic transverse frequency,  $a_2/d$ . Data are shown for three driver mixtures and two pressure ratios, where driver mixtures are plotted using the sound speed ratio,  $a_{42}/a_1$ .  $a_{42}$  is the CJ state sound speed.

the speed of the implosion process affects the transmitted disturbance frequency or that the higher sound speed transmits a stronger wave.

#### 5.2.4 Test Gas

Figure 5.22 shows the effect of varied test gas composition, where argon and an argon-helium mixture were examined. Argon has a lower sound speed than air, however its high post-shock temperatures give it a higher sound speed than for air. The nominal post-shock sound speeds are 718 m/s for air, 910 m/s for argon, and 1,120 m/s for 0.5Ar+0.5He. The peak frequency from periodograms is shown to trend toward  $a_2/d$  as  $a_2$  increases.

### 5.3 Results: Helium Driver

Observations of shock oscillations from both forward and reverse-mode detonation driver operation motivated investigation of the typical unheated high-pressure helium driver. Shock speed measurements, predicted shock speeds, and corresponding power spectra are plotted in Figure 5.23 for the two shot conditions studied. Shock speed measurements in (a) show that the shock accelerates from early time, overshoots the predicted shock speed, then decays below it. These dynamics are consistent with the classic analysis of diaphragm-opening effects by White (1958).

Data are noisier than for the detonation driver, so power spectra are estimated using Welch's method (Welch, 1967) with a Hann window, where each averaged segment

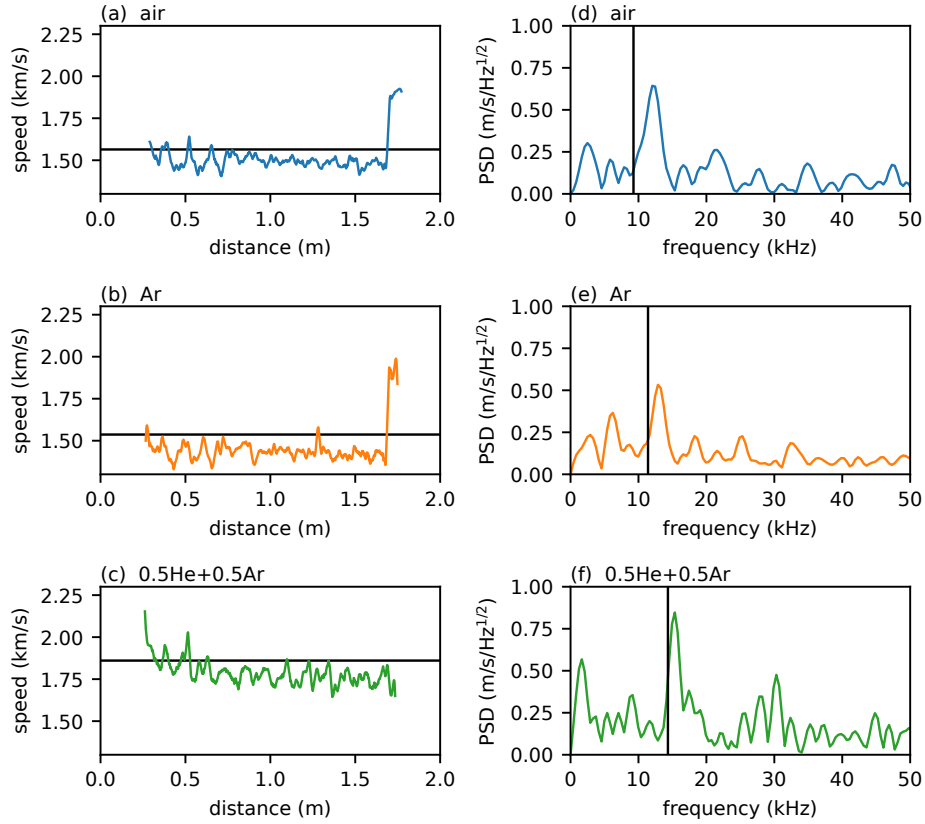


Figure 5.22: Shock speed measurements and power spectral densities for various test gases. The black line in (d-f) corresponds with  $a_2/d$ .

is half the record length. The power spectra in Figure 5.23(b) show some frequency content around the transverse acoustic frequency,  $a_2/d$ , but the amplitudes are much smaller than any observed from the detonation driver. RMS signal amplitudes are computed by integrating the PSD up to 50 kHz and are  $14.9 \pm 11.8$  m/s and  $19.8 \pm 12.7$  m/s for  $P_4/P_1 = 106.2$  and 219.2, respectively. The uncertainty value is the RMS noise amplitude over the signal bandwidth, which shows that the RMS signal amplitudes are only slightly greater than the measurement noise.

## 5.4 Discussion

Comparison between experimental shock speed measurements and predictions from ideal one-dimensional inviscid shock tube theory showed that theory overpredicts shock speeds for larger pressure ratios in both the forward and reverse-mode driver. Interpretation of forward-mode results are complicated by interactions with the TZ wave. In particular, diaphragm thickness effects were shown to be significant. However, extrapolation to zero diaphragm thickness showed a residual discrepancy

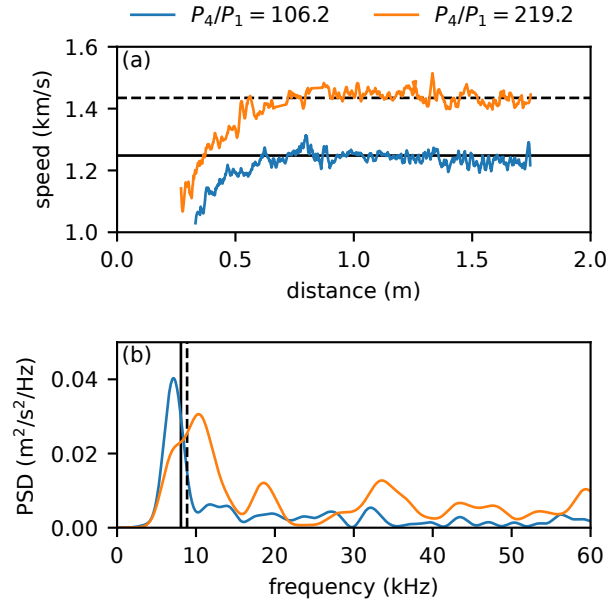


Figure 5.23: Measurements of shock speed using unheated high-pressure helium driver for two pressure ratios in (a). Both cases use  $P_1 = 5$  kPa, and the black lines denote predicted shock speeds. (b) shows power spectra estimates using Welch's method, where the black lines are the acoustic frequencies,  $a_2/d$ , corresponding with the lines in (a).

with the ideal model that was larger for increasing pressure ratios. For reverse-mode drivers, steady attenuation per meter also increased with increasing pressure ratio, which is a well-known effect from wall boundary layers. Although the experimental TZ wave was shown to be consistent with an isentropic expansion, wall effects becomes more significant with increasing time. Attenuation from wall effects may not be separable from experimental results due to the much greater decay by the transmitted TZ wave. The variable that was not studied in this investigation was the driver length-to-diameter ratio, which would help uncouple sources of shock decay.

Large oscillations in the shock speed were observed for both the forward and reverse mode driver. Shock oscillations are significant because they are directly related to acoustic perturbations behind the shock and hence acoustic noise in a facility's test flow. The amplitude of these oscillations decreased as the shock propagated away from the diaphragm, indicating some attenuation. However, for larger pressure ratios where oscillations are more significant the attenuation is reduced.

Acoustic disturbances behind primary shocks are particularly important for expansion tubes, which motivated the study by Paull and Stalker (1992). They concluded

that transverse or lateral acoustic waves were the culprit of test flow noise, and examined the transmission of these waves into the test gas from an undefined source in the driver. The ratio of sound speeds across the contact surface,  $a_3/a_2$ , was identified as a controlling factor for transmission. The high-temperatures of detonation products results in large sound speeds, even after isentropic expansion to the contact surface state. For all shot conditions in this chapter,  $a_3/a_2 > 1$ .

The origin of the shock oscillations observed in this work cannot be unambiguously identified. However, they were shown to be substantially affected by the bulging diaphragm for the forward-mode driver, which could be mitigated by mechanically supporting the diaphragm to prevent it from bulging. Post-shock flow perturbations from diaphragm bulge have been investigated before (Daru and Damion, 1995). Hornung and Quirk (1998) showed that another effect is to distort the contact surface.

Diaphragm bulge was not found to be important for the reverse-mode. Instead, a likely source for these oscillations is the detonation initiation process. For the reverse-mode operation, the detonation is imploded directly at the diaphragm plane, generating very large transverse pressure transients (Jackson and Shepherd, 2007). It was shown that the frequency of shock oscillation normalized by  $a_2/d$  increased for increasing CJ sound speed (or the CJ speed, itself). Normalization by  $a_2/d$  takes into account variation in the post-shock sound speed, so these trends illustrate the dependence of measured frequencies on driver conditions.

No remedy was identified for the reverse-mode driver, since initiation at the diaphragm is fundamental to the driver's operation. Detonation wave implosion is possibly especially prone to exciting these shock oscillations. However, the transverse detonation tubes used for initiation in other facilities (Yu et al., 1992, Zhao et al., 2005) likely also introduce transverse waves. It is important to note that these shock oscillations are only observable in the present shock tube due to the high-frequency shock speed measurement technique employed. In other facilities, these oscillations may be present and go unobserved due to typically coarse measurements using time-of-arrival gauges.

Conventional shock tubes with high-pressure helium drivers also have bulging diaphragms, and so shock oscillations for this driver operation were also investigated. It was found that the oscillation amplitude was comparable to measurement noise. To compare this with detonation drivers, RMS shock speed oscillation amplitudes are collected below in Table 5.1 for conditions with roughly 1.45 km/s shock speeds.

These results show that the forward-mode driver with supported diaphragm is nearly as “quiet” as the conventional high-pressure helium driver.

Table 5.1: Comparison of RMS shock speed oscillation amplitudes between driver techniques

driver technique	RMS shock oscillation (m/s)
forward-mode detonation driver	$53.3 \pm 13.1$
forward-mode detonation driver with diaphragm support	$22.5 \pm 14.0$
reverse-mode detonation driver	$32.3 \pm 16.6$
helium driver	$19.8 \pm 12.7$

A final point is to consider the spacing of time-of-arrival gauges necessary to resolve the frequencies observed here. For a steady shock with speed  $U_s$ , the effective sampling rate obtained by an array of sensors with spacing  $\Delta x$  is  $U_s/\Delta x$ . In one representative shot, a roughly 1.6 km/s shock was observed to have 12 kHz oscillations. Consider this to be at the Nyquist frequency of the sensor array. Then,  $\Delta x$  must be less than 6.6 cm in order to resolve these oscillations. Sensors spaced 2-cm apart would give roughly six samples per period of oscillation. Over a 1.5-m long measurement region, this would require 75 sensors.

## 5.5 Conclusions

A unique method of using shadowgraphy through a polycarbonate shock tube enabled high-resolution measurements of shock speeds along the entire driven section length. Diaphragm effects were identified, and overall performance could be calibrated against model calculations. With a correction factor, the forward-mode shock decay model presented in Chapter 3 was shown to be accurate. An important consequence of this is that it can be used to estimate shock unsteadiness for a given facility and shot condition.

Time-resolved shock speed measurements enabled original observations of shock speed frequency content. Conventional time-of-arrival shock speed measurements only coarsely sample shock position, and so the present work’s ability to perform spectral analysis of shock speed is unique. Shock speed oscillations are important considerations for assessing the quality of flows generated by a shock tube, and perturbations from these oscillations should be observable in the post-shock flow. Methods for interrogating the post-shock flow is the subject of the next chapter.

*Chapter 6***HETERODYNE FOCUSED LASER INTERFEROMETER:  
THEORY, METHODS, AND VALIDATION**

Optical interferometry is an exceptionally sensitive method for interrogating transparent media. When coherent light transmits through a variable density gas flow, the light wave is phase modulated. By interfering this signal beam with a reference beam, the phase modulation of the electric field is converted to amplitude modulation of the optical intensity, something measurable with a photosensitive detector.

Like shadowgraphy and schlieren, interferometry is a historic method for investigating shock-tube flows. Although earlier applications to compressible flows exist, Bleakney et al. (1949) provide one of the first uses of an interferometer in a shock tube. Interferometric measurement of density jumps across shock waves is particularly challenging due to the very large density gradients in shocks causing apparently discrete fringe shifts in interferograms. The pioneering work by Bleakney et al. (1949) included a method of overcoming this by transmitting the signal beam obliquely through the test section so that the resulting fringes remained continuous through the widened shock front. This technique was extensively used by Blackman (1956), Matthews (1959), and Alpher and White (1959a,b) to measure relaxation and reaction rates behind shock waves. Interferometric measurements make up a large portion of the empirical data used in the famous study of relaxation rates by Millikan and White (1963). Results from White's shock-tube interferometry also include the first observations of the cellular and turbulent structure of gaseous detonations (White, 1961).

Early uses of shock-tube interferometry employed simple constructions with only the requisite optical components: beam splitting elements, mirrors, lenses, a spatially-filtered light source, and film. Experimental applications of the basic technique have grown enormously with the advent of new technologies like the laser, digital electronics, and fiber optics. Advances in electronics have enabled a new kind of interferometry where beams are not imaged but rather focused onto a single detector, the optical power is converted to electrical current, and the signal is digitized at high speed with modern oscilloscopes. Phase modulation is measured as a time-varying

signal instead of from the spatial modulation of fringes in an image. This application extends far beyond scientific research and makes up many of the sensors used in modern technologies, where it is often no longer referred to as interferometry but rather *coherent detection*. Telecommunications technologies make up a significant portion of these applications. In fluid dynamics applications, the great advantage of this technique is the improved bandwidth and signal-to-noise ratio over photography of finite fringe diagrams. Additionally, tightly focused laser beams can enable much greater spatial resolution or at least spatial selectivity. However, the challenge is that the temporal signal cannot be phase unwrapped as with a finite fringe diagram. Shock-tube flows often generate very large fringe shifts, making an interferometer signal nearly useless in these cases as the ability to invert the signal to density is completely lost by rapid phase wrapping.

The challenge of phase wrapping is greatly reduced in the case of a *differential* laser interferometer. If the signal and reference beams instead both transmit through the shock-tube flow and are spatially displaced by a length scale that is small compared to those of the flow, then the rapid phase change from large density gradients occurs in both beams, so that only their difference is detected. This is the technique employed in the Focused Laser Differential Interferometer (FLDI), which has found recent widespread use in hypersonic flow research facilities. The instrument was developed by Smeets and George (1973) but was only recently popularized by Parziale et al. (2012). The operation of FLDI was analyzed in greater detail by Schmidt and Shepherd (2015) and then extensively by Lawson and Austin (2023). Lenses are used to focus the beam at a desired position in the test flow and then refocus the beam onto a photodetector. By locating a pair of Wollaston prisms at the focal planes of each focusing lens, the transmitted beam is split into two closely-spaced parallel beams and then recombined. Wollaston prisms are a kind of polarizing beam splitter, and so the phase modulation in each signal beam is carried by orthogonal polarizations. Subsequent transmission of the recombined beams through a linear polarizer causes the two signal beams to interfere, so that the beam optical intensity is now modulated by the differential phase signal.

FLDI is a powerful technique with several advantages. The common beam paths eliminate a significant amount of common-mode noise such as from vibration but also low-frequency fluid motion such as from ambient air currents. Construction and alignment is much simpler than with other interferometers, which has certainly aided its widespread adoption. The differential signal enables use of high-speed

photodetectors and therefore measurements of signals with large bandwidths. By focusing the beams, the frequency response of the interferometer is spatially distributed, so that high frequencies are passed at the focus while being suppressed at boundaries. The typical use for FLDI is to make measurements of density fluctuations in some test flow. High bandwidths enable spectral techniques, allowing both measurements of signal amplitude and frequency. A common adaptation to the instrument is to incorporate additional beam splitting elements to create additional foci pairs and therefore additional measurement locations (Gillespie et al., 2022, Hameed et al., 2020).

As a laboratory instrument using coherent detection the theoretical signal-to-noise ratio of FLDI is limited only by shot noise from the photocurrent. Laser power is typically not a restriction, so shot noise can be made to greatly exceed thermal Johnson noise in detection circuits. To the author's knowledge, there are no documented examples of this being accomplished due to nearly all implementations of FLDI containing a significant degree of laser intensity noise. This limitation was identified by Lawson (2021) as an important avenue for future improvements to FLDI. Overcoming this challenge is especially important for applications in low-density flows, such as those generated in expansion tubes, where signals are weak.

An alternative method of coherent detection is to interfere the signal beam with one at a different optical frequency, known as *optical heterodyne detection*, distinguished from homodyne detection where signal and references frequencies are the same. If the optical frequency difference is in radio-frequency (RF) or microwave bandwidths, then detection of the optical intensity returns an alternating current at this frequency difference. This is the phenomenon of beat formation from mixing two frequencies. Information contained in the phase modulation of the optical signal beam is converted to phase modulation of the heterodyne signal. This is a key difference from prior interferometric techniques: phase information is not converted to amplitude modulation. Instead, the phase signal can be measured directly, enabling powerful signal processing techniques to unwrap large phase changes. Additionally, the beat frequency can be chosen so that heterodyne detection is performed in a quiet band far from amplitude noise sources. Since typical laser noise is less than 10 MHz, heterodyne detection in RF bandwidths provides a possible method for eliminating SNR limitations of FLDI. These advantages motivated the present work to apply heterodyne detection to FLDI.

Optical heterodyne detection grew out of the heterodyne techniques used for RF



communication and is merely the same principles applied to optical frequencies. Beat formation from optical frequencies was first reported by Forrester et al. (1955), but McMurtry and Siegman (1962) were the first to use a laser. As examples, early work used the technique to investigate atmospheric turbulence (Fried, 1967, Goldstein et al., 1965), measure surface vibrations (Massey, 1968, Whitman et al., 1968), and probe plasmas (Jacobson and Call, 1978, Kristal and Peterson, 1976). See NASA (1980) for a history and other early work. In condensed shock physics, the VISAR technique employs heterodyne detection using the beat formed by mixing with a doppler-shifted reflected beam (Strand et al., 2006). In Laser-Induced Thermal Acoustics (LITA) (Cummings, 1995) and similar techniques (Jakobs et al., 2023, Sander et al., 2022) the signal beam is scattered from an opto-acoustic grating, incurring a Doppler frequency shift. By interfering the Doppler-shifted signal beam with a reference beam, coherent heterodyne detection is used to also obtain flow velocity measurements. Frequency-modulated spectroscopy (Lenth, 1983, Philippe and Hanson, 1993) generates alternating signals that can be demodulated using RF techniques, however this is not coherent heterodyne detection.

Examples of heterodyne interferometry used to make direct phase measurements in fluid dynamics are sparse. Authors at Bethel University implemented a heterodyne interferometer to investigate the gas dynamics in a “Ping-Pong Cannon” (Olson et al., 2006, Peterson et al., 2005) and in an under-expanded jet (Fredrick et al., 2015). Recently, Choudhary et al. (2024) applied heterodyne techniques to a focused interferometer, where signal beams were imaged on a high-speed detector.

In this work, a heterodyne focused laser interferometer is constructed, validated, and employed to interrogate the post-shock flow in a detonation-driven shock tube. The instrument uses the same construction as the FLDI, however heterodyne detection enables both differential and absolute phase measurements. With some caveats, the instrument overcomes limitations of phase wrapping with some measurements in this work spanning nearly  $100\pi$  radians. Differential signal-to-noise ratios were not improved beyond the conventional FLDI, however, while developing the heterodyne instrument, an alternative method for improving FLDI SNR was investigated using balanced detection. Described in Appendix C, this simple method is shown to produce shot-noise limited measurements with an astounding 30 dB increase in SNR.

In this chapter, essential background is established before the heterodyne focused laser interferometer is presented. A set of experiments were performed to validate

its operation, and these are discussed here. Results are reported from using the interferometer in GUST in the next chapter.

## 6.1 Theory

### 6.1.1 Governing Equations

Interference of two beams of coherent light with a common polarization is a consequence of the wave nature of light. If the wavefronts, identified by spatial contours of constant phase, are not exactly coincident, then regions of constructive and destructive interference produce fringes, and the resulting fringe pattern encodes this wavefront variation.

Wavefront perturbations result from spatial variation of the wave speed. The speed of light,  $v$ , propagating through a dielectric medium is reduced from its vacuum speed,  $c$ , by a factor  $n$ , i.e.,

$$v = \frac{c}{n} . \quad (6.1)$$

$n$  is known as the index of refraction and is an intrinsic property of the medium. Since  $c$  is a constant, optical wavefronts are perturbed when they propagate through variations in  $n$ .

The propagation of light is described by Maxwell's equations (Born and Wolf, 1999). In a homogeneous dielectric medium, free of charge and currents, Maxwell's equations can be combined to obtain the wave equation,

$$\nabla^2 \mathbf{E} - \frac{1}{v^2} \partial_t^2 \mathbf{E} = 0 , \quad (6.2)$$

where  $\mathbf{E}$  is the vector electric field. For linearly-polarized monochromatic light with frequency  $\omega$ , the scalar electric field can be given as

$$E(\mathbf{x}, t) = \mathcal{E}(\mathbf{x}) e^{-j\omega t} . \quad (6.3)$$

Substitution into the wave equation gives

$$(\nabla^2 + k^2) \mathcal{E} = 0 , \quad (6.4)$$

where  $k = 2\pi/\lambda$  and  $\lambda$  is the wavelength of light in the medium. Equation (6.4) is the Helmholtz equation.

### 6.1.2 Gaussian Beam Propagation

Real laser beams are often modeled as Gaussian beams, an important solution to the Helmholtz equation. Milonni and Eberly (2010) give a derivation, however the

key steps and assumptions are simple and will be summarized here. Consider a “beamlike” solution to the Helmholtz equation

$$\mathcal{E}(\mathbf{x}) = \mathcal{E}_0(\mathbf{x})e^{jkz}, \quad (6.5)$$

where the beam propagates along the  $z$  axis. Substituting (6.5) into (6.4) and applying the paraxial approximation, then the paraxial wave equation is obtained,

$$\left(\partial_x^2 + \partial_y^2 + 2jk\partial_z\right)\mathcal{E}_0(\mathbf{x}) = 0. \quad (6.6)$$

The Gaussian beam parameters can be derived by assuming a Gaussian intensity profile for  $\mathcal{E}_0$ , i.e., consider

$$\mathcal{E}_0(\mathbf{x}) = Ae^{jk(x^2+y^2)/2q(z)}e^{jp(z)}, \quad (6.7)$$

where  $A$  is the field amplitude. The required functions  $q(z)$  and  $p(z)$  are to be determined by substitution into (6.6). The results are

$$q(z) = \left(\frac{1}{R(z)} + \frac{j\lambda}{\pi w(z)^2}\right)^{-1}, \quad (6.8)$$

$$e^{jp(z)} = \frac{w_0}{w(z)}e^{-j\varphi(z)}, \quad (6.9)$$

where  $R(z)$  is the radius of curvature of the wavefront,  $w(z)$  is the beam radius,  $w_0$  is the beam waist radius where  $R \rightarrow \infty$ , and  $\varphi(z)$  is the Guoy phase, given by

$$\varphi(z) = \tan^{-1}(z/z_0). \quad (6.10)$$

$z_0$  is the Rayleigh range,

$$z_0 = \frac{\pi w_0^2}{\lambda}, \quad (6.11)$$

and the beam radius is given by

$$w(z) = w_0\sqrt{1 + z^2/z_0^2}. \quad (6.12)$$

So, putting it all together, the scalar electric field for a Gaussian beam is given by

$$E(\mathbf{x}, t) = A \frac{w_0}{w(z)} e^{jk(x^2+y^2)/2R(z)} e^{-(x^2+y^2)/w(z)^2} e^{-j\varphi(z)} e^{jkz} e^{-j\omega t}. \quad (6.13)$$

Photosensitive detectors respond to the optical intensity. For a paraxial beam, the optical intensity is given by

$$I = \frac{nc\epsilon_0}{2} \langle |E|^2 \rangle, \quad (6.14)$$

where  $\epsilon_0$  is the permittivity of free space. All detectors have some finite response time, and so the angled brackets denote a short-time average over a period large compared to the period of the optical oscillation. In other words, the theoretical optical intensity is convolved with the impulse response of the detector (Hobbs, 2008). Then, the intensity of a Gaussian beam is

$$I(\mathbf{x}) = \frac{I_0 w_0^2}{w(z)^2} e^{-2(x^2+y^2)/w(z)^2}, \quad (6.15)$$

where  $I_0 = nc\epsilon_0|A|^2/2$ .

As a solution to the wave equation, the Gaussian beam scalar field equation includes the essential effects of diffraction, which is responsible for the expanding beam radius.

The Gaussian beam is paraxial, however focused laser interferometers often operate at larger numerical apertures, so it is worth verifying this remains a reasonable approximation. This was studied by Nemoto (1990), who showed that for  $w_0 k > 4$  the paraxial Gaussian beam remains a good approximation. For  $\lambda = 532$  nm, then this gives a minimum beam waist radius of  $0.34 \mu\text{m}$ . In the present work, the minimum radius used was  $5.7 \mu\text{m}$ , which is much more than this limit.

The Gaussian beam is merely the lowest-order mode of a more general solution to the paraxial wave equation. Real lasers rarely propagate as perfect Gaussian beams because some energy occupies higher-order modes, leading them to diffract at steeper angles than pure Gaussian beams. There are many beam quality metrics that quantify this, but a simple one is the  $M^2$ , defined by

$$\theta = M^2 \lambda / \pi w_0, \quad (6.16)$$

where  $\theta$  is the measured beam divergence and  $\lambda/\pi w_0$  is the diffraction-limited beam divergence. If  $M^2 = 1$  then the beam is perfectly Gaussian. In modern interferometry, high-quality lasers are typically used with small, near unity  $M^2$  values. For example, a common specification is  $M^2 < 1.1$ . However, even a  $M^2 = 1.1$  can lead to a much wider beam than expected. If need be, the  $M^2$  can be incorporated into beam propagation calculations by using it to scale the wavelength. This was not necessary in the present work as the laser used was measured to have an  $M^2 \approx 1.02$ .

The signal beam of an interferometer transmits through a region of nonuniform index. If these index perturbations are large, then the nonhomogeneous Helmholtz

equation must be solved to obtain the  $E$  field propagation. Powerful and simple computational methods exist for performing these beam propagation calculations (Feit and Fleck, 1978). However, for this work, index perturbations are considered sufficiently small that wavefront propagation is negligibly affected, and therefore the Gaussian beam may be used. This is appropriate for many gas dynamics applications, but not for cases with strong density gradients such as in shock waves.

### 6.1.3 Phase, Index, and Density

Phase perturbations are accumulated continuously as the wavefront propagates. In a homogeneous medium, wavefronts propagate along trajectories everywhere orthogonal to the wavefront surface. These paths provide an interpretation for the “rays” of a Gaussian beam. Rays are typically an artifice of geometric optics where the optical wavelength is assumed to be infinitesimal. The result is that in a homogeneous medium, rays are straight lines. However, Gaussian beams, as solutions to the Helmholtz equation, include the essential physics of diffraction, which causes focused beams to form waists, something not described by ray optics.

Integration along ray paths is often used to formulate the accumulated phase change from propagation through a nonuniform index field. For a ray path with arc length parametrized by  $s$ , the accumulated phase change from an index perturbation is

$$\phi - \phi_0 = \frac{2\pi}{\lambda} \int_0^L \Delta n(\mathbf{x}) \, ds , \quad (6.17)$$

where  $L$  is the total arc length,  $\phi_0$  is the initial phase, and  $\lambda$  is the wavelength of light in the ambient medium.

For the Gaussian beam, the same formalism can be used where instead of considering straight rays, the integration paths are contours that are everywhere perpendicular to wavefront surfaces (Born and Wolf, 1999). Near the optical axis, these contours are hyperbolas given by

$$r(z) = r_0 \frac{w(z)}{w_0} . \quad (6.18)$$

For small angles,  $s \approx z$ , and (6.17) becomes

$$\phi(r(l), \theta, l) - \phi_0 = \frac{2\pi}{\lambda} \int_{-l}^l \Delta n(r(z), \theta, z) \, dz , \quad (6.19)$$

where cylindrical coordinates are now used, and  $r(l)$  and  $l$  define the coordinates of the detector plane.

The phenomenon of image inversion through a focus, a result from geometric optics, is not accounted for by assuming hyperbolic ray paths. Lawson (2021) included image inversion in a numerical solution by artificially rotating the domain in  $\theta$  for  $z > 0$ . In the present work, only index fields that are symmetric about the  $z = 0$  plane are considered. Since the index perturbations are assumed weak enough to not deflect rays and there are no apertures to clip the beam, there is no effect on the result by neglecting image inversion. Hence, (6.19) can be used to compute phase changes along Gaussian beam “ray” paths.

The refractive index of a dielectric medium is determined by intrinsic material properties and its density. In gases, the refractive index is small,  $n - 1 \ll 1$ , and is accurately modeled as directly proportional to the gas density,

$$n - 1 = K\rho , \quad (6.20)$$

where  $K$  is the Gladstone-Dale constant.  $K$  is particular to a given molecule, and so the index of a gas mixture with  $N$  constituents is given by

$$n - 1 = \sum_i^N K_i \rho_i . \quad (6.21)$$

It is useful to define a single Gladstone-Dale constant for a given mixture. From (6.20) and (6.21) this is

$$K_{\text{mix}} = \sum_i^N K_i Y_i , \quad (6.22)$$

where  $Y_i$  is the constituent’s mass fraction and  $K_i$  is defined in terms of the mass density. Tabulated data for many gases are given by Gardiner et al. (1981), which was used in this work with Cantera and Shock and Detonation Toolbox calculations to determine values for  $K_{\text{mix}}$ .

The variable gas density in a shock-tube flow causes a nonuniform index field. As a Gaussian beam propagates through this nonhomogeneous medium, its wavefront incurs an integral phase change given by (6.19). The key assumption is that density and therefore index changes are sufficiently small that ray paths remain unperturbed.

The action of an interferometer is to convert the phase modulation of the wavefront into amplitude modulation of intensity. This is coherent detection.

### 6.1.4 Coherent Detection

In an interferometer, the signal beam is combined with a reference beam by linear superposition,

$$E_{\text{sig}} + E_{\text{ref}} = \mathcal{E}_{\text{sig}}(\mathbf{x}, t) e^{j(\omega_{\text{sig}} t + \phi_{\text{sig}}(\mathbf{x}, t))} + \mathcal{E}_{\text{ref}}(\mathbf{x}, t) e^{j(\omega_{\text{ref}} t + \phi_{\text{ref}}(\mathbf{x}, t))} , \quad (6.23)$$

where  $\phi_{\text{sig}}(\mathbf{x}, t)$  and  $\phi_{\text{ref}}(\mathbf{x}, t)$  are each given by (6.19).

Photosensitive detectors, like film, photodiodes, and the retina, respond to optical intensity. Assuming the incident beam is nearly normal to the detector face and the numerical aperture of the beam is small (Hobbs, 2008), then the optical intensity is given by (6.14). The intensity of the interfering electric fields (6.23) is

$$\begin{aligned} I(\mathbf{x}, t) &= \frac{nc\epsilon_0}{2} \langle |E_{\text{sig}} + E_{\text{ref}}|^2 \rangle , \\ &= \frac{nc\epsilon_0}{2} [ |\mathcal{E}_{\text{sig}}|^2 + |\mathcal{E}_{\text{ref}}|^2 + 2|\mathcal{E}_{\text{sig}}||\mathcal{E}_{\text{ref}}| \cos(\Delta\omega t + \Delta\phi(\mathbf{x}, t)) ] , \quad (6.24) \\ &= I_{\text{sig}}^2 + I_{\text{ref}}^2 + 2\sqrt{I_{\text{sig}}I_{\text{ref}}} \cos(\Delta\omega t + \Delta\phi(\mathbf{x}, t)) . \end{aligned}$$

Equation (6.24) shows how phase modulation of the electric field is converted to amplitude modulation of the optical intensity, where  $\mathbf{x}$  describes detector plane coordinates.

The electrical current produced by a photodetector is proportional to the total optical power,  $P$ , obtained from integrating intensity over the detector area, i.e.,

$$i(t) \propto P(t) = \int_{\text{det}} I(\mathbf{x}, t) \, dA . \quad (6.25)$$

$i(t)$  is the current resulting from photon conversion, often referred to as the photocurrent. The proportionality constant is referred to as the detector's responsivity,  $\mathcal{R}$ , so that  $i(t) = \mathcal{R}P(t)$ . Responsivity is a figure of merit for a specific photodetector construction and is a function of wavelength. For reference, the silicon photodiodes used throughout this work have a typical responsivity of 0.25 A/W at 532 nm, where the power here refers to incident optical power.

In most interferometers, the two beams have the same frequency and  $\Delta\omega = 0$ . This is referred to as *homodyne* detection. If the phase is spatially modulated, then the intensity field displays fringes. Phase unwrapping requires capturing the fringe pattern, so if these fringes are integrated over the detector plane, then this information is lost. When using photodetectors to record the total optical power, interferometers are aligned for infinite fringe so that the resting phase field is spatially uniform. Additionally, beams are typically assumed much smaller than fluid perturbations,

so that fringes are not formed and  $\Delta\phi(\mathbf{x}, t) = \Delta\phi(t)$ . Considering phase spatial variation is important for determining an instrument's exact response and will be revisited later.

Therefore, applying (6.25) to (6.24) for homodyne detection gives the alternating current (AC) signal,

$$i_{AC}(t) = 2\sqrt{i_{sig}i_{ref}} \cos(\Delta\phi(t)) . \quad (6.26)$$

Current is then converted to voltage with a transimpedance amplifier or terminating resistance.  $\Delta\phi$  can be obtained by inverting (6.26). This is accomplished in practice by calibrating the instrument, so that the voltage signal is given by

$$v_{AC}(t) = A \cos(\Delta\phi(t)) \quad (6.27)$$

where  $A$  is a calibration factor. Thus, the inverted phase change is

$$\Delta\hat{\phi}(t) = \cos^{-1}\left(\frac{v_{AC}(t)}{A}\right) , \quad (6.28)$$

where  $v_{AC}/A \in [0, \pi]$ . Clearly, if  $|\Delta\phi| > \pi$ , then this information is lost and cannot be recovered by the inversion (6.28). This is referred to as *phase wrapping*. Furthermore, since near the phase-wrapping boundaries the signal derivative goes to zero, the phase signal-to-noise ratio becomes poor. This constrains a homodyne measurement to an even smaller acceptable range of phase changes. Another consequence of the phase-to-amplitude signal conversion is that the phase signal is inseparable from other variations in amplitude such as from laser noise.

If instead the two interferometer beams have different optical frequencies, then the signal photocurrent has a constant frequency given by their difference,  $\Delta\omega$ . This is *heterodyne* detection. The phase information  $\Delta\phi(t)$  now modulates this new frequency, referred to as the carrier frequency. There are several advantages. First,  $\Delta\omega$  can be chosen to enable detection in more desirable, less-noisy bandwidths. More importantly, the phase of the heterodyne signal can be measured directly without any inversion.

### 6.1.5 Frequency Down Conversion

For a heterodyne signal in an RF bandwidth, consider a reference signal with the same carrier frequency,  $\omega$ .<sup>1</sup> This reference signal is referred to as the Local Oscillator (LO).

---

<sup>1</sup>The  $\Delta$  denoting optical frequency difference is dropped here.



The most simple phase-measurement system is mix the RF signal with the LO. Mixers are circuit elements and perform the function of signal multiplication. The output is referred to as the Intermediate Frequency (IF) and is

$$\begin{aligned} S_{\text{IF}} &= S_{\text{RF}} S_{\text{LO}} , \\ &= A(t) \cos(\omega t + \phi(t)) \cos(\omega t) , \end{aligned} \quad (6.29)$$

where  $A(t)$  and  $\phi(t)$  are the amplitude and phase modulation of  $S_{\text{RF}}$ . The LO is assumed to have unity amplitude and zero phase. From trigonometry,

$$S_{\text{IF}} = \frac{1}{2} A(t) \cos(\phi(t)) + \frac{1}{2} A(t) \cos(2\omega t + \phi(t)) . \quad (6.30)$$

So, the effect of an ideal mixer is to generate two signals with frequencies given by the sum and difference of the RF and LO frequencies. If  $S_{\text{IF}}$  is now low-pass filtered with cutoff frequency  $\omega_c < 2\omega$ , then the resulting signal is

$$S_{\text{IF,LPF}} = \frac{1}{2} A(t) \cos(\phi(t)) . \quad (6.31)$$

This signal processing architecture is often illustrated in block diagrams as shown in Figure 6.1.

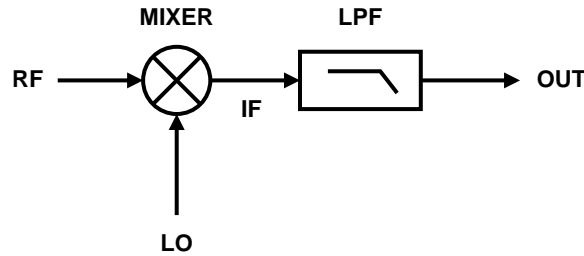


Figure 6.1: Block diagram of frequency down converter.

The above example illustrates frequency down conversion to baseband, the frequency band containing the phase modulation. Mixer down conversion is ubiquitous in RF engineering applications, e.g., it is the technique used to convert frequency-modulated radio to audible frequencies. The RF and LO frequencies do not need to be the same, and the system is often used in receivers to down convert very high frequencies to lower bandwidths that are still RF. Likewise, the mixer is often used for up conversion, necessary for transmission.

If  $S_{\text{RF}}$  is the signal obtained from a heterodyne interferometer, then frequency down conversion can be used to obtain the signal phase in the form of (6.31). However,

all of the same issues of phase wrapping and amplitude discrimination are present in this output. Heterodyne detection can be performed in quiet bandwidths, but with only this signal processing system the advantages are limited. With only a slightly more complicated system, much more information can be extracted from the heterodyne signal. This is known as IQ demodulation.

### 6.1.6 IQ Demodulation

IQ demodulation is a signal processing method used to obtain the in-phase (I) and quadrature (Q) components of a signal. The signal acquired using only down conversion is merely the in-phase component. With an additional signal path, the signal quadrature component can be obtained, enabling powerful and simple methods for extracting the desired signal information like phase and amplitude modulation.

To obtain the signal quadrature component, the key additional step is to phase delay the LO by one quadrature, i.e.,  $90^\circ$ , before frequency down conversion. To see how this works, consider the simple example above again, where now the LO has a phase delay. Then, the mixer output is

$$\begin{aligned}
 S_{\text{IF}} &= S_{\text{RF}} S_{\text{LO}} , \\
 &= A(t) \cos(\omega t + \phi(t)) \cos(\omega t - \pi/2) , \\
 &= -A(t) \cos(\omega t + \phi(t)) \sin(\omega t) , \\
 &= \frac{1}{2} A(t) \sin(\phi(t)) - \frac{1}{2} A(t) \sin(2\omega t + \phi(t)) .
 \end{aligned} \tag{6.32}$$

After low-pass filtering, the quadrature component is obtained,

$$Q(t) = \frac{1}{2} A(t) \sin(\phi(t)) . \tag{6.33}$$

Clearly, the quadrature component is merely the in-phase component with a quadrature phase difference. If both the in-phase and quadrature components are extracted, then the signal can now be constructed as

$$S(t) = I(t) + jQ(t) , \tag{6.34}$$

$$= A(t) e^{j\phi(t)} . \tag{6.35}$$

The phasor representation in (6.35) illustrates how the IQ data enable the amplitude and phase modulation to be separated and independently measured. They are given

simply by

$$\phi(t) = \tan^{-1}(Q(t)/I(t)) , \quad (6.36)$$

$$A(t) = \sqrt{I(t)^2 + Q(t)^2} . \quad (6.37)$$

It is in this sense that heterodyne detection and subsequent IQ demodulation enables direct phase measurement. The block diagram illustrating this system is shown in Figure 6.2.

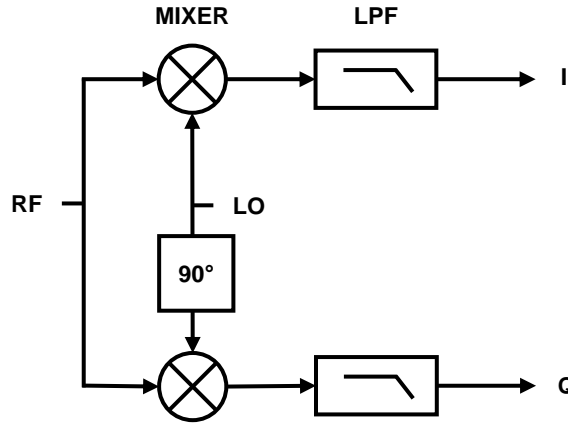


Figure 6.2: Block diagram of IQ demodulator.

Typically in interferometry phase wrapping occurs every  $\pi$  radians. Equation (6.36) increases this limit to  $2\pi$  because, although  $\tan(x)$  is defined for  $x \in (-\pi/2, \pi/2)$ , the sign of  $Q(t)$  can be used to identify the quadrant on the phase plane. This signed inverse tangent is implemented in a variety of computational tools as the `arctan2` function, and the NumPy version is used in this work (Harris et al., 2020). An essential consequence of these phase data is that wrapping at  $2\pi$  increments results in discrete jumps in the signal, identification of which is simple, and since the direction of phase change is known, the wrapped signal can be unwrapped using only a simple algorithm. In this work, the NumPy algorithm `unwrap` is used. Figure 6.3 illustrates how this works. The true signal is

$$\phi(t) = 3\pi \cos(\omega t) . \quad (6.38)$$

The amplitude is uniformly unity. The in-phase and quadrature components are then given by

$$\begin{aligned} I(t) &= \Re(e^{j\phi(t)}) , \\ Q(t) &= \Im(e^{j\phi(t)}) . \end{aligned} \quad (6.39)$$

Figure 6.3 shows true phase variation, the inverted in-phase component, the inverted phase using  $\arctan2$ , and the unwrapped signal. The distinct jumps in the inverted IQ data are apparent, enabling the unwrapping algorithm. The phase information clearly cannot be recovered using only the in-phase component. An additional important point seen from Figure 6.3 is that the unwrapped IQ data cannot recover the initial phase, and so the unwrapped phase signal is displaced. So some additional information is required to correct for this shift, such as the phase signal amplitude or initial condition.

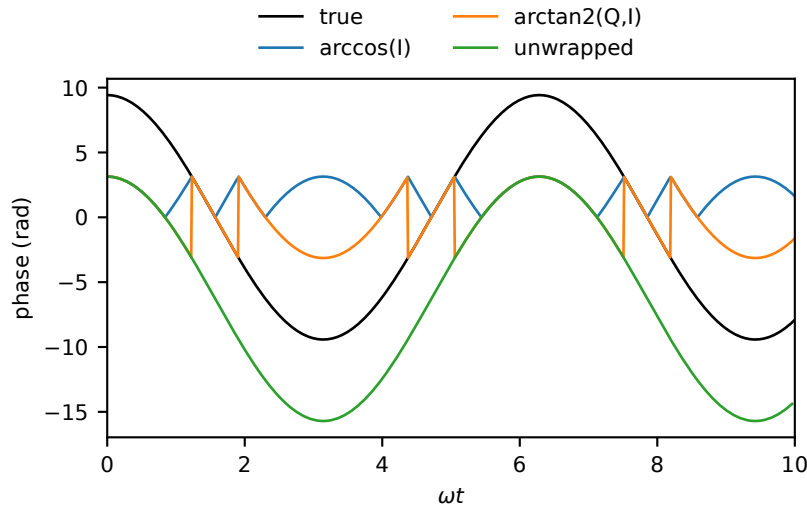


Figure 6.3: Illustration of phase unwrapping using IQ data.

Heterodyne detection enables using IQ demodulation to obtain IQ data, however IQ data can also be obtained using other methods. A clever technique is to introduce the quadrature delay *optically* in the reference beam of an interferometer. One way to do this is to use a quarter wave plate, which delays one polarization component of the reference beam by one quadrature. Interference in a polarizing beam splitter generates two signals, the in-phase and quadrature components. An interferometer of this type is described by Hogenboom and DiMarzio (1998). Another approach is to use an imaging interferometer and introduce the quadrature delay spatially in the reference beam. This is the approach used recently by Wang and Mazumdar (2021) to make index measurements through shock waves.

### 6.1.7 Amplitude and Phase Noise

Given an RF signal measured with some noise power spectral density, an important question is how does this signal noise determine the noise of the IQ demodulated

signal and the phase and amplitude data.

By mixing the RF and LO signals, a process of ideal multiplication, the power spectra of each signal are convolved. For simplicity, assume that the SNR of the RF signal is much worse than the SNR of the LO, such that the LO noise power can be neglected and the noise characteristics of the in-phase and quadrature components are driven by the RF signal. Then the SNR of the IQ data is the same as that of the incoming RF signal.

Given IQ data with some SNR, the objective is to determine the SNR of the phase and amplitude data. Goodman (2015) presents a solution using concepts of random phasor sums, and this analysis is repeated here. Consider  $I$  and  $Q$  to be Gaussian random variables with means  $\mu_I$  and  $\mu_Q$  and a common variance  $\sigma^2$ . The phasor defined by  $I$  and  $Q$ ,

$$I + jQ = Ae^{j\phi}, \quad (6.40)$$

can be separated into the sum of a constant phasor and a random phasor,

$$I + jQ = s + ae^{j\theta}, \quad (6.41)$$

where  $s$  is the constant phasor with amplitude  $\sqrt{\mu_I^2 + \mu_Q^2}$  and phase  $\tan^{-1}(\mu_Q/\mu_I)$ . Without loss of generality, the constant phasor phase can be set to zero by taking  $\mu_Q = 0$ . The joint probability density function for  $a$  and  $\theta$  is (Goodman, 2015)

$$p_{A\Theta}(a, \theta) = \frac{a}{2\pi\sigma^2} \exp\left(-\frac{(a \cos \theta - s)^2 + (a \sin \theta)^2}{2\sigma^2}\right), \quad (6.42)$$

assuming  $\theta \in (-\pi, \pi]$  and  $a > 0$ . Goodman (2015) gives the marginal densities for  $a$  and  $\theta$ , which are complicated for general values of  $s$ . Worth noting is that the marginal density for  $a$  is known as the Rician distribution, often discussed in other relevant applications (Papoulis and Pillai, 2002). In the limit  $s \gg \sigma$ , the marginal distributions can approximated as

$$p_A(a) \approx \frac{1}{\sqrt{2\pi}} \exp\left(-\frac{(a - s)^2}{2\sigma^2}\right), \quad (6.43)$$

$$p_\Theta(\theta) \approx \frac{k}{\sqrt{2\pi}} \exp\left(-\frac{k^2\theta^2}{2}\right), \quad (6.44)$$

where  $k = s/\sigma$ . Thus, the essential result is that for IQ data with a sufficiently large SNR,  $s \gg \sigma$ , the marginal densities for the amplitude and phase data are normally distributed around the constant phasor that is given by the mean IQ data. The amplitude variance is equal to the variance of the IQ data, and the phase variance

is equal to  $\sigma^2/s^2$ , i.e., the phase-noise floor is equal to  $1/\text{SNR}$  of the IQ data. For example, if a heterodyne signal is measured with an SNR of 100 dB/Hz, then the phase-noise floor is  $10^{-10}$  rad<sup>2</sup>/Hz. To obtain microradian resolution in a 1 MHz bandwidth requires IQ data, and therefore photodetector signals, with an SNR of more than 180 dB.

This was simulated by generating synthetic signals with white band-limited Gaussian noise. A bandwidth  $f_{\text{BW}}$ , center frequency  $f_c$ , RMS carrier power  $P_c$ , record length  $N$ , sampling rate  $f_s$ , and signal-to-noise ratio SNR were chosen. For digital signals, the resolution bandwidth (RBW) is given by  $1/T$  where  $T$  is the sampling period. Welch's method is used to compute the power spectral density, so the RBW is instead given by the size of each averaging segment,  $N_{\text{seg}}$ , i.e.,  $\text{RBW} = 1/N_{\text{seg}}$ .

The root-mean-square noise amplitude is

$$\sigma_N = \sqrt{\frac{f_{\text{BW}}}{\text{SNR}}} . \quad (6.45)$$

The noise-free signal is given by

$$S[n] = \sqrt{2P_c} \sin(2\pi f_c n / f_s) . \quad (6.46)$$

White Gaussian noise,  $\hat{G}[n]$ , is generated by drawing  $N$  samples from a zero-mean normal distribution with arbitrary variance.  $S[n]$  and  $\hat{G}[n]$  are band-pass filtered with -3 dB cutoff frequencies given by  $f_c - f_{\text{BW}}$  and  $f_c + f_{\text{BW}}$ . The band-limited Gaussian noise is now scaled to obtain the correct noise power,

$$G_{\text{BL}} = \frac{\sigma_N}{\sqrt{\text{Var}[\hat{G}_{\text{BL}}]}} \hat{G}_{\text{BL}} . \quad (6.47)$$

The noised signal is now obtained by the sum,

$$S[n] = S_{\text{BL}}[n] + G_{\text{BL}}[n] . \quad (6.48)$$

The resulting PSD for the noised signal is shown in Figure 6.4 using the following parameters:  $f_c = 200$  MHz,  $N = 12.5$  Mpts,  $f_{\text{BW}} = 40$  MHz,  $f_s = 6.25$  GS/s, and  $\text{SNR} = 80$  dB/Hz. The PSD is shown in dBc, which is

$$\text{dBc} = 10 \log_{10} \left( \frac{P}{P_c} \right) . \quad (6.49)$$

Using the above procedure, synthetic IQ data were generated for a range of SNRs. The resulting histograms are scaled and plotted together in Figure 6.5. This shows

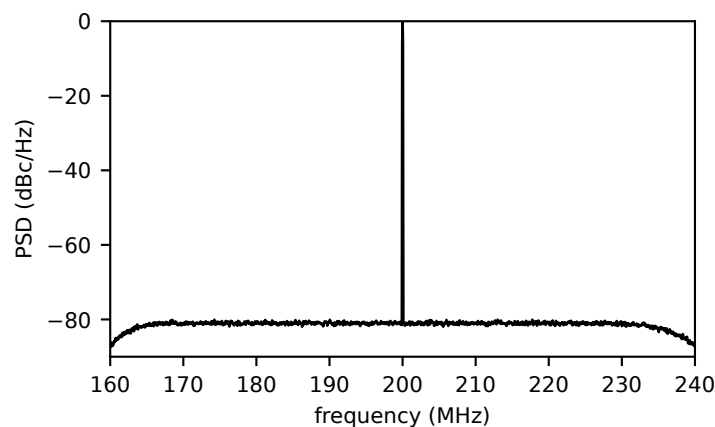


Figure 6.4: Power spectral density of synthetic signal with band-limited Gaussian noise and 80 dB SNR.

that the amplitude noise in IQ data results in a point “cloud” in the IQ-plane. Resolution of amplitude and phase measurements is determined by the diameter of the cloud. Figure 6.6 compares phase noise measured from simulated signals with the value expected from the random phasor analysis above.

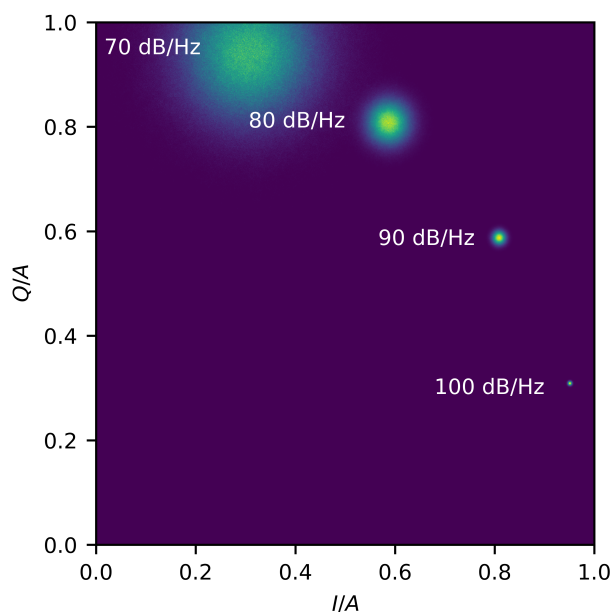


Figure 6.5: Histograms of IQ data calculated from simulated signals with four different SNRs.

The above results assume that IQ data only contain band-limited additive Gaussian white noise. This models noise in real band-limited circuits, such as shot noise.

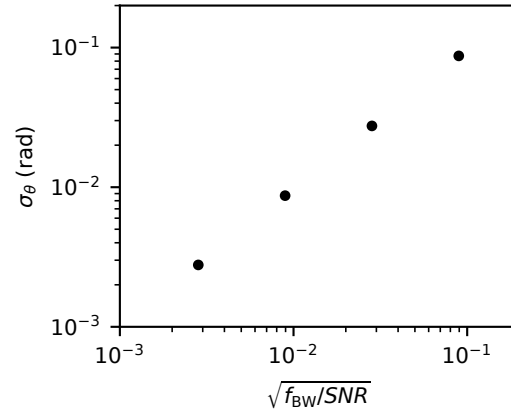


Figure 6.6: Phase noise from IQ data with band-limited additive Gaussian noise.

However, other noise sources may not be additive, Gaussian, or white. Therefore, the above results provide estimates for only the *minimum* expected measurement noise. A particular challenge for the heterodyne system that does not exist for the typical homodyne interferometer is sensitivity of LO phase noise.

### 6.1.8 Small-Signal Response

Previously, when analyzing the conversion of phase modulation to optical intensity, it was assumed that spatial variation in the phase field is sufficiently small as to be neglected. Including these effects are essential for understanding aspects of the focused laser interferometer used in this work. Here, index perturbations are still assumed sufficiently small that Gaussian beam propagation is preserved. Hence, this analysis gives the small-signal response of the interferometer.

Settles and Fulghum (2016), Schmidt and Shepherd (2015), and Lawson (2021) all analyze the optical response of an FLDI, with Lawson (2021) providing the most comprehensive investigation. The result from this work is a transfer function that relates harmonic plane waves in the refractive index,

$$n(x, t) = A \cos(kx - \omega t + \varphi) , \quad (6.50)$$

to the integrated optical phase signal,

$$\Delta\Phi = Ah(k) \sin(\omega t - \varphi) . \quad (6.51)$$

$k$  and  $\omega$  are the wavenumber and frequency describing the index plane wave and are related by

$$k = \frac{\omega}{v} , \quad (6.52)$$



where  $v$  is the plane wave speed. The function,  $h(k)$ , can then be used to invert measurements of phase into units of refractive index or density, using the Gladstone-Dale constant. For plane waves in fluid flows, there are three families of characteristics on which the signal can travel,  $C^-$ ,  $C^0$ , and  $C^+$ . The wave speeds for these cases are  $u - a$ ,  $u$ , and  $u + a$ .

With heterodyne detection and IQ demodulation, the *absolute* phase response can be measured, and therefore a corresponding small-signal transfer function is required. Derivation of this is a simple variation on the work by Lawson (2021), and so will not be detailed here. Lawson's analysis is more general, including plane wave propagation at angles relative to the beam axis and foci orientation. These effects are not considered here, and plane waves are assumed to propagate perpendicular to the beam axis and perpendicular to the plane defined by the FLDI foci.

The transfer functions for differential and absolute signals are

$$h_{\text{diff}}(k) = \frac{8\sqrt{2}\pi^{5/2}w_0}{k\lambda_L^2} \exp\left(-\frac{w_0^2k^2}{8}\right) \text{erf}\left(\frac{kl\lambda_L}{2\sqrt{2}\pi w_0}\right) \sin\left(\frac{k\Delta x}{2}\right), \quad (6.53)$$

$$h_{\text{abs}}(k) = \frac{1}{2} \cdot \frac{8\sqrt{2}\pi^{5/2}w_0}{k\lambda_L^2} \exp\left(-\frac{w_0^2k^2}{8}\right) \text{erf}\left(\frac{kl\lambda_L}{2\sqrt{2}\pi w_0}\right), \quad (6.54)$$

where  $\lambda_L$  is the optical wavelength and  $l$  is the domain half length, i.e.,  $L = 2l$ . The correspondence between (6.53) and (6.54) is obvious, and we find that

$$\frac{h_{\text{diff}}}{h_{\text{abs}}} = 2 \sin\left(\frac{k\Delta x}{2}\right). \quad (6.55)$$

For high wavenumbers, the sine term in  $h_{\text{diff}}$  causes signal aliasing and the exponential term causes the signal amplitude to roll off. This is not a useful region of bandwidth. We can consider small wavenumbers in the following limits,

$$\frac{k\Delta x}{2} \ll 1, \quad \frac{w_0^2k^2}{8} \ll 1, \quad \frac{kl\lambda_L}{2\sqrt{2}\pi w_0} \ll 1. \quad (6.56)$$

If these limits are satisfied, then the transfer functions can be given to first order as

$$h_{\text{diff}} = \frac{2\pi}{\lambda_L} L \cdot k\Delta x, \quad (6.57)$$

$$h_{\text{abs}} = \frac{2\pi}{\lambda_L} L. \quad (6.58)$$

These are, of course, only equal when  $k\Delta x = 1$ .

Figure 6.7 plots the full transfer functions, (6.53) and (6.54), with the first-order limits, (6.57) and (6.58). The absolute response has a uniform pass band, while the differential response shows low frequency roll off. This roll-off is a consequence of the differentiation. If the differential signal is instead compared with the phase *derivative*, then the transfer function shows a flat pass band (Schmidt and Shepherd, 2015). The FLDI gives a measurement of the spatial index gradients. Gradients are, of course, directly proportional to frequencies. So, differential signal amplitudes are reduced for longer frequencies. This is the behavior shown in Figure 6.7 and by (6.57).

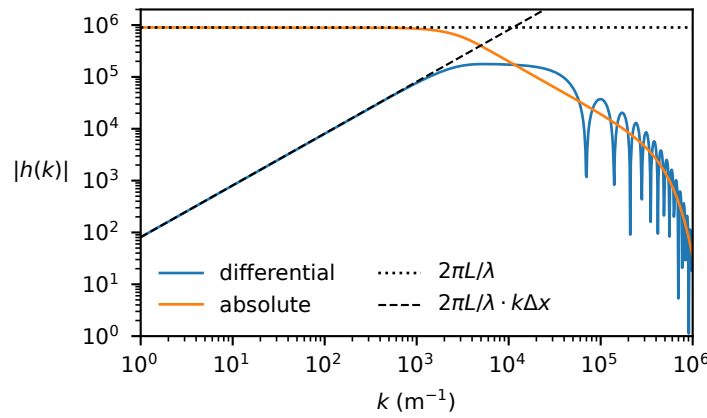


Figure 6.7: Comparison of absolute and differential focused laser interferometer transfer functions, using parameters  $\Delta x = 90 \mu\text{m}$ ,  $w_0 = 6 \mu\text{m}$ ,  $\lambda_L = 532 \text{ nm}$ , and  $l = 38.1 \text{ mm}$ .

The absolute signal transfer function illustrates that the interferometer response is a low-pass filter. A -3 dB cutoff can be derived by solving

$$-3 \text{ dB} = 20 \log_{10} \left( \frac{h_{\text{abs}}(k_c)}{2\pi L / \lambda_L} \right). \quad (6.59)$$

Note that decibels are typically defined for signal powers, and so the logarithm is multiplied by 20 instead of 10.  $k_c$  was solved numerically for relevant optical parameters ( $w_0 = 6 \mu\text{m}$ ,  $\lambda_L = 532 \text{ nm}$ ,  $L = 76.2 \text{ mm}$ , and  $\Delta x = 90 \mu\text{m}$ ) and converted to frequency  $f_c$  using the dispersion relation (6.52). In this work, shock Mach numbers of interest range are  $M_s \in [2, 10]$ . For simplicity, consider only air shocks with  $\gamma = 1.4$  and  $a_1 = 345 \text{ m/s}$ . Assume index plane waves are traveling on incoming  $C^+$  characteristics. Since  $u_2 + a_2$  varies approximately linearly with  $M_s$ , the interferometer response -3 dB cut-off frequency can be approximated by

$$f_c \approx 0.2 M_s \text{ (MHz)}. \quad (6.60)$$

So, for a  $M_s = 5$  shock,  $f_c = 1$  MHz. The cut-off frequency can be increased by using a less focused beam. For example, for a  $24 \mu\text{m}$  beam waist, the cut-off frequency is approximately  $0.8M_s$  MHz.

The above transfer functions do not describe the spatial selectivity of a focused interferometer, since the index perturbation is assumed to uniformly span  $L$ . If the perturbation is instead confined to a small region along the  $z$  axis, then the response depends upon the local beam diameter. This effect was examined by Schmidt and Shepherd (2015) by considering the index field perturbation to be

$$n(x, z, t) = A \sin(kx - \omega t + \varphi) \delta(z - z_0) , \quad (6.61)$$

where  $\delta$  is the Dirac delta function and  $z_0$  is the index perturbation's position. The relevant transfer function is

$$H_w(k) = \exp\left(-\frac{k^2 w^2}{8}\right) , \quad (6.62)$$

where  $w$  is the local beam radius.  $H_w(k)$  behaves as a first-order low-pass filter with -3 dB cut-off given by

$$k_c w = \sqrt{\frac{1.2}{\log_{10} e}} \approx 1.66 . \quad (6.63)$$

If  $\lambda$  is the wavelength of the index plane wave, then  $\lambda_c \approx 3.8w$ . Put simply, beam focusing only begins significantly rolling off higher frequencies when wavelengths are less than 50% of the beam diameter. Therefore, for index perturbations local to the focus, by reducing the beam waist the cut-off frequency increases. It is in this manner that the focused interferometer achieves spatial selectivity.

Throughout the following work it will be assumed that phase signals are uniformly distributed spanwise, so that the response functions (6.53) and (6.54) may be used.

A final point is that, for a significant portion of the bandwidth of interest, the absolute phase signal has a response orders of magnitude greater than the differential signal. There is fundamentally no additional information obtained from using the differential signal. The advantages come from implementation with real optics where, for example, vibration sensitivity can be a major challenge. Since the differential signal is only redundant with a weaker response, all of the work in the following chapter employs only the absolute phase signal.

## 6.2 Methods

### 6.2.1 Electro-Optical System

The complete heterodyne focused laser interferometer (HFLI) is diagrammed in Figure 6.8, where all components are labeled except for three mirrors. Optical and electrical components are tabulated in Appendix D.

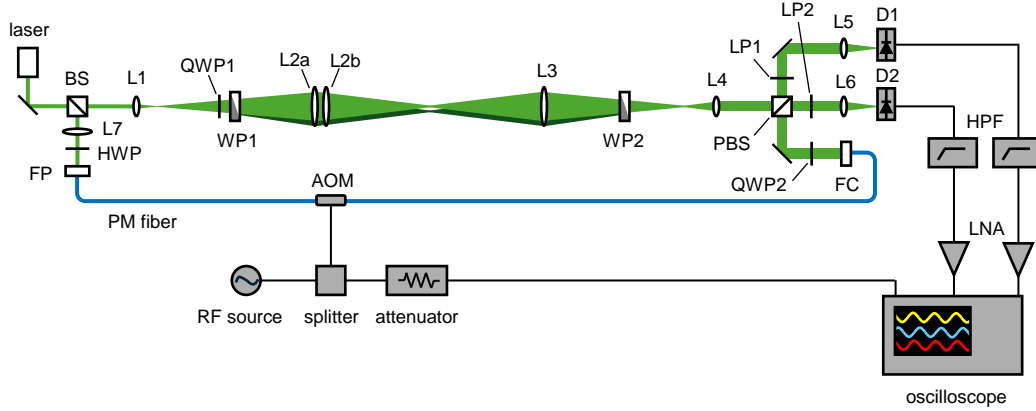


Figure 6.8: Diagram of heterodyne focused laser interferometer.

The overall construction is one of a Mach-Zehnder interferometer, where the reference beam is fiber coupled. The signal beam path is transmitted through a typical FLDI, where the only missing component is a linear polarizer at the output of WP2. The FLDI beams carry phase modulation in orthogonal polarization states. These signals are subsequently split again by a polarizing beam splitter (PBS) and coherently detected by interfering them with the reference beam. The reference beam is frequency shifted by 200 MHz by a fiber-coupled acousto-optic modulator (AOM), so that the coherent detection is heterodyne. The detector signals are high-pass filtered (HPF), amplified using Low-Noise Amplifiers (LNA), and finally digitized by the oscilloscope.

The AOM is driven by a 1 W, 200 MHz RF source. The RF power is split, sending roughly 0.5 W to the AOM. The other half is attenuated (-23 dB) and then also digitized by the oscilloscope. The measured insertion loss of the AOM is minimized in the 0.5 W range, so splitting the source power leads to no loss in performance.

Three signals are acquired: two signals from heterodyne detection of the signal beams and an LO reference signal. Any pair of these signals can be IQ demodulated to measure the phase and amplitude modulation of the optical signals. It must be emphasized that the FLDI beams are not interfered, rather each is detected separately. The signal of the FLDI, i.e., the differential phase, is recovered by IQ demodulating

the heterodyne signals with each other. If the heterodyne signal is demodulated with the LO, then the absolute phase and amplitude modulations are measured.

There are many details to the electro-optical system and its final performance that required significant effort to make it all work. Throughout this process, Hobbs (2008) proved an indispensable resource. Some of the instrument details will be described here, but additional information is given in Appendix D.

By far, the most troublesome subsystem was coupling the reference beam into the polarization-maintaining (PM) fiber. A Thorlabs FiberPort (PAF2-A4A) was used for this, which has five degrees of freedom for adjustment. The L7 is a 300 mm plano-convex lens and was necessary to collimate the laser, or at least place the beam waist behind the FiberPort, in order to achieve good coupling efficiency. The beam splitter was mounted on a tip-tilt kinematic and one translation stage. From an initially unfocused FiberPort, alignment was performed in stages beginning with a 105  $\mu\text{m}$  multimode fiber, stepping down to a 25  $\mu\text{m}$  fiber, and finally the single-mode PM fiber (Thorlabs P3-488PM-FC). Not including fiber insertion losses, typical alignment could achieve 80-90% coupling efficiency.

PM fiber does not polarize the input beam, instead polarization modes are uncoupled by large stress-induced birefringence in the fiber core. If light is coupled into both axes of a PM fiber, then each polarization rapidly loses phase coherence, and if any light jumps modes, e.g., from vibration, then there is interference. Since there is only a single mode for the electric field to propagate in the fiber, then there is perfect spatial coherence between any beams combined in the fiber, and so immediate interference. This leads to significant conversion of phase modulation to amplitude modulation, and therefore effectively noise in the output beam. It is important to ensure that the input beam is linearly polarized and accurately aligned with the PM fiber axis to mitigate some of these effects. Hobbs (2008) gives a procedure for this using a half-wave plate (HWP) to rotate the input polarization, while monitoring the output with a detector and linear polarizer, aligned perpendicular to the fiber axis. The HWP and output polarizer are iteratively adjusted to minimize the output power. For much of the present work, an additional linear polarizer was located after the beam splitter (BS). Polarizers are lossy and so to increase signal level during shock-tube experiments it was later removed.

At some point during the development of the instrument it was identified that the AOM was damaged, leading to a much greater insertion loss than given by the specification sheet. The maximum insertion loss was measured to be 7.2 dB, whereas

the calibration data sheet reported a 1.74 dB insertion loss. Some of this loss is from the fiber connectors, but this is at most 2 dB. The most likely source for damage is the AOM fiber itself. Given the time constraints of completing development of this instrument and employing it for shock-tube measurements, work proceeded with the damaged unit.

Another challenge from using a fiber-coupled reference beam was that the reference signal phase was not steady, and instead drifted quite significantly over time. This was identified to be from the fiber itself by realigning the system as a homodyne free-space Mach-Zehnder interferometer. Using a fiber for the reference beam path was in part motivated by the success of the finite-fringe interferometer built by Jones (2021). A partial explanation for the present instrument's comparatively large drift is that operating an interferometer at zero-fringe with coherent detection is inherently much more sensitive.

A significant advantage from using a fiber-coupled reference beam was that the AOM could be easily "short circuited" by just directly connecting the input and output PM fibers and thereby converting the instrument into a homodyne interferometer. This proved essential for alignment, since fringes are only visible by eye with a homodyne system. When heterodyne, fringes are flickering at 200 MHz, and so the output beam appears uniform. Fringes significantly reduce the signal amplitude, so even if the instrument is only slightly out of alignment a signal might not be observable on the oscilloscope. There is then no way to know whether PBS adjustment is improving alignment, and adjustments are performed blind. By short-circuiting the AOM and operating the instrument as a homodyne system, fringes are observable by eye. A flip mirror located before L5 was used to redirect a portion of the beam and monitor alignment. Furthermore, it was only in this homodyne configuration that beam aberrations became apparent.

As a homodyne interferometer, it was identified that the beams transmitted through the FLDI optics incur significant spherical aberration. FLDI uses a focused beam, so the larger numerical apertures cause greater sensitivity to effects of real optics like aberrations. Spherical aberrations were reduced by replacing the FLDI lenses with achromatic doublets. L2a and L2b are a pair of 300 mm doublets, and the lens system they form has a focal length of 150 mm with near zero spherical aberration. Appendix D gives more details on this.

The pair of linear polarizers, LP1 and LP2, serve an essential function. Polarizing beam splitters reflect s- and transmit p-polarization components, regardless of the

beam input plane. Therefore, the reference beam and signal beam polarizations are orthogonal at the output of the PBS. The linear polarizers, LP1 and LP2, are aligned at  $45^\circ$  to rotate the polarizations and cause interference. Without the polarizers, fringes might still be observable but with terrible contrast.

The two detectors used in this work are reverse-biased photodiodes (Thorlabs DET10A). The BNC output of the detectors is terminated at  $50\ \Omega$  to convert the photocurrent to a voltage and impedance match the input of the RG58 coaxial cable. Because of the DC component from coherent detection, the 200 MHz RF signals are sitting on a positive constant DC value, which is eliminated by the HPFs. The LNAs amplify the signal with minimal reduction in SNR. Initially, amplified high-bandwidth detectors (Thorlabs PDA015A2) were employed. However, these detectors were found to be remarkably noisy. Additionally, the photodiode active area was very small, requiring an extremely sensitive alignment. Using a pair of DET10A detectors with external RF amplification was found to be superior in every way. Some issues were encountered with RF pickup from the 200 MHz source. A possible remedy for this would be to build the detectors and bring the  $50\ \Omega$  termination closer to the photodiode. When the system was operated in homodyne, the detector signals were amplified using a baseband low-noise preamplifier (Stanford Research SR560).

The AOM and RF system are designed for 200 MHz, which is a sufficiently low frequency that the signals could be directly digitized using a high-speed oscilloscope. This work used a Tek MSO44B with a maximum sample rate of 6.25 GS/s and bandwidth of 500 MHz. The oscilloscope was run at its maximum sample rate, so the main limitation of this approach is record length and file sizes. With a maximum record length of 62.5 Mpts, the maximum measurement duration was 10 ms. For four signals (three RF signals and the trigger), this generates roughly 5 GB of data. Significant subsequent digital signal processing is required, so minimizing the file size was important for efficiency. Fortunately, shock-tube experiments are short, so only 2-ms record lengths were used for almost all experiments. If the AOM and RF system were operating at a higher frequency, then direct digitization and signal processing may not be viable, and an analog system would have to be used for IQ demodulation.

A final point is that the interferometer can be quickly converted to a conventional FLDI by installing a linear polarizer at the output of WP2 and a detector at the focus of L3. This does not require any alignment adjustment except translation of

WP2 so that the FLDI is resting at a half fringe. Conventional FLDI measurements were performed for the validation experiments presented in this chapter using this technique.

### 6.2.2 Digital Signal Processing

Phase measurements were performed by implementing IQ demodulation digitally as a software algorithm. In digital IQ demodulation, there is no power loss from splitting a signal (it is literally copied), and there is no additional noise added from subsequent electronics. Analog electronics all have a Noise Figure (NF), which is the magnitude the SNR is reduced. The NF of digital IQ demodulation is zero. Signal multiplication is achieved by straightforward multiplication of the discrete signals at each sampled time. The important steps in digital IQ demodulation are the algorithms chosen to implement a quadrature phase delay in the LO and the low-pass filter employed.

Since the center frequency of the RF signal and the sampling rate of the digitizer are not necessarily even multiples of each other, the signal cannot be truncated by some number of samples to achieve a quadrature delay. One possibility is that the signal is linearly interpolated to a new time base with the correct shift. The method chosen in this work is to construct a linear-time-invariant phase-delay filter and apply it to the Fourier transform of the signal. Inversion of the signal back to the time domain returns a signal with the desired phase delay. Pei and Lai (2012) present the phase-delay filter employed in this work. The filter is

$$H[k] = \begin{cases} 1, & k = 0 \\ e^{-jD(2\pi/N)k}, & k = 1, 2, \dots, N/2 - 1 \\ \cos(D\pi), & k = N/2 \\ e^{jD(2\pi/N)(N-k)}, & k = N/2 + 1, \dots, N - 1 \end{cases} \quad (6.64)$$

where  $D$  is the fractional sample delay. For sampling rate  $f_s$ , and time delay  $\tau$ , then  $D = f_s\tau$ . For input signal,  $S[n]$ , then the delayed output is

$$S[n - D] = \mathcal{F}^{-1}\{H[k]\mathcal{F}\{S[n]\}\} \quad (6.65)$$

where  $\mathcal{F}$  and  $\mathcal{F}^{-1}$  denote the discrete-Fourier transform (DFT) and inverse DFT, respectively. This algorithm preserves the amplitude spectrum exactly, and only changes the phase data of the signal.

After frequency multiplication, the frequency sum component must be filtered. Many algorithms exist for low-passing filtering digital signals. The method cho-



sen here is to use an infinite-impulse response (IIR) Butterworth filter in cascaded second-order sections, implemented forward and backward. These filters are straightforward to employ using SciPy (Virtanen et al., 2020). The cascaded second-order sections construction enables stable high-order filters to be used. Applying the filter forward and then to the reversed signal is a clever technique of digital signal processing that cancels the phase delay of IIR filters. Hence, unlike analog filters, these filters give signals with a zero phase change. These methods are discussed in common digital signal processing textbooks (Oppenheim and Schaffer, 2010). The Python program used to implement these signal-processing steps is reproduced in Appendix D.

The disadvantage of using digital techniques is that the entire signal *and carrier* must be digitized. The 200 MHz carrier frequency itself contains no useful information, but the digitizer dynamic range must be filled by the carrier instead of the small signal. As a consequence, the effective number of bits available to acquire the desired signal is reduced, and loss of resolution can reduce SNR. Because of these considerations, an analog IQ demodulation system was constructed and tested. This work is discussed in Appendix D. For the present signals and electronics, no SNR improvement was found by using analog techniques, since the noise figure of analog components is much more significant. However, an important benefit of using an analog system is that the digitizer can be operated at a lower sampling rate, so that longer duration measurements can be performed. The present system was limited to milliseconds, which is appropriate for shock-tube applications.

### 6.2.3 Noise Performance

The noise floor of the instrument is illustrated in Figure 6.9 by two sets of power spectra. In (a), the spectrum of the heterodyne signal from detector D1 is compared with background signals from shuttering the laser and the oscilloscope. The oscilloscope noise floor is measured by terminating the input externally at  $50\ \Omega$ , which is the output impedance of the LNAs. (a) shows that the signal noise is significantly greater than the limitations of the oscilloscope digitizer. The small difference between the oscilloscope and the “laser off” signal is from the noise output from the detectors and LNAs. The noise source in the heterodyne signal is apparent by comparison with the LO in (b). The LO is the reference 200 MHz signal split from the AOM RF driver. In order to compare these signals, their spectra are plotted in dBc units, which properly scales each signal relative to the carrier power. (b) shows that the power spectra of the detector signal and LO are approximately the same,

indicating that the noise is coming from the 200 MHz RF source itself. This is particularly true for  $f_{\text{BW}} \leq 1$  MHz. For higher bandwidths, there is additional noise apparent in the detector signal. The origin is unclear, but the author suspects this comes from RF pickup in the detectors or RF reflections between the photodiode and  $50\ \Omega$  termination. For most of the spectrum the LO appears to be the primary contributor. Although not shown in Figure 6.9, if the resolution is increased, it is clear that LO noise is not so significant for low frequencies, less than 10 kHz. This is consistent with the unstable signals discussed above, which are suspected to come from the fiber.

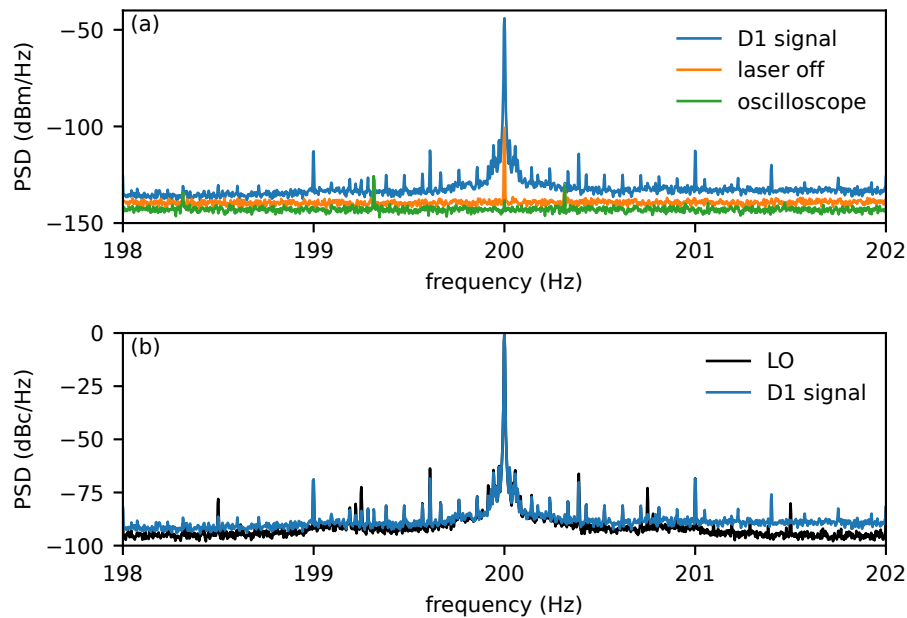


Figure 6.9: Power spectra compare heterodyne signal from detector D1 with background signals in (a) and the local oscillator (LO) in (b).

An important question is how does measurement noise depend upon the sampling rate. This was tested with results plotted in Figure 6.10, showing that the minimum phase noise is obtained with the highest sampling rate possible. It is possible that an even greater sampling rate could further reduce signal noise.

The ultimate noise floor obtained with the instrument varied depending upon alignment. In particular loss of fringe visibility due to spherical aberration when using smaller beam waists (higher NA) reduced detector SNR and therefore increased the phase noise floor. For the measurements presented in this chapter, typical values for the noise floor in the 10 kHz to 10 MHz band was 1 mrad or  $10^{-13}$  rad<sup>2</sup>/Hz.

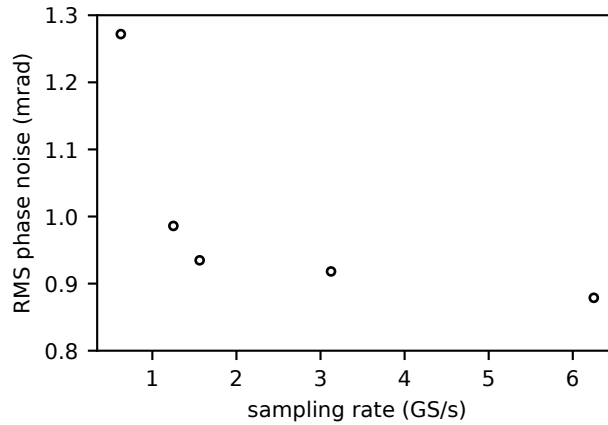


Figure 6.10: RMS phase noise measurements in 10 kHz to 10 MHz band for various sampling rates. 6.25 GS/s is the maximum speed of the Tek MSO44B.

The data in Figure 6.10 show an example where the noise floor was 0.9 mrad. For comparison, the FLDI using balanced detection described in Appendix C achieved a noise floor of  $6 \cdot 10^{-17} \text{ rad}^2/\text{Hz}$  in a 1 MHz bandwidth.<sup>2</sup>

Figure 6.11 shows typical absolute and differential signals, both the time series in (a) and spectrum in (b). A 10 MHz low-pass filter was used to process these data. Most significant to observe is the behavior of the absolute signal: it is not steady. This was acquired with the interferometer at rest on a vibration-isolating optical table and room air conditioning off. Unfortunately this is the typical behavior of the instrument. The reference fiber seems to be a leading contributor to this signal drift. The drift was random, and analysis over long time records shows  $1/f$  frequency dependence. In the present work, this is not a significant limitation because shock-tube signals are  $O(10^2)$  rad and data are analyzed over less than 200  $\mu\text{s}$ , where drift is expected to be about 20 mrad.

## 6.3 Validation

### 6.3.1 Small-Signal Response

The small-signal response of the HFLI was tested using an ultrasonic transducer to generate a constant source of weak acoustic waves. The methods and equipment used are the same as those used by Lawson (2021).

Figure 6.12 shows measurements of the ultrasonic source operated at 100 kHz. The

<sup>2</sup>In terms of RMS resolution, the HFLI achieves about 0.3 mrad in a 1 MHz bandwidth versus 8  $\mu\text{rad}$  with balanced detection.

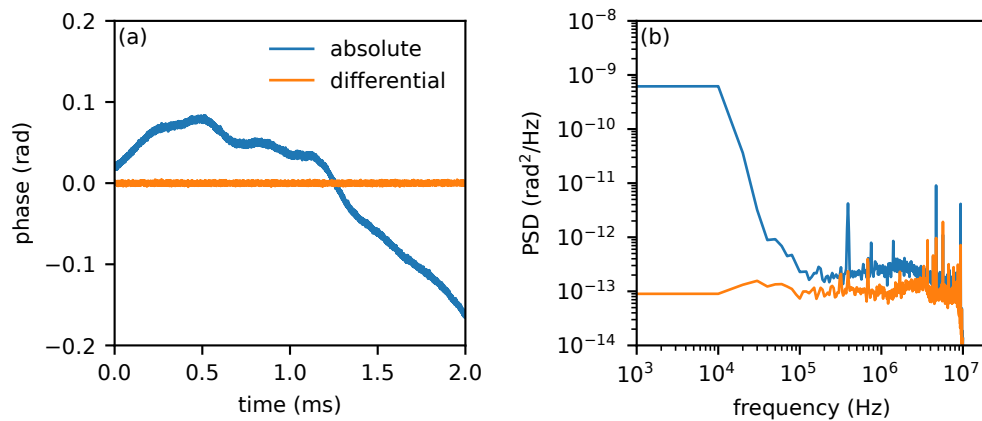


Figure 6.11: Typical phase signals for resting interferometer.

HFLI signals are demodulated to obtain differential and absolute phase signals, and these measurements are compared with those from a conventional FLDI. The time-series signals are shown in (a) and the power-spectral densities in (b). Clearly, the differential HFLI and the conventional FLDI produce the same signals with slightly different noise characteristics. This confirms that digitally demodulating heterodyne signals is equivalent to directly interfering the optical signals. In contrast, the absolute HFLI signal has a much greater magnitude and is  $90^\circ$  out of phase with the differential signals. This is consistent with the small-signal response functions discussed above.

The ultrasonic source was swept over a range of frequencies from 30 kHz to 100 kHz, and the absolute and differential signal amplitudes were ratioed. Amplitudes were measured from the power spectral densities using a “flat-top” window. The results are plotted in Figure 6.13 and compared with the analytical expression. Good agreement is obtained. Deviations are possibly from wave propagation components along the beam axis.

### 6.3.2 Dynamic Response

The dynamic response of the interferometer to a large index gradients was tested by sending weak shocks through the signal beam pair using an open-ended shock tube. The shock tube was constructed from 0.75-inch diameter iron pipe. The driver was built from an 8-inch nipple and a tee, in which a 100-psi dial pressure gauge was installed. The driven section was built from a 12-inch nipple, where the end pipe threads were cut off and the end was squared. The diaphragm was clamped between

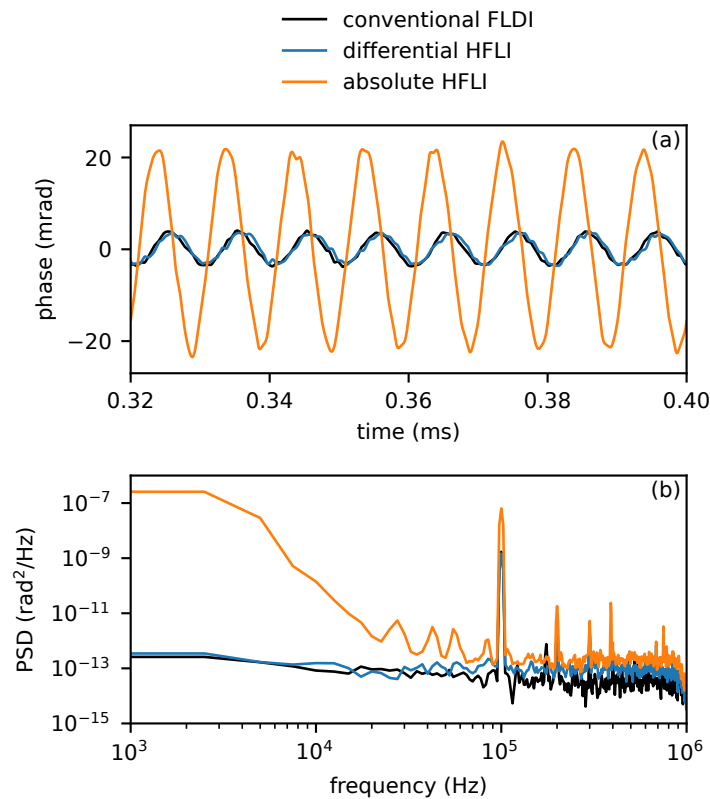


Figure 6.12: Comparison of measurements of 100 kHz ultrasonic waves using a conventional FLDI, the differential HFLI, and absolute HFLI.

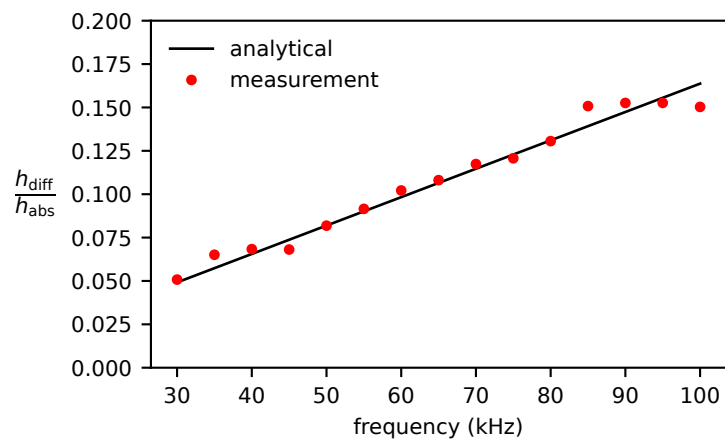


Figure 6.13: Ratio of differential to absolute phase signals comparing measurements with analytical result (6.55).

the tapered faces of a pipe union. Two thicknesses of 1100-O aluminum sheet were used for diaphragms to generate two shot conditions: 0.7 mil and 2.0 mil, which

ruptured at 16 psi and 54 psi, respectively. Nitrogen was used as the driver gas. Data were collected for two positions of the interferometer beam pairs relative to the shock-tube exit: 2.5 mm and 10 mm. Figure 6.14 shows a diagram of the setup.

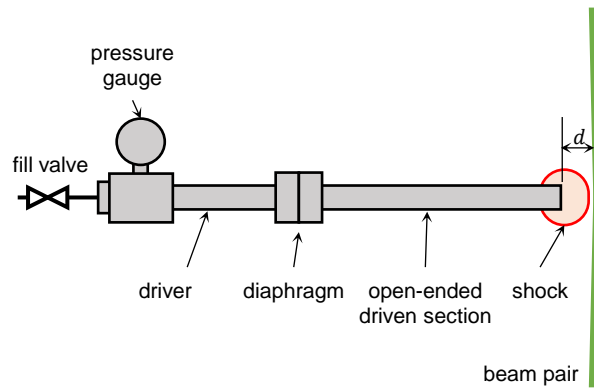


Figure 6.14: Diagram of open-ended shock-tube experimental setup for validating HFLI dynamic response.

First, differential phase measurements using a conventional FLDI and the HFLI are compared in Figure 6.15. All data are for the 54-psi shot condition. (b) and (d) show detail of the shock response in (a) and (c), respectively. The long-time small-signal response of the FLDI and HFLI measurements are consistent, as expected. There is clearly discrepancy in the shock response. There are two factors causing this difference. First, large phase changes, such as the peaks above 6 radians, cause phase wrapping which can only be recovered by the HFLI but not the FLDI. Second, the large density gradients in the shock distort the signal beam. Signals obtained from interfering these distorted beams together, as with the conventional FLDI, are likely different than those obtained from subtracting the two signals obtained from interfering the distorted beams with undistorted reference beams, as with the HFLI.

Absolute phase measurements from four shots at the 54-psi condition are shown in Figure 6.16. The signals range over 50 radians illustrating the unwrapping capability of the heterodyne technique. (a) shows the signals unwrapped and zeroed based on their initial value before the shock arrives. (b) zooms in on the shock arrival in these signals. There is clearly inconsistency between these shots, but more significantly the theoretical shock speed should produce a roughly 50 radian jump in phase. This is not observed, providing a first indication of the interferometer's inability to measure phase change through shocks. Assuming that the remainder of the signal is viable, (c) shows them zeroed by the maximum signal value. In this case, the signals collapse and show good repeatability.

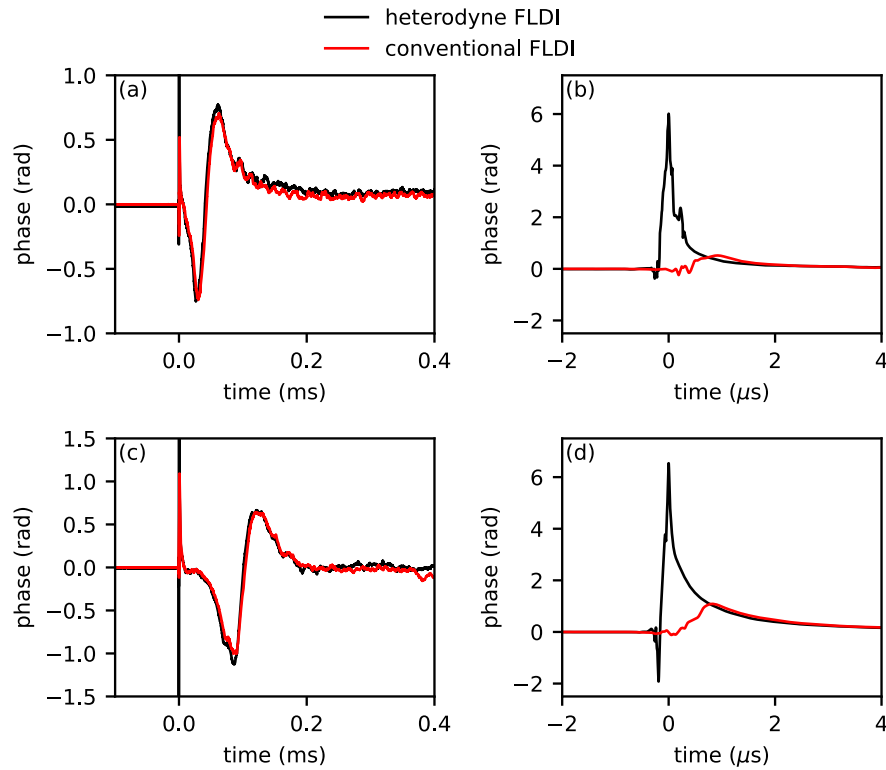


Figure 6.15: Comparison between differential phase measurements from a conventional and heterodyne FLDI for 54-psi condition. (a) and (b) correspond with  $d = 2.5$  mm, (c) and (d) correspond with  $d = 10$  mm.

A partial explanation for the interferometer's apparent inability to track phase changes through shocks is found from inspecting the signal amplitudes. Figure 6.17 shows heterodyne signal amplitudes over 1 ms in (a) and the 1  $\mu$ s shock response in (b). Amplitude is normalized by the pre-shock stationary value. When the shock arrives, a sharp downward spike is observed in the amplitude data, showing that the shock causes the signal amplitude to decrease near zero. This amplitude reduction indicates some distortion to the signal beams. Recall from Chapter 4 the image obtained from a shock propagating through a beam of collimated light. Strong refractive effects produce a shadow and focused band of light. When transmitting through a focused laser beam, the wavefront is distorted and the beam path could be steered out of alignment with the reference beam producing fringes. Fringes averaged over the detector significantly reduce heterodyne signal amplitudes. It appears then that the present interferometer cannot be used to measure phase continuously through large jumps in refractive index.

In order to validate the absolute phase signals, numerical simulations were performed

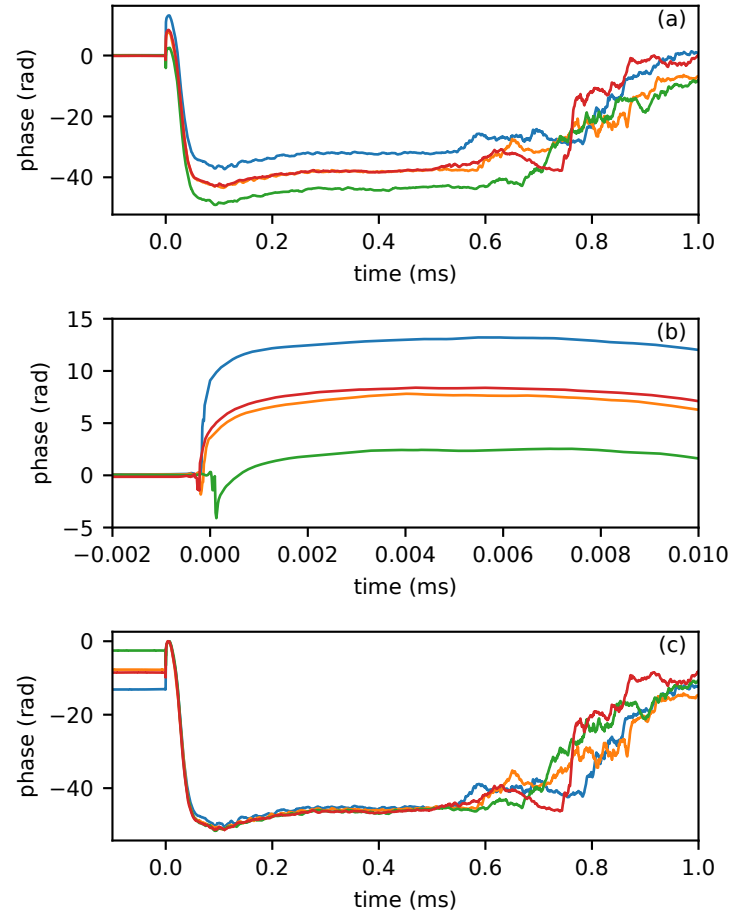


Figure 6.16: Unwrapped phase signals from four shots at 54-psi condition and  $d = 2.5$  mm. Each subplot show the same data, however in (a) the phase signals are zeroed by their initial values, the shock response is shown in (b), and (c) shows the phase signals zeroed by the maximum.

to model the two shot conditions. The same simulation methods as those used in Chapters 2 and 3 are employed here: OpenFOAM-9 (Greenshields, 2021) and blastFoam-5 (Heylmun et al., 2021). A coarse grid was generated based on the measured inner and outer diameters of the pipe: 21.9 mm and 27.2 mm, respectively. The domain was axisymmetric with the pipe protruding 43.8 mm and with a 87.6-mm high clear area above the pipe. The domain radius was 87.6 mm. The initial grid contained uniformly 1.825 mm cells. BlastFoam's adaptive mesh refinement with four levels of refined was used to obtain a minimum cell size of 0.11 mm. Only the shock in air was modeled without any driver gas or contact surface. Air was modeled as inviscid and a perfect gas. Representative time steps from the two simulations are shown in Figure 6.18. The primary features are the shock, which diffracts out



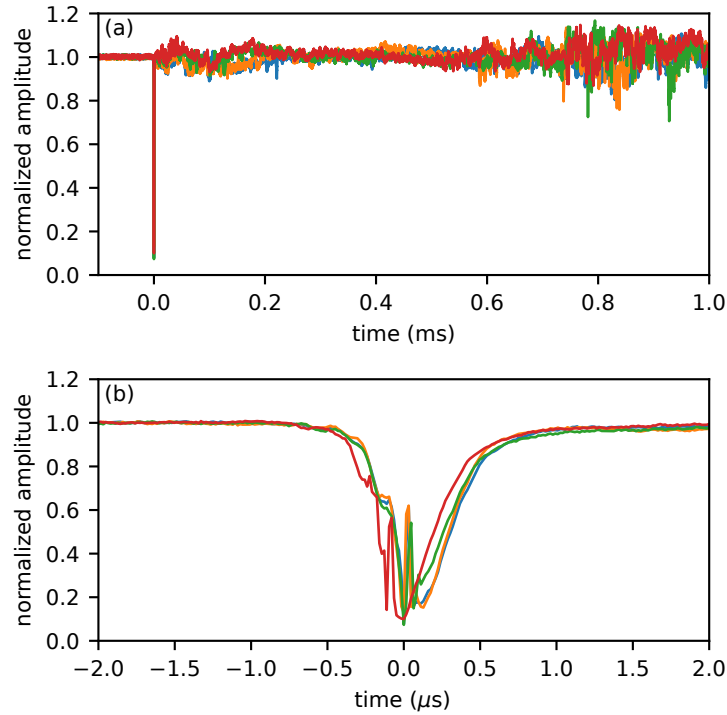


Figure 6.17: Signal amplitudes from IQ data for four shots at 54-psi condition and  $d = 2.5$  mm.

of the open shock-tube end, and the shear layer that rolls up into a vortex ring. Kelvin-Helmholtz instability in the shear layer generates fine eddies, particularly in the 54-psi case. These eddies cause noise in the simulated measurements.

Interferometer measurements of the simulation data were modeled by extracting density along horizontal lines located 2.5 mm and 10 mm from the shock tube exit. Density was converted to index using the Gladstone-Dale constant for ambient air. Index changes were line integrated to obtain the phase changes. The beam shapes were not simulated for simplicity, but (6.58) shows this is accurate in the transfer function pass band.

Figure 6.19 compares experimental and simulated phase measurements for the two shot conditions and two measurement locations tested. All measurements are zeroed by the phase maximum. Experimental measurements from at least four shots are averaged and used to generate 95% confidence intervals. After the shock, experimental and simulation phase measurements show good agreement, particularly for cases (a), (b), and (c). As mentioned above, shear layer eddies cause the apparent noise in the simulated measurements for the 54-psi shot condition.

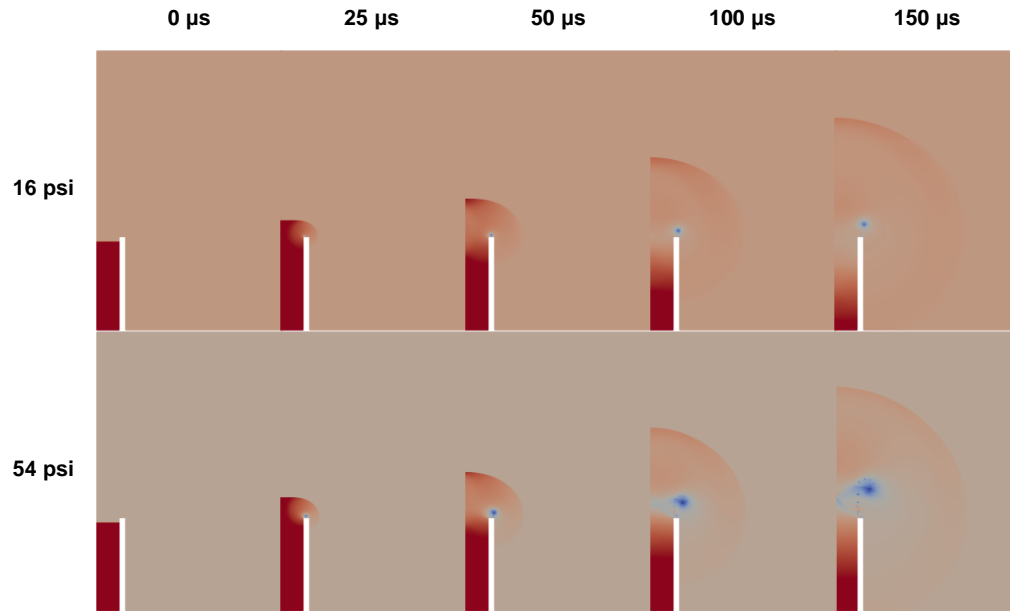


Figure 6.18: Representative time steps of density profiles from numerical simulations of open-ended shock-tube validation experiment.

Agreement could possibly be improved with higher-fidelity fluid dynamics simulation including viscosity and heat transfer. Additionally, the shock tube used here had a crude construction and approximate alignment. The iron pipes were very rough internally with a large weld bead that ran the length of the pipe. Given these considerations, the above results reasonably validate the use of the HFLI for measurements in post-shock flows.

#### 6.4 Conclusions

Optical heterodyne interferometry provides a powerful technique for density measurements in shock-tube experiments. Based on the highly successful design of the FLDI, a heterodyne focused laser interferometer (HFLI) was constructed. There are two major novelties of this instrument that are made possible by heterodyne detection. First, detection at 200 MHz enables theoretically improved SNR by elimination of laser noise. This is important for FLDI applications, where signal levels can be low, especially in low-density flows. Second, heterodyne detection enables direct phase measurement by IQ demodulation, so that arbitrarily large phase changes can be measured. Success on both of these fronts was mixed.

Signal-to-noise ratio was not improved beyond what is possible with a conventional FLDI because of limitations of the RF driver. It should be noted that a particularly quiet laser was employed for this work, and so effects of eliminating laser noise were

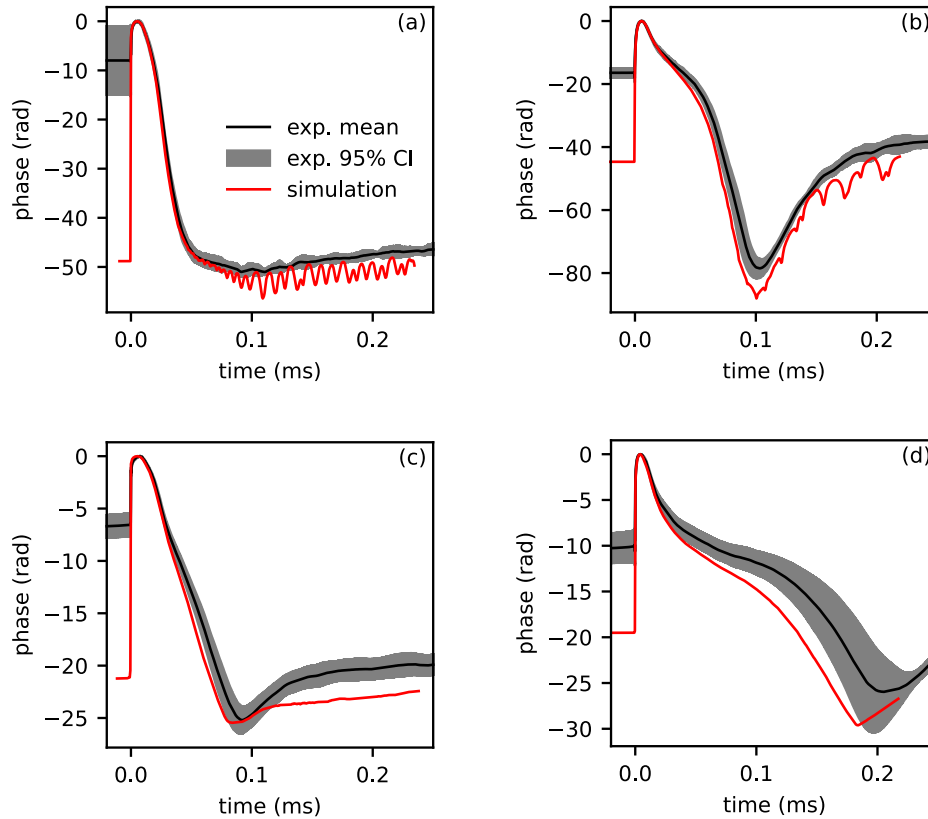


Figure 6.19: Comparison between experimental measurements of absolute phase change using heterodyne interferometer and phase signals modeled from numerical simulations for four cases. Experimental data from several shots are averaged, and the plots show both the mean signal and 95% confidence intervals (CI). (a) 54 psi  $d = 2.5$  mm, (b) 54 psi  $d = 10$  mm, (c) 16 psi  $d = 2.5$  mm, and (d) 16 psi  $d = 10$  mm.

potentially minimized. In the course of this work, a method for achieving excellent SNR was investigated. Use of balanced detection and differential amplification was demonstrated to increase SNR of FLDI measurements by 30 dB, an astounding improvement from a simple modification to the typical FLDI construction. If ultra-sensitive FLDI measurements are required for an application, then this technique is recommended. See Appendix C for details.

Validation experiments showed that large phase signals are measurable using IQ demodulation of the heterodyne signals. However, it was shown that phase changes could not be tracked through shock waves. For large phase gradients, such as those in shocks, optical rays can no longer be considered straight, and refraction should be expected. Refraction distorts the signal beam so that subsequent coherent de-

tection no longer gives meaningful phase signals. Nonetheless, it was shown that large amplitude phase signals could be successfully measured in the post-shock flow. In particular, it was shown that heterodyne detection enables measurement of *absolute* phase changes and thereby a new method for directly probing gas densities. Differential measurements via FLDI require *a priori* knowledge of acoustic wave velocities to invert phase to index coordinates. Additionally, FLDI signals significantly attenuate lower wavenumbers. These challenges are not present for absolute phase measurements, and so the advantages of FLDI are retained while greatly extending measurement ranges.

## Chapter 7

### HETERODYNE FOCUSED LASER INTERFEROMETER: RESULTS

This chapter presents results from using the heterodyne focused laser interferometer to make high-resolution measurements of post-shock gas density in GUST. Experiments were performed for a forward-mode and reverse-mode detonation driver and for a conventional high-pressure helium driver, looking at effects from pressure ratios, diaphragm parameters, driver gas mixtures, and test gas mixtures. These experiments complement the shock speed measurements from Chapter 5. All of the interferometry data presented in this chapter use the absolute phase signals obtained from one of the FLDI beams. Differential data were largely not found to add any additional information. Differential and amplitude data are given as supplementary material in Appendix E.

#### 7.1 Additional Methods

##### 7.1.1 Shock-Tube Modifications

The driven section of GUST was replaced with three stainless-steel sections, giving it a full length of 1.93 m from the diaphragm. The middle section contains two sets of optical-access ports for beam transmission through the shock tube. Only the near-diaphragm ports were used, positioned 1.22 m from the diaphragm. Fused-silica windows (Thorlabs WG41050-A) were glued using UV-cured adhesive (CRL-701) into plugs that mount to the test section.

Five ports along the top of the driven section were used to mount dynamic pres-

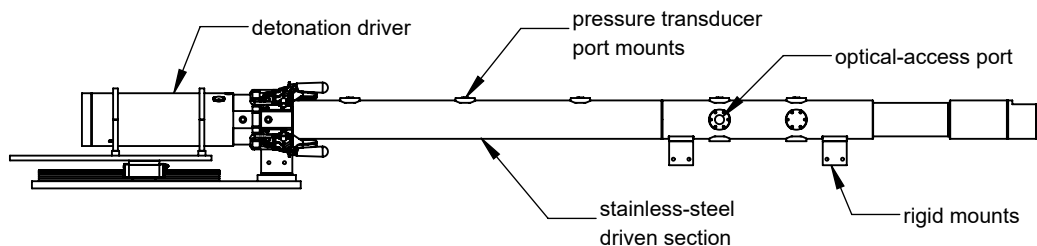


Figure 7.1: Diagram of GUST with stainless-steel driven section ports for optical access and pressure transducers.

Table 7.1: GUST pressure transducer positions

Sensor No.	P1	P2	P3	P4	P5	P6	P7	P8
Position (in)	-15.27	-1.5	0.9	9.65	21.65	33.65	48.15	56.15

sure transducers (PCB 113B26). Sensors were mounted using a novel construction, where the shock-tube plug was 3D printed with FormLabs Clear Resin v4, and the transducer itself was mounted in a stainless-steel plug with O-ring seal. The stainless-steel plug screwed into the plastic plug, which mounted to the shock tube. Using plastic introduced sufficient damping to substantially reduce structural-vibration noise in pressure measurements, and 3D printing affording quick prototyping. These methods are discussed further in the Appendix F, where measurements are compared with those using rigid aluminum plugs. The position of each sensor relative to the diaphragm plane is given in Table 7.1. P1 and P2 are located in the driver, and the tabulated positions are only for forward-mode operation.

Since the shock tube is rigidly mounted to the wall, the third segment of the driven section was designed so that it could be removed without disturbing the test section. This was important for routinely cleaning the tube, since the end accumulated significant diaphragm debris.

### 7.1.2 In Situ Verification

In order to verify the interferometer operation once aligned, isentropic expansion waves were transmitted down the shock tube, so that density measurements from the interferometer could be compared with co-located pressure measurements.

There are principally two aspects of the interferometer measurements that are important to verify: first, that the correct optical path length is used, and, second, that the Gladstone-Dale constants are accurate. The latter point is particularly important when considering detonation products.

To launch an isentropic expansion down the driven section, the shock-tube was operated backward by evacuating the driver and filling the driven section to high pressure. 12.7- $\mu\text{m}$  Mylar diaphragms were used, which ruptured at roughly 25 psia. Upon diaphragm rupture, the shock-tube centered expansion is launched down stream and so was interrogated with the interferometer and pressure transducer, P7. These experiments were performed using  $\text{N}_2$  and He as the driver gas.

Figure 7.2 shows the measured isentropes plotted with those calculated using thermodynamics. Agreement is excellent with helium data and shows a slight discrepancy

with nitrogen data. A significant source of error for these measurements is from the inaccuracy of the pressure transducer in these ranges. The optical path length used to invert phase measurements was 76.2 mm, the inner diameter of the shock tube.

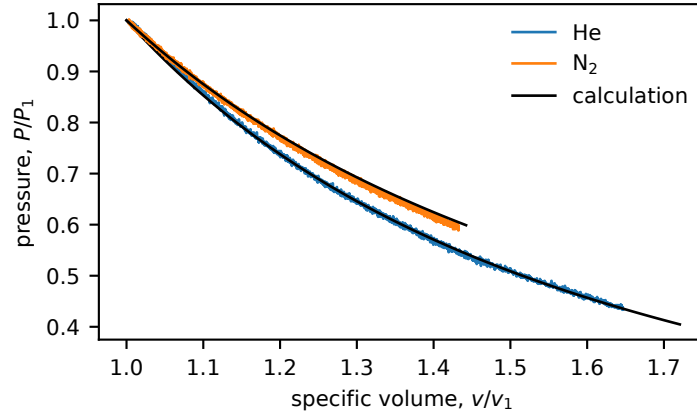


Figure 7.2: Comparison of isentropes from pressure and density measurements with thermodynamic calculations. Density is obtained from interferometer.

The CJ isentrope behind a steady detonation wave was used to investigate the interferometer's accuracy regarding measurements of detonation products. The shock tube was therefore operated as a single detonation tube by filling it with 25 kPa of  $C_2H_4 + 3O_2$  and initiating using the driver like normal.

Pressure transducers were used to record detonation time-of-arrival and estimate its speed. The measured speed was 1.006% of the CJ speed. At 25 kPa, the cell size is on the order of a millimeter. Hence, it is reasonable to model the detonation as a one-dimensional CJ detonation.

Data from P7 and the HFLI are shown in Figure 7.3(a) and (b), respectively. The red dot in (a) shows the calculated CJ pressure, notably greater than the measurement peak. This is considered to be both a consequence of the sensor's finite bandwidth and sensitive area. Following the detonation front is the TZ wave. The absolute phase data in (b) show a large negative jump when the detonation intersects the beam. This negative jump is not physical and a consequence of the beam distortion by the detonation. After the jump, the phase data show a similar variation in time through the TZ wave as in the pressure data. The phase data in (b) are zeroed by the post-detonation value. Both pressure and phase data are extracted up to the reflected shock that appears after 0.8 ms. Phase data are converted to density using the Gladstone-Dale constant  $K = 2.84 \cdot 10^{-4} \text{ m}^3/\text{kg}$ . This value was computed using

the Shock and Detonation Toolbox and the tabulated data given by Gardiner et al. (1981). The post-detonation density is assumed to lie on the CJ isentrope and so is computed as

$$\rho_2 = \rho(P_2, s_{\text{CJ}}), \quad (7.1)$$

where  $P_2$  is the *measured* post-detonation pressure and  $s_{\text{CJ}}$  is the CJ entropy.

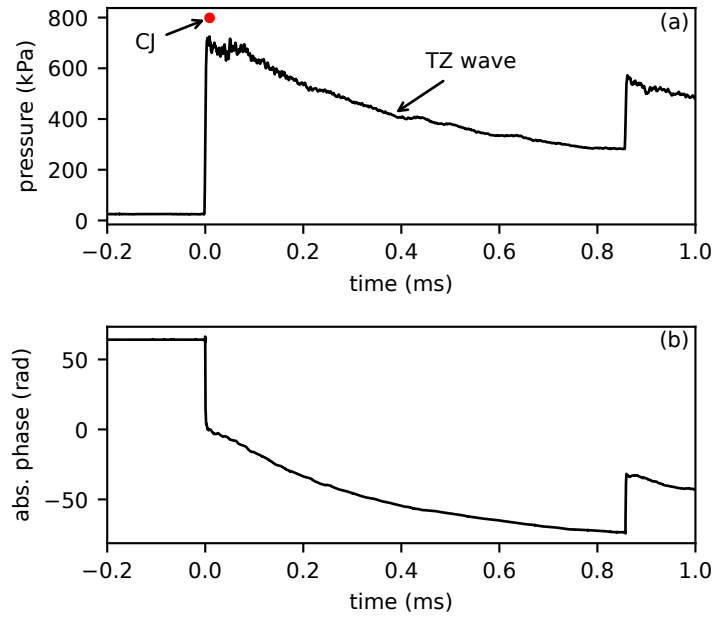


Figure 7.3: (a) pressure and (b) absolute phase data from 25 kPa  $\text{C}_2\text{H}_4 + 3\text{O}_2$  detonation.

The pressure and density data are plotted with the calculated isentrope in Figure 7.4. Agreement is good, although not as close as that obtained from the inert isentropes above. At a minimum, this illustrates the greater difficulty in performing accurate measurements of detonation products. However, the instrument clearly still provides meaningful data. The root-mean-square error between the calculation and measurement is 1.9%.

A final point is that the detonation products in a detonation-driven shock tube are expanded to even lower pressures, and so this calibration is only over part of the relevant range.

### 7.1.3 Additional Signal Processing

Because the phase change cannot be reliably measured through a shock, as shown in Chapter 6, an additional post-processing algorithm is required to obtain absolute



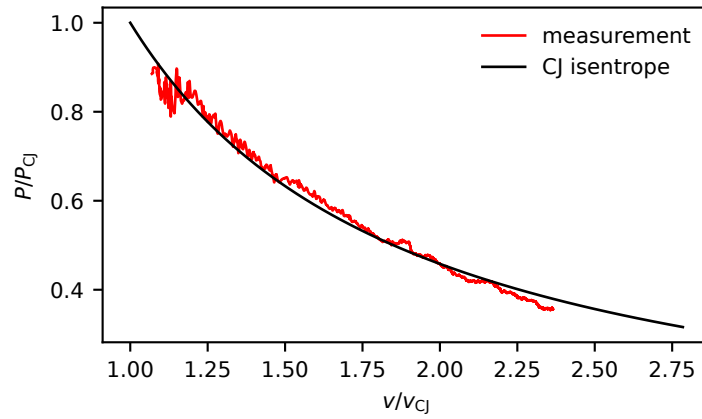


Figure 7.4: Comparison of measured and calculated CJ isentrope for a 25 kPa  $\text{C}_2\text{H}_4 + 3\text{O}_2$  detonation.

density measurements. The shock speed is first estimated using time-of-arrival measurements at pressure transducers. With the shock speed, the post-shock density is calculated using the Shock and Detonation Toolbox. The measured post-shock phase is identified and used to zero the signal. Finally, the zeroed signal is shifted to match the calculated post-shock density. The interferometer time response is sufficient that relaxation phenomena must be considered for shocks in air. These steps will be described in more detail below.

Time of arrival at pressure transducers was identified by the first sample with  $P > 10P_1$ . Sensor positions and time-of-arrival measurements were then differentiated using centered differences – this is important for preserving accuracy with a decaying shock. Figure 7.5 compares these speed measurements with data from Chapter 5 and shows that they accurately capture the low-frequency shock decay. Therefore, time of arrival can be used to estimate the mean shock speed at the beam position, which was obtained by linear interpolation.

The most robust method for identifying the post-shock phase was to first find the time when the shock intersects the beam waist,  $t_0$ , and then choosing the point at time  $t_0 + w/U_s$ , where  $w$  is the beam radius at the inner diameter. Intersection with the beam waist was identified from the amplitude data. Figure 7.6 demonstrates this method's results for six representative shot conditions.

Using the shock speed and initial test gas conditions, the post-shock density can be calculated with some assumptions regarding the thermodynamic state of air. Vibrational relaxation times are estimated using the correlations and data given

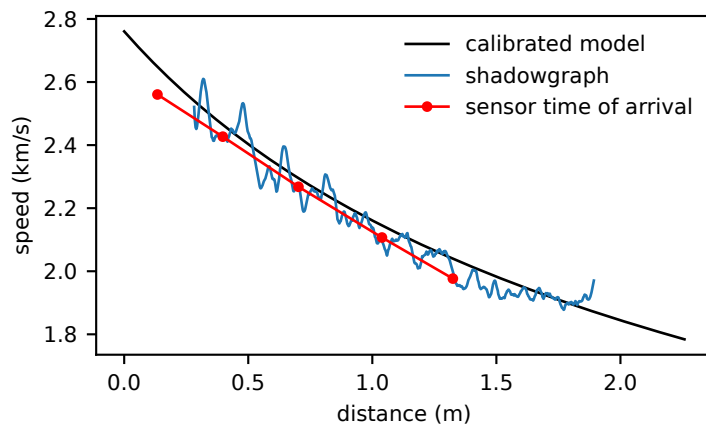


Figure 7.5: Comparison shock-speed measurements using shadowgraphy and pressure sensor time of arrival for shot condition: 100 kPa  $\text{C}_2\text{H}_4 + 3\text{O}_2$  and 10 kPa air. The calibrated decay model is also shown.

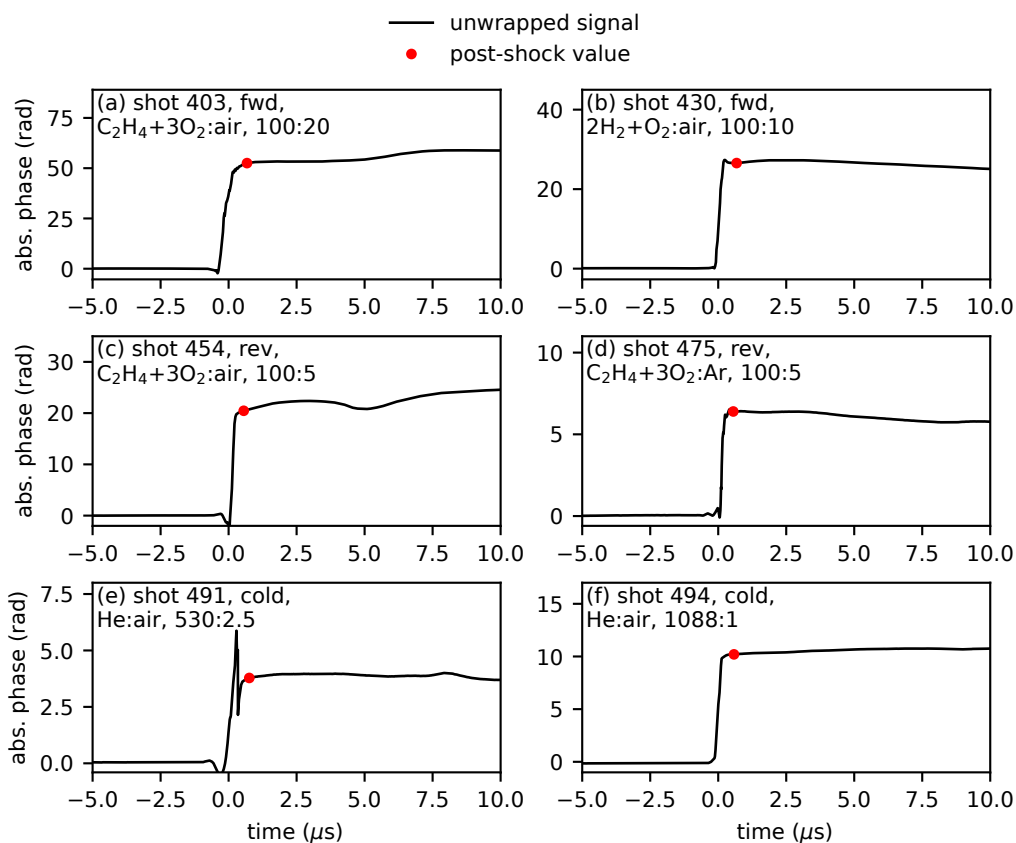


Figure 7.6: Examples of post-shock phase value identified for representative shot conditions.

by White and Millikan (1964). White (1968) also gives additional data for these systems. Figure 7.7(a) shows relaxation times of oxygen dilute in nitrogen calculated for the three driver modes and a range of  $P_1$  pressures. The oxygen molecules in air vibrationally relax quickly behind the shock front, however nitrogen relaxation takes significantly longer. In air, vibrationally excited oxygen accelerates the relaxation of nitrogen compared to in pure nitrogen by as much as an order of magnitude. Nonetheless, even accounting for this, relaxation times for nitrogen in air,  $\tau_{N_2} \sim O(100 \mu s)$ , remain much longer than those for oxygen,  $\tau_{O_2-N_2} \sim O(1 \mu s)$ . An exception is for shot conditions using a high-pressure helium driver, where  $P_1$  pressures are reduced and so oxygen relaxation times are longer,  $\tau_{O_2-N_2} \sim O(10 \mu s)$ . So, for the present experiments using a detonation driver, post-shock air is assumed to be comprised of vibrationally-equilibrated oxygen and vibrationally-frozen nitrogen. Post-shock densities are calculated accordingly using the Shock and Detonation Toolbox, where the nitrogen species is a perfect diatomic molecule with constant heat capacity,

$$c_{P,N_2} = \frac{7}{2}R, \quad (7.2)$$

and  $R$  is the gas constant. For experiments using a helium driver, post-shock air is assumed to be comprised of vibrationally-frozen oxygen and nitrogen, so the gas is perfect with  $\gamma = 7/5$ . These calculations are only for estimating the immediate post-shock density resolved with the interferometer.

Relaxation causes a significant change in density, and so accounting for these effects is important. Figure 7.7(b) compares post-shock densities using the above assumptions with values obtained by assuming complete vibrational equilibrium. Densities change by over 5% in almost all cases. Shot conditions with a forward-mode detonation driver see density changes over 10%.

An additional complication was from diaphragm particulate intersecting the beams, since phase also cannot be tracked through these interruptions. However, since the beams are narrow the blips in the signal are short, and the phase was approximated as unchanged through the blip. These events were easy to identify as they cause spikes in the amplitude data. The algorithm looks for these spikes where there are no shocks, which is known from the pressure data. Before unwrapping, the phase signal is adjusted so that it stays constant through the event.

Each experiment used four channels with 12.5 MS each, ultimately about 1 GB of data. In order to accelerate plotting and subsequent analysis, after IQ demodulation all phase and amplitude data were decimated, giving an effective sampling rate of

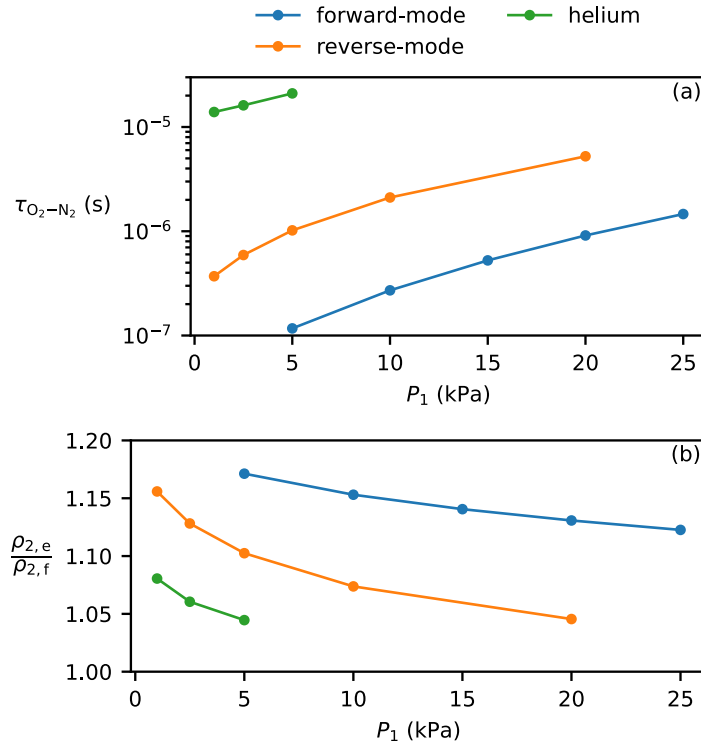


Figure 7.7: (a) Vibrational relaxation times for  $O_2$  in air. (b) comparison of post-shock densities for vibrationally frozen and equilibrium gases. Detonation driver calculations use 100 kPa of  $C_2H_4 + 3O_2$ , and calculations for a cold Helium driver use a pressure of 1.1 MPa.

625 MS/s. Signal bandwidths were limited to 40 MHz, so this reduction in sample rate after IQ demodulation has no effect on the signal.

The primary consequence of losing phase information through the shock is a reduction in measurement accuracy. Additional uncertainty is incorporated through the shock speed estimate and density calculation. However, the exceptional measurement resolution possible with this interferometer is preserved.

## 7.2 Results: Forward-Mode Detonation Driver

### 7.2.1 Pressure Ratio

Experimental results for a range of  $P_1$  pressures are plotted in Figure 7.8 with numerical simulation data from Chapter 3. Experimental and simulation signals are zeroed in time by the shock arrival. Experimental data preceding shock arrival are not shown so as to avoid confusion from the erroneous phase jump. Because the Gladstone-Dale constant jumps across the contact surface, and the contact sur-

face is only approximately identifiable in experimental results, data are plotted in units of refractive index. Measured phase is converted to index by the first-order approximation (6.58).

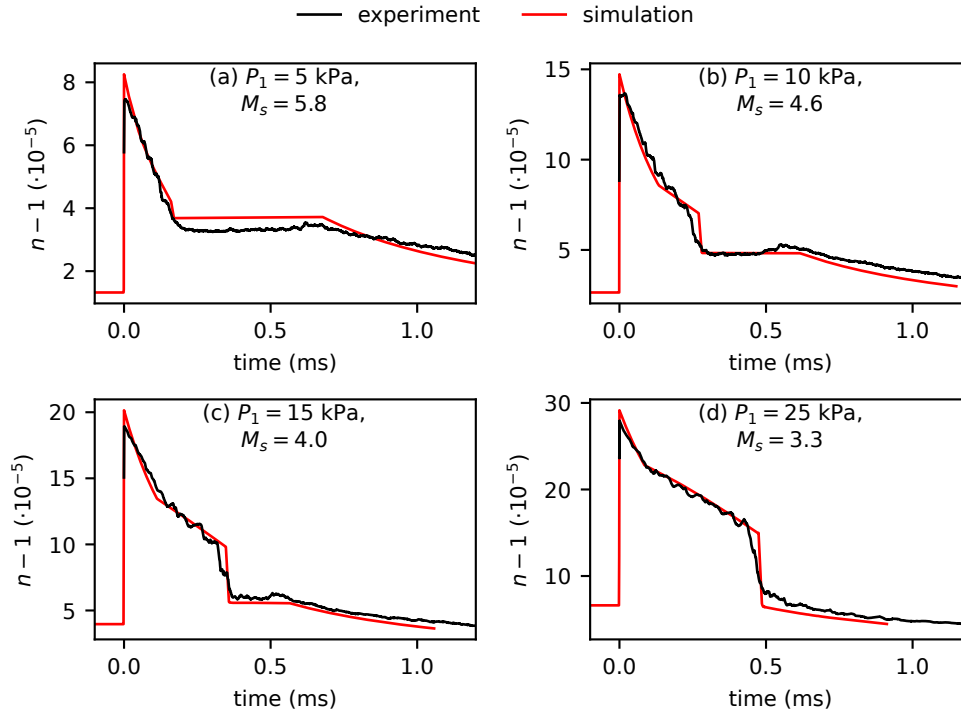


Figure 7.8: Comparison between results from experiments and numerical simulations for shot conditions using 50 kPa  $\text{C}_2\text{H}_4 + 3\text{O}_2$ . Air is the test gas.

Figure 7.8 shows that the key features from the 1D simulation data are visible in the experimental results. As expected from Chapter 5, the shock speed is lower than the simulation value, so the post-shock density is lower. In all cases, there is a rapid decrease in post-shock density from expansion by the transmitted TZ wave. Subplots (b), (c), and (d) show the kink at the terminal TZ wave characteristic (most visible in (d)). The contact surface is also evident from the experimental measurements. The comparison shows how the discrete contact surface in 1D gas dynamics is smeared over a finite spatial region in the real shock tube. In general, agreement is good between experiments and simulations, illustrating the effectiveness of 1D simulations for investigating these flows.

There are some features in the experimental data not present in the simulations. At the arrival of the reflected centered expansion wave, there is a small rise in density in the experimental data. A possible explanation is that this is from the expansion's

interaction with the additional gas volume in the initiation channels at the driver end. Additionally, particularly in (a) and (b), the decrease in index following arrival of the reflected expansion is slower in experiments.

Of most importance, the immediate post-shock flow exhibits clear signs of fluctuations on top of the mean gradients. These fluctuations appear directly behind the shock, but their amplitude appears greatest later in time, particularly in the region driven by the TZ-wave plateau. This is most clearly seen in (b), (c), and (d).

Figure 7.9 shows the same data as in Figure 7.8 but with the immediate post-shock signal magnified. Data are plotted now in density coordinates using the Gladstone-Dale constant for air. Additionally, a line is plotted for all cases with slope calculated using the appropriate shock-change equation, i.e.,

$$\rho_{t,2} = \rho_1 \hat{H} \dot{M} , \quad (7.3)$$

where  $\hat{H}$  is defined in Appendix A.2.5. Use of a shock-change equation requires knowledge of the shock acceleration. This was estimated by differentiating the shock time-of-arrival data twice and by using the calibrated shock-decay model. Both estimates were close and produced no significant change in the resulting line. As an additional check, note that the post-shock gradient in the simulation data is consistent with the shock-change equation estimate.

The comparison in Figure 7.9 shows that the experimental data do not exhibit a post-shock gradient consistent with either simulation data or the shock-change equation, except in (d). An important competing effect on these time scales is vibrational relaxation of nitrogen. This is certainly affecting the signals to some extent, as evidenced by the positive post-shock density gradient in (a) and (b). In (c) and (d), gradients are uniformly negative, however some relaxation effects are still expected to be observable at these conditions. A possible explanation for the variation in these observations could be the variation in relaxation time scales between each case, from short time scales in (a) to longer time scales in (d). If the fluid time scale is sufficiently small compared to relaxation, then the post-shock gradients observed would coincide with those calculated by the shock-change equation. Further analysis of these phenomena is beyond the present scope but could proceed by formulating a thermicity and using the nonequilibrium form of the shock-change equation.

### 7.2.2 Diaphragm Effects

In Chapter 5, it was found that supporting the diaphragm produced a distinct reduction in observable shock speed oscillations. Figure 7.10 compares interferom-

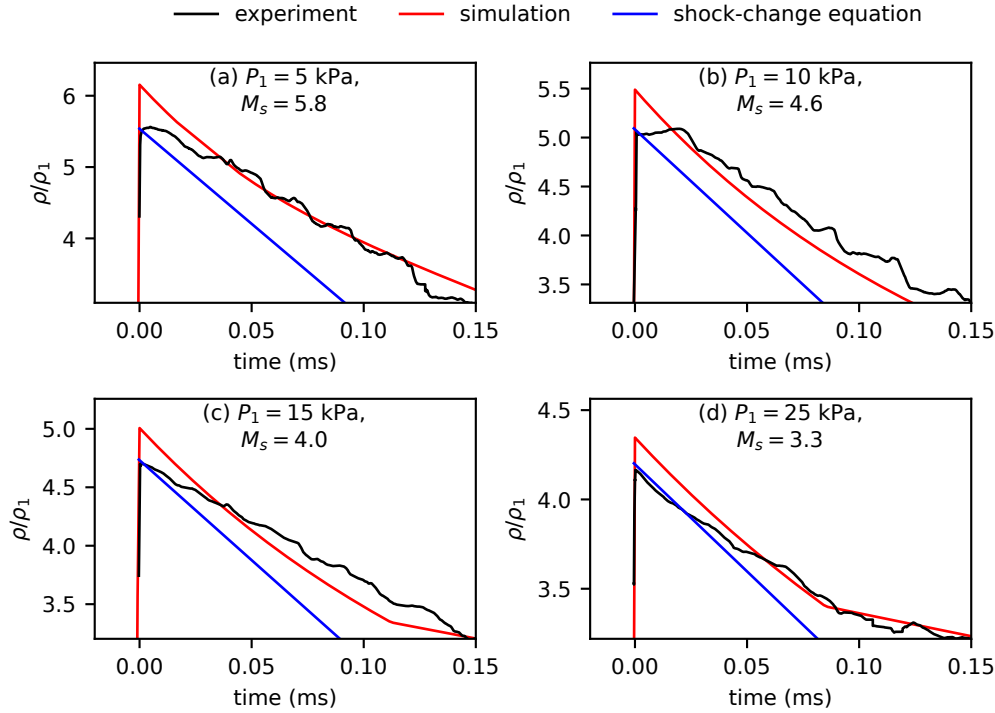


Figure 7.9: Detailed view of post-shock data from Figure 7.8, plotted in density units.

etry measurements for two shot conditions with both supported and unsupported diaphragms. These data are presented in density coordinates using the Gladstone-Dale constant for air, hence densities are only accurate for the shocked air upstream of the contact surface, which can be identified by the kinks in (a) and (b) at roughly 0.2 ms. These data are also shown zeroed in time based on the detonation's arrival at the shock-tube diaphragm. Prior to arrival of the contact surface, there is no prominent difference from supporting the diaphragm with similar-magnitude oscillations observable in both signals. However, after the contact surface the oscillations are clearly of a much greater amplitude for the unsupported diaphragm. Shock speed measurements from Chapter 5 showed that oscillation amplitude decreased as the shock propagated, and so they may be weak by the time the shock reaches the interferometer position. However the residual of these oscillations would nonetheless be expected to be observable in the post-shock flow. There are oscillations apparent in the post-shock flow for both cases, which suggests that these are not from the diaphragm bulge.

Pressure data provide useful additional information on the effects of diaphragm

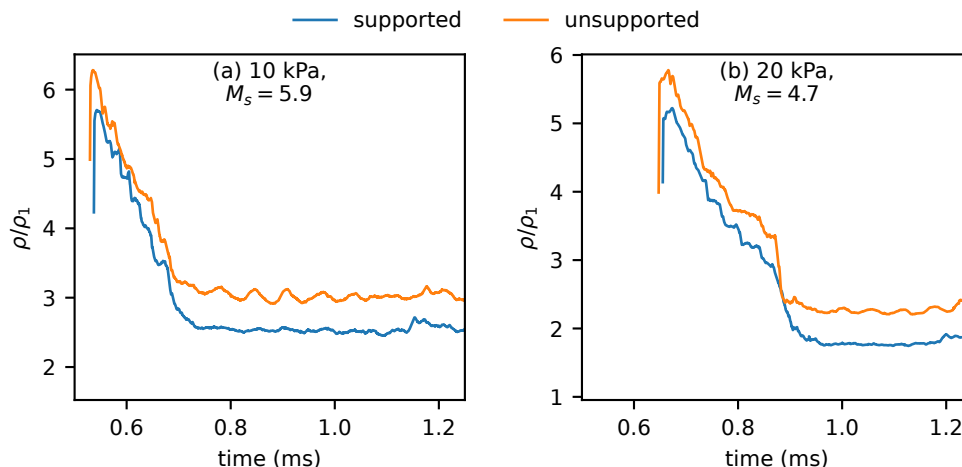


Figure 7.10: Post-shock density data for supported and unsupported diaphragms. Data are from shots with a 100 kPa  $\text{C}_2\text{H}_4 + 3\text{O}_2$  driver, air test gas, and  $25.4 \mu\text{m}$  Mylar diaphragm. Unsupported data have been shifted vertically by an increment of 0.5 to improve visibility.

support. Figure 7.11 shows pressure measurements from sensor P7, which is located at the same axial position as the interferometer beams. The pressure data show the post-shock decay, followed by the plateau period, and then the arrival of the reflected expansion wave. The large oscillations observed in the plateau period in the density data are apparent in these measurements as well. The fluctuations observable in density data nearer to the shock are not evident from the pressure measurements. Important factors are the much reduced measurement resolution as compared to data from the interferometer, and added noise from residual vibration. However the near shock frequencies observed from density data are less than 100 kHz and should be within the sensor's bandwidth.

Three diaphragm thicknesses and materials were tested for the same shot condition, and results are shown in Figure 7.12. For all of these cases, the diaphragm was supported. (a) show only minor differences between diaphragm thicknesses regarding the post-shock density or fluctuation amplitudes. There is some variation in the near-shock flow for the  $50.8 \mu\text{m}$  case, but otherwise data are similar for each thickness. In particular the large amplitude oscillations are unchanged.

In Chapter 5 diaphragm thickness was shown to impact driven shock speeds and delayed their arrival. This is consistent with the present measurements, which show an increase in shock arrival time and reduction in shock Mach number.

Diaphragm material has not been investigated thus far, and two alternatives to Mylar



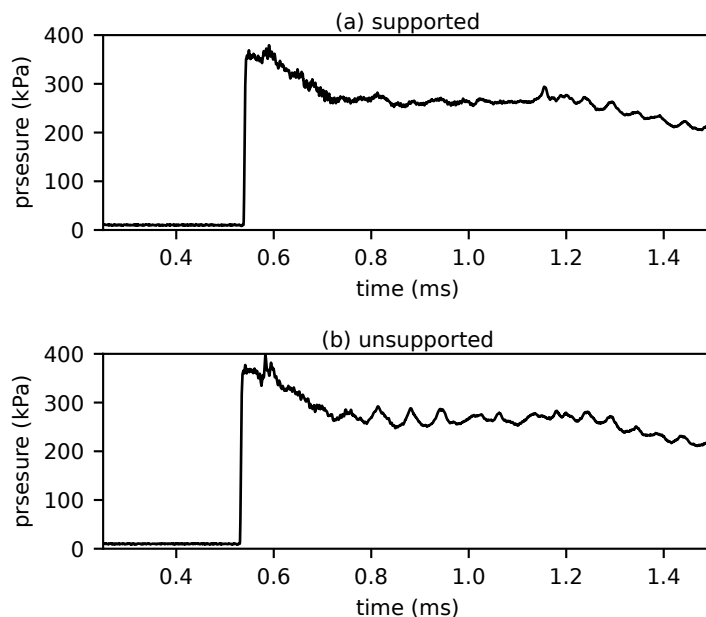


Figure 7.11: P7 pressure data for shots with a supported and unsupported diaphragm. Shot conditions are those from Figure 7.10(a).

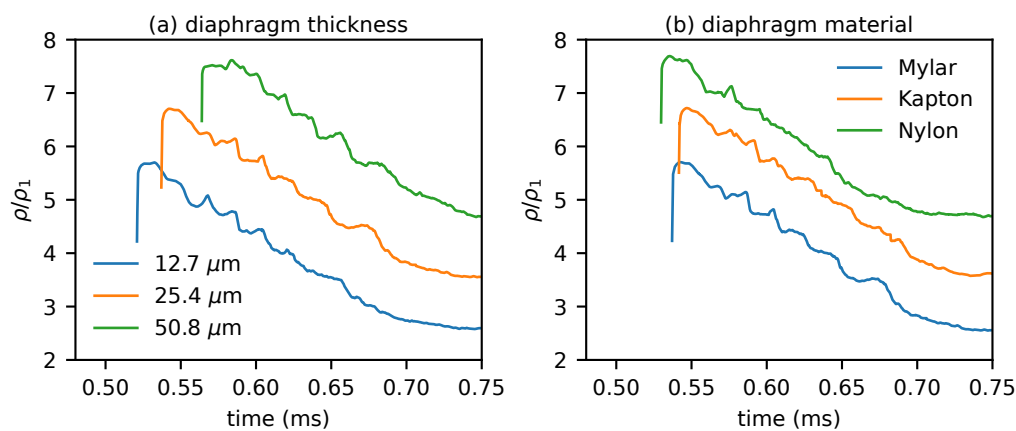


Figure 7.12: Post-shock density data for different diaphragm thicknesses in (a) and materials in (b). All are for shot the same condition: 100 kPa  $\text{C}_2\text{H}_4 + 3\text{O}_2$  and 10 kPa air. Data are shifted vertically in increments of 1 to improve visibility.

are shown in Figure 7.12(b): Kapton and Nylon. Both plastics have densities, elastic moduli, and tensile strengths different from Mylar. Relevant data are tabulated below.<sup>1</sup> Kapton has a higher density and tensile strength than Mylar, and Nylon

<sup>1</sup>Values for density and tensile strength are those reported by the distributor, McMaster-Carr. Elastic moduli are from the materials database MatWeb.

has a lower density and tensile strength than Mylar. Density is important as it determines the diaphragm mass and response to shock impact. From results for varied thickness, diaphragm mass does not seem to significantly affect the post-shock flow (at least for the values tested). Since solid-phase plastic densities are much greater than those of the detonation gas, the waves transmitted into the plastic are weak and only marginally different for the different densities. Testing different materials was of interest to observe the effect of the material strength and stiffness. Note that the difference between signals for the different materials is greater than the difference between signals for different thicknesses, indicating material property effects. Nylon in particular shows an apparently steadier post-shock flow, with only some perturbations near the shock. The oscillation amplitudes are also decreased for Kapton. These results are repeatable, however it is not clear what particular properties are causing the signal variations. Minimally this illustrates that alternative materials may be superior to Mylar.

Table 7.2: Diaphragm material properties

Material	Density (g/cm <sup>3</sup> )	Elastic Modulus (GPa)	Tensile Strength (MPa)
Mylar	1.38	3.5	170
Kapton	1.42	2.5	230
Nylon 66	1.14	3.0	81

### 7.2.3 Driver Mixture

Figure 7.13 shows results for two test gas pressures (10 kPa and 20 kPa) and three driver gas mixtures ( $\text{C}_2\text{H}_4 + 3\text{O}_2$ ,  $\text{C}_2\text{H}_4 + 3\text{O}_2 + 4\text{Ar}$ , and  $2\text{H}_2 + \text{O}_2$ ). These data are all zeroed in time by the shock arrival.

A surprising result is that the post-shock gradients for the hydrogen driver are notably free from large amplitude oscillations. This was not expected due to the much higher driver gas sound speeds for hydrogen as opposed to ethylene, given the theory by Paull and Stalker (1992). Results show “quieter” post-shock flows for a hydrogen driver in all cases. The post-shock oscillations are also weaker for the argon diluted driver, where the post-shock sound speed is reduced. An important difference between the different mixtures is the shock speed attained. Data for the undiluted ethylene driver show the largest amplitude oscillations but the shock speed is also the greatest. However, the oscillations in (c) appear smaller than those in (b), where the shock is stronger in the former case. Clearly, the oscillation strength is not determined by the driver gas sound speed or shock strength.

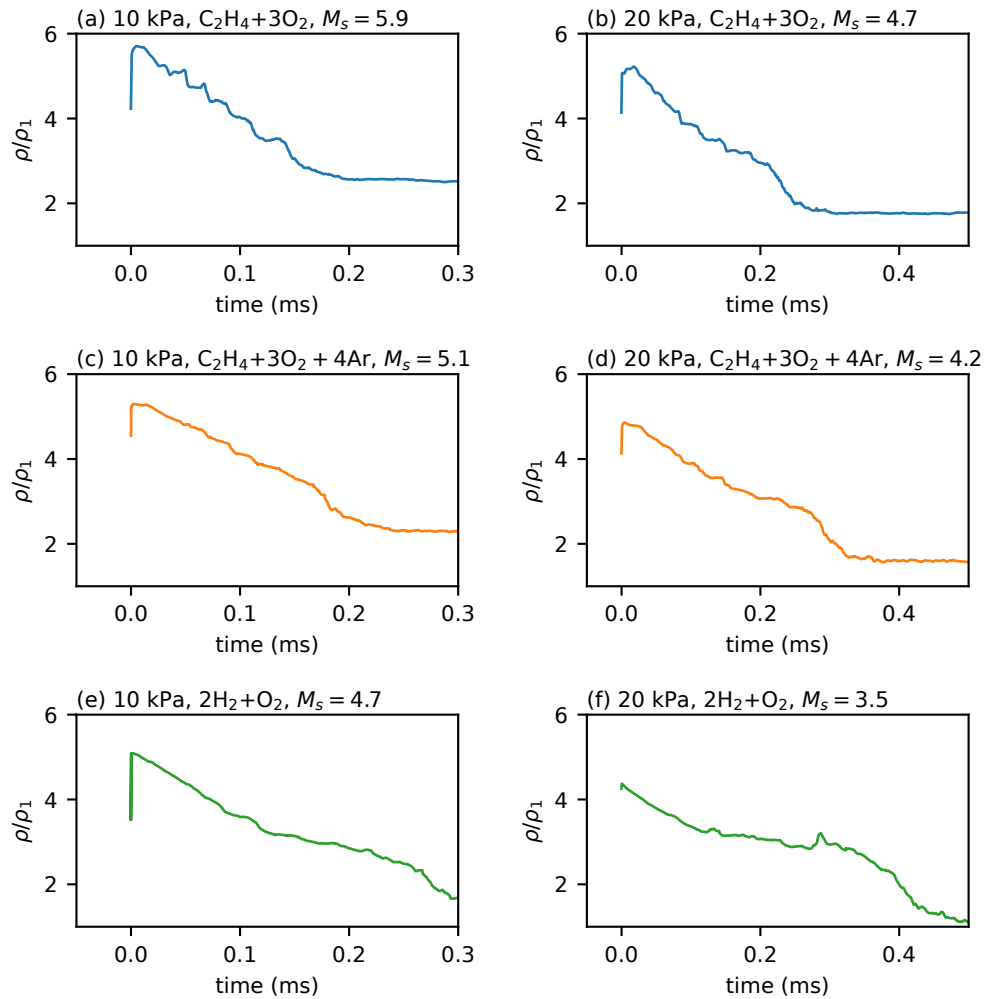


Figure 7.13: Post-shock density data for three driver mixtures and two pressure conditions. All conditions use supported 25.4- $\mu\text{m}$  Mylar diaphragms and air as test gas.

### 7.3 Results: Reverse-Mode Detonation Driver

#### 7.3.1 Pressure Ratio

Figure 7.14 shows density measurements for four driven gas pressures. As stated previously, density data are calculated only for post-shock air, and so densities are inaccurate regarding the detonation products.

Reverse-mode driven shocks are approximately steady, and data show generally small post-shock gradients. Test time of usable post-shock flow is determined by arrival of either the contact surface, as in (a) and (b), or reflected shock from detonation reflection in the driver, as in (c) and (d). An additional line is drawn for the expected post-shock density at vibrational equilibrium, and its length is meant

to roughly indicate the test-time duration. Relaxation effects are confined to early time, and the density later in time is consistent with the relaxed values. Contact surfaces are again observed to be elongated and not sharp jumps.

All data in Figure 7.14 show large fluctuations in the shocked gas. Oscillations are observable not just in the air, but prominently in the detonation products too, although at a distinctly lower frequency. Analysis of these effects is presented later.

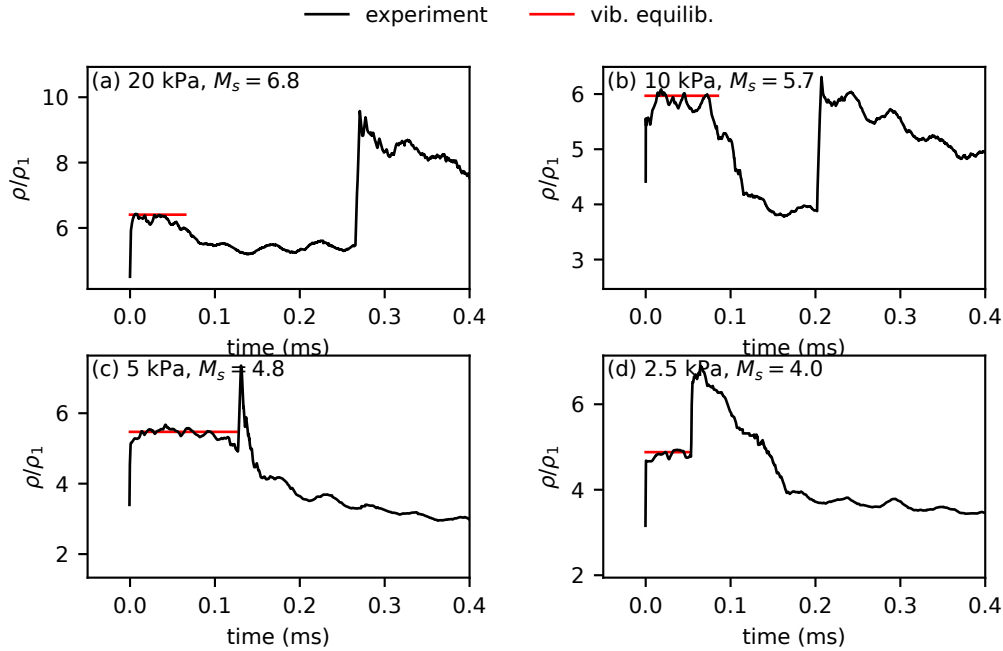


Figure 7.14: Post-shock density measurements for four  $P_1$  pressures, where all shot conditions use a 100 kPa  $C_2H_4 + 3O_2$  driver and a supported 25.4- $\mu$ m Mylar diaphragm. Density data are valid up to contact surface or reflected shock.

### 7.3.2 Diaphragm Effects

In Chapter 5, diaphragm support was found to have lesser importance for the reverse-mode driver. This is consistent with the results in Figure 7.15. These data are zeroed in time based on the detonation arrival at the diaphragm. The primary shock arrives earlier for the unsupported diaphragm case. This makes sense, given that a bulging diaphragm has the effect of lengthening the driver and shortening the driven section. The reflected shock from detonation reflection arrives at the same time in both cases. Because of the variation in arrival times of the contact surface and reflected shock, the contact surface can be observed in (b) for the unsupported case. Density fluctuations in the post-shock flow are obvious for both cases, reinforcing the conclusion that they are not from diaphragm effects.

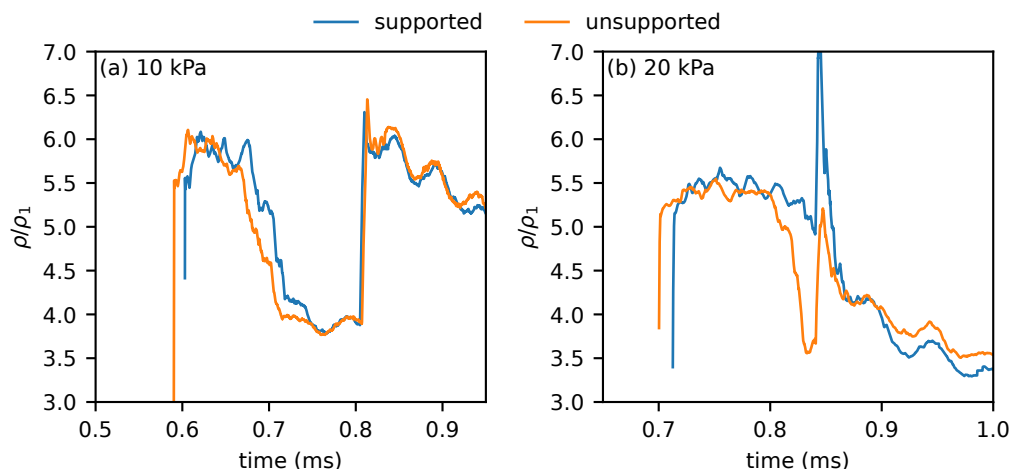


Figure 7.15: Post-shock density measurements for four  $P_1$  pressures, where all shot conditions use a 100 kPa  $C_2H_4 + 3O_2$  driver and a supported 25.4- $\mu m$  Mylar diaphragm.

Figure 7.16 shows data for two diaphragm thicknesses. The thicker diaphragm significantly delays shock arrival and reduces available test time. Oscillations are apparent in both signals.

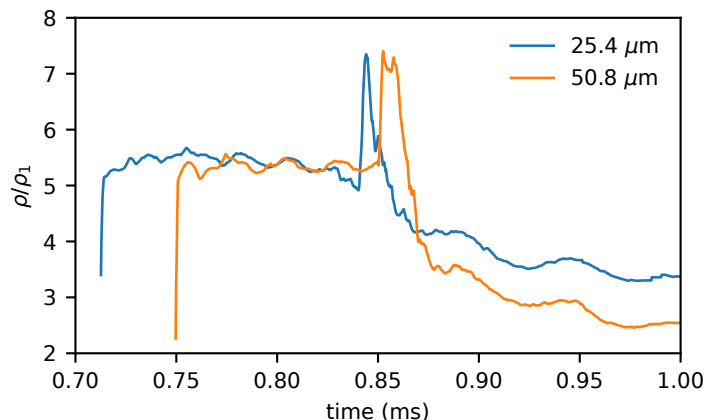


Figure 7.16: Post-shock density measurements for two diaphragm thicknesses. Shot conditions use a 100 kPa  $C_2H_4 + 3O_2$  driver, 10 kPa air test gas, and a supported diaphragm.

### 7.3.3 Driver Mixture

Results for the three driver mixtures are shown in Figure 7.17. Post-shock fluctuations are obvious in (a)-(d). Comparing (b) and (c), which have similar shock Mach numbers, shows that test time duration is similar, however (b) shows much

larger oscillations in the detonation gas. In the shocked air itself, oscillations are apparent for both cases. (d) also shows oscillations in the test gas but not clearly in the detonation gas. (e) and (f) show that for the hydrogen driver the reflected shock arrives far sooner than for any other condition. Data in (f) are largely unusable because the reflected shock has nearly overtaken the primary shock. Test time in (e) is too short for analysis of the post-shock flow except for a general observation of no large amplitude oscillations as those shown in (a)-(d).

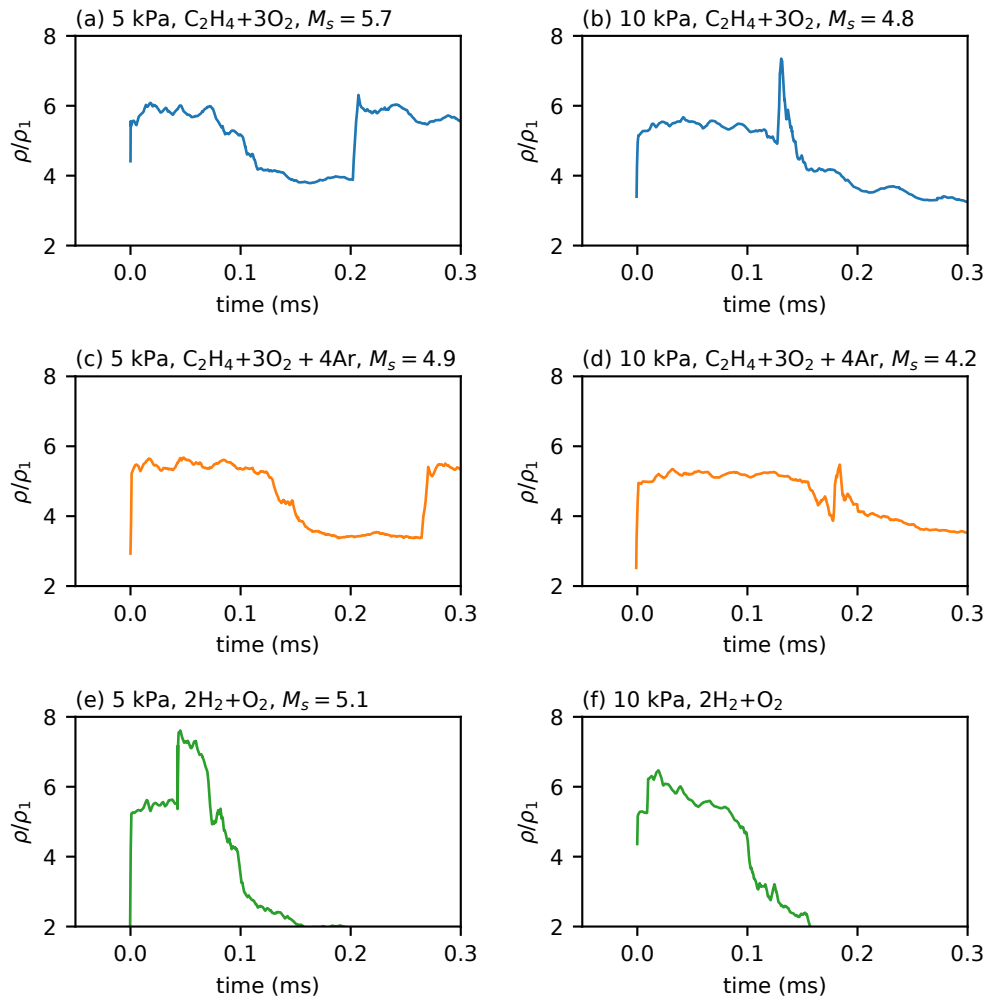


Figure 7.17: Post-shock density measurements for three driver mixtures and two pressure conditions.

### 7.3.4 Test Gas

In order to investigate the effect of the contact surface sound speed ratio, while preserving the same driver conditions, shots were performed with argon and helium

as test gases. Because helium has a low molecular weight, both shocked and unshocked helium have a high sound speed. Argon has a low sound speed initially, enabling strong shocks. However, because it has a low heat capacity its post-shock temperatures are very large, and so shocked argon also has a sound speed higher than for shocked air. Results for these test gases are shown in Figure 7.18. (c), (e), and (f) clearly show a strikingly more steady post-shock flow than for all results in air. For these cases, the post-shock flow has a high sound speed and therefore low  $a_3/a_2$ , consistent with the theory by Paull and Stalker (1992). Large amplitude oscillations are present in (d) but not (c). A possible explanation for this is that the weaker shock results in reduced values for  $a_2$  and therefore higher values for  $a_3/a_2$ .

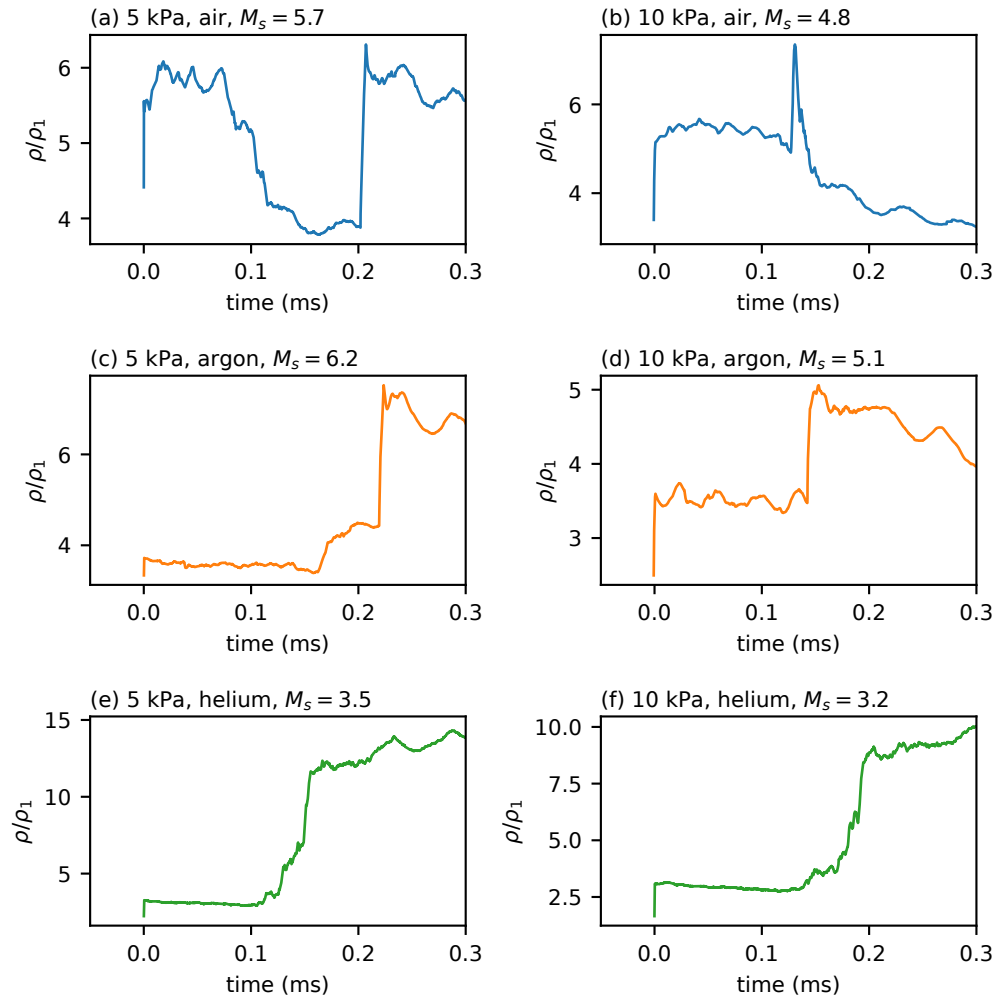


Figure 7.18: Post-shock density measurements for three test gases and two pressure conditions.

To investigate shocks in argon further, additional experiments were performed for

lower test gas pressures, and therefore lower values of  $a_3/a_2$ . These data are shown in Figure 7.19 in density units normalized by the post-shock value. Each signal is shifted vertically by 0.1 units to improve clarity. There is distinct contrast between the 10 kPa condition and all lower pressures, where large amplitude oscillations are not seen. As the shock strength increases and  $a_3/a_2$  decreases, the post-shock flow does not become observably more steady. Note that test time for the 10 kPa case is terminated by arrival of the reflected shock, and for all other cases by the arrival of the contact surface.

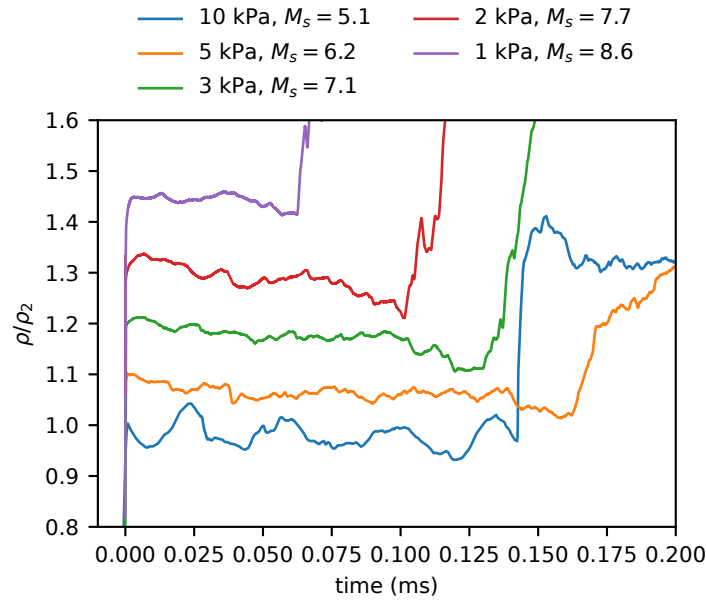


Figure 7.19: Additional data at more pressure conditions where argon is the test gas. Data are shifted vertically by increments of 0.1.

### 7.3.5 RMS Oscillation Amplitudes

In order to quantify post-shock oscillations, test time data from all reverse-mode shots with common diaphragm conditions (supported 25.4  $\mu\text{m}$  Mylar) were processed to obtain root-mean-square estimates of fluctuation amplitudes. Test time was identified manually in all cases using arrival of the contact surface or reflected shock. To account for the mean gradients, the baseline was subtracted using a linear fit. The root-mean-square value of these data was then normalized by the mean post-shock density. These results are plotted in Figure 7.20 against calculated values of the contact surface sound speed ratio  $a_3/a_2$ . Markers with a common color are for the same driver mixture. Different marker symbols are used to denote different



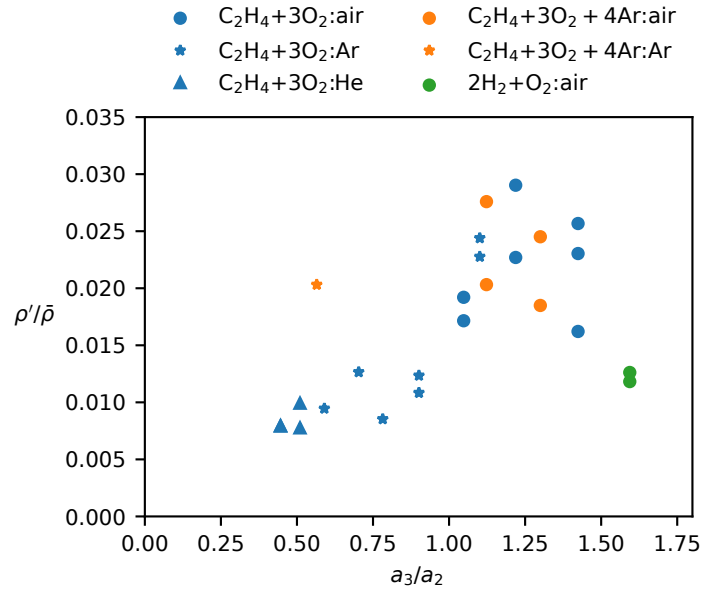


Figure 7.20: Measurements of root-mean-square density fluctuations,  $\rho'$ , normalized by the mean density during the test time,  $\bar{\rho}$ , using a reverse-mode detonation driver.

test gases.

The majority of data were acquired for a  $C_2H_4 + 4O_2$  driver mixture, for which Figure 7.20 shows a clear positive correlation between the RMS density fluctuations and the contact surface sound speed ratios. This is consistent with the theory by Paull and Stalker (1992) regarding the transmission of acoustic lateral waves through the contact surface from the driver gas. Data for an argon-diluted ethylene driver are also consistent with this positive correlation, except for an outlier point for one shot using an argon test gas. Data using a hydrogen driver are not consistent with the trend, however there is low confidence in these data due to the short test times as shown in Figure 7.17. Assuming there is sufficient test time to assess the post-shock flow, then this might be consistent with observations from forward-mode experiments, where hydrogen-driven flows do not exhibit significant oscillations, despite the much increased driver gas sound speed.

#### 7.4 Results: Helium Driver

Experiments were performed using a cold high-pressure helium driver for two diaphragm thicknesses and three air pressures. Results are shown in Figure 7.21. Although conventional static high-pressure driver operation theoretically generates

steady shock waves, results show that in all cases, except (e), shocks have a positive post-shock gradient, indicating that they are accelerating. This is consistent with results from Chapter 5 and the analysis by White (1958). The metal diaphragms are much more massive than plastic diaphragms requiring more time to open. For strong shock conditions, this produces a significant area-change effect in early time, ultimately causing the shock to overshoot its nominal steady shock speed. This process takes some time, and (e) shows that after the initial transients have passed the post-shock flow is more uniform.

Some fluctuations are apparent in the data, however generally there do not appear to be any large amplitude oscillations such as those observed with a detonation driver. Quantifying these RMS fluctuations was not performed because identification of the contact surface arrival is less obvious for these data and prone to biasing calculations. Using ideal shock tube calculations has generally been found to overestimate test times, since the real contact surface is spatially broad and accelerating from boundary layer effects.

## 7.5 Frequency Analysis

In order to extract the oscillations from time-series data, particularly for forward-mode cases with significant mean gradients, the background must be removed. This was accomplished by fitting the post-shock data up to the contact surface with a fifth-order polynomial and subtracting the fit from the data. Examples of background subtracted signals are shown in Figure 7.22 for forward-mode data obtained at different  $P_1$  pressures. For lower pressures, the test time is shorter, however frequency content is still evident. By inspection, the background-subtracted signals show that for lower pressures the oscillation frequency is greater. There is also some time-varying component, where greater amplitudes are observed later in time. This is consistent with the claim that the oscillations are residual density perturbations from shock oscillations. It was shown in Chapter 5 that shock oscillation amplitudes decrease with time, so the magnitude of perturbations should also decrease toward the shock.

Power spectra were estimated using periodograms. The record lengths are short, and there is no significant noise for averaging with Welch's method to be useful. Power spectra of signals with and without background subtraction are shown in Figure 7.23, where the signal with background is black. In all four cases there is a higher frequency peak that is consistent with the visible periodicity in the time series data.

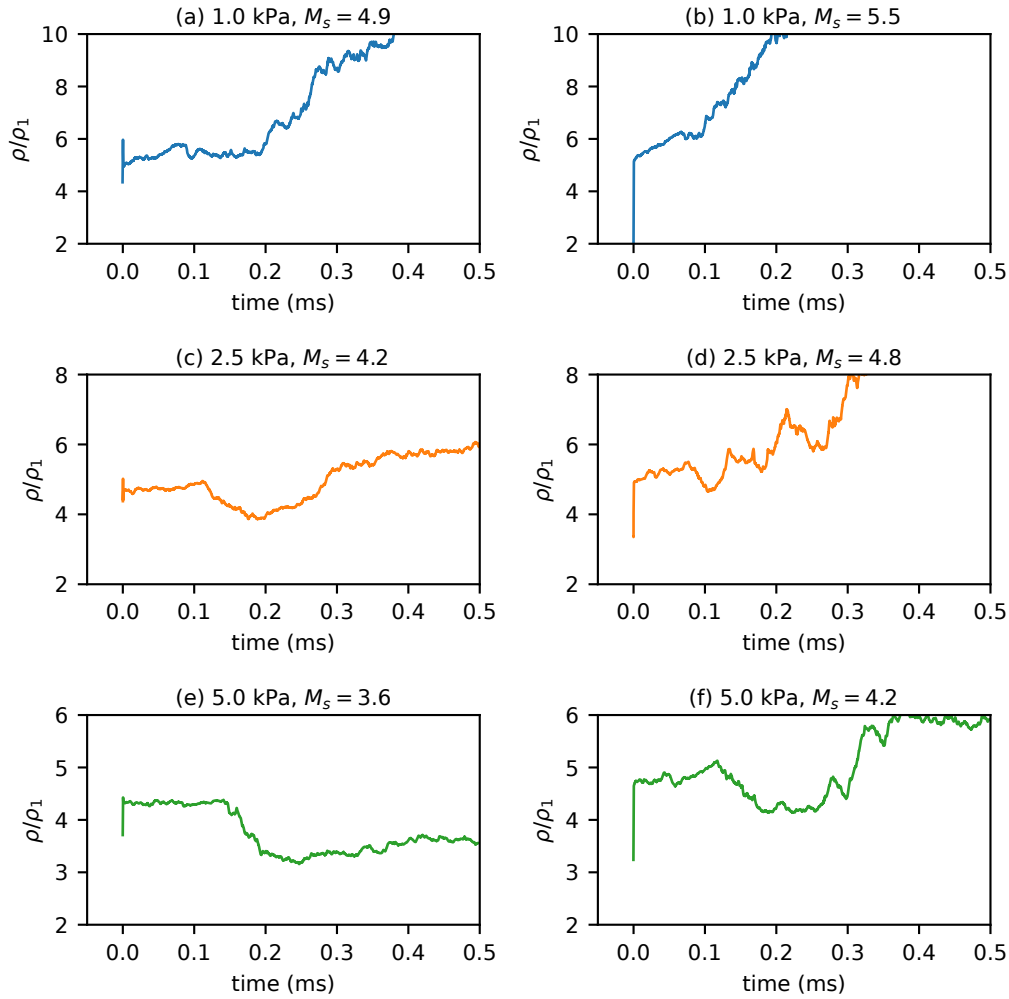


Figure 7.21: Post-shock density data for six pressure conditions using a cold high-pressure helium driver.

The lower frequency peak in background subtracted data is residual power from the background. The higher frequency peak can be readily extracted for all shot data with sufficient record lengths. For example, this precludes reverse-mode data using a hydrogen driver.

Peak frequencies measured from density data for viable shot conditions are plotted in Figure 7.24. Data are plotted against the initial pressure ratio. Error bars indicate the DFT frequency resolution.

In Chapter 5, shock speeds were observed to oscillate with some peak frequency, and these peak frequencies were measured. Interferometry measurements show fluctuations in density in the post-shock flow. If these frequencies are coming from

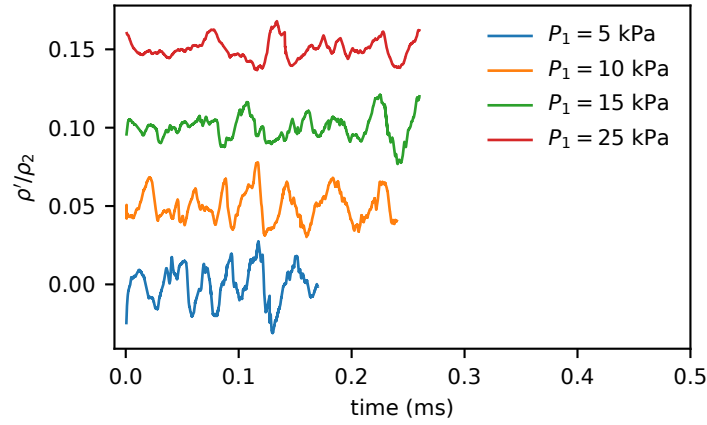


Figure 7.22: Background subtracted data for forward-mode detonation-driven shocks with a 50 kPa  $\text{C}_2\text{H}_4 + 3\text{O}_2$  driver and air test gas.

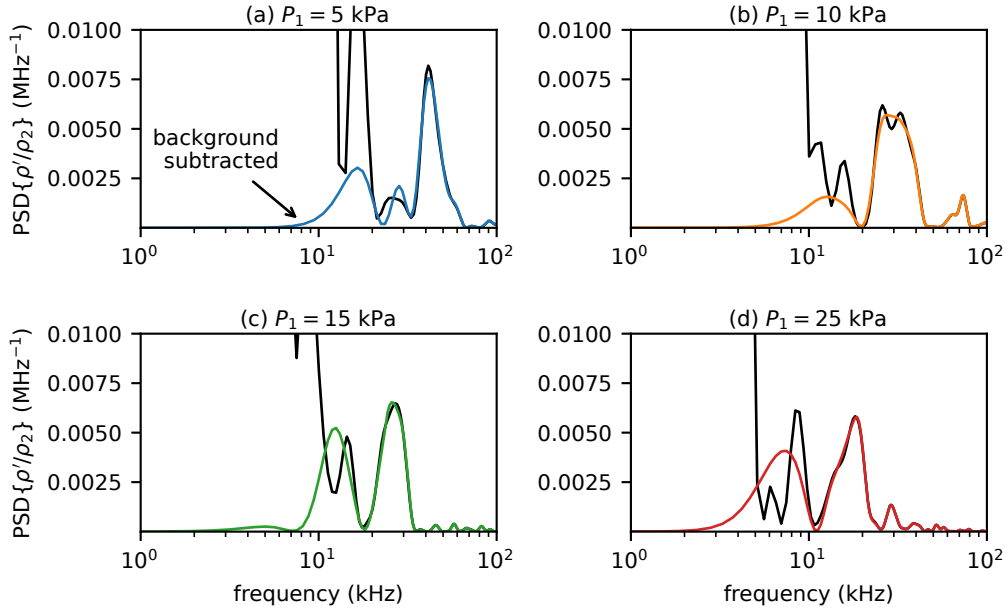


Figure 7.23: Power spectra of data with (colored) and without (black) background-subtraction.

a common source, then they are related by some Doppler shift. Shock oscillation measurements were performed in the shock-fixed frame, and interferometry measurements were performed in the lab-fixed frame.

First, consider the disturbances to be one-dimensional plane waves, then they can propagate along any of the three families of characteristics, or they can propagate supersonically as shock waves. Therefore there are four possibilities for the Doppler

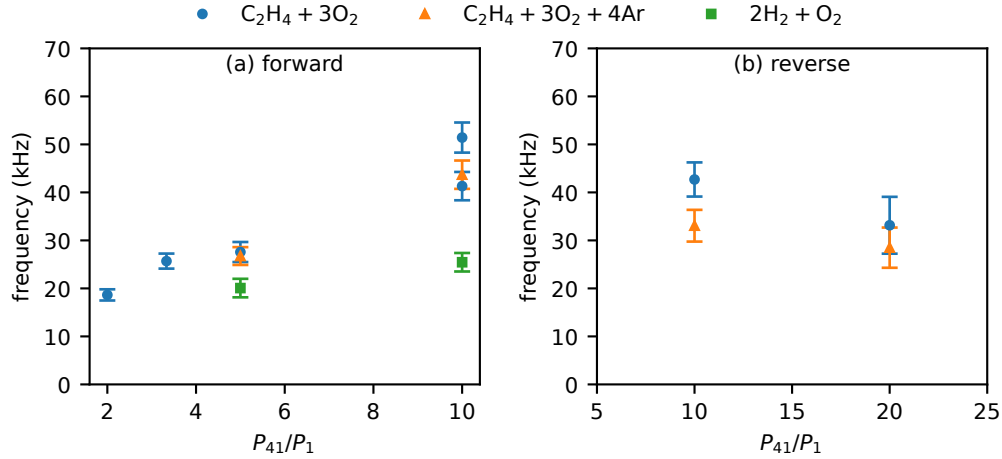


Figure 7.24: Peak frequencies from power spectra of density data for (a) forward-mode and (b) reverse-mode detonation drivers.

shift. Figure 7.25 shows these possibilities with four cartoon space-time diagrams, where in (a) the disturbance is carried by particle paths (p.p.) or  $C^0$  characteristics, in (b) by  $C^-$  characteristics, in (c) by  $C^+$  characteristics, and in (d) by weak shocks. For (a) and (b), the shock itself is acting like the source of the disturbance, whereas in (c) and (d) the disturbance is coming from upstream and the primary shock is the receiver. The observed shock oscillation frequency,  $f_w$ , and shock speed,  $U_s$ , give the spatial length for one oscillation. From the characteristics' geometry the period,  $\Delta t$ , of the disturbance in the lab-frame can be identified. Then, the frequency measured in the lab-frame is  $f_l = 1/\Delta t$ . Relating  $f_w$  and  $f_l$  gives the four possible Doppler shifts:

$$f_l = \frac{u_2}{U_s - u_2} f_w = b_0 f_w \quad C^0 \text{ characteristics ,} \quad (7.4)$$

$$f_l = \frac{(u_2 - a_2)}{U_s - (u_2 - a_2)} f_w = b_- f_w \quad C^- \text{ characteristics ,} \quad (7.5)$$

$$f_l = \frac{u_2 + a_2}{(u_2 + a_2) - U_s} f_w = b_+ f_w \quad C^+ \text{ characteristics ,} \quad (7.6)$$

$$f_l = \frac{U_d}{U_d - U_s} f_w = b_s f_w \quad \text{weak shock .} \quad (7.7)$$

For case (d), the disturbance shock is propagating at speed  $U_d$  in the lab-frame. The strength of this shock is given by

$$M_d = \frac{U_d - u_2}{a_2} , \quad (7.8)$$

so that

$$b_s = \frac{u_2 + M_d a_2}{(u_2 + M_d a_2) - U_s} , \quad (7.9)$$

which clarifies the connection with  $b_+$ . This model is useful only for interpreting flows with steady shock waves, where  $b_0$ ,  $b_-$ , and  $b_+$  are functions of the shock speed and medium,<sup>2</sup> and  $b_s$  requires knowledge of  $M_d$ . More work is required to relate lab-frame and shock-frame frequencies for decaying shocks.

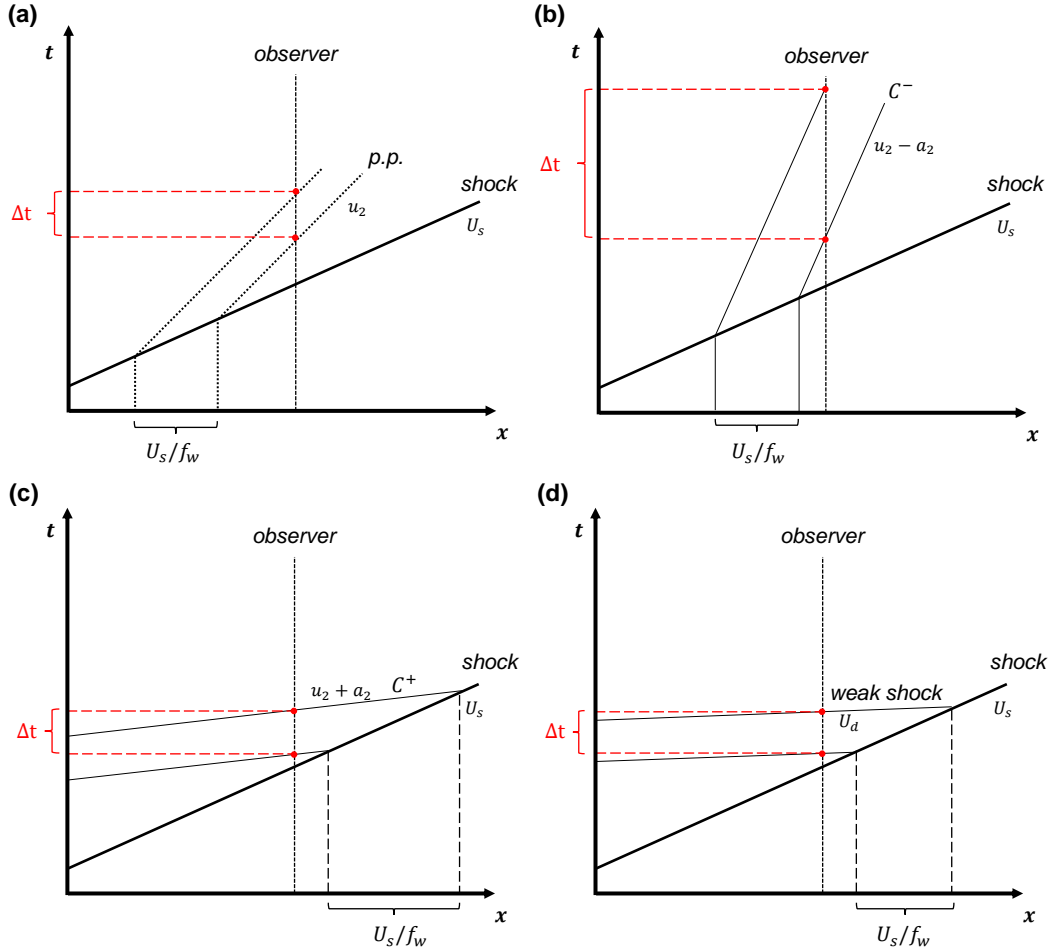


Figure 7.25: Space-time diagrams illustrating four possible modes for a plane disturbance to propagate between the observation plane and the shock wave.

For experiments with a reverse-mode detonation driver, there are three viable shot conditions that were used for both shock-speed and interferometry measurements. The ratio of peak frequencies measured using these methods is plotted in Figure 7.26 with values for Doppler shift coefficients calculated for vibrationally-equilibrated air. First, note  $b_0$ ,  $b_+$ , and  $b_s$  are all greater than one, indicating that  $f_l > f_w$ , consistent with observations.  $b_- < 1$  and so it can be ruled out that the observed disturbances are being carried on  $C^-$  characteristics. The experimental data do not

<sup>2</sup>For a perfect gas, they are functions of only  $M_s$  and  $\gamma$ .

overlap curves for  $b_0$  or  $b_+$ . Because of this disagreement,  $M_d$  was adjusted so that data points lie on the curve for  $b_s$ . Here  $M_d = 1.3$ , which is not a weak shock. If this were accurate, pressure fluctuations on the order of 50%-100% would be observed in the post-shock flow, which is not the case. Therefore, an alternative model for the disturbances must be considered.

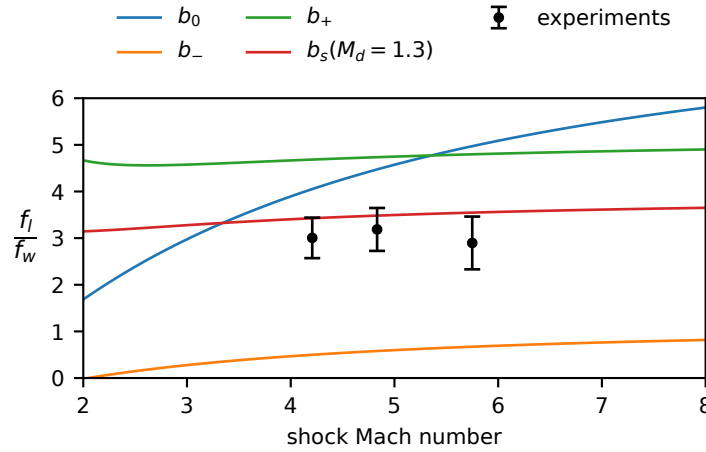


Figure 7.26: Comparison between experimentally measured frequency ratio and calculated Doppler shifts for a plane wave disturbance and reverse-mode data.

Paull and Stalker (1992) formulated an acoustic wave theory to model disturbances in cylindrical ducts. In acoustics, by assuming small perturbations the equations of motion can be linearized. By introducing the velocity potential,  $\mathbf{u} = \nabla\phi$ , the linearized equations can be combined to obtain the wave equation

$$\frac{\partial^2 \phi}{\partial t^2} = a^2 \nabla^2 \phi . \quad (7.10)$$

Paull and Stalker (1992) proposed the following form for the velocity potential:

$$\phi = J_0(\lambda r) \exp(i\omega(t \pm \beta x/a)) , \quad (7.11)$$

where  $J_0$  is the zeroth-order Bessel function of the first kind,  $\omega$  is the fundamental frequency, and  $\beta$  is the dispersive term, given by

$$\beta = \sqrt{1 - (\lambda a/\omega)^2} . \quad (7.12)$$

It can be verified that (7.11) does indeed solve the wave equation. To satisfy no penetration boundary conditions at the tube radius,  $r_0$ , requires that  $\lambda r_0$  is equal to any zero of the first-order Bessel function of the first kind. Paull and Stalker (1992)

focused their analysis on “lateral” waves for which  $\lambda r \neq 0$  and in particular for the lowest order where  $\lambda r_0 \approx 3.83$ .

Paull and Stalker (1992) formulated Doppler shifts by translating the spatial coordinate in (7.11) by a constant velocity. If the wave source is convected with the post-shock gas velocity and subsequently observed from the stationary lab-frame, where the wave source is propagating toward the observer, then the Doppler-shifted frequency is

$$f_l = (1 + u_2\beta/a_2)f_0, \quad (7.13)$$

where  $f_0 = \omega/2\pi$ . This describes the interferometric measurements. Similarly, the Doppler-shifted frequency in the shock-fixed frame is

$$f_w = (1 + (u_2 - U_s)\beta/a_2)f_0. \quad (7.14)$$

Equations (7.13) and (7.14) can be combined to find the Doppler-shift relating lab-frame and shock-frame measurements, and the result is

$$f_l = \frac{u_2 + a_2/\beta}{u_2 + a_2/\beta - U_s} f_w = b_L f_w. \quad (7.15)$$

The Doppler shift formulation for lateral waves (7.15) is precisely the same as for  $C^+$  characteristics, except with the local sound speed scaled by the dispersion term. Generally  $\beta < 1$ , which gives the subtle result that the phase velocity of lateral waves exceeds the local sound speed. This is a physical consequence of guided wave propagation. The potential function (7.11) is not unique to this problem and describes wave propagation in a cylindrical waveguide. Phase velocity can exceed the sound speed as a consequence of interference phenomena inside the waveguide. Energy is transmitted with the group velocity, which is, for one-dimensional wave propagation,

$$v_g = \frac{\partial \omega}{\partial k}. \quad (7.16)$$

For the potential function (7.11), the group velocity is

$$v_g = \beta a. \quad (7.17)$$

Since  $\beta \leq 1$ , this illustrates that  $v_g \leq a$  inside the tube, as expected. The group velocity also gives the minimum frequency that can be coupled into the waveguide. This is given by  $\beta = 0$ , which is obtained for cut-off frequency

$$\omega_c = \lambda a. \quad (7.18)$$



For first-order lateral waves, the cut-off frequency is  $\omega_c \approx 3.83a/r_0$ .

In order to apply this formulation to experimental data, the fundamental frequency must be obtained, which is not directly measured in experiments. Instead, the lab-frame frequencies measured by interferometry can be used with (7.13) and a root solver to obtain  $f_0$  and consequently  $\beta$ . Results from these calculations are given in Table 7.3 with the ratio of experimentally measured lab-frame and shock-frame frequencies. Since  $b_L$  is calculated using the lab-frame frequencies, measurement uncertainty was propagated through the calculation and is included.

Table 7.3: Experimental frequency ratio,  $f_l/f_s$ , and predicted Doppler shift of first-order lateral waves,  $b_L$

experimental $f_l/f_s$	$b_L$
$3.19 \pm 0.46$	$3.15 \pm 0.09$
$2.90 \pm 0.57$	$2.86 \pm 0.11$
$3.01 \pm 0.43$	$3.00 \pm 0.09$

Agreement between the experimental frequency ratio and calculated Doppler shift is striking with all calculated values well inside uncertainty bounds. This result indicates that measured lab-frame frequencies and shock-frame frequencies for reverse-mode experiments are indeed coupled and accurately modeled as first-order lateral waves.

The same analysis cannot be so easily implemented with forward-mode data. For decaying shock waves, the post-shock flow has nonuniform velocity and sound speed. We can make some approximate conclusions from analyzing the same plane wave Doppler shifts plotted with the experimental frequency ratios. These data are shown in Figure 7.27, where the shock Mach number for experimental data is the value measured at the interferometer position. The primary observation is that, unlike for reverse-mode data, for forward-mode data the frequency ratios show a clear positive trend with increasing shock Mach number. The only Doppler shift that shows this dependence is for  $C^0$  characteristics. The experimental data sit beneath this line, and this disagreement could be attributed to the unsteady flow behind a decaying shock. Observations regarding an absence of post-shock pressure perturbations for forward-mode data are consistent with disturbances propagating on  $C^0$  characteristics. This is only an approximate analysis with low confidence. Doppler shifts could be more accurately estimated by integrating along characteristics from numerical simulation data. However, this is not performed here.

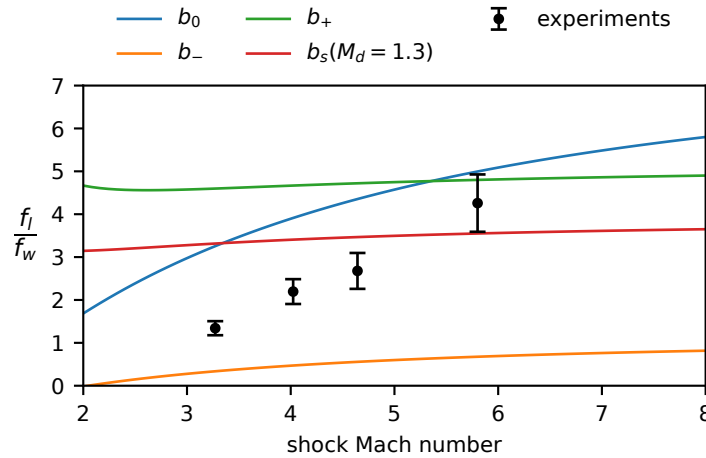


Figure 7.27: Comparison between experimentally measured frequency ratio and calculated Doppler shifts for a plane wave disturbance and forward-mode data.

## 7.6 Discussion

To compare the three driver modes, Figures 7.28 and 7.29 show density data for cases with similar shock Mach numbers where the test gas is air. There are clear differences in the post-shock flows between the three cases. Figure 7.28 shows that the magnitude of the post-shock density gradients is actually comparable for the forward-mode detonation driver and helium driver. This illustrates the significance of diaphragm effects on the conventional static high-pressure shock-tube driver. The length of the driven section that is impacted by diaphragm effects is expected to scale with the shock-tube diameter, so that for a fixed diameter the shock tube can be elongated to allow transients to pass and obtain a more steady shock. For the detonation-driven facility, the post-shock gradient is reduced by lengthening the driver.

In Figure 7.28 large amplitude oscillations, approximately 5-10%, are only observed in the detonation-driven post-shock flows, not for the helium-driven shock. However, in Figure 7.29, there are clearly fluctuations in the helium-driven post-shock flow, but the forward detonation-driven shock appears quiet. The forward-mode data displayed are those from a case using a hydrogen driver mixture. A quite surprising result is how steady the hydrogen-driven flows appeared.

Large amplitude oscillations have been observed in much of the density data presented above. If these oscillations propagate into a facility's test flow, then they would corrupt the flow as "noise". However, it is important to note that all mea-

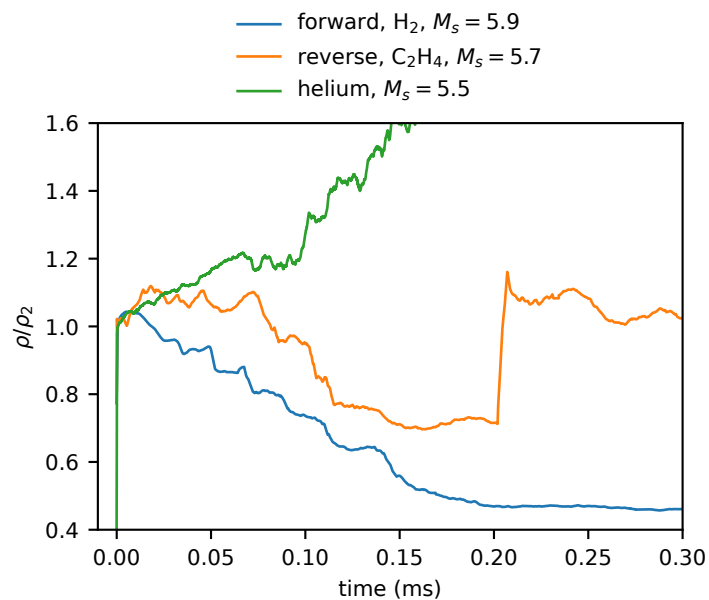


Figure 7.28: Comparison between post-shock density data for the three driver types where shock Mach numbers are all similar.

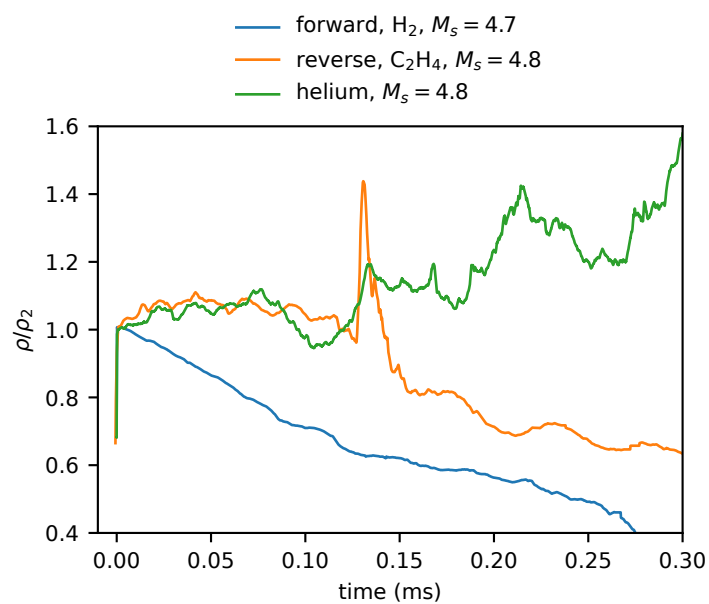


Figure 7.29: A second comparison between post-shock density data for the three driver types where shock Mach numbers are all similar, where the forward-mode driver uses hydrogen.

measurements of oscillations have been deterministic and highly repeatable. There is no randomness associated with the observed oscillations. This indicates that the source of the oscillations is something repeatable and intrinsic to the system construction and operation. They could potentially be eliminated by changes to, e.g., diaphragm rupture and detonation initiation.

## 7.7 Summary & Conclusions

A heterodyne focused laser interferometer was employed to make high-resolution density measurements in the flows generated by a detonation-driven shock tube. The advanced capabilities of this instrument enabled phase measurements spanning nearly  $100\pi$  radians. Signals could be adjusted through the shock so that post-shock density could be measured. Relaxation effects were prominent, particularly for forward-mode shocks where relaxation must compete with the decaying shock gradients. Away from shocks, the interferometer afforded unambiguous insight into the post-shock flows.

Results from forward-mode operation consistently showed perturbations in the test flow, regardless of whether the diaphragm was supported. Previous shock speed measurements showed that oscillation amplitudes were reduced by supporting the diaphragm and thereby mitigating diaphragm bulge. The oscillations in density data were consistent for different diaphragm thicknesses, but changed for different materials, indicating some sensitivity to the diaphragm. The oscillations were reduced for driver conditions using ethylene diluted with argon, but also for conditions using hydrogen. Hydrogen was particularly surprising with post-shock flows remarkably free from perturbations. Frequency analysis of forward-mode data is challenging because the shocks are decaying and the post-shock flow is nonuniform. The origin of the observed flow oscillations, not caused by diaphragm bulge, could not be unambiguously identified.

Results from reverse-mode operation similarly showed significant post-shock flow perturbations. Hydrogen could not be characterized completely because of how rapidly the reflected shock overtook the primary shock. Experiments using gases with large post-shock sound speeds appeared to show suppression of flow oscillations. This was evident from strong shocks in argon and helium. An estimate of the root-mean-square density fluctuations showed that the amplitude of fluctuations was positively correlated with the contact surface sound speed ratio for data using the same driver conditions, i.e., only the test gas was varied. This observation is

consistent with the theory by Paull and Stalker (1992). Frequency analysis was used to related lab-frame frequencies measured by interferometry and shock-fixed-frame frequencies measured in Chapter 5. Analysis showed that the Doppler shift relating these frequencies cannot be explained by plane waves. By implementing the acoustic wave model from Paull and Stalker's analysis, it was shown that the Doppler shifts are in excellent agreement with those predicted for lateral waves propagating downstream. These are likely generated by detonation implosion, which is used to initiate the reverse-mode driver. These effects should be a concern for any transverse initiation tube.

Results from operating the driver with high-pressure helium emphasize the significance of diaphragm opening times. Post-shock density gradients were positive from accelerating shocks. The gradients were sufficiently large as to be comparable with those behind decaying shock waves from forward-mode operation.

## CONCLUSIONS & FUTURE WORK

### 8.1 Conclusions

This work was motivated by the application of a detonation driver to expansion tube research facilities. There were primarily three objectives: develop an analytical model for forward-mode shock decay, develop a high-resolution shock-speed measurement technique to investigate detonation-driven shock dynamics, and develop a heterodyne interferometer to probe post-shock flows.

The shock decay resulting from forward-mode detonation driver operation results from the interaction between a simple wave and a plane shock. This general problem was analyzed in detail using higher-order shock-change equations. It was shown that the model presented is a significant advance over predecessors and provides a simple solution to a classic problem in gas dynamics.

The shock propagation law derived from this general analysis was shown to excellently model the motion of detonation-driven shocks. An empirical approach of fitting simulation data was used to develop correlations of critical independent variables for the two parameters of the decay model. The new model was used to investigate the decay-rate characteristics of different driver gases, and it was shown how reduced sound speeds have the effect of decreasing shock decay rates. This gives new insight into the trade between shock strength and steadiness in choosing a facility's operating conditions. The model provides a tool that can be used for optimizing a test condition based on given shock-tube lengths.

A time-resolved shock-speed measurement technique was developed and implemented to characterize shock propagation in a small-scale detonation-driven shock tube. Results were used to calibrate the analytical decay model for various pressure ratios.

The new shock-speed measurement technique provided insight into the shock dynamics in these facilities. Prominent shock-speed oscillations were observed and shown to result from diaphragm bulging in forward-mode operation and driver initiation in reverse-mode operation. Shock-speed oscillations are significant for expansion tubes since they indicate the presence of large disturbances in the post-

shock flow. A simple fix for diaphragm bulge issues was found to be mechanically supporting the diaphragm with a blunt cross. This technique could be used to enable thinner diaphragms for high-pressure detonation driver applications as well.

A heterodyne focused laser interferometer was designed, built, and implemented to characterize post-shock flows. The technique gave high-resolution measurements of flow perturbations and mean gradients, including from vibrational relaxation. The presence of flow perturbations was shown to depend significantly on driver operating conditions. In particular, a surprising result was to find greatly reduced perturbations for hydrogen-oxygen forward-mode drivers. Operation with hydrogen-oxygen generates stronger shocks, yet mean gradients are also greater. However, flow perturbations are of more significance regarding expansion tube operation.

Frequency analysis of lab-frame density measurements and shock-frame speed measurements was used to show that the observed flow perturbations are consistent with the first-order lateral waves described by Paull and Stalker (1992). Agreement between measured and calculated Doppler shifts using this model was excellent. A principal source for these waves is the initiation of the reverse-mode driver at the diaphragm. The facility in this work uses wave implosion, which is possibly particularly prone to generating these waves. However, this should be a concern for any transverse initiation, which is typical for reverse-mode detonation drivers.

Heterodyne interferometry is not original but has been rarely applied to fluid dynamics research. The heterodyne focused laser interferometer built in this work demonstrates the significant capabilities of the technique. The spatial filtering effects of FLDI that have popularized its use are preserved in the new instrument, however heterodyne detection can be used to make new measurements of absolute phase changes, which have several advantages. Perhaps most significantly, the absolute phase measurements have a uniform frequency response below some cut-off defined by the beam shape. A uniform frequency response in measurement bandwidths is desired for all instruments. The differentiation used in FLDI introduces frequency sensitivity, requiring a more complicated spectral inversion with some additional knowledge about acoustic disturbances, namely their phase velocity. In the present work, only waves propagating perpendicular to the beam were considered, however propagation along the optical axis should be analyzed as Lawson (2021) demonstrated for FLDI.

Absolute phase measurements with heterodyne interferometry enable a new capability of directly probing gas densities. This gives the instrument new utility for

applications beyond fluctuating flows. In particular, it could be used to measure relaxation times. Large amplitude oscillations in the post-shock flows examined in this work prevented a detailed study of this. Although there have been significant advancements with absorption spectroscopy techniques (Streicher et al., 2020), it remains challenging to measure these quantities in gases composed of nonpolar molecules like nitrogen and oxygen. The present technique could be employed for these applications, enabling high-resolution measurements to complement those obtained with spectroscopy.

## **8.2 Future Work**

### **8.2.1 Shock Decay Modeling**

One aspect of the model that was not explored in depth is its generality for other equations of state. Application to shocks in media not described by the ideal gas law is a straightforward extension of the theory and could be of interest.

In order to simplify analysis, thermodynamic equilibrium was assumed throughout the flow, however for shocks in real gases relaxation phenomena are important. The time scales of these relaxation phenomena will compete with those of the unsteady post-shock flow. Investigating how both the relaxation zone and the shock motion are coupled would be interesting.

For application of the shock decay model to other problems, the challenge is how to obtain the initial shock acceleration. For detonation-driven shocks, an empirical approach was used, but an analytical method would provide more generality. The power-law exponent does not vary significantly, and so in many cases the value might be estimated from a small number of simulations and extrapolation to other conditions would remain reasonably accurate. Estimating the decay rate for general conditions, however, is more challenging. One analytical strategy might be to employ the fundamental solution of gas dynamics (Courant and Friedrichs, 1948, Landau and Lifshitz, 1987), which is valid for the isentropic flow confined behind the shock-tube contact surface. This could enable one to estimate the initial post-shock gradients and therefore the initial decay rate. With this solution, a more detailed parameter study could be employed. These results could also be applied to model expansion tube operation using a decaying primary shock.

The modeling in this work focused on one-dimensional inviscid gas dynamics. Consideration of viscous and heat transfer effects is important, especially for facilities with larger length-to-diameter ratios. It should be investigated how shock decay



from an unsteady expansion is coupled with boundary layer effects. Additionally, the shock-tube boundary layer forms in a flow with a significant adverse pressure gradient, likely affecting growth rates.

### **8.2.2 Detonation Driver Optimization**

The lateral waves measured in reverse-mode operation are significant. Reducing contact-surface sound-speed ratios endeavors to reduce their transmission into test flows, however this can significantly constrain operating conditions and may not be viable for air test gases. Lateral waves are coupled with the waveguide formed by the tube, and so perhaps they could be damped using baffles.

The dynamic operation of a detonation driver also provides a means for overcoming diaphragm issues in general. If the diaphragm is quickly ruptured prior to detonation arrival, then transients from diaphragm opening result from much smaller pressures differences and are therefore weaker. When the detonation arrives, a possibly higher-quality shock is formed with fewer flow perturbations. Methods for fast diaphragm rupture are therefore an avenue for future work, and the technique might be transferrable to the expansion tube secondary diaphragm as well.

Detonation-driven expansion tube operation should be investigated experimentally, where the steadiness of test flows is related to primary shock dynamics. The heterodyne interferometer in this work could be employed to record both background gradients and perturbations.

### **8.2.3 Shock-Speed Measurements**

Almost all shock-tube-based facilities have some method for measuring shock speeds. As the present work has shown, a diagnostic that can measure shock speeds continuously would be very useful for facility characterization. The shadowgraphy technique used here is not transferrable to large-scale metal shock tubes, so a new method is needed. A possible technique might construct some kind of linearly distributed sensor that can be unrolled down the length of a shock tube. Some candidates for this might be: an array of thin-film gauges printed on a flexible circuit board or using an optical fiber as an intrinsic sensor.

### **8.2.4 Interferometric Techniques**

The absolute phase measurements possible with the heterodyne technique were limited by the physical optics of a shock transmitting through a focused laser beam. The instrument's utility would be greatly advanced by overcoming this issue. A

possible method would be to send the beam through the test section at an angle, similar to the original technique used by Bleakney et al. (1949).

For a heterodyne FLDI without absolute phase measurement capabilities, one possibility for simplifying the construction in this work is to use a Zeeman-split He-Ne laser. Two optical frequencies with a difference in the MHz range are emitted directly by the laser. They can be separated by their polarization and used directly as the beam pair in an FLDI. Interference in the FLDI analyzer generates a signal modulated at the beat frequency. The simple construction of an FLDI is preserved while enabling heterodyne detection. If signal amplitudes are large, phase unwrapping can be employed, but there is also the possibility of greatly reduced phase noise. Balanced detection is possibly still the best choice for low-noise measurements, but heterodyning does not limit signal amplitudes and techniques like lock-in amplification can be employed.

Heterodyning is only one method for obtaining the IQ data required for direct phase measurements. IQ data can also be acquired by implementing the quadrature delay optically in the fashion used by Hogenboom and DiMarzio (1998) or Wang and Mazumdar (2021). This technique has promise for visualization applications, where the in-phase and quadrature components are both recorded with one or two high-speed cameras. Phase can then be unwrapped using the spatial techniques common with finite-fringe interferometry but also with the temporal unwrapping possible with IQ data. Fringe shifts could therefore be measured with improved resolution. This technique has applications beyond interferometry, for example, it could be used for high-resolution photoelastic stress measurements.

## Bibliography

- Alpher, R. A. and White, D. R. (1959a). Optical refractivity of high-temperature gases. I. effects resulting from dissociation of diatomic gases. *The Physics of Fluids*, 2(2):153–161.
- Alpher, R. A. and White, D. R. (1959b). Optical refractivity of high-temperature gases. II. effects resulting from ionization of monatomic gases. *The Physics of Fluids*, 2(2):162–169.
- Ardavan-Rhad, H. (1970). The decay of a plane shock wave. *Journal of Fluid Mechanics*, 43(4):737–751.
- Bakos, R., Calleja, J., Erdos, J., Sussman, M., and Wilson, G. (1996). An experimental and computational study leading to new test capabilities for the HYPULSE facility with a detonation driver. In *Advanced Measurement and Ground Testing Conference*, New Orleans, LA. American Institute of Aeronautics and Astronautics.
- Bakos, R. and Erdos, J. (1995). Options for enhancement of the performance of shock-expansion tubes and tunnels. In *33rd Aerospace Sciences Meeting and Exhibit*, Reno, NV. American Institute of Aeronautics and Astronautics.
- Balcerzak, M. J. and Johnson, M. R. (1966). The gaseous-detonation driver and its application to shock tube simulation techniques. In *5th International Shock Tube Symposium*, pages 1111–1128.
- Barenblatt, G. I. and Zel'dovich, Y. B. (1972). Self-similar solutions as intermediate asymptotics. *Annual Review of Fluid Mechanics*, 4(1):285–312.
- Benitez, E. K., Jewell, J. S., and Schneider, S. P. (2021). Focused laser differential interferometry with contoured tunnel windows. *AIAA Journal*, 59(2):419–429.
- Best, J. P. (1991). A generalisation of the theory of geometrical shock dynamics. *Shock Waves*, 1(4):251–273.
- Bird, G. (1957). A note on combustion driven shock tubes. Technical Report 146, RAE.
- Blackman, V. (1956). Vibrational relaxation in oxygen and nitrogen. *Journal of Fluid Mechanics*, 1(1):61–85.
- Bleakney, W., Weimer, D. K., and Fletcher, C. H. (1949). The shock tube: A facility for investigations in fluid dynamics. *Review of Scientific Instruments*, 20(11):807–815.
- Blum, R. J. and Dunn, M. G. (1966). Continuous measurement of shock velocity using a microwave technique. Technical Report CR-490, NASA.

- Born, M. and Wolf, E. (1999). *Principles of Optics*. Cambridge University Press, 7th edition.
- Bradski, G. (2000). The OpenCV Library. *Dr. Dobb's Journal of Software Tools*.
- Brinkley, S. R. and Kirkwood, J. G. (1947). Theory of the propagation of shock waves. *Physical Review*, 71(9):606–611.
- Burnside, R. R. and Mackie, A. G. (1965). A Problem in shock wave decay. *Journal of the Australian Mathematical Society*, 5(2):258–272.
- Cassen, B. and Stanton, J. (1948). The decay of shock waves. *Journal of Applied Physics*, 19(9):803–807.
- Chandrasekhar, S. (1943). On the decay of plane shock waves. Technical Report No. 423, Aberdeen Proving Ground.
- Chen, H., Feng, H., and Yu, H. (2004). Double detonation drivers for a shock tube/tunnel. *Sci China Ser G: Phy & Ast*, 47(4):502–512.
- Chen, P. J. and Gurtin, M. E. (1971). Growth and decay of one-dimensional shock waves in fluids with internal state variables. *Phys. Fluids*, 14(6):1091–1094.
- Chester, W. (1954). CXLV. The quasi-cylindrical shock tube. *The London, Edinburgh, and Dublin Philosophical Magazine and Journal of Science*, 45(371):1293–1301.
- Chisnell, R. F. (1957). The motion of a shock wave in a channel, with applications to cylindrical and spherical shock waves. *Journal of Fluid Mechanics*, 2(3):286–298.
- Choudhary, R., Dewey, J. M., and Limbach, C. (2024). Towards spatially resolved imaging of high-frequency density fluctuations using quasi-tomographic space-time interferometry. In *AIAA SciTech 2024 Forum*. American Institute of Aeronautics and Astronautics.
- Chue, R. S. M., Bakos, R. J., and Tsai, C. Y. (2003). Driver gas contamination in a detonation-driven reflected-shock tunnel. *Shock Waves*, 13(5):367–380.
- Coates, P. B. and Gaydon, A. G. (1965). A simple shock tube with detonating driver gas. *Proc. Math. Phys. Sci.*, 283(1392):18–32.
- Cooper, M. A. (2004). *Impulse Generation by Detonation Tubes*. PhD thesis, California Institute of Technology.
- Cottet, F. and Romain, J. P. (1982). Formation and decay of laser-generated shock waves. *Physical Review A*, 25(1):576–579.
- Courant, R. and Friedrichs, K. O. (1948). *Supersonic Flow and Shock Waves*. Interscience.

- Crane, J., Shi, X., Xu, R., and Wang, H. (2022). Natural gas versus methane: Ignition kinetics and detonation limit behavior in small tubes. *Combustion and Flame*, 237:111719.
- Cummings, E. B. (1995). *Laser-Induced Thermal Acoustics*. Phd, California Institute of Technology.
- Damazo, J. and Shepherd, J. E. (2017). Observations on the normal reflection of gaseous detonations. *Shock Waves*, 27:795–810.
- Daru, V. and Damion, J. P. (1995). Analysis of the flow perturbations in a shock tube due to the curvature of the diaphragm. In Brun, R. and Dumitrescu, L. Z., editors, *Shock Waves @ Marseille I*, pages 451–456, Berlin, Heidelberg. Springer.
- Dufrene, A., Sharma, M., and Austin, J. M. (2007). Design and characterization of a hypervelocity expansion tube facility. *Journal of Propulsion and Power*, 23(6):1185–1193.
- Dufrene, A. T. (2013). *Expansion Tunnel Characterization and Development of Non-Intrusive Microwave Plasma Diagnostics*. PhD thesis, University at Buffalo, State University of New York.
- Eckett, C. A., Quirk, J. J., and Shepherd, J. E. (2000). The role of unsteadiness in direct initiation of gaseous detonations. *J. Fluid Mech.*, 421:147–183.
- Eilers, P. H. C. (2003). A perfect smoother. *Analytical Chemistry*, 75(14):3631–3636.
- Erdos, J. and Bakos, R. (1994). Prospects for a quiet hypervelocity shock-expansion tunnel. In *25th Plasmadynamics and Lasers Conference*, Fluid Dynamics and Co-located Conferences. American Institute of Aeronautics and Astronautics.
- Erdos, J., Bakos, R., Castrogiovanni, A., Rogers, R., Erdos, J., Bakos, R., Castrogiovanni, A., and Rogers, R. (1997). Dual mode shock-expansion/reflected-shock tunnel. In *35th Aerospace Sciences Meeting and Exhibit*, Reno, NV. American Institute of Aeronautics and Astronautics.
- Feit, M. D. and Fleck, J. A. (1978). Light propagation in graded-index optical fibers. *Appl. Opt.*, AO, 17(24):3990–3998.
- Fickett, W. and Davis, W. C. (1979). *Detonation*. University of California Press, Berkeley.
- Forrester, A. T., Gudmundsen, R. A., and Johnson, P. O. (1955). Photoelectric mixing of incoherent light. *Phys. Rev.*, 99(6):1691–1700.
- Fowles, G. R. (1960). Attenuation of the shock wave produced in a solid by a flying plate. *Journal of Applied Physics*, 31(4):655–661.

- Fredrick, C. D., Greenlee, T. R., Peterson, R. W., Schaffer, A. J., Stein, K. R., and Woetzel, A. W. (2015). Complementary studies on supersonic nozzle flow: Heterodyne interferometry, high-speed video shadowgraphy, and numerical simulation. In *Computational Methods and Experimental Measurements XVII*, pages 223–234.
- Fried, D. (1967). Optical heterodyne detection of an atmospherically distorted signal wave front. *Proceedings of the IEEE*, 55(1):57–77.
- Friedlander, F. D. (1958). *Sound Pulses*. Cambridge University Press.
- Friedrichs, K. O. (1948). Formation and decay of shock waves. *Communications on Pure and Applied Mathematics*, 1(3):211–245.
- Gardiner, W. C., Hidaka, Y., and Tanzawa, T. (1981). Refractivity of combustion gases. *Combustion and Flame*, 40:213–219.
- Gillespie, G. I., Ceruzzi, A. P., and Laurence, S. J. (2022). A multi-point focused laser differential interferometer for characterizing freestream disturbances in hypersonic wind tunnels. *Exp Fluids*, 63(11):180.
- Goldstein, I., Miles, P., and Chabot, A. (1965). Heterodyne measurements of light propagation through atmospheric turbulence. *Proceedings of the IEEE*, 53(9):1172–1180.
- Goodman, J. W. (2015). *Statistical Optics*. Wiley, 2nd edition.
- Goodwin, D. G., Moffat, H. K., and Speth, R. L. (2021). Cantera: An Object-oriented Software Toolkit for Chemical Kinetics, Thermodynamics, and Transport Processes. <https://www.cantera.org>.
- Greenshields, C. (2021). *OpenFOAM v9 User Guide*. The OpenFOAM Foundation, London, UK.
- Grönig, H., Olivier, H., and Habermann, M. (1998). Development of a detonation driver for a shock tunnel. *Rev. High Pressure Sci. Technol.*, 7:879–884.
- Grunthaner, M., Jackson, S. I., and Shepherd, J. E. (2001). Design and construction of an annular detonation initiator. Technical Report FM01-5, GALCIT.
- Haloua, F., Brouillette, M., Lienhart, V., and Dupré, G. (2000). Characteristics of unstable detonations near extinction limits. *Combustion and Flame*, 122(4):422–438.
- Hameed, A., Parziale, N. J., Paquin, L. A., Butler, C., and Laurence, S. J. (2020). Hypersonic slender-cone boundary-layer instability in the UMD HyperTERP Shock Tunnel. In *AIAA Scitech 2020 Forum*, AIAA SciTech Forum. American Institute of Aeronautics and Astronautics.

- Hanson, R. K., Spearrin, R. M., Goldenstein, C. S., et al. (2016). *Spectroscopy and Optical Diagnostics for Gases*, volume 1. Springer.
- Harris, C. R., Millman, K. J., van der Walt, S. J., Gommers, R., Virtanen, P., Cournapeau, D., Wieser, E., Taylor, J., Berg, S., Smith, N. J., Kern, R., Picus, M., Hoyer, S., van Kerkwijk, M. H., Brett, M., Haldane, A., del Río, J. F., Wiebe, M., Peterson, P., Gérard-Marchant, P., Sheppard, K., Reddy, T., Weckesser, W., Abbasi, H., Gohlke, C., and Oliphant, T. E. (2020). Array programming with NumPy. *Nature*, 585(7825):357–362.
- Henderson, S. J. and Menart, J. A. (2008). Equilibrium properties of high-temperature air for a number of pressures. *Journal of Thermophysics and Heat Transfer*, 22(4):718–726.
- Henshaw, W. D., Smyth, N. F., and Schwendeman, D. W. (1986). Numerical shock propagation using geometrical shock dynamics. *Journal of Fluid Mechanics*, 171:519–545.
- Hertzberg, A. and Smith, W. E. (1954). A method for generating strong shock waves. *Journal of Applied Physics*, 25(1):130–131.
- Heylmun, J., Vonk, P., and Brewer, T. (2021). blastFoam version 5.0 User Guide.
- Hobbs, P. C. D. (1997). Ultrasensitive laser measurements without tears. *Appl. Opt.*, 36(4):903–920.
- Hobbs, P. C. D. (2008). *Building Electro-Optical Systems*. Wiley, 2nd edition.
- Hogenboom, D. O. and DiMarzio, C. A. (1998). Quadrature detection of a Doppler signal. *Appl. Opt.*, 37(13):2569.
- Hongru, Y. (1999). Oxyhydrogen combustion and detonation driven shock tube. *Acta Mechanica Sinica*, 15(2):97–107.
- Hornung, H. G. (2010). Ground testing for hypervelocity flow, capabilities and limitations. Technical Report RTO-EN-AVT-186, NATO Research and Technology Organization.
- Hornung, H. G. and Quirk, J. J. (1998). Two effects of diaphragm bulge on shock tubes. In Rath, H. J. and Egbers, C., editors, *Advances in Fluid Mechanics and Turbomachinery*, pages 57–66. Springer, Berlin, Heidelberg.
- Hu, Z., Wang, W., and Zhang, Z. (2025). A review on the development of large-scale detonation-driven shock tunnels and the application in hypersonic flow tests. *International Journal of Fluid Engineering*, 2(1):010601.
- Jackson, S. I. (2005). *Gaseous Detonation Initiation Via Wave Implosion*. PhD thesis, California Institute of Technology.

- Jackson, S. I. and Shepherd, J. E. (2007). Toroidal imploding detonation wave initiator for pulse detonation engines. *AIAA Journal*, 45(1):257–270.
- Jackson, S. I. and Short, M. (2013). The influence of the cellular instability on lead shock evolution in weakly unstable detonation. *Combustion and Flame*, 160(10):2260–2274.
- Jacobson, A. R. and Call, D. L. (1978). Novel interferometer for the measurement of plasma density. *Review of Scientific Instruments*, 49(3):318–320.
- Jakobs, L., Sander, T., and Mundt, C. (2023). Temperature and velocity measurement in a shock tube with homodyne and heterodyne grating spectroscopy. In *AIAA Aviation 2023 Forum*. American Institute of Aeronautics and Astronautics.
- Jayamani, A. and Lu, F. K. (2022). Method-of-characteristics model for a low-enthalpy, detonation-driven shock tube. *Physics of Fluids*, 34(6):066109.
- Jiang, Z., Lin, J., and Zhao, W. (2011). Performance tests of JF-10 high-enthalpy shock tunnel with a FDC driver. *International Journal of Hypersonics*, 2(1):29–36.
- Jiang, Z., Wu, B., Gao, Y., Zhao, W., and Hu, Z. (2015). Development of the detonation-driven expansion tube for orbital speed experiments. *Science China Technological Sciences*, 58(4):695–700.
- Jiang, Z. and Yu, H. (2016). Development and calibration of detonation-driven high-enthalpy and hypersonic test facilities. In *Experimental Methods of Shock Wave Research*, pages 285–313. Springer International Publishing.
- Jiang, Z., Yu, H. R., and Lin, Z. B. (2007). Research progress on high-enthalpy and hypersonic flows. In *New Trends in Fluid Mechanics Research*, pages 37–44. Springer Berlin Heidelberg.
- Jiang, Z. L., Zhao, W., Wang, C., and Takayama, K. (2002). Forward-running detonation drivers for high-enthalpy shock tunnels. *AIAA Journal*, 40(10):2009–2016.
- Johnston, C. O. and Brandis, A. M. (2014). Modeling of nonequilibrium CO fourth-positive and CN violet emission in CO<sub>2</sub>–N<sub>2</sub> gases. *Journal of Quantitative Spectroscopy and Radiative Transfer*, 149:303–317.
- Jones, S. M. (2021). *Thermal Ignition by Vertical Cylinders*. PhD thesis, California Institute of Technology.
- Kao, S. T., Ziegler, J. L., Bitter, N. P., Schmidt, B. E., Lawson, J., and Shepherd, J. E. (2020). SDToolbox: Numerical Tools for Shock and Detonation Wave Modeling. GALCIT Report FM2018.001, California Institute of Technology, Pasadena, CA.
- Korobeinikov, V. P. (1991). *Problems of Point-Blast Theory*. American Institute of Physics, New York.



- Kramer, D. (2023). Helium prices surge to record levels as shortage continues. *Physics Today*, 76(9):18–20.
- Kristal, R. and Peterson, R. W. (1976). Bragg cell heterodyne interferometry of fast plasma events. *Review of Scientific Instruments*, 47(11):1357–1359.
- Kurganov, A., Noelle, S., and Petrova, G. (2001). Semidiscrete central-upwind schemes for hyperbolic conservation laws and hamilton–jacobi equations. *SIAM J. Sci. Comput.*, 23(3):707–740.
- Landau, L. D. and Lifshitz, E. M. (1987). *Course of Theoretical Physics - Vol. 6, Fluid Mechanics*. Pergamon Press, 2nd edition.
- Lawson, J. M. (2021). *Focused Laser Differential Interferometry*. PhD thesis, California Institute of Technology.
- Lawson, J. M. and Austin, J. M. (2018). Design of conventional and detonation-driven hypervelocity expansion tubes. In *2018 Aerodynamic Measurement Technology and Ground Testing Conference*, Atlanta, GA. American Institute of Aeronautics and Astronautics.
- Lawson, J. M. and Austin, J. M. (2023). Recovering density disturbance spectra from FLDI. Part 1. *Appl. Opt.*, AO, 62(12):3042–3053.
- Lee, B. H. K. (1967). Detonation-driven shocks in a shock tube. *AIAA Journal*, 5(4):791–792.
- Lee, J. H. S. (2008). *The Detonation Phenomenon*. Cambridge University Press, New York.
- Lee, J. H. S. (2016). *The Gas Dynamics of Explosions*. Cambridge University Press.
- Lenth, W. (1983). Optical heterodyne spectroscopy with frequency- and amplitude-modulated semiconductor lasers. *Opt. Lett.*, OL, 8(11):575–577.
- Lu, F. K. and Wilson, D. R. (2003). Detonation driver for enhancing shock tube performance. *Shock Waves*, 12(6):457–468.
- Lu, F. K., Wilson, D. R., Bakos, R. J., and Erdos, J. I. (2000). Recent advances in detonation techniques for high-enthalpy facilities. *AIAA Journal*, 38(9):1676–1684.
- MacLean, M., Dufrene, A., Wadhams, T., and Holden, M. (2010). Numerical and experimental characterization of high enthalpy flow in an expansion tunnel facility. In *48th AIAA Aerospace Sciences Meeting Including the New Horizons Forum and Aerospace Exposition*. American Institute of Aeronautics and Astronautics.
- Massey, G. (1968). An optical heterodyne ultrasonic image converter. *Proceedings of the IEEE*, 56(12):2157–2161.

- Matthews, D. L. (1959). Interferometric measurement in the shock tube of the dissociation rate of oxygen. *The Physics of Fluids*, 2(2):170–178.
- McBride, B. J., Gordon, S., and Reno, M. A. (1993). Coefficients for calculating thermodynamic and transport properties of individual species. Technical Memorandum TM-4513, NASA.
- McBride, B. J., Zehe, M. J., and Gordon, S. (2002). NASA Glenn coefficients for calculating thermodynamic properties of individual species. Technical Memorandum NASA/TP-2002-211556, NASA Glenn Research Center.
- McMurtry, B. J. and Siegman, A. E. (1962). Photomixing experiments with a ruby optical maser and a traveling-wave microwave phototube. *Appl. Opt.*, AO, 1(1):51–53.
- Merzkirch, W. (1987). *Flow Visualization*. Academic Press, 2nd edition.
- Millikan, R. C. and White, D. R. (1963). Systematics of vibrational relaxation. *J. Chem. Phys.*, 39(12):3209–3213.
- Milonni, P. W. and Eberly, J. H. (2010). *Laser Physics*. Wiley.
- Mirels, H. (1957). Attenuation in a shock tube due to unsteady-boundary-layer action. Technical Report TR-1333, NACA.
- Nagamatsu, H. T. and Martin, E. D. (1959). Combustion investigation in the hypersonic shock tunnel driver section. *Journal of Applied Physics*, 30(7):1018–1021.
- NASA (1980). Heterodyne systems and technology, part 1. Technical Report NASA-CP-2138-PT-1.
- Nemoto, S. (1990). Nonparaxial Gaussian beams. *Appl. Opt.*, AO, 29(13):1940–1946.
- Norfleet, G. D., Lacey, J. J., and Whitfield, J. D. (1966). Results of an experimental investigation of the performance of an expansion tube. Technical Report TR-66-10, AEDC.
- Olivier, H. (2016). The Aachen shock tunnel TH2 with dual driver mode operation. In Igra, O. and Seiler, F., editors, *Experimental Methods of Shock Wave Research*, pages 111–129. Springer International Publishing.
- Olson, G., Peterson, R., Pulford, B., Seaberg, M., Stein, K., Stelter, C., and Weber, R. (2006). The role of shock waves in expansion tube accelerators. *American Journal of Physics*, 74(12):1071–1076.
- Oppenheim, A. V. and Schaffer, R. W. (2010). *Discrete-Time Signal Processing*. Pearson, 3rd edition.

- Oshima, K., Sugaya, K., Yamamoto, M., and Totoki, T. (1965). Diffraction of a plane shock wave around a corner. Technical Report 393, ISAS.
- Papoulis, A. and Pillai, S. U. (2002). *Probability, Random Variables, and Stochastic Processes*. McGraw-Hill, 4th edition.
- Parziale, N., Shepherd, J., and Hornung, H. (2012). Reflected shock tunnel noise measurement by focused differential interferometry. In *42nd AIAA Fluid Dynamics Conference and Exhibit*, Fluid Dynamics and Co-Located Conferences. American Institute of Aeronautics and Astronautics.
- Paull, A. and Stalker, R. J. (1992). Test flow disturbances in an expansion tube. *Journal of Fluid Mechanics*, 245(-1):493.
- Peace, J. T. and Lu, F. K. (2018a). Detonation-to-shock wave transmission at a contact discontinuity. *Shock Waves*, 28(5):981–992.
- Peace, J. T. and Lu, F. K. (2018b). On the propagation of decaying planar shock and blast waves through non-uniform channels. *Shock Waves*, 28(6):1223–1237.
- Pei, S.-C. and Lai, Y.-C. (2012). Closed form variable fractional time delay using FFT. *IEEE Signal Processing Letters*, 19(5):299–302.
- Pert, G. J. (1980). Self-similar flows with uniform velocity gradient and their use in modelling the free expansion of polytropic gases. *Journal of Fluid Mechanics*, 100(2):257–277.
- Petersen, E. L. and Hanson, R. K. (2001). Nonideal effects behind reflected shock waves in a high-pressure shock tube. *Shock Waves*, 10(6):405–420.
- Peterson, R. W., Pulford, B. N., and Stein, K. R. (2005). The ping-pong cannon: A closer look. *The Physics Teacher*, 43(1):22–25.
- Philippe, L. C. and Hanson, R. K. (1993). Laser diode wavelength-modulation spectroscopy for simultaneous measurement of temperature, pressure, and velocity in shock-heated oxygen flows. *Appl. Opt., AO*, 32(30):6090–6103.
- Radulescu, M. I. (2020). On the shock change equations. *Phys. Fluids*, 32(5):056106.
- Radulescu, M. I. and Hanson, R. K. (2005). Effect of Heat Loss on Pulse-Detonation-Engine Flow Fields and Performance. *Journal of Propulsion and Power*, 21(2):274–285.
- Ridoux, J., Lardjane, N., Monasse, L., and Coulouvrat, F. (2019). Beyond the limitation of geometrical shock dynamics for diffraction over wedges. *Shock Waves*, 29(6):833–855.
- Rościszewski, J. (1960). Calculations of the motion of non-uniform shock waves. *Journal of Fluid Mechanics*, 8(3):337–367.

- Sachdev, P. (2004). *Shock Waves & Explosions*. Monographs and Surveys in Pure and Applied Mathematics. Taylor & Francis.
- Sander, T., Weber, J., and Mundt, C. (2022). Simultaneous thermometry and velocimetry for a shock tunnel using homodyne and heterodyne detection. *Appl. Phys. B*, 128(8):150.
- Schafer, R. W. (2011). What Is a Savitzky-Golay Filter? [Lecture notes]. *IEEE Signal Processing Magazine*, 28(4):111–117.
- Schmidt, B. E. and Shepherd, J. E. (2015). Analysis of focused laser differential interferometry. *Appl. Opt., AO*, 54(28):8459–8472.
- Schoeffler, D. T. and Shepherd, J. E. (2023). Analysis of shock wave acceleration from normal detonation reflection. *Shock Waves*, 33:205–222.
- Settles, G. S. (2001). *Schlieren and Shadowgraph Techniques*. Springer Berlin, Heidelberg.
- Settles, G. S. and Fulghum, M. R. (2016). The focusing laser differential interferometer, an instrument for localized turbulence measurements in refractive flows. *Journal of Fluids Engineering*, 138(10):101402.
- Sharma, V. D. and Radha, C. (1994). On one-dimensional planar and nonplanar shock waves in a relaxing gas. *Phys. Fluids*, 6(6):2177–2190.
- Sharma, V. D., Ram, R., and Sachdev, P. L. (1987). Uniformly valid analytical solution to the problem of a decaying shock wave. *Journal of Fluid Mechanics*, 185:153–170.
- Singh, M. and Arora, R. (2021). Propagation of one-dimensional planar and non-planar shock waves in nonideal radiating gas. *Physics of Fluids*, 33(4):046106.
- Skews, B. W. (1967). The shape of a diffracting shock wave. *Journal of Fluid Mechanics*, 29(2):297–304.
- Smeets, G. and George, A. (1973). Laser-differential interferometer applications in gas dynamics. Technical Report 28/73, Institut Franco-Allemand de Recherches de Saint-Louis.
- Stalker, R. J. (1967). A study of the free-piston shock tunnel. *AIAA Journal*, 5(12):2160–2165.
- Straede, H. G., Jenkinson, I., Herik, T. v. d., and James, C. M. (2024). Implementation of microwave interferometry for continuous shock speed measurement in shock and expansion tubes. In *AIAA SCITECH 2024 Forum*, number 2569. American Institute of Aeronautics and Astronautics.

- Strand, O. T., Goosman, D. R., Martinez, C., Whitworth, T. L., and Kuhlow, W. W. (2006). Compact system for high-speed velocimetry using heterodyne techniques. *Review of Scientific Instruments*, 77(8):083108.
- Streicher, J. W., Krish, A., and Hanson, R. K. (2020). Vibrational relaxation time measurements in shock-heated oxygen and air from 2000 K to 9000 K using ultraviolet laser absorption. *Physics of Fluids*, 32(8):086101.
- Stuessy, W., Lu, F., and Wilson, D. (1998). Shock-induced detonation wave driver for enhancing shock tube performance. In *36th AIAA Aerospace Sciences Meeting and Exhibit*, Reno, NV. American Institute of Aeronautics and Astronautics.
- Taylor, G. I. (1939). The propagation and decay of blast waves. In Batchelor, G. K., editor, *The Scientific Papers of Sir Geoffrey Ingram Taylor*, page 221. Cambridge University Press.
- Thompson, P. A. (1971). A fundamental derivative in gasdynamics. *The Physics of Fluids*, 14(9):1843–1849.
- Thompson, P. A. (1972). *Compressible Fluid Dynamics*. McGraw-Hill, New York.
- Trimpi, R. L. (1962). A preliminary study of a new device for producing high-enthalpy, short-duration gas flows. Technical Report R-133, NASA.
- van Albada, G. D., van Leer, B., and Roberts, W. W. (1997). A comparative study of computational methods in cosmic gas dynamics. In Hussaini, M. Y., van Leer, B., and Van Rosendale, J., editors, *Upwind and High-Resolution Schemes*, pages 95–103. Springer.
- van Leer, B. (1974). Towards the ultimate conservative difference scheme. II. Monotonicity and conservation combined in a second-order scheme. *Journal of Computational Physics*, 14(4):361–370.
- Vincenti, V. G. and Kruger, C. H. (1965). *Introduction to Physical Gas Dynamics*. Wiley, New York.
- Virtanen, P., Gommers, R., Oliphant, T. E., Haberland, M., Reddy, T., Cournapeau, D., Burovski, E., Peterson, P., Weckesser, W., Bright, J., van der Walt, S. J., Brett, M., Wilson, J., Millman, K. J., Mayorov, N., Nelson, A. R. J., Jones, E., Kern, R., Larson, E., Carey, C. J., Polat, İ., Feng, Y., Moore, E. W., VanderPlas, J., Laxalde, D., Perktold, J., Cimrman, R., Henriksen, I., Quintero, E. A., Harris, C. R., Archibald, A. M., Ribeiro, A. H., Pedregosa, F., van Mulbregt, P., and SciPy 1.0 Contributors (2020). SciPy 1.0: Fundamental Algorithms for Scientific Computing in Python. *Nature Methods*, 17:261–272.
- Waldron, H. F. (1958). An experimental investigation of the flow properties behind strong shock waves in nitrogen. Technical Report 50, University of Toronto, Institute of Aerophysics.

- Wang, G. and Mazumdar, Y. C. (2021). High-gradient index of refraction measurements with a quadrature fringe imaging interferometer. In *AIAA Scitech 2021 Forum*, AIAA SciTech Forum. American Institute of Aeronautics and Astronautics.
- Welch, P. (1967). The use of fast Fourier transform for the estimation of power spectra: A method based on time averaging over short, modified periodograms. *IEEE Transactions on Audio and Electroacoustics*, 15(2):70–73.
- White, D. R. (1958). Influence of diaphragm opening time on shock-tube flows. *Journal of Fluid Mechanics*, 4(6):585–599.
- White, D. R. (1961). Turbulent structure of gaseous detonation. *The Physics of Fluids*, 4(4):465–480.
- White, D. R. (1968). Shock-tube study of vibrational exchange in N<sub>2</sub>–O<sub>2</sub> mixtures. *The Journal of Chemical Physics*, 49(12):5472–5476.
- White, D. R. and Millikan, R. C. (1964). Vibrational relaxation in air. *AIAA Journal*, 2(10):1844–1846.
- Whitham, G. B. (1958). On the propagation of shock waves through regions of non-uniform area or flow. *J. Fluid Mech.*, 4(4):337–360.
- Whitham, G. B. (1999). *Linear and Nonlinear Waves*. John Wiley & Sons, Ltd.
- Whitman, R., Laub, L., and Bates, W. (1968). Acoustic surface displacement measurements on a wedge-shaped transducer using an optical probe technique. *IEEE Transactions on Sonics and Ultrasonics*, 15(3):186–189.
- Willert, C. E. and Gharib, M. (1991). Digital particle image velocimetry. *Experiments in Fluids*, 10(4):181–193.
- Woodward, P. and Colella, P. (1984). The numerical simulation of two-dimensional fluid flow with strong shocks. *Journal of Computational Physics*, 54(1):115–173.
- Wright, T. W. (1976). An intrinsic description of unsteady shock waves. *The Quarterly Journal of Mechanics and Applied Mathematics*, 29(3):311–324.
- Yamanaka, A., Ariga, Y., Obara, T., Cai, P., and Ohyagi, S. (2002). Study on performance of detonation-driven shock tube. *JSME International Journal Series B Fluids and Thermal Engineering*, 45(2):425–431.
- Yousaf, M. (1974). The effect of overtaking disturbances on the motion of converging shock waves. *Journal of Fluid Mechanics*, 66(3):577–591.
- Yousaf, M. (1982). Effect of overtaking disturbances on the motion of a shock wave due to an intense explosion. *The Physics of Fluids*, 25(1):45–47.

- Yu, H. r., Esser, B., Lenartz, M., and Grönig, H. (1992). Gaseous detonation driver for a shock tunnel. *Shock Waves*, 2(4):245–254.
- Yu, W. M., Luo, Y., Austin, J. M., Hornung, H., Finch, P. M., Schwartz, T., Strand, C. L., and Hanson, R. K. (2024). High-frequency static pressure measurements in the T5 reflected shock tunnel. In *AIAA SCITECH 2024 Forum*. American Institute of Aeronautics and Astronautics.
- Zel'dovich, Y. and Raizer, Y. P. (1967). *Physics of Shock Waves and High Temperature Hydrodynamic Phenomena*. Academic Press.
- Zhao, W., Jiang, Z. L., Saito, T., Lin, J. M., Yu, H. R., and Takayama, K. (2005). Performance of a detonation driven shock tunnel. *Shock Waves*, 14(1-2):53–59.

## Appendix A

### ADDITIONAL MATERIAL ON PLANE SHOCK DECAY

Schoeffler, D. T. and Shepherd, J. E. (2024). Decay of plane shock waves in equilibrium flows. *Under consideration for J. Fluid Mech.*

#### A.1 Irreversible Chemical Reaction

The shock decay model can also be applied if there is some nonzero heat of reaction,  $\Delta h$ , where  $\Delta h > 0$  is exothermic and  $\Delta h < 0$  is endothermic. If  $\gamma_2 = \gamma_1 = \gamma$ , and  $Q = \Delta h/RT_1$ , then the shock jump relations are

$$\frac{P_2}{P_1} = \frac{1 + \gamma M^2}{1 + \gamma M_2^2}, \quad (\text{A.1})$$

$$\frac{v_2}{v_1} = \frac{P_2 M_2^2}{P_1 M^2}, \quad (\text{A.2})$$

$$M_2^2 = \frac{-2\gamma\zeta + 1 - \sqrt{1 - 2(\gamma + 1)\zeta}}{(2\gamma\zeta - 1)\gamma + 1}, \quad (\text{A.3})$$

$$\zeta = \frac{M^2}{(1 + \gamma M^2)^2} \left[ \frac{\gamma - 1}{\gamma} Q + 1 + \frac{\gamma - 1}{2} M^2 \right], \quad (\text{A.4})$$

where  $M_2 = w_2/a_2$ . If  $Q > 0$ , then  $M > M_{\text{CJ}}$ , where  $M_{\text{CJ}}$  is the Chapman-Jouguet (CJ) Mach number, given by

$$M_{\text{CJ}} = \sqrt{\frac{\gamma^2 - 1}{2\gamma} Q + 1} + \sqrt{\frac{\gamma^2 - 1}{2\gamma} Q}. \quad (\text{A.5})$$

If  $M \geq 1$ , then admissible values for  $Q$  are

$$Q \geq -\frac{\gamma}{2} \frac{\gamma + 1}{\gamma - 1}. \quad (\text{A.6})$$

Thompson (1972) discusses this model for CJ detonations. The above equations can be used to compute  $K$  and  $B$  for implementation of the decay model.

Figure A.1 shows the effect of  $Q$  on  $K^{-1}$  for  $\gamma = 1.2$ . Positive  $Q$  shifts the  $K^{-1}$  to the right, so that  $K^{-1} = 0$  when  $M > 1$ . The value of  $M$  when  $K^{-1} = 0$  is equal to the CJ Mach number. Therefore, the overdriven detonation decays toward the CJ Mach number and approaches it asymptotically with infinite time. Negative  $Q$  results in faster decay for a given shock Mach number. As  $M \rightarrow 1$ ,  $K^{-1}$  remains nonzero and



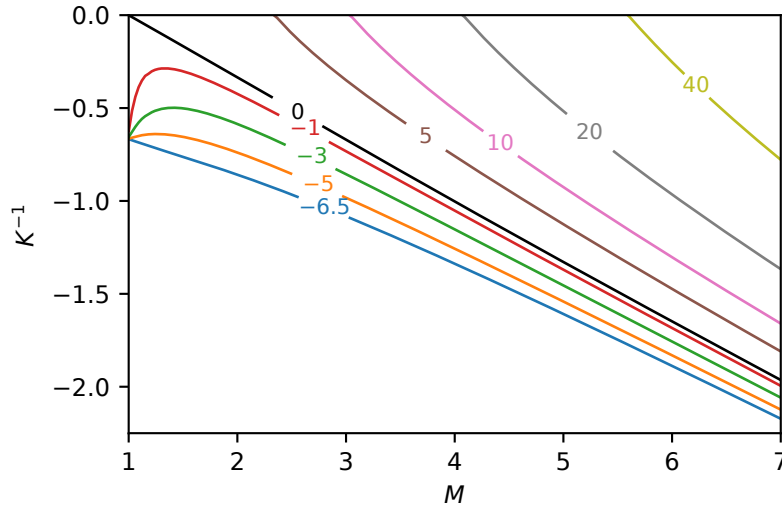


Figure A.1: Effect of  $Q$  on  $K^{-1}$  for  $\gamma = 1.2$ .

approaches a finite value. As a result, the decaying shock in an endothermic gas approaches  $M = 1$  in finite time. Even small endothermicity results in significant increase in decay as  $M \rightarrow 1$ . These effects are shown by numerical solutions of the shock decay model in figure A.2.

For  $Q > 0$ , the power-law approximation can be formulated as

$$\delta(t) = \frac{1}{(1 + \beta t / \alpha)^\alpha},$$

$$\delta(t) = \frac{M(t) - M_{\text{CJ}}}{M_0 - M_{\text{CJ}}}, \quad \beta = \frac{-\dot{M}_0}{M_0 - M_{\text{CJ}}}, \quad \alpha = -\frac{1}{K(M_0)(M_0 - M_{\text{CJ}}) + 1}. \quad (\text{A.7})$$

## A.2 Implementation of Prior Theories

### A.2.1 Chandrasekhar (1943)

Chandrasekhar's solution is given by equation (31) of his work, reproduced here as

$$\frac{M}{(M-1)^2} \frac{(M_0-1)^2}{M_0} e^{M_0-M} = 1 + qt,$$

where  $q$  is a required time scale. If  $\dot{M}_0$  is known,  $q$  can be obtained from

$$q = -\left(1 + \frac{1}{M_0^2}\right) \frac{M_0}{M_0 - 1} \dot{M}_0.$$

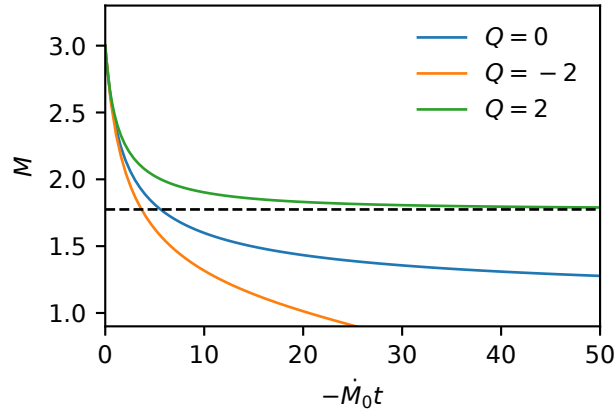


Figure A.2: Solutions of shock decay model for  $M_0 = 3$ ,  $\dot{M}_0 = -1$ , and  $\gamma = 1.2$  with nonzero values for  $Q$ . The dashed line is the CJ Mach number for  $Q = 2$  and is  $M_{CJ} = 1.77$ .

### A.2.2 Brinkley and Kirkwood (1947)

Brinkley and Kirkwood (1947) derive a propagation equation for one-dimensional shocks in a medium with an arbitrary equation of state. The derivation is based on the equivalence between the work done by some generating surface, e.g., the piston motion, and the residual enthalpy in shocked gas after having isentropically expanded back to the initial pressure,  $P_1$ . The enthalpy increment is nonzero because of the entropy increment by the shock. Lee (2016) discusses this theory in more detail. The Brinkley-Kirkwood shock propagation equations are given by (14) in their work, which were integrated here as they are given. The second-order shock propagation equation requires two initial conditions, given by the shock speed or strength and the blast energy or, equivalently, the initial shock acceleration. The shock acceleration was computed using this article's solution (2.86) and converted to their variables to give

$$\begin{aligned} \frac{dp}{dR} &= \frac{\partial p}{\partial R} + \frac{1}{U} \frac{\partial p}{\partial t}, \\ &= \rho_1 a_1 (G + \hat{G}/M) \dot{M}, \end{aligned}$$

where  $R$  is the shock position,  $p$  is the pressure increment at the shock, and  $\hat{G}$  is given in section A.2.5.

The critical assumption in Brinkley-Kirkwood theory is that the time-evolution of the shock-energy integrand is spatially similar. As a result, the integral over scaled time gives a constant parameter,  $\nu$ . Brinkley and Kirkwood assume the shock-energy

time integrand to be exponential and show that a strong shock limit gives  $\nu = 1$  and a weak shock limit gives  $\nu = 2/3$ . For the calculations used in this article,  $\nu = 1$  was used. This was found to be more accurate than  $\nu = 2/3$ . Accuracy was improved for  $\nu > 1$ , but further discussion of this is beyond the scope of the present work.

### A.2.3 Friedrichs (1948)

Friedrichs's solution for the shock position as a function of time is given by equation (10.13) of his paper. Reproduced here using our nomenclature, the equation is

$$x_s = x_R + a_1 \left[ t - t_R + \frac{4k((t_1 - t_R)(t - t_R))^{1/2}}{1 + k \left( \frac{t_1 - t_R}{t - t_R} \right)^{1/2}} \right], \quad (\text{A.8})$$

where

$$k = \frac{u_2}{4(1 - \mu^2)a_1 - u_2}$$

and

$$\mu^2 = \frac{\gamma - 1}{\gamma + 1}.$$

$t_R$  and  $x_R$  are the time and position where the piston impulsively stops.  $t_1$  is the time when the head characteristic intersects the shock wave. Friedrichs uses the weak shock approximation, so  $t_1$  is given by

$$t_1 = 8t_R \frac{1 + \mu^2 \sigma_1}{\sigma_1(4 - \sigma_1)},$$

where

$$\sigma_1 = \frac{u_2}{(1 - \mu^2)a_1}.$$

To obtain the shock speed over time, we differentiated (A.8), using the value of  $u_2$  given by the shock jump equations for  $M_0$ . The characteristic time  $t_R$  was scaled to match our time scale.

### A.2.4 Sharma et al. (1987)

The shock propagation equation obtained by Sharma et al. (1987) is given by equation (38) of their work. To ensure correct implementation of their solution, it was verified that Figure 2 and Figure 3(b) from their work could be reproduced. Peace and Lu (2018b) also implemented this solution, and it was verified that their Figure 4 could be reproduced.

### A.2.5 Best (1991)

Best (1991) uses a truncation term of the form

$$Q_2 = \frac{1}{\rho_1 a_1^2} \frac{\partial}{\partial t} \left( \frac{\partial P}{\partial t} + \rho a \frac{\partial u}{\partial t} \right) \quad (\text{A.9})$$

as a generalization of Whitham's geometric shock dynamics. For constant area shock propagation, Best's hierarchy of shock-change equations can be reduced to a single equation in the same form as above. We consider the second-order equation and compare it with our  $u_{xx,2}$  result (2.54). The algebra is simplified by manipulating the equations in terms of the coefficients derived in section 2.2.

Expanding (A.9) gives

$$Q_2 = \frac{P_{tt,2}}{\rho_1 a_1^2} + \frac{\rho_2 a_2}{\rho_1 a_1} \frac{u_{tt,2}}{a_1} + \frac{\rho_2}{\rho_1} \frac{a_{t,2}}{a_1} \frac{u_{t,2}}{a_1} + \frac{\rho_{t,2}}{\rho_1} \frac{a_2}{a_1} \frac{u_{t,2}}{a_1}. \quad (\text{A.10})$$

The partial-time shock-change equations are given by

$$\left. \frac{1}{a_1} \frac{\partial u}{\partial t} \right|_2 = \hat{F} \dot{M}, \quad \left. \frac{1}{\rho_1 a_1^2} \frac{\partial P}{\partial t} \right|_2 = \hat{G} \dot{M}, \quad \left. \frac{1}{\rho_1} \frac{\partial \rho}{\partial t} \right|_2 = \hat{H} \dot{M}, \quad \left. \frac{1}{a_1} \frac{\partial a}{\partial t} \right|_2 = \hat{E} \dot{M}, \quad (\text{A.11})$$

where the coefficients are given by

$$\begin{aligned} \hat{F} &= \frac{\partial u_2}{\partial w_1} - MF, & \hat{G} &= \frac{1}{\rho_1 a_1} \frac{\partial P_2}{\partial w_1} - MG, \\ \hat{H} &= \frac{a_1}{\rho_1} \frac{\partial \rho_2}{\partial w_1} - MH, & \hat{E} &= \frac{\partial a_2}{\partial w_1} - ME. \end{aligned}$$

The second-order shock-change equation for  $u_{tt,2}$  is

$$\begin{aligned} \frac{u_{tt,2}}{a_1} &= \frac{1}{a_1} \frac{du_t}{dt} - M u_{xt,2} \\ &= \frac{1}{a_1} \frac{du_t}{dt} - M \left( \frac{du_x}{dt} - M a_1 u_{xx,2} \right) \\ &= \hat{F}' \dot{M}^2 + \hat{F} \ddot{M} - M F' \dot{M}^2 - M F \ddot{M} - M^2 (\ddot{M} + K \dot{M}^2) / L \\ &= (\hat{F} - M F - M^2 / L) \ddot{M} + (\hat{F}' - M F' - M^2 K / L) \dot{M}^2. \end{aligned} \quad (\text{A.12})$$

The result for  $P_{tt,2}$  is derived similarly.

Substituting into (A.10) and grouping terms gives the second-order shock-change equation for  $Q_2$ ,

$$\begin{aligned} Q_2 &= \left( \hat{G} - M G - M^2 / N + \frac{\rho_2 a_2}{\rho_1 a_1} (\hat{F} - M F - M^2 / L) \right) \ddot{M} \\ &+ \left( \hat{G}' - M G' - J M^2 / N + \frac{\rho_2 a_2}{\rho_1 a_1} (\hat{F}' - M F' - K M^2 / L) + \frac{\rho_2}{\rho_1} \hat{E} \hat{F} + \frac{a_2}{a_1} \hat{H} \hat{F} \right) \dot{M}^2. \end{aligned} \quad (\text{A.13})$$

Best's theory is to assume  $Q_2 = 0$ , which can be used to solve (A.13) with appropriate initial conditions.

### A.2.6 Sharma and Radha (1994)

Sharma and Radha (1994) use a series expansion in terms of  $\partial_x^n P$ , where truncation at order  $n$  is used to close the hierarchy of shock-change equations. The required second-order shock-change equation is given by (2.57) and is reproduced here as

$$\ddot{M} + J\dot{M}^2 + N\frac{P_{xx,2}}{\rho_1} = 0.$$

The coefficients,  $J$  and  $N$ , are given by (2.58) and (2.59). The truncation at second order then gives  $P_{xx,2} = 0$ , which reduces (2.57) to a second-order ordinary differential equation requiring the initial conditions  $M_0$  and  $\dot{M}_0$ . The latter is provided by our solution (2.86).

## *Appendix B*

### ADDITIONAL METHODS & DATA: SHOCK SPEED MEASUREMENTS

#### B.1 Detonation Spectrum

Figure B.1 plots spectra acquired for flash lamp and detonation products using an Ocean Optics FX spectrometer. The fiber-coupled collection optic was located on the same optical bread board as the high-speed camera and faced the polycarbonate tube. The shadowgraphy setup was repositioned so that the line-of-sight between the tube and the collection optic was unobstructed. The spectrometer was run in “burst” mode at its highest sampling rate (4.5 kHz). The detonation products spectrum shows broadband emission with saturation at lines associated with sodium and potassium, common contaminants. The flash lamp spectrum is similarly broadband and there is no clear region of the spectrum where filtering would be advantageous.

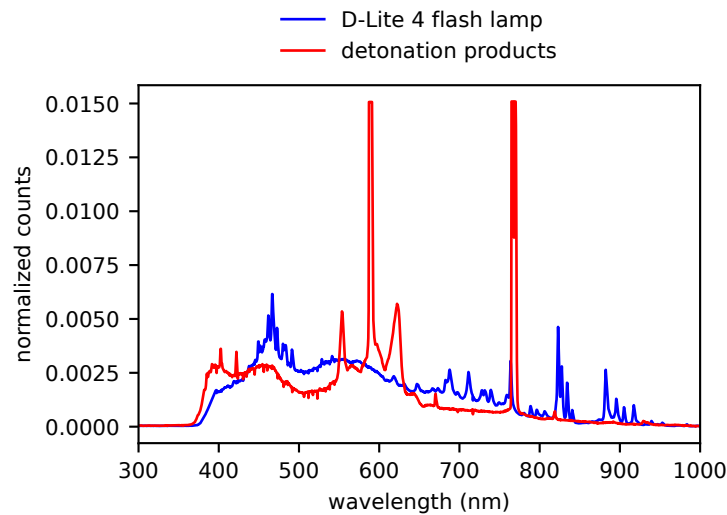


Figure B.1: Spectra of luminous detonation products and flash lamp normalized by the integrated intensity.

#### B.2 Calibration Methods

High-speed videos give shock motion in units of pixels and frames. Conversion of these results to lab-frame coordinates requires three calibrations. First, the motion of the shock shadow on the screen must be converted to the shock’s motion inside

the tube. Second, the position of the shock shadow must be adjusted relative to shock tube reference features. Third, pixel units are converted to real length units. As described in Chapter 5, length calibration was performed using a precision 450-mm scale that was adhered to the screen. Shadow corners were used to measure the scale length in pixels and obtain the spatial calibration. This neglects lens distortion and assumes a flat image field, which was found to be sufficient for the present measurements.

The first two calibration steps were accomplished using an alignment tool that was placed in the shadowgraphy test field on the polycarbonate tube. A photograph of the tool is shown in Figure B.2. The tool is constructed from two segments of T-slot extruded aluminum and two plates. The T-slot rails align the tool parallel with the tube, so that each plate is parallel to a tangent plane. The top plate is aligned horizontally with a bubble level so that the plate in front is normal to the optical axis. The tool is placed on the tube so that the tube lies between the plate and the viewing screen. The shadowgraphy flash lamps are pulsed and a full FOV record of the flash is captured with the high-speed camera. An example frame is shown in Figure B.3 where the alignment tool is placed in front of the left Fresnel lens. Features from these images are used to verify alignment and spatially locate the FOV relative to the shock tube.

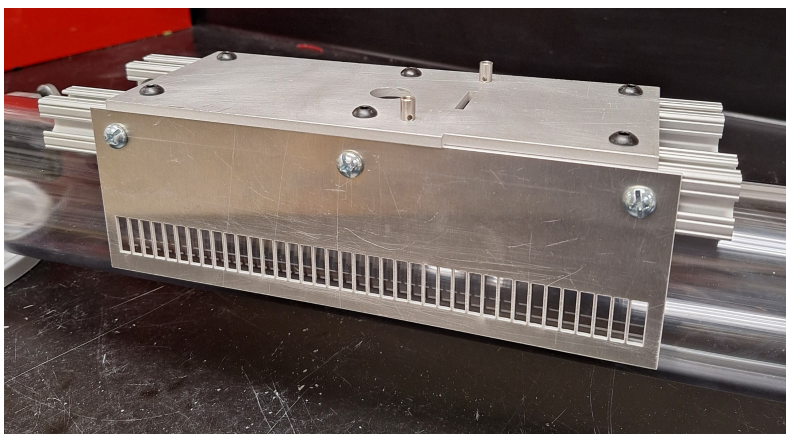


Figure B.2: Photograph of alignment tool positioned on polycarbonate tube.

The front plate of the alignment tool has a linear grid of 37 ribs that project shadows on the screen. Each rib is 1.27-mm wide. A 16-pixel wide strip along the tube centerline that matches the narrow FOV used for high-speed shadowgraphy measurements is extracted from each frame, and the position of each rib's shadow is identified. This is demonstrated in Figure B.4(a) and (b), respectively. The rib shadow posi-

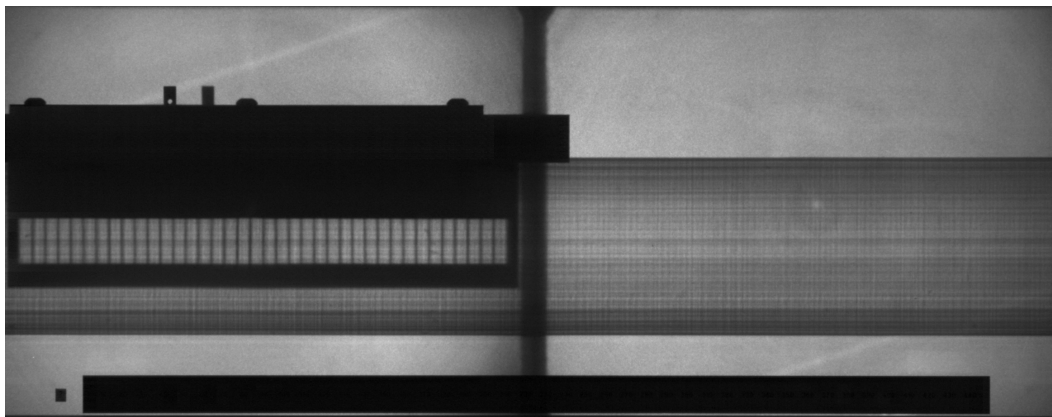


Figure B.3: Calibration image used to obtain pixel size, FOV position, and verify unity magnification.

tions are then compared with the known dimensions of the array to verify that the optical alignment gives a unity magnification, i.e., the measured and true positions are one-to-one. Figure B.4 illustrates these measurements with a linear fit, showing a fitted line with near-unity slope. This shows that the average magnification over the width of the Fresnel lens is nearly unity, however shadowgraphy displacement measurements are performed over only a few pixels, where the magnification must not deviate significantly. Figure B.6 shows the measurements differentiated to illustrate the local magnification variation. Measurements are coarse and results are noisy, so a 4-point moving average is also shown. Typical deviation from unity is within 1%.

On the top plate of the alignment tool, there is a 0.25-in diameter post that is used to identify the position of the shadowgraphy FOV relative to the shock tube. The corners of the post are picked out from the image using a corner detection algorithm (`cv2.cornerSubPix`) in the OpenCV library (Bradski, 2000). A tape measure is used to measure the distance between reference features on the diaphragm closure and the top plate. This method gives measurements accurate to roughly 1 mm.

These calibration and alignment steps were repeated every time the shadowgraphy set-up was repositioned along the tube length. During early experiments, this was also performed on every new day of shots. Early experiments also used a different front plate, where, instead of ribs, a coarser array of 19 slots was used.

### B.3 Post-Processing Algorithm

In Chapter 5, the methods used to post-process high-speed shadowgraphy records was described. These methods were implemented as an algorithm in Python, and



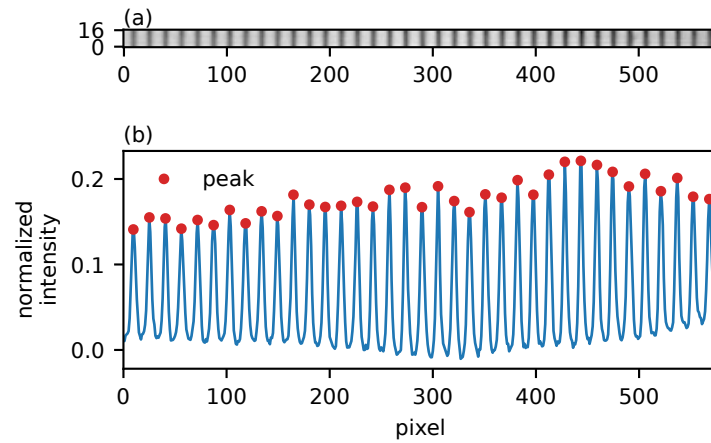


Figure B.4: (a) linear array of shadows from the alignment tool. In (b), the image is vertically averaged and inverted. Peaks are identified.

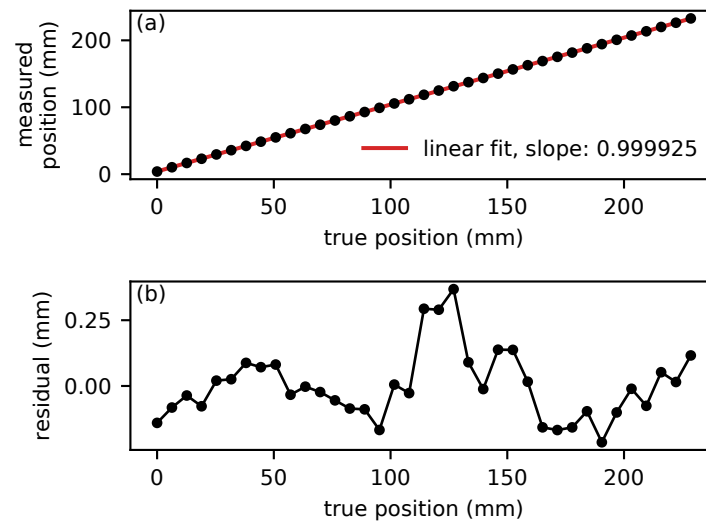


Figure B.5: Measured rib positions from alignment tool are compared with their known true positions.

the code used is reproduced below. The outputs from this script are in units of pixels and frames and are subsequently converted to lab-frame coordinates using calibration data. These additional processing steps, including saving data to file, are excluded below.

```
1 import numpy as np
2 import os
3 import cv2
```

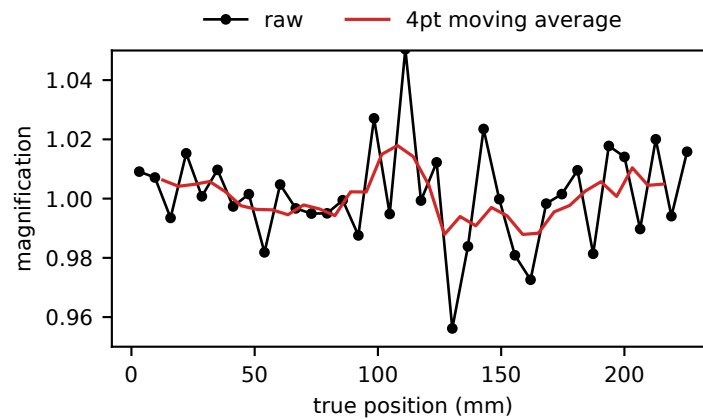


Figure B.6: Spatial variation of magnification from differentiating measured rib positions.

```

4 from scipy import signal
5
6
7 def cine2pxfr(dynamic=True, path=os.getcwd()):
8     # tifs are 16 bit, however v2512 captures 12 bit
9     tifpath_shot = path + '/tifs_shot/'
10    tifpath_ref = path + '/tifs_ref/' # background reference
11    files = os.listdir(tifpath_shot)
12
13    pxfr = np.zeros((len(files), 1280))
14    for i, file in enumerate(files):
15        fullpath_shot = tifpath_shot + file
16        fullpath_shot1 = tifpath_shot + files[0] # 'img000.tif', single reference
17        fullpath_ref = tifpath_ref + file # each reference frame matches each
18        # shot frame
19
20        im_shot = cv2.imread(fullpath_shot, cv2.IMREAD_ANYDEPTH)
21        if dynamic is True:
22            im_ref = cv2.imread(fullpath_ref, cv2.IMREAD_ANYDEPTH)
23        else:
24            im_ref = cv2.imread(fullpath_shot1, cv2.IMREAD_ANYDEPTH)
25
26        #background subtraction
27        im_sub = im_shot.astype('double') - im_ref.astype('double')
28
29        # normalize and vertically average
30        pxfr[i, :] = np.mean(im_sub.astype('double')/65535, axis=0)
31    return pxfr
32
33 def pxfr_hpf(pxfr, wx=71, wt=71, p=5, filter_time=False):
34     filt_x = signal.savgol_filter(pxfr, wx, p, axis=1)
35     if filter_time is True:
36         filt_t = signal.savgol_filter(pxfr-filt_x, wt, p, axis=0)

```

```

37     pxfr_filtered = pxfr - filt_x - filt_t #subtract savgol to hpf
38 else:
39     pxfr_filtered = pxfr - filt_x
40     return pxfr_filtered
41
42
43 def isolate_shocks(pxfr, iso_window=50, threshold=0.01, center_edges=(622, 658)):
44     nf = np.shape(pxfr)[0]
45     shock_fr = []
46     single_shocks = []
47     px = 0
48     # loop through each frame and find shock pixels
49     for f in range(nf):
50         frame = pxfr[f, :]
51         min_px_value = np.min(frame[px:]) # minimum from shadow
52         contrast = -1*min_px_value
53
54         shock_pxi = np.argmin(frame[px:])+px # minimum pixel index
55         sz = len(frame)-1 # 1279
56         # check if shock is near edges
57         if shock_pxi < 5 or shock_pxi > sz-5:
58             valid = False
59         elif shock_pxi > center_edges[0] and shock_pxi < center_edges[1]:
60             valid = False
61         else:
62             valid = True
63
64         if contrast > threshold and valid is True:
65             shock_fr.append(f)
66             px = np.copy(shock_pxi)
67
68             # construct window around shock
69             if shock_pxi < iso_window:
70                 shock_window = range(0, shock_pxi+iso_window)
71             elif shock_pxi > sz-iso_window:
72                 shock_window = range(shock_pxi-iso_window, sz)
73             else:
74                 shock_window = range(shock_pxi-iso_window, shock_pxi+iso_window)
75
76             # clean_frame contains the shock shadow pixels but excludes all other
77             # features, such as from diaphragm particulate
78             clean_frame = np.zeros((np.shape(pxfr)[1],))
79             clean_frame[shock_window] = frame[shock_window]
80             single_shocks.append(clean_frame)
81     return single_shocks, shock_fr
82
83 # Find shock position. subpx_estimate uses 3pt Gaussian fit
84 def find_positions(single_shocks, subpx_estimate=True):
85     Nshocks = len(single_shocks)
86     minima_positions = np.zeros((Nshocks,))
87     maxima_positions = np.zeros((Nshocks,))
88     for j in range(len(single_shocks)):
89         shockjn = np.argmin(single_shocks[j])
90         shockjp = np.argmax(single_shocks[j])

```

```

91     if subpx_estimate is True:
92         Rm, R0, Rp = -1*single_shocks[j][shockjn-1:shockjn+2]
93         inc_n = three_point_Gaussian(R0, Rm, Rp)
94
95         Rm, R0, Rp = -1*single_shocks[j][shockjp-1:shockjp+2]
96         inc_p = three_point_Gaussian(R0, Rm, Rp)
97     else:
98         inc_n = 0
99         inc_p = 0
100     minima_positions[j] = shockjn + inc_n
101     maxima_positions[j] = shockjp + inc_p
102     return minima_positions, maxima_positions
103
104
105 def three_point_Gaussian(R0, Rm, Rp):
106     if Rm <= 0 or Rp <= 0:
107         return 0
108     else:
109         inc = (np.log(Rm)-np.log(Rp))/(2*(np.log(Rm)+np.log(Rp)-2*np.log(R0)))
110         return inc
111
112
113 def displacement_estimator(correlation, lags):
114     int_peak = np.argmax(correlation)
115     Rm, R0, Rp = correlation[int_peak-1:int_peak+2]
116     peak_increment = three_point_Gaussian(R0, Rm, Rp)
117     return lags[int_peak] + peak_increment
118
119
120 def correlate_shock_pairs(single_shocks):
121     Ns = len(single_shocks)
122
123     displacements = np.zeros((Ns-1,))
124     for i in range(1, Ns):
125         shockj0 = single_shocks[i-1]
126         shockj1 = single_shocks[i]
127         corr = signal.correlate(shockj1, shockj0)
128         lags = signal.correlation_lags(shockj1.size, shockj0.size)
129
130         displacement = displacement_estimator(corr, lags)
131         displacements[i-1] = displacement
132     return displacements
133
134
135 if __name__ == '__main__':
136     shot = 212
137     shotpath = 'shot'+str(shot)
138
139     # background subtract cine, vertically average, and save contrast stretched
140     # tiff to file
141     # pxfr is a 2D array. Each row corresponds to a frame. Each column is a
142     # vertically averaged pixel.
143     pxfr = cine2pxfr(path=shotpath)

```

```

143     # high-pass filter pxfr data to remove artifacts from combustion gas,
    diaphragm, lens margins, etc.
144     pxfr_filtered = pxfr_hpf(pxfr, filter_time=True)
145
146     # identify shock in each frame. Check for valid data, threshold
147     single_shocks, pframes = isolate_shocks(pxfr_filtered, )
148
149     # find shock positions
150     positions, _ = find_positions(single_shocks)
151
152     # calculate shock displacements
153     displacements = correlate_shock_pairs(single_shocks)
154
155     # adjust for centered differences
156     px_positions = positions[:-1] + np.diff(positions)/2
157     dframes = pframes[:-1] + np.diff(pframes)/2
158
159     # compute speeds
160     px_speeds = displacements/np.diff(pframes) # units: px/fr

```

## B.4 Shot Conditions

Tables B.1, B.2, and B.3 list all shot conditions tested. For each condition, results from three to four individual experiments are combined to produce the final shock-speed record along the driven section. Calculated parameters from ideal models are also included in each table.

Table B.1: Shot conditions and model parameters for forward-mode driver experiments.  $P_{41}$  is unburnt driver pressure,  $P_1$  is initial pressure of air (20.91%  $O_2$ ) in driven section,  $l$  is Mylar diaphragm thickness.  $M_{s,0}$ ,  $\beta$ , and  $\alpha$  are model parameters.  $\beta$  is reported here nondimensionalized by the driver time scale,  $L/a_1 = 1.27$  ms. The asterisk denotes that the shot condition used a blunt cruciform to support the diaphragm.

no.	driver mixture	$P_{41}$ (kPa)	$P_1$ (kPa)	$l$ ( $\mu\text{m}$ )	$M_{s,0}$	$\beta$	$\alpha$
1	$C_2H_4+3O_2$	50	50	12.7	4.71	2.42	.293
2	$C_2H_4+3O_2$	50	25	12.7	5.72	1.92	.309
3	$C_2H_4+3O_2$	50	15	12.7	6.54	1.62	.315
4	$C_2H_4+3O_2$	50	10	12.7	7.23	1.41	.317
5	$C_2H_4+3O_2$	50	6.5	12.7	7.99	1.22	.315
6	$C_2H_4+3O_2$	50	5	12.7	8.47	1.12	.312
7	$C_2H_4+3O_2$	100	20	25.4	7.31	1.44	.317
8	$C_2H_4+3O_2$	100	13	25.4	8.08	1.24	.315
9	$C_2H_4+3O_2$	100	10	25.4	8.57	1.14	.313
10	$C_2H_4+3O_2$	100	20	25.4*	7.31	1.44	.317
11	$C_2H_4+3O_2$	50	25	25.4	5.72	1.92	.309
12	$C_2H_4+3O_2$	50	15	25.4	6.54	1.62	.315
13	$C_2H_4+3O_2$	50	6.5	25.4	7.99	1.22	.315
14	$C_2H_4+3O_2$	50	25	50.8	5.72	1.92	.309
15	$C_2H_4+3O_2$	50	15	50.8	6.54	1.62	.315
16	$C_2H_4+3O_2$	50	6.5	50.8	7.99	1.22	.315
17	$C_2H_4+3O_2+4Ar$	63.3	18.02	25.4	5.72	1.28	.305
18	$C_2H_4+3O_2+4Ar$	63.3	10.2	25.4	6.54	1.06	.308
19	$C_2H_4+3O_2+4Ar$	63.3	3.92	25.4	8.02	0.76	.300
20	$2H_2+O_2$	87	32.12	25.4	5.72	2.96	.317
21	$2H_2+O_2$	87	20.21	25.4	6.54	2.53	.325
22	$2H_2+O_2$	87	9.56	25.4	7.99	1.96	.329

Table B.2: Shot conditions and model parameters for reverse-mode driver experiments.  $P_{41}$  is unburnt driver pressure,  $P_1$  is initial pressure of air (20.91%  $O_2$ ) in driven section,  $l$  is Mylar diaphragm thickness.  $M_s$  is ideal shock Mach number. The asterisk denotes that the shot condition used a blunt cruciform to support the diaphragm.

no.	driver mixture	test gas	$P_{41}$ (kPa)	$P_1$ (kPa)	$l$ ( $\mu\text{m}$ )	$M_s$
23	$C_2H_4+3O_2$	air	50	50	25.4	2.45
24	$C_2H_4+3O_2$	air	100	50	25.4	3.13
25	$C_2H_4+3O_2$	air	100	25	25.4	3.89
26	$C_2H_4+3O_2$	air	100	15	25.4	4.53
27	$C_2H_4+3O_2$	air	100	10	25.4	5.07
28	$C_2H_4+3O_2$	air	100	5	25.4	6.09
29	$C_2H_4+3O_2$	air	100	25	50.8	3.89
30	$C_2H_4+3O_2$	air	50	12.5	25.4	3.85
31	$C_2H_4+3O_2$	air	100	25	25.4*	3.89
32	$C_2H_4+3O_2+4Ar$	air	100	25	25.4	3.40
33	$C_2H_4+3O_2+4Ar$	air	100	10	25.4	4.39
34	$2H_2+O_2$	air	100	25	25.4	3.45
35	$2H_2+O_2$	air	100	10	25.4	4.64
36	$C_2H_4+3O_2$	Ar	100	15	25.4	4.80
37	$C_2H_4+3O_2$	He+Ar	100	15	25.4	4.31

Table B.3: Shot conditions for high-pressure helium driver using 1100-O aluminum diaphragms

no.	$P_4$ (kPa)	$P_1$ (kPa)	$l$ ( $\mu\text{m}$ )	$M_s$
38	531	5	152.4	3.61
39	1096	5	304.8	4.15

## B.5 Shock Speed Data

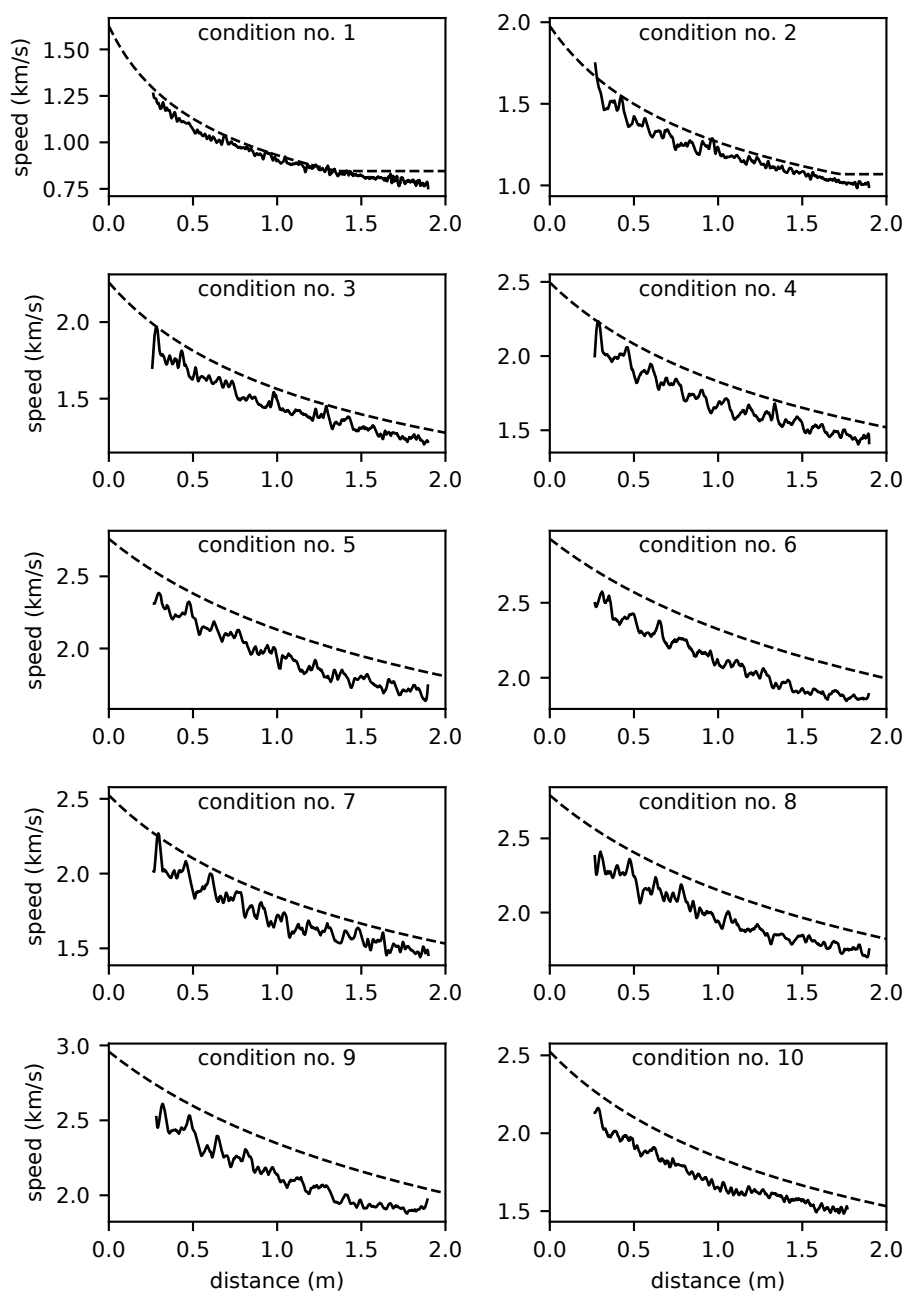


Figure B.7: Shock speed measurements for forward-mode shot condition numbers 1 to 10. Solid line is measurement, dashed line is model. Driver length is 438.6 mm.



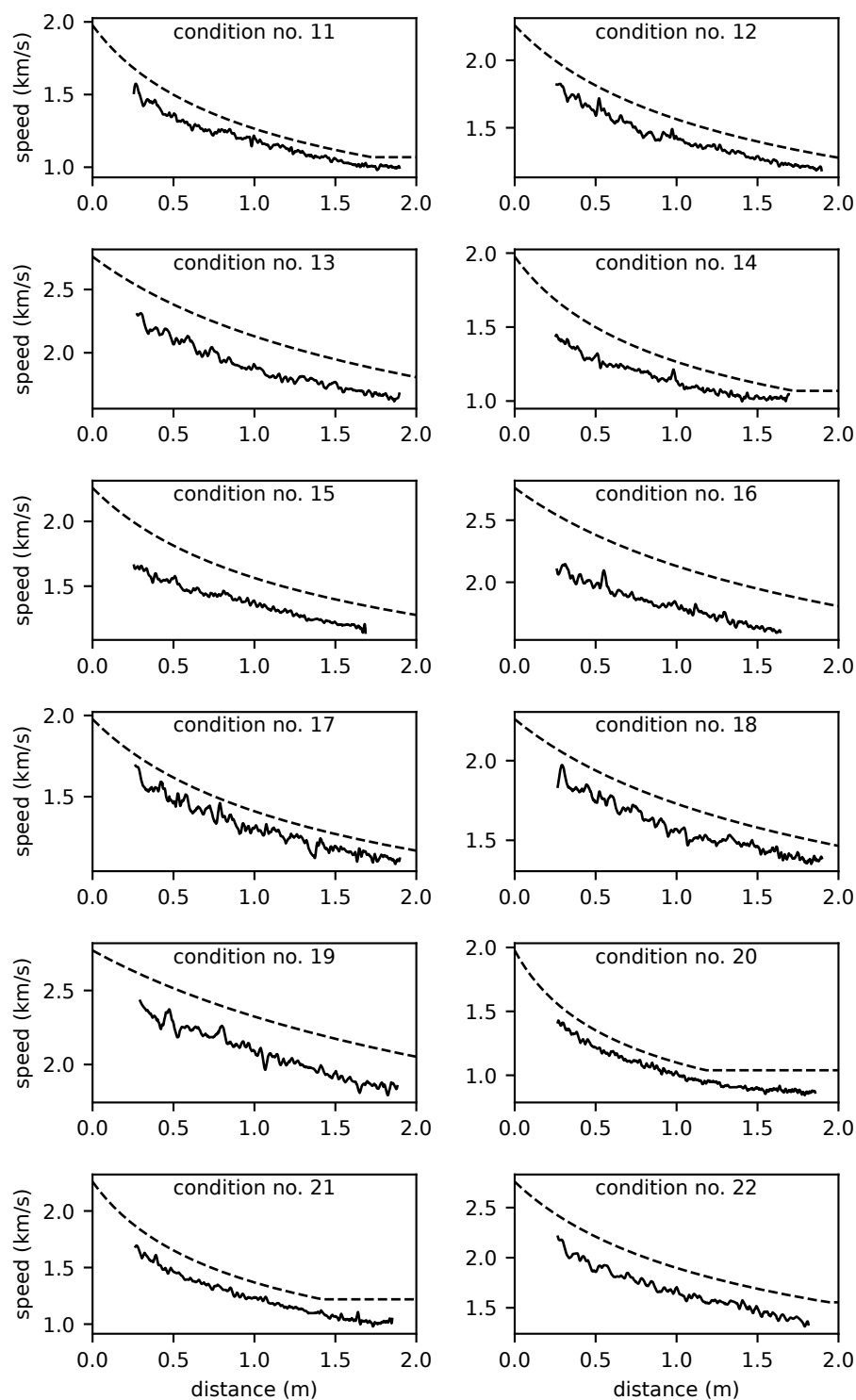


Figure B.8: Shock speed measurements for forward-mode shot condition numbers 11 to 22. Solid line is measurement, dashed line is model. Driver length is 438.6 mm.

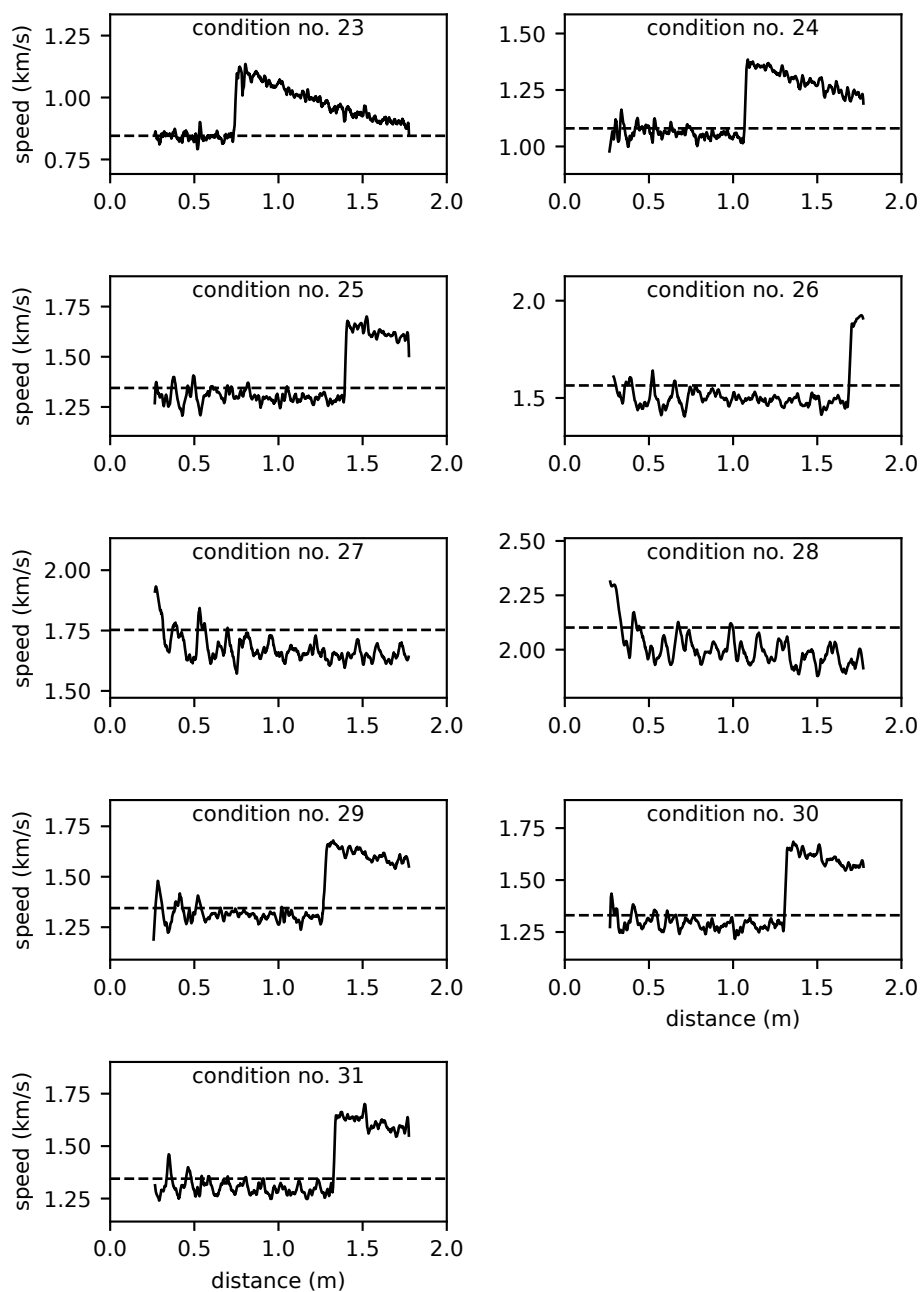


Figure B.9: Shock speed measurements for reverse-mode shot condition numbers 23 to 31. Solid line is measurement, dashed line is model.

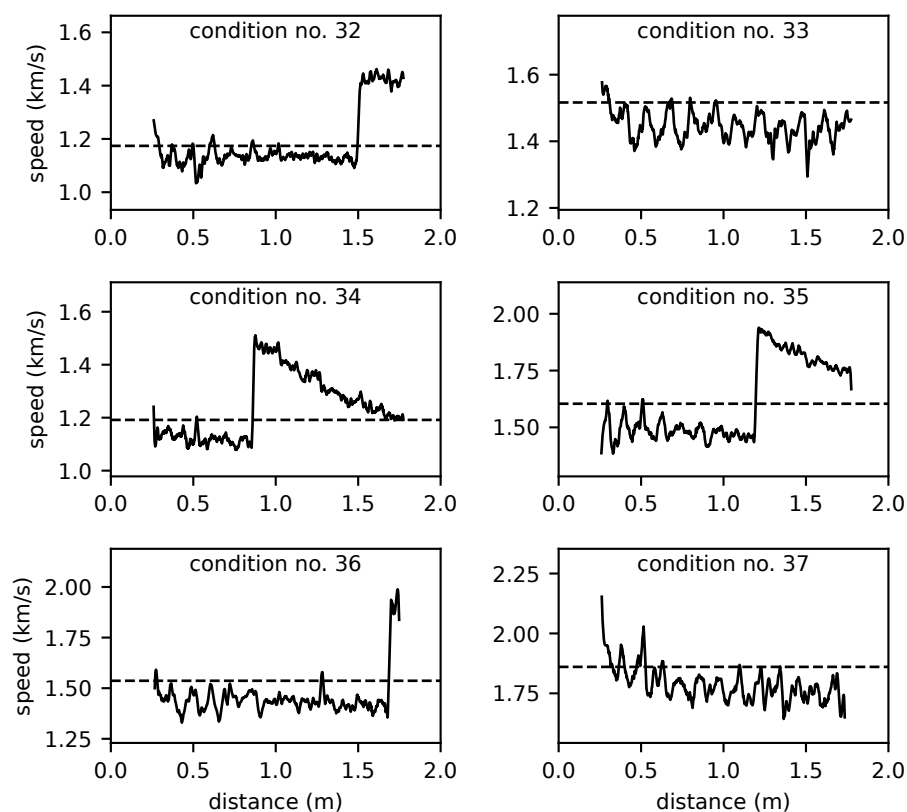


Figure B.10: Shock speed measurements for reverse-mode shot condition numbers 32 to 37. Solid line is measurement, dashed line is model.

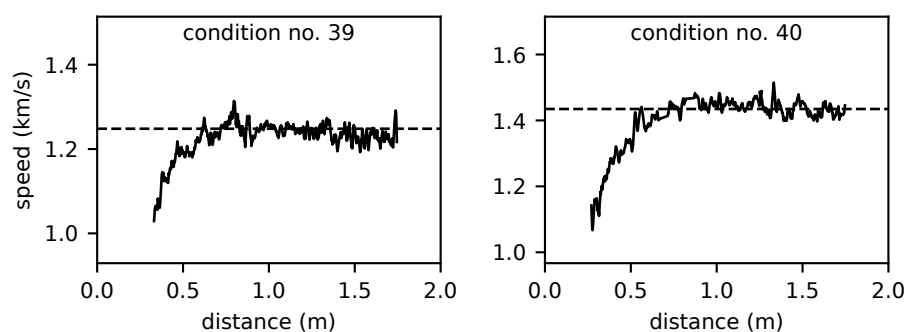


Figure B.11: Shock speed measurements for shot condition numbers 38 and 39 using high-pressure helium driver. Solid line is measurement, dashed line is model.

## B.6 All Calibration Factors

Decay model calibration factors,  $c$ , for all forward-mode shot conditions are plotted in Figure B.12. Values for  $c$  can be used with the decay model to estimate shock trajectories in shock tubes with length-to-diameter ratios comparable to GUST. See (5.4) for the decay model formulated with  $c$ .

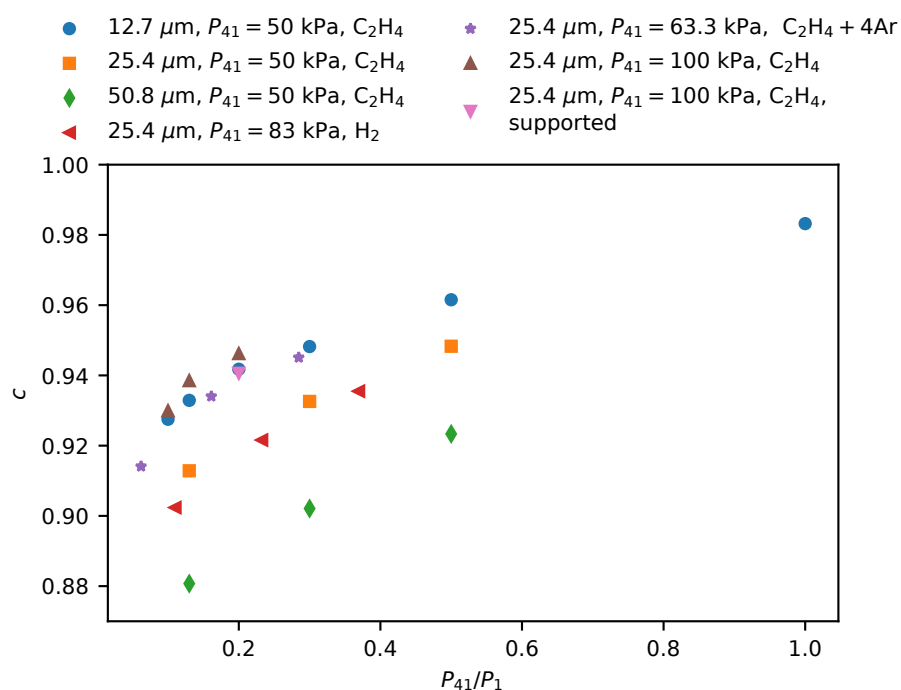


Figure B.12: Calibration factors for all tested shot conditions.

## *Appendix C*

### ULTRA-SENSITIVE FLDI USING BALANCED DETECTION

Signal-to-noise ratio (SNR) is limited in most FLDI implementations by residual intensity noise in the laser. This is true even for high-quality lasers designed to minimize intensity noise. Methods to eliminate laser intensity noise include heterodyne interferometry and laser-noise canceling techniques, like balanced detection. Balanced detection uses either subtraction or division of two signals to cancel common-mode noise. Several auto-balancing circuits are presented and described in detail by Hobbs (1997), and some balanced detectors are commercially available. Here, a simple construction is employed for balanced detection using two reverse-biased photodiodes and a low-noise differential amplifier. Settles and Fulghum (2016) and Benitez et al. (2021) employed balanced detection in FLDI previously with comments on its improvement to SNR, however its performance has not been investigated in detail.

Figure C.1 shows the optical construction used to implement balanced detection. The key difference between this setup and a conventional FLDI is that the signal beams are interfered in a polarizing beam splitter (PBS) instead of with a linear polarizer. The first quarter-wave plate (QWP) is used to generate circularly polarized light, enabling Wollaston prism 1 (WP1) and therefore the foci pair to be oriented at any angle in the  $xy$ -plane. WP2 recombines the beams, and the second QWP allows the analyzer to again be oriented at any angle relative to the foci pair. This is essential for employing a PBS as an analyzer, since the PBS is most conveniently aligned parallel to the optical bench. From the advice given by Hobbs (1997), a linear polarizer was placed at the laser output. This was found to be essential for achieving good noise cancellation.

Photocurrents from the two reverse-biased photodiodes (Thorlabs DET10A) were converted to a voltage signals through  $500\ \Omega$  terminations. The two signals are then differentially amplified with a low-noise amplifier (Stanford Research SR560). Various gain settings were used on the amplifier depending upon the signal level. The differential signal was then balanced by adjusting WP2.

To illustrate the performance of this setup, the ultrasonic source from Chapter 6 is used as a reference signal at 100 kHz. Figure C.2 shows a comparison between

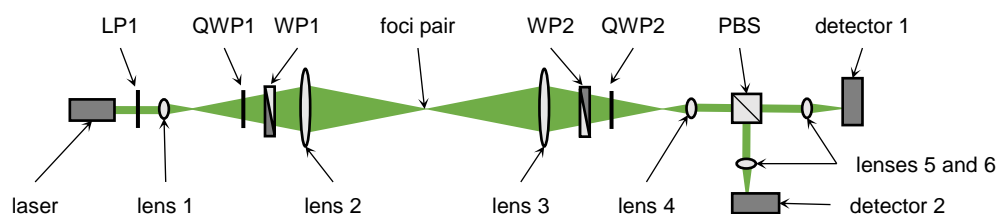


Figure C.1: Schematic for FLDI modified to implement balanced detection. Abbreviated element names refer to linear polarizer (LP), quarter-wave plate (QWP), Wollaston prism (WP), and polarizing beam splitter (PBS).

resulting FLDI signals. (a) shows a single FLDI channel with unity gain, equivalent to the signal produced by a conventional FLDI. (b) shows the effect of amplifying the AC coupled signal, a significant improvement upon (a). This is *not* equivalent to the signal from an amplified photodetector. An FLDI using amplified photodetectors is typically aligned at a half fringe where phase changes are most linear. The signal then carries a significant DC component. Signals are usually AC-coupled with a digitizer's input and vertical resolution is adjusted to fill the instrument's dynamic range. At no point is the AC-signal amplified, and so for low signal levels it must compete with the noise floor of the oscilloscope front end. This can be considerable. In (b), the single-ended signal is AC-coupled with a preamplifier, where it is amplified before digitizing. Noise in (b) is residual laser intensity noise. (c) shows the differential signal for unity gain, i.e., without amplification. Assuming laser noise is canceled, then the noise in (c) is principally from the oscilloscope. Finally, (d) shows the signal obtained with differential amplification, a remarkable improvement upon the conventional measurement in (a).

Power-spectral densities (PSD) are estimated using the method by Welch (1967) for the four cases and plotted in Figure C.3. By implementing balanced detection, the noise floor has been dropped by such a degree that ninth-order signal harmonics are clearly observable. SNR is improved by 30 dB over conventional methods!

In order to quantify how good the laser-noise cancellation is, the instrument noise floor can be compared with the expected shot noise limit from the photocurrent. Hobbs (2008) gives a procedure for making these measurements, where an incandescent light bulb is powered with a low-noise DC supply (better yet, batteries) to generate broadband light, free from intensity noise. By matching photocurrents from detectors obtained with this light source and with the laser, the resulting noise

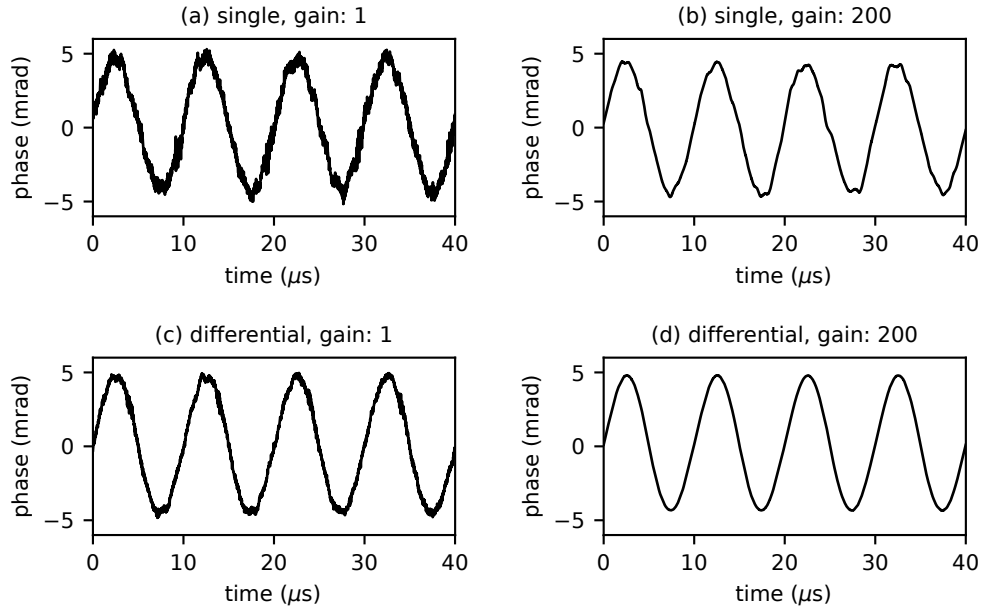


Figure C.2: Comparison of signals obtained using FLDI with balanced detection and differential amplification. (a) shows the signal obtained from a conventional FLDI.

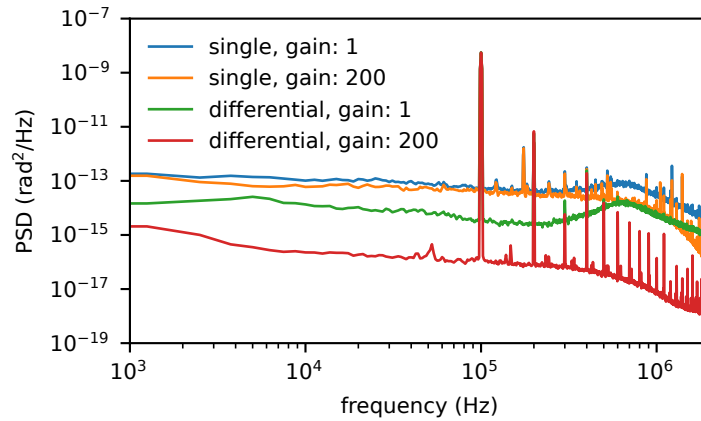


Figure C.3: Comparison of power-spectra of signals obtained using FLDI with balanced detection and differential amplification.

spectra can be compared. To focus enough light onto the photodetectors, a pair of aspheric condenser lenses was used. Power delivered to the light bulb and its position were adjusted until the output voltage from both detectors matched the 1.09 V signal level when using the laser and hence gave a null differential signal. The same gain and low-pass filters were used. Figure C.4 shows these signals. The

white-noise light is barely distinguishable from the balanced FLDI reference signal. Additionally, results can be compared with theoretical expectations for shot noise. The power spectral density,  $S$ , of shot noise from a photocurrent  $i$  is

$$S = 2ie, \quad (\text{C.1})$$

where  $e$  is the charge of an electron, and units of  $S$  are  $\text{A}^2\text{Hz}^{-1}$ . Shot noise is an example of white noise exhibiting a uniform power spectral density across all frequencies. The current noise is converted to voltage noise in the terminating resistor of the photodiode, which is  $500\ \Omega$  in the present case. The voltage noise is assumed to be linearly amplified by the pre-amplifier gain (200). The DC photocurrent was measured to be 2.18 mA, giving an amplified voltage noise density of  $7 \cdot 10^{-12} \text{ V}^2\text{Hz}^{-1}$ . The shot noise from both detectors is uncorrelated, so their subtraction in the amplifier gives an output noise spectral density that is the sum of both. Hence the expected power spectral density from photocurrent shot noise in the detected signal is  $1.4 \cdot 10^{-11} \text{ V}^2\text{Hz}^{-1}$ .

The Stanford Research DS345 function generator was used to generate 10 MHz band-limited white noise. In this bandwidth, the theoretical shot-noise root-mean-square voltage is 8.35 mV in each channel. Two DS835 function generators were configured to deliver 8.35 mV<sub>rms</sub> noise to the differential input of the SR560 preamplifier, configured to unity gain. Figure C.4 shows the resulting power spectral density. The simulated photocurrent shot noise accurately reproduces the measured shot-noise spectral densities from the incandescent light bulb and the FLDI. These two methods verify that the measurements obtained using FLDI with differential amplification are limited only by the shot-noise of the photocurrent.

Figure C.4 shows that white noise measurements are rolled off above 1 MHz. To determine where this roll-off is coming from, the same noise power was directly connected to the oscilloscope input, bypassing the pre-amplifier. As expected the spectrum is flat, verifying that this roll-off is from the SR560 preamplifier.



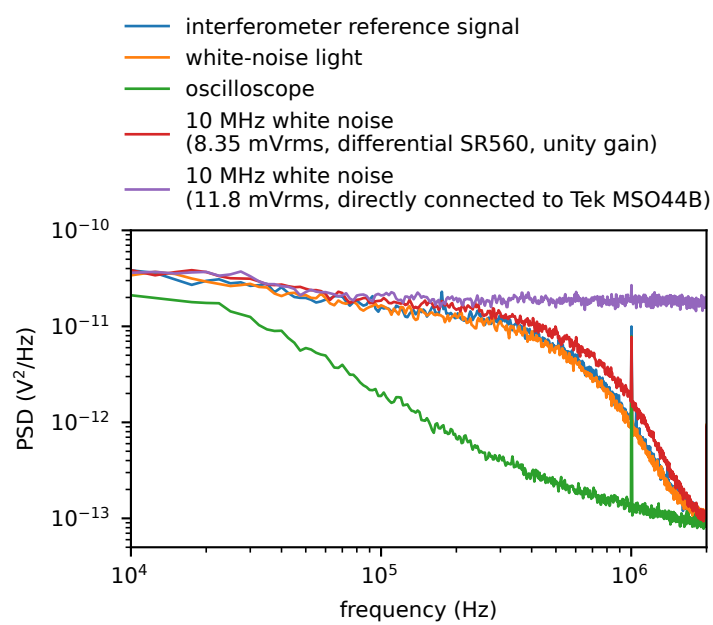


Figure C.4: Comparison of power-spectral densities from balanced FLDI with white-noise sources.

## ADDITIONAL HFLI METHODS

### D.1 Optical Construction

The interferometer schematic is duplicated here for reference as Figure D.1. Tables D.1 and D.2 detail all of the optical and electrical components used in this work with the exception of the Wollaston prisms. 2 arc min Wollaston prisms were repurposed from the FLDI built by Lawson (2021).

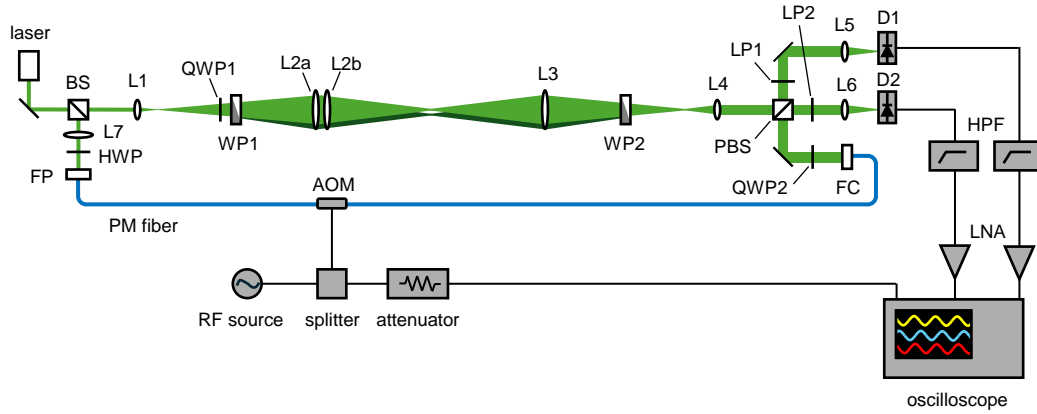


Figure D.1: Diagram of heterodyne focused laser interferometer.

The heterodyne focused laser interferometer was installed in the laboratory test cell by constructing it on a custom optical table. The interferometer was designed so that all free-space optics could be mounted to a 2.5-m optical rail (Newport X95-2.5). All detection optics were fit onto a 12-in square breadboard mounted to the rail. The rail was mounted to the custom optical table and ran underneath the shock-tube test section. Figure D.2 shows a diagram of the optical table construction. It was built from 0.75-in plywood and stacked steel strut channel. This design gave the table sufficient stiffness and some vibration damping through the plywood. The table itself was mounted to the test-cell walls using 1-in thick steel angle braces. The table was floated using four air mounts (Newport SLM-3A). The shape of the table was driven by test-cell mounting location, and consequently the design was asymmetric with the center-of-mass shifted toward one side of the table. In order to evenly load each air mount, an additional 20 kg of ballast was added to each side of the table.

Table D.1: Optical components of interferometer

item	product	description
laser	Coherent Sapphire SF	532 nm, 55 mW max
AOM	G&H Fibre Q	200 MHz, 532 nm, PM fiber, FC/APC
FP	Thorlabs PAF2-A4A	achromatic fiber port
FC	Thorlabs TC25APC-532	FC/APC 25 mm triplet collimator
PM fibers	Thorlabs P3-488PM-FC-1	FC/APC
BS	Thorlabs BS004	50:50 nonpolarizing beam splitter
L1	Thorlabs AC127-025-A	25 mm achromat
L2a & b	Thorlabs AC508-300-A	300 mm achromat
L3	Thorlabs AC508-150-A	150 mm achromat
L4	Thorlabs AC254-200-A	200 mm achromat
L5 & L6	Thorlabs LA1131-A	50 mm plano-convex
L7	Thorlabs LA1484-A-ML	300 mm plano-convex
QWP1 & 2	Thorlabs WPQ10M-532	zero-order quarter-wave plate
HWP	Thorlabs WPH05M-532	zero-order half-wave plate
PBS	Edmund Optics 48-574	25 mm, 532 nm
LP1 & 2	Thorlabs LPVISA050-MP2	linear polarizer
mirrors	Thorlabs BB1-E02	broadband

Table D.2: Electrical components of interferometer

item	product	description
D1 & 2	Thorlabs DET10A	12 V biased Si diode, 350 MHz BW
RF source	G&H 3910	200 MHz, 1 W
splitter	Mini-Circuits Z99SC-62-S+	two-way power splitter
attenuator 1	Mini-Circuits HAT-10A+	10 dB, BNC
attenuator 2	Mini-Circuits BW-S10W2+	10 dB, SMA
attenuator 3	Mini-Circuits BW-S3W2+	3 dB, SMA
LNA	Mini-Circuits ZFL-500LN+	28.8 dB gain, 3 dB NF
HPF	Crystek CHPFL-0010-BNC	10 MHz high-pass, 7 <sup>th</sup> -order Chebyshev
oscilloscope	Tek MSO44B	6.5 GS/s, 500 MHz, 4 Channel

Only optical components and the AOM RF driver were mounted directly to the optical table. All other electrical components were mounted separately with strain-relieved cables to minimize disturbances to the interferometer.

## D.2 Beam Profiling

Real laser beams are not perfectly Gaussian with all energy occupying the lowest order transverse electric and magnetic field mode, TEM-00. Occupation of higher modes leads to more rapid diffraction of a beam and is a typical feature of real lasers. This can also occur in the form of aberrations introduced by optical components.

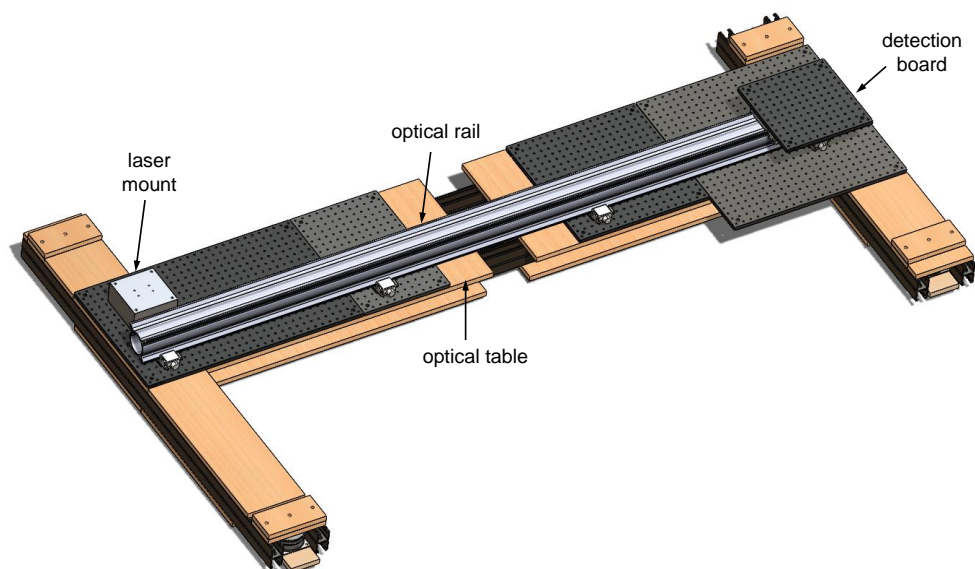


Figure D.2: Diagram of optical table constructed from 0.75-in plywood and steel channels. All free-space optics are rail-mounted.

Deviation from a TEM-00 beam is quantified by the  $M^2$ .

Measurement of a focused beam's waist, typically on the order of micron, requires specialized equipment. The Thorlabs BP209-VIS is used for this. Several representative measurements are included here. These measurements are performed with the test section of GUST removed with the window plugs mounted in their respective positions in the beam path.

Figure D.3 shows the FLDI foci pair, measured using the “slit” mode with 5- $\mu\text{m}$  slits. In this mode, the foci pair separation can be measured and is shown to be 90  $\mu\text{m}$ . Measurement of the beam waist requires use of the BP209-VIS “knife-edge” mode. This is accomplished by rotating QWP1 until it is aligned with the input polarization axis, and so only a single focus is produced. Removing the QWP is not advised as this can affect the focus diameter and position. The “reconstructed knife-edge” profiles generated by the beam profiler software are plotted in Figure D.4. The edges in the wings of both (a) and (b) are thought to be artifacts from the beam profiler. The knife-edge mode requires good alignment. Note, that the beam focus was measured here slightly off center of the device, and the profiles in Figure D.3 are zeroed by their maxima. The dashed lines show the  $1/e^2$  clip-level. The beam is slightly elliptical with the  $x$  and  $y$  widths equal to 13.9 and 8.9  $\mu\text{m}$ , respectively. The beam waist radius is estimated from the mean of the  $x$  and  $y$  widths divided by two and is 5.7  $\mu\text{m}$ .

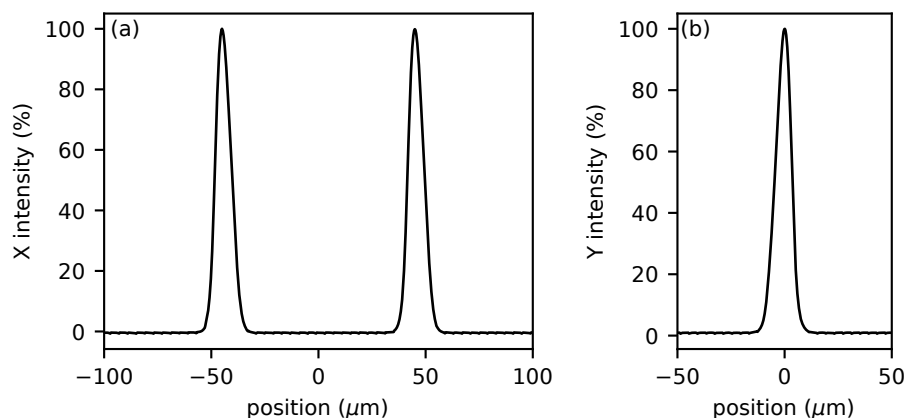


Figure D.3: Foci pair using Thorlabs BP209-VIS in “slit” mode.

A small beam waist results in rapid diffraction. Measurements of the beam radius along the  $z$  axis are shown in Figure D.5. An  $M^2 = 1.02$  most accurately fits the data. This is consistent with the laser manufacturer specification,  $M^2 < 1.1$ .

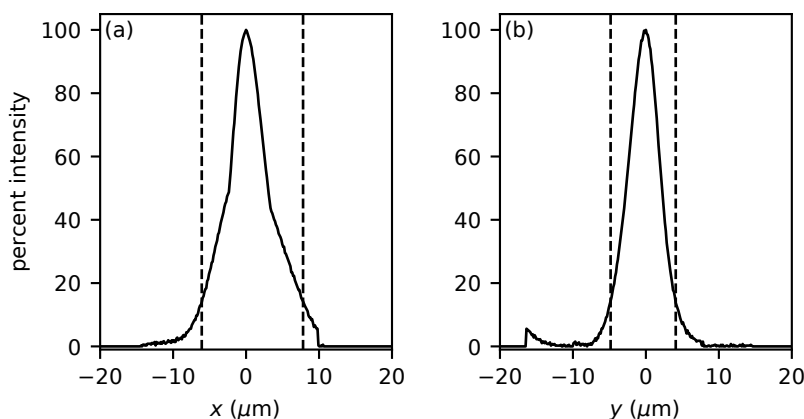


Figure D.4: Focused beam diameter measurements using Thorlabs BP209-VIS in “knife-edge” mode.

### D.3 Spherical Aberration

An initial construction of the interferometer with a fiber-coupled reference beam generated interference patterns with distinct circular or curved fringes. Fringe patterns were photographed by expanding them with a lens and projecting them onto a ground glass screen. Figure D.6(a) and (b) show the fringe pattern obtained with beams slightly tilted and parallel, respectively. Circular fringes can also be obtained from interfering beams with unmatched collimations, however in these

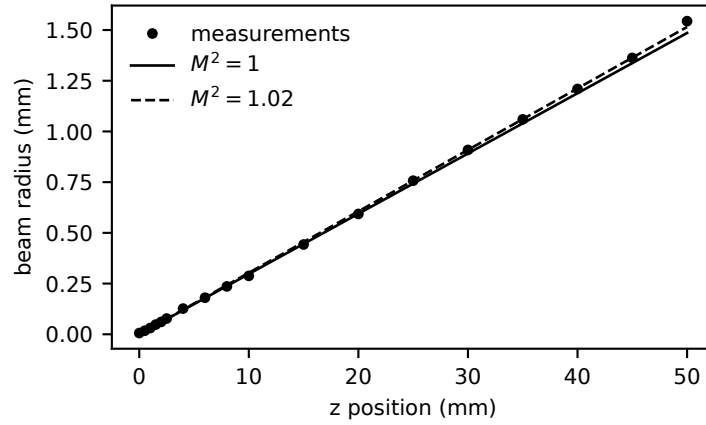


Figure D.5: Beam  $M^2$  measurement.

cases circular fringes extend to the center of the pattern. The fringes shown in Figure D.6(a) and (b) were identified to result from spherical aberration in the free-space beam, which transmits through the optics of an FLDI. The focusing optics in an FLDI generate a system that operates at a high numerical aperture and so is sensitive to the aberrations from real optics. If the system was realigned to a lower numerical aperture, then the number of fringes was reduced, as expected. These fringes are significant because, when the beam is focused onto a single detector, they reduce the fringe visibility and therefore SNR that is achievable.

To compensate for the aberration, all FLDI lenses were replaced with achromatic doublets, and for the pitch focusing lens a pair of doublets were used. Figure D.6(c) shows the fringe pattern and reduced aberration obtained with these new optics. In the final alignment used for the experiments in GUST, a very high numerical aperture was used to achieve a tight focus. Consequently, aberrations were worse than shown in (c).

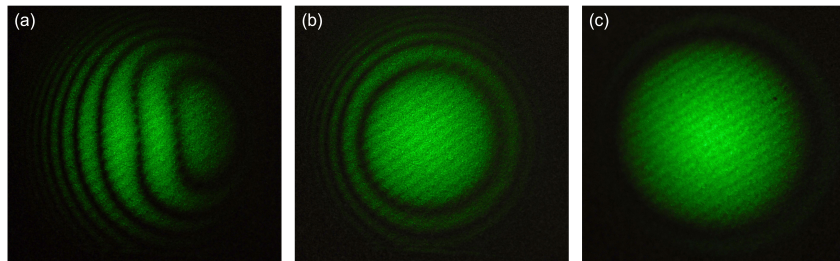


Figure D.6: Fringe patterns obtained from homodyne interferometer setup. Biconvex and plano-convex lenses are used in (a) and (b), where signal and reference beams are slightly tilted in (a). Achromatic doubles are used in (c).

## D.4 IQ Demodulation

### D.4.1 Digital

The methods used for digital IQ demodulation were described in Chapter 6 and were implemented in Python using a slight modification of the code reproduced below. The function actually employed includes additional processing of the wrapped phase data to eliminate artifacts resulting from diaphragm particulate that intersects the laser beam.

```

1 import numpy as np
2 from scipy import signal
3
4 def IQ_demodulate(time, RF, LO, fs=6.25e9, fc=200e6, lpfc=40e6):
5     '''
6     Function used to IQ demodulate experimental data obtained from
7     heterodyne focused laser interferometer.
8     Absolute measurements: LO is reference signal from AOM driver
9     Differential measurements: RF is D1 signal, LO is D2 signal
10
11     Parameters
12     -----
13     time : array of time data
14     RF : array of voltage data for RF
15     LO : array of voltage data for LO
16     fs : sampling rate (S/s)
17     fc : center frequency (Hz)
18     lpfc : low-pass filter cut-off frequency (Hz)
19
20     Returns
21     -----
22     phase : array of unwrapped phase data
23     amplitude: array of amplitude data
24
25     '''
26
27     # see Pei and Lai (2012)
28     def phase_delay_filter(D, N):
29         freqs = np.fft.fftfreq(N)
30         H = np.exp(-1j*D*2*np.pi*freqs)
31         H[0] = 1
32         H[N//2] = np.cos(D*np.pi)
33         return H
34
35     # construct phase delay filter
36     N = len(time)
37     D = -1/fc/4*fs # delay
38     H = phase_delay_filter(D, N)
39
40     # apply phase delay filter
41     LO_fft = np.fft.fft(LO)
42     LO_fft_shift = LO_fft*H
43     LO_delay = np.real(np.fft.ifft(LO_fft_shift))
44

```

```

45 # mix signals
46 I = RF*LO
47 Q = RF*LO_delay
48
49 #8th order Butterworth low-pass filter, second-order sections, forward-
    backward
50 sos = signal.butter(8, lpfc, fs=fs, output='sos', btype='lowpass')
51 I_lpf = signal.sosfiltfilt(sos, I)
52 Q_lpf = signal.sosfiltfilt(sos, Q)
53
54 phase_wrapped = np.arctan2(Q_lpf, I_lpf)
55 amplitude = np.sqrt(I_lpf**2+Q_lpf**2)
56
57 # code used to eliminate blips in wrapped phase is excluded
58 phase = np.unwrap(phase_wrapped)
59
60 return phase, amplitude

```

### D.4.2 Analog

IQ demodulation using analog RF electronics was also investigated with the advantage of enabling long-duration measurements. Figure D.7 shows a block diagram of the prototype system. IQ demodulation was accomplished using an Analog Devices integrated circuit, the ADL5387. In particular, the chip's Evaluation Board was used. The default configuration for the ADL5387-EVAL uses a pair of baluns at the chip's output to convert the differential signal to single-ended. The specific baluns have a usable bandwidth beginning at 900 kHz, so signal cannot be measured at lower baseband frequencies. Consequently, the evaluation board was configured to use the differential baseband output. Figure D.7 shows two of the differential outputs passed through high-pass filters to eliminate the DC bias. By not including the other signal half from the differential output, SNR is reduced by 3 dB.

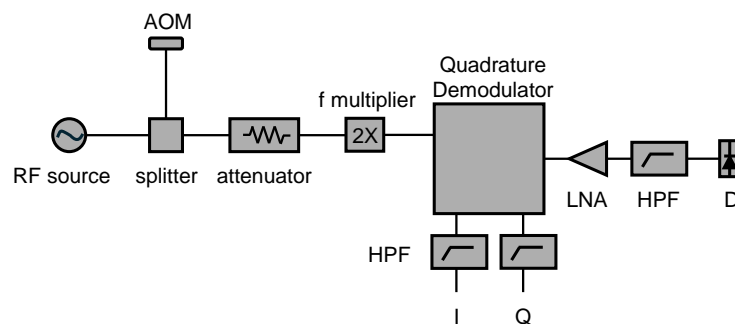


Figure D.7: Schematic of analog IQ demodulation system.

The ADL5387 uses a frequency division architecture to achieve high phase accuracy, and so the LO frequency required is twice the design frequency, i.e., to demodulate



the RF signal at 200 MHz required an input 400 MHz LO. This was generated by attenuating the AOM RF driver and passing the signal through a 2X frequency multiplier (Mini-Circuits ZX90-2-13-S+). The RF input of the ADL5387-EVAL was driven directly by the output of one LNA.

Figure shows an example of the IQ data acquired from this construction where the heterodyne interferometer is resting. As expected, the SNR obtained using analog IQ demodulation was worse than that from the above digital algorithm, and so the analog setup was not used for further measurements. In this case, the ADL5387 has a specified NF of -12 dB. Additionally, by using the heterodyne signals with an analog IQ demodulator, both differential and absolute phase measurements cannot be obtained without further splitting the signals. By digitizing the heterodyne signal, any of the three RF signals can be demodulated in software, and the lost SNR from the reduced ENOB is less significant.

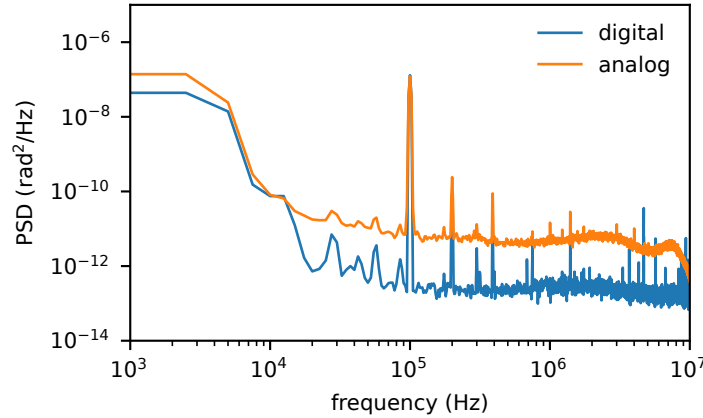


Figure D.8: Comparison of phase measurement using analog and digital IQ demodulation.

## D.5 Noise and Drift

### D.5.1 Laser Noise

Hobbs (2008) discusses laser noise at length, including measurement procedures and mitigation strategies. Of most concern for FLDI measurements is residual intensity noise. This intensity noise is spectrally confined to lower bandwidths, which of course motivates heterodyne detection. Laser noise must be distinguished from photocurrent shot noise or detector noise. For the reverse-biased photodiodes used in this work, noise from dark current is totally swamped by photocurrents. Amplified detectors can add quite a bit of noise from the internal amplification. In

order to discriminate laser noise from shot noise, an incandescent light bulb powered by a regulated DC supply can be used to illuminate detectors until output currents or signal voltages match those with the laser on (Hobbs, 2008). This was described also in Appendix C.

Figure D.9 shows laser noise measurements for two lasers using a Thorlabs PDA36A2 amplified detector. Voltage levels were matched from both lasers using ND filters. The Spectra-Physics Excelsior is the laser used by Lawson (2021), which clearly contains more intensity noise than the Coherent Sapphire SF used in this work. Fancy detection can be used to reduce laser noise, but using a better laser helps too. “White-noise” light refers to the incandescent light bulb. Above about 10 kHz, the additive shot noise is apparent. Below 10 kHz, the noise floor is limited by the oscilloscope itself (this is measured by terminating the output at  $50\ \Omega$ , which is the output impedance of the PDA36A2 detector). Laser noise drops off as frequencies approach 10 MHz.

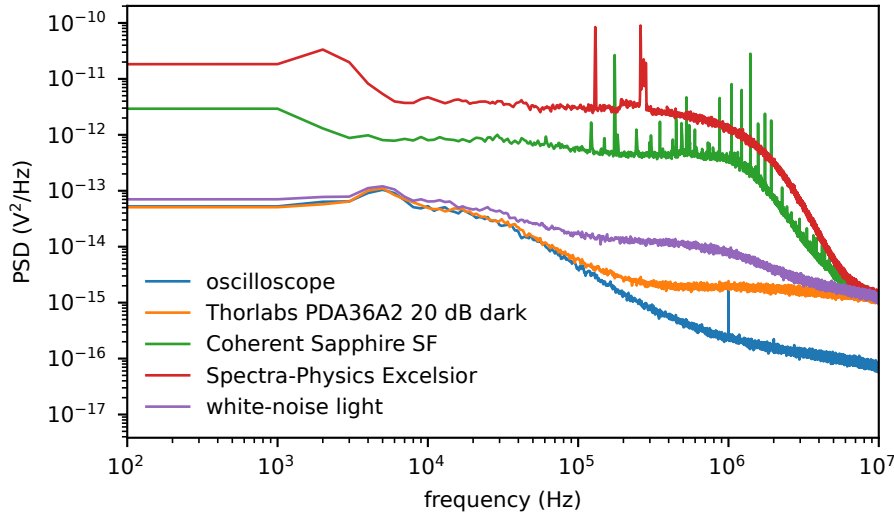


Figure D.9: Laser noise measurements.

### D.5.2 Free-Space Mach-Zehnder Interferometer

While troubleshooting the HFLI, the fiber-coupled reference beam was removed and replaced with mirrors to align the setup as a free-space Mach-Zehnder interferometer. In order to make large amplitude phase measurements over long durations, the analog IQ demodulator was used for the HFLI. For the free-space interferometer, optical IQ demodulation was employed using the QWP trick described by Hogenboom and DiMarzio (1998). Optical IQ demodulation could have been used for the

fiber-coupled interferometer and that would provide a more one-to-one comparison, but in separate studies the AOM was not found to significantly affect the signal drift. Figure D.10 shows a comparison between the resting phase signal for the fiber-coupled versus the free-space interferometers. The drift in the fiber-coupled interferometer is huge.

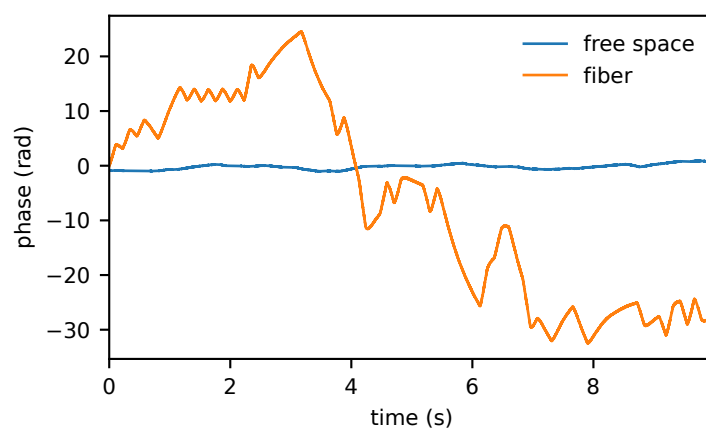


Figure D.10: Comparison between phase signals measured using a reference beam that was fiber-coupled versus in free-space.

## Appendix E

## ADDITIONAL HFLI DATA

**E.1 Shot Conditions**

Shot conditions are listed in Table E.1. For forward (fwd) and reverse (rev) mode shot conditions, the driver gas is the fuel with or without diluent. For conditions where the driven gas is air, bottled Ultra-Zero air was used (20.91% O<sub>2</sub>). All conditions use a stoichiometric mixture with pure oxygen. The backward (bwd) mode refers to calibration conditions where the driven section is filled to a static high-pressure so that the shock tube is operated backwards. High-pressure (HiP) mode refers to operation as a conventional shock-tube with a static high-pressure driver gas.  $l$  denotes the diaphragm thickness and whether the diaphragm is supported (sup.) or unsupported (unsup.) is noted. For all conditions using an aluminum diaphragm, the alloy is 1100-O.

Table E.1: Shot conditions for HFLI measurements.

shot no.	$P_{41}$ (kPa)	$P_1$ (kPa)	driver	driven	mode	$l$ ( $\mu\text{m}$ )	material	note
375	50.0	10.0	C <sub>2</sub> H <sub>4</sub>	air	fwd	25.4	Mylar	unsup.
376	50.0	10.0	C <sub>2</sub> H <sub>4</sub>	air	fwd	25.4	Mylar	unsup.
377	50.0	5.0	C <sub>2</sub> H <sub>4</sub>	air	fwd	25.4	Mylar	unsup.
378	50.0	5.0	C <sub>2</sub> H <sub>4</sub>	air	fwd	25.4	Mylar	unsup.
379	50.0	10.0	C <sub>2</sub> H <sub>4</sub>	air	fwd	25.4	Mylar	unsup.
380	50.0	5.0	C <sub>2</sub> H <sub>4</sub>	air	fwd	25.4	Mylar	unsup.
381	50.0	5.0	C <sub>2</sub> H <sub>4</sub>	air	fwd	12.7	Mylar	unsup.
382	50.0	5.0	C <sub>2</sub> H <sub>4</sub>	air	fwd	12.7	Mylar	unsup.
383	50.0	10.0	C <sub>2</sub> H <sub>4</sub>	air	fwd	12.7	Mylar	unsup.
384	50.0	10.0	C <sub>2</sub> H <sub>4</sub>	air	fwd	12.7	Mylar	unsup.
385	50.0	10.0	C <sub>2</sub> H <sub>4</sub>	air	fwd	12.7	Mylar	sup.
386	50.0	5.0	C <sub>2</sub> H <sub>4</sub>	air	fwd	12.7	Mylar	sup.
387	50.0	5.0	C <sub>2</sub> H <sub>4</sub>	air	fwd	12.7	Mylar	sup.

Continued on next page

Table E.1: Shot conditions for HFLI measurements. (Continued)

shot no.	$P_{41}$ (kPa)	$P_1$ (kPa)	driver	driven	mode	$l$ ( $\mu\text{m}$ )	material	note
388	50.0	2.0	C <sub>2</sub> H <sub>4</sub>	air	fwd	12.7	Mylar	sup.
389	50.0	2.0	C <sub>2</sub> H <sub>4</sub>	air	fwd	12.7	Mylar	sup.
390	50.0	1.0	C <sub>2</sub> H <sub>4</sub>	air	fwd	12.7	Mylar	sup.
391	40.0	1.0	C <sub>2</sub> H <sub>4</sub>	air	fwd	12.7	Mylar	sup.
392	40.0	1.0	C <sub>2</sub> H <sub>4</sub>	air	fwd	12.7	Mylar	sup.
393	50.0	15.0	C <sub>2</sub> H <sub>4</sub>	air	fwd	12.7	Mylar	sup.
394	50.0	15.0	C <sub>2</sub> H <sub>4</sub>	air	fwd	12.7	Mylar	sup.
395	50.0	25.0	C <sub>2</sub> H <sub>4</sub>	air	fwd	12.7	Mylar	sup.
396	50.0	25.0	C <sub>2</sub> H <sub>4</sub>	air	fwd	12.7	Mylar	sup.
398	100.0	10.0	C <sub>2</sub> H <sub>4</sub>	air	fwd	25.4	Mylar	sup.
399	100.0	20.0	C <sub>2</sub> H <sub>4</sub>	air	fwd	25.4	Mylar	sup.
400	100.0	10.0	C <sub>2</sub> H <sub>4</sub>	air	fwd	25.4	Mylar	sup.
401	100.0	10.0	C <sub>2</sub> H <sub>4</sub>	air	fwd	25.4	Mylar	sup.
402	100.0	20.0	C <sub>2</sub> H <sub>4</sub>	air	fwd	25.4	Mylar	sup.
403	100.0	20.0	C <sub>2</sub> H <sub>4</sub>	air	fwd	25.4	Mylar	sup.
404	50.0	5.0	C <sub>2</sub> H <sub>4</sub>	air	fwd	12.7	Mylar	unsup.
405	100.0	10.0	C <sub>2</sub> H <sub>4</sub>	air	fwd	25.4	Mylar	unsup.
406	100.0	10.0	C <sub>2</sub> H <sub>4</sub>	air	fwd	25.4	Mylar	unsup.
407	100.0	10.0	C <sub>2</sub> H <sub>4</sub>	air	fwd	25.4	Mylar	unsup.
409	100.0	20.0	C <sub>2</sub> H <sub>4</sub>	air	fwd	25.4	Mylar	unsup.
410	100.0	20.0	C <sub>2</sub> H <sub>4</sub>	air	fwd	25.4	Mylar	unsup.
411	25.0	25.0	C <sub>2</sub> H <sub>4</sub>	C <sub>2</sub> H <sub>4</sub>	det			none
412	0.0	170.9	vac	He	bwd	25.4	Mylar	unsup.
413	0.0	164.0	vac	He	bwd	25.4	Mylar	unsup.
414	0.0	177.8	vac	He	bwd	25.4	Mylar	unsup.
417	0.0	188.2	vac	N <sub>2</sub>	bwd	25.4	Mylar	unsup.
418	100.3	1.0	N <sub>2</sub>	Ar	HiP	50.8	alum.	unsup.

Continued on next page

Table E.1: Shot conditions for HFLI measurements. (Continued)

shot no.	$P_{41}$ (kPa)	$P_1$ (kPa)	driver	driven	mode	$l$ ( $\mu\text{m}$ )	material	note
419	100.3	1.0	N <sub>2</sub>	Ar	HiP	50.8	alum.	unsup.
420	100.3	2.0	N <sub>2</sub>	Ar	HiP	50.8	alum.	unsup.
421	229.5	1.0	N <sub>2</sub>	Ar	HiP	76.2	alum.	unsup.
422	226.1	1.0	N <sub>2</sub>	Ar	HiP	76.2	alum.	unsup.
423	229.5	2.0	N <sub>2</sub>	Ar	HiP	76.2	alum.	unsup.
424	229.5	2.0	N <sub>2</sub>	Ar	HiP	76.2	alum.	unsup.
425	100.0	10.0	C <sub>2</sub> H <sub>4</sub> +4Ar	air	fwd	25.4	Mylar	sup.
426	100.0	10.0	C <sub>2</sub> H <sub>4</sub> +4Ar	air	fwd	25.4	Mylar	sup.
427	100.0	20.0	C <sub>2</sub> H <sub>4</sub> +4Ar	air	fwd	25.4	Mylar	sup.
428	100.0	20.0	C <sub>2</sub> H <sub>4</sub> +4Ar	air	fwd	25.4	Mylar	sup.
429	100.0	10.0	H <sub>2</sub>	air	fwd	25.4	Mylar	sup.
430	100.0	10.0	H <sub>2</sub>	air	fwd	25.4	Mylar	sup.
431	100.0	20.0	H <sub>2</sub>	air	fwd	25.4	Mylar	sup.
432	100.0	20.0	H <sub>2</sub>	air	fwd	25.4	Mylar	sup.
433	100.0	5.0	C <sub>2</sub> H <sub>4</sub>	air	fwd	25.4	Mylar	sup.
434	100.0	5.0	C <sub>2</sub> H <sub>4</sub>	air	fwd	25.4	Mylar	sup.
435	100.0	10.0	C <sub>2</sub> H <sub>4</sub>	air	fwd	12.7	Mylar	sup.
436	100.0	5.0	C <sub>2</sub> H <sub>4</sub>	air	fwd	12.7	Mylar	sup.
437	0.0	184.7	vac	N <sub>2</sub>	bwd	25.4	Mylar	unsup.
438	0.0	181.1	vac	N <sub>2</sub>	bwd	25.4	Mylar	unsup.
439	0.0	181.1	vac	N <sub>2</sub>	bwd	25.4	Mylar	unsup.
440	0.0	184.6	vac	N <sub>2</sub>	bwd	25.4	Mylar	unsup.
441	0.0	174.2	vac	He	bwd	25.4	Mylar	unsup.
442	100.0	10.0	C <sub>2</sub> H <sub>4</sub>	air	fwd	50.8	Mylar	sup.
443	100.0	10.0	C <sub>2</sub> H <sub>4</sub>	air	fwd	50.8	Mylar	sup.
444	100.0	10.0	C <sub>2</sub> H <sub>4</sub>	air	fwd	25.4	Kapton	sup.
445	100.0	10.0	C <sub>2</sub> H <sub>4</sub>	air	fwd	25.4	Kapton	sup.

Continued on next page

Table E.1: Shot conditions for HFLI measurements. (Continued)

shot no.	$P_{41}$ (kPa)	$P_1$ (kPa)	driver	driven	mode	$l$ ( $\mu\text{m}$ )	material	note
446	100.0	10.0	C <sub>2</sub> H <sub>4</sub>	air	fwd	25.4	Nylon 6/6	sup.
447	100.0	10.0	C <sub>2</sub> H <sub>4</sub>	air	fwd	25.4	Nylon 6/6	sup.
448	35.2	35.2	C <sub>2</sub> H <sub>4</sub>	C <sub>2</sub> H <sub>4</sub>	det			none
449	100.0	40.0	H <sub>2</sub>	air	fwd	25.4	Mylar	sup.
450	100.0	50.0	H <sub>2</sub>	air	fwd	25.4	Mylar	sup.
451	100.0	10.0	C <sub>2</sub> H <sub>4</sub>	air	rev	25.4	Mylar	sup.
452	100.0	10.0	C <sub>2</sub> H <sub>4</sub>	air	rev	25.4	Mylar	sup.
453	100.0	5.0	C <sub>2</sub> H <sub>4</sub>	air	rev	25.4	Mylar	sup.
454	100.0	5.0	C <sub>2</sub> H <sub>4</sub>	air	rev	25.4	Mylar	sup.
455	100.0	2.5	C <sub>2</sub> H <sub>4</sub>	air	rev	25.4	Mylar	sup.
456	100.0	10.0	C <sub>2</sub> H <sub>4</sub>	air	rev	25.4	Mylar	unsup.
457	100.0	10.0	C <sub>2</sub> H <sub>4</sub>	air	rev	25.4	Mylar	unsup.
458	100.0	5.0	C <sub>2</sub> H <sub>4</sub>	air	rev	25.4	Mylar	unsup.
459	100.0	5.0	C <sub>2</sub> H <sub>4</sub>	air	rev	25.4	Mylar	unsup.
460	100.0	20.0	C <sub>2</sub> H <sub>4</sub>	air	rev	25.4	Mylar	sup.
461	100.0	2.5	C <sub>2</sub> H <sub>4</sub>	air	rev	25.4	Mylar	sup.
463	50.0	5.0	C <sub>2</sub> H <sub>4</sub>	air	rev	25.4	Mylar	sup.
464	100.0	10.0	C <sub>2</sub> H <sub>4</sub>	air	rev	50.8	Mylar	sup.
465	100.0	10.0	C <sub>2</sub> H <sub>4</sub> +4Ar	air	rev	25.4	Mylar	sup.
466	100.0	10.0	C <sub>2</sub> H <sub>4</sub> +4Ar	air	rev	25.4	Mylar	sup.
467	100.0	5.0	C <sub>2</sub> H <sub>4</sub> +4Ar	air	rev	25.4	Mylar	sup.
468	100.0	5.0	C <sub>2</sub> H <sub>4</sub> +4Ar	air	rev	25.4	Mylar	sup.
469	100.0	1.0	C <sub>2</sub> H <sub>4</sub>	air	rev	25.4	Mylar	sup.
470	100.0	10.0	H <sub>2</sub>	air	rev	25.4	Mylar	sup.
471	100.0	5.0	H <sub>2</sub>	air	rev	25.4	Mylar	sup.
472	100.0	5.0	H <sub>2</sub>	air	rev	25.4	Mylar	sup.
473	100.0	10.0	C <sub>2</sub> H <sub>4</sub>	Ar	rev	25.4	Mylar	sup.

Continued on next page

Table E.1: Shot conditions for HFLI measurements. (Continued)

shot no.	$P_{41}$ (kPa)	$P_1$ (kPa)	driver	driven	mode	$l$ ( $\mu\text{m}$ )	material	note
474	100.0	10.0	C <sub>2</sub> H <sub>4</sub>	Ar	rev	25.4	Mylar	sup.
475	100.0	5.0	C <sub>2</sub> H <sub>4</sub>	Ar	rev	25.4	Mylar	sup.
476	100.0	5.0	C <sub>2</sub> H <sub>4</sub>	Ar	rev	25.4	Mylar	sup.
477	100.0	10.0	C <sub>2</sub> H <sub>4</sub>	He	rev	25.4	Mylar	sup.
478	100.0	10.0	C <sub>2</sub> H <sub>4</sub>	He	rev	25.4	Mylar	sup.
479	100.0	5.0	C <sub>2</sub> H <sub>4</sub>	He	rev	25.4	Mylar	sup.
480	100.0	5.0	C <sub>2</sub> H <sub>4</sub>	He	rev	25.4	Mylar	sup.
481	100.0	1.0	C <sub>2</sub> H <sub>4</sub> +4Ar	air	rev	25.4	Mylar	sup.
482	100.0	1.0	C <sub>2</sub> H <sub>4</sub> +4Ar	air	rev	25.4	Mylar	sup.
483	100.0	1.0	C <sub>2</sub> H <sub>4</sub> +4Ar	N <sub>2</sub>	rev	25.4	Mylar	sup.
484	100.0	1.0	C <sub>2</sub> H <sub>4</sub>	Ar	rev	25.4	Mylar	sup.
485	100.0	1.0	C <sub>2</sub> H <sub>4</sub> +4Ar	Ar	rev	25.4	Mylar	sup.
486	100.0	2.0	C <sub>2</sub> H <sub>4</sub>	Ar	rev	25.4	Mylar	sup.
487	100.0	3.0	C <sub>2</sub> H <sub>4</sub>	Ar	rev	25.4	Mylar	sup.
488	526.1	5.0	He	air	HiP	152.4	alum.	unsup.
489	531.2	5.0	He	air	HiP	152.4	alum.	unsup.
490	527.8	1.0	He	air	HiP	152.4	alum.	unsup.
491	529.5	2.5	He	air	HiP	152.4	alum.	unsup.
492	1098.2	5.0	He	air	HiP	304.8	alum.	unsup.
493	1089.6	5.0	He	air	HiP	304.8	alum.	unsup.
494	1087.8	1.0	He	air	HiP	304.8	alum.	unsup.
495	1098.2	1.0	He	air	HiP	304.8	alum.	unsup.
496	1087.8	2.5	He	air	HiP	304.8	alum.	unsup.
497	1093.0	2.5	He	air	HiP	304.8	alum.	unsup.
498	528.8	2.5	He	N <sub>2</sub>	HiP	152.4	alum.	unsup.



## E.2 Additional Data: Absolute Phase

HFLI data from all shots in Table E.1 are plotted below in units of unwrapped absolute phase. The complete 2-ms record is plotted. For all cases the spanwise distance is  $L = 76.2$  mm, which can be used to convert phase to index units by  $\Delta n = \Delta\phi/2\pi \cdot \lambda/L$  within the wavenumber bandwidth defined by (6.59). For post-shock flows, the measured shock speed is included.

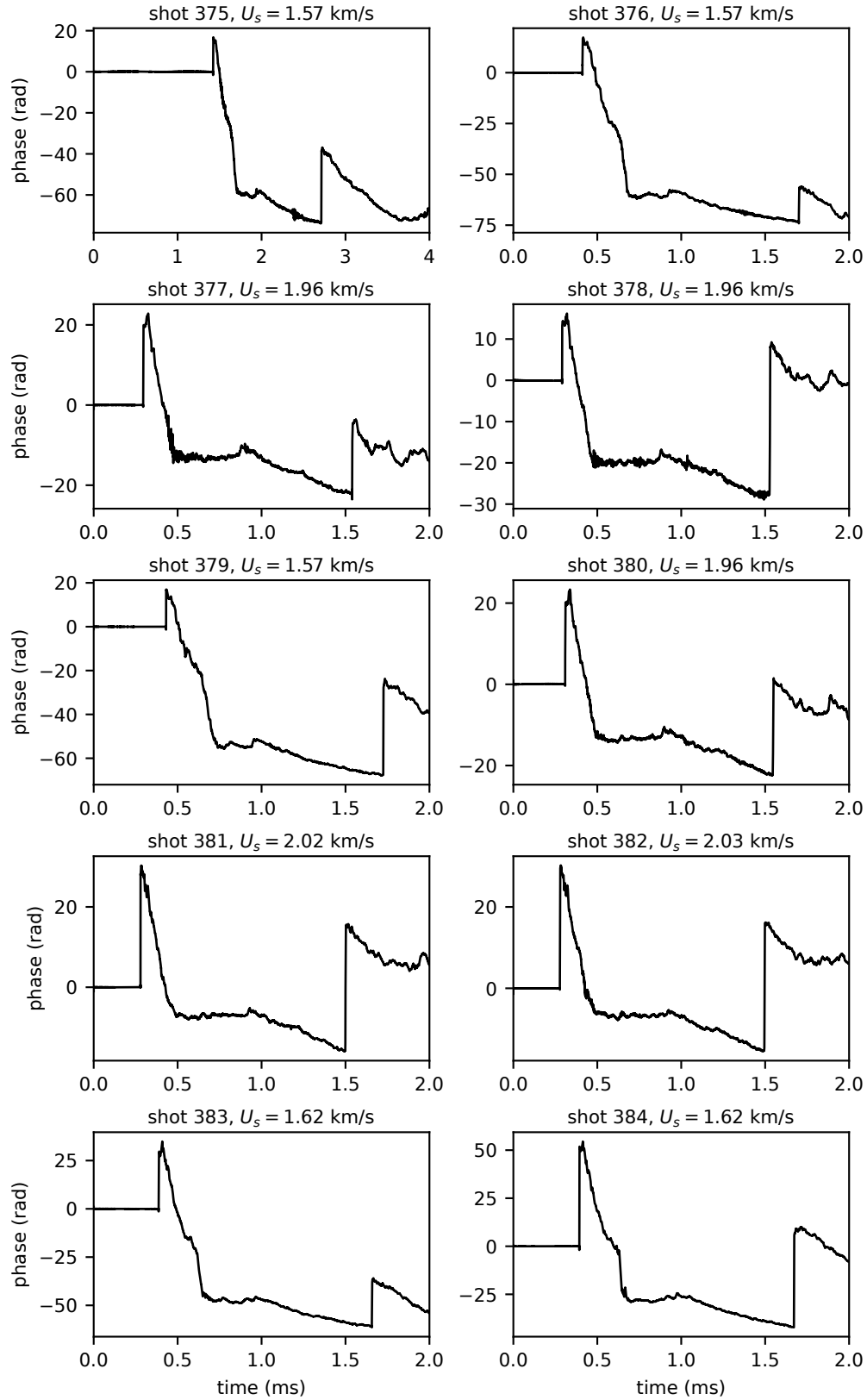


Figure E.1: Absolute phase data for shots 375 to 384.

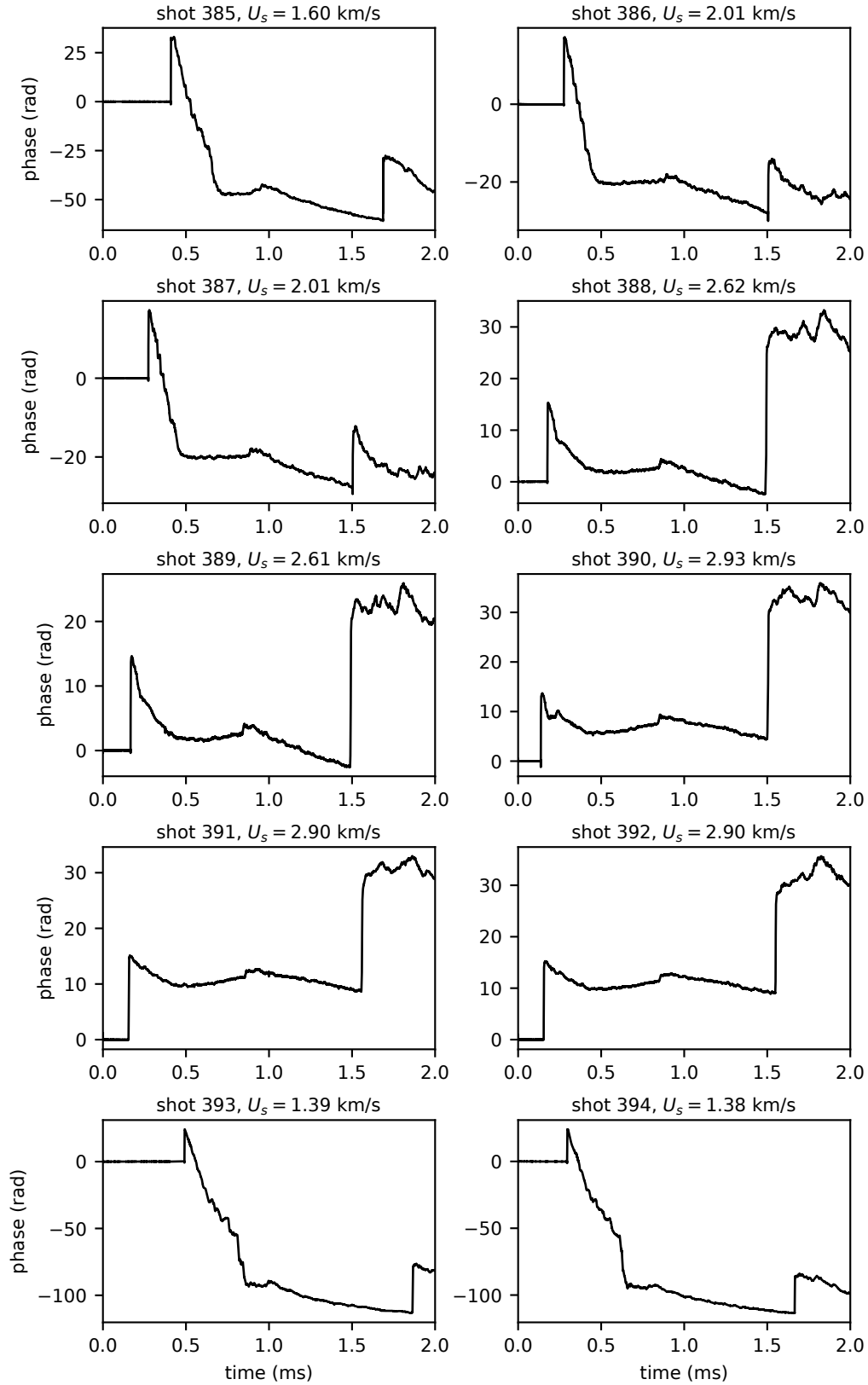


Figure E.2: Absolute phase data for shots 385 to 394.

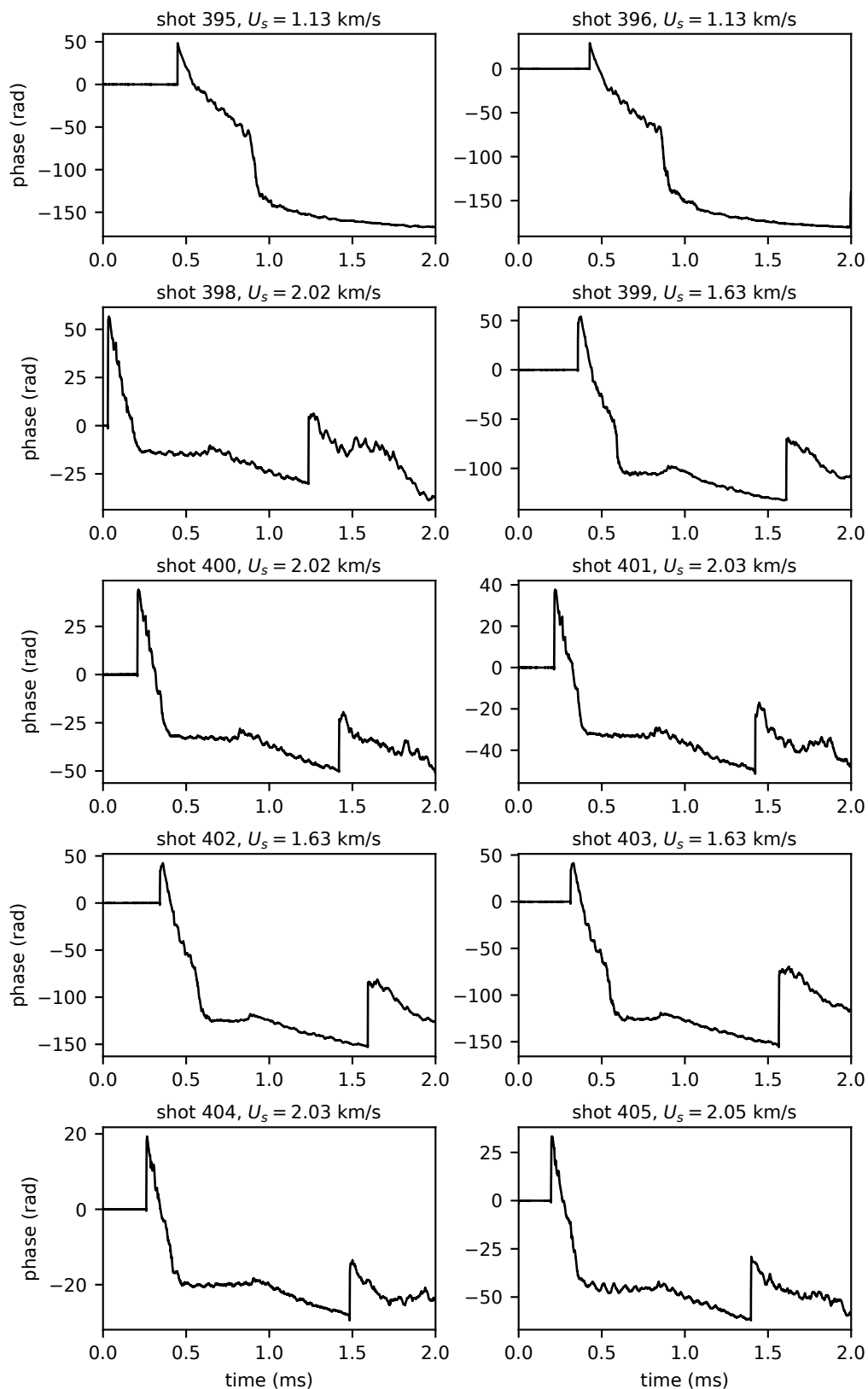


Figure E.3: Absolute phase data for shots 395 to 405.

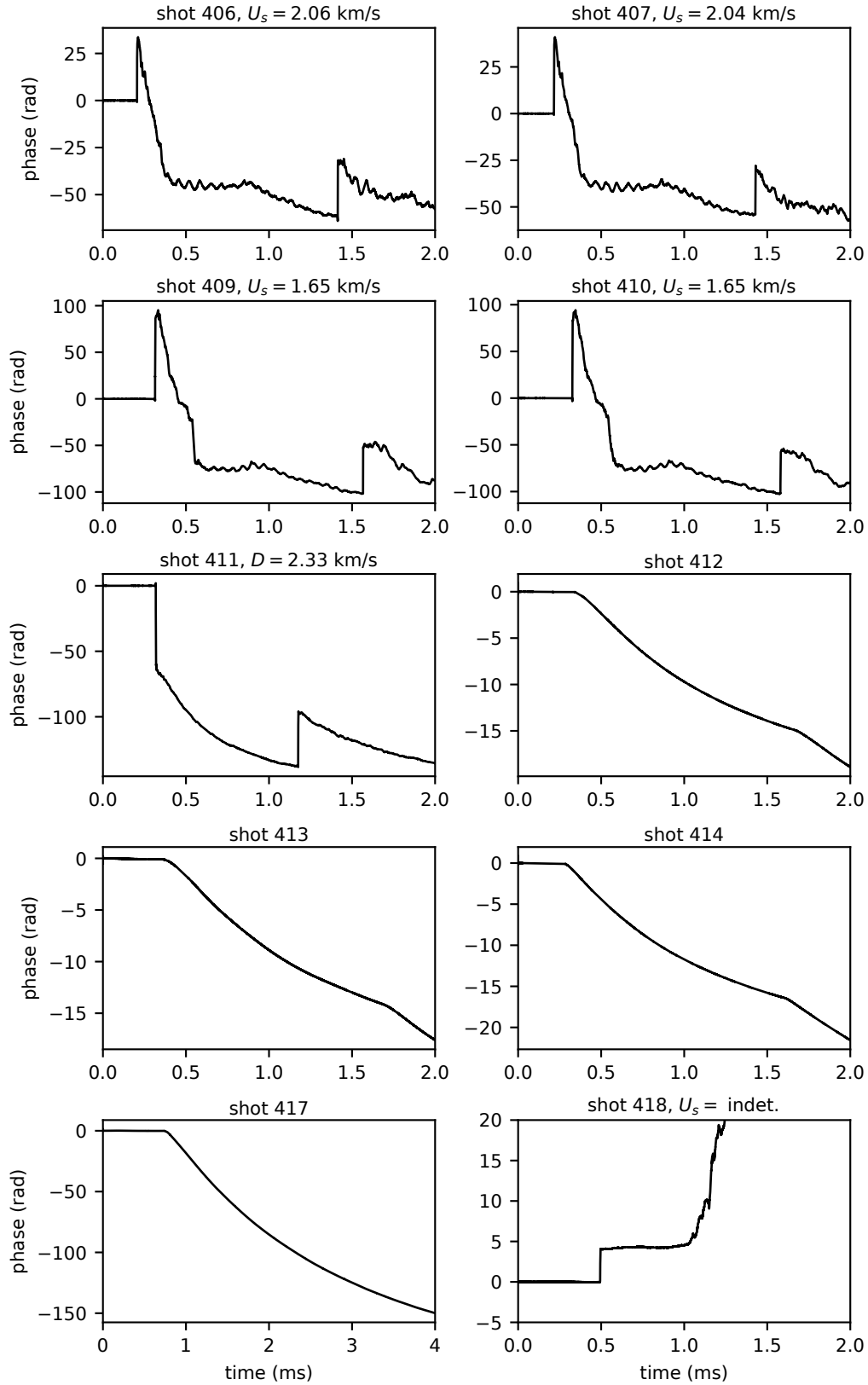


Figure E.4: Absolute phase data for shots 406 to 418.

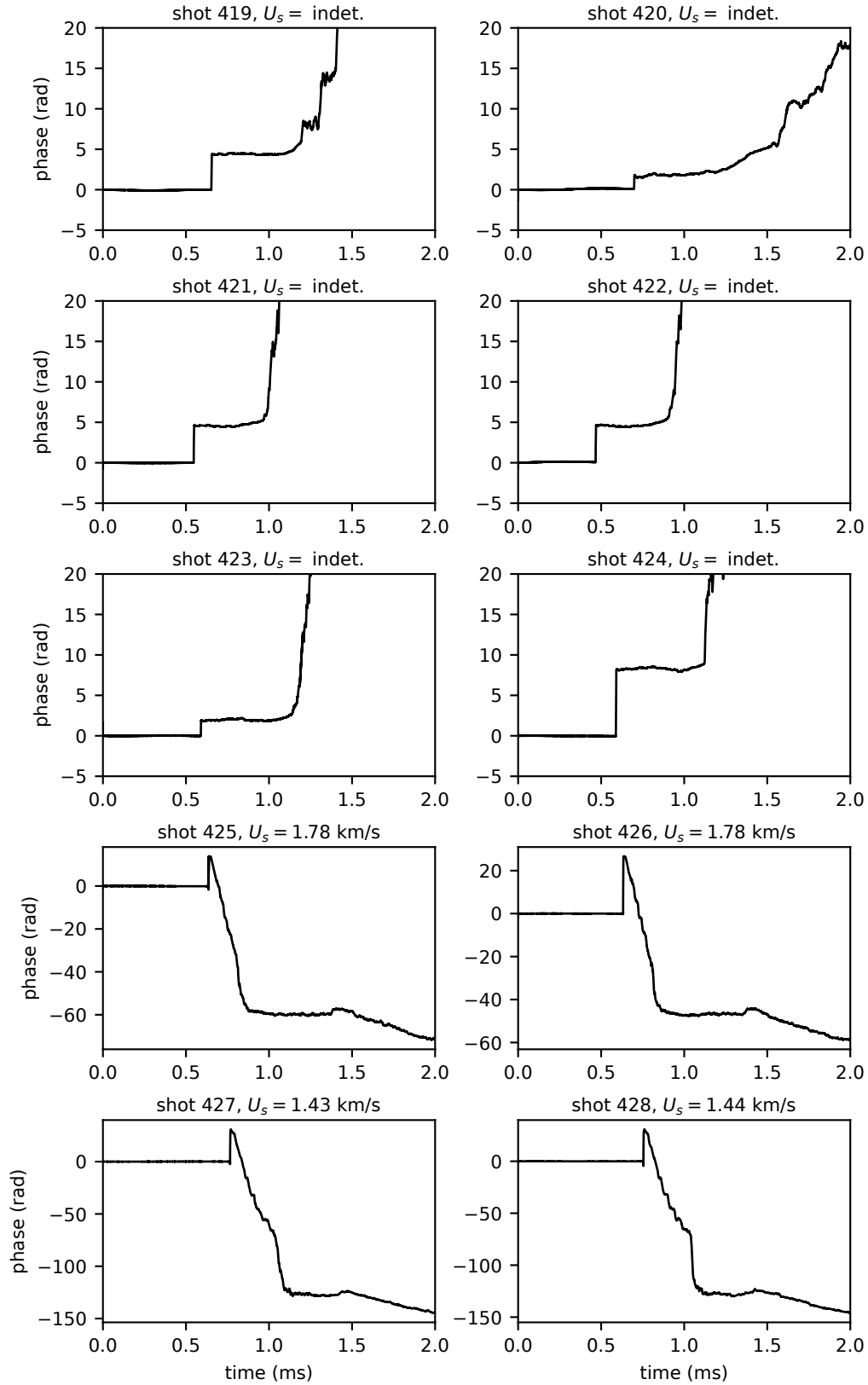


Figure E.5: Absolute phase data for shots 419 to 428.

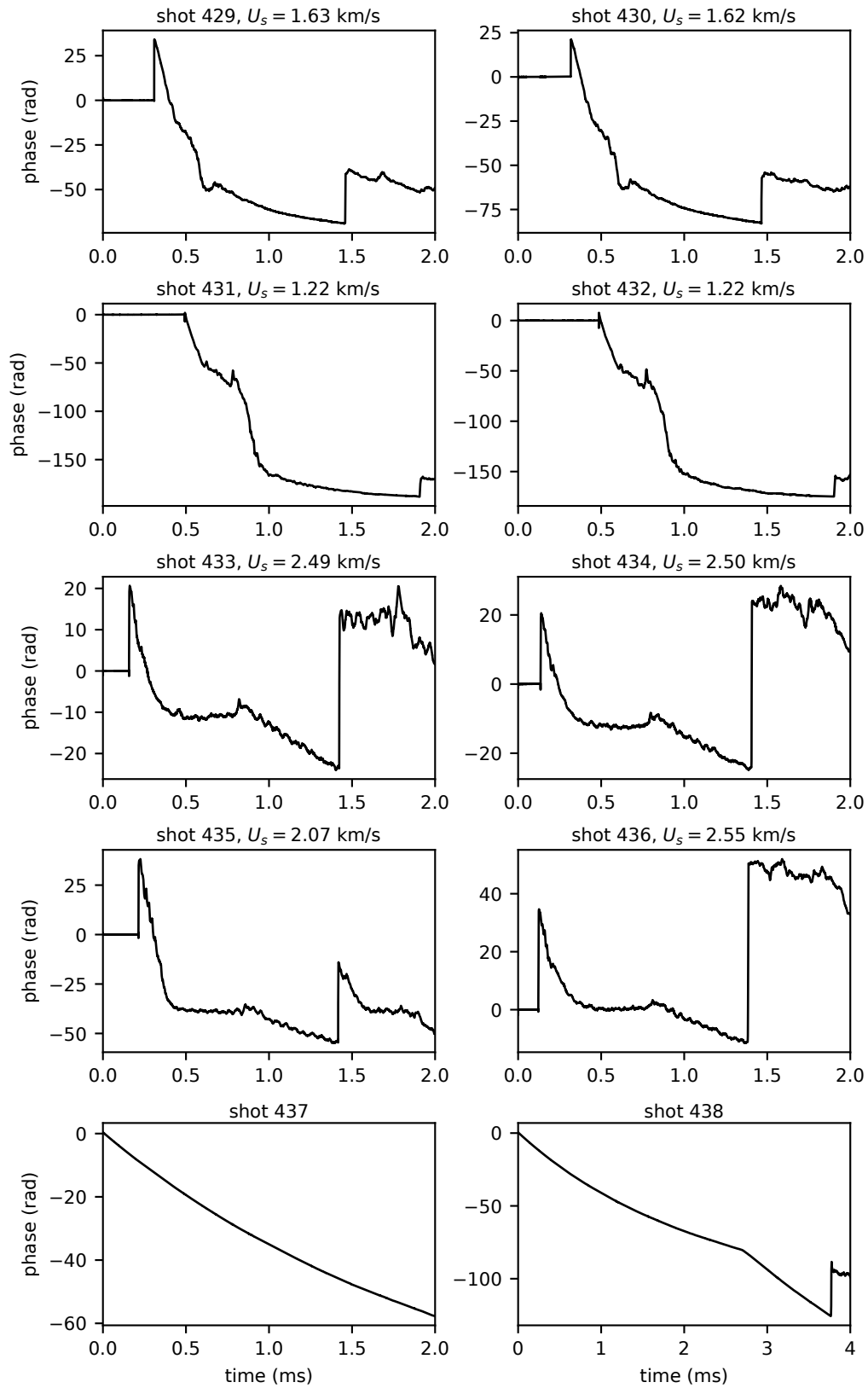


Figure E.6: Absolute phase data for shots 429 to 438.

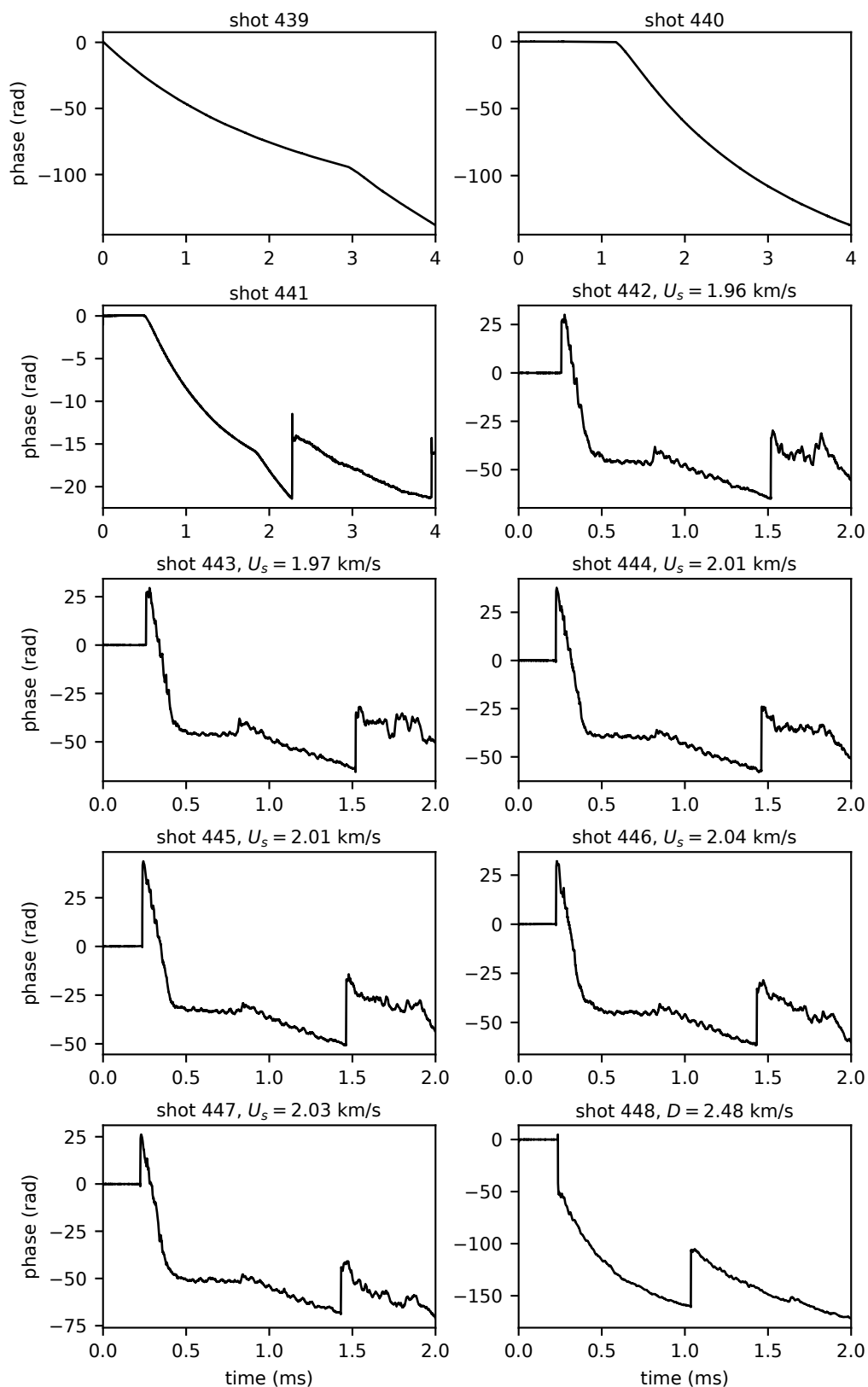


Figure E.7: Absolute phase data for shots 439 to 448.



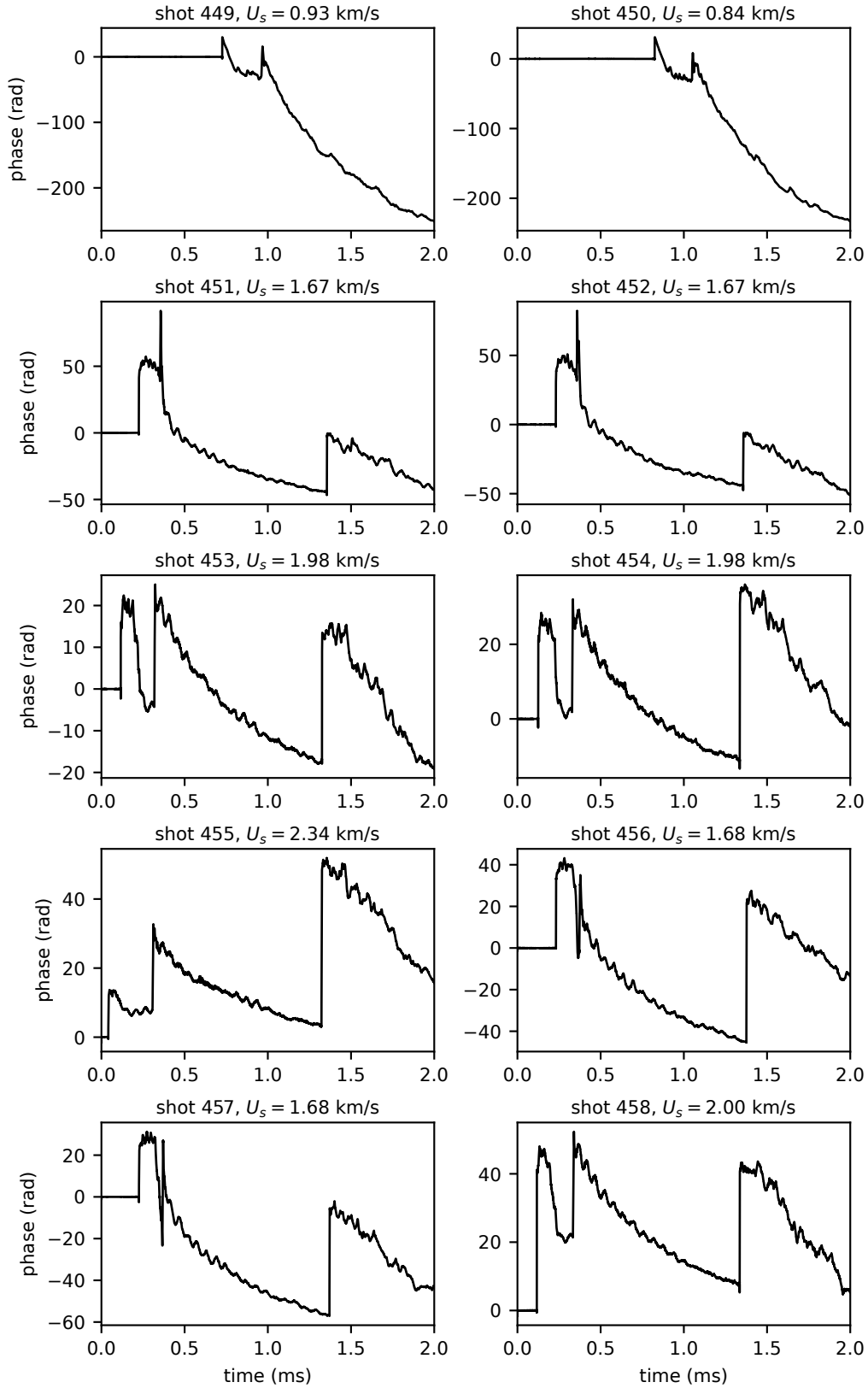


Figure E.8: Absolute phase data for shots 449 to 458.

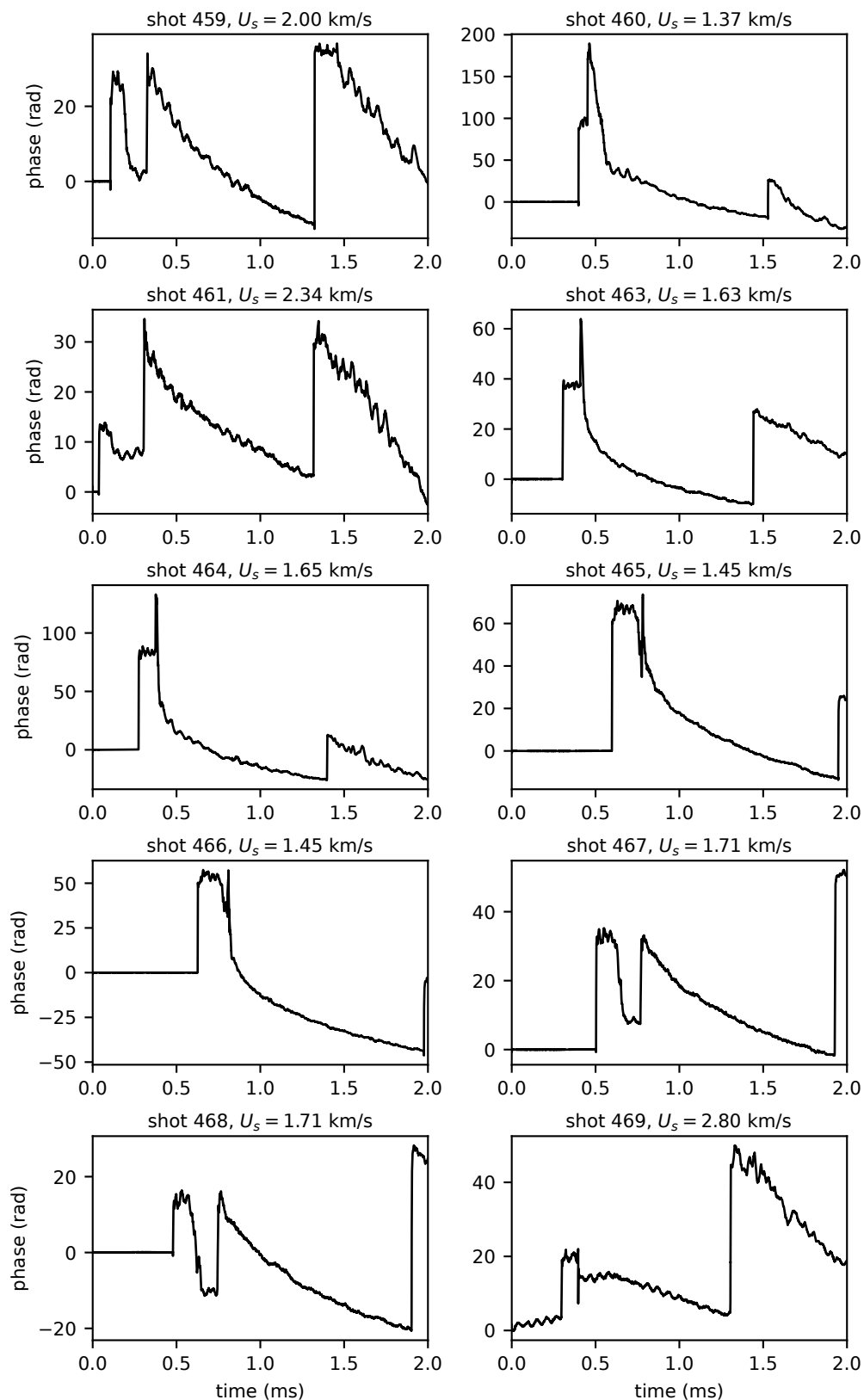


Figure E.9: Absolute phase data for shots 459 to 469.

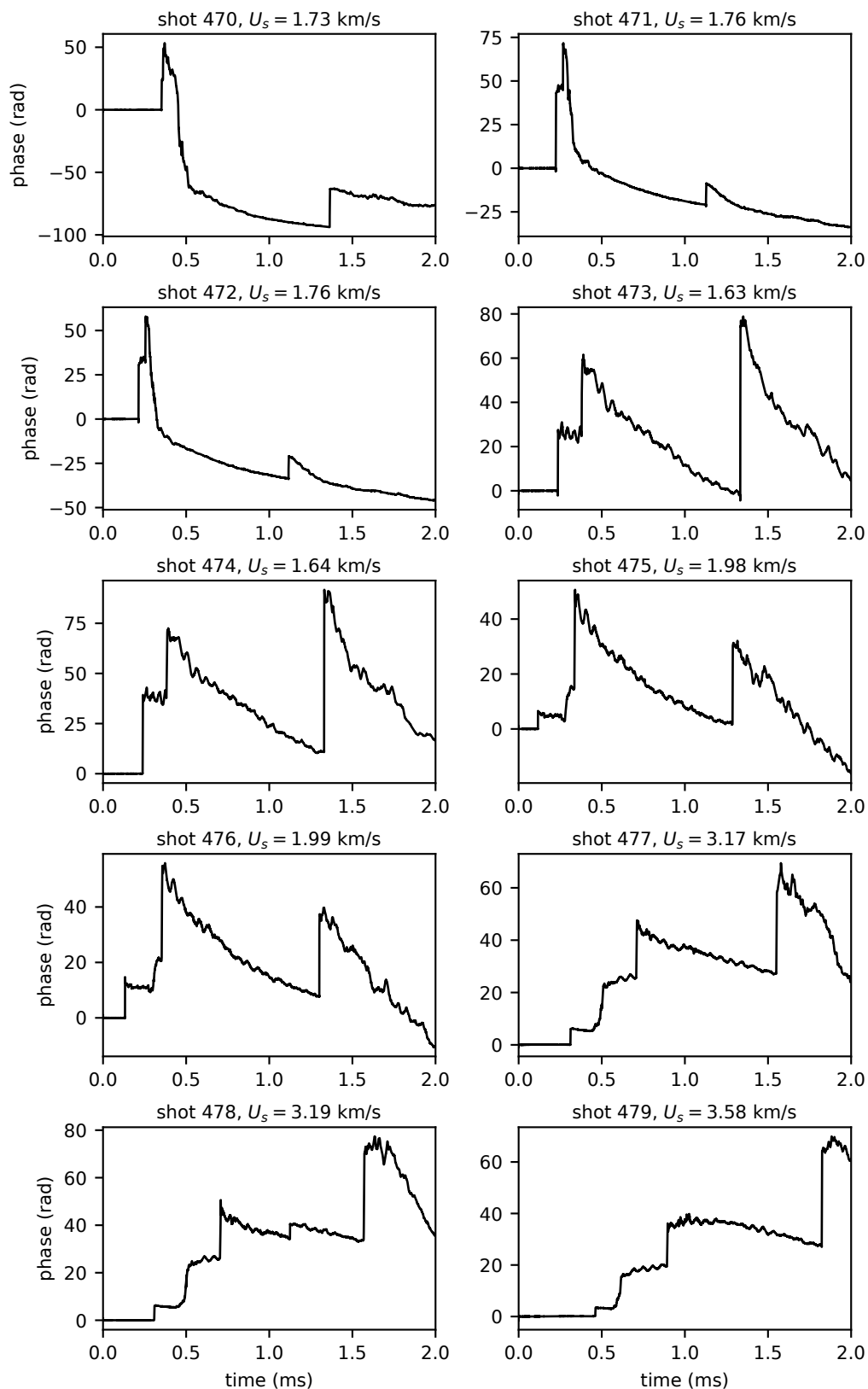


Figure E.10: Absolute phase data for shots 470 to 479.

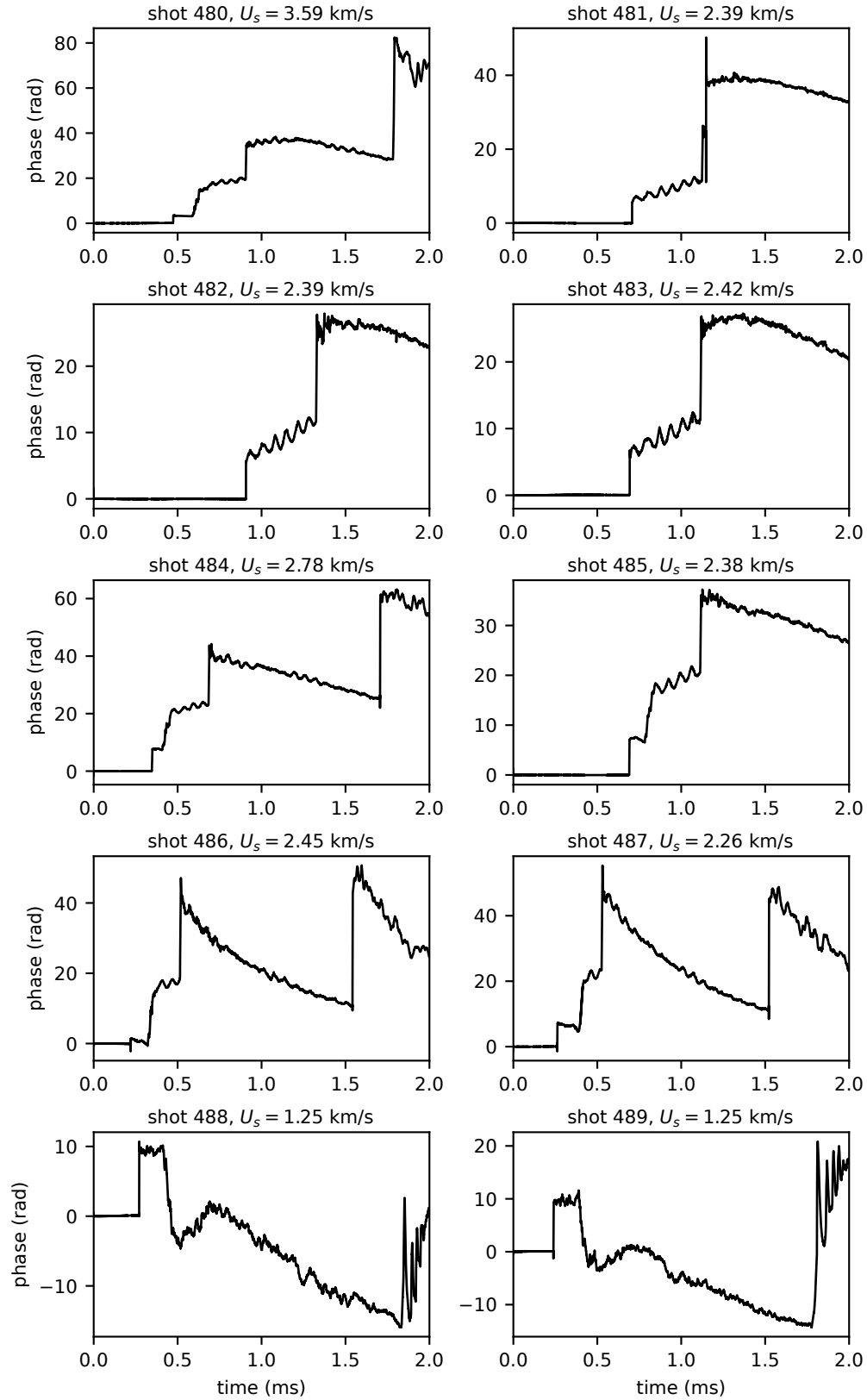


Figure E.11: Absolute phase data for shots 480 to 489.

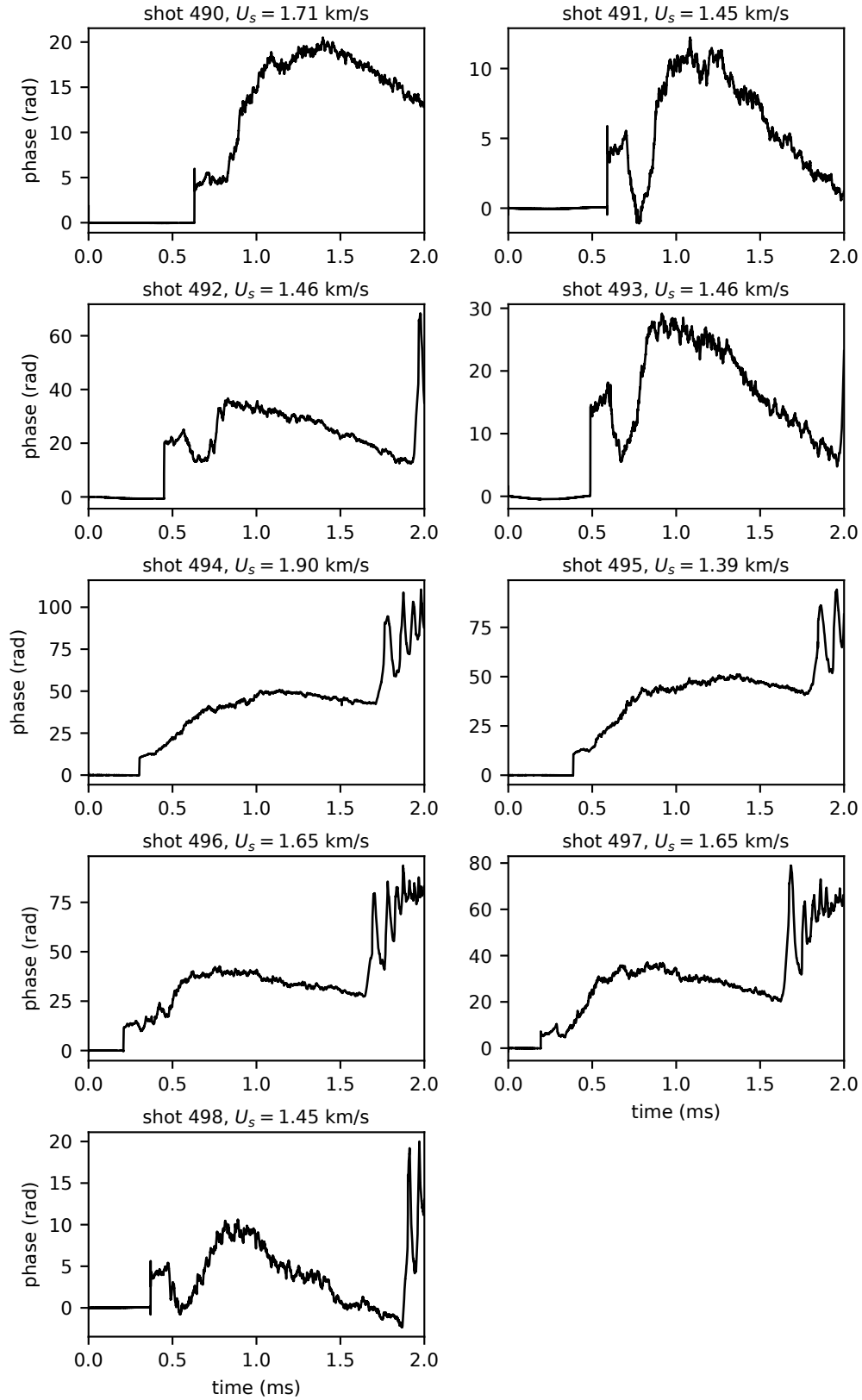


Figure E.12: Absolute phase data for shots 490 to 498.

### E.3 Additional Data: Differential Phase

The HFLI was designed so that both absolute and differential phase signals could be measured, where the differential signal is equivalent to that obtained by a conventional FLDI. Spatial differencing causes wavenumber-dependence of the signal, which complicates both its inversion to density units and seriously attenuates lower-wavenumber disturbances. Consequently, only the absolute phase measurements have so far been presented and analyzed. Differential phase signals for all shots are similar, and Figure E.13 illustrates a representative result from shot 405. The post-shock disturbances are zoomed in upon in (b) and the shock response is shown in (c). There are two spikes, corresponding to the primary and reflected shocks. The reflected shock peak is negative due to its propagation in the opposite direction.

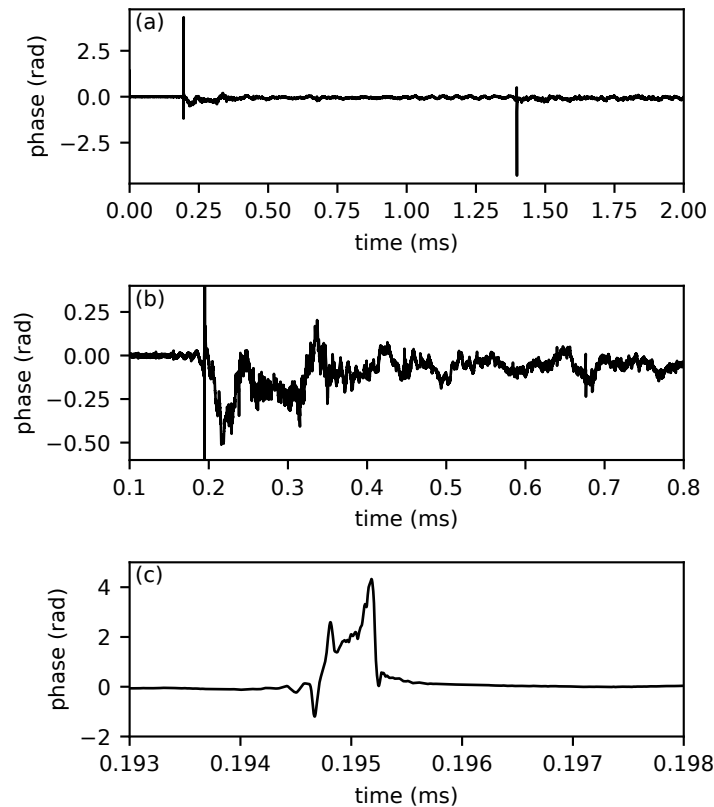


Figure E.13: Differential phase measurement from shot 405.

The disturbance spectrum for signal between the two shocks is plotted in Figure E.14 along with the spectrum calculated from the absolute phase data. There is a peak at around 21 kHz in both spectra, however observe the enormous difference in signal amplitudes. The peak from the absolute phase measurement is over 26 dB greater than from the differential phase measurement (or roughly a factor of 400).

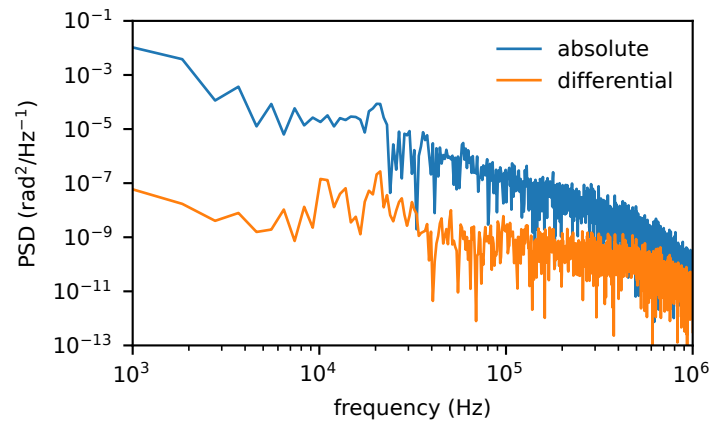


Figure E.14: Power spectral densities for differential and absolute phase measurements from shot 405.

#### E.4 Additional Data: Amplitude

IQ demodulation enables independent measurement of both phase and amplitude modulation. Phase modulation is directly proportional to density fluctuations in the test flow and is the primary object of interferometry. Amplitude modulation provides new information relevant to physical optics effects like refraction and diffraction. Distortion of the signal beam causes the formation of fringes when interfered with the reference beam, which reduce the RF signal amplitude. The variation in this signal amplitude is acquired from IQ demodulation of the RF signal with the AOM driver.

The amplitude signal is normalized by its initial value, so deviation from unity indicates an increase or decrease in the signal amplitude. Signal and reference beam wavefronts are not exactly identical due to both imperfect alignment and different aberrations, and so fringe visibility is not unity. Consequently, perturbation of the signal wavefront can result in an improved interference with the reference beam and an increased heterodyne signal amplitude.

The entire amplitude signal from a representative shot (shot 400) is shown in Figure E.15. The subplots show various features in detail, namely the spikes from (b) the shock and (c) diaphragm particulate traversing the beam. Figure E.16 compares the amplitude signal with a background reference signal and shows their power spectral densities in (b). In this case, the PSD is calculated for the entire record. There is clearly significant broadband signal from shock-tube flows. For typical homodyne interferometers without IQ demodulation schemes, phase modulation is converted

to amplitude modulation and indistinguishable from these other disturbances.

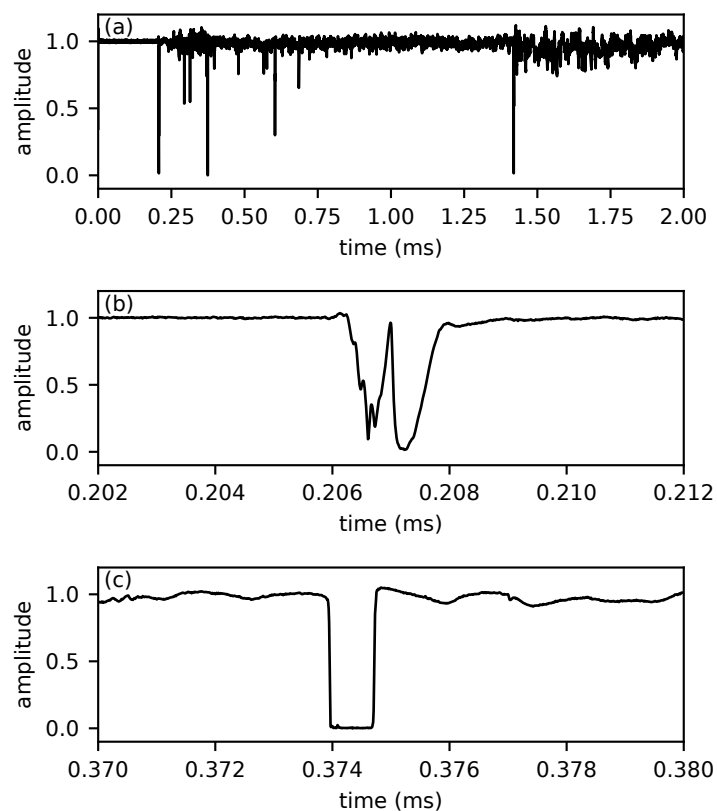


Figure E.15: Amplitude modulation from heterodyne signal obtained for shot 400.

The signal obtained from the interaction between the shock and laser beam in Figure E.15(b) shows a distinct two-lobed structure with some finer oscillations in one lobe. This signal is unique to these measurements, and so it is plotted below for each relevant shot.



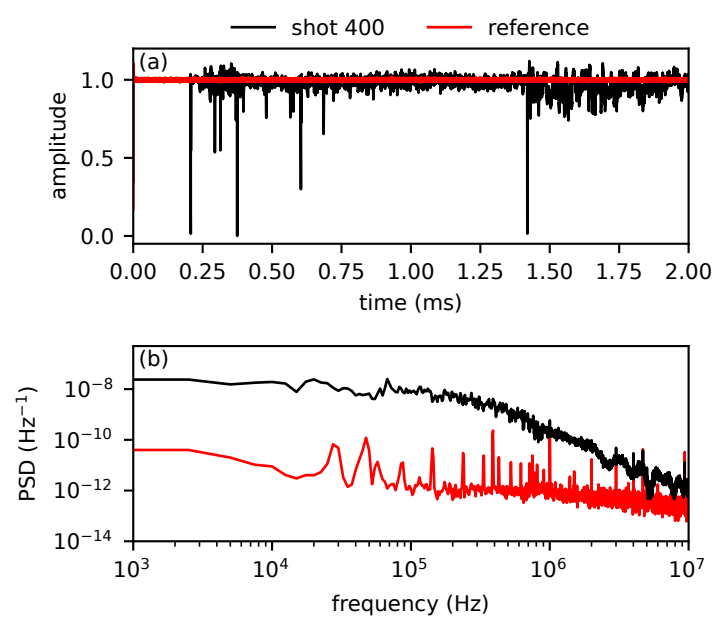


Figure E.16: Amplitude modulation compared with background reference signal and estimates of their power spectral densities.

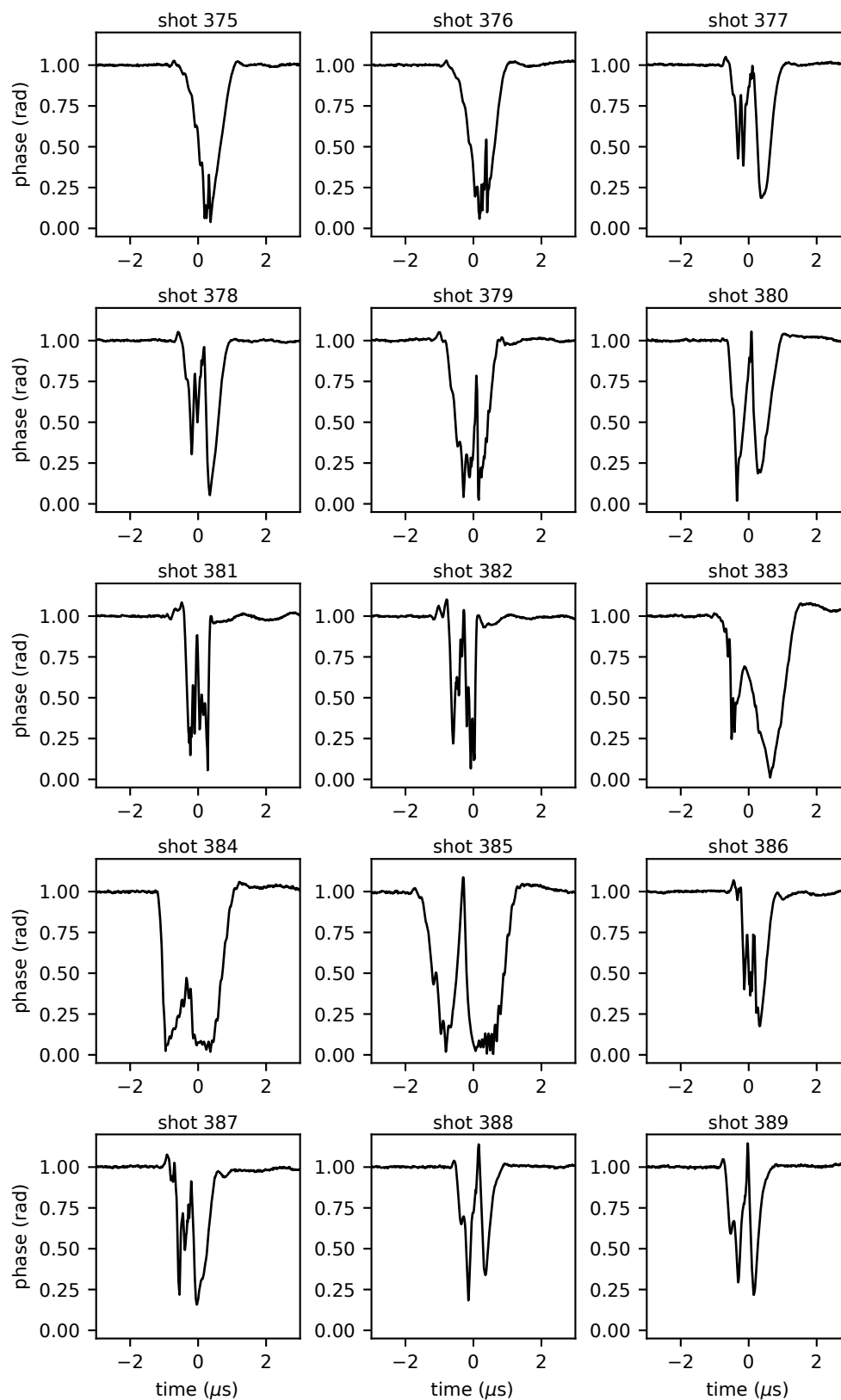


Figure E.17: Shock-response amplitude data for shots 375 to 389.

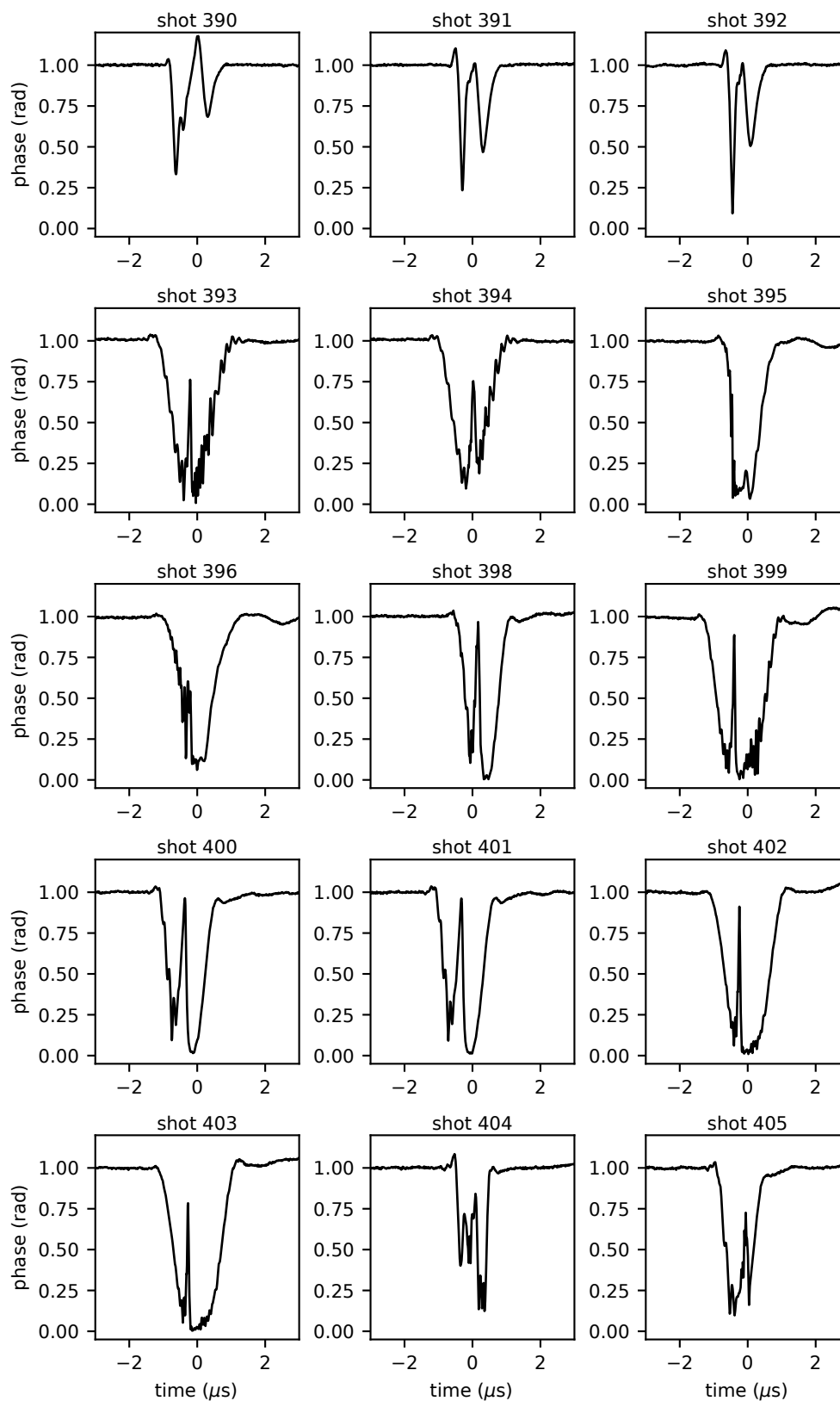


Figure E.18: Shock-response amplitude data for shots 390 to 405.

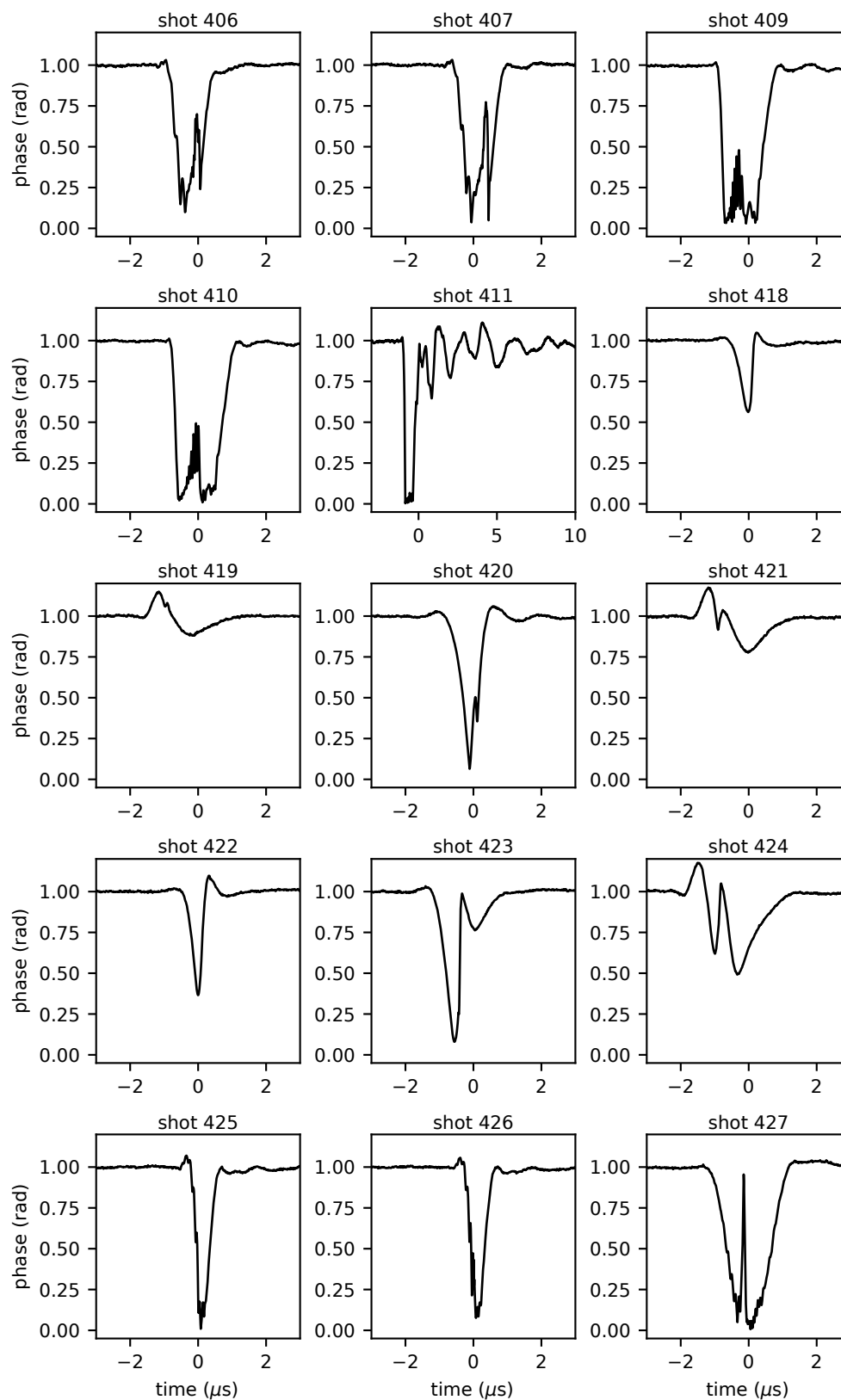


Figure E.19: Shock-response amplitude data for shots 406 to 427.

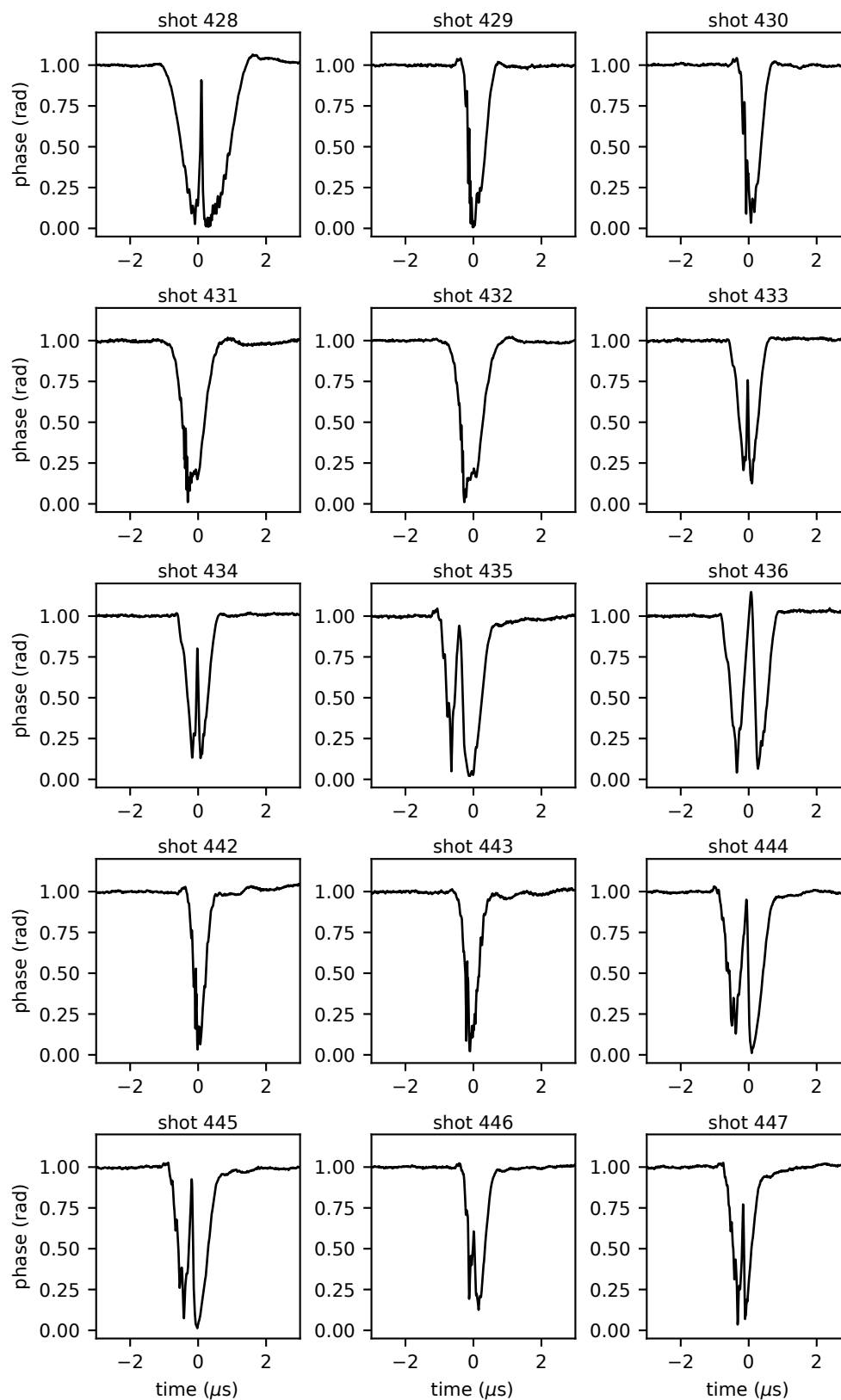


Figure E.20: Shock-response amplitude data for shots 428 to 447.

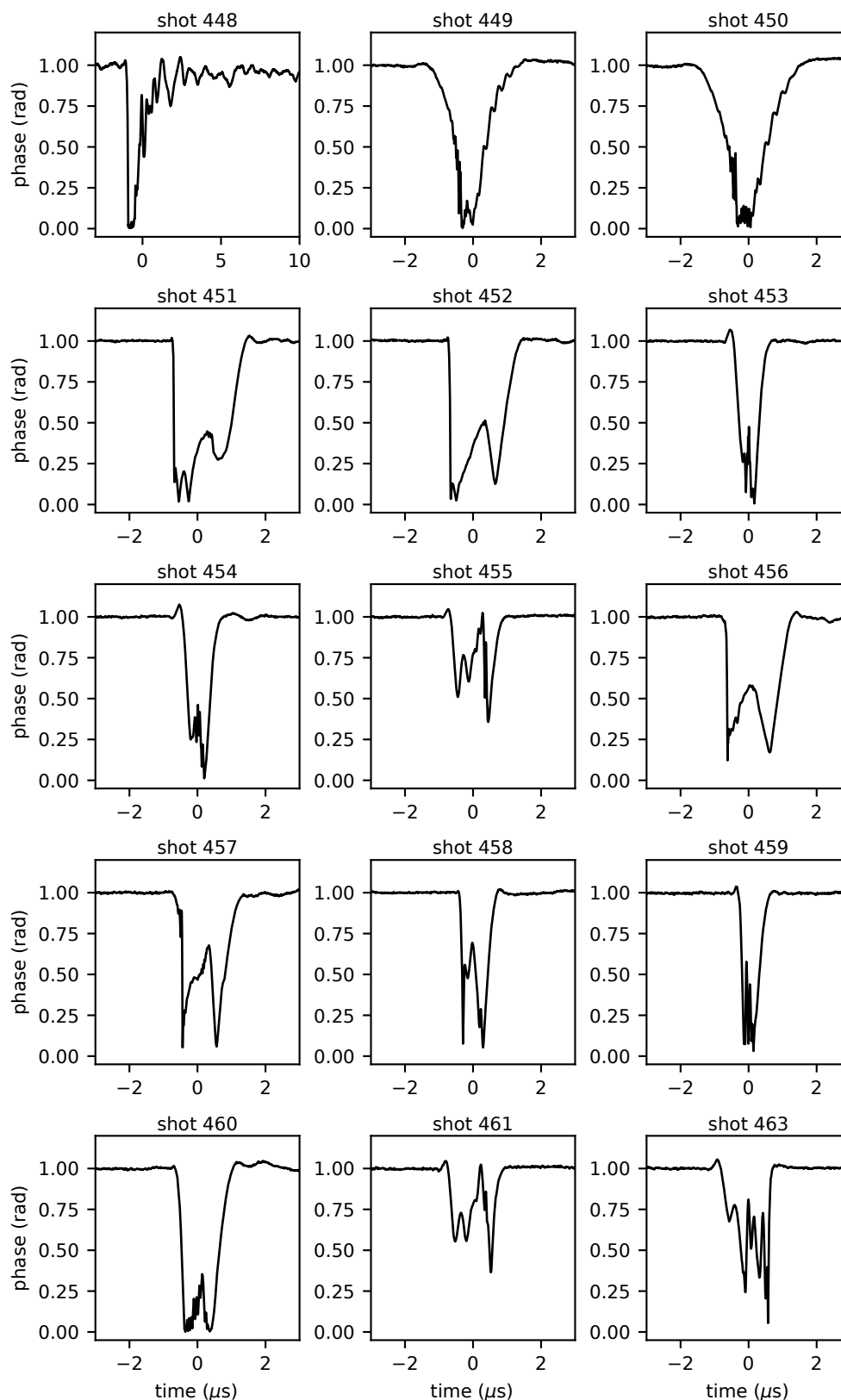


Figure E.21: Shock-response amplitude data for shots 448 to 463.

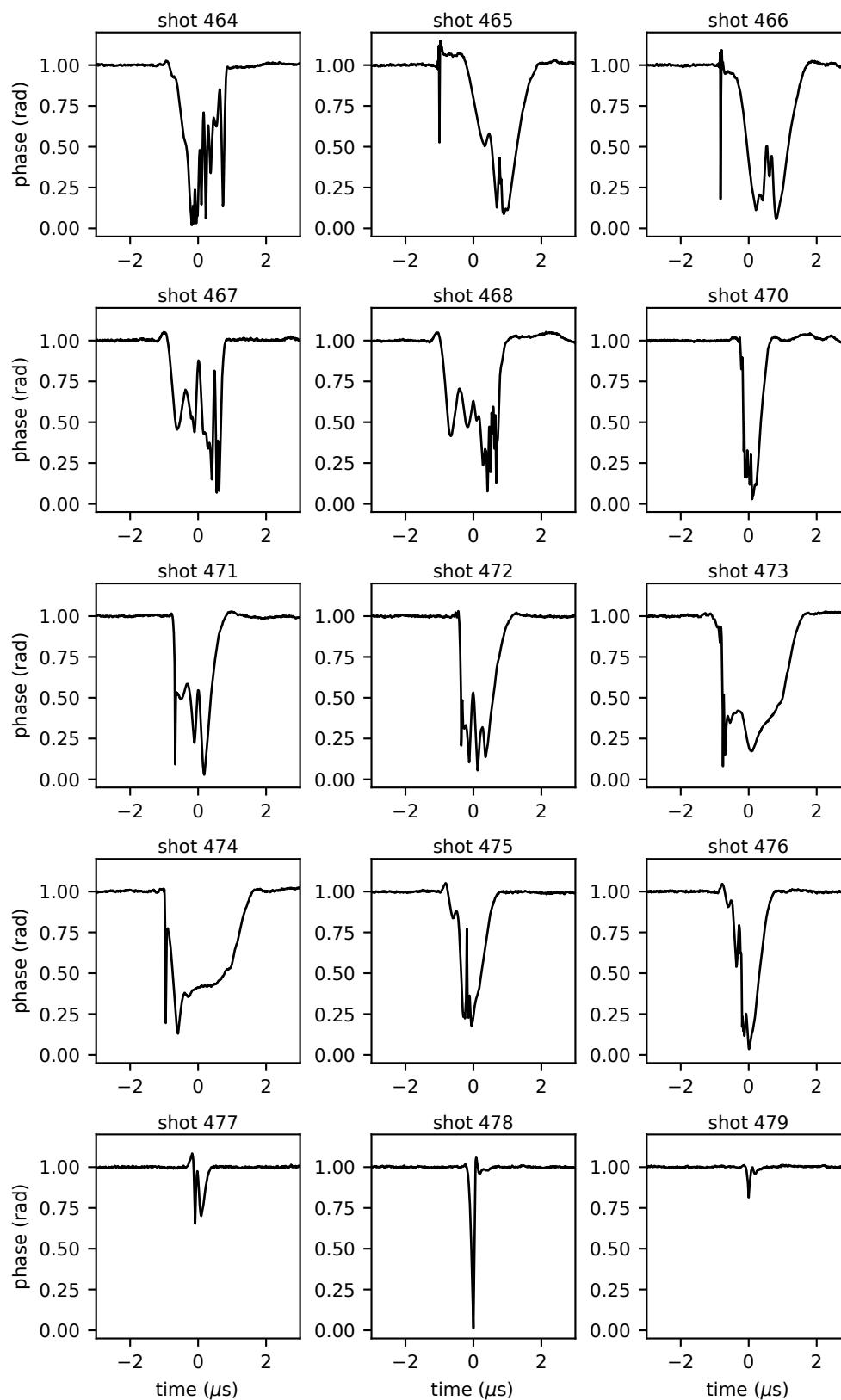


Figure E.22: Shock-response amplitude data for shots 464 to 479.

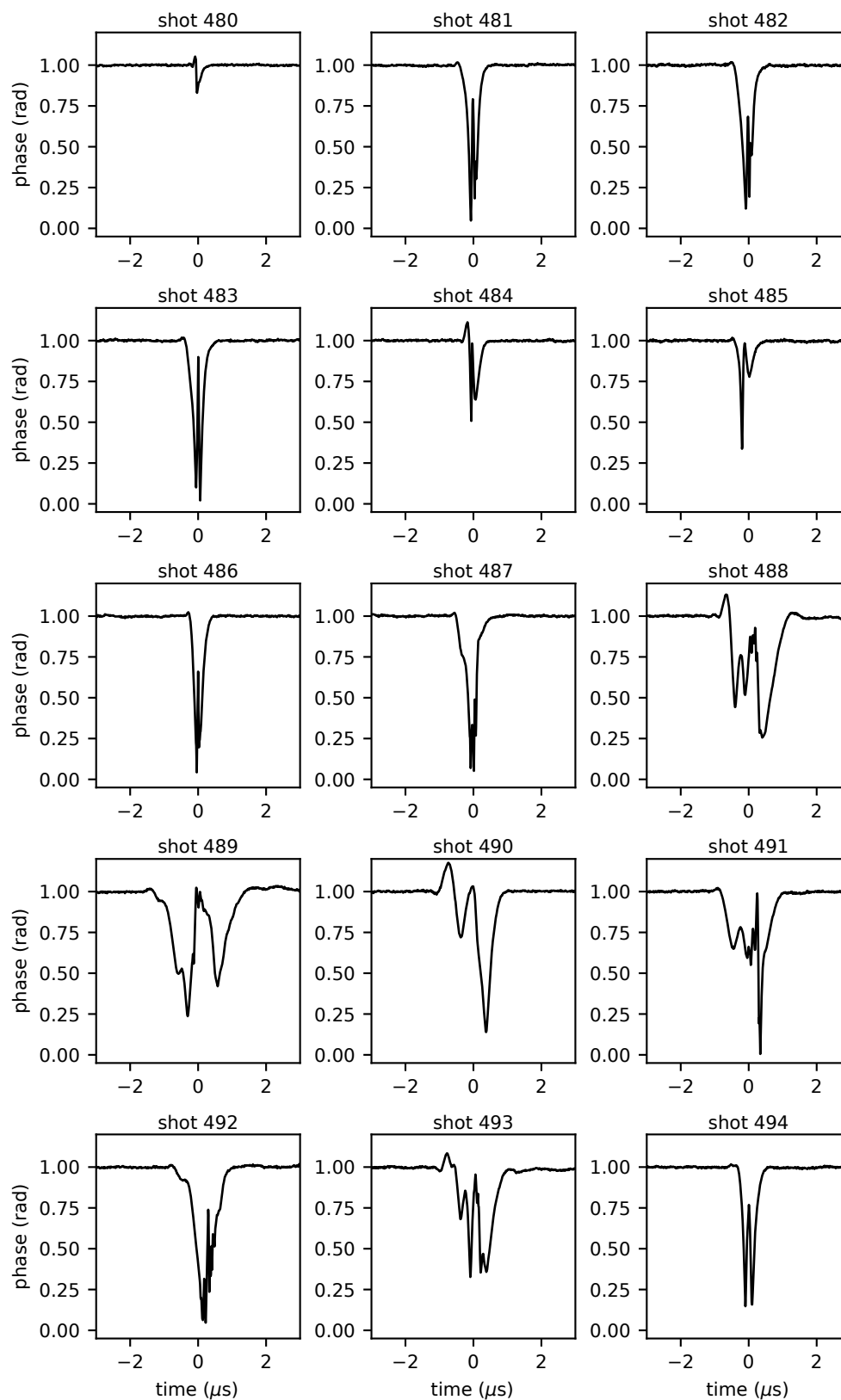


Figure E.23: Shock-response amplitude data for shots 480 to 494.



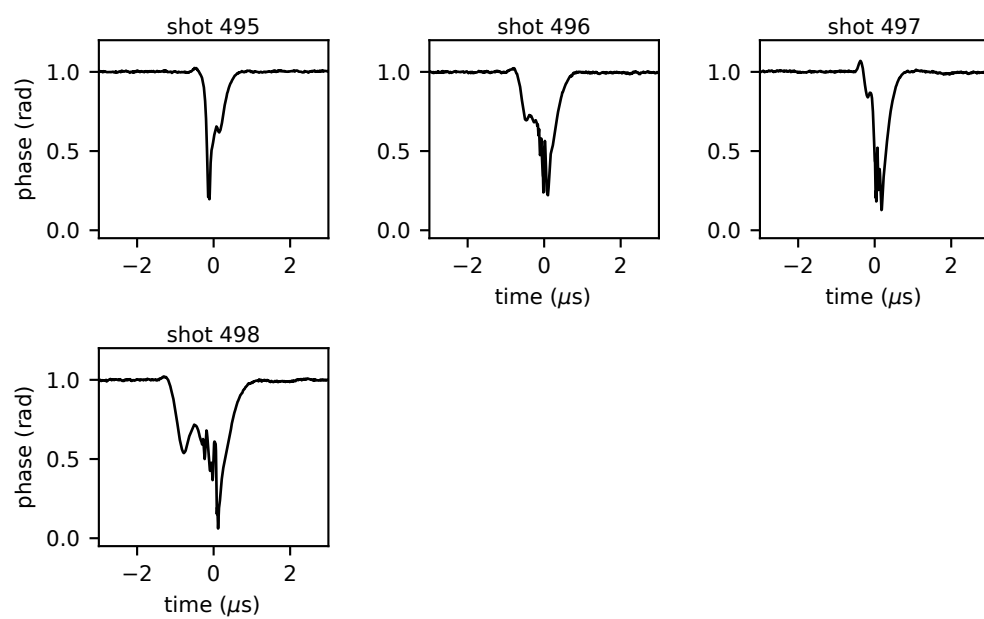


Figure E.24: Shock-response amplitude data for shots 495 to 498.

### E.4.1 Local Shock-Speed Measurement

As the shock propagates through the two signal beams of the HFLI, the signal amplitude decreases significantly before returning to the nominal baseline amplitude. The amplitude data from each beam are nearly identical but displaced by some  $\Delta t$ . The beam pair has a known separation, measured using a beam profiler, and so the  $\Delta t$  may be used to estimate the instantaneous shock speed as it intersects the beams. The  $\Delta t$  can be measured using cross correlation of the two amplitude signals. Figure E.25 demonstrates this for three representative shot conditions for each of the driver configurations.

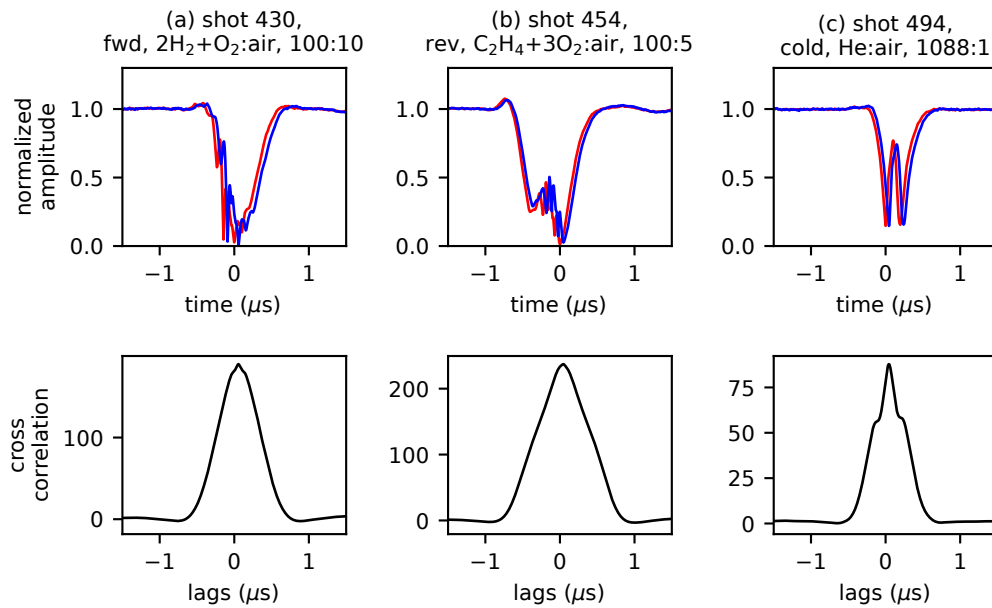


Figure E.25: Shock  $\Delta t$  estimate using cross-correlation of amplitude signals.

This method was found to sometimes be inaccurate. Consequently, pressure sensor time-of-arrival was used instead. Figure E.26 compares measurements using amplitude data cross-correlation with pressure sensor time-of-arrival and shadowgraphy results. In (a) agreement is good, whereas there is clearly a discrepancy in (b). Measurement uncertainty is determined by SNR, spatial and temporal resolution, and varied signal shapes. Uncertainty for ideal Gaussian amplitude signals was estimated numerically by simulating signals with SNR comparable to measurements. Simulation results showed a predicted uncertainty of approximately 2.5%, however Figure E.26(b) shows an error of nearly 6%. The non-Gaussian signal shape and beam-to-beam variation is expected to be the source for this inconsistent measure-

ment accuracy. This cross-correlation technique would be much improved if the beam separation was larger. For this work it was small,  $\Delta x = 90 \mu\text{m}$ .

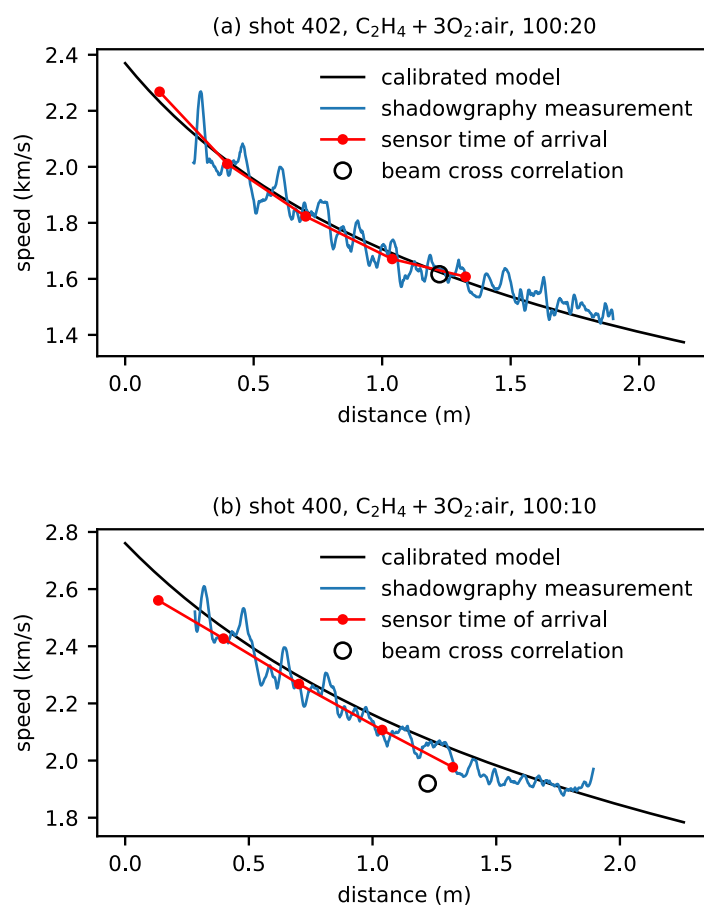


Figure E.26: Comparison between shock speed measurement techniques for two shot conditions.

*Appendix F*

## ADDITIONAL DATA: PRESSURE MEASUREMENTS

**F.1 Vibration Isolation**

Shocks in shock tubes drive structural vibrations that can have serious effects on wall-mounted pressure transducers. This was mitigated in the present work by using plastic plugs instead of aluminum plugs for mounting the PCB sensor. The plastic plugs were 3D printed using a Formlabs SLA printer and Clear Resin V4. The plugs were tapped to receive an SAE-1926 plug that contained the PCB sensor. Figure F.1 shows a comparison between a pressure measurement using the plastic plug and an aluminum plug. Figure F.1 compare spectra. The plastic clearly damps a significant portion of high-frequency vibrations. In particular, note the absence of oscillation ahead of the shock. These are from dilatational and shear waves excited by the traveling load. These do not transmit into the PCB sensor when mounted in the plastic plug.

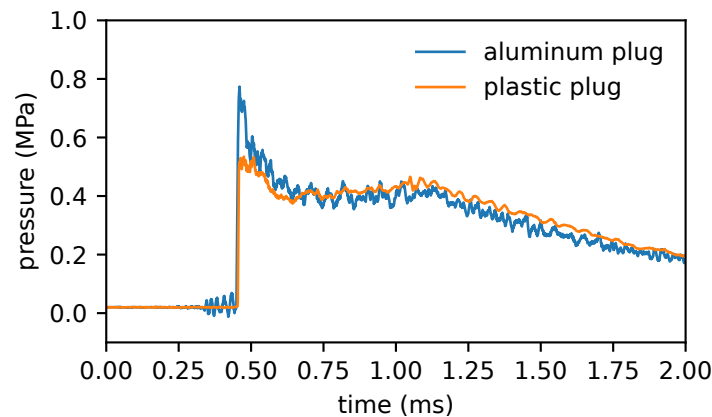


Figure F.1: Comparison between pressure measurements using a PCB mounted in an aluminum and in a plastic plug.

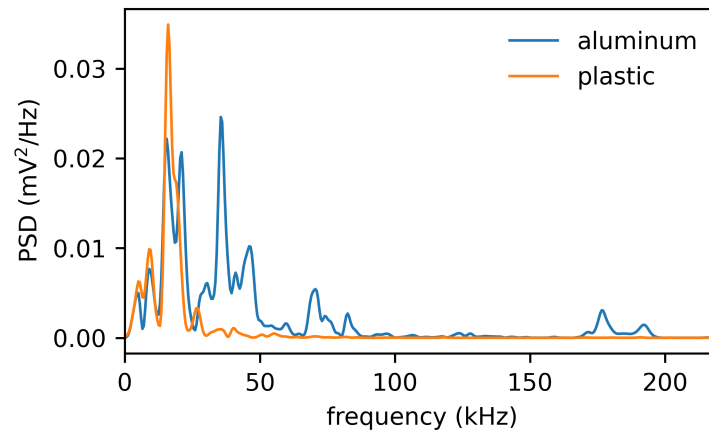


Figure F.2: Post-shock pressure signal spectrum for PCB mounted in an aluminum and in a plastic plug.

## F.2 Shot Data

Driven-section pressure data for a selection of shots are shown below. Shot conditions are given in Table E.1 and transducer positions are given in Table 7.1. Time is zeroed by the detonation's estimated arrival at the diaphragm. For all shot data below, transducers P4-P8 are mounted in plastic plugs for vibration isolation. Transducer P3 is always mounted directly downstream in the diaphragm closure. Pressure measurements from the driver are excluded.

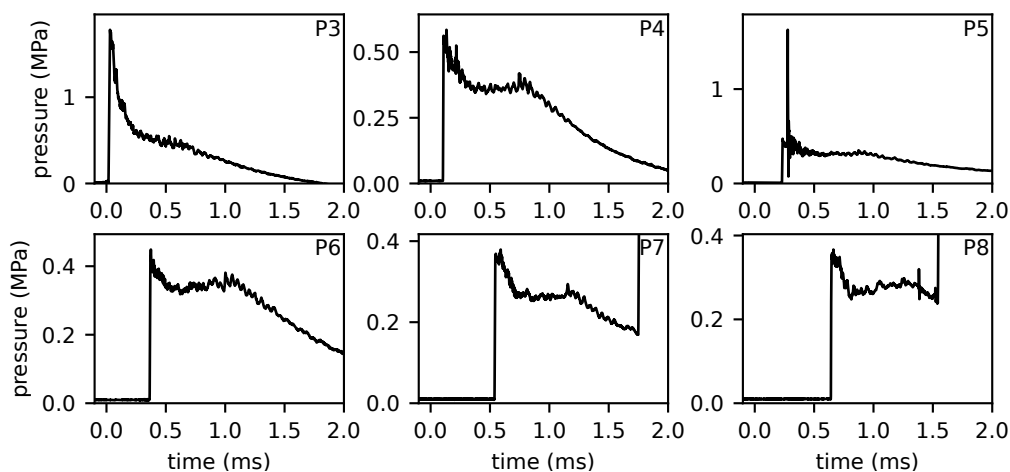


Figure F.3: Pressure data for shot 400.

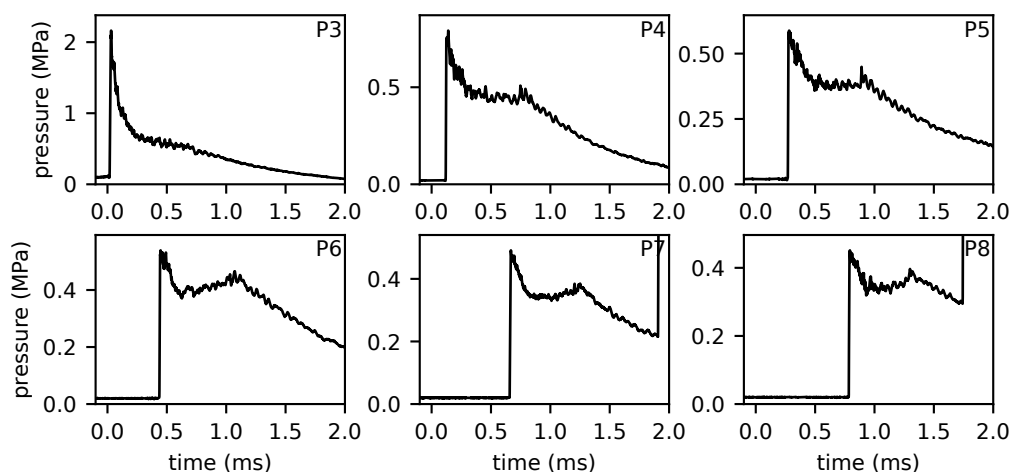


Figure F.4: Pressure data for shot 402.

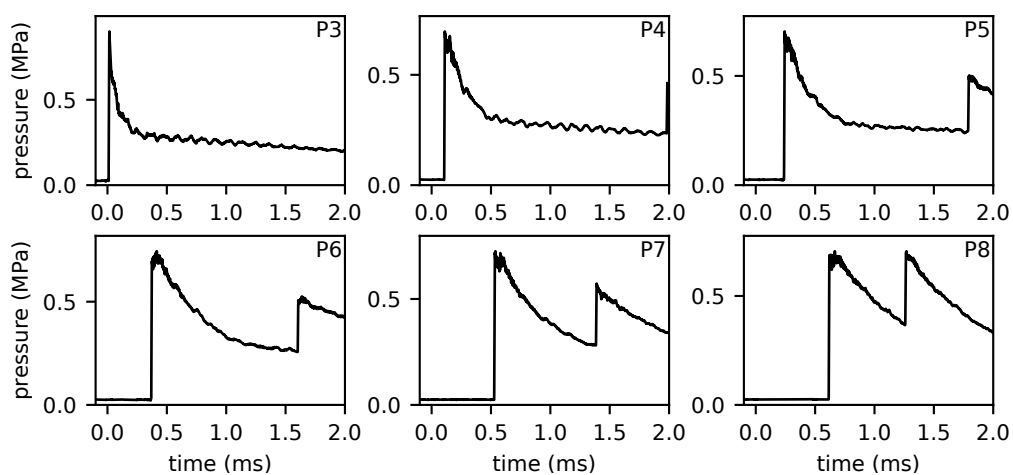


Figure F.5: Pressure data for shot 411.

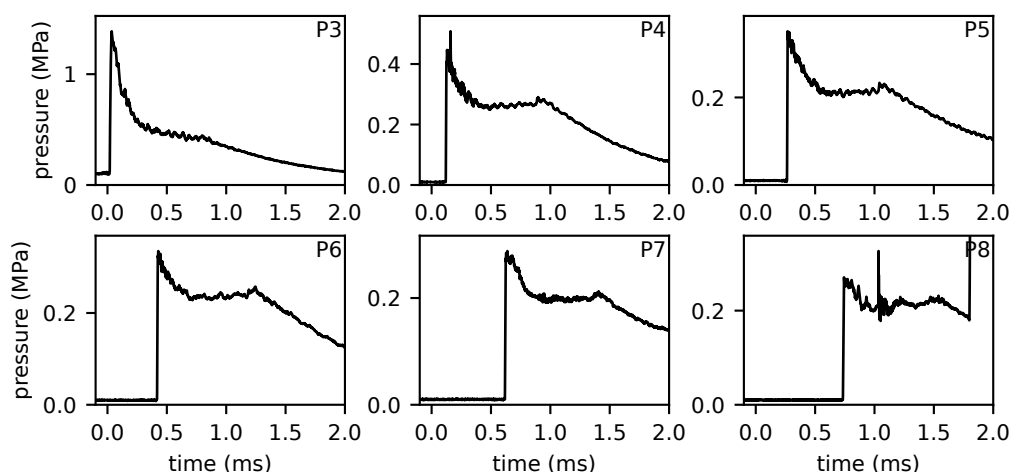


Figure F.6: Pressure data for shot 425.

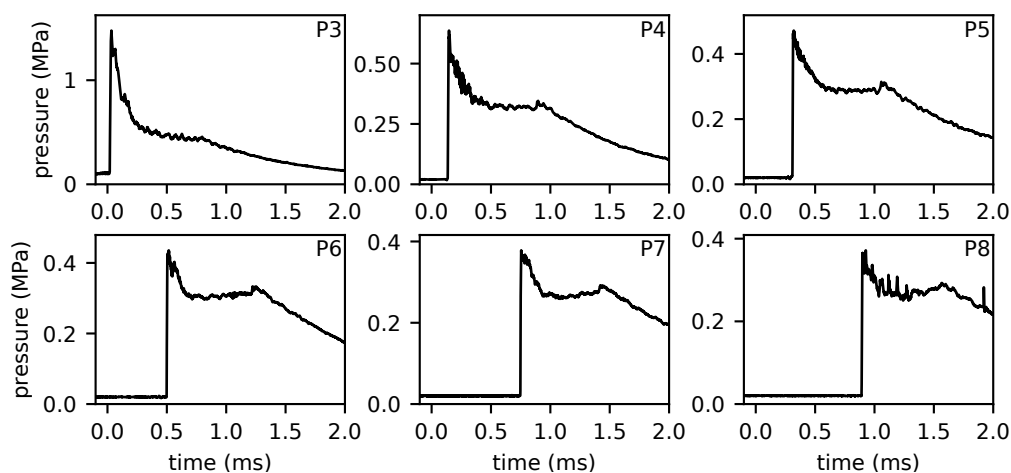


Figure F.7: Pressure data for shot 427.

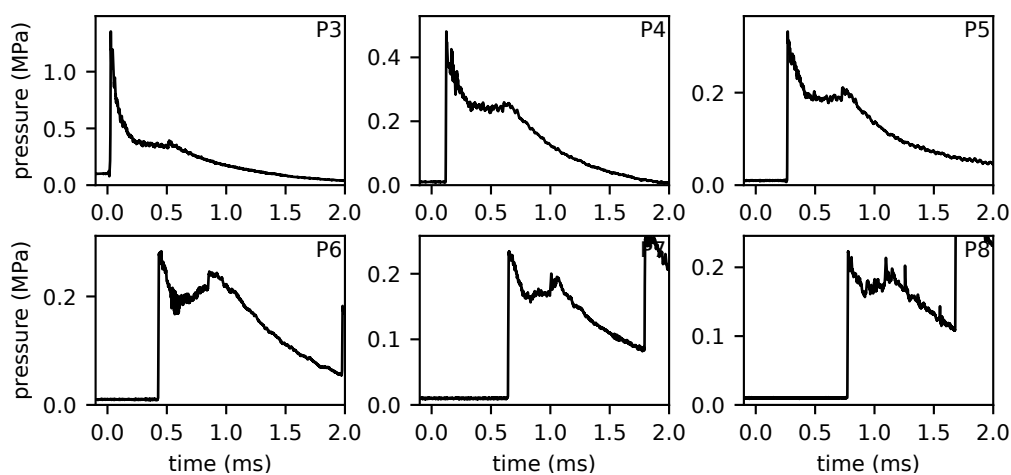


Figure F.8: Pressure data for shot 429.

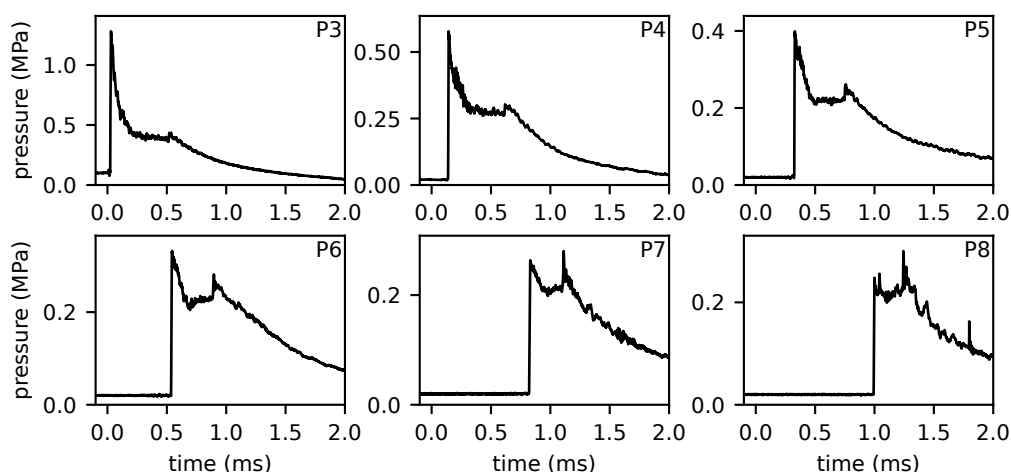


Figure F.9: Pressure data for shot 431.

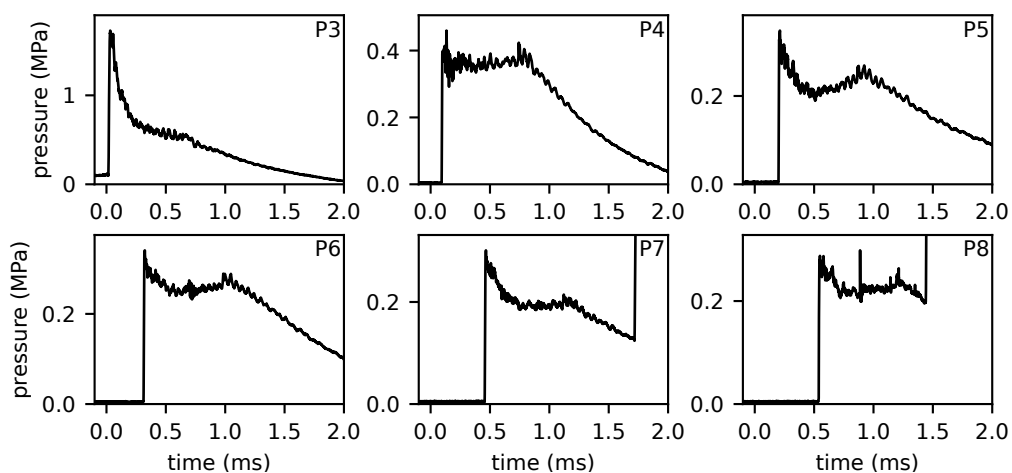


Figure F.10: Pressure data for shot 433.

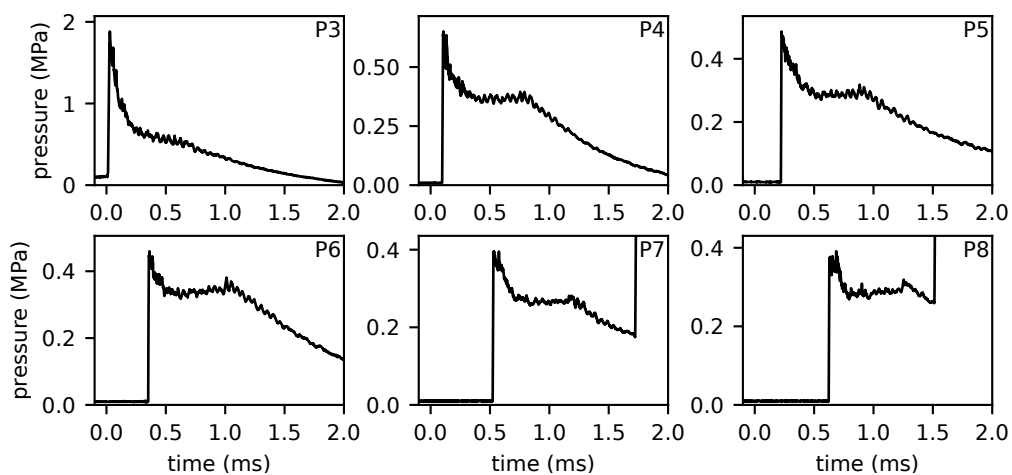


Figure F.11: Pressure data for shot 435.

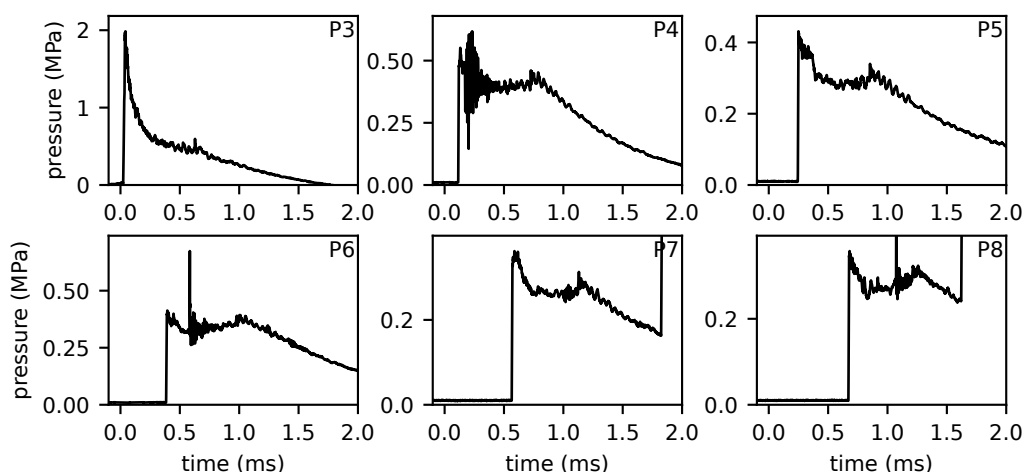


Figure F.12: Pressure data for shot 442.



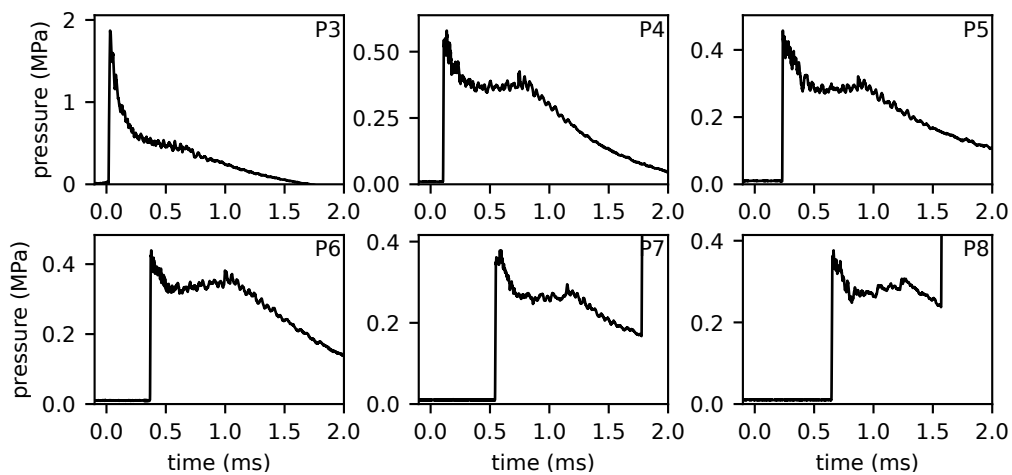


Figure F.13: Pressure data for shot 444.

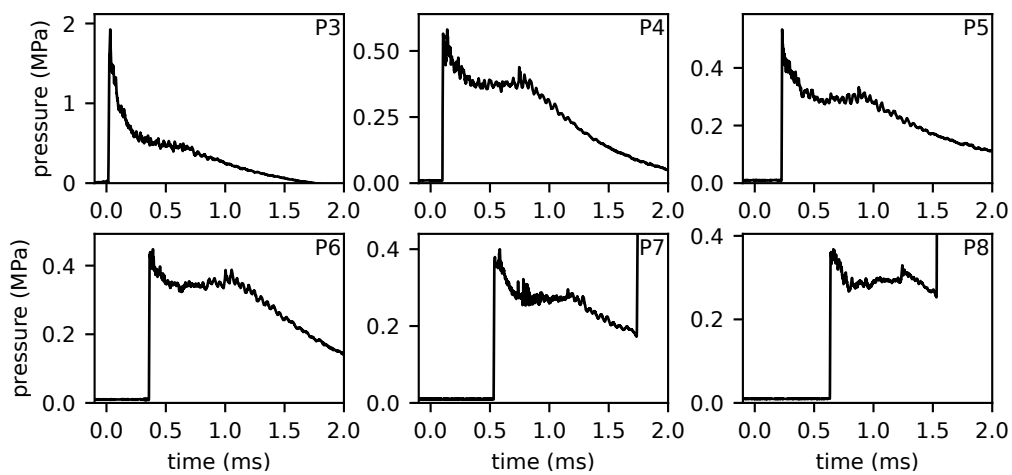


Figure F.14: Pressure data for shot 446.

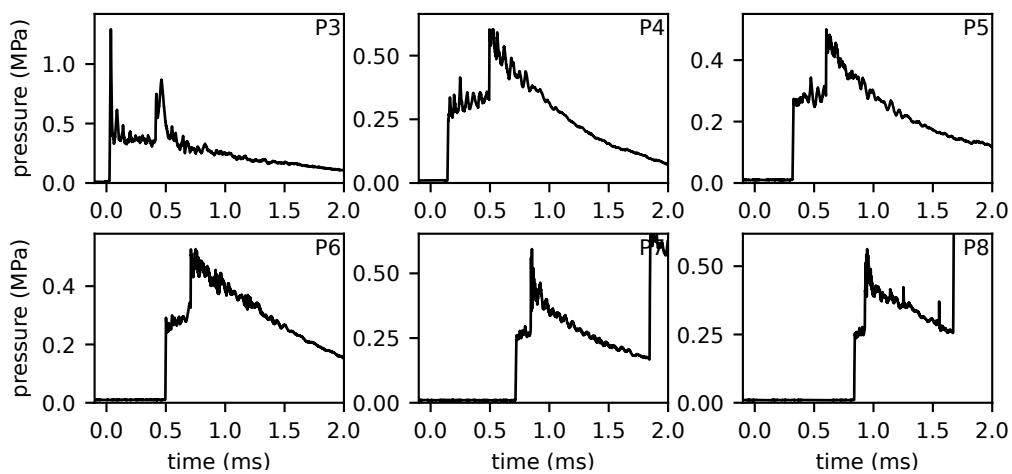


Figure F.15: Pressure data for shot 451.

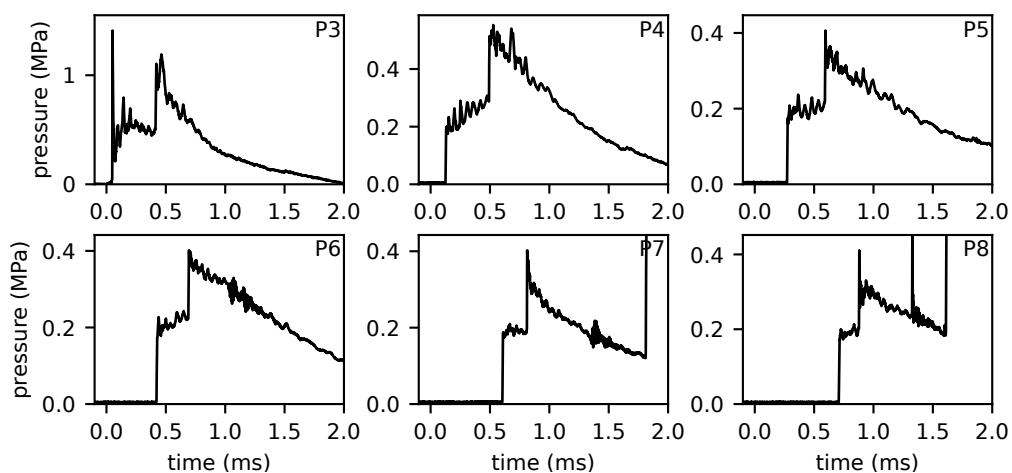


Figure F.16: Pressure data for shot 453.

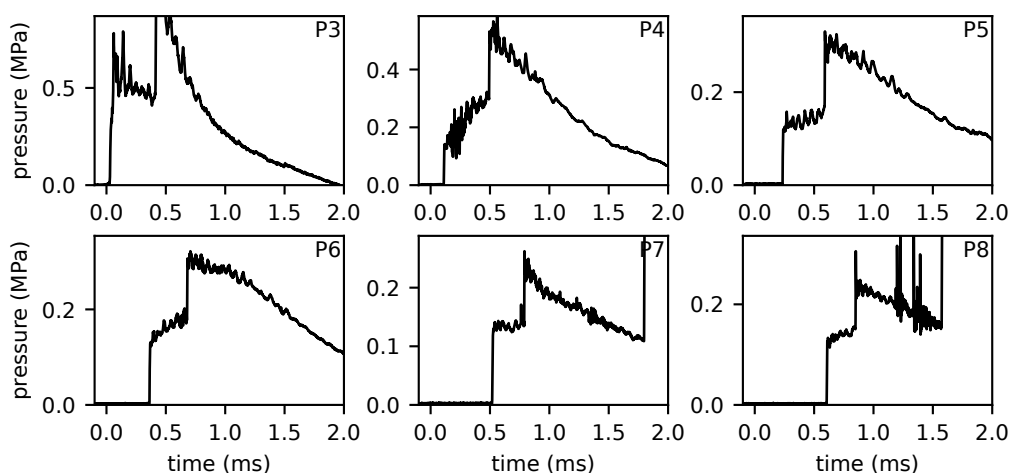


Figure F.17: Pressure data for shot 455.

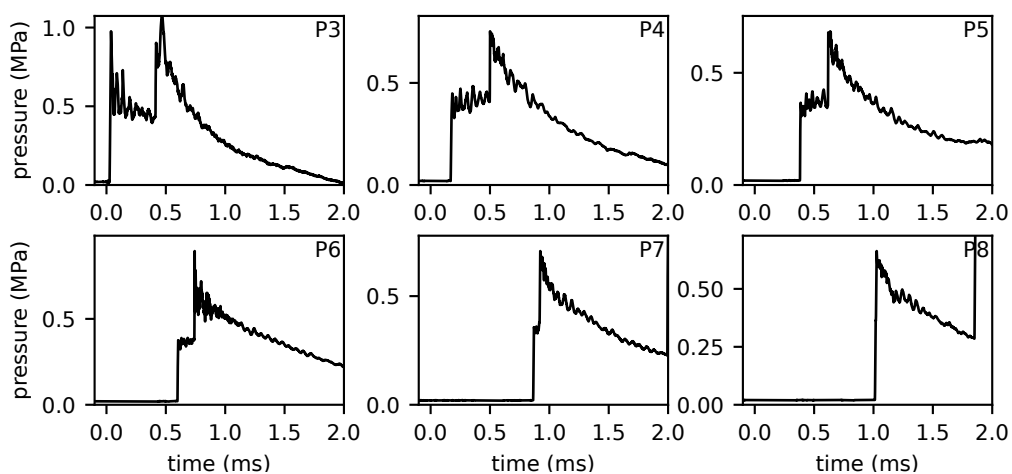


Figure F.18: Pressure data for shot 460.

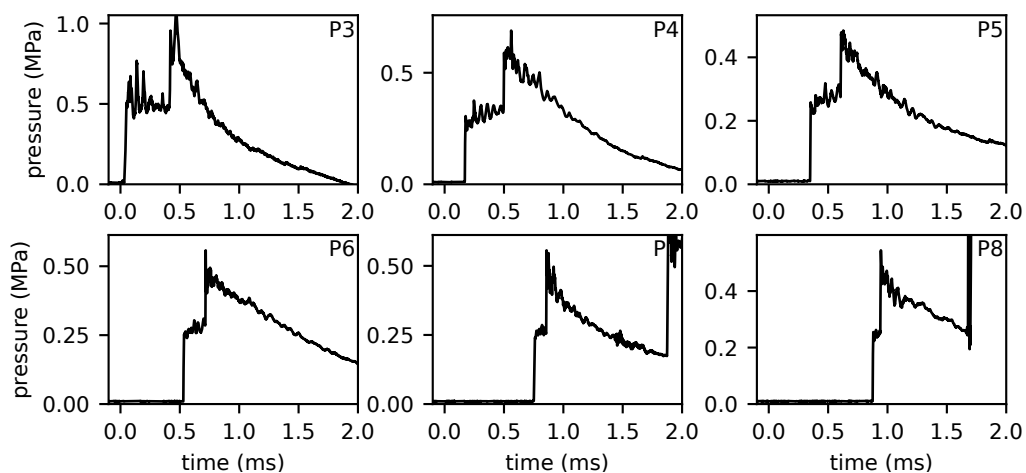


Figure F.19: Pressure data for shot 464.

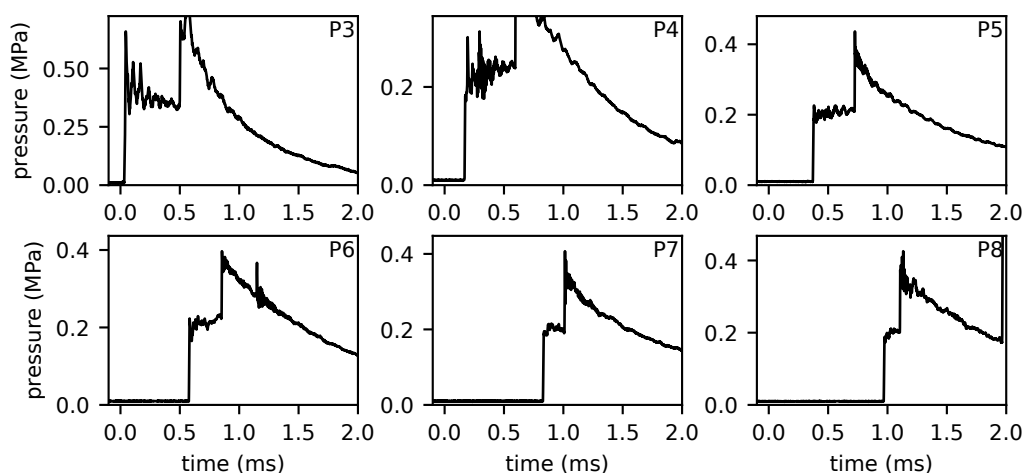


Figure F.20: Pressure data for shot 465.

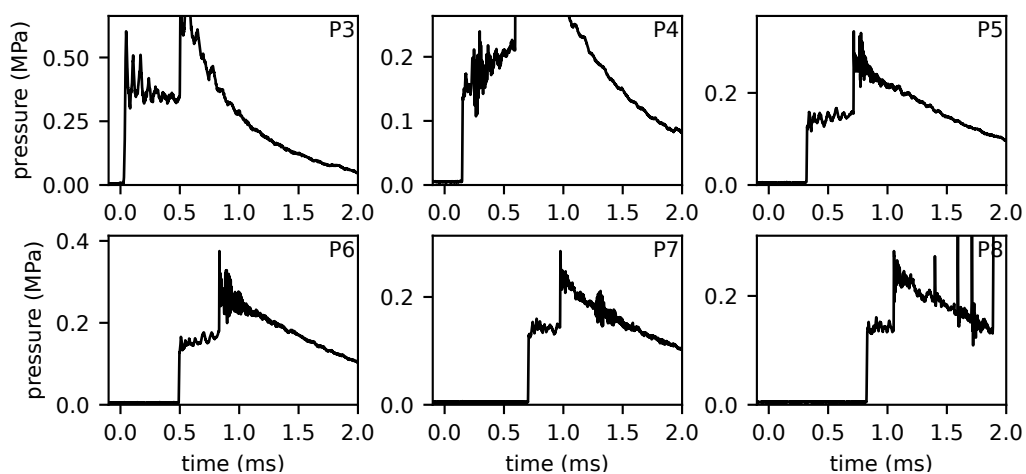


Figure F.21: Pressure data for shot 467.

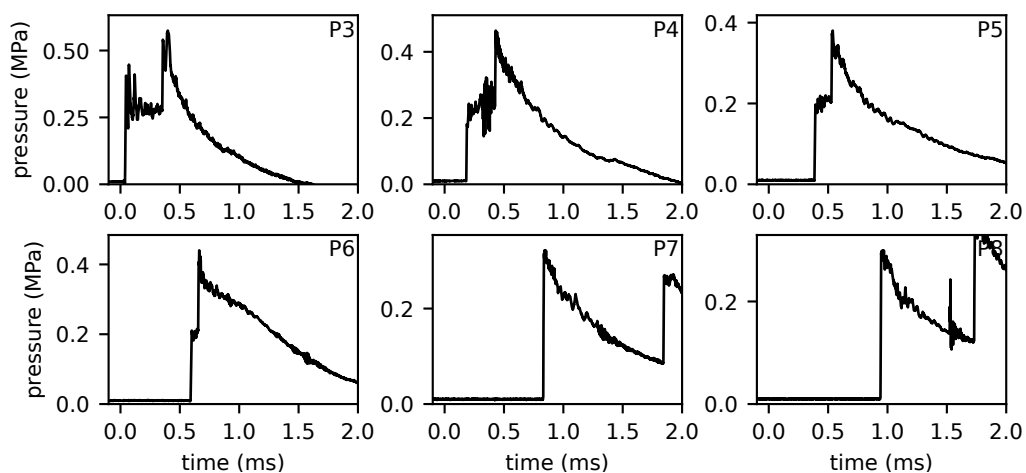


Figure F.22: Pressure data for shot 470.

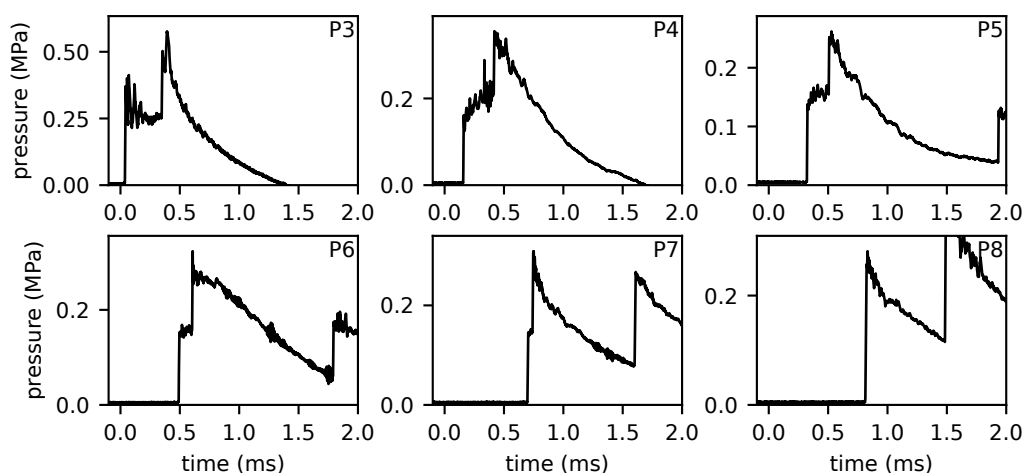


Figure F.23: Pressure data for shot 471.

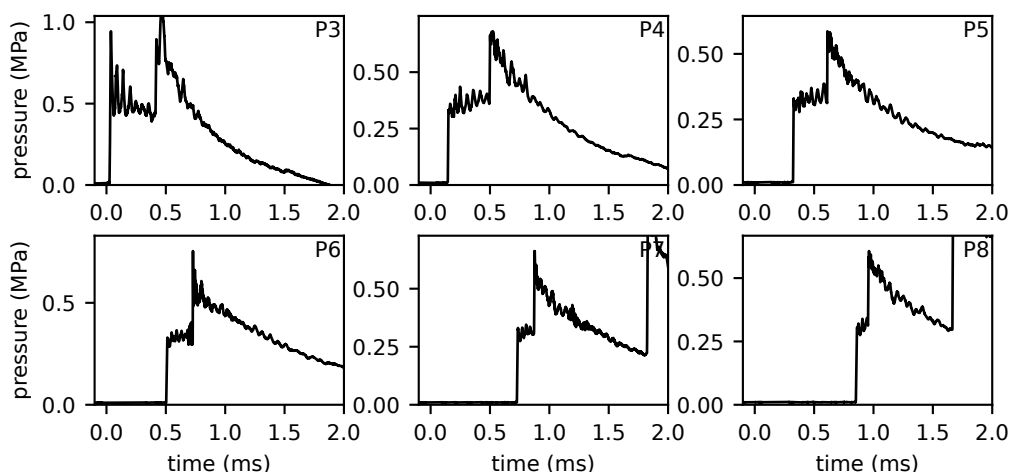


Figure F.24: Pressure data for shot 473.

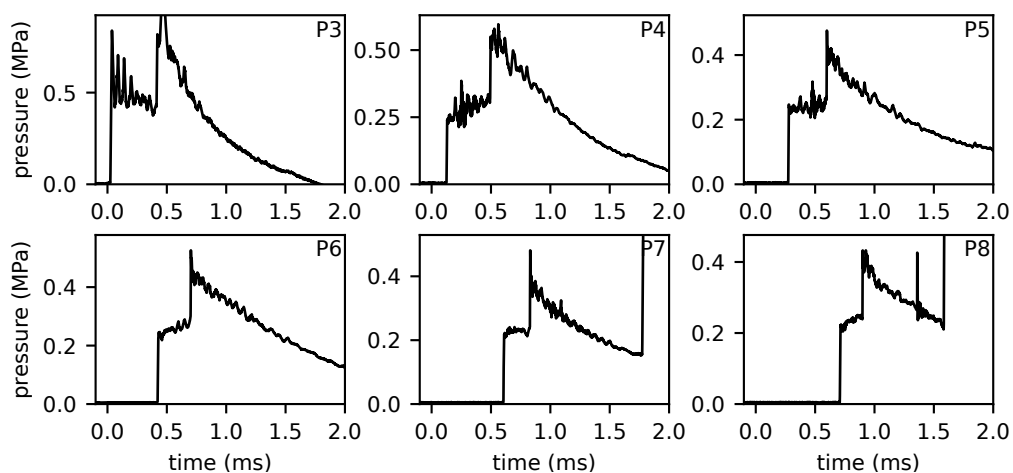


Figure F.25: Pressure data for shot 475.

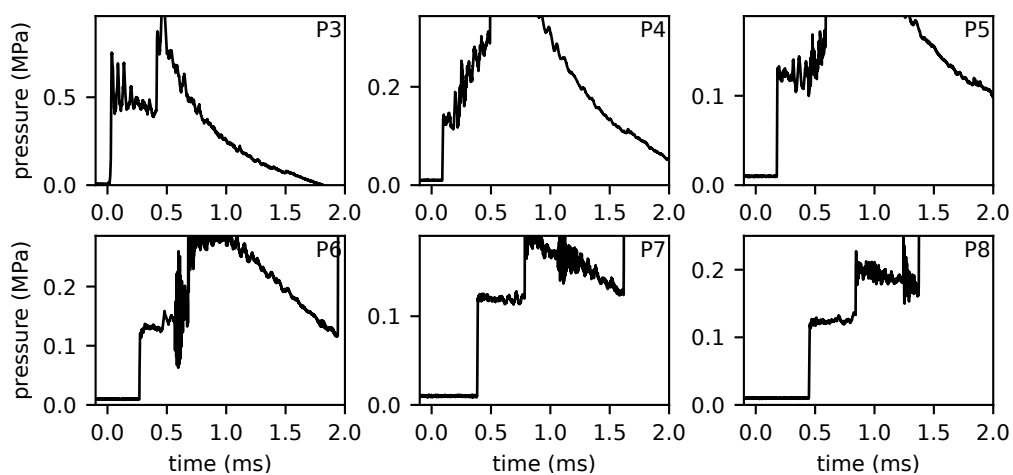


Figure F.26: Pressure data for shot 477.

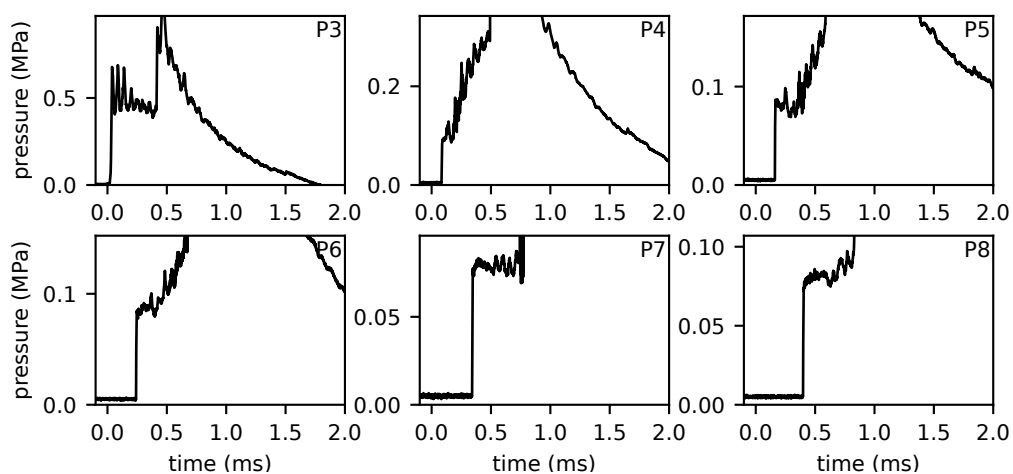


Figure F.27: Pressure data for shot 479.

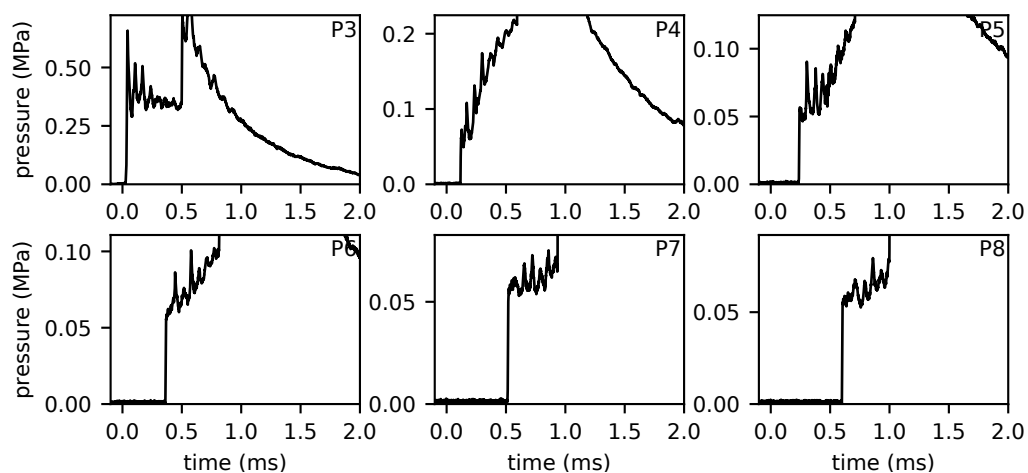


Figure F.28: Pressure data for shot 481.

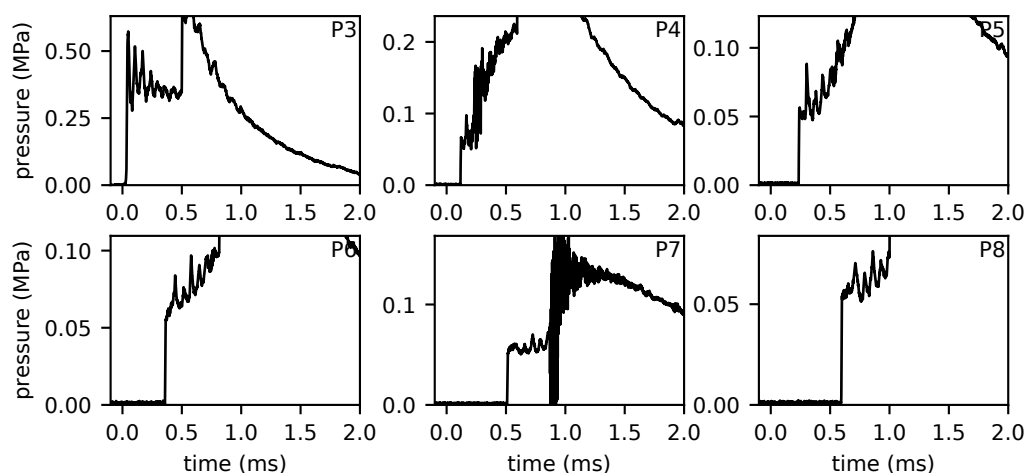


Figure F.29: Pressure data for shot 483.

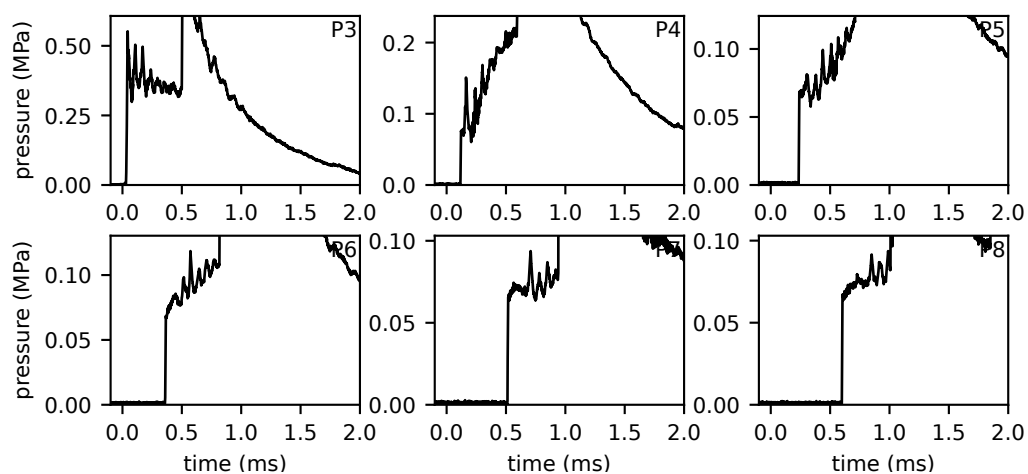


Figure F.30: Pressure data for shot 485.

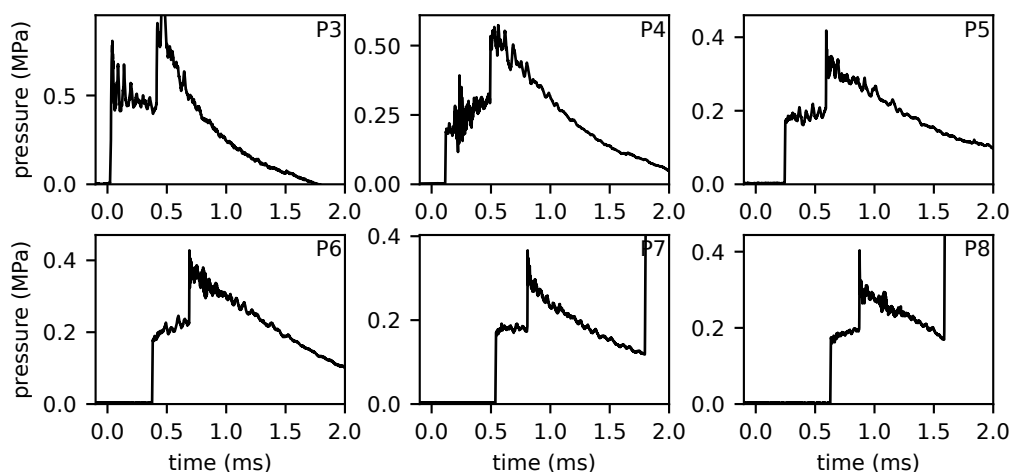


Figure F.31: Pressure data for shot 487.

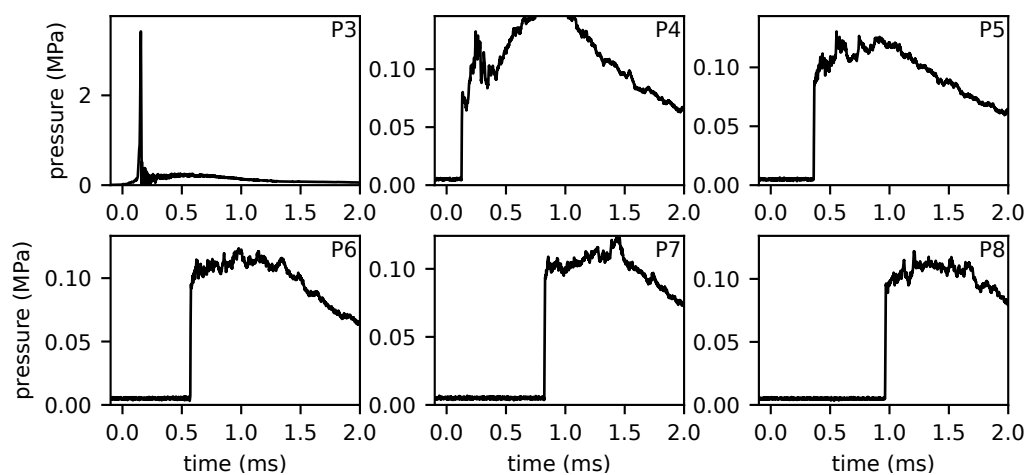


Figure F.32: Pressure data for shot 493.

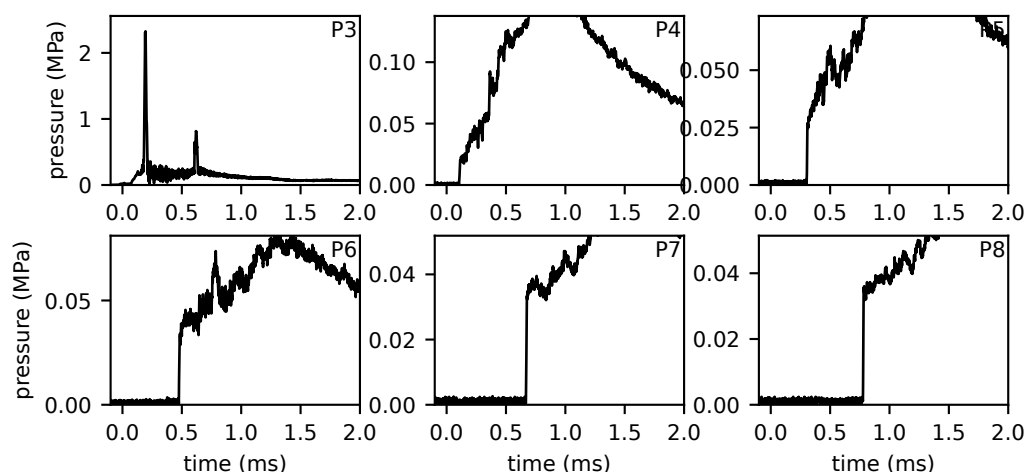


Figure F.33: Pressure data for shot 494.

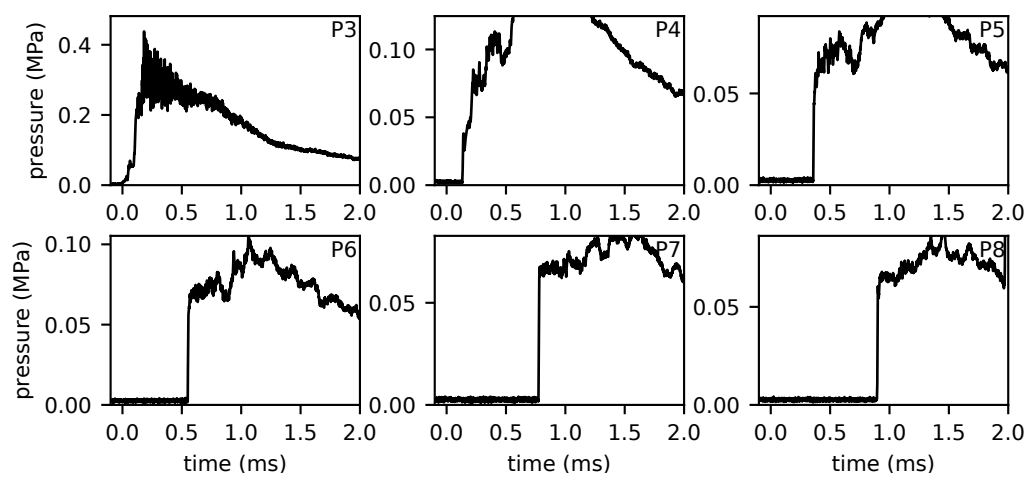
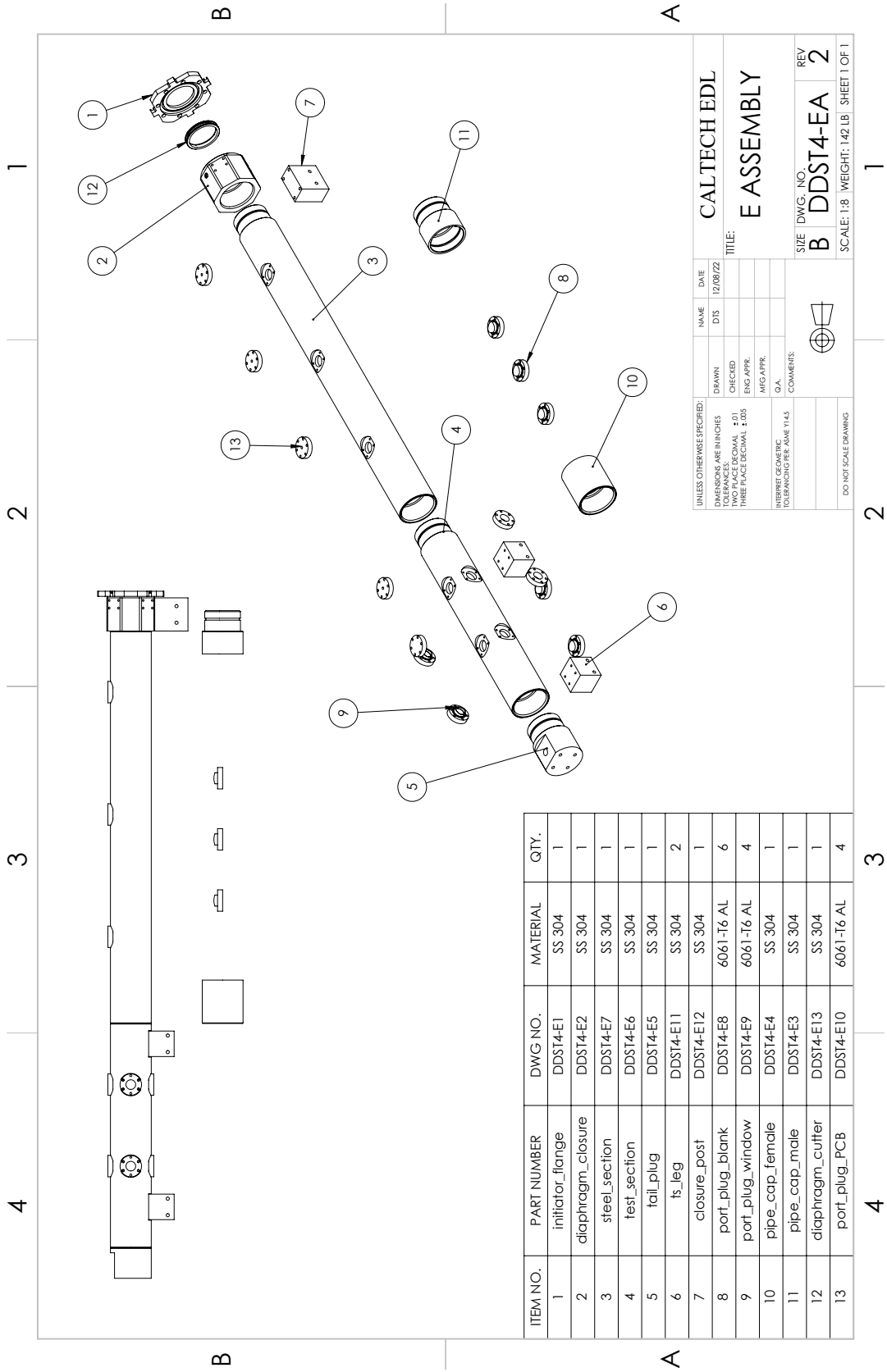


Figure F.34: Pressure data for shot 496.



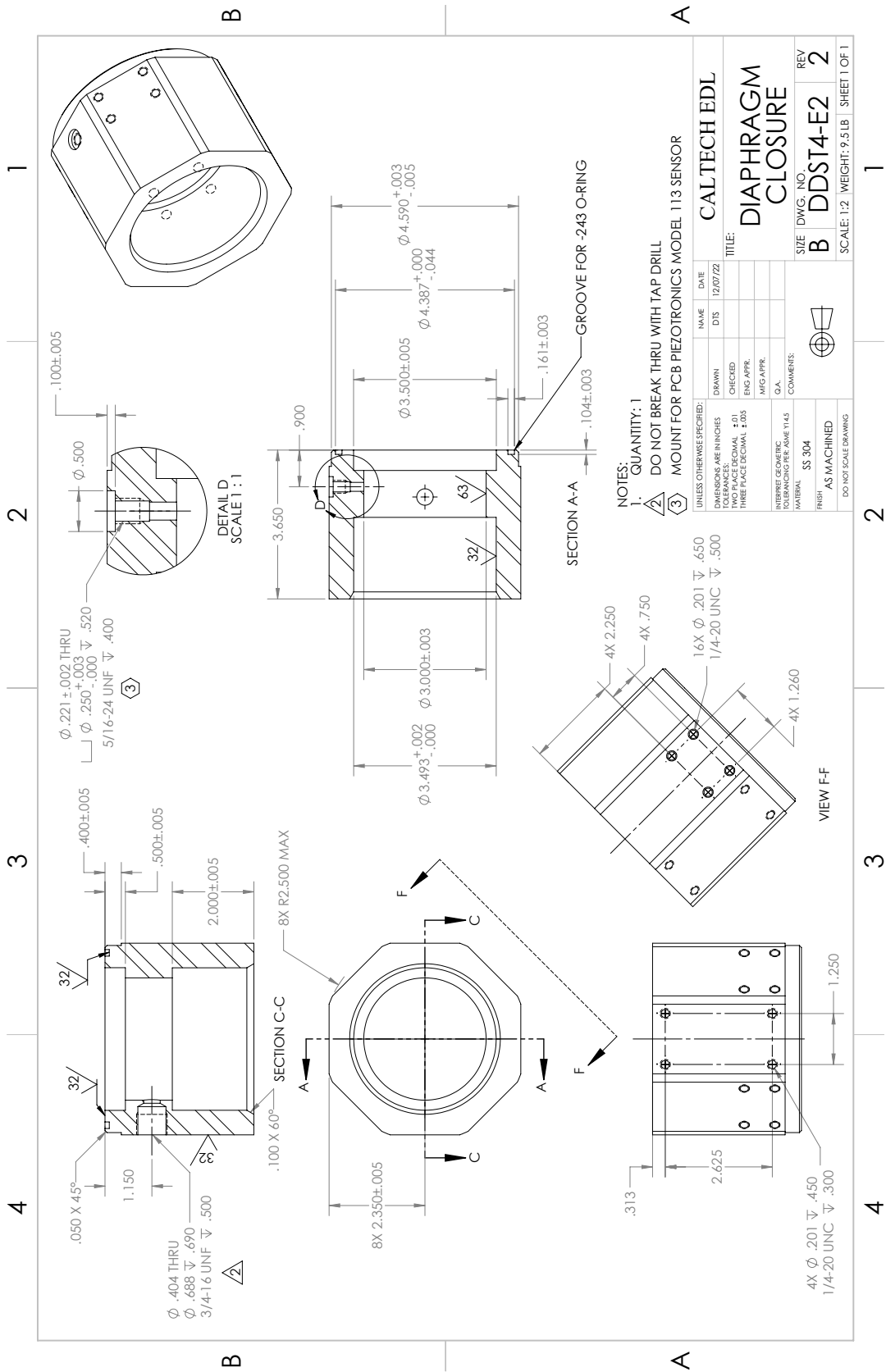
*Appendix G***ENGINEERING DRAWINGS**

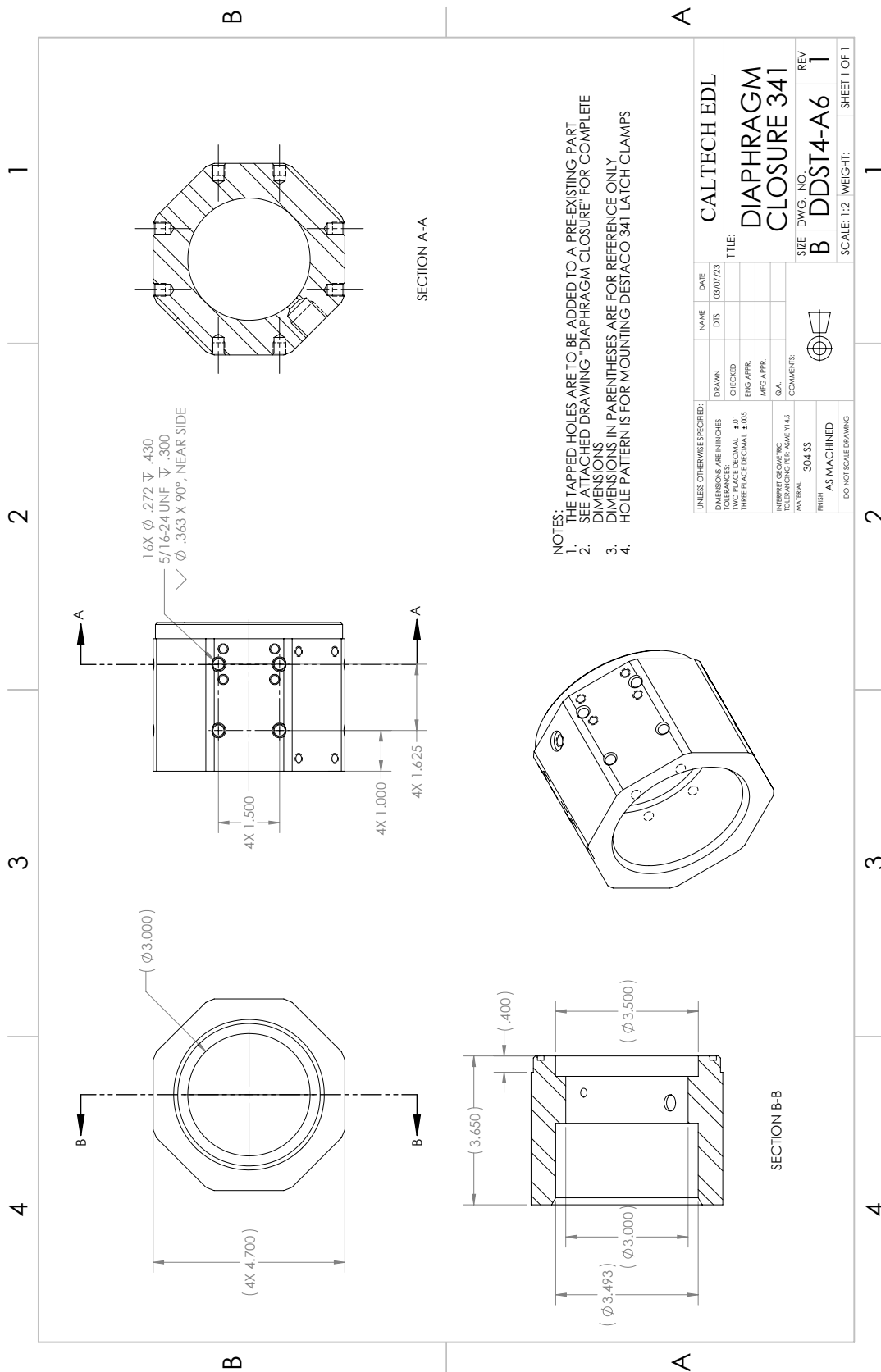
Engineering drawings for parts used to construct GUST are listed below. Several parts required modification or replacement from their initial designs. In particular, the diaphragm closure was modified to use four Destaco 341 clamps. Both the initial and modified drawing are below. Some parts, like block spacers, are not included below. Also not included are drawings for the polycarbonate driven section, however drawings DDST-E3 and DDST-E4 are the pipe caps that retained the polycarbonate tube.

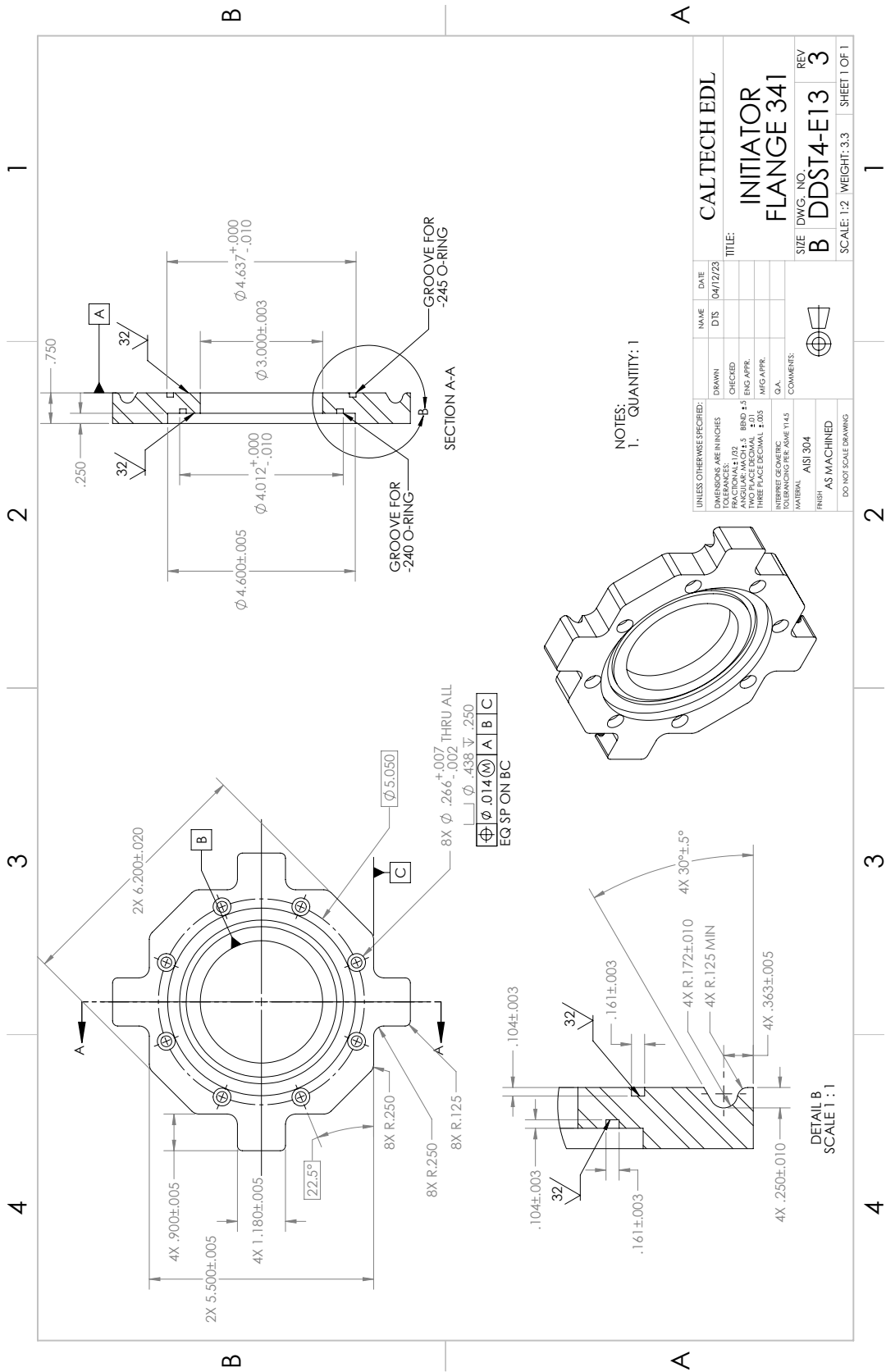


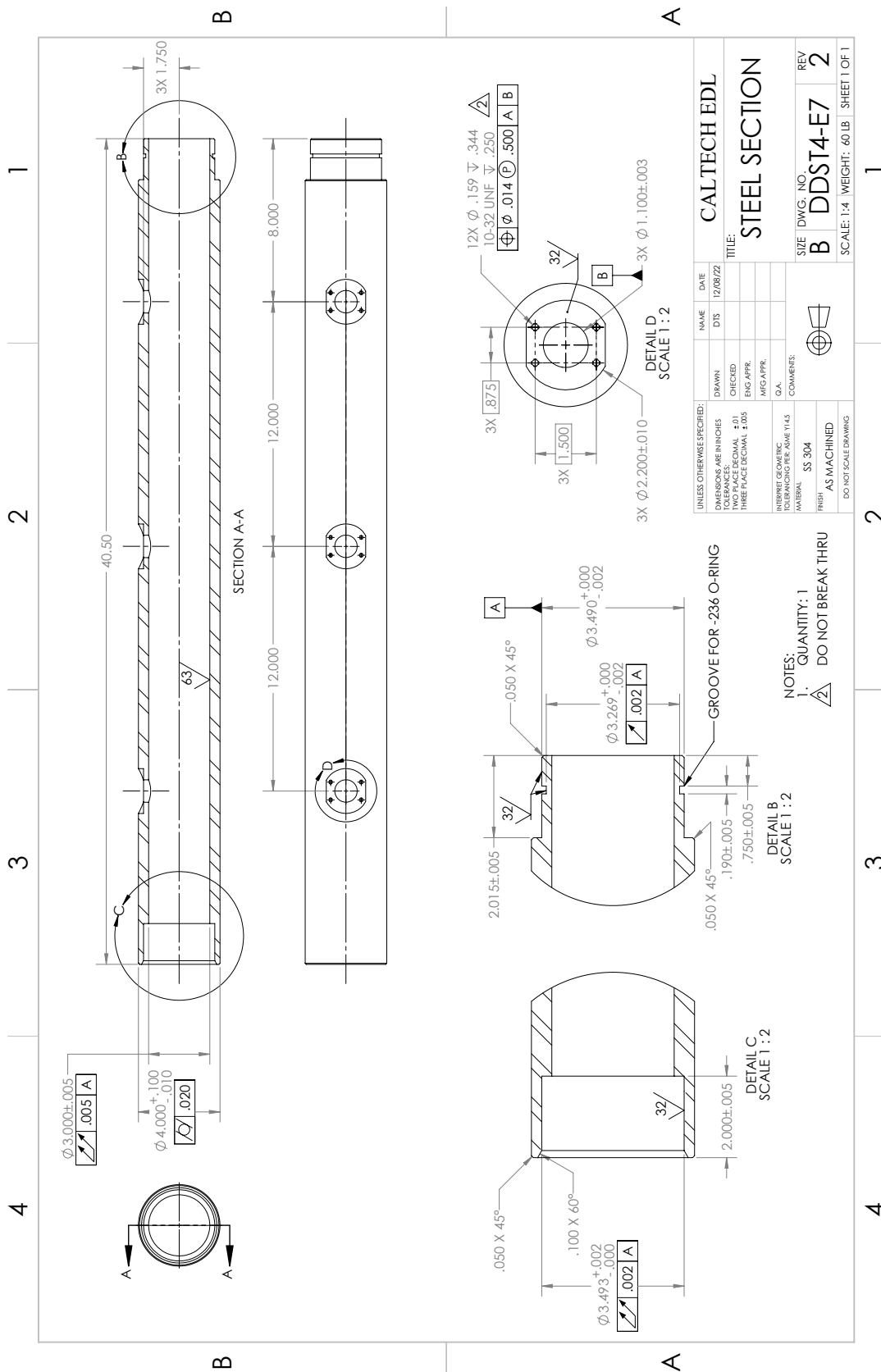
ITEM NO.	PART NUMBER	DWG NO.	MATERIAL	QTY.
1	initiator_flange	DDST4-E1	SS 304	1
2	diaphragm_closure	DDST4-E2	SS 304	1
3	steel_section	DDST4-E7	SS 304	1
4	test_section	DDST4-E6	SS 304	1
5	tail_plug	DDST4-E5	SS 304	1
6	ts_leg	DDST4-E11	SS 304	2
7	closure_post	DDST4-E12	SS 304	1
8	port_plug_blank	DDST4-E8	6061-T6 AL	6
9	port_plug_window	DDST4-E9	6061-T6 AL	4
10	pipe_cap_female	DDST4-E4	SS 304	1
11	pipe_cap_male	DDST4-E3	SS 304	1
12	diaphragm_cutter	DDST4-E13	SS 304	1
13	port_plug_PCB	DDST4-E10	6061-T6 AL	4

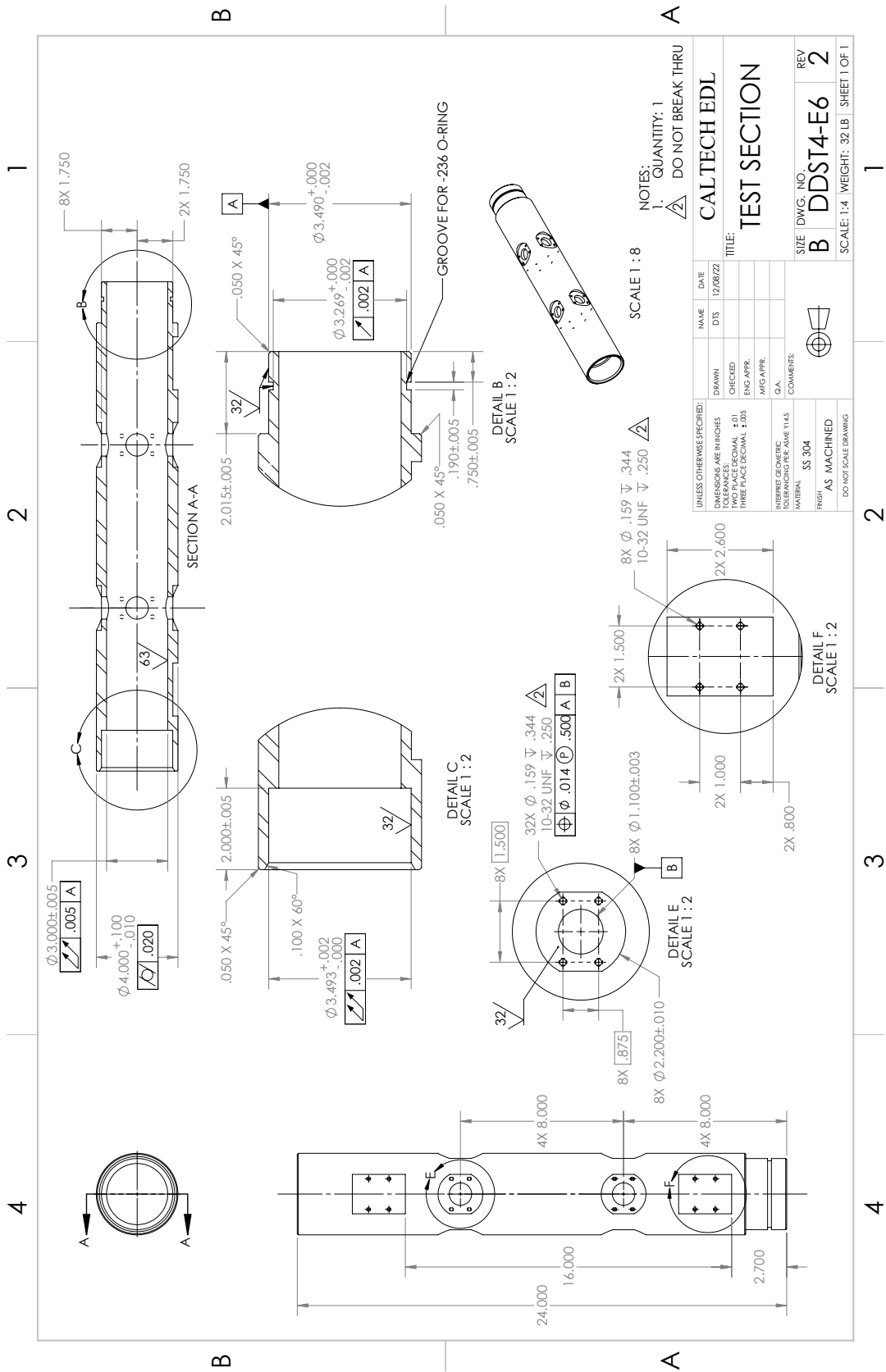
UNLESS OTHERWISE SPECIFIED:		NAME	DATE
DIMENSIONS ARE IN INCHES		DTS	12/08/22
TOLERANCES ARE:		CHECKED	
FRACTIONS DECIMAL ±.01		ENG APPR.	
THREE PLACE DECIMAL ±.005		MFG APPR.	
INTERPRET GEOMETRIC TOLERANCING PER ASME Y14.5		Q.A.	
COMMENTS:		TITLE: E ASSEMBLY	
DO NOT SCALE DRAWING		SIZE DWG. NO. REV	
		B DDST4-EA 2	
		SCALE: 1:8 WEIGHT: 142 LB SHEET 1 OF 1	

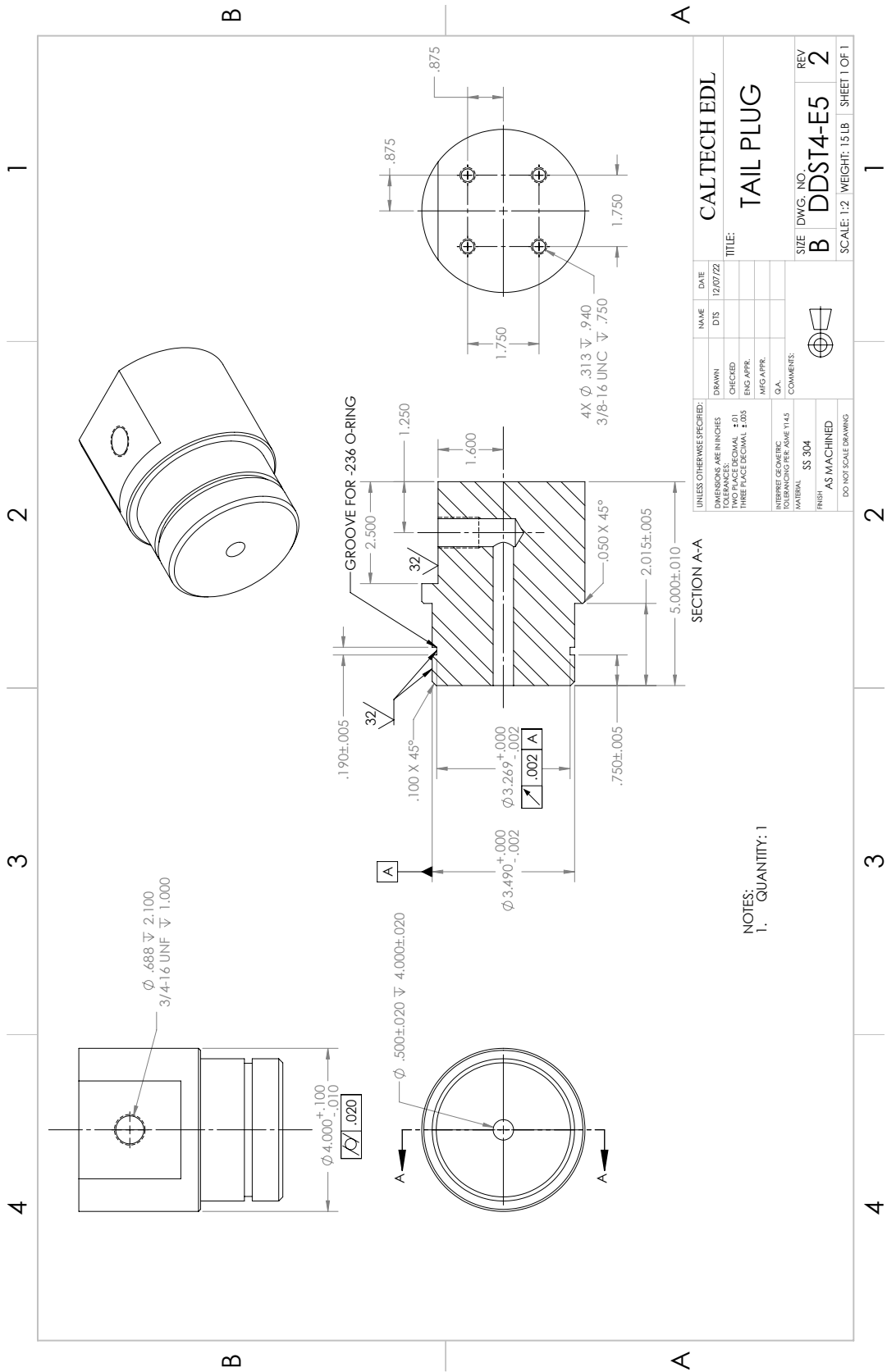






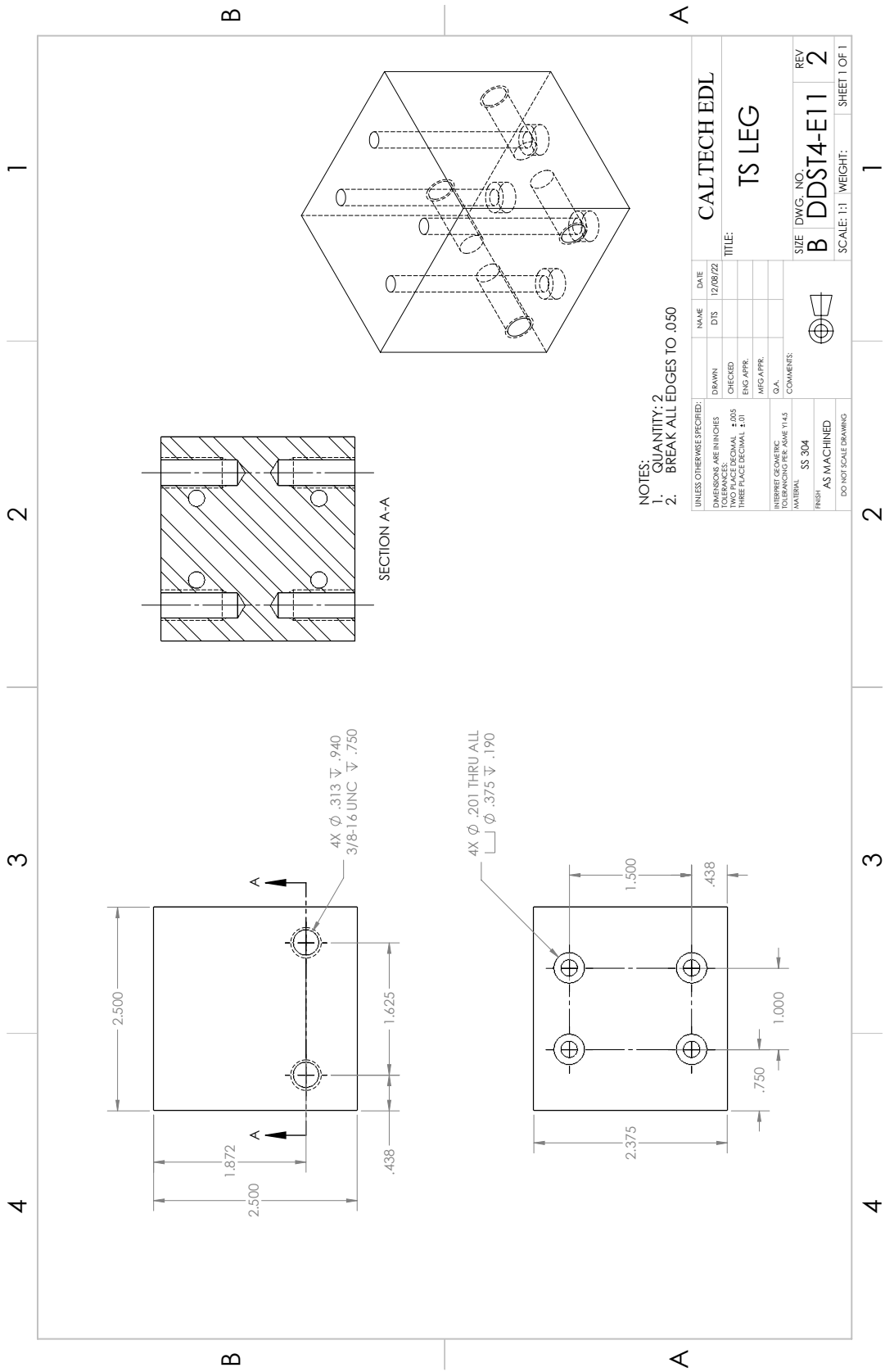


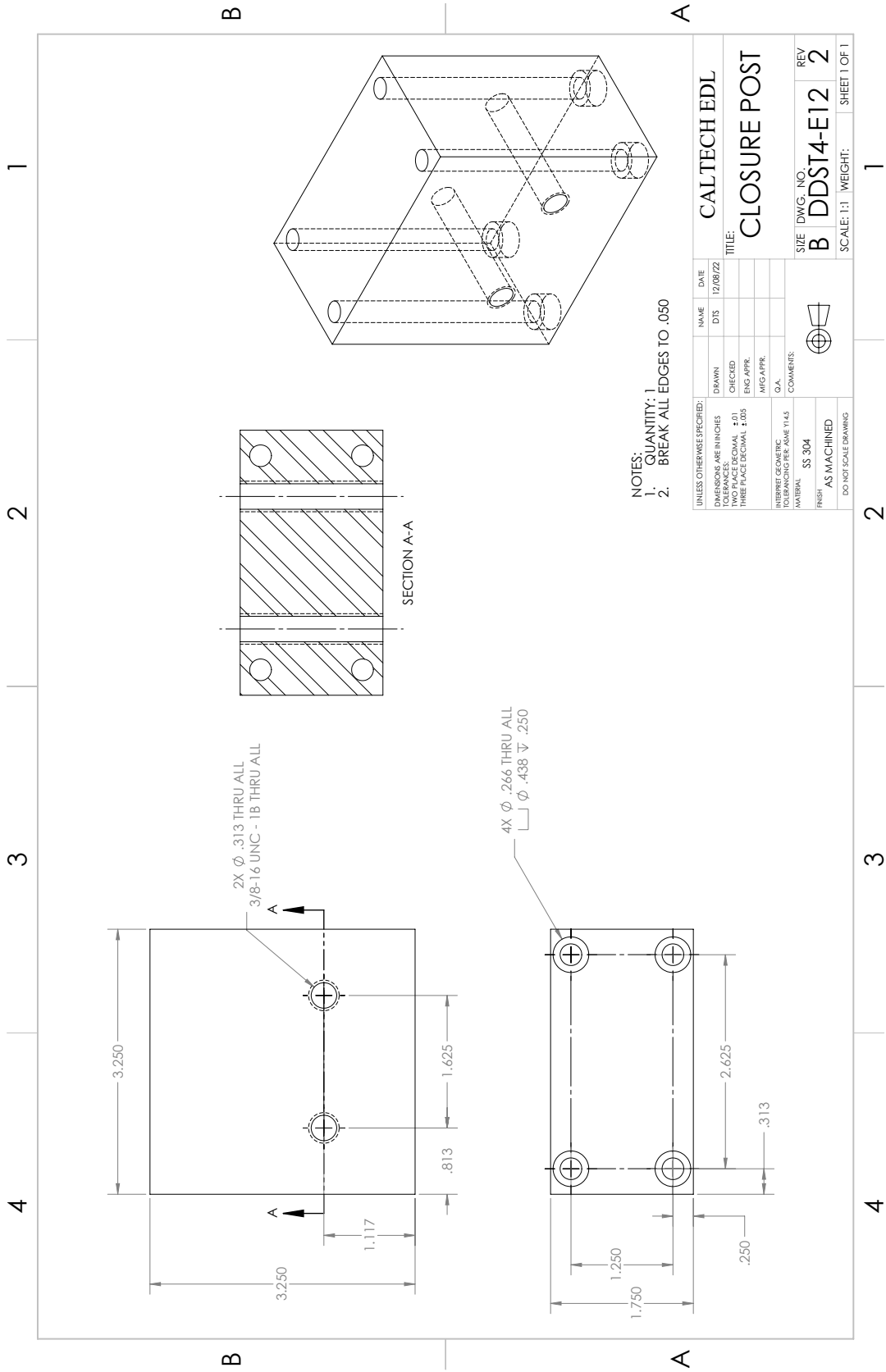


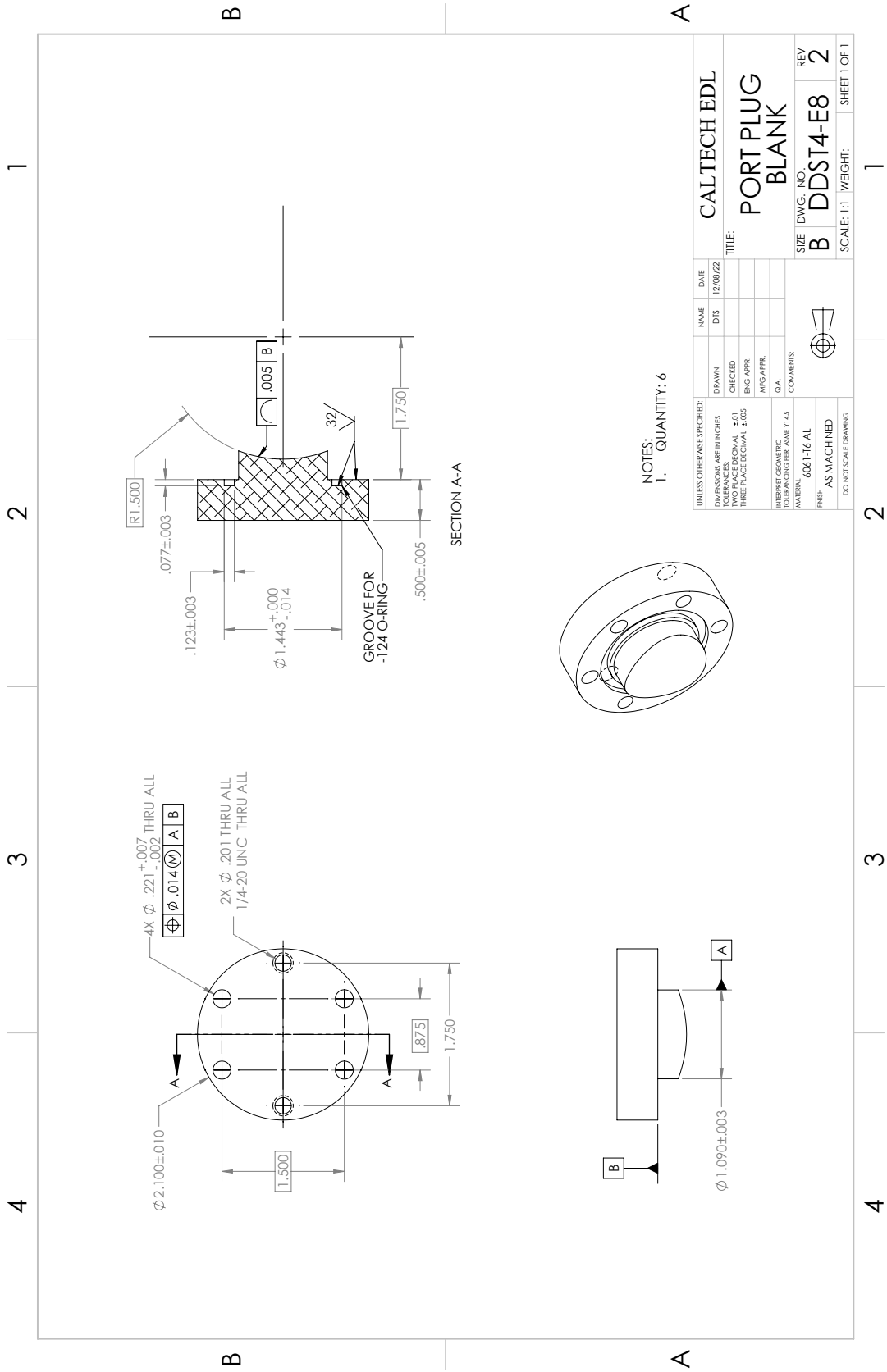


UNLESS OTHERWISE SPECIFIED:				CALTECH EDL			
DRAWN	NAME	DATE		DRAWN	NAME	DATE	
CHECKED	DTS	12/07/22		CHECKED	DTS	12/07/22	
ENG APPR				ENG APPR			
MFG APPR				MFG APPR			
Q.A.				Q.A.			
INTERPRET GEOMETRIC TOLERANCES PER ASME Y14.5				TITLE: TAIL PLUG			
MATERIAL: SS 304				SIZE: DDST4-E5			
FINISH: AS MACHINED				REV: 2			
DO NOT SCALE DRAWING				SCALE: 1:2			
				SHEET 1 OF 1			









4

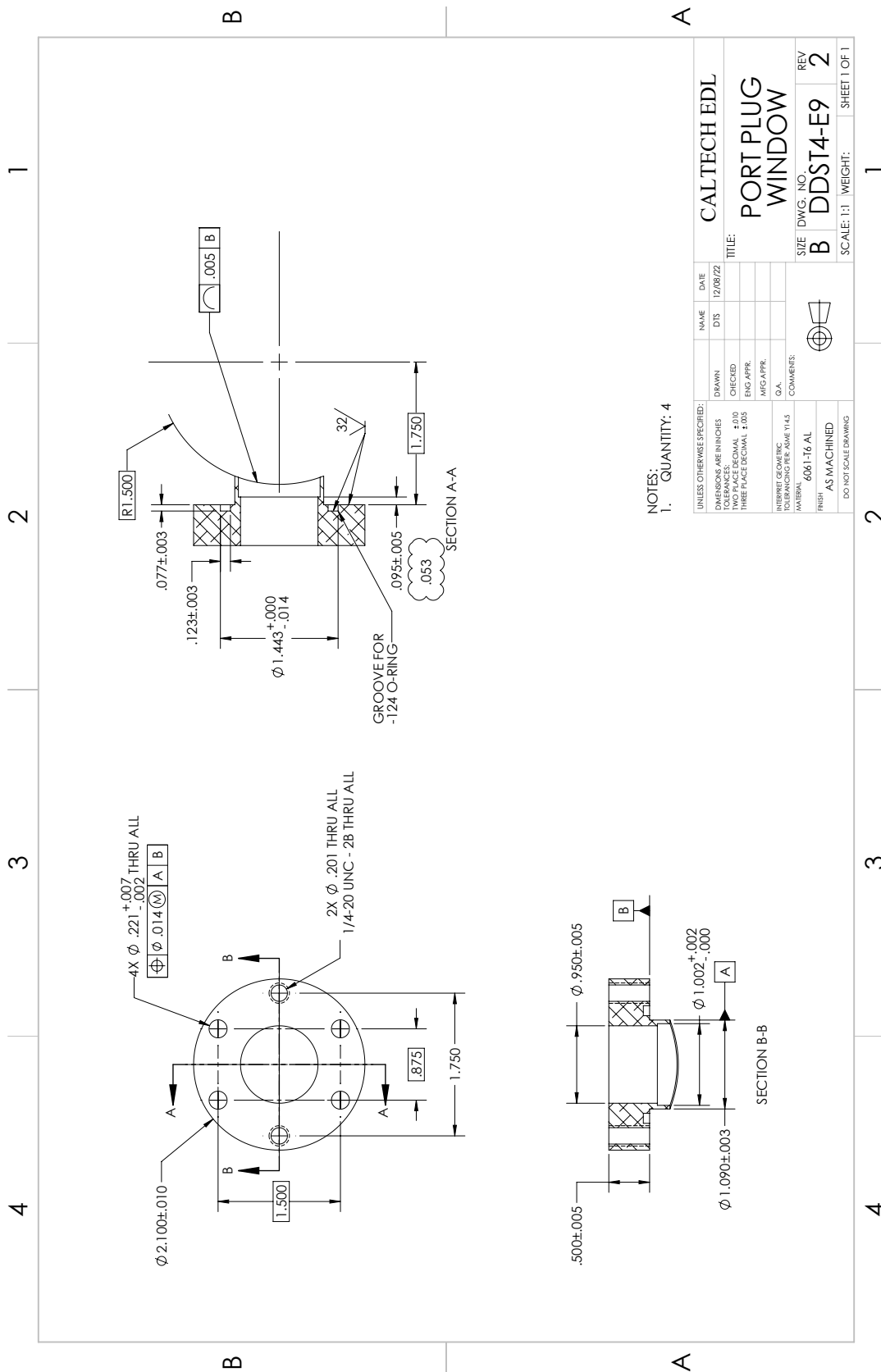
3

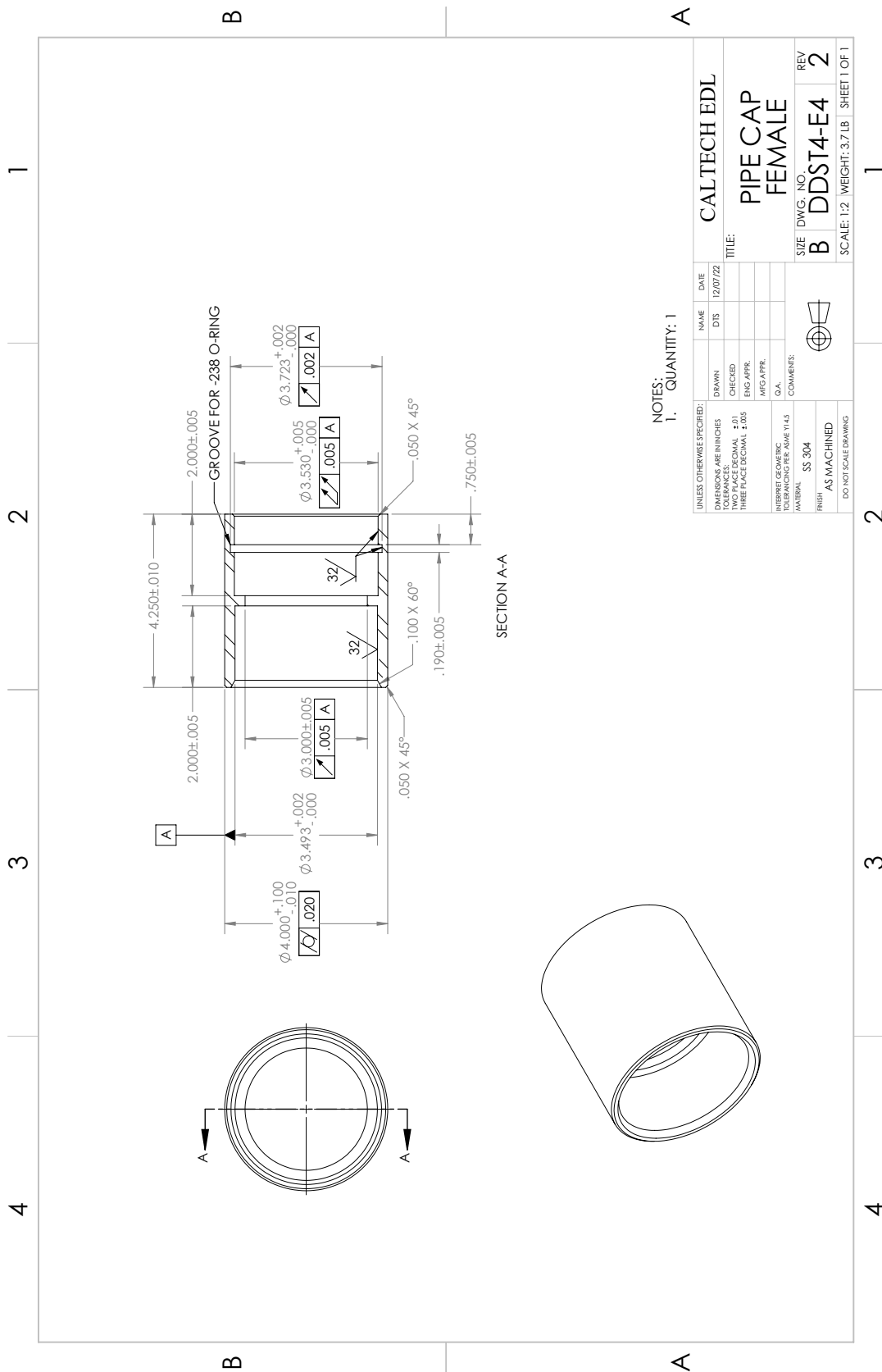
2

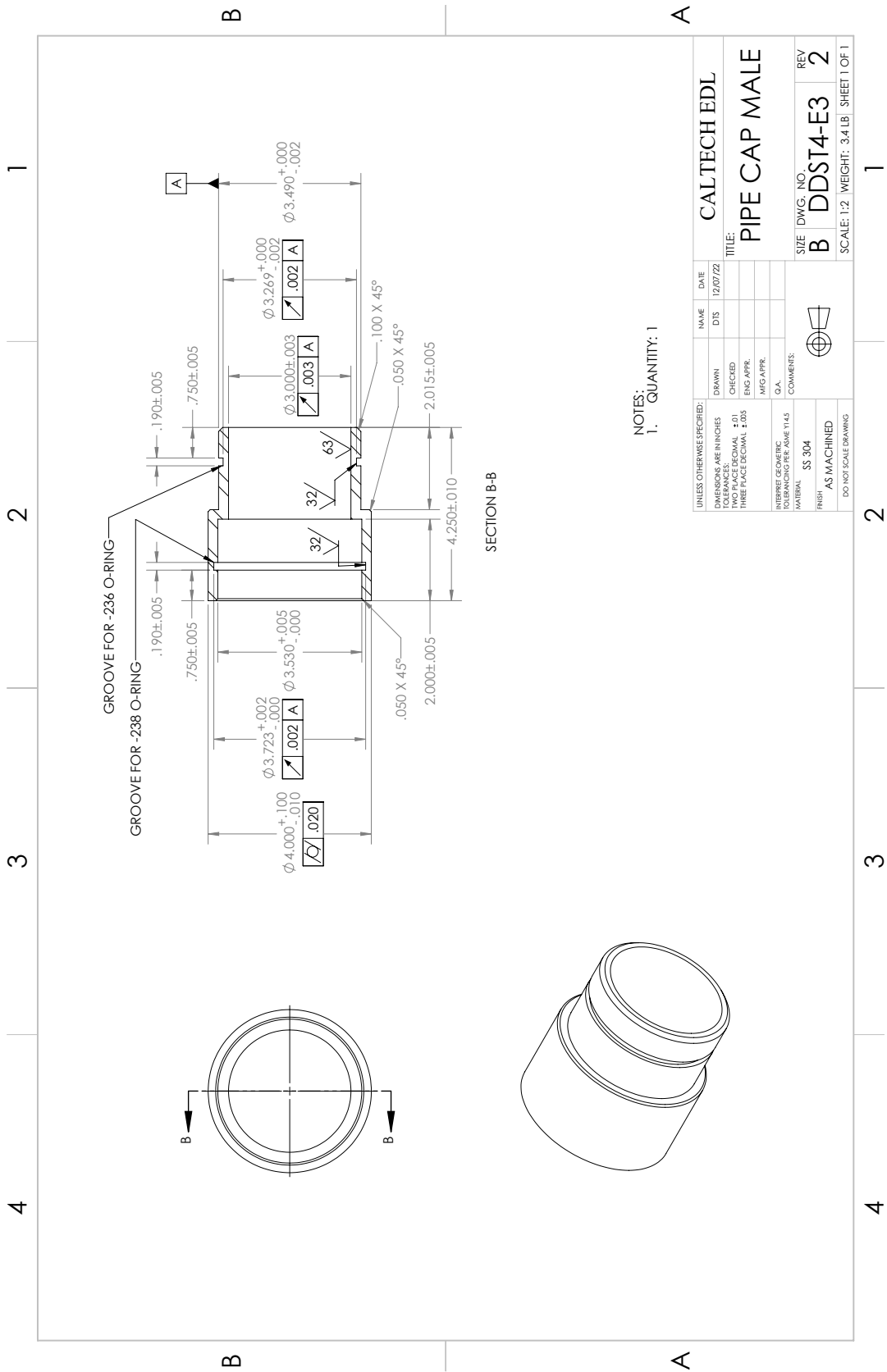
1

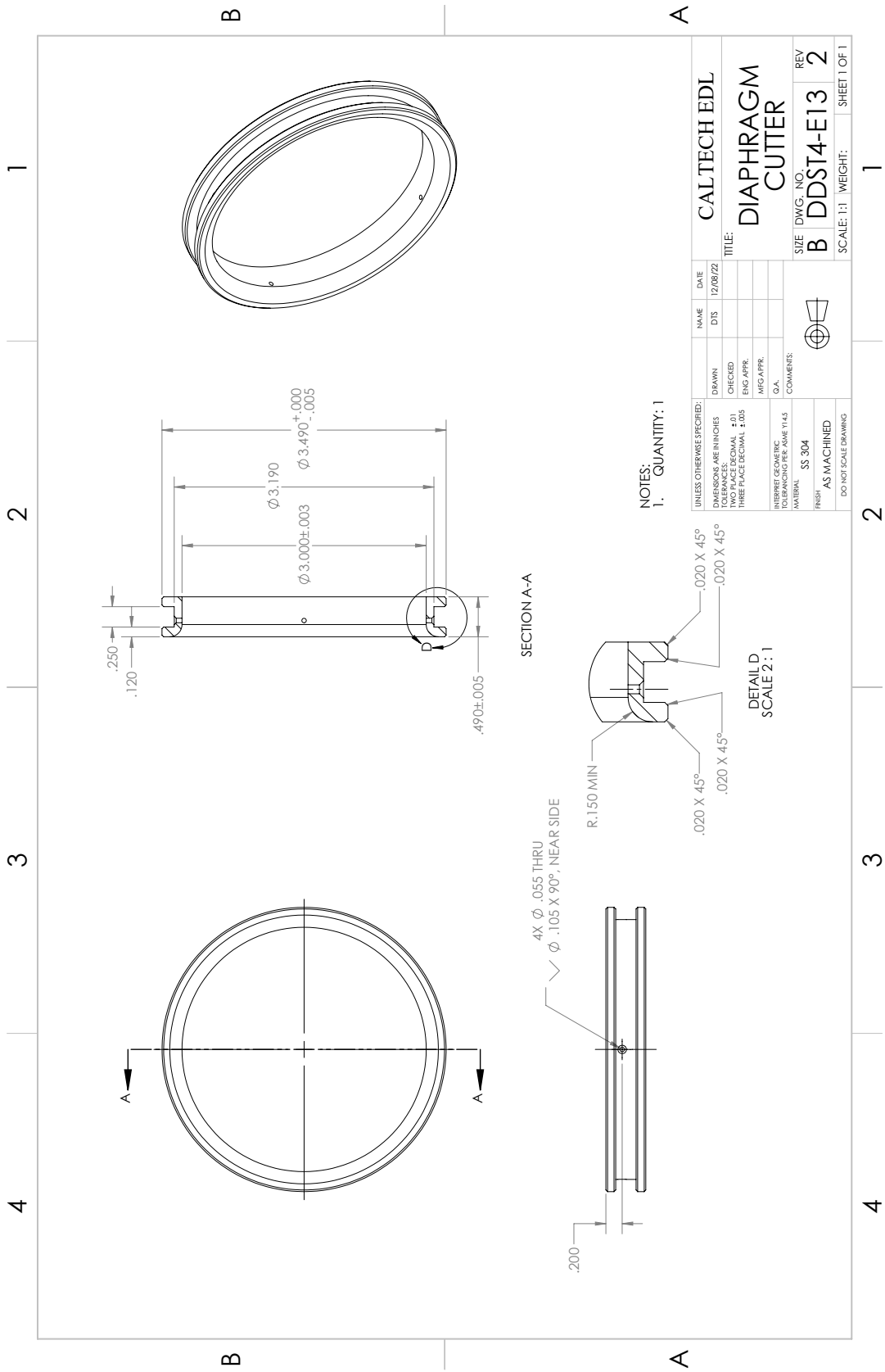
B

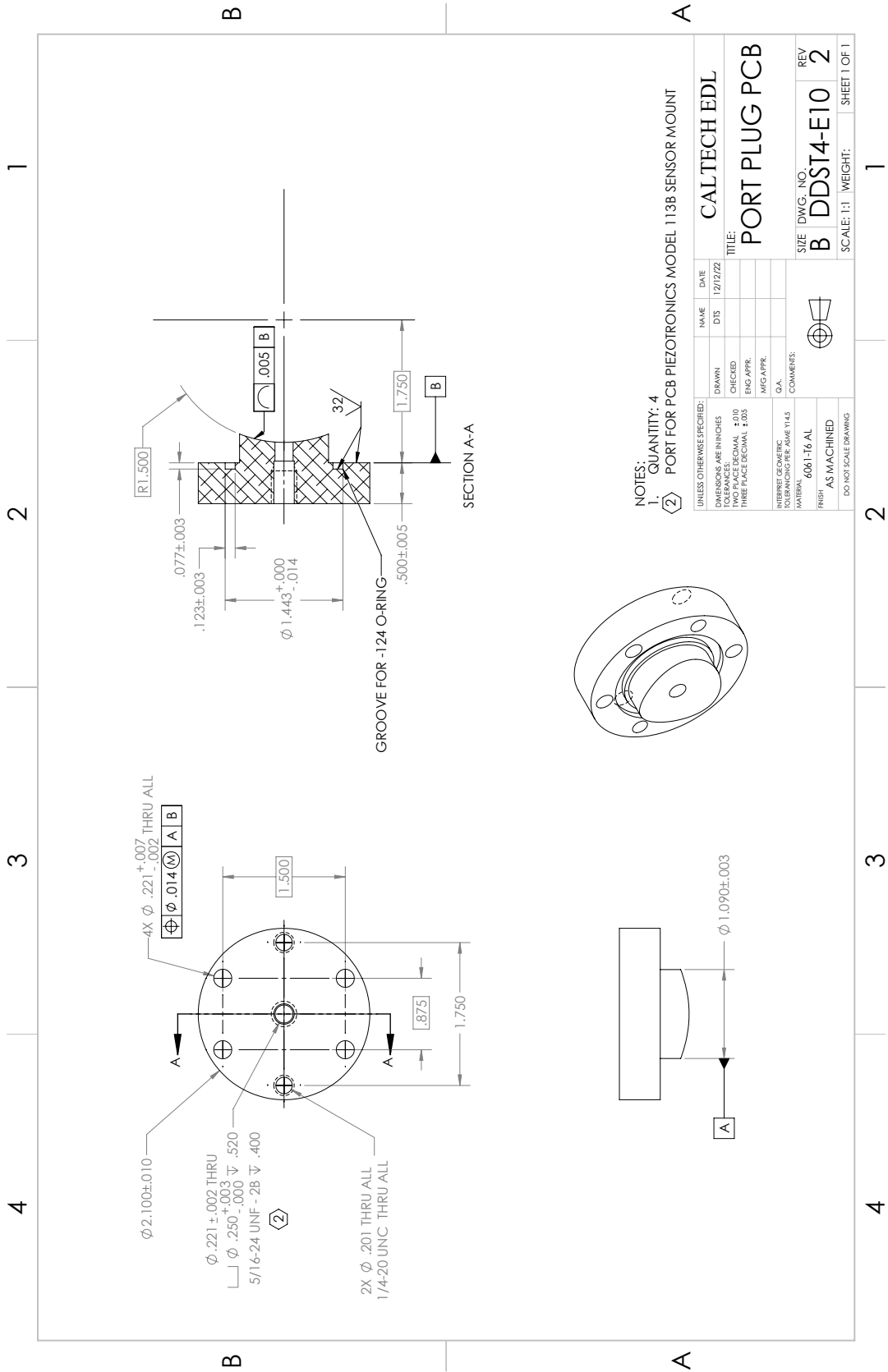
A











NOTES:

1. QUANTITY: 4

2. PORT FOR PCB PIEZOTRONICS MODEL 113B SENSOR MOUNT

UNLESS OTHERWISE SPECIFIED:	NAME	DATE
DIMENSIONS ARE IN INCHES	DTS	12/12/22
TOLERANCES ARE IN INCHES	CHECKED	
THREE PLACE DECIMAL $\pm .010$	ENG APPR.	
THREE PLACE DECIMAL $\pm .005$	MFG APPR.	
	Q.A.	

INTERPRET GEOMETRIC TOLERANCES USING Y14.5

MATERIAL: 6061-T6 AL

FINISH: AS MACHINED

DO NOT SCALE DRAWING

SIZE: DWG. NO. B DDST4-E10

REV: 2

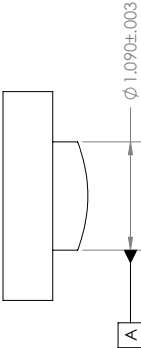
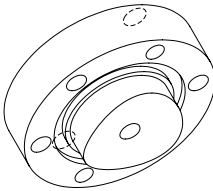
SCALE: 1:1

WEIGHT: 1

SHEET 1 OF 1

CALTECH EDL

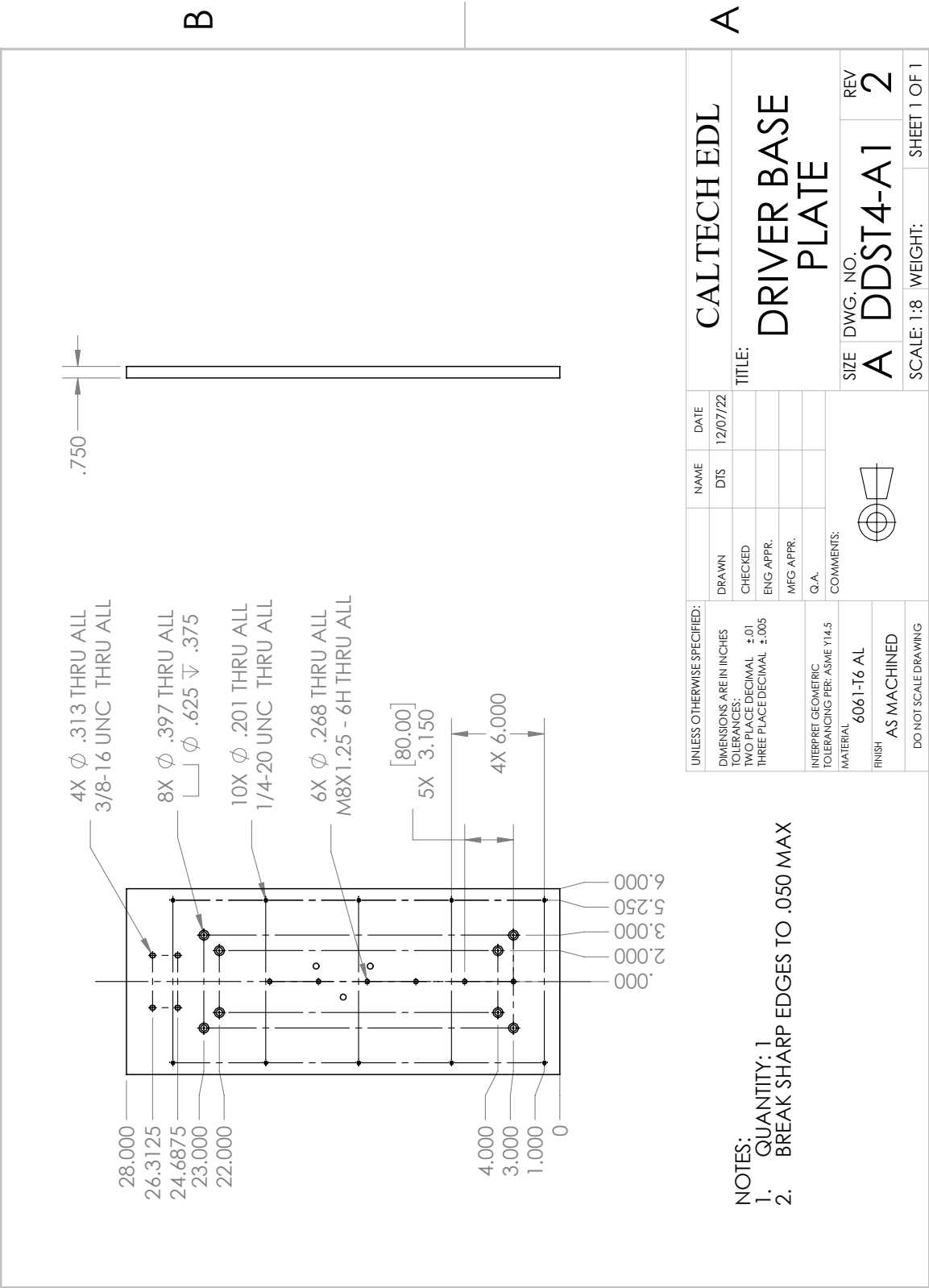
TITLE: PORT PLUG PCB





2

1



B

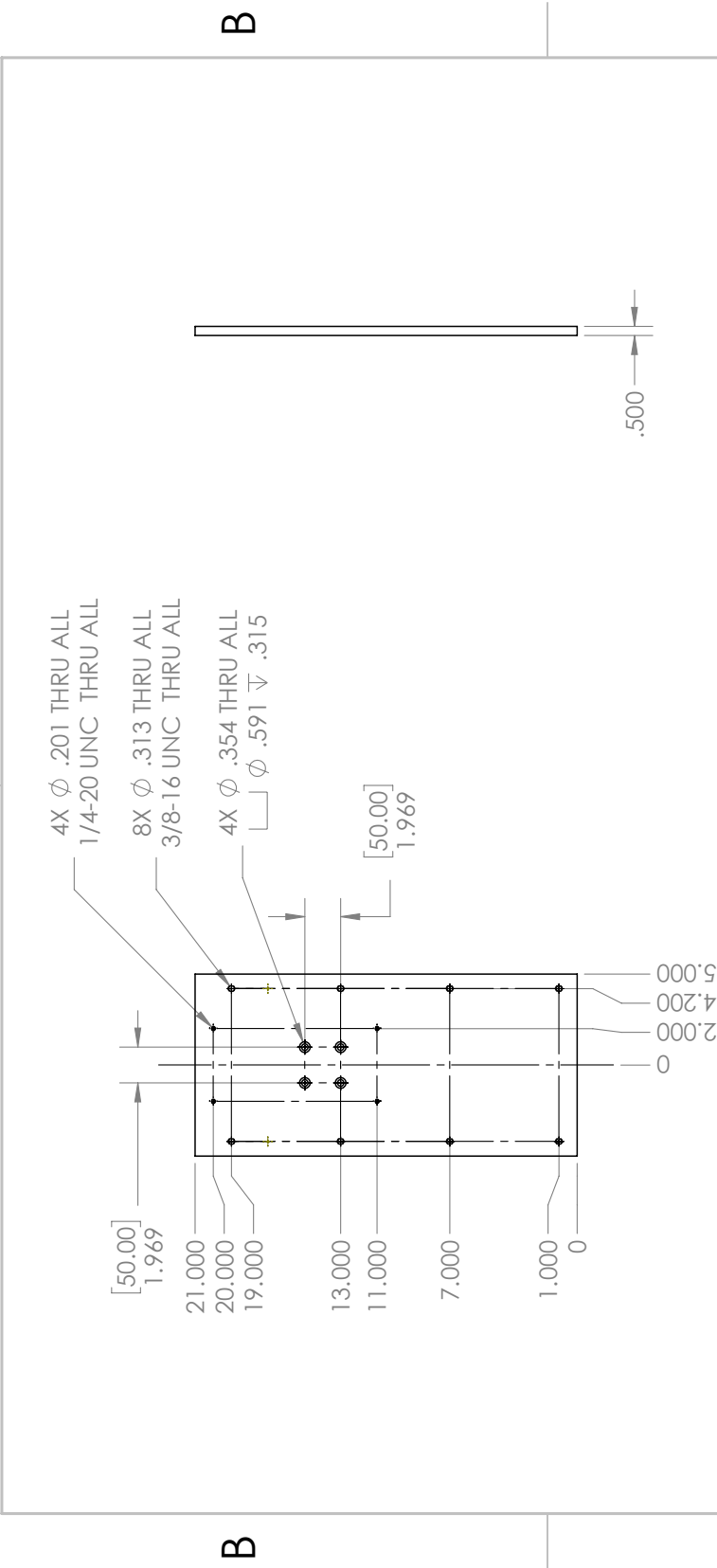
A

2

1

2

1



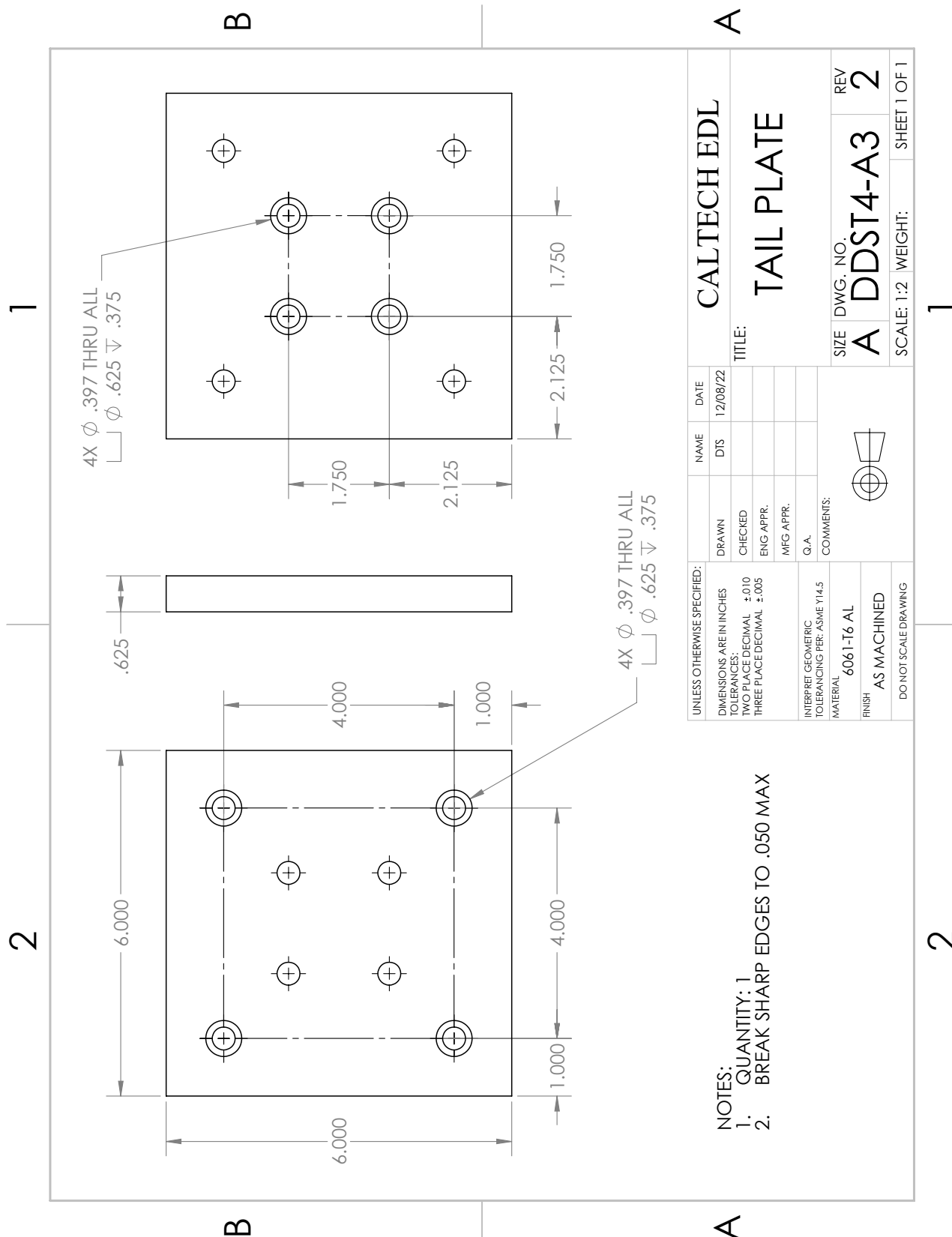
UNLESS OTHERWISE SPECIFIED:			CALTECH EDL		
DIMENSIONS ARE IN INCHES			NAME	DATE	TITLE:  DRIVER CARRIAGE PLATE
TOLERANCES:			DTS	12/07/22	
TWO PLACE DECIMAL ±.01					
THREE PLACE DECIMAL ±.005					
INTERPRET GEOMETRIC TOLERANCING PER: ASME Y14.5			COMMENTS:		
MATERIAL 6061-T6 AL			SIZE DWG. NO. REV		
FINISH AS MACHINED			A DDST4-A2 2		
DO NOT SCALE DRAWING			SCALE: 1:8 WEIGHT:		SHEET 1 OF 1

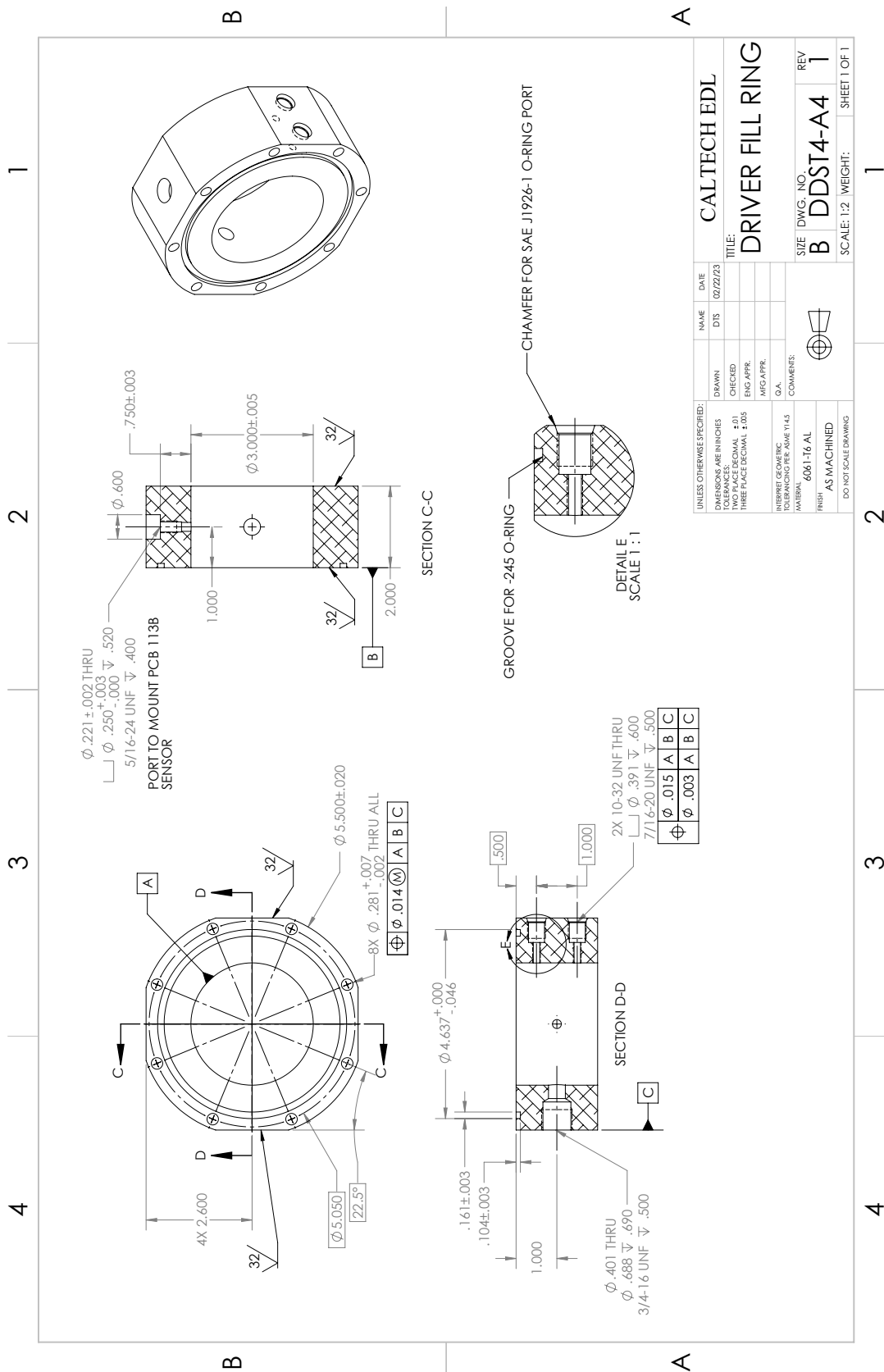
A

NOTES:

1. QUANTITY: 1
2. BREAK SHARP EDGES TO .050 MAX

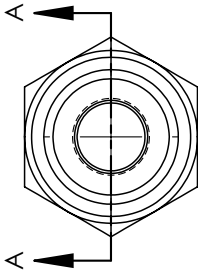
A



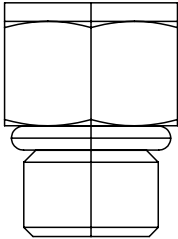


2

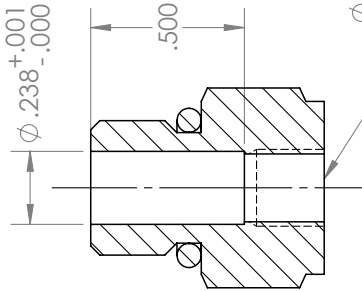
1



B



B



SECTION A-A

$\phi .221 \pm .003$   
1/4-36 UNS  $\pm .020$

SWAGELOK SS-4-PST

NOTES:  
1. QUANTITY: 2

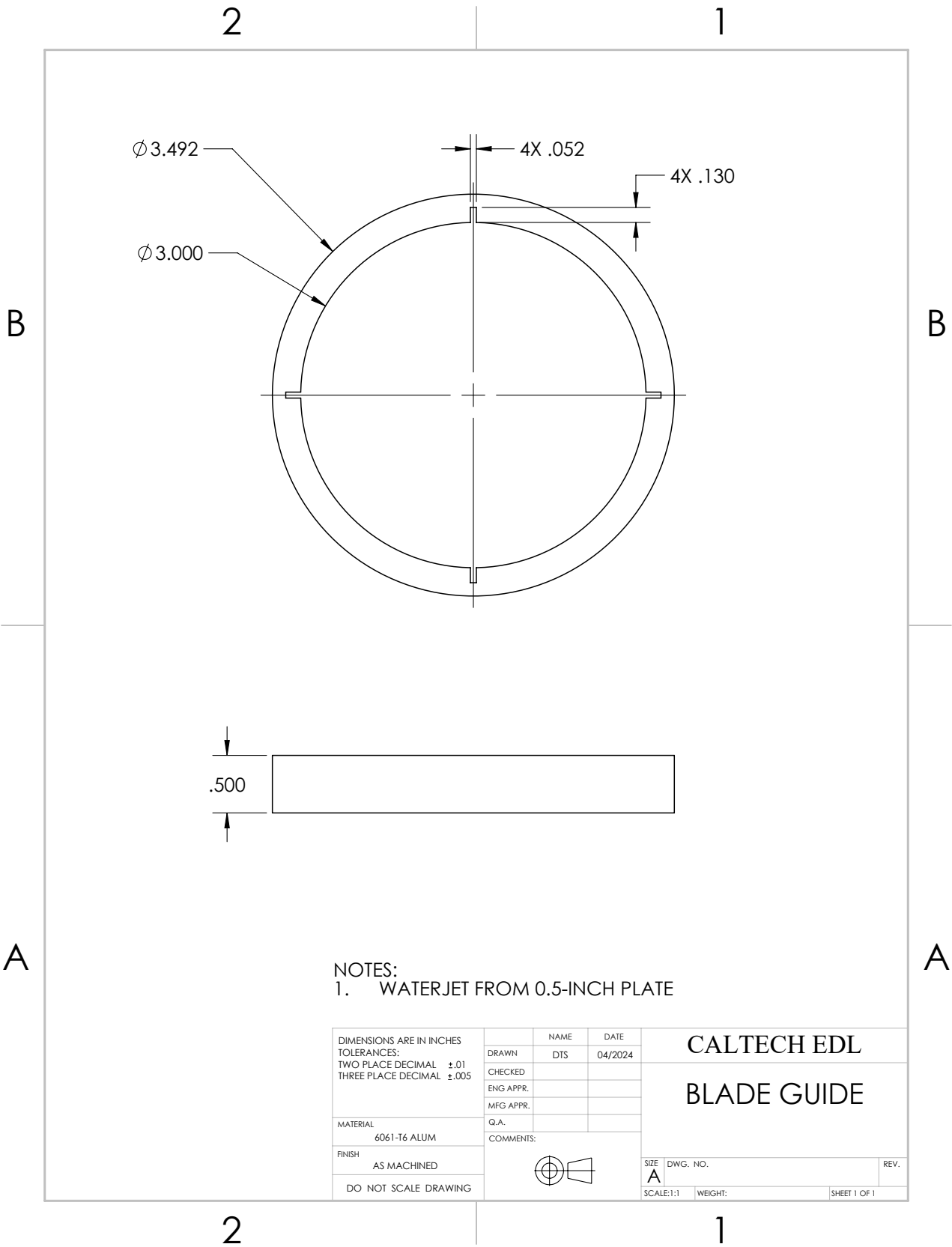
A

A


UNLESS OTHERWISE SPECIFIED:		DRAWN	NAME	DATE	CALTECH EDL	
DIMENSIONS ARE IN INCHES		CHECKED	DTS	02/24/23	TITLE:	
TOLERANCES:		ENG APPR.			FIBER-COUPLING	
TWO PLACE DECIMAL $\pm .01$		MFG APPR.			PLUG	
THREE PLACE DECIMAL $\pm .005$		Q.A.			SIZE DWG. NO.	
INTERPRET GEOMETRIC TOLERANCING PER: ASME Y14.5		COMMENTS:			A DDST4-A5	
MATERIAL					REV	
SS					1	
FINISH					SCALE: 2:1	
AS MACHINED					WEIGHT:	
DO NOT SCALE DRAWING					SHEET 1 OF 1	

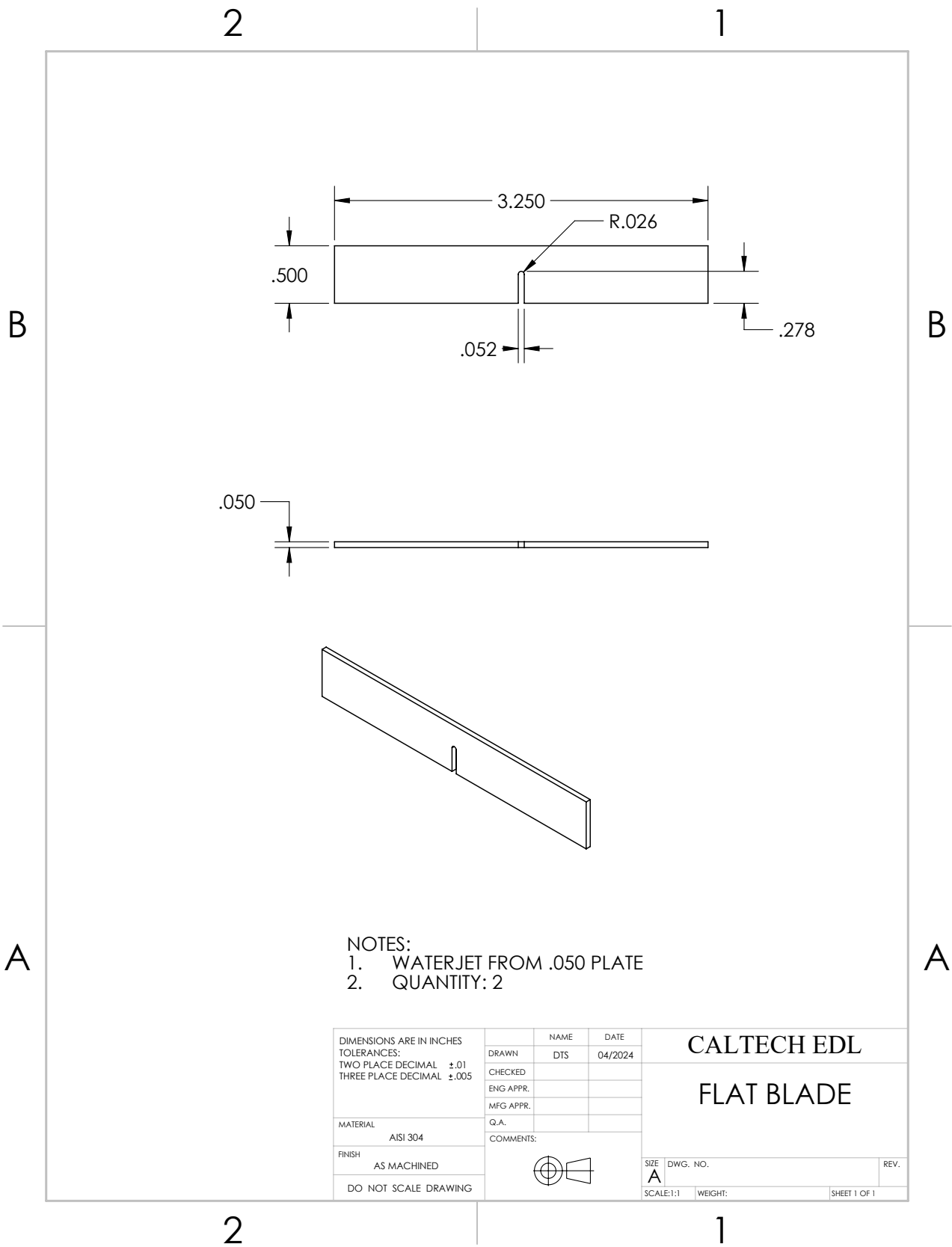
2

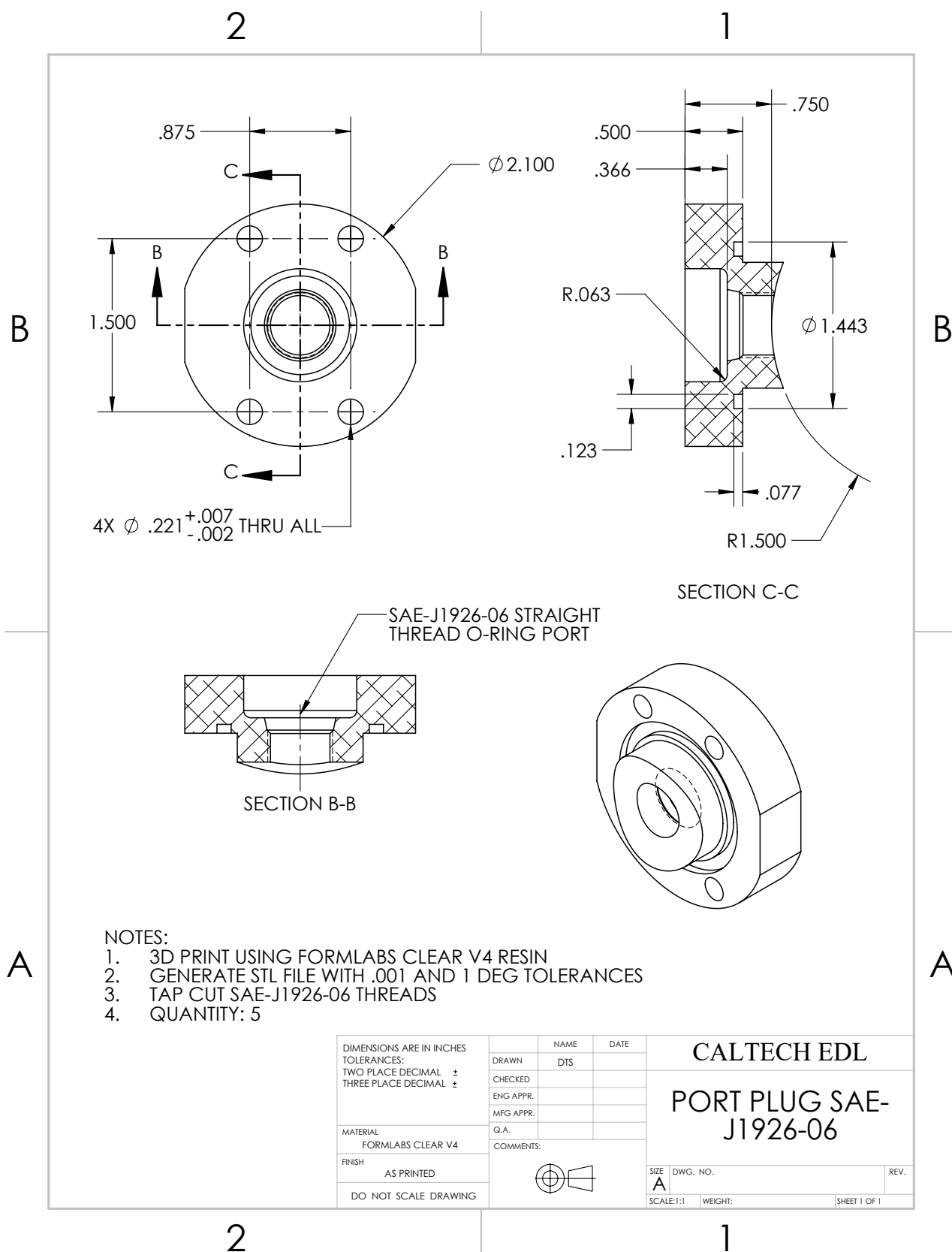
1



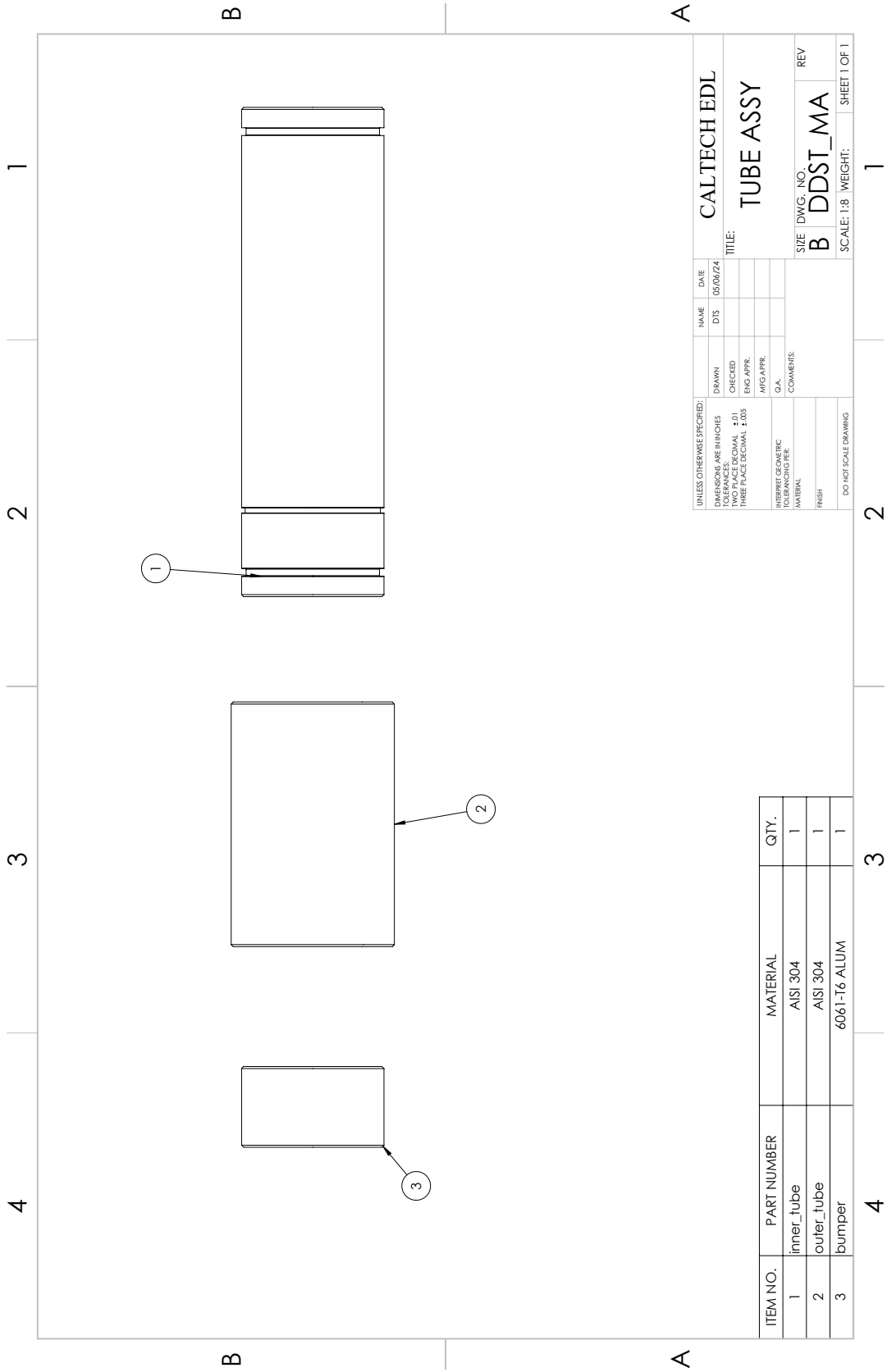
NOTES:  
1. WATERJET FROM 0.5-INCH PLATE

DIMENSIONS ARE IN INCHES TOLERANCES: TWO PLACE DECIMAL ±.01 THREE PLACE DECIMAL ±.005		NAME	DATE	CALTECH EDL  BLADE GUIDE			
		DRAWN	DTS			04/2024	
		CHECKED					
		ENG APPR.					
		MFG APPR.					
MATERIAL		Q.A.		BLADE GUIDE			
6061-T6 ALUM		COMMENTS:					
FINISH						SIZE	
AS MACHINED						DWG. NO.	REV.
DO NOT SCALE DRAWING						SCALE:1:1	WEIGHT:





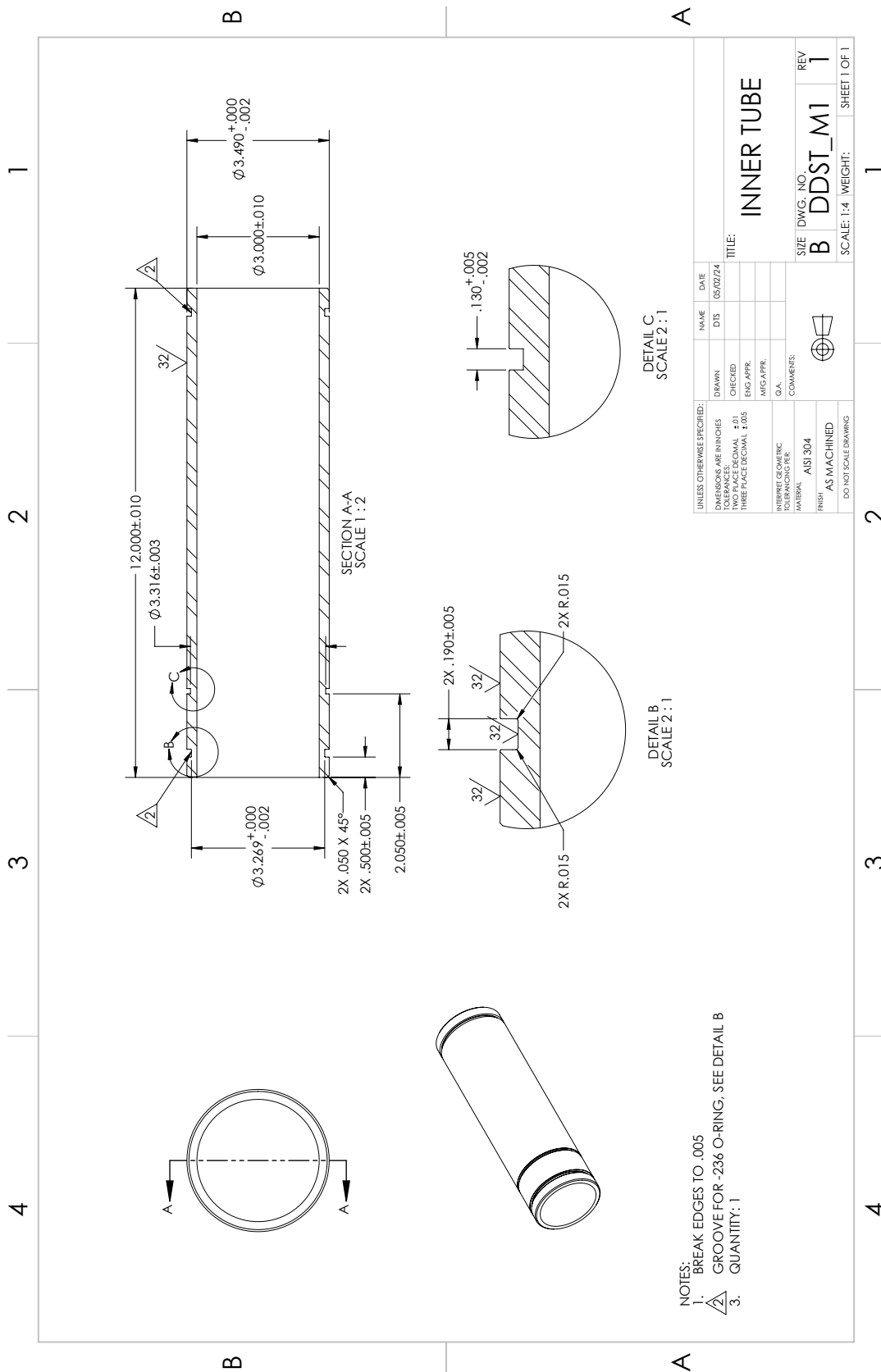




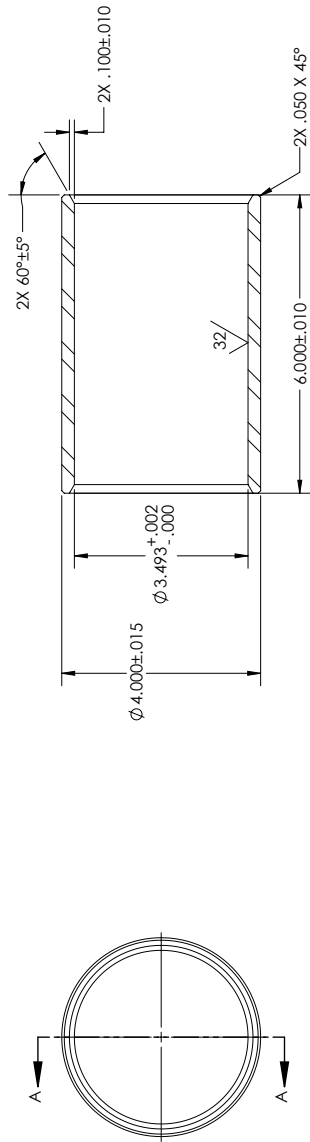
ITEM NO.	PART NUMBER	MATERIAL	QTY.
1	innerTube	AlSi 304	1
2	outerTube	AlSi 304	1
3	bumper	6061-T6 ALUM	1

UNLESS OTHERWISE SPECIFIED:		NAME	DATE
DIMENSIONS ARE IN INCHES		DTS	05/06/24
TOLERANCES ARE DECIMALS		CHECKED	
FRACTIONS ARE DECIMALS		ENG APPR	
THREE PLACE DECIMALS		MFG APPR	
INTERPRET GEOMETRIC		Q.A.	
FEATURES AND DIMENSIONS		COMMENTS:	
MATERIAL			
FINISH			
DO NOT SCALE DRAWING			

CALTECH EDL		TITLE:	
		TUBE ASSY	
SIZE		DWG. NO.	REV
B		DDST_MA	
SCALE: 1:8		WEIGHT:	SHEET 1 OF 1



4 3 2 1

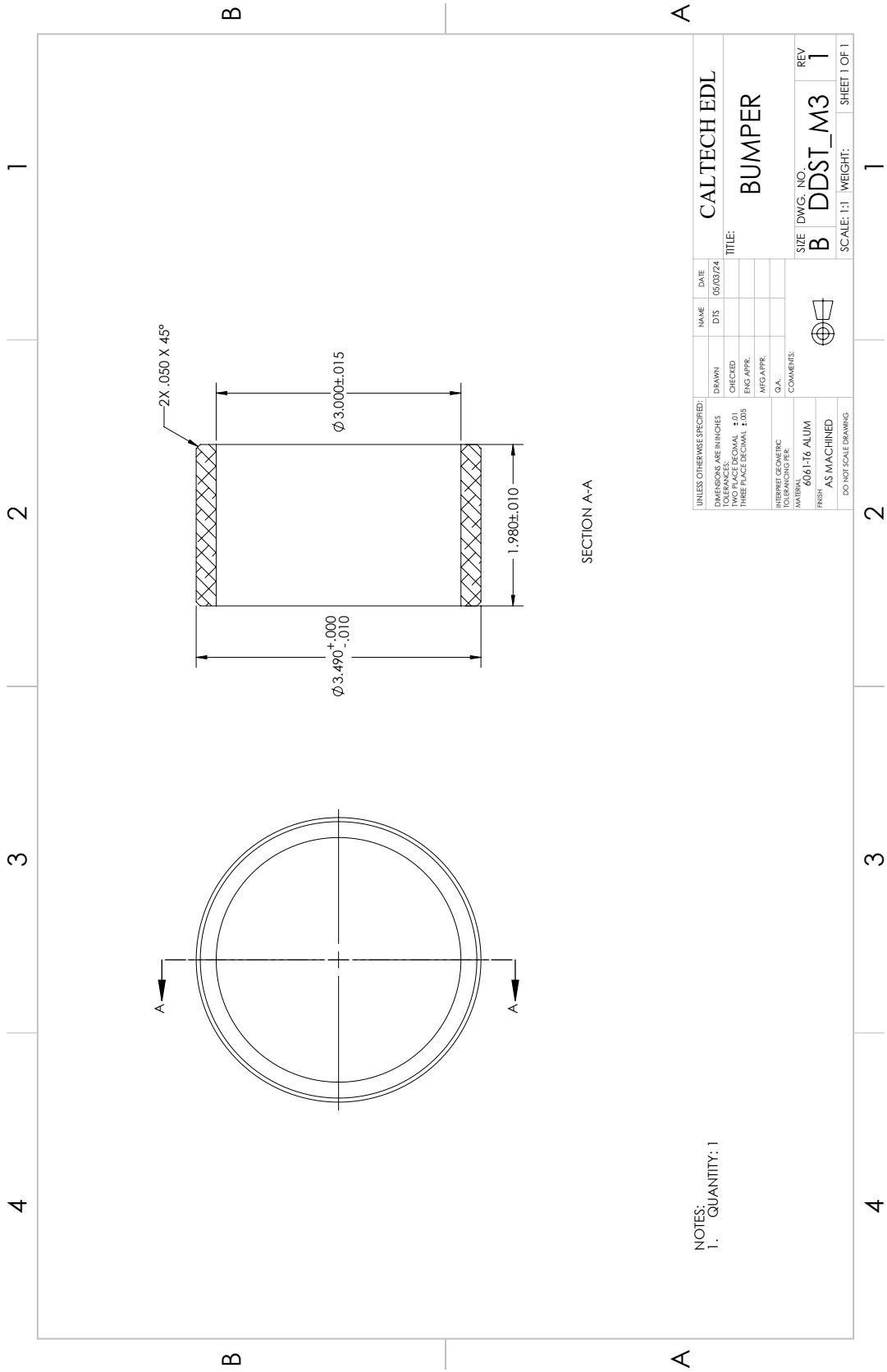


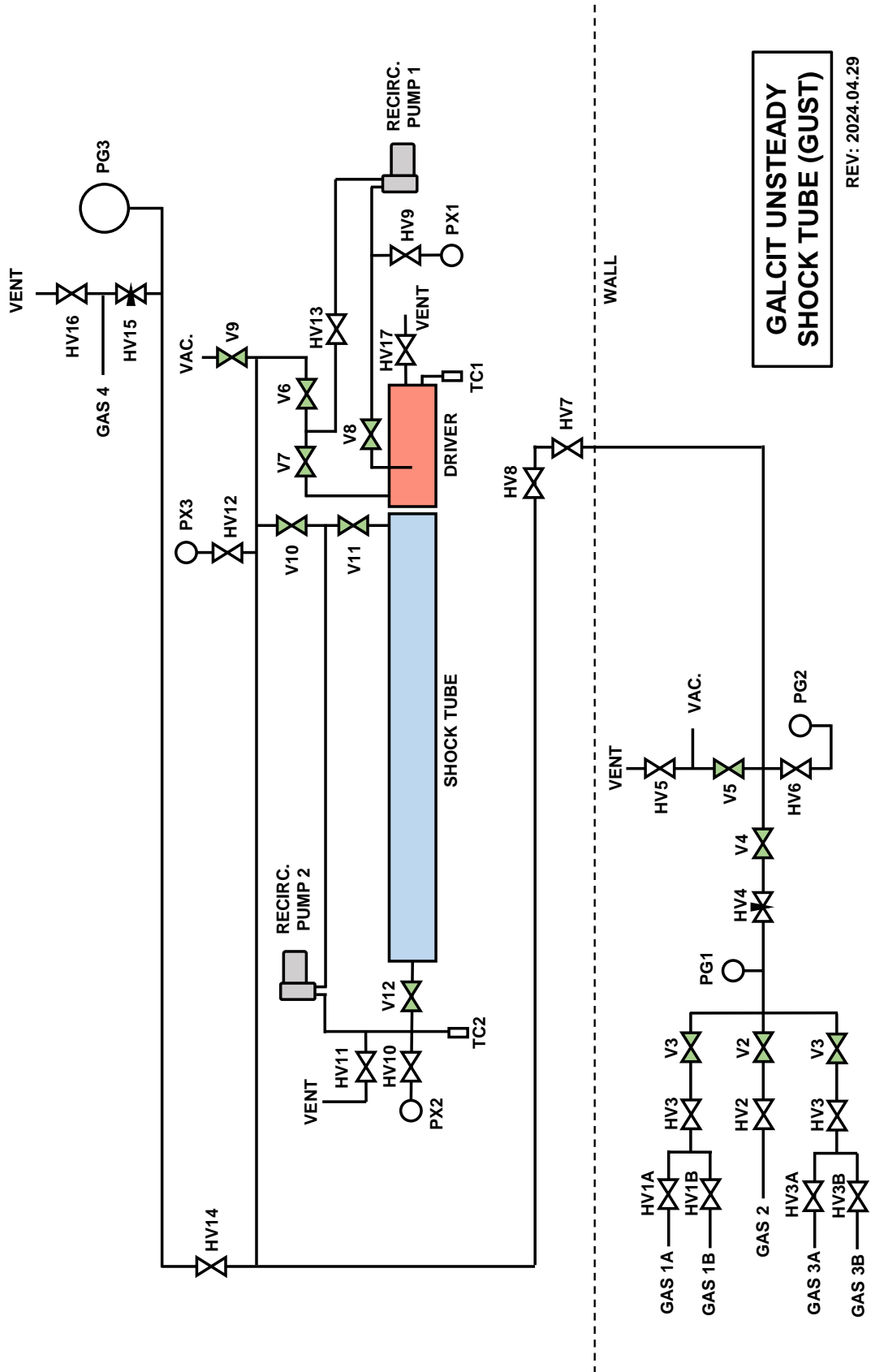
SECTION A-A

- NOTES:
1. 32 MICRO-INCH SURFACE FINISH APPLIES EVERYWHERE ON ID
  2. QUANTITY:

UNLESS OTHERWISE SPECIFIED:		NAME	DATE	CALTECH EDL	
DIMENSIONS ARE IN INCHES		DTS	05/02/24	TITLE:	
TOLERANCES:		DRAWN		OUTER TUBE	
FRACTIONS DECIMAL ±.01		CHECKED			
THREE PLACE DECIMAL ±.005		ENG APPR.			
		MFG APPR.			
		Q.A.			
INTERPRET GEOMETRIC TOLERANCES		COMMENTS:		SIZE	DWG. NO.
MATERIAL				B	DDST_M2
FINISH				REV	1
AS MACHINED				SCALE: 1:2	WEIGHT:
DO NOT SCALE DRAWING				1	SHEET 1 OF 1

4 3 2 1





**GALCIT UNSTEADY  
SHOCK TUBE (GUST)**

REV: 2024.04.29